Characterisation of porous materials for the adsorption of volatile organic compounds

By

Elwin Hunter Sellars

A dissertation submitted to Imperial College London for the degree of Doctor of Philosophy

Department of Materials
Imperial College London
Exhibition Road
London, UK
SW7 2AZ

August 2021

Declaration of Originality and Copyright

I hereby declare that this thesis and the work presented herein is entirely my own work. Any information presented and derived from the published and unpublished work of others, as well as any assistance received or collaborations undertaken, have been acknowledged in the text and references as given.

‘The copyright of this thesis rests with the author. Unless otherwise indicated, its contents are licensed under a Creative Commons Attribution-Non Commercial 4.0 International Licence (CC BY-NC). Under this licence, you may copy and redistribute the material in any medium or format. You may also create and distribute modified versions of the work. This is on the condition that: you credit the author and do not use it, or any derivative works, for a commercial purpose. When reusing or sharing this work, ensure you make the licence terms clear to others by naming the licence and linking to the licence text. Where a work has been adapted, you should indicate that the work has been changed and describe those changes. Please seek permission from the copyright holder for uses of this work that are not included in this licence or permitted under UK Copyright Law.

Elwin Hunter Sellars

August 2021

Acknowledgements

I want to thank my academic supervisors Daryl Williams and Ivan Parkin for all their help and guidance throughout the project, without which I'm sure I could not have succeeded. I also want to thank my industrial supervisor JJ Tee and the many team members from Procter & Gamble for keeping our work grounded and providing support and funding for the project. Thank you to Stephen Skinner and Neil Curson for giving me the opportunity to conduct research as part of the Centre for Doctoral Training in Advanced Characterisation of Materials, and the researchers and staff within the CDT who have organised so many training sessions, social events, and conferences to attend.

Thank you to everyone within the Surfaces and Particle Engineering Laboratory and at Surface Measurement Systems, not only for giving me advice and constructive criticism on my work and ideas, but also for keeping me sane with all the coffee breaks, picnics, and Christmas dinners that I will sorely miss. A special thank you to Paola for her help and support in designing and constructing the breakthrough curve analyser, and for being able to bend stainless steel piping without making it look 'avant garde'.

A PhD is a stressful undertaking, especially when it's interrupted by a worldwide pandemic and leaves your project's future, and so many others, uncertain. I want to thank my family and friends, particularly Kübra and Meghann, who encouraged me to keep going and see this work through. Most of all, thank you to my wonderful girlfriend Belle who made what would normally be an anxiety- and stress-filled period of my life a genuinely enjoyable experience.

Finally, I want to thank my granddad Bill and late grandma Sheila for supporting me in all my academic endeavours. They are both a huge part of the reason I pursued engineering and science in the first place, and I am certain I wouldn't be where I am now without them.

Abstract

Volatile organic compounds (VOCs) are a broad class of chemicals which, at elevated levels, can contribute negatively to the health and quality-of-life of affected individuals. Adsorption using porous materials a common method of reducing the levels of VOCs in indoor spaces. This work investigates the VOC adsorption performance of industrial and synthetic porous materials in real-world conditions via a comprehensive experimental study.

Adsorbent hydrophobicity is a key parameter when considering application in environments with high relative humidity. To illustrate the humidity-dependant nature of a material's adsorption hydrophobicity, single- and two-component gravimetric adsorption experiments were carried out. A new method of determining hydrophobicity indexes as a function of humidity was developed to illustrate the importance of the adsorption environment on selectivity, which correlated well with toluene adsorption following pre-exposure of humidity. To better understand the mechanism of competition occurring between water and toluene, a breakthrough analyser was designed and constructed. Fixed-bed measurements largely confirmed findings from gravimetric experiments, while revealing that displacement of toluene could occur in microporous adsorbents providing the critical pore filling pressure for water vapour was reached.

A single-step, modulator-based synthesis procedure was devised for ZIF-8/67 and MIL-100, producing millimetre-centimetre scale monoliths with enhanced density while still possessing the base MOF's physicochemical and morphological characteristics. ZIF monoliths demonstrated gravimetric VOC capture performances up to 217 and 232% higher than their powder counterparts at 0% and 80% RH respectively. These monoliths may be a promising technology for applications where volume is a critical consideration, such as packed-bed columns and air filtration.

A comprehensive evaluation of VOC adsorption behaviour as a function of relative humidity for a range of adsorbents is reported. These results aim to highlight the interplay between pore size, aperture chemistry, and selectivity in determining the effectiveness of adsorbents in real world VOC capture.

Table of Contents

Declaration of Originality and Copyright 2
Acknowledgements 3
Abstract 4
Table of Contents 5
List of peer-reviewed journal publications 14
Published work 14
In preparation/ submission/ review 15
Conference papers and oral presentations 16
List of figures 17
List of tables 29
Chapter 1: Introduction and Motivation 33
1.1. Motivation: Volatile organic compounds 33
1.2. Motivation: Malodour removal in consumer care products 36
1.3. Project aims and objectives 37
Chapter 2: Review of industrial and synthetic porous materials, their properties, and their role in gas and vapour adsorption applications 38
2.1. Principles of gas adsorption in porous materials 38
2.1.1. Fundamentals of adsorption and intermolecular interactions 38
2.1.2. Adsorption of gases via surface filling 42
2.1.2.1. Langmuir 42
2.1.2.2. Brunauer-Emmett-Teller 43
2.1.3. Polanyi potential theory of adsorption 44
2.1.3.1. Dubinin Radushkevich and Dubinin Astakhov 46
2.2. Defining and characterising porous materials 47
2.2.1. Surface area in porous materials 47
2.2.1.1. Specific surface area 47
2.2.1.2. External surface area 49
2.2.2. Types of porosity 51

2.2.2.1. Determining porosity by adsorption isotherm 52
2.2.2.2. Determining pore size distribution using adsorption models 55
2.2.3. Pore volume 56
2.2.3.1. Micropore volume determination 56
2.2.3.2. Mesopore volume determination 57
2.2.3.3. Total pore volume determination 57
2.3. Measuring adsorption performance 59
2.3.1. Equilibrium adsorption capacity 59
2.3.1.1. Gravimetric measurement 59
2.3.1.2. Volumetric measurement 61
2.3.1.3. Fixed bed adsorption methods 61
2.3.2. Adsorption kinetics and diffusion 65
2.3.2.1. Adsorption kinetics models 65
2.3.2.2. Diffusion analysis based on sorption uptake 67
2.3.2.3. Kinetic modelling in fixed-bed columns 70
2.3.3. Adsorption enthalpy 72
2.3.4. Selectivity 73
2.4. Industrial porous materials 76
2.4.1. Zeolite structure 76
2.4.1.1. Zeolite families 77
2.4.1.2. Silica: alumina ratio and its influence on zeolite chemistry and structure 78
2.4.2. Activated carbons 80
2.4.3. Porous silicas 81
2.5. Metal-organic frameworks 82
2.5.1. Structural flexibility 83
2.5.2. Zeolitic imidazolate frameworks 86
2.5.2.1. ZIF-8 87
2.5.3. Structured and monolithic MOFs 89
2.6. Adsorption of volatile organic compounds 91

2.6.1. Adsorption by zeolites 93
2.6.1.1. Impact of water vapour on adsorption in zeolites 96
2.6.2. Adsorption by activated carbons 99
2.6.2.1. Impact of water vapour on adsorption in activated carbons 101
2.6.3. Adsorption by porous silicas 104
2.6.3.1. Impact of water vapour on adsorption in porous silicas 104
2.6.4. Adsorption by metal-organic-frameworks 106
2.6.4.1. Impact of water vapour on adsorption by metal-organic frameworks 110
2.6.4.2. Adsorption by modified MOFs and composites 114
2.7. Conclusions 115
Chapter 3: Methodology 117
3.1. Materials, chemicals, and standard synthesis procedures 117
3.1.1. Materials 117
3.1.1.1. Industrial adsorbents 117
3.1.1.2. Solvents and synthesis reagents 118
3.1.2. Synthesis of metal-organic frameworks 119
3.1.2.1. Synthesis of powder ZIF-8 and ZIF-67 119
3.1.2.2. Synthesis of monolithic ZIF-8 and ZIF-67 119
3.1.2.3. Synthesis of powder and monolithic MIL-100 120
3.2. Physical and chemical material characterisation 120
3.2.1. X-ray diffraction 121
3.2.2. Thermogravimetric analysis 123
3.2.3. Fourier transform infrared spectroscopy 124
3.2.4. Gas and solid-medium pycnometry 124
3.2.5. Contact angle 127
3.2.6. Scanning electron microscopy 128
3.2.7. Low-temperature nitrogen sorption 130
3.2.7.1. Analysis of nitrogen sorption data 131
3.2.8. X-ray fluorescence 132

3.3. Measurement of material sorption properties using dynamic vapour sorption 133
3.3.1. Design of dynamic vapour sorption methods 135
3.3.1.1. Single-component isotherm method 136
3.3.1.2. Single-component cycling method 136
3.3.1.3. Two-component competitive adsorption method 137
3.3.2. Sample preparation for dynamic vapour sorption 138
3.3.3. Analysis of dynamic vapour sorption data 139
3.3.3.1. Humidity-dependant hydrophobicity indexes 139
3.4. Design and construction of bench-top breakthrough analyser 141
3.4.1. Construction materials 142
3.4.1.1. Building materials 142
3.4.1.2. Generation of concentration and temperature 143
3.4.1.3. Sensory components 143
3.4.1.4. Testing materials 143
3.4.2. Construction of the breakthrough analyser 144
3.4.2.1. Gas inlets 144
3.4.2.2. Mass flow controller manifold 144
3.4.2.3. Concentration generation 145
3.4.2.4. Packed-bed column and pre-heater 145
3.4.2.5. Sensory components 147
3.4.2.6. Photoionization detector 148
3.4.2.7. Experimental operation and controls 148
3.4.2.8. Operation of photoionisation detector 149
3.4.3. Leak tests 149
3.4.4. Sensor testing and calibration 149
3.4.4.1. Humidity sensor calibration 150
3.4.4.2. Photoionization detector (PID) calibration 150
3.4.5. Dead time determination 151
3.4.5.1. Dead time of humidity sensors 152

3.4.5.2. Dead time of PID 153
3.4.5.3. Comparisons between dead volume and sample volume 155
3.4.6. Testing of column pre-heater 156
3.4.7. Measurement of fixed bed pressure drop 157
3.4.8. Validation of adsorption capacity of porous materials 157
3.4.9. Generation of experimental breakthrough curve datasets 158
3.5. Dataset fitting, standard deviations, significance, and repeat measurements 159
3.5.1. Isotherm models 159
3.5.1.1. Langmuir 159
3.5.1.2. Freundlich 160
3.5.1.3. Combined Langmuir-Freundlich models 160
3.5.1.4. Brunauer-Emmett-Teller 162
3.5.1.5. Guggenheim-Anderson-de Boer 162
3.5.1.6. Dubinin Radushkevich and Dubinin Astakhov models 163
3.5.2. Fitting experimental adsorption kinetics 163
3.5.3. Fitting experimental breakthrough curves 164
3.5.3.1. Fitting adsorbate 'rollover' in competitive breakthrough curves 164
3.5.4. Methodology for fitting of experimental datasets 165
3.5.5. Standard deviation and repeat measurements 166
3.7. Conclusions 167
Chapter 4: Characterisation of porous materials for solvent vapour removal 168
4.1. Introduction 168
4.2. Results and discussion 169
4.2.1. X-ray diffraction 169
4.2.2. X-ray fluorescence 170
4.2.3. Fourier-transform infrared spectroscopy 171
4.2.4. Thermogravimetric analysis 173
4.2.5. Density of industrial adsorbents 173
4.2.6. Surface area and pore volume measurements 174

4.2.7. Advancing contact angles and surface hydrophobicity 177
4.2.8. Single-component vapour adsorption performance 178
4.2.8.1. Unusual isotherm of zeolite Y and polar adsorbates 181
4.2.8.2. Hydrophobicity indexes 182
4.2.9. Two-component vapour adsorption performance 185
4.2.9.1. Relationship between hydrophobicity indexes and two-component capacities 187
4.2.10: Cycling performance of adsorbents 188
4.2.10.1. Estimated productivity of toluene adsorption 190
4.2.12: Fitting of adsorption kinetics 191
4.2.12.1: Investigation of Simonin data range 191
4.2.12.2: Adsorption rate constant trends of adsorbent-adsorbate pairs 193
4.2.12.3: Impact of humidity on toluene adsorption kinetic rate constants 197
4.3. Conclusions 199
Chapter 5: Synthesis of metal-organic frameworks possessing hydrophobic apertures 201
5.1. Introduction 201
5.2. Experimental methods 202
5.2.1. Optimisation of ZIF-8 synthesis 202
5.2.2. Synthesis of MIL-100 202
5.3. Results and discussion 203
5.3.1. Synthesis of MOF powders 203
5.3.2. Initial screening of ZIF powders 204
5.3.2.1. Product yield 204
5.3.2.2. Product crystallinity 205
5.3.2.3. Adsorption performance for toluene vapour 206
5.3.2.4. Summary of screening of ZIF synthesis methods 207
5.3.3. Crystallinity and yield of MIL-100 powder 208
5.3.4. Influence of ZIF-8 reaction conditions on crystal size 208
5.3.5. Thermal stability of ZIF-8/67 and MIL-100 adsorbents 211
5.3.6. Surface area and pore volume of powder MOFs 211

5.3.6.1. Pore size distributions of powder MOFs 214
5.3.7. Adsorption of VOCs and water vapour by MOFs 217
5.3.7.1. Hydrophobicity indexes of MOF adsorbents 219
5.3.7.2. Influence of VOC diameter and crystal size on ZIF-8 adsorption kinetics 220
5.3.8. Impact of humidity on toluene adsorption by ZIF-8/67 and MIL-100 221
5.4. Conclusions 222
Chapter 6. Modulator-based synthesis of high-density monolithic MOF adsorbents 224
6.1. Introduction 224
6.2. Experimental methods 226
6.2.1. Hydrophobic modification of MIL-100 226
6.3. Results and discussion 226
6.3.1. Synthesis of monolithic MOFs 226
6.3.1.1. Monolithic ZIF-8 and ZIF-67 226
6.3.1.2. Monolithic MIL-100 228
6.3.1.3. Loading of acids on powder and monolithic MIL-100 229
6.3.2. Impact of monolith formation on crystallinity 229
6.3.2.1. Impact of acid modification on crystallinity 231
6.3.3. FTIR of monolithic MOFs 232
6.3.4. Thermogravimetric analysis of monolithic MOFs 233
6.3.5. Comparisons between powder and monolith density 235
6.3.6. Surface area and pore volume of ZIF and MIL monoliths 236
6.3.6.1. Pore size distributions of monolithic ZIFs 239
6.3.6.2. Impact of acid modification on surface area and pore volume of MIL-100 240
6.3.7. Scanning electron microscopy of monolithic MOFs 242
6.3.8. Advancing water contact angles of powder and monolithic MOFs 244
6.3.9. Single-component VOC adsorption by monolithic ZIFs 246
6.3.10. Single-component VOC adsorption by monolithic MIL-100 249
6.3.11. Comparing hydrophobicity indexes of powder and monolithic MOFs 250
6.3.11.1. Impact of acid modification on hydrophobicity indexes of MIL-100 252

6.3.12. Impact of humidity on toluene adsorption by monolithic MOFs 253
6.3.12.1. Impact of acid modification on humid toluene adsorption performance of MIL-100 256
6.3.13. Fitting of experimental adsorption kinetics 256
6.3.13.1. Impact of humidity on toluene kinetics 258
6.4. Conclusions 262
Chapter 7: Multicomponent fixed-bed adsorption of dilute VOCs on porous materials 264
7.1. Introduction 264
7.2. Results and discussion 266
7.2.1. Choice of flowrate for fixed-bed adsorption measurements 266
7.2.2. Dilute toluene adsorption by industrial porous materials 270
7.2.2.1. Impact of humidity on toluene adsorption by industrial porous materials 272
7.2.3. Dilute toluene adsorption by powder and monolithic ZIFs 277
7.2.3.1. Comparison of n-hexane and toluene breakthrough curves 279
7.2.3.2. Impact of humidity on toluene adsorption by ZIF adsorbents 281
7.2.4. Dilute toluene adsorption by MIL-100 284
7.2.4.1. Impact of humidity on toluene adsorption by MIL-100 286
7.2.5. Fitting of experimental breakthrough curves 289
7.2.5.1. Fitting of experimental BTCs for industrial adsorbents 289
7.2.5.2. Fitting of experimental BTCs for MOF adsorbents 292
7.4. Conclusions 296
Chapter 8: Conclusions and future work 300
8.1. Summary 300
8.1.1. Adsorption hydrophobicity 300
8.1.2. Monolithic metal-organic frameworks 302
8.1.3. Competitive adsorption of VOCs in humidified environments 303
8.2. Future work 304
8.2.1. Investigation of adsorption enthalpy and multi-temperature breakthrough curves 304
8.2.2. Effect of ZIF-8 pore expansion on toluene adsorption kinetics 305

8.2.3. Palladium-doped ZIF-8 monoliths 305
8.2.4. Photocatalytic oxidation of VOCs using breakthrough analyser 306
References 307
Appendix 346
Adsorption fitting parameters 369

List of peer-reviewed journal publications

Published work

Paola A. Sáenz Cavazos, Mariana L. Díaz-Ramirez, **Elwin Hunter-Sellars**, Sean R. McIntyre, Enrique Lima, Ilich A. Ibarra, Daryl R. Williams. *Fluorinated MIL-101 for carbon capture utilisation and storage: uptake and diffusion studies under relevant industrial conditions.* RSC Advances, 2021, 11, 13304-13310.

Elwin Hunter-Sellars, Paola A. Saenz-Cavazos, Anthony R. Houghton, Sean R. McIntyre, Ivan P. Parkin, and Daryl R. Williams. *Sol–Gel Synthesis of High-Density Zeolitic Imidazolate Framework Monoliths via Ligand Assisted Methods: Exceptional Porosity, Hydrophobicity, and Applications in Vapor Adsorption.* Advanced Functional Materials, 2021, 31 (5), 2008357-2008367. (Based on work in Chapter 6 and 8).

Mehzabin Patel, Anand N. P. Radhakrishnan, Ludovic Bescher, **Elwin Hunter-Sellars**, Benjamin Schmidt-Hansberg, Esther Amstad, Stuart Ibsen, Stefan Guldin. *Temperature-induced liquid crystal microdroplet formation in a partially miscible liquid mixture*. Soft Matter, 2021, 4, 947-954.

Elwin Hunter-Sellars, J.J. Tee, Ivan P. Parkin, Daryl R. Williams. *Adsorption of volatile organic compounds by industrial porous materials: Impact of relative humidity.* Microporous and Mesoporous Materials, 2020, 298, 10090-10098. (Based on work in Chapter 4)

Isabella del Gaudio, **Elwin Hunter-Sellars**, Ivan P. Parkin, Daryl Williams, Simoní Da Ros, Katherine Curran. *Water sorption and diffusion in cellulose acetate: the effect of plasticisers*. Carbohydrate Polymers, 2021, 267, 118185-118195.

In preparation/ submission/ review

Chunchun Ye; Anqi Wang, Rui Tan, C. Grazia Bezzu, **Elwin Hunter-Sellars**, Daryl R. Williams, Anthony Kucernak, Neil McKeown, Qilei Song. *Highly conductive and selective ion-exchange membranes from sulfonated polymers of intrinsic microporosity boost the performance of aqueous organic redox flow batteries*. Energy & Environmental Science. Under review.

Luqman Hakim Mohd Azmi, Pavani Cherukupally, **Elwin Hunter-Sellars**, Bradley P. Ladewig, Daryl R. Williams. *Polydimethyl siloxane/MIL-101 composites for real world enhanced VOC adsorption.* Submitted to Separation and Purification Technology

Elwin Hunter-Sellars, Paola A. Saenz-Cavazos, J.J. Tee, Ivan P. Parkin, Daryl R. Williams. *Impact of humidity on VOC filtration media, measured using fixed-bed adsorption.* Energy and Buildings, 2021, Special Issue: 'Resilient Ventilation Technologies for Building Energy Conservation'. Invited for submission, in preparation. (Based on work in Chapter 4 and Chapter 8)

Elwin Hunter-Sellars, Paola A. Saenz-Cavazos, Sean R. McIntyre, Ivan P. Parkin, Daryl R. Williams. *Dilute toluene adsorption by metal-organic-frameworks: influence of hydrophobic apertures on performance in humid conditions*. In preparation.

Sean R. McIntyre, **Elwin Hunter-Sellars**, Peter R. Haycock, Daryl R. Williams. *Determining Counter-diffusion Constants in Liquid Phase Catalytic Reactions using the Zero Length Column (ZLC) Method.* Submitted to ChemCatChem.

Sean R. McIntyre, **Elwin Hunter-Sellars**, Daryl R. Williams. *Novel zero-length column (ZLC) analysis of desorption curves for single cylindrical pellets.* In preparation.

Sean R. McIntyre, Paola A. Saenz-Cavazos, **Elwin Hunter-Sellars**, Daryl R. Williams. *The significance of diffusion control towards product selectivity in the transfer hydrogenation of levulinic acid by monolithic MOF and ZIF supports.* In preparation.

Conference papers and oral presentations

Elwin Hunter-Sellars, Paola A. Saenz-Cavazos, Luqman Hakim Mohd Azmi, Ivan P. Parkin, Daryl R. Williams. *Multicomponent adsorption of volatile organic compounds: gravimetric and spectrometric characterisation*. AIChE Annual Meeting. San Francisco, USA (Virtual due to COVID-19 pandemic). November 16th-20th 2020. Virtual oral and poster presentations.

Elwin Hunter-Sellars, Paola A. Saenz-Cavazos, Ivan P. Parkin, Daryl R. Williams. *Energy-efficient air filtration media for removal of volatile chemicals*. The 16th Conference of the International Society of Indoor Air Quality & Climate (Indoor Air 2020). Seoul, South Korea (Virtual due to COVID-19 pandemic). July 20th-24th 2020. Virtual oral presentation.

Elwin Hunter-Sellars, Paola A. Saenz-Cavazos, Ivan P. Parkin, Daryl R. Williams. *Monolithic ZIF-8/ ZIF-67 adsorbents for gas adsorption and air cleaning.* EuroMOF 2019. Paris, France. October 27th-30th 2019. Poster presentation.

Elwin Hunter-Sellars, Ivan P. Parkin, Daryl R. Williams. *Gravimetric and spectrometric methods of assessing VOC interactions for improved air quality.* International Societies of Exposure Science (ISES) and Indoor Air Quality and Climate (ISIAQ) Joint Conference 'The built, natural, and social environments: impacts on exposures, health and well-being'. Kaunas, Lithuania. August 18th-22nd 2019. Oral presentation.

Elwin Hunter-Sellars, Ivan P. Parkin, Daryl R. Williams. *Coadsorption and competitive sorption of water vapour and organic species in zeolite adsorbents.* 13th International Conference on the Fundamentals of Adsorption (FOA13). Cairns, Australia. May 27th-31st 2019. Oral presentation.

Elwin Hunter-Sellars, Meishan Guo, Lulu Cao, Naima Ali, Daryl R, Williams. *Adsorption Interactions between Volatile Organic Compounds and Natural and Synthetic Fibres: Impact of Relative Humidity.* 8th Pacific Basin Conference on Adsorption Science and Technology (PBAST-8). Sapporo, Japan. September 3rd-6th 2018. Oral presentation.

List of figures

Figure 1.1: Number of publications associating VOCs with environment (left) and VOCs with health (right), illustrating the growing focus on volatile chemicals. Reproduced from Pubmed on 17th May 2021.

Figure 1.2: Methods of VOC removal, reproduced from a review by Khan & Ghoshal [10] with permission.

Figure 2.1: Illustration of Keesom forces (left), Debye forces (middle), and London forces (right) between molecules with different bonding chemistries. Adapted from work by Leite et al [18] under Creative Commons licensing.

Figure 2.2: Approximate schematic model for a region of a pore, showing equipotential surfaces corresponding to successively lower adsorption potentials with increasing pore size. Condensation of the vapour occurs wherever the adsorption potential required to concentrate it to saturation, i.e. its vapour pressure, is equalled or exceeded. Reproduced from the book 'Partition and Adsorption of Organic Contaminants in Environmental Systems' by Cary T. Chiou [26], with permission.

Figure 2.3: Illustration of effect of internal pores on available surface area, made up of three regions: solid material (black), pores and gaps (white), area for potential adsorption sites (blue).

Figure 2.4: t-plot method for nitrogen adsorption data collected at -196˚C for microporous FAU zeolite (left) and mesoporous MCM-41 (right). Blue and red lines correspond to adsorption regimes at low and high pressures respectively. Reproduced from work by Galarneau et al [46] with permission.

Figure 2.5: Effect of pore diameter on diffusivity and diffusion activation energy, showing different diffusion regimes, reproduced from work by Ruthven et al [55] with permission.

Figure 2.6: Illustration of adsorption isotherm types, reproduced from IUPAC Technical Report [40].

Figure 2.7: Theoretical argon isotherms based on DFT (left) and BJH (right) models, using a variety of assumed pore sizes. Note the increasing unusual isotherm shape in the BJH plot with decreasing pore size. Reproduced from a whitepaper published by Micromeritics [60], with permission.

Figure 2.8: Application ranges of different pore size distribution determination techniques- specifically gas adsorption, mercury porosimetry, and water retention. Reproduced from a similar figure in Encyclopedia of Agrophysics [69].

Figure 2.9: Schematic of symmetric gravimetric adsorption apparatus incorporating a recording microbalance connected to both a sample pan and reference pan to register changes in mass of a sample after exposure to a vapour or gas (blue arrow).

Figure 2.10: Illustration of concentration profiles (C/C0) of adsorbate along the length of the packed bed (L/LTotal) at different time stages (t1-t4). The light and dark grey regions represent unsaturated and saturated adsorbent regions in the column respectively [75].

Figure 2.11: Illustration of breakthrough curve. Times t¬B and tE¬ show the breakthrough and equilibration times for the adsorbent bed, respectively. The dotted line at C/C¬inlet = 0.9 shows the 'operating limit' of the column [76], and the line at C/Cinlet = 1 is the species concentration in the inlet to the column.

Figure 2.12: Illustration of bias towards pseudo second order model: example kinetic dataset (top); fitting using pseudo first order model (left); fitting using pseudo second order model (right), and naturally alignment of close-to equilibrium data and t/q(t) term of PSO (red region). Reproduced from work by Simonin [88] with permission.

Figure 2.13: Illustration of diffusivities in adsorbent pellets composed of individual crystals, reproduced from work by Douglas M. Ruthven [55], with permission.

Figure 2.14: Example breakthrough curves plotted using simplified (left) and full (right) mathematical expressions of breakthrough models, equations 2.31 and 2.32 respectively.

Figure 2.15: Illustration of the temperature dependence of the required pressure to reach a fixed adsorption capacity. Reproduced from the book 'Partition and Adsorption of Organic Contaminants in Environmental Systems' by Cary T. Chiou [26], with permission.

Figure 2.16: Illustration of adsorption competition on a hydrophilic surface: displacement of adsorbed benzene molecules by water molecules (top); and inability of benzene molecules to displace adsorbed water molecules (bottom).

Figure 2.17: Multicomponent breakthrough curves of hexane isomers on zeolite beta pellets, reproduced from work by Bárcia et al [78], with permission.

Figure 2.18: Examples of zeolite structure: (a) primary and (b) secondary building units (SBUs), the latter showing 4- and 6-ring; (c) 3-dimensional sodalite building units; and (d) 3-dimensional A-type (bottom) and sodalite (top) zeolite cages.

Figure 2.19: Zeolite framework structures, showing metal positions and bridges of LTA (left), FAU (middle), and MFI (right). Collected from the IZA-Structure Database of Zeolite Structures [115], with permission.

Figure 2.20: Schematic showing mechanism of mesopore formation during dealumination, reproduced from work by Silaghi et al [44] with permission. The terms ASA and EFAL refer to 'amorphous silica-alumina' and 'extra-framework aluminium' respectively.

Figure 2.21: Schematic of charcoal activation using both chemical and gasification methods, reproduced from work by Li et al [129] under Creative Commons licensing.

Figure 2.22: Illustration of silica xero- and aero-gel formation from a sol-gel solution, reproduced from work by Buckley and Greenblatt [132] with permission.

Figure 2.23: Number of publications using the term 'Metal-organic framework', found using Pubmed. Date of search: 17th May 2021.

Figure 2.24: Mechanisms of framework flexibility due to inclusion or displacement of guest molecules, reproduced from work by Schneemann et al [139] under Creative Commons licensing.

Figure 2.25: Illustration of the bridging angle in zeolites (left), sodalite-like ZIF-8 (middle), and RHO-like ZIF-11 (right), the latter two synthesised using 2-methylimidazole and benzimidazole, respectively. Adapted from work by Wang et al [144] with permission.

Figure 2.26: Examples of imidazolate linkers used in the synthesis of zeolitic imidazole frameworks

Figure 2.27: Schematic of ZIF-8 flexibility via linker rotation (left) and shift in low-angle XRD peak (right) upon exposure to bulky molecule. Reproduced from work by Ueda et al [151] under Creative Commons licensing.

Figure 2.28: Strategies for producing monolithic MOF composites through depositing on monolithic supports (a) and extrusion of composites consisting of active MOF materials and binder. Reproduced from work by Hou et al [159] under Creative Commons licensing.

Figure 2.29: Examples of functional groups and subsequent bonding and interaction types in VOCs with multiple chemistries, in this example ortho-cresol.

Figure 2.30: Isotherms of the four most common behaviours of hydrophilic/ hydrophobic adsorbents, assuming the materials have similar pore volumes and surface areas.

Figure 2.31: Illustration of molecular sieving of benzene by smaller pore zeolite LTA 4A compared to molecular sieve 13X.

Figure 2.32: Adsorption of vapours onto high-silica zeolite Y (top), and mass dispersion maps of methanol vapour on/ in the surface and pores of the hydrophobic zeolite at a concentration below (left) and above (right) the Type V inflection point. Reproduced from work by Halasz et al [172] with permission.

Figure 2.33: Breakthrough curves of toluene and water vapour, exposed to adsorbents HiSiv1000 (left) and zeolite 13X (right) simultaneously. Note the outlet toluene flux exceeding the inlet flux in the zeolite 13X system due to displacement of toluene molecules by water. Reproduced from work by Kraus et al [177] with permission.

Figure 2.34: Experimental and modelled breakthrough curves of a mixture of VOCs in a column of activated carbon. Reproduced from work by Tefera et al [179] with permission.

Figure 2.35: Summary of adsorption capacities of toluene (TOL) and benzene (BNZ) vapours onto activated charcoal at a wide range of concentrations (top), and a focus towards lower concentrations

(bottom). Legend format: reference-relative humidity of measurement- material- vapour; GAS- granular activated carbon; ACF- activated carbon fibre; ACM- activated carbon monolith; N/A- relative humidity not reported in reference. Reproduced from work by Pei & Zhang [189] with permission.

Figure 2.36: Breakthrough curves of toluene vapour on silica and carbon adsorbents, carried out at relative humidities of 80 % (left) and 0 % (left). Reproduced from work by Lu et al [199] with permission.

Figure 2.37: Sizes of small cages (a), large cages (b), and pentagonal and hexagonal windows in MIL-100 and MIL-101. Reproduced from work by Trung et al [201] with permission.

Figure 2.38: Vapour isotherms of n-pentane and n-heptane in MIL-100 (left) and MIL-101 (right), measured at 303 K. Reproduced from work by Trung et al [201] with permission.

Figure 2.39: Stepped isotherms of high-silica zeolite Y (left), MIL-100 (Fe) (right), and ZIF-8 (bottom) when exposed to methanol vapour, showing hydrophobic screening effect. Reproduced from work by Halasz et al [172], Iacomi et al [203], and Zhang et al [207], with permission.

Figure 2.40: Theoretical degradation mechanisms of Cu3(BTC)2, HKUST-1, by ligand displacement or hydrolysis in the presence of water. Reproduced from work by Xue et al [209] with permission.

Figure 3.1: Illustration of X-ray diffraction in a crystalline material. Blue circles and black lines represent atoms and X-rays respectively. The left image represents an incidence angle resulting in constructive interference of diffractive X-rays, while the right image shows destructive interference of diffractive X-rays. Reproduced from Wikipedia [223] under Creative Commons licensing.

Figure 3.2: Powder X-ray diffraction spectra for TiO2 nanoparticles (1, 2, and 3) alongside characteristic peaks for rutile- and anatase-phase TiO2. Reproduced from work by Wang et al [225] through Creative Commons licensing.

Figure 3.3: Schematic of gas pycnometry equipment, including chambers, valves and pressure gauge.

Figure 3.4: Schematic of bulk density measurement using dry flow medium. Points A and B represent the plunger position without (top) and with (bottom) the addition of sample respectively.

Figure 3.5: Illustration of water contact angles on more (left) and less (right) hydrophobic solid surfaces.

Figure 3.6: Illustration of back scattering analysis of samples: SEM images of sample containing aluminium and copper (a); schematics for scattering potential of larger Cu atoms (b), and smaller Al atoms (c). Reproduced from whitepaper article by AZO Materials and Thermo Fisher Scientific [230] with permission.

Figure 3.7: Linear fits of BET plots for activated charcoal, using the Rouquerol (top) and standard BET (bottom) partial pressure ranges. Note the negative intercept when fitting the standard BET range.

Figure 3.8: Kinetic mass profile (top) and corresponding sorption isotherm (bottom) of water vapour interacting with zeolite Y, measured using DVS Endeavour at 25˚C.

Figure 3.9: Mass profiles of zeolite Y in a two-component adsorption experiment, in which the sample is pre-exposed to water vapour following an initial drying step, and then exposed to a step change in toluene vapour concentration. Q represents the adsorption capacity of the material for a particular adsorbate. Measurement carried out using DVS Endeavour, T = 25˚C.

Figure 3.10: Schematic for breakthrough curve analyser, including: mass flow controller manifold and bubbling unit (generation); adsorption column with heating jacket (adsorption); and relative humidity (RH), pressure (P), and photoionisation detector (PID) sensors (detection).

Figure 3.11: Schematic of mass flow controller manifold. Solid black lines show gas flow between inlet and outlet valves. Coloured boxes and dotted lines show dependence links between MFCs (e.g. Dry B and Wet B, red, have flowrates and control systems dependant on one other).

Figure 3.12: Simplified schematic of pre-heater setup for fixed-bed sample analysis column.

Figure 3.13: Photograph of the sensory housing unit. Connections from top clockwise: gas inlet; gas outlet; CO2 probe; and combined temperature and humidity probe.

Figure 3.14: Photograph of integration board (left), sensor control board (middle), and photoionization detector (right).

Figure 3.15: Target and actual toluene concentrations in the breakthrough analyser over two cycles, as a function of time for cycle 1 (left) and cycle 2 (right). Experiments were carried out at T = 25˚C and a total flowrate through the column of 100 mL/min.

Figure 3.16: Target and actual relative humidities measured by the pre-column humidity sensor for flowrates between 20-80 mL/min. Right plot shows close-up of 0-40 % RH step. T = 25˚C.

Figure 3.17: Target and actual toluene concentrations measured by the photoionization detector for flowrates between 20-80 mL/min. Right plot shows close-up of 5ppmv step. T = 25˚C.

Figure 3.18: Breakthrough curve of water vapour on MS13X, carried out at a flowrate of 10 mL/min, relative humidity of 49.5 % and a temperature of 25˚C.

Figure 3.19: Illustration of constants for the Boltzmann (a) and EMG (b) equations, reproduced from work by Shu-Jiang et al [259] with permission.

Figure 4.1: X-ray diffraction patterns for industrial adsorbents: molecular sieve 13X, MS13X; zeolite Y, A88Y; ZSM-5 zeolite, A14Z; activated charcoal, AC; amorphous silica, AS.

Figure 4.2: FTIR spectra for industrial adsorbents, in wavenumber ranges of 650-1450 cm-1 (left), and 650-4000 cm-1 (right). Inset graph shows zeolite samples in 3620-3690 cm-1 region. AC not shown on left graph due to broad peaks and to improve clarity.

Figure 4.3: Nitrogen isotherms for adsorbent samples: activated charcoal, AC; amorphous silica, AS; molecular sieve 13X, MS13X; zeolite Y, A88Y; ZSM-5 zeolite, A14Z. Solid and dashed lines correspond to adsorption and desorption points respectively. T = -196˚C.

Figure 4.4: Advancing contact angles: activated charcoal, AC (left); and ground zeolite Y, A88Y (right)

Figure 4.5: Vapour adsorption isotherms of water (a), toluene (b), n-hexane (c), ethanol (d), 2-propanol (e), and 2-butanone (f). Adsorbents studied: activated charcoal, AC; amorphous silica, AS; molecular sieve 13X, MS13X; zeolite Y, A88Y; ZSM-5 zeolite, A14Z. T = 25˚C.

Figure 4.6: Isotherms of polar and non-polar vapours on high-silica zeolite Y, A88Y. T = 25˚C.

Figure 4.7: Molar hydrophobicity indexes (H.I.s) calculated as a function of RH for adsorbent samples: activated charcoal, AC; amorphous silica, AS; molecular sieve 13X, MS13X; zeolite Y, A88Y; ZSM-5 zeolite, A14Z. (P/P0)toluene = 0.005, T = 25˚C.

Figure 4.8: Two-component adsorption capacities of toluene (top) and ethanol (bottom) after pre-exposure to different levels of RH. Adsorbent samples studied: activated charcoal, AC; amorphous silica, AS; molecular sieve 13X, MS13X; zeolite Y, A88Y; ZSM-5 zeolite, A14Z. T = 25˚C.

Figure 4.9: Relationship between hydrophobicity indexes and relative toluene capacities, measured using single- and two- component adsorption data respectively. Adsorbent samples studied: activated charcoal, AC; amorphous silica, AS; molecular sieve 13X, MS13X; zeolite Y, A88Y; ZSM-5 zeolite, A14Z. T = 25˚C.

Figure 4.10: Quantities of toluene adsorbed as a function of cycle number, under dry (left) and humid (right) conditions. Samples studied: activated charcoal, AC; amorphous silica, AS; molecular sieve 13X, MS13X; zeolite Y, A88Y; ZSM-5 zeolite, A14Z. Partial pressure of toluene in all cycling experiments, P/P0 = 0.005. RH in humid experiments = 50 %. Desorption carried out under 200 mL/min of dry air flow, T = 25˚C.

Figure 4.11: Toluene adsorption kinetics curve for AC, showing Simonin uptake limit, and linear fitting of kinetics data within this range of 0-0.85 qmax. P/P0,TOL = 0.005, T = 25˚C.

Figure 4.12: Ethanol uptake profiles by zeolite Y (A88Y), highlighting two mechanisms of adsorption occurring at two different partial pressures- surface filling (a) and micropore filling (b).

Figure 4.13: PFO adsorption rate constants for water adsorption as a function of relative humidity, for all industrial adsorbents studied. Kinetic model fitting in the uptake range of 0-1 qmax. T = 25˚C. Calculated error for parameters smaller than symbols.

Figure 4.14: PFO adsorption rate constants (left) and the kinetic productivities (right) for toluene adsorption as a function of pre-exposure relative humidity, for all industrial adsorbents studied. Kinetic model fitting in the uptake range of 0-1 qmax. T = 25˚C.

Figure 5.1: ZIF-8 (left) and ZIF-67 (middle) and MIL-100 (right) powders following cleaning, centrifuging and drying.

Figure 5.2: PXRD patterns for ZIFs synthesised under different salt and solvent conditions (left) and synthesised using different molar ratios of zinc nitrate and 2-methylimidazole (right).

Figure 5.3: Scanning electron microscopy images collected for ZIF samples: zinc: linker ratios of 1:4 (a), 1:6 (b), 1:8 (c); zinc acetate (d) and bromide (e) salts; and ZIF-67 using cobalt nitrate (f).

Figure 5.4: Nitrogen sorption isotherms for MOF adsorbents: ZIF-8, synthesised using a metal: linker ratio of 1:8 and zinc nitrate as the metal source (top); and MIL-100 (bottom). T = -196˚C.

Figure 5.5: Comparison of Tarazona NLDFT and Horvath-Kawazoe models, both assuming cylindrical pore geometry, in predicting the pore size distribution of ZIF-8 synthesised using zinc nitrate and a metal: linker ratio of 1:8. Calculated using nitrogen sorption data at T = 196˚C.

Figure 5.6: Pore size distributions of powder ZIF-8 (top) and MIL-100 (bottom), calculated using Tarazona NLDFT model assuming cylindrical pore geometry, using nitrogen sorption data at T = 196˚C.

Figure 5.7: Water (left) and toluene (right) adsorption isotherms for ZIF-8 and MIL-100. T = 25˚C.

Figure 5.8: Molar hydrophobicity indexes (H.I.s) calculated as a function of RH for ZIF-8, synthesised using zinc nitrate and a metal: linker ratio of 1:8, and MIL-100. Plots for zeolite Y and activated charcoal shown for comparison. (P/P0)toluene = 0.005, T = 25˚C.

Figure 5.9: Adsorption kinetics curves for toluene and n-hexane vapour on ZIF-8 (1:8). Partial pressure of vapour in all experiments is P/P0 = 0.005. T = 25˚C.

Figure 5.10: Toluene adsorption capacities for ZIF-8 and MIL-100 as a function of pre-exposure relative humidity. P/P0, toluene = 0.005, T = 25˚C.

Figure 6.1: State of ZIF-8 synthesis at different time periods without (left) and with (right) addition of n-butylamine. All reactions carried out in a fume hood at room temperature.

Figure 6.2: Photographs of ZIF-8 (NB-1) (left) and ZIF-67 (NB-1) (right) monoliths. British 20 pence coin shown for scale.

Figure 6.3: Photograph of MIL-100 (NB) monolith. British 20 pence coin shown for scale.

Figure 6.4: Photograph of MIL-100 powders: unmodified (left); DPA-modified (middle); and OPA-modified (right).

Figure 6.5: PXRD patterns for zinc- (left) and cobalt- (right) based ZIFs synthesised using different types and amounts of modulating ligands.

Figure 6.6: PXRD patterns for unmodified and acid-modified MIL-100 powders (left) and monoliths (right) formed using n-butylamine as a modulating ligand.

Figure 6.7: FTIR spectra for powder (left) and monolithic (right) MIL-100 samples

Figure 6.8: Thermogravimetry profiles for powder (left) and monolithic (right) MIL-100 in N2.

Figure 6.9: Nitrogen adsorption isotherms for ZIF (left) and MIL (right) powder and monolithic adsorbents. T = -196˚C.

Figure 6.10: Pore size distributions of zinc (left) and cobalt (right) ZIFs, calculated using Tarazona NLDFT model assuming cylindrical pore geometry, using nitrogen sorption data at T = 196˚C.

Figure 6.11: Nitrogen adsorption isotherms for modified powder (left) and monolithic (right) MIL-100 adsorbents. T = -196˚C.

Figure 6.12: Pore size distributions of powder (left) and monolithic (right) MIL-100 with and without acid modification, calculated using Tarazona NLDFT model assuming cylindrical pore geometry, using nitrogen sorption data at T = 196˚C.

Figure 6.13: Scanning electron microscopy images of ZIF monoliths, including scale bars.

Figure 6.14: Scanning electron microscopy of MIL-100 powder (left) and monolith (right).

Figure 6.15: Advancing contact angles of ZIF samples: ZIF-8, (a); ZIF-8 (NB-1), (b); ZIF-8 (ML), (c); ZIF-67, (d); ZIF-67 (NB-1), (e); ZIF-67 (ML), (f). N = 5.

Figure 6.16: Advancing contact angles of MIL-100 samples: MIL-100, (a); MIL-100/ DPA, (b); MIL-100/ OPA, (c); MIL-100 (NB), (d); MIL-100 (NB)/ DPA, (e); MIL-100 (NB)/ OPA, (f).

Figure 6.17: Vapour adsorption isotherms for zinc (left) and cobalt (right) ZIF samples. From top to bottom, vapours studied are water, toluene, and methanol. All measurements carried out at 25ºC.

Figure 6.18: Vapour adsorption isotherms for powder (left) and monolithic (right) MIL-100 samples. Vapours studied are toluene (top) and water (bottom). All measurements carried out at 25ºC.

Figure 6.19: Molar hydrophobicity indexes for powder and monolithic MOFs, including industrial adsorbents for comparison. All measurements carried out at 25ºC.

Figure 6.20: Molar hydrophobicity indexes for acid modified MIL-100 in powder and monolithic form. All measurements carried out at 25ºC.

Figure 6.21: Adsorption of toluene vapour following pre-exposure of water vapour at different humidity levels for MOF adsorbents, expressed in mass- (top) and volume- (bottom) relative terms. Partial pressure of toluene in all experiments, P/P0 = 0.005. T = 25˚C.

Figure 6.22: Impact of water vapour pre-exposure on pseudo-first order model kinetic parameters (left) and kinetic productivities (right) for toluene adsorption. T = 25˚C, P/P0, toluene = 0.005.

Figure 7.1: Breakthrough curves of water vapour on molecular sieve 13X using carrier gas flowrates of 10 and 30 mL/min. T = 25˚C. Left plot uses standard time axis, right plot normalises axis by flowrate.

Figure 7.2: Breakthrough curves of 10 ppmv toluene vapour on molecular sieve 13X using carrier gas flowrates of 40, 60, and 80 mL/min. T = 25˚C. Left plot uses standard time axis, right plot normalises axis by flowrate.

Figure 7.3: Toluene breakthrough curves for industrial adsorbents. Gas flowrate = 60 mL/min. Cin = 10 ppmv, T = 25˚C.

Figure 7.4: Multicomponent breakthrough curves for toluene and water vapour on granular activated charcoal, at concentrations of 10 ppmv and 40 % (a) or 80 % (b) RH. A combined plot of the three toluene vapour breakthrough curves (c) is shown for comparison. Flowrate = 60 mL/min, T = 25˚C.

Figure 7.5: Multicomponent breakthrough curves for toluene and water vapour on zeolite Y, at concentrations of 10 ppmv and 40 % (a) or 80 % (b) RH. A combined plot of the three toluene vapour breakthrough curves (c) is shown for comparison. Flowrate = 60 mL/min, T = 25˚C.

Figure 7.6: Multicomponent breakthrough curves for toluene and water vapour on molecular sieve 13X, at concentrations of 10 ppmv and 40 % RH (left). A combined plot of the toluene vapour breakthrough curves (right) is shown for comparison. Flowrate = 60 mL/min, T = 25˚C.

Figure 7.7: Toluene breakthrough curves for zinc (left) and cobalt (right) ZIF adsorbents at 10 ppmv. Flowrate = 60 mL/min, T = 25˚C.

Figure 7.8: Breakthrough curves for toluene and n-hexane on ZIF-8 powder, carried out in separate single-component experiments at 10 ppmv. Flowrate = 60 mL/min, T = 25˚C.

Figure 7.9: Multicomponent breakthrough curves for toluene and water vapour on ZIF-8 powder, at concentrations of 10 ppmv and 40 % or 80 % RH. Flowrate = 60 mL/min, T = 25˚C.

Figure 7.10: Multicomponent breakthrough curves for toluene and water vapour on ZIF-8 (NB-1) (left) and ZIF-67 (ML) (right), at a toluene concentration of 10 ppmv and 0 and 80 % RH. Flowrate = 60 mL/min. Cin = 10 ppmv, T = 25˚C.

Figure 7.11: Toluene breakthrough curves for MIL-100 powder at 10 ppmv. Flowrate = 60 mL/min, T = 25˚C.

Figure 7.12: Multicomponent breakthrough curves for toluene and water vapour on MIL-100, at concentrations of 10 ppmv and 20 % (a), 40 % (b), and 80 % (c) RH. A combined plot of the four toluene vapour breakthrough curves (d) is shown for comparison. Flowrate = 60 mL/min. T = 25˚C.

Figure 7.13: Comparison of experimental and fitted water BTCs for GAC at 40 % (left) and 80 % (right) relative humidity. Fitting carried out using Bohart-Adams Logistic model. Flowrate = 60 mL/min. T= 25˚C.

Figure 7.14: Comparison of experimental and fitted toluene BTCs for zeolite Y at 80 % RH (left) and MS13X at 40 % RH (right). Fitting carried out using Bohart-Adams Logistic and Boltzmann-EMG models. Flowrate = 60 mL/min. T= 25˚C.

Figure 7.15: Comparison of experimental and fitted BTCs for toluene (left) and n-hexane (right) on ZIF-8 powder at 0 % RH. Shaded region on toluene curve indicates 'lost' capacity due to traditional breakthrough curve symmetry. Fitting carried out using Bohart-Adams Logistic model. Flowrate = 60 mL/min. T= 25˚C.

Figure 7.16: Comparison of experimental and fitted water (left) and toluene (right) BTCs for MIL-100 at 40 % RH. Fitting carried out using Bohart-Adams Logistic and Boltzmann-EMG models. Flowrate = 60 mL/min. T= 25˚C.

Figure 7.17: Fixed-bed total and useable toluene capacities expressed in volume-relative terms, measured at 10 ppmv and an RH equal to the bracket, between 0-80 %. T = 25˚C.

List of tables

Table 1.1: Typical VOCs and levels present in different industrial and indoor environmental spaces.

Table 3.1: Summary of literature methods for determining adsorbent hydrophobicity.

Table 3.2: Dead times of pre- and post-column humidity sensors, measured at relative humidities between 10-40 % RH, and carrier gas flowrates between 20-80 mL/min. T =25˚C.

Table 3.3: Dead times of PID sensor, measured at toluene concentrations between 5-50 ppmv, and carrier gas flowrates between 20-80 mL/min. T =25˚C.

Table 3.4: Measured pressure drop for adsorbent beds during dynamic breakthrough adsorption experiments, measured at two different gas flowrates. Temperature in all experiments was 25ºC. Adsorbent bed length and diameter were 2 cm and 0.4 cm respectively.

Table 4.1: Metal compositions of adsorbents: molecular sieve 13X, MS13X; zeolite Y, A88Y; ZSM-5 zeolite, A14Z; activated charcoal, AC; amorphous silica, AS. Measured by X-ray fluorescence.

Table 4.2: BET surface areas, micropore volumes, and total pore volumes of industrial adsorbents, determined using N2 gas adsorption data at -196ºC.

Table 4.3: Comparison of experimental and literature values for surface area, micropore, and total pore volumes of adsorbents. Standard deviations for values in this work can be found in Table 4.2.

Table 4.4: Summary of literature comparisons for single-component water and toluene capacities of adsorbents.

Table 4.5: Metrics of hydrophobicity for industrial porous materials. Water capacities and hydrophobicity indexes calculated using an RH of 70 %. T = 25˚C.

Table 4.6: Toluene adsorption capacities and estimated productivities of adsorbents during the 4th performance cycle in dry and humid conditions. All experiments carried out using a toluene partial pressure of 0.005, humid experiments used 50 % RH for both pre-exposure and regeneration.

Table 4.7: Summary of pseudo first order kinetic rate constants for each adsorbent for different VOC molecules and water vapour. T = 25˚C. Red numbers indicate fits that did not converge.

Table 5.1: Summary of ZIF synthesis conditions, all carried out at room temperature.

Table 5.2: Summary of yield, crystallinity, and toluene capacities for synthesised ZIF samples

Table 5.3: BET surface areas, micropore volumes, and total pore volumes of ZIF adsorbents, determined using N2 gas adsorption data at -196ºC.

Table 6.1: Bulk densities, surface areas, and porosities of powder and monolithic adsorbents, determined using dry medium displacement at 25˚C, and nitrogen sorption at -196˚C respectively.

Table 6.2: Densities, surface areas, and porosities of MIL-100 adsorbents, determined using dry medium displacement at 25˚C, and nitrogen sorption at -196˚C.

Table 6.3: Dry and humid capacities for toluene at a partial pressure of 0.005, expressed in volume-relative terms, for MOF adsorbents, with zeolite Y and activated charcoal shown for comparison. T = 25˚C.

Table 6.4: Summary of pseudo first order kinetic rate constants for each adsorbent for different VOC molecules and water vapour. T = 25˚C. Red numbers indicate fits that did not converge.

Table 6.5: Summary of pseudo first order kinetic rate constants for all microporous MIL-100 adsorbents for toluene and water vapour. T = 25˚C.

Table 7.1: Impact of carrier gas flowrate on breakthrough time and capacities of molecular sieve 13X when exposed to water vapour or toluene at fixed concentrations. T = 25˚C.

Table 7.2: Fixed-bed toluene capacities for industrial materials. Flowrate in all experiments set to 60 mL/min. Cin = 10 ppmv. T = 25˚C.

Table 7.3: Fixed-bed capacities for toluene vapour for multicomponent vapour mixtures on industrial adsorbents. Experiments carried out in ‘wet adsorbate’ mode where toluene and water vapour were eluted simultaneously through the adsorbent bed. Flowrate = 60 mL/min. Cin = 10 ppmv. T = 25˚C.

Table 7.4: Fixed-bed toluene capacities for ZIF materials. Flowrate = 60 mL/min. Cin = 10 ppmv, T = 25˚C.

Table 7.5: Fixed-bed capacities for toluene vapour for multicomponent vapour mixtures on ZIF adsorbents. Experiments carried out in ‘wet adsorbate’ mode where toluene and water vapour were eluted simultaneously through the adsorbent bed. Flowrate = 60 mL/min. Cin = 10 ppmv. T = 25˚C.

Table 7.6: Fixed-bed capacities for toluene vapour for multicomponent vapour mixtures on MIL-100. Experiments carried out in ‘wet adsorbate’ mode where toluene and water vapour were eluted simultaneously through the adsorbent bed. Flowrate = 60 mL/min. Cin = 10 ppmv. T = 25˚C.

Table 7.7: Experimental and fitted values for capacity and useability of adsorbents for toluene. Values calculated by integrating BTCs generated using the Bohart-Adams Logistic or Boltzmann-EMG models. Flowrate = 60 mL/min. Cin = 10 ppmv, T = 25˚C.

Chapter 1: Introduction and Motivation

1.1. Motivation: Volatile organic compounds

Volatile organic compounds, or VOCs, are a broad class of compounds defined by their organic chemistry, low boiling point, and high vapour pressure. Despite their potential dangers, chemicals producing VOCs are extensively utilised in several industries to produce the materials and services we use in everyday life, thanks to the plethora of bonding and chemical groups present in the species. There are increasingly observed health risks associated with exposure to many types of VOCs, from alkanes to alcohols, with some of the more dangerous groups such as acids, bases and aromatics requiring extensive protection for handling. In high enough concentrations these chemicals can lead to acute problems such as nausea, lack of breathing, blindness and even death but what is often less considered is the chronic issues that can affect individuals who are continuously exposed to lower, less noticeable, levels of these compounds. While heightened levels of VOCs have typically been considered an environmental problem, the recent global focus on air pollution has led to VOCs being considered a major health risk.

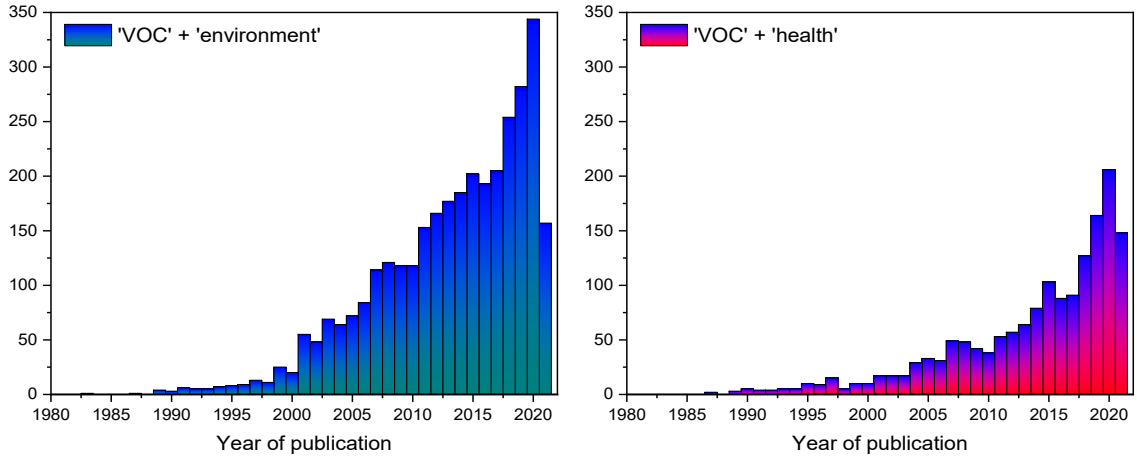


Figure 1.1: Number of publications associating VOCs with environment (left) and VOCs with health (right), illustrating the growing focus on volatile chemicals. Reproduced from Pubmed on 17th May 2021.

A study by Shuai et al in 2018 [1] quantified these increased health risks by surveying groups housed in areas both inside and outside of a dyeing industrial park in South Korea, as well as the indoor and

outdoor concentrations of the 8 most common VOCs released. The concentrations of all VOCs were higher in regions exposed to the industrial plant compared to those in the controlled region. For example, the indoor toluene concentration found in the exposed region was over 7 times higher than the controlled region, 125 μg m^{-3} compared to 17 μg m^{-3}. Similarly, people living in these exposed areas had significantly lower satisfaction with their ambient environment, with more people reporting serious issues with odour and air pollution in exposed areas. Finally, the levels of health problems such as were all higher in exposed regions compared to non-exposed regions, with the percentage of participants with a history of asthma in exposed and controlled regions being 3.7% and 1.6% respectively. While not definitive, these findings highlight the enhanced risk associated with high levels of VOCs in peoples' lives, and the need for capturing or removing these dangerous chemicals to a reasonable degree.

The emission of VOCs from industrial chemical processes is a well-known and established risk, although several indoor sources of VOCs also exist including fragranced consumer products [2], paints and varnishes, and even the building materials of the dwellings themselves [3]. Common side effects of elevated VOC levels, including those found in consumer products, have been associated with 'sick building syndrome' (SBS). SBS describes a range of symptoms including sensory and skin irritation, hypersensitivity, general health problems, and malodour that are present for individuals exposed to indoor built environments [4]. In recent years it has been hypothesised that the complex mixture of VOCs in indoor air might be a primary cause of several SBS symptoms, even at concentration levels far below what are typically considered 'dangerous'. For example, while the short (15 minute) and long (8 hour) work place exposure limits for toluene are 384 and 191 mg/m^3 respectively, as dictated by UK Health and Safety Executive [5], WHO-recommended indoor exposure limits are several orders of magnitude lower (260 $\mu g/m^3$) [6]. Additionally, a study in Dalian, China [7] found that individuals experienced symptoms of SBS even at VOC concentrations far below their exposure limit; toluene levels in the bedroom, kitchen, and outdoor varied between 2.4-97.4, 3.0-80.0, and 3.9-40.6 $\mu g/m^3$ respectively. Even below the limits put in place by health organisations, elevated levels of VOCs can contribute significantly to poorer living conditions for affected individuals. Examples of these concentration levels and types of compounds is outlined in **Table 1.1.**

Table 1.1: Typical VOCs and levels present in different industrial and indoor environmental spaces.

Environment	VOCs present (concentration level [mg/m^3]) [a]
Wooden furniture manufacturing [8]	Toluene (0.09 ± 0.04 – 0.67 ± 0.17) Dichloromethane (0.16 ± 0.05 – 7.52 ± 1.23) 2-Butanone (0.63 ± 0.10 – 3.32 ± 0.50)
Office building [9]	Toluene (0.094 ± 0.039) Formaldehyde (0.127 ± 0.025)
Residential home, autumn (exposed) [1]	Toluene (0.167 ± 0.221) Chloroform (0.012 ± 0.006) 2-Butanone (0.015 ± 0.0014)
Residential home, autumn (controlled) [1]	Toluene (0.073 ± 0.057) Chloroform (0.007 ± 0.002) 2-Butanone (0.031 ± 0.138)

[a] Due to complex mixture of VOCs, list is non-exhaustive.

Reducing the concentration of VOCs in indoor spaces where the levels of species are elevated could provide significant improvements to the quality of life and health of individuals in these spaces. Many methods of reducing VOC concentrations exist, with some of the most common being adsorption using zeolites or activated charcoals. Activated charcoal has an advantage of containing a large number of sites for VOCs to adsorb onto while being relatively inexpensive to produce [10] although a study by Blocki [11] recommends the use of hydrophobic zeolites in certain applications due to charcoal's difficulty in regeneration when adsorbing high boiling solvents and its ability to promote polymerisation and oxidation of adsorbed species to potentially toxic compounds. Zeolites, while typically more expensive to produce than charcoals, allow for selective adsorption of compounds based on chemistry or size. The choice of an adsorbent depends strongly on the system in which it is being applied. Understanding how a material's properties can influence its effectiveness in VOC filtration requires in-depth understanding of both the material and the space in which it is being applied, and testing must reflect that. Considering the omnipresence of VOCs in industrial and household spaces, the range of compounds and their concentrations can vary significantly. This work will assess VOC adsorption in concentrations ranges between those of indoor and long-time VOC exposure limits while accounting

for the limitations of standard analytical adsorption equipment. Studying VOC levels between 10-1000 mg/m^3 (10s-100s of part-per-million) aims to bridge the gap between the fields of analytical and environment VOC adsorption studies.

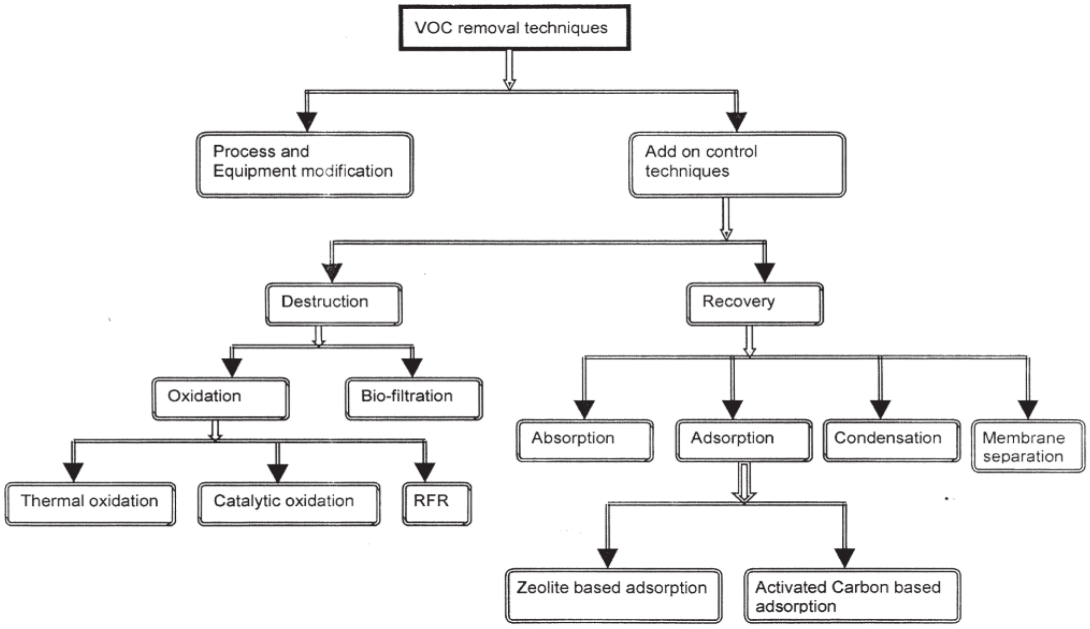


Figure 1.2: Methods of VOC removal, reproduced from a review by Khan & Ghoshal [10] with permission.

1.2. Motivation: Malodour removal in consumer care products

Many of the concerns associated with VOCs as a health hazard can be extended to their role in malodour. Any chemistry student can attest to the variety of harsh smells present in a laboratory utilising organic solvents, whether those are aromatic, halogenated, or aminated. Indoor malodourous VOCs can be emitted from a wide range of sources including biological [12], consumer products [13]; or the building itself, with the most commonly studied VOC emission being formaldehyde [14]. The odour threshold limit for these malodourous VOCs can vary but is typically in the range of a few parts-per-million down to tens or hundreds of parts-per-trillion [15]. Technologies designed for removal of these compounds must be effective at dilute levels to effectively prevent or reduce detection by humans.

1.3. Project aims and objectives

Based on the previous sections, this project's primary goal is to gain a deeper understanding of the properties of porous adsorbent materials, and how these can influence their performance in removing volatile organic compounds from environments representative of indoor air. To this end, several aims were laid out:

1) Review existing literature on the properties of both traditional industrial materials, such as zeolites and activated carbons, and recent advancements in adsorbent technologies, such as mesoporous silicas and metal-organic-frameworks. Particularly, how these properties may influence their adsorption of VOCs in ambient conditions and in the presence of water vapour.

2) Validate standard practises for material characterisation by analysing widely available industrial odour adsorbent materials, based on reviewed literature and the recommendations of this project's industrial partner, Procter & Gamble Co. USA. Use gravimetric techniques and mathematical modelling to provide parameters related to the capacity, kinetics, and selectivity of adsorbents for VOC species. Relate physicochemical and adsorption properties to provide screening tools for consumer care malodour removal and inform future material choice or synthesis.

3) Evaluate current experimental capabilities within the research group and institution, and how this apparatus can be used to assess the role of environmental conditions, particularly relative humidity, on the performance and efficiency of porous adsorbents. If necessary, determine which additional experimental assets will be required to address these research aims and where to source these assets, e.g. home institution, industrial partner, academic collaboration, home-built system.

4) Use experimental findings, combined with reviewed literature, to provide recommendations to industrial partners in the selection or development of adsorbent technologies for the removal of VOCs from indoor air environments.

Chapter 2: Review of industrial and synthetic porous materials, their properties, and their role in gas and vapour adsorption applications

2.1. Principles of gas adsorption in porous materials

2.1.1. Fundamentals of adsorption and intermolecular interactions

Adsorption is defined as the increase in density of a fluid adsorbate at a phase boundary or surface, differentiating itself from absorption by its constraint to the surface or interface of the sorbent [16]. If adsorption occurs via the formation of chemical bonds, the adsorption is referred to chemical adsorption, or chemisorption. When adsorption occurs via weaker physical bonds between atoms and molecules, the process is called physical adsorption, or physisorption. Physisorption occurs due to weak, intermolecular attractive forces between a fluid, the adsorbate, and a solid, the adsorbent [17]. The most common attractive forces in adsorption processes are long-range van der Waals forces, encompassing both polar and non-polar interactions, and short-range chemical forces including covalent and ionic bonding, although the interplay between these forces has been debated.

Van der Waals (vdW) forces are the general name given to a set of individual forces [18], all inversely proportional to the 7^{th} power of distance between the atoms or molecules. The three contributions to vdW are [18]:

- Keesom forces, electrostatic interactions between permanent dipoles or charged particles.
- Debye forces between permanent dipoles and induced dipoles.
- London forces, due to fluctuations in the electron cloud of atoms and molecules, leading to temporary changes in charge distribution or fluctuating dipole-induced dipoles forces.

Debye (induced) and Keesom (orientation) contributions are referred to as a form of polar interaction due to their prerequisite of a permanent dipole, while London forces exist in any material since any atom can have a temporary induced dipole, and are considered the most important contribution in non-polar bonding [18]. These attractive forces are assumed to be additive and can be written in the form [18]:

$$F_{vdW}(r) = \frac{d}{dr} w_{vdW}(r) = -\frac{6 \cdot C_{vdW}}{r^7} \quad (2.1)$$

Where F_{vdW} and w_{vdW} are the vdW force and free energy, r is the distance between atoms or molecules, and C_{vdW} is the vdW coefficient, a sum of the contributions of Keesom, Debye, and London (C_{Keesom}, C_{Debye}, C_{London}). This attractive force term, when combined with a repulsive, short-range potential due to the overlap between atoms' electron clouds, describes the net sum interactions between isolated molecules in a vacuum, known as the Leonard-Jones potential [19], a commonly used intermolecular potential equation.

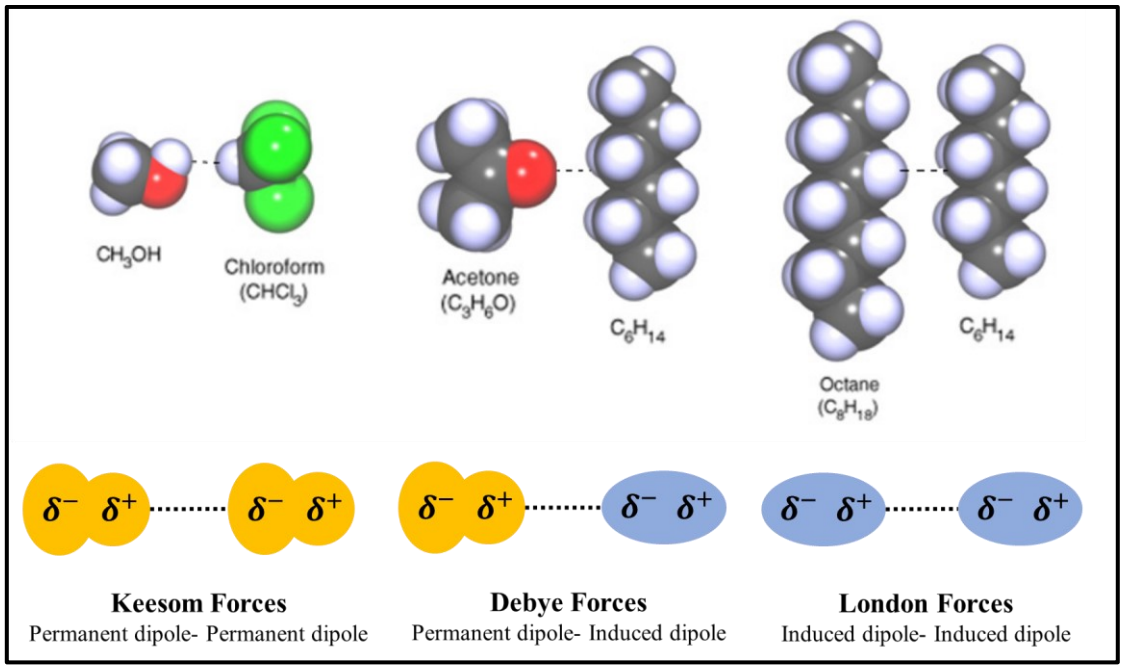


Figure 2.1: Illustration of Keesom forces (left), Debye forces (middle), and London forces (right) between molecules with different bonding chemistries. Adapted from work by Leite et al [18] under Creative Commons licensing.

Acid-base interactions are another important category of forces that can occur between adsorbent and adsorbate. Based on the Lewis theory of acid-base reactions [20], a base is a species that donates an electron for a reaction, commonly from the highest occupied molecular orbital (HOMO), while an acid is a species that accepts an electron, commonly into its lowest energy unoccupied molecular orbital

(LUMO). For example, in the reaction of a proton (H^+) and a hydroxide ion (OH^-), the latter donates a pair of electrons to the former to form a covalent bond. Therefore, Lewis bases are electron-pair donors and Lewis acids are electron-pair acceptors. This definition also extends to solid materials- in zeolites, the framework oxygens have an ability to donate electrons during adsorption, and the extra framework cations have an ability to accept electrons, defining them as Lewis bases and acids respectively. The acidity or basicity of zeolites will be discussed later in this Chapter. One special case of Lewis acid-base interactions, and one of the most fundamental considerations for gas-solid or vapour-solid adsorption, is the hydrogen bond.

Hydrogen bonds are, despite their name, non-bonded electrostatic interactions formed between covalently bonded hydrogen atoms and a strongly electronegative atom, such as oxygen or nitrogen, with a lone pair of electrons [21]. A hydrogen atom, when bonded to an atom such as fluorine, oxygen, or nitrogen will have a partial positive charge due to the ability of those electronegative atoms to attract the hydrogen's electron. In general, the interaction can occur between two groups, X-H and Y [22], where X is any atom with an electronegativity higher than hydrogen, and Y can be any of the elements encompassing X as well as π electrons from benzene rings . There are many debates around the exact nature of hydrogen bonds, whether they are purely electrostatic or contain some components of covalent bonding [23]. These forces are often described as being distinct from vdW, despite fitting the definition of a dipole-dipole interaction, due to the hydrogen bonds' directional, non-isotropic nature. In simple terms, hydrogen bonds favour linear geometries over bent ones, while vdW contacts are isotropic and their interaction energy is independent of the bond angle. Steiner & Desiraju [24] showed this difference is present even for weak hydrogen bonds, being able to distinguish between C-H - - H-C and C-H - - O, with the methyl group acting as a weak hydrogen bond donor. Acid-base interactions, including hydrogen bonds, are exothermic and short-range in nature, typically acting at intermolecular distances of ~0.3 nm (compared to a range up to several dozen nm for vdW [25]) and not exceeding energy ranges of 155 kJ/mol [20]. The nature of acid-base interactions, i.e. the donation or acceptance of an electron, directly affects the configuration of the electrons in the molecules when the interaction occurs, whilst dipole interactions are due to pre-defied and notionally fixed charge separations, i.e. dipole moments,

within the molecules of interest. The exact nature of the hydrogen bond, while debated, likely exists on a spectrum depending on the strength of the interaction, which itself is dependent on the bond donor and acceptors, i.e. the environment of the electronegative element and the hydrogen it interacts with.

In the most extreme cases, chemical forces and interactions can lead to reactions occurring between the adsorbent and adsorbate, resulting in either covalent or ionic bonds forming. As these bonds involve the sharing of electrons, they are much stronger than van der Waals forces, and processes involving the formation of these bonds are typically distinguished by the term 'chemisorption'. However, the distinction between 'physisorption' and 'chemisorption' is not always clear. As noted by Chiou [26], the adsorption of polar vapours onto a polar solid may fall under either category, depending on the strength of interaction and the adsorption energy and indeed there in a continuum of adsorption energies between 'physisorption' and 'chemisorption' processes.

Between the London dispersive component of vdW and acid-base interactions, the latter encompassing hydrogen bonding for the sake of simplicity, the two most significant components of physisorption interactions, described as non-polar and polar interactions, or dispersive and specific interactions, respectively [27] are defined. Non-polar interactions increase with the size of the adsorbing molecule due to the greater number of electrons and therefore a greater magnitude of electron fluctuations, as well as the amount of surface contact [20]. This means that larger molecules and higher surface area materials will both contribute to an increase in their non-polar adsorption strength. Non-dispersive bonding tends to change in strength based on the type of chemical bonding group (such as -OH or -NH) present, the proportion of these groups, and their environment in the molecule. For example, despite both having the same molecular weight and number of hydroxyl groups, 1-propanol has a higher polarity index than 2-propanol due to the latter molecule's -OH group being shielded by methyl groups on both sides [28]. Materials with a high proportion of polar bonding chemistry (e.g. containing electronegative atoms or charged ions) are often described as 'hydrophilic' due to their affinity towards water molecules, whereas materials with few polar bonding sites are described as 'hydrophobic'. This definition also extends to the adsorbate species with the proportion of polar to non-polar chemical groups defining the molecule as more or less hydrophilic or polar.

Adsorption occurs when the combination of polar and non-polar interactions between the surface and adsorbate exceeds the attractive forces between the adsorbate's own molecules. The enthalpy change accompanying physical adsorption is expressed by:

$$\Delta H = \Delta G + T\Delta S \tag{2.2}$$

The entropy change, ΔS, is negative since the adsorbed state is inherently more ordered than that of the fluid state. For physisorption which occurs spontaneously, the change in Gibbs free energy, ΔG, is negative, resulting in an enthalpy change, ΔH, that is also negative, or exothermic.

The readiness at which adsorption occurs depends on a few factors including the driving force within the environment (i.e. relative concentration), the temperature of the system, the number of available sites for molecules to occupy on the sorbent, and the chemistry of these sites with respect to adsorbing molecules. Taking these factors into account means that the removal of volatile species from the air will depend not only the physical structure of the material and how that contributes to adsorption site density, but also the chemistry or hydrophobicity of the adsorbent material relative to the adsorbate molecule(s) of interest.

2.1.2. Adsorption of gases via surface filling

The adsorption of gas molecules onto a surface is a complex phenomenon, the fundamentals and driving forces behind which are still being studied today. However, many theories for the adsorption mechanism have been developed over the years.

2.1.2.1. Langmuir

Langmuir is perhaps the most famous adsorption model, which considers the adsorption of gases or vapours onto a surface with a fixed number of adsorption sites. At equilibrium, the rate of desorption from occupied sites is defined as equal to the rate of adsorption onto the unoccupied sites [26]:

$$k_{des}\theta = k_{ads} \cdot P_P \cdot (1 - \theta) \tag{2.3}$$

Where P_P is the partial pressure of adsorbate, calculated as the fraction of adsorbate pressure to the saturation or vapour pressure of that adsorbate in that environment, θ is the fraction of total sites

occupied, and k is the rate constant for adsorption or desorption. The amount of gas adsorbed, being proportional to θ, can then be determined as a function of partial pressure in the isotherm equation:

$$q = \frac{q_m \cdot K_L \cdot P_P}{1 + K_L \cdot P_P} \tag{2.4}$$

Where q is the quantity adsorbed, q_m is the capacity of the material when the surface is covered with a completed monolayer of the adsorbed gas or vapour, and K_L is the Langmuir constant related to the heat of adsorption relative to the quantity of adsorbate, considered to be independent of the adsorbed amount. At low concentrations, the quantity adsorbed becomes directly proportional to the partial pressure, often referred to as the Henry region where the gas molecules can interact with the entire of the surface independently due to a lack of adsorbate-adsorbate interactions.

2.1.2.2. Brunauer-Emmett-Teller

An extension of the Langmuir model was devised by Brunauer in 1938 [29] to describe submonolayer-to-multilayer gas and vapour adsorption on a solid, known as the Brunauer-Emmett-Teller (or BET) model. This provided the basis for calculating a theoretical surface area for materials, but makes several assumptions: the Langmuir equation applies to each adsorbed layer, i.e. uniform surface and localised sites with no interference between them; adsorption and desorption occur only for the exposed layer surfaces; at equilibrium, the rate of adsorption onto a layer is balanced by the rate of desorption from the layer above it; and the molar heat of adsorption for the first layer is higher than for additional layers, the latter of which are assumed to have a heat of adsorption which is similar to the liquefaction heat of the gas/ vapour. The final BET isotherm has the equation [30]:

$$q = \frac{q_m \cdot C_{BET} \cdot P_P}{(1 - P_P) \cdot \left(1 + P_P(C_{BET} - 1)\right)} \tag{2.5}$$

The constant, C_{BET}, is related to the difference between the heat of adsorption in the first layer and the heat of liquefaction of the vapour. Using the quantity q_m and the molecular surface area in the experiment, the surface area of the material can be determined. This determination requires the BET equation to be rearranged and plotted, using the slopes parameters for calculation. This method is typically valid in the region that multilayers can form indefinitely [26]. The specifics of this process

will be discussed in future sections. Due to its assumption of site energy uniformity, the BET model accounts for multilayer adsorption on surfaces with low degrees of heterogeneity, such as those with small to moderate surface areas. The applicability of the BET model increases when an inert gas is considered which does not contribute to polar interactions, one reason why nitrogen is commonly utilised for surface area analysis. Analysing the sample at nitrogen's boiling point of -196˚C allows the molecule to condense onto the surface and inside of the pores.

2.1.3. Polanyi potential theory of adsorption

In energetically heterogeneous materials, such as those with high surface areas and high degrees of microporosity, adsorption data commonly deviates from Langmuir and BET models, as the force field within an adsorption space in these materials varies considerably with location. The Polanyi theory [31], [32] has been recognised as one of the most powerful models for describing vapour adsorption on energetically heterogeneous solids. The theory considers that an adsorption potential (ε) exists between a molecular located within the attractive force field of a microporous solid, and that microporous solid's surface. This attraction is derived from London dispersion forces between the atoms of the molecule and surface atoms. The magnitude of ε is therefore dependent on proximity of the molecule to the surface and may be viewed as the energy required to remove that molecule from that location to a point outside of the attractive force field of the solid. It is highest in the narrower portion of a pore due to the adsorbate being close to attractive forces on more than one surface, e.g. overlapping van der Waals forces from the pore walls.

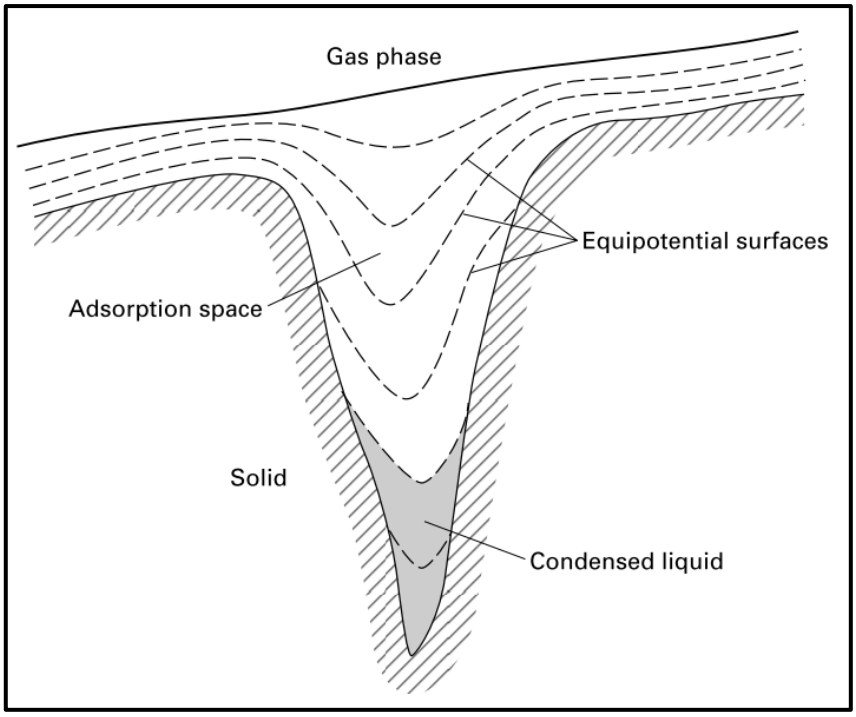


Figure 2.2: Approximate schematic model for a region of a pore, showing equipotential surfaces corresponding to successively lower adsorption potentials with increasing pore size. Condensation of the vapour occurs wherever the adsorption potential required to concentrate it to saturation, i.e. its vapour pressure, is equalled or exceeded. Reproduced from the book 'Partition and Adsorption of Organic Contaminants in Environmental Systems' by Cary T. Chiou [26], with permission.

A vapour molecule inside this attractive field is exposed to two opposing thermodynamic effects: the entropy is reduced due the more ordered adsorption state; and the system potential energy is reduced due to a loss in vapour concentration. In a system at adsorption equilibrium (i.e. the change in molar free energy is zero) these two effects are equal:

$$d\epsilon = \bar{V} dP \tag{2.6}$$

Where dε is the differential potential energy change per mole of vapour, $\bar{V}$ is the molar volume of vapour, and dP is the differential change in vapour partial pressure. According to Polanyi theory, a vapour will condense to form a liquid-like adsorbate if the value of ε is greater than or equal to the work

required to concentrate the vapour from ambient pressure (i.e. when the adsorption potential, ε, is zero) to its saturate pressure at the surface. Applying the ideal gas law to the system yields:

$$\epsilon = \int \bar{V} dP = RTln\left(\frac{P_0}{P}\right) \tag{2.7}$$

Where R is the molar gas constant, T is the temperature, and P and P_0 are the equilibrium and saturation pressures of the vapour. Thus, as a porous solid is exposed to increasing partial pressures of a vapour, condensation and the formation of a liquid-like adsorbate will form within regions of the highest adsorption potential, or those within the smallest pores. This trend will continue in regions with progressively lower potentials until all adsorption spaces are filled as the equilibrium pressure saturates resulting in an adsorption potential of zero.

2.1.3.1. Dubinin Radushkevich and Dubinin Astakhov

Based on the potential theory of Polaniyi, Dubinin and Radushkevich developed a micropore volume filling theory (MVFT), and proposed an empirical expression for describing the adsorption of gases on microporous adsorbents [33], [34]:

$$q = a_0 \cdot \exp\left[-\left(\frac{\varepsilon}{E}\right)^2\right] \tag{2.8}$$

Where a_0 is the micropore capacity of the solid, ε is the Polanyi adsorption potential expressed in **equation 2.7**, and E is a constant related to the characteristic adsorption energy for the given system:

$$E = E_0 \cdot \beta, \quad E_0 = reference, \quad \beta = \left(\frac{\varepsilon}{\varepsilon_0}\right)_v \tag{2.9}$$

The value of E is computed using the characteristic adsorption energy for a reference gas E_0 (usually benzene), and multiplying by a similarity constant, β. The similarity constant is calculated by comparing the adsorption potentials of two gases or vapours at equal distances from the adsorbent surface, or equal surface layer volumes (v). A modified form, the Dubinin Astakhov equation [35], introduced an additional parameter (n) in placed of the power term within the exponential of **equation 2.8**, which has been related to the heterogeneity of the surface/ material's pore size distribution [36].

2.2. Defining and characterising porous materials

Porous materials can be defined as any solid material containing ‘pores’ or ‘spaces’ throughout their structure, resulting in lower density and, typically, higher surface area [37]. The surfaces of these materials, whether external or internal, provide sites that can accommodate ions or fluid molecules. Examples of naturally occurring porous materials include beach sand, limestone, and wood [38].

2.2.1. Surface area in porous materials

By virtue of having a large amount of pore volume within their structure, porous materials possess higher than average surface areas. Surface area can be defined as the available area on or inside of a material for fluid molecules to attach to through physical or chemical interactions, i.e. physisorption- or chemisorption. **Figure 2.3** shows a simplified illustration of how gaps and spaces increase surface area.



Figure 2.3: Illustration of effect of internal pores on available surface area, made up of three regions: solid material (black), pores and gaps (white), area for potential adsorption sites (blue).

As the number of gaps and spaces increases, the number of molecules that can ‘fit’ onto the surface of that material increases. Surface areas are related to standard units of square metres by multiplying the number of molecules occupying the surface by the molecule’s cross-sectional area of adsorbing species.

2.2.1.1. Specific surface area

The calculation of the specific surface area, i.e. relative to the mass of material, is commonly carried out by determining the monolayer capacity of a material, i.e. the number of molecules that can occupy

a single layer covering the available surface of a material. One method for carrying this out uses a 'BET plot', a linearised form of the adsorbate (typically nitrogen) isotherm using the following equation:

$$\frac{1}{q_e\left[\left(\frac{P_0}{P}\right)-1\right]} = \frac{c_{BET}-1}{q_m\, c_{BET}}\left(\frac{P}{P_0}\right) + \frac{1}{q_m\, c_{BET}} \tag{2.10}$$

Where q_e is the equilibrium quantity of N_2 adsorbed at pressure P, q_m is the monolayer adsorbed gas quantity (typically in units of volume adsorbed per unit mass), P and P_0 are the pressure and saturation pressure of nitrogen in the system, and c_{BET} is the BET constant related to the magnitude of adsorbent-adsorbate interactions. By multiplying the parameter q_m by the Avogadro number and constants related to the molar volume and cross sectional area of the adsorbate molecule, the cross section area occupied by the monolayer can be calculated which, when divided by sample mass, provides the 'BET' specific surface area. An important consideration in calculating the BET surface area is the partial pressure range used for generating the line of best fit, especially for microporous adsorbents [39], to ensure that only monolayer formation has occurred. Typically this range is within $0.05 < P/P_0 < 0.35$ [40], although values outside of this range have been used for materials exhibiting high degrees of microporosity using the Rouquerol method [39].

The 'monolayer adsorbed capacity' can also be determined using the Langmuir equation, as seen in **equation 2.4**. This value can be calculated either by linearising the Langmuir equation or fitting the experimental data through error minimisation. The pressure range used for linearisation has been found to drastically effect the deviation between Langmuir and BET surface areas [41], with the former often having lower linear correlation coefficients when using the standard 0.05-0.35 partial pressure range. Since the Langmuir model assumes only monolayer formation, and that the formation of this monolayer is the hard limit for capacity, it leads to surface area overestimations as it considers any multilayer formation to be instead occurring directly on the surface of the material. It is also important to consider the interaction strength between the adsorbate and adsorbent material, as any non-preferential interactions, such as polar molecules and hydrophobic materials, will lead to decreases in the adsorbed quantity, and may lead to underestimations in the monolayer adsorbed quantity.

2.2.1.2. External surface area

The external surface area of the material is an important factor to consider when optimising diffusion of fluid molecules into a porous solid. This area is often increased through the generation of larger aperture sizes within the material, producing hierarchical micro-/ meso-/ macro- porosity. External surface area increases molecular accessibility due to an increased number of interconnected pore openings, and shortened diffusion pathlengths between active sites in the micropores [42]. Introducing hierarchical porosity into adsorbents is possible through various methods: with activated carbons, the activation temperature and use of chemical agents can influence pore size distribution [43]; whilst with zeolites, post-synthetic modification of the material's ion content can result in mesopore generation [44]. Specific details of pore size distribution modification for different adsorbents will be elaborated on later in this review.

The t-plot method is widely used for determining external surface areas, as well as pore volumes, for porous materials as it utilises the same experimental datasets as specific surface area (i.e. gas isotherms). The t-plot method uses a 'statistical thickness' which describes the thickness of an adsorbed film as a function of partial pressure on a reference material that is both non-porous and has the same surface chemistry as the studied material. These reference materials are described by several models for the film thickness, often included in isotherm analysis software such as Harkins and Jura, Halsey, and Lecloux [45]. The t-plot itself is created by plotting the adsorbed volume of gas for the studied material at a pressure against the average thickness of the adsorbate film at the same pressure on the non-porous reference material. In microporous materials, adsorption can be described by two regimes: adsorption in and filling of micropores; and adsorption on the external surface area. In a microporous t-plot, adsorption at higher pressures follows a linear trend, the gradient of which can be used to estimate the external surface area of the material. Similarly, mesoporous materials have two adsorption regimes: prior to capillary condensation, adsorption occurs on the internal surface of mesopores and on the external surface of mesoporous particles; above condensation pressures, adsorption occurs only on the external surface. Again, the external surface area can be estimated using the gradient of points following

mesopore filling (i.e. the linear region following steep increase in adsorbed quantities). These regimes are illustrated below in **Figure 2.4**.

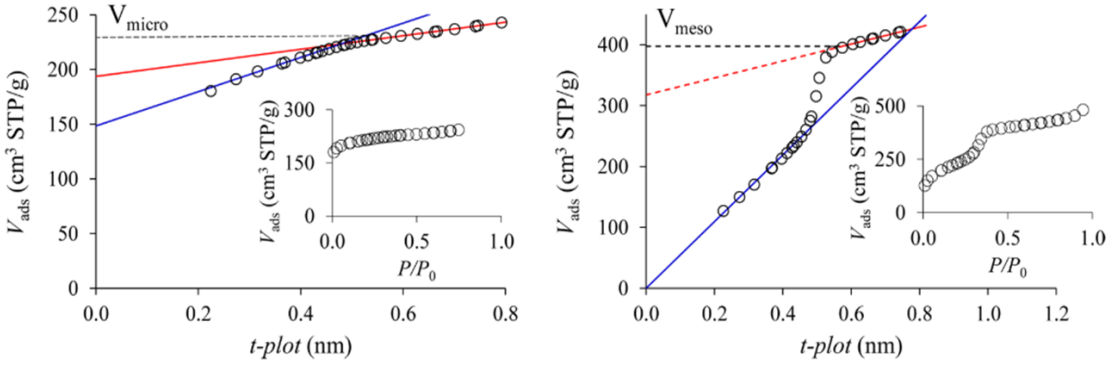


Figure 2.4: t-plot method for nitrogen adsorption data collected at -196˚C for microporous FAU zeolite (left) and mesoporous MCM-41 (right). Blue and red lines correspond to adsorption regimes at low and high pressures respectively. Reproduced from work by Galarneau et al [46] with permission.

The t-plot method, while valid for purely micro- and mesoporous materials, has difficulties in accurately determining external surface areas in hierarchically porous materials. A study by Galarneau et al [46] studied the impact of pore size and on curvature and the resulting thickness of the adsorbate layer, using experimental data from Kruk & Jaroniec [47] on argon adsorption in MCM-41 with varying pore sizes. They found that while this curvature effect is negligible for large pores, a correction for determining the micropore volume is required for pores smaller than 10 times the size of the adsorbate (i.e. around 3.5 nm for nitrogen). In the case of external surface area, Villemot et al [48] found the t-plot method is suitable for hierarchical porous solids, but only when there exists a pressure range for which micropores are completely filled but not mesopores. This results in two linear regimes in the t-plot which can be used for determining surface areas.

2.2.2. Types of porosity

The pore size distribution of a porous material is an important property, as it can dictate the molecules the material is capable of adsorbing, as well as the concentration range in which it will be most effective. In general, pore sizes are split in three IUPAC categories [40]:

- Micropores, with diameters below 2 nm.
- Mesopores, with diameters between 2 nm and 50 nm.
- Macropores, with diameters above 50 nm.

As the concentration, or partial pressure, of a gas molecule decreases, the size of the pores it can fill will also decrease [49]. Therefore, if a material is predominantly microporous, it will often have high effectiveness at adsorbing low-concentration gas molecules. This relationship is commonly described using the Kelvin equation which, for cylindrical pore geometry, is expressed as [40], [50]:

$$r_K = \frac{-2 \cdot \sigma \cdot V_m \cdot cos\theta}{R \cdot T \cdot \ln\left(\frac{P}{P_0}\right)} \tag{2.11}$$

Where r_K is the Kelvin radius, P/P_0 is the partial pressure of gas or vapour, σ and V_m are the surface tension and molar volume of the liquid/ vapour, θ is the contact angle between capillary condensate and pore walls (usually assumed to be zero), and R and T have their usual meanings. For example, water vapour at a partial pressure of 0.5 and a temperature of 25˚C will fill a pore with Kelvin radius of 1.45 nm [51]. However, due to the assumption that the molecules form a liquid-like meniscus inside of the pore, the Kelvin equation is typically utilised in pore sizes above 2 nm [50], i.e. outside of the microporous range.

The aperture size of a porous material can influence adsorption via size exclusion of molecules with larger diameters than the accessible pore radius. This molecular sieving effect has been shown to occur in VOC adsorption with narrow and wide pore zeolites [52], with the latter being more capable of adsorbing large diameter aromatic volatiles due to its channel size. Zeolites, a class of aluminosilicate minerals, have been used for their molecular sieving properties, to the extent that many classes of zeolites are described by their sieving properties and their pore size (molecular sieve 4A, 5A, 13X etc).

This sieving property has also been observed in metal organic frameworks [53], although this effect is often dependant on the extent of the material's pore flexibility [54].

Pore size distribution also influences the rate at which gas phase molecules can adsorb onto the surface of a material, and the energy barrier for this process to occur [55]. Diffusion can generally be divided into three phenomena [55]: molecular diffusion, where the pore diameter is greater than the mean free path of the molecules and collisions are assumed to only occur between fluid molecules; Knudsen diffusion, where pores are small enough for fluid molecules to collide with the aperture walls; and intracrystalline diffusion, where significant interactions exist between diffusing molecules and the porous structure. In intracrystalline diffusion, or micropore diffusion, the process can be affected by steric hindrance and the nature of the fluid molecule. In addition, diffusion through micropores is an activated process where molecules must overcome the repulsive interactions of the pore walls- this activation is dependent on the chemistry, shape, and size of molecule. These diffusion differences can lead to a 'kinetic selectivity' between molecules with similar structures [56], when size-based molecule sieving is not feasible.

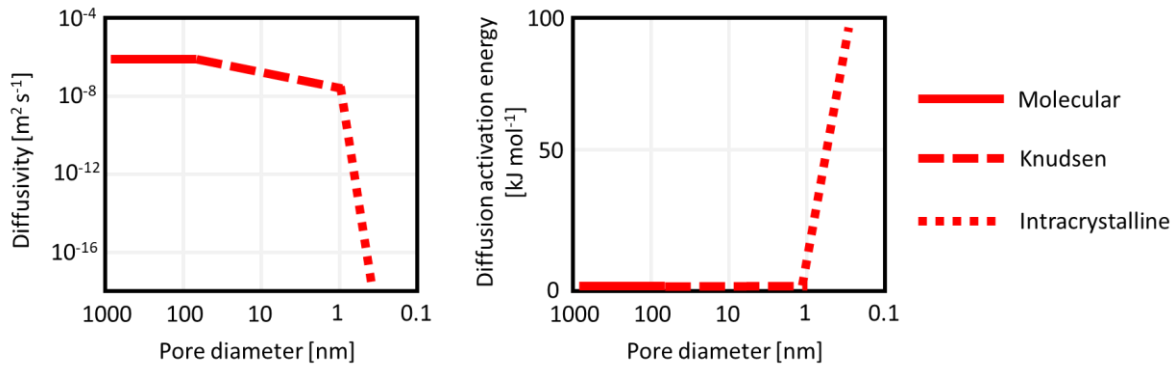


Figure 2.5: Effect of pore diameter on diffusivity and diffusion activation energy, showing different diffusion regimes, reproduced from work by Ruthven et al [55] with permission.

2.2.2.1. Determining porosity by adsorption isotherm

The type of porosity a material has can be qualitatively ascertained by the measurement the adsorption isotherm of an inert gas. A gas isotherm, i.e. at constant temperature, is constructed by measuring the

amount of gas or vapour adsorbed by a material as a function of partial pressure. There are generally eight isotherm shapes as defined by IUPAC [40], shown in **Figure 2.6**, which give an impression of the materials physical structure, porosity, and the nature of solid-fluid interaction:

- Type I describes microporous materials, with high uptake at lower pressures followed by a plateau. Type I(a) and (b) are distinguished by the former containing only narrow (< 1 nm) pores, and the latter having a broader range of sizes.
- Type II describes nonporous or macroporous materials, where multilayers of adsorbate molecules form on the surface, with the initial inflection point (x) denoting the completion of the first monolayer.
- Type III shows initially negligible uptake followed by a sharp increase at the highest pressures due to clustering of molecules on particular surface sites, rather than the gradual formation of mono- and multilayers.
- Type IV are typical for mesoporous materials, which are determined not only by adsorbent-adsorbate interactions but also interactions between adsorbate molecules in the condensed state. This follows similarly to Type II but, as pressure increases, the gas molecules within the pores condense into a liquid-like state below the saturation pressure of the liquid. This 'capillary condensation' is often accompanied by hysteresis, as shown in Type IV(a), as molecules are more difficult to displace once in this liquid-like state and so require a greater pressure driving force to remove. In cases where the mesopore diameter is low (< 4 nm [40]), there can be a lack of hysteresis, as shown in Type IV(b).
- Type V describes unfavourable adsorbent-adsorbate interaction followed by pore filling at higher pressures. This is typical for water adsorption onto hydrophobic micro- and mesoporous materials.
- Type VI describes layer-by-layer adsorption onto uniform, nonporous materials.

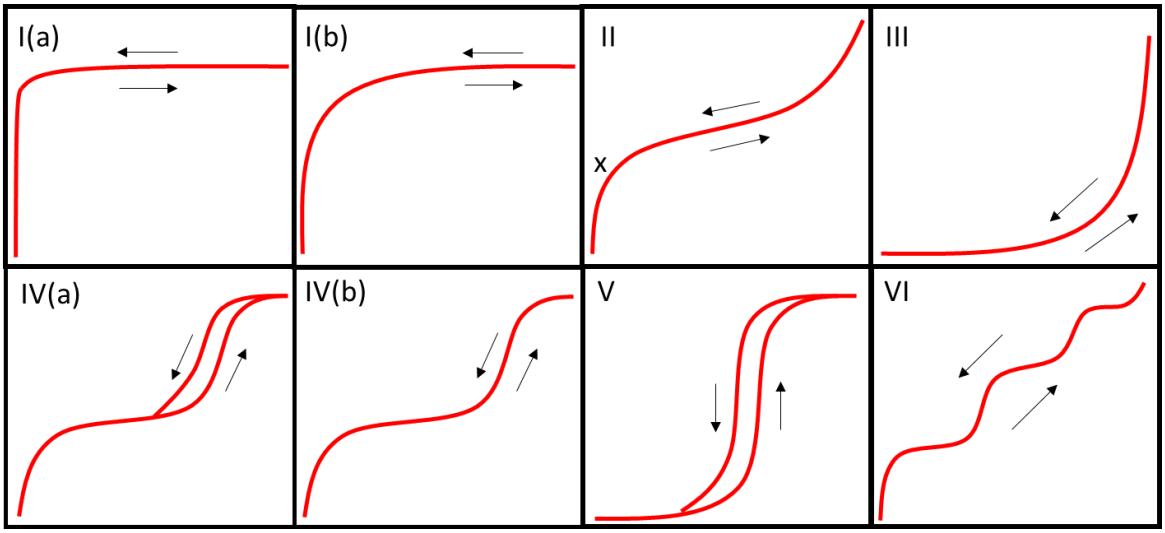


Figure 2.6: Illustration of adsorption isotherm types, reproduced from IUPAC Technical Report [40].

Adsorption hysteresis is the term for a difference in adsorbed quantities in the adsorption and desorption branches at a certain partial pressure, as seen in isotherm types IV(a) and V in **Figure 2.6**. Adsorption hysteresis in porous materials is commonly associated with capillary condensation. In the adsorption branch there is monolayer formation on the wall of the pores for lower pressures. As pressure increases, multilayers form and eventually the adsorbate condenses into a 'liquid-like' state. During desorption the geometry of the adsorbate-adsorbent interface is assumed to have changed, leading to a change in the resultant evaporation pressure. Using the Kelvin equation, shown in **equation 2.11**, the pore-filling partial pressure can be expressed in terms of the pore radius. The value of this radius will decrease in the desorption branch due to the formation of a condensed layer on the walls of the pore. In more complex pore structures, the desorption pathway for the molecules will often be dependent on network effects and pore blocking. For example, in ink-bottle pore shapes the wider pores are filled via narrow necks, which then restrict the desorption of molecules following condensation. The overall shape of the hysteresis loop can be related to the nature of the hysteresis and the features of the pore structure [40], [57].

2.2.2.2. Determining pore size distribution using adsorption models

Adsorption models have been used to relate the experimental adsorption capacity and isotherms to the pore size distribution of the material. The Barrett-Joyner-Halenda (BJH) method [58] uses a form of the Kelvin equation modified by Broekhoff-De Boer, the Kelvin-BdB expression [57], [59]:

$$R \cdot T \cdot \ln\left(\frac{P}{P_0}\right) = \frac{\sigma \cdot V_m}{r_{K,BdB} - t_c} + F(t_c) \tag{2.12}$$

Where R, T, P, P_0, σ and V_M have their regular meanings, $r_{K,BdB}$ is the modified Kelvin radius, t_c is the critical thickness of adsorbed film on a cylindrical pore wall at which capillary condensation occurs. The term $F(t_c)$ relates to the contribution of adsorbent-adsorbate attractive forces to the adsorption potential and, for N_2 adsorption at -196˚C on a plane surface, can be expressed using a relationship developed by Harkins and Jura [59]:

$$F(t) = R \cdot T \cdot \ln(10)\left(\frac{13.99}{t^2} - 0.034\right) \tag{2.13}$$

However, the expression for F(t) differs depending on the adsorbate, environment, and pore geometry of the material. The BJH method, like the Kelvin equation, is only valid for pores outside of the micropore range [50], as it assumes the density of the adsorbed fluid is equal to the bulk fluid. As pore size decreases, the strength of interactions between the pore surface and fluid become more significant- making the BJH method less valid [60]. As many adsorbent materials contain a significant amount of micropores, the applicability of the BJH method for pore size distribution determination is limited.

Non-local density functional theory (NLDFT) has also been applied to the generation of theoretical adsorption isotherms depending on an assumed pore size distribution. Fluid density distributions as a function of distance from the pore wall can be generated via the application of the Leonard-Jones potential at different gas partial pressures, or driving forces [61]. These profiles can be used to construct a series of theoretical adsorption isotherms for different pore shapes and sizes, known as kernels. The calculation of pore size distribution is based on the solution of the general adsorption isotherm, which correlates the kernel of the theoretical isotherm to experimental isotherm data [40]. This method's applicability strongly depends on the choice of model system and how well it relates to the adsorbate/

adsorbent pair in question. DFT is the recommended method for determining PSDs by the International Standard Organisation (ISO) [62], as the reliability of the technique can be improved by careful selection or development of descriptors for adsorbate-adsorbent interactions [57].

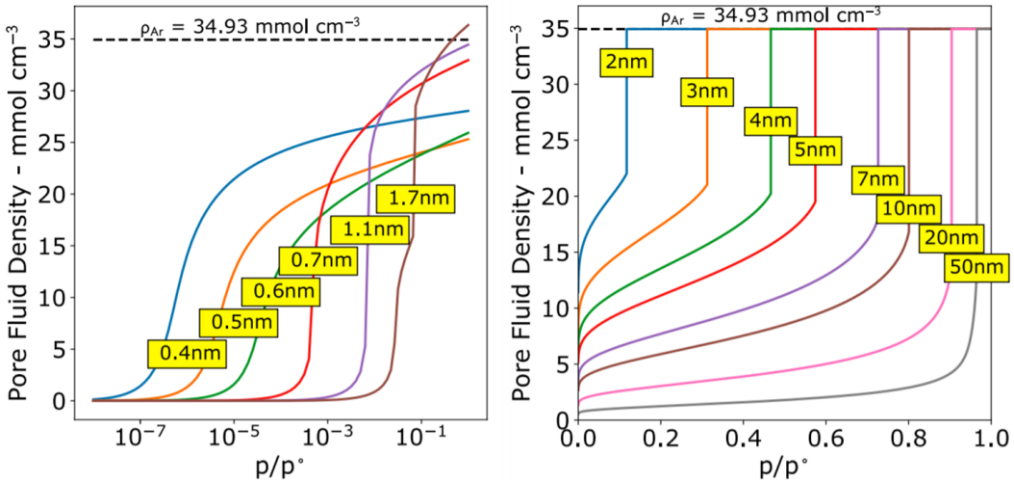


Figure 2.7: Theoretical argon isotherms based on DFT (left) and BJH (right) models, using a variety of assumed pore sizes. Note the increasing unusual isotherm shape in the BJH plot with decreasing pore size. Reproduced from a whitepaper published by Micromeritics [60], with permission.

2.2.3. Pore volume

Related to the pore size distribution, the distribution of pore volume within the microporous and mesoporous size regimes often dictates the applicability of an adsorbent. For example, while the adsorption of dilute gases may be carried out using a predominantly microporous zeolite [63], molecules at higher concentrations, such as water vapour, are commonly adsorbed and controlled using mesoporous desiccants such as silica gel [64]. Generally, three quantities are of interest for porous materials- micropore volume, mesopore volume, and total pore volume.

2.2.3.1. Micropore volume determination

The t-plot method, mentioned earlier for the determination of external surface area, is also used for calculating micropore volume [45]. By plotting the adsorbed condensed quasi-liquid volume against the adsorbed layer thickness, the micropore volume can be found from the intercept of the straight line

in the multi-layer region. However, the t-plot has been found to underestimate micropore volumes for materials possessing a range of porosities (i.e. micro-mesoporous materials) due to a 'curvature effect' in small apertures requiring correction [46]. The t-plot method is derived from the adsorbed layer thickness in a non-porous material, which is determined using BET theory. The BET model typically provides good results for Type II isotherms, but for materials that deviate from this model significantly the t-plot may not be applicable. The α_s-plot, proposed by Sing [45], replaces the monolayer capacity using a factor related to the amount adsorbed at a particular partial pressure and constructs a standard isotherm for a non-porous material with chemical properties similar to the material being analysed. A study by Villarroel-Rocha et al [65] compared the t-plot, α_s-plot, Dubinin-Radushkevich (DR), and density functional theory (DFT) methods for calculating micropore volume in a range of materials including activated carbons, zeolites, and mesoporous silicas. The DR method was found to overestimate the micropore volume in samples with a high proportion of mesoporosity, while the other methods showed similar results for all other materials. The t-plot showed slight deviations when compared to α_s and DFT, which was hypothesised to be due to its dependence on the chemical nature of the samples. The α_s-plot and DFT methods were found to be in good agreement with each other.

2.2.3.2. Mesopore volume determination

As with pore size distributions, the BJH method can be used for determining the quantity of gas adsorbed inside of mesopores, and by extension the volume of those mesopores by using the cumulative volume of pores located in the size range of 2- 50 nm [66]. Another method is to subtract the estimated micropore volume, determined via methods such as DR, t-plot, or DFT as shown above, from the total single-point pore volume calculated in the same gas adsorption experiment. This somewhat simple method has been used for characterising zeolites [67] and activated carbons [68], but will carry with it the core assumptions of whatever method was used to determine the sample's micropore volume.

2.2.3.3. Total pore volume determination

The total accessible pore volume of a material can be determined directly using experimental data. For example, the single-point pore volume of a material can be calculated using the quantity of nitrogen gas

adsorbed at a temperature of -196˚C and a partial pressure close to $P/P_0 = 1$, although this approach is less applicable to macroporous adsorbents due to the lack of a plateau region in the isotherm at high pressures [40]. The pore volume of a material can also be determined using the intrusion and extrusion of liquid mercury, although this method is a destructive technique with the added complication of mercury contaminated sample disposal [69]. Gas sorption and mercury porosimetry have 'application ranges' of 0.3- 50 nm and 3- 10,000 nm respectively [69]. To analyse over the full range of pore sizes (i.e. micro, meso, and macro), a combination of these techniques is often employed [70].

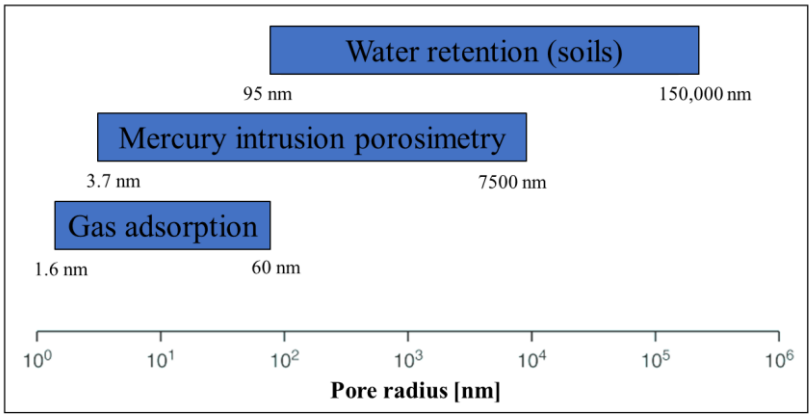


Figure 2.8: Application ranges of different pore size distribution determination techniques- specifically gas adsorption, mercury porosimetry, and water retention. Reproduced from a similar figure in Encyclopedia of Agrophysics [69].

The validity of the two techniques has been compared by Conner et al [71] for compressed silica aerosols in the pore size regime of 2-30 nm, finding that the two techniques were equivalent in this size range, with the nitrogen adsorption data assuming either spherical or cylindrical pores connected via cylindrical throats. For materials where micro- and meso-porosity is of upmost importance, such as adsorbents, gas adsorption typically allows for assessing the most pertinent pore volumes, with the added benefit of being non-destructive.

2.3. Measuring adsorption performance

The 'performance' of an adsorbent can be linked to several factors: the adsorption capacity, how much of a particular species can be adsorbed by the material; adsorption kinetics, how fast the material can adsorb these species; how strong the interaction between adsorbate and adsorbent is; and adsorption selectivity, how well a material can adsorb a particular species when placed in an environment with multiple competing adsorbates. Any one of these parameters, or indeed all of them, may be important for evaluating the performance of the material depending on its application.

2.3.1. Equilibrium adsorption capacity

The equilibrium capacity of a porous material for a gas or vapour is commonly carried out using gravimetric or volumetric methods [72]. This involves exposing the sample to a series of partial pressures or concentration of adsorbate and, at each step, recording the amount of gas adsorbed by the sample as a function of time until the system reaches equilibrium.

$$q_x\left(\frac{P_x}{P_{x,0}}\right) = \frac{(n_x)_{\frac{P_x}{P_{x,0}}}}{m_0}\left[\frac{mol}{g}\right] \tag{2.14}$$

Where q_x is the molar adsorption capacity for species x, n_x is the number of moles of x adsorbed by the sample when at equilibrium with a certain pressure of x, and m_0 is the dry mass of sample. It is essential that the material being studied is completely dry and clean. Any adsorption sites filled by occupying molecules such as water vapour or contaminants will influence the adsorptive attachment of gas-phase probes and provide inaccurate calculations of adsorption capacity [73]. Usually, the final sample mass following exposure can be calculated at multiple pressures or concentrations to construct an adsorption isotherm.

2.3.1.1. Gravimetric measurement

Gravimetric experimentation uses the change in mass a sample undergoes to characterise the amount of adsorbate that has become attached. At each pressure or concentration interval the sample is given time to reach mass equilibrium before recording the amount adsorbed during that interval. The 'adsorption capacity' of the material for that adsorbate can then be calculated:

$$q_{grav} = \frac{m - m_{dry}}{m_{dry}} \left[\frac{g}{g}\right] \tag{2.15}$$

Where q_{grav} is the gravimetric adsorption capacity, m and m_{dry} are the equilibrium and dry masses of sample (i.e. post- and pre-adsorption). In order to accurately measure the capacity of a material, the change in mass must be quantifiable. In cases where adsorption is unfavourable, negligible changes in mass may be difficult to detect, without using high sensitivity mass balances. As the partial pressure of certain gases increases, the density of the gas environment also changes, resulting in changes in buoyancy forces and by extension the apparent sample mass. These buoyancy forces may skew the mass readings of the equipment, although this effect can be minimised by using two inert, non-adsorbing sample holders: one sample holder contains the material being studied; the second sample holder containing an inert non-porous blank material with the same volume as the sample being studied. This approach will minimise the effect of buoyancy forces. In addition, materials that undergo a phase change may produce confusing mass versus time profiles, making the assessment of adsorption capacity difficult. For example, the release of water vapour upon crystallisation of lactose [74] occurs at a relative humidity (RH) around 55 % (T = 25˚C), leading to a loss in moisture content of around 10 %.

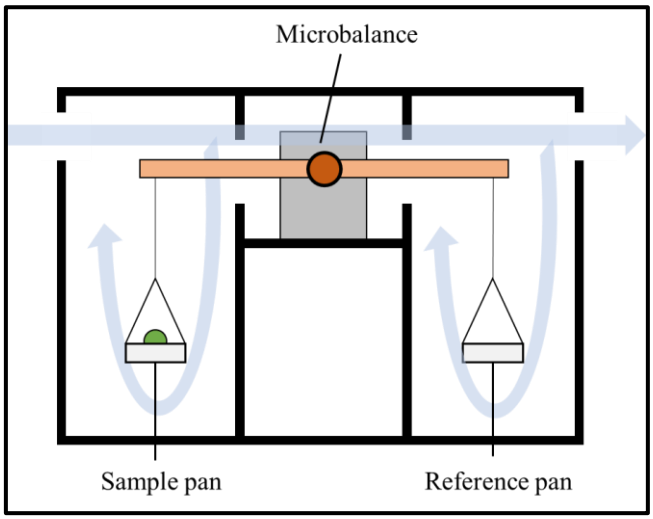


Figure 2.9: Schematic of symmetric gravimetric adsorption apparatus incorporating a recording microbalance connected to both a sample pan and reference pan to register changes in mass of a sample after exposure to a vapour or gas (blue arrow).

2.3.1.2. Volumetric measurement

Volumetric experimentation uses equipment containing a series of pressure valves and transducers as a gas delivery manifold, typically with the ability to work at high pressure and under vacuum. Following manifold evacuation under high vacuum, a certain amount of the gas is allowed to enter the sample chamber, with the initial and final pressures being recorded for each interval. Using the ideal gas law, the difference in pressure can be used to calculate the adsorbed quantity of gas. The same principle can also be applied to a closed volumetric system in which step changes in vapour concentration are introduced. The change in partial pressure, or concentration, of the adsorbate molecule(s) can be used to calculate adsorption capacities:

$$q_{vol,x} = \frac{\Delta n_x}{m_{dry}} = \frac{\Delta C_x \cdot V}{m_{dry}} = \frac{\frac{\Delta P_x \cdot V}{R \cdot T}}{m_{dry}} \left[\frac{mol}{g}\right] \tag{2.16}$$

Where Δn_x is the change in moles of the adsorbate x in the chamber, ΔC_x is the change in molar concentration of the adsorbate species x in the chamber at equilibrium, ΔP_x is the change in pressure of the gas x, V is the volume of the adsorption chamber, R is the molar gas constant, and T is the temperature. The species x is specified in this capacity as volumetric measurements allow for the determination of adsorption capacities for multiple species simultaneously, i.e. multicomponent adsorption. In addition, the sample mass requirement is dictated by the sensitivity of the pressure transducers used, with less sensitive equipment requiring larger pressure changes to measure accurately, and therefore a larger mass with which to adsorb the gas molecules. For systems using gas or vapour concentration as a measurement variable, the same principle applies, with the additional consideration that the sensing element must be non-destructive, as any reduction in concentration will affect the determination of capacity.

2.3.1.3. Fixed bed adsorption methods

In fixed-bed adsorption a packed bed of adsorbent material, such as a molecular sieve or activated carbon, is exposed to a continuous solute-solvent mixture which is eluted through the column.

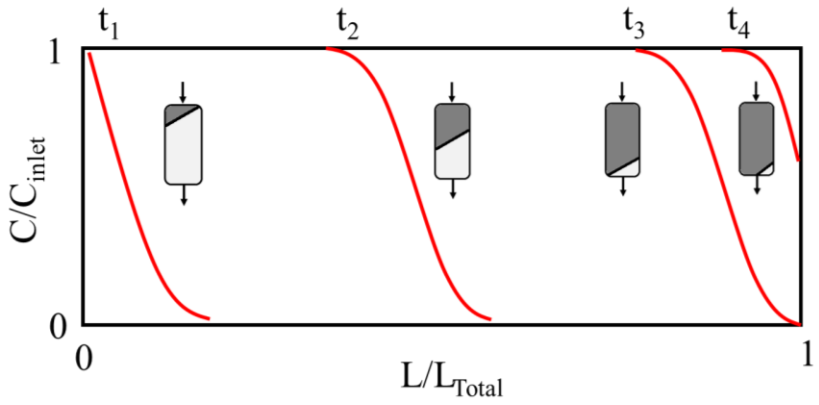


Figure 2.10: Illustration of concentration profiles (C/C_0) of adsorbate along the length of the packed bed (L/L_{Total}) at different time stages (t_1-t_4). The light and dark grey regions represent unsaturated and saturated adsorbent regions in the column respectively [75].

Initially the adsorbate species are fully adsorbed by the packed bed, resulting in a concentration profile across the length of the column, the shape of which depends on several factors related to the process and the adsorbate-adsorbent interactions. This profile between the regions of completely saturated length and completely unsaturated length is known as the 'mass transfer zone' and is an important property when determining the effectiveness of a packed bed adsorber. Once this zone reaches the outlet of the column the adsorbate species 'breaks through' until reaching equilibrium at a concentration equal to the inlet, signifying the adsorbent bed has reached saturation for that adsorbate. By monitoring the concentration profile in the outlet of the adsorption bed as a function of time, a breakthrough curve (BTC) can be plotted.

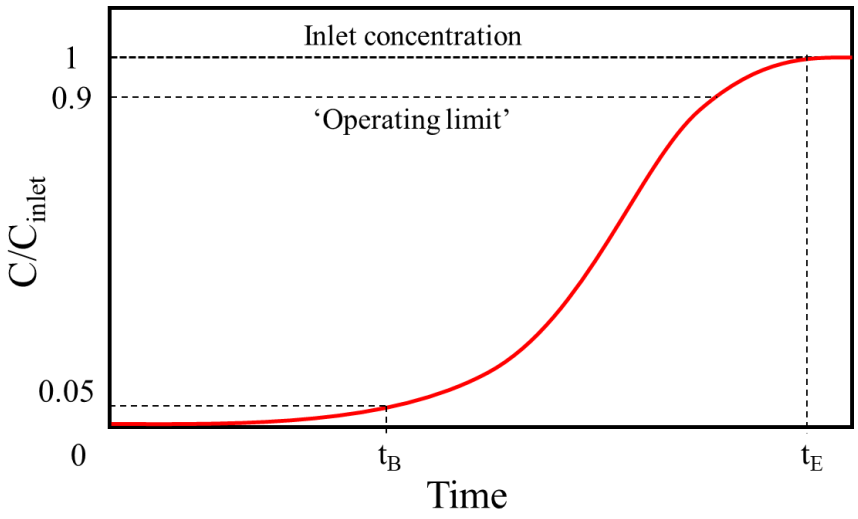


Figure 2.11: Illustration of breakthrough curve. Times t_B and t_E show the breakthrough and equilibration times for the adsorbent bed, respectively. The dotted line at $C/C_{inlet} = 0.9$ shows the 'operating limit' of the column [76], and the line at $C/C_{inlet} = 1$ is the species concentration in the inlet to the column.

Various parameters for the BTC are discussed in literature, especially for industrial gas and liquid adsorption processes. The 'breakthrough time' is defined as the time at which the outlet concentration of the bed reaches a certain percentage (e.g. 5%) of the inlet, while the 'saturation time' or 'equilibration time' is defined as the time taken for the ratio of outlet to inlet concentration to reach unity, when the packed bed has become completely saturated. By integrating down from either a ratio of 1 (complete saturation) or 0.9 (a typical industrial 'operating limit') the quantity of adsorbed species can be determination and the adsorption capacity at the breakthrough point or saturation point can be calculated [77], [78]:

$$q_{breakthrough}\left[\frac{g}{g}\right] = \frac{1}{m_{dry}}\left[\frac{1}{g}\right] \cdot C_{inlet}\left[\frac{g}{mL}\right] \cdot \dot{V}\left[\frac{mL}{\min}\right] \cdot \int_0^{t_B} \frac{C_{outlet}(t)}{C_{inlet}} dt \qquad (2.17)$$

$$q_{total}\left[\frac{g}{g}\right] = \frac{1}{m_{dry}}\left[\frac{1}{g}\right] \cdot C_{inlet}\left[\frac{g}{mL}\right] \cdot \dot{V}\left[\frac{mL}{\min}\right] \cdot \int_0^{t_E} \frac{C_{outlet}(t)}{C_{inlet}} dt \qquad (2.18)$$

The ratio of these capacities gives the 'useable fraction' of the column, which is often linked to a 'useable' length of bed to indicate the efficiency of the process [79]. To accurately assess the adsorption

capacity of a bed, the parameters of **equations 2.17 or 2.18** must be well defined and accurate. For example, the flowrate and inlet species concentration are assumed to be constant throughout the process, but sensors for monitoring these parameters may be necessary if a large amount of deviation is present. The process of adsorption or desorption within the packed bed will also lead to changes in the exit flowrate, in all cases except those where the fraction of adsorbable component in the feed during the breakthrough is very small (dilute gases, VOCs etc.). For example, a carbon capture process using a feed stream of 10% CO_2 would have a reduction in flowrate of up to 10% due to the CO_2 not travelling directly through the column and instead being adsorbed. Wilkins et al [80] suggest the use of a flowmeter calibrated for a series of adsorbate/ inert compositions to account for the changes in meter response with different gases and vapours. If the inlet to the bed contains a mixture of components, separate breakthrough curves can be plotted for each species, allowing for the quantitative determination of multicomponent adsorption capacities. However, this approach requires that the sensing element for a species is unaffected by the presence of other species or that it can independently measure the concentrations of multiple species simultaneously. For example, Heinen et al [81] measured the simultaneous adsorption of water and toluene onto activated charcoal by monitoring the outlet of the packed bed using gas chromatography.

One of the more important considerations for evaluating capacity in a BTC is the dead time, or dead volume of the process. This volume can include several terms: the distance between the gas delivery manifold and the adsorption column; the volume of the column not occupied by the packed-bed; the distance between the outlet of the column and the concentration sensors; and the response time of the sensors. Minimising this volume reduces the uncertainty in the inlet and outlet concentration profiles, and by extension the calculation of fixed-bed adsorption capacity. For example, if a CO_2 sensor is located 50 cm further down the line from the adsorption column, the time taken for the gas to travel that distance could be misinterpreted as the residence time of the species within the bed, and would lead to an overestimation in the adsorption capacity [80]. Therefore, dead volume measurements are required to accurately correct BTCs. These are typically carried out through ‘empty column’ experiments, where

the same total volume is present but without the solid bed itself [80], or using a non-interacting gas probe to be detected post-bed [82].

2.3.2. Adsorption kinetics and diffusion

The speed at which species are adsorbed by adsorbents, like adsorption capacity, can be measured relatively simply. For gravimetric systems, the change in mass of a sample as a function of time following a step change in adsorbate concentration will yield plots that allow for the quantification of adsorption kinetics. Similar profiles can in principle be generated in volumetric systems, by converting the change in pressure or concentration in the measurement chamber to a corresponding mass of species being adsorbed. Breakthrough curve analysis (BCA) data does not provide any direct quantitative measures of adsorption kinetics, although fixed-bed models used for assessing kinetic parameters do exist and will be discussed.

2.3.2.1. Adsorption kinetics models

The pseudo first order (PFO) and pseudo second order (PSO) models describe the rate of adsorption as being dependent on the difference between the adsorption capacity at time t (q_t), and the equilibrium capacity (q_e) [83]:

$$\frac{dq_t}{dt} = k(q_e - q_t)^n \tag{2.19}$$

Where k is the rate constant, and n is an integer of value 1 (PFO) or 2 (PSO). The value of k is often reported as a metric for the speed at which a material can adsorb a fluid species, although has been found to have some dependence on initial adsorbate concentration [84] and therefore can only compare materials which are exposed to identical adsorbate environments. The PFO and PSO carry several assumptions [85]: sorption only occurs on localised sites with no adsorbate-adsorbate interactions; a constant concentration of adsorbate in the fluid phase; the energy of adsorption is independent of surface coverage, and the maximum adsorption corresponds to a saturated monolayer, similar to the Langmuir model. While the fluid phase concentration can be kept constant using certain experimental tools, such as gravimetric adsorption apparatus, the other assumptions are material and concentration dependent.

For example, high concentrations of adsorbate interacting with a mesoporous material is likely to cause capillary condensation [86], rather than monolayer formation. For materials with hierarchical porosity, the adsorption sites in small, medium, and large pores are likely to be different, as shown by isosteric heat of adsorption profiles for activated charcoal [87]. An extensive study by Simonin [88] compared PFO and PSO for modelling adsorption kinetics from a wide range of experimental publications, with several interesting conclusions. First, the applicability of the two models are often determined by constructing linear forms of the models and comparing the goodness of fit for these points [89]:

$$PFO:\ \ln\big(q_e - q_t(t)\big) = \ln(q_e) - k_{PFO}t \tag{2.20}$$

$$PSO: \frac{t}{q_t(t)} = \frac{t}{q_e} + \frac{1}{k_{PSO}q_e^2} \tag{2.21}$$

However, it was found that in a significant number of studies, large amounts of the experimental data used in PSO plots were at, or close to, equilibrium, which makes little sense for a kinetics model which predicts the evolution of fractional uptake from 0 to 1. In addition, as q approaches q_e the value for t/q will be approximately equal to the gradient of t/q_e, leading to the points in this range being naturally well aligned. This leads to an overestimation in the accuracy of PSO in predicting kinetic profiles of adsorbate uptake.

To counter this issue, Simonin [88] recommends that non-linear regression be carried out to minimise the values of various error functions for the value of q for the two rate laws. In addition, to counteract the influence of near-equilibrium data, an upper limit for the fractional uptake was set at 0.85. This approach was applied to experimental adsorption data from over a dozen previous studies and found that PFO and PSO gave superior fits in ~33 and ~35 % of cases, and neither gave satisfactory fits in ~31 % of cases.

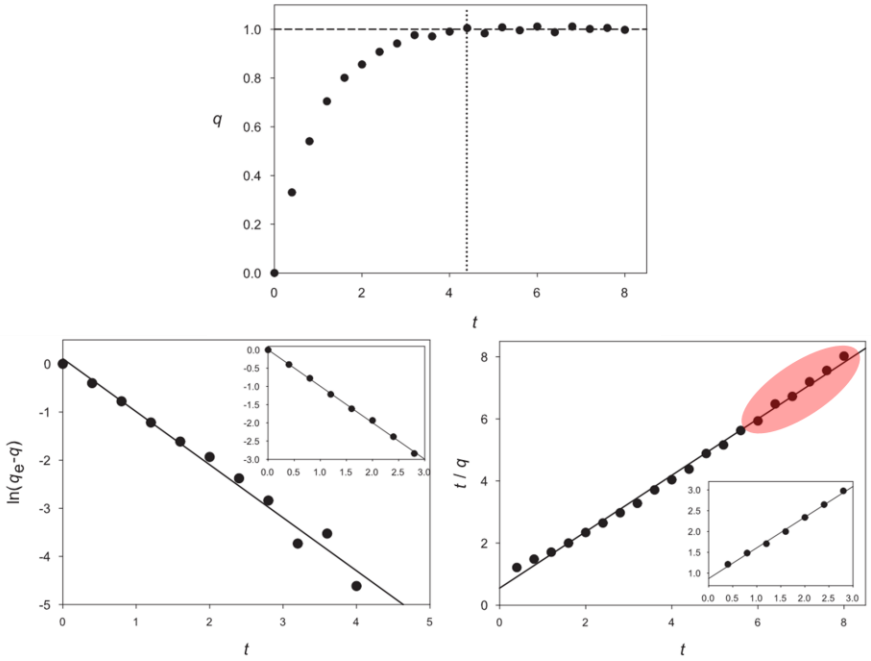


Figure 2.12: Illustration of bias towards pseudo second order model: example kinetic dataset (top); fitting using pseudo first order model (left); fitting using pseudo second order model (right), and naturally alignment of close-to equilibrium data and t/q(t) term of PSO (red region). Reproduced from work by Simonin [88] with permission.

2.3.2.2. Diffusion analysis based on sorption uptake

While adsorption kinetics are useful in determining the performance of an adsorbent, it is more common to study the diffusion of species into porous materials, as it can provide information about the nature of the adsorption process(es) itself. The starting point of any diffusion calculation starts with the definition of diffusivity by Fick [55]:

$$J = -D\frac{\delta C}{\delta z} \tag{2.22}$$

Where J is the molar flux of a fluid species, D is the diffusivity, and δC/δz is the concentration gradient. Diffusion in a porous crystalline material, such as a zeolite, has added complexity due to the multitude of kinetic processes occurring. A zeolite pellet will consist of many crystals, which have their own intrinsic diffusivity into their micropores. The spaces in between these crystals packed in the pellets,

and any defects within the crystals or pellets, will impart their own meso and microporosity, each of which will also have their own effective diffusivity.

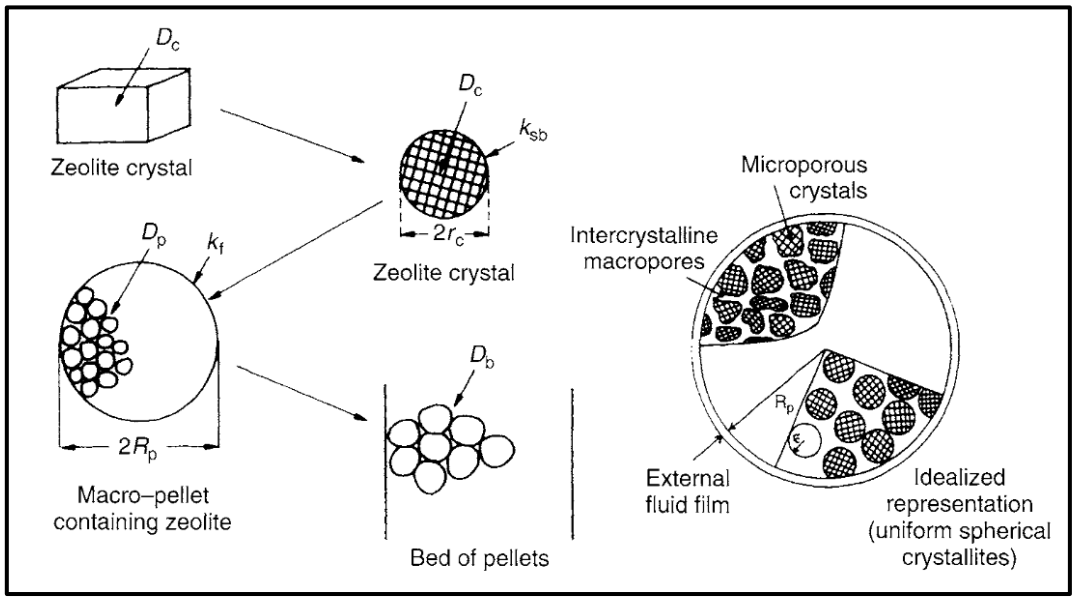


Figure 2.13: Illustration of diffusivities in adsorbent pellets composed of individual crystals, reproduced from work by Douglas M. Ruthven [55], with permission.

Simplifications are often required in order to describe diffusion kinetics in hierarchically porous media due to the contributions of micro- and macro-pores. For a spherical particle undergoing a step change in adsorbate concentration at its external surface, the approach to equilibrium, assuming diffusion controlled, can be expressed as [90]:

$$\frac{M_t}{M_\infty} = 1 - \frac{6}{\pi^2}\sum_{1}^{\infty}\frac{1}{n^2}\exp\left(\frac{-n^2 \cdot \pi^2 \cdot D \cdot t}{R^2}\right) \tag{2.23}$$

Where M/M_∞ is the fractional approach to equilibrium for the material, n is an integer, D is the diffusion coefficient, t is the time, and R is the radius of the sphere. For a crystal, R is the crystal radius and D is the crystal diffusivity. For a pellet consisting of several crystals, R is the pellet radius and D is the effective diffusivity in the macropores and is related to the pore diffusivity (D_P), particle porosity (ε_P), and dimensionless Henry's Law constant based on particle volume (K_{HL}):

$$D_e = \frac{\varepsilon_P \cdot D_P}{1 + (1 - \varepsilon_P) \cdot K_{HL}} \tag{2.24}$$

At short- and long-time asymptotes, the diffusivities can be calculated using the following expressions [55]:

$$Short\ time: \frac{M_t}{M_\infty} = \frac{6}{R}\sqrt{\frac{D \cdot t}{\pi}} \tag{2.25}$$

$$Long\ time: \frac{M_t}{M_\infty} = 1 - \frac{6}{\pi^2}\exp\left(\frac{-\pi^2 \cdot D \cdot t}{R^2}\right) \tag{2.26}$$

These equations have been applied to a number of non-crystalline materials as well, using gravimetric adsorption kinetics data, and are now used as a general solution for measuring diffusivity in powders containing spherical particles [91]. For the same system, but for a particle where the limiting step is surface mass transfer [55]:

$$\frac{M_t}{M_\infty} = 1 - \exp\left(\frac{-3 \cdot k_s \cdot t}{R}\right) \tag{2.27}$$

Where k_S is the surface mass transfer coefficient. Interestingly, equations 2.26 and 2.27 appear to be mathematically similar, albeit with the former depending on R to the power of negative two rather than negative 1 and will therefore likely result in similar, or identical, correlation coefficients when fitting the same dataset. These equations and calculation methods for diffusivity appear relatively simple, and the measurement of intracrystalline diffusion works well for slow diffusion processes (i.e. large crystals and/ or low diffusivity). However, when sorption rates are rapid, the uptake rate may be controlled by extra-crystalline diffusion through the interstitial spaces in the adsorbent pellets. This effect can be detected by changing the sample quantity or the state of the sample (e.g. fine grinding of the pellets to reduce the discrepancy in particle and crystallite size). In addition, the particle size or crystal size of the material needs to be well understood and quantified in order to accurately analyse the system's diffusion and calculate diffusivities or mass transfer coefficients.

2.3.2.3. Kinetic modelling in fixed-bed columns

Due to the nature of breakthrough curve analysis, the uptake kinetics of gas molecules cannot be directly measured. However, several methods exist for approximating the kinetics of the adsorption process using the maximum and outlet concentrations from the column, C_0 and C(t) respectively. The first is by fitting the experimental breakthrough curve with one of several adsorption models, one of the most common of which is the Thomas model, with the linear form below [92]:

$$\ln\left(\frac{C_0}{C(t)} - 1\right) = \frac{k_T \cdot q_0 \cdot M}{\dot{V}} - k_T \cdot C_0 \cdot t \tag{2.28}$$

Where k_T is the Thomas rate coefficient, q_0 is the equilibrium mass uptake, M is the mass of adsorbent, and $\dot{V}$ is the volumetric flowrate. This model describes plug flow behaviour in a fixed bed, assuming no axial dispersion, and is based on the Langmuir isotherm for equilibrium systems [76]. However, the model is used extensively in systems that do not follow the Langmuir equilibrium relationship and the values of q_0 and k_T are instead treated as empirical parameters.

The Yoon Nelson model [93] was developed as a relatively simple model, presuming the rate of decrease in probability of adsorption for each molecule is proportional to the probability of adsorbate adsorption and the probability of adsorbate breakthrough on the adsorbent. In other words, as the bed adsorbs more species and reaches closer to breakthrough, the probability for further adsorption decreases [94]. The linearised model is expressed as:

$$\ln\left(\frac{C(t)}{C_0 - C(t)}\right) = k_{YN} \cdot (t - \tau) \tag{2.29}$$

Where k_{YN} is the Yoon-Nelson rate coefficient, and τ is the time required for 50 % adsorbate breakthrough.

Bohart and Adams [95] proposed a model for column adsorption dynamics for chlorine on charcoal, predicting that equilibrium is not instantaneous and that the rate of adsorption is proportional to the remaining capacity of the adsorbent and the concentration of the adsorbate:

$$\ln\left(\frac{C_0}{C(t)}\right) = \frac{k_{BA} \cdot N_0 \cdot L}{u} - k_{BA} \cdot C_0 \cdot t \tag{2.30}$$

Where k_{BA} is the Bohart-Adams rate coefficient, N_0 is the adsorption capacity of the adsorbent bed per unit volume, L is the bed length, u is the superficial velocity. Despite being a century old, Bohart-Adams has been found by Chu to be mathematically equivalent to both Thomas and Yoon-Nelson models [92], as all three express the breakthrough curve in terms of a logistic equation of population growth. The study advises caution in using various simplifications of the Bohart-Adams model which may be unable to fit the sigmoidal shape of the breakthrough curves, and that the 'proper' version gives similar fitting quality to more modern fitting models.

$$Simplified\ expression: \frac{C(t)}{C_0} = \exp(bt - a) \tag{2.31}$$

$$Full\ expression: \frac{C(t)}{C_0} = \frac{1}{1 + \exp(a - bt)} \tag{2.32}$$

Where the terms for a and b vary depending on the use of Bohart-Adams, Yoon-Nelson, or Thomas models. To illustrate the importance of using the full expression, example datasets for these mathematical expressions **2.31** and **2.32** were plotted, giving the curves shown in **Figure 2.14**.

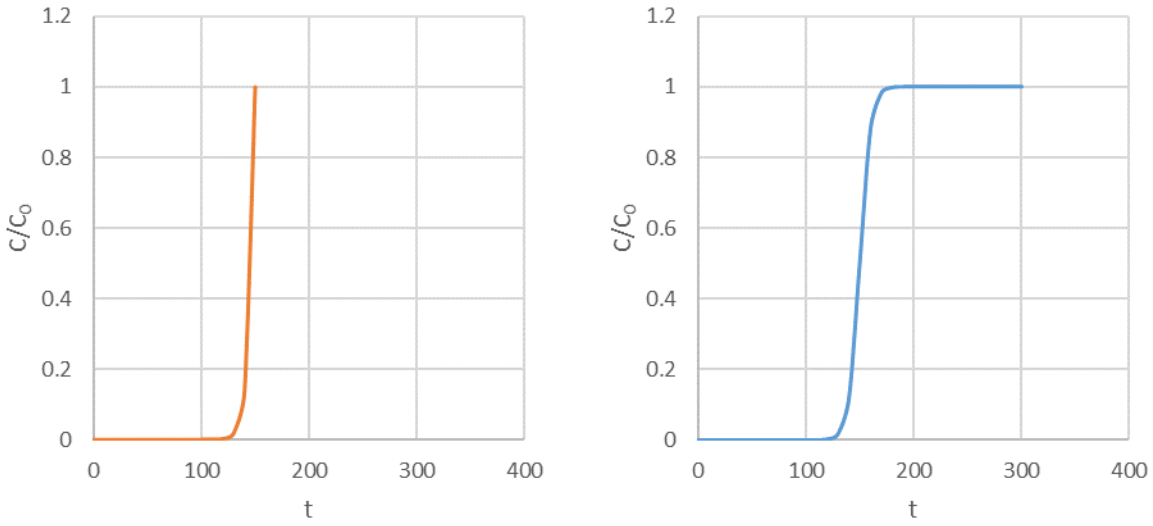


Figure 2.14: Example breakthrough curves plotted using simplified (left) and full (right) mathematical expressions of breakthrough models, equations 2.31 and 2.32 respectively.

2.3.3. Adsorption enthalpy

As mentioned previously, the enthalpy change associated with physical adsorption is negative and has a negative correlation with the temperature of the system. Determining the adsorption enthalpy gives an indication of how strong the fluid-solid interaction is. The isosteric, i.e. the same number of adsorbed molecules, heat of adsorption can be calculated using the partial pressures required at several temperatures to reach the same adsorption capacity, or loading.

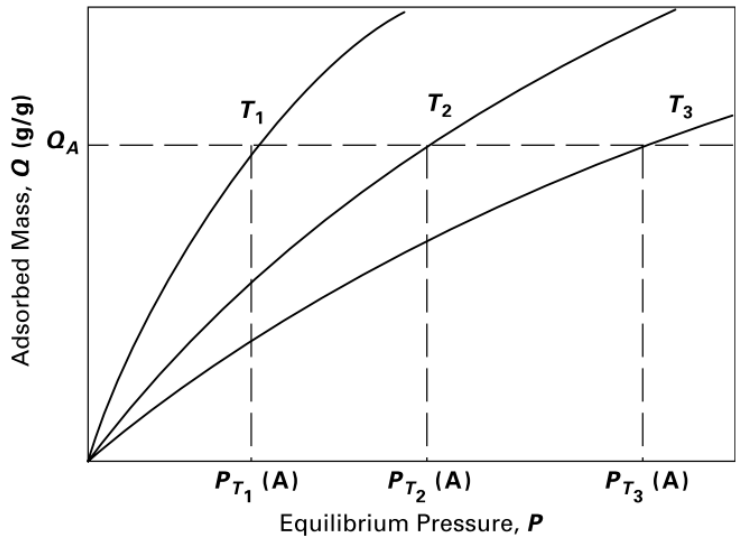


Figure 2.15: Illustration of the temperature dependence of the required pressure to reach a fixed adsorption capacity. Reproduced from the book 'Partition and Adsorption of Organic Contaminants in Environmental Systems' by Cary T. Chiou [26], with permission.

This method is based on the Clausius-Clapeyron equation [96], which expresses the isosteric heat of adsorption as a function of capacity or loading:

$$\ln\left(\frac{P_2}{P_1}\right) = \frac{\Delta H_{ads}(q)}{R}\left(\frac{1}{T_1} - \frac{1}{T_2}\right) \tag{2.33}$$

Where, for a fixed loading q, P_x is the required pressure or concentration of adsorbate when the system has temperature T_x, where x = 1 or 2. While calculating this constant can technically be carried out experimentally by varying temperature and pressure while maintaining a constant mass, it is generally

easier to use isotherm fitting models to determine the relationship between pressure and loading for a series of experimentally generated isotherms. For example, using the Langmuir-Freudlich isotherm [96] the partial pressure can be expressed as:

$$q_{LF} = \frac{q_{m,LF} \cdot K_{LF} \cdot P^{\frac{1}{n}}}{1 + K_{LF} \cdot P^{\frac{1}{n}}} \tag{2.34}$$

$$P(q) = \sqrt[\frac{1}{n}]{\frac{q_{LF}}{q_{m,LF} \cdot K_{LF} - q_{,LF} \cdot K_{LF}}} \tag{2.35}$$

Where q_{LF} is the predicted loading, $q_{m,LF}$ is the Langmuir-Freundlich maximal loading, K_{LF} is the affinity constant, and 1/n is the adsorption heterogeneity constant. For a fixed loading, plotting the natural log of pressure against the reciprocal of absolute temperature, the product of the plot's gradient and the molar gas constant will give the isosteric heat of adsorption. These heats of adsorption can be used to compare the readiness for adsorbents to interact with a species [97]- the greater the value of ΔH_{ads}, the stronger the interaction. This value can be calculated at multiple loadings to determine how the strength of interaction varies as more molecules occupy the surface. Typically, this trend follows an initially higher value before decreasing towards an enthalpy value equal to the heat of vaporisation. The higher energy sites are filled at lower coverages corresponding to lower pressures or concentrations, such as those in micropores [98].

2.3.4. Selectivity

The adsorption capacity of a species has been defined earlier in this section. In cases where multiple adsorbate species are present, they will compete for the limited number of adsorption sites within the material. Adsorption selectivity is the propensity for an adsorbent to interact with one adsorbate species over another and is an important parameter when assessing a material's chemistry, as well as its adsorption performance in realistic conditions. For example, water vapour molecules are omnipresent and can be found in every industrial adsorption process worldwide, and are known to have a profound impact on the efficiency of porous adsorbents [99]. In the case of VOCs, water vapour exists at a

concentration several orders of magnitude greater than VOCs [1] and, due to water's hydrogen bonding interactivity, has sufficient ability to displace other species [99].

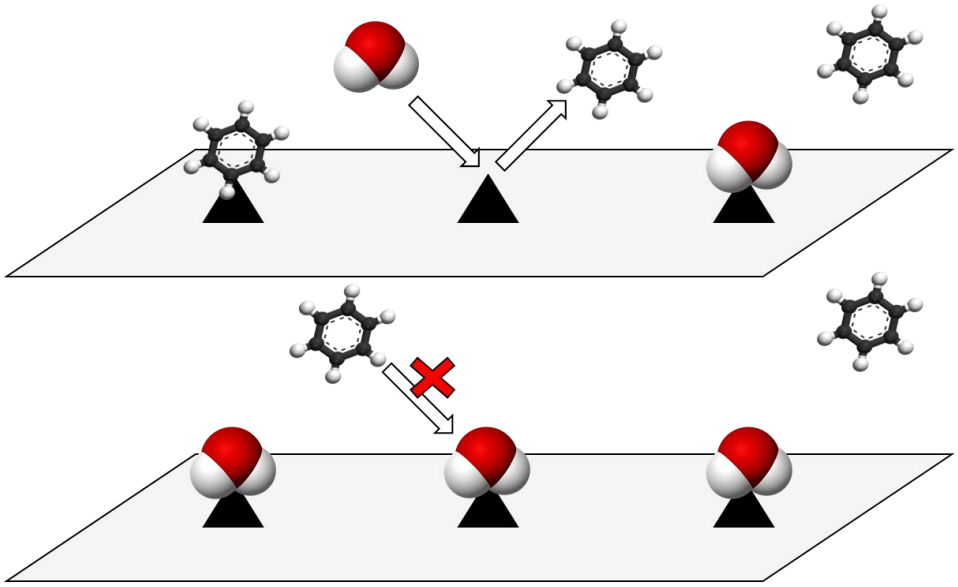


Figure 2.16: Illustration of adsorption competition on a hydrophilic surface: displacement of adsorbed benzene molecules by water molecules (top); and inability of benzene molecules to displace adsorbed water molecules (bottom).

Adsorption selectivity is a broadly used term and can be measured in several ways for VOC adsorption systems. The first and simplest approach uses single-component adsorption data to derive a selectivity criterion based on the adsorption capacities of two different adsorbates. This method has been used for determining static 'hydrophobicity indexes' by Halasz et al [100] who compared the adsorption of n-hexane and water on various zeolite adsorbents. Another approach uses co-adsorption measurements involving the pre-adsorption of one component before adsorbing the other, allowing equilibration between each step. This approach has been used for assessing octane-water selectivity by Fletcher et al [101] using combined gravimetric-spectrometric methods. The method of 'pre-exposure' gives a clear advantage to the first species introduced to the material, and likely gives a better indication of industrial adsorption performance rather than fundamental selectivity. One of the most popular methods of determining selectivity is directly through multicomponent dynamic adsorption experiments, such as

breakthrough curve (BTC) analysis. By analysing the BTCs of each component when the packed bed is exposed to a multicomponent inlet gas, the real capacities of each individual species can be determined, providing the sensor can detect each species' concentration independently. This process has been carried out for systems with chemistry-based selectivity, such as VOC- water competition in metal organic frameworks [102], and size-based selectivity such as the selective adsorption of hexane isomers by zeolite beta [78].

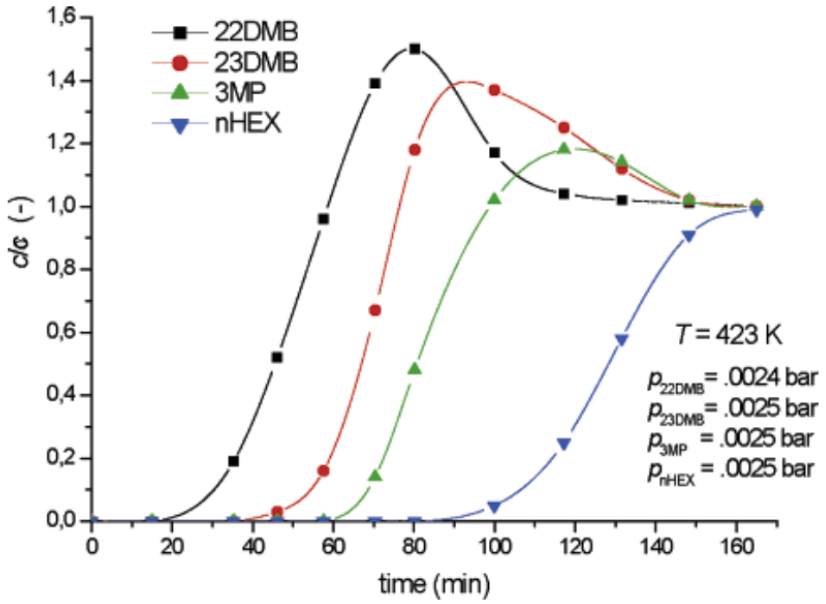


Figure 2.17: Multicomponent breakthrough curves of hexane isomers on zeolite beta pellets, reproduced from work by Bárcia et al [78], with permission.

For multicomponent adsorption where one species is preferentially adsorbed over the other, displacement of the less preferential species can occur. As shown in **Figure 2.17**, n-hexane is adsorbed preferentially over its branched isotopes, leading to the other species being detected at concentrations higher than the inlet due to displacement. The quantity of a species displaced can be calculated by integrating the area between the curve above the line of $C/C_0 = 1$, which will then need to be subtracted from the area below the line to find the 'actual' adsorbed quantity. This analysis allows for quantitative assessment of the selectivity of a material for a species when exposed to theoretically any mixture of gases or vapours.

2.4. Industrial porous materials

While a variety of porous materials have been tested for their ability to adsorb or remove gas phase compounds, three classes of industrial adsorbents are ubiquitous in these applications: zeolites, activated carbons, and porous silicas.

2.4.1. Zeolite structure

Zeolites are a class of aluminosilicate minerals with well-defined aperture sizes and porosity. The primary 'building blocks' of zeolites are tetrahedrons of silicon or aluminium cations bonded to 4 oxygen anions, with each oxygen ion being shared by two metal cations [103]. These building blocks can then form secondary units, such as 4-12 member rings, and more complicated composite building units, the final number and orientation of which determine the final crystal structure of the zeolite. The resultant three-dimensional framework of SiO_2 and AlO_2, due to the latter's valency of -1, has a net negative charge often offset by the inclusion of extra-framework cations such as K^+, Na^+, and Ca^{2+} [104]. These ions are mobile, as they are bound to the external surface of the zeolite by weaker, electrostatic interactions [105]. Diagrammatic representations of these building blocks and structures are shown in **Figure 2.18**. Over 150 zeolites have been synthesised over the years due to the variety of configurations that these building blocks can have [106], the most ubiquitous forms of which are types A, X, Y and ZSM-5 [106].

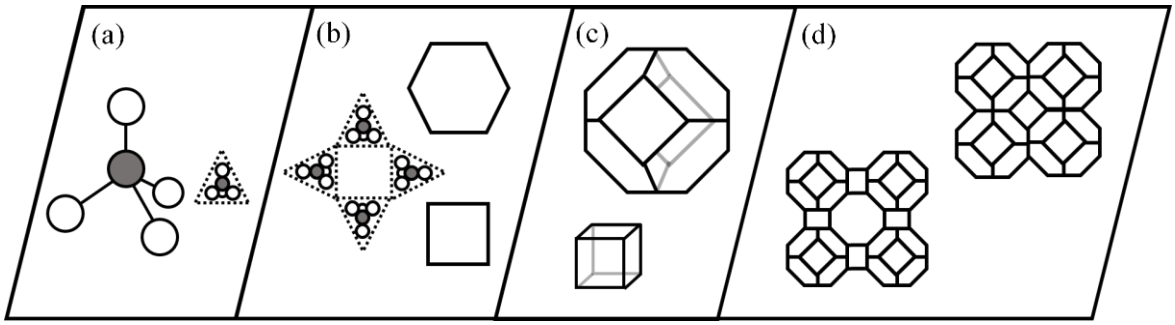


Figure 2.18: Examples of zeolite structure: (a) primary and (b) secondary building units (SBUs), the latter showing 4- and 6-ring; (c) 3-dimensional sodalite building units; and (d) 3-dimensional A-type (bottom) and sodalite (top) zeolite cages.

2.4.1.1. Zeolite families

Zeolite A, Linde Type A, or LTA zeolites consist of 8 sodalite units linked by cuboids, with α and β 'cages' with diameters based on the cations present during synthesis. The most common form, Type 4A contains sodium ions and has an aperture of '4A' or 4 Å (Angstroms) [107]. Zeolite A is a synthetic zeolite produced under low temperature, pressure, and alkaline conditions by reaction of alkali metal aluminosilicate gels. Its low pore size provides LTA zeolites with molecular sieving properties, making them the most popular option for detergents as the sodium ions can be exchanged with the magnesium and calcium ions contained in hard water [108].

Faujasite zeolites X and Y have similar structures to LTA, consisting of sodalite cages- but in the former materials the cages are arranged in the same way as carbon atoms in a diamond via hexagonal prisms, or double 6-rings [109]. This structure leads to apertures of 8 Å, and supercages of approximately 12 Å, which allow encapsulation of much larger molecules such as volatile fragrances [110]. The difference between zeolite X and Y is the ratio of silica to alumina atoms within the framework, with X having Si:Al ratios lower than 3, while Y has ratios of 3 and higher [109], [111].

ZSM-5, like LTA, is another synthetic zeolite prepared in alkali conditions at elevated temperatures using alumina and silica sources alongside directing agents to ensure the correct structure is obtained. ZSM-5 has an MFI (Mobil Five) framework structure consisting of linked pentasil units linked by oxygen bridges to form sheets, which are in tern connected via additional bridges [112]. This results in a 3D structure with 10-ring channels with straight and zigzag geometry formed parallel and perpendicular to the corrugations respectively with sizes between 5 and 6 Å [113]. These 10-ring channels provide the material with shape selectivity in adsorption processes, making ZSM-5 zeolites popular in catalytic petrochemical applications such as hydrocarbon isomerisation and alkylation [114].

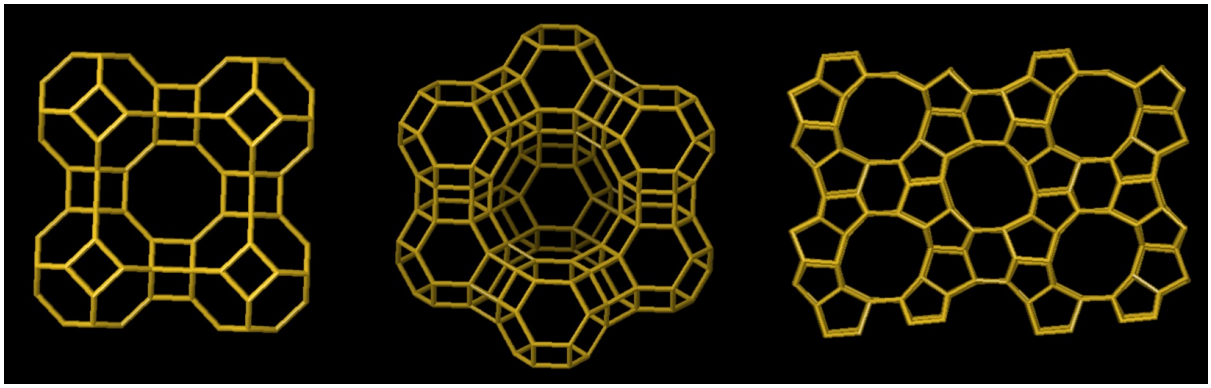


Figure 2.19: Zeolite framework structures, showing metal positions and bridges of LTA (left), FAU (middle), and MFI (right). Collected from the IZA-Structure Database of Zeolite Structures [115], with permission.

2.4.1.2. Silica: alumina ratio and its influence on zeolite chemistry and structure

An important property of zeolites is the ratio of silica to alumina molecules within its framework, the Si:Al ratio. A zeolite's hydrophobicity is dictated largely by the content of alumina within its framework, with greater alumina content resulting in greater affinity towards polar molecules such as water. Early work by Chen [116] found that the adsorption of water molecules in zeolites involves the specific (polar) interaction between the water molecule and the hydrophilic centres, including silanol groups or cations associated with coordinated aluminium. Chen found that the adsorption capacity for water increased for lower ratios of SiO_2 to Al_2O_3, while the capacity for cyclohexane reached a plateau at ratios exceeding 40. This analysis implies that modifying the Si:Al ratio confers two changes in the material that reduce adsorption capacity: a decrease in surface area or micropore volume [117]; and a decrease in the overall hydrophilicity of the surface and pores of the material, which has also been studied experimentally in ZSM-5 type zeolites [118], [119]. This Si:Al ratio can be altered by dealumination or desilication processes where the concentration of the two ions is reduced [44], either in vapour phase by thermal treatment or steaming [120], or in liquid phase by hydrothermal treatment [121], acid [121], or alkali leaching [122]. These treatments have been found to generate mesopores within the zeolite due to the partial collapse of the microporous structure [117] and, for dealumination,

a reduction in crystallinity [123]. One possible mechanism for this process is shown in **Figure 2.20**, showing the migration of silicon atoms and the formation of amorphous silica-alumina, and extra-framework aluminium. NMR studies by Coster et al [124] used the chemisorption of isotopically enriched ammonia to probe the surface active sites of high-silica zeolite Y, among other zeolites and γ-alumina. This procedure hypothesised that γ-alumina contained two Lewis acid sites, one tetrahedral and one pentagonal, and that the same kinds of sites exist in the non-framework, or extra-framework aluminium of the dealuminated faujasite. On the other hand, the framework aluminium was hypothesised to be a Bronsted acid site. Unlike Lewis acids, which are defined due to their ability to accept electrons, Bronsted acids act as donors of protons. Regardless, both forms of alumina contribute to the acidity, and by extension hydrophilicity of the zeolite, even in high-silica forms.

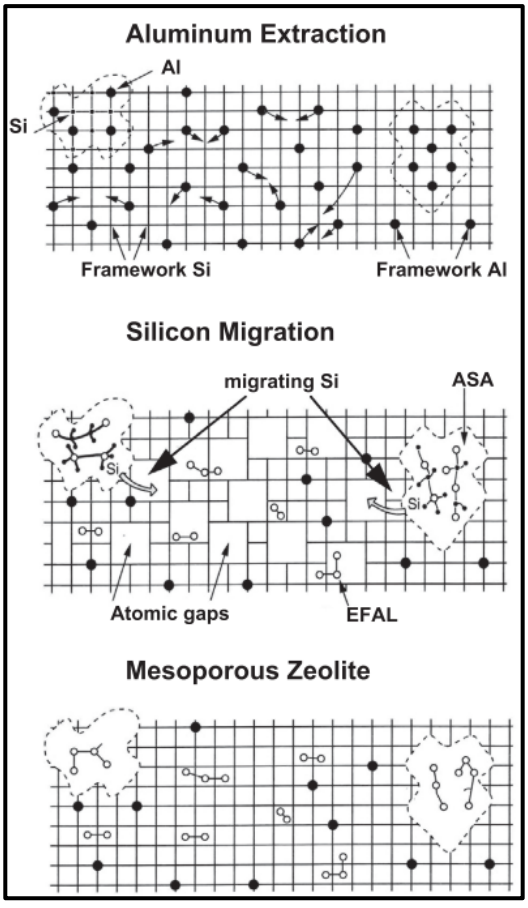


Figure 2.20: Schematic showing mechanism of mesopore formation during dealumination, reproduced from work by Silaghi et al [44] with permission. The terms ASA and EFAL refer to 'amorphous silica-alumina' and 'extra-framework aluminium' respectively.

However, the generation of mesopores is often viewed as beneficial as it has been found to improve molecular transport properties within the material [125]. In some research, desilication is used primarily as a post-synthetic method of introducing mesoporosity into zeolites [122]. Unlike other materials in this review, the micropore size distribution of zeolites is dictated primarily by the arrangement of building blocks, while the synthesis conditions or post-synthetic modification may alter the pore volume or surface area available within the final material.

2.4.2. Activated carbons

Activated carbon or charcoal (AC) is produced from the preparation, typically thermal or chemical activation, of carbon-rich materials to produce an amorphous, highly porous carbonaceous material. Precursors for these carbons are commonly from natural sources such as biomass residues [126] or coal, the latter of which have been found to produce ACs with excellent BET surface areas in the range of 1200-1800 m^2/g [127]. The first preparation step is the formation of charcoal by pyrolysis at high temperatures, removing volatile components and introducing small amounts of porosity. The second preparation step is the activation of the charcoal, the two most conventional methods for which are: physical activation, where the precursor is carbonised at high temperature under an inert atmosphere, followed by exposure to light gases or vapour (gasification) [128]; and chemical activation, where the precursor is mixed with a chemical compound before heating at high temperature in an inert atmosphere Following activation, the final activated product is an amorphous, carbonaceous material typically containing a network of randomly sized and shaped pores.

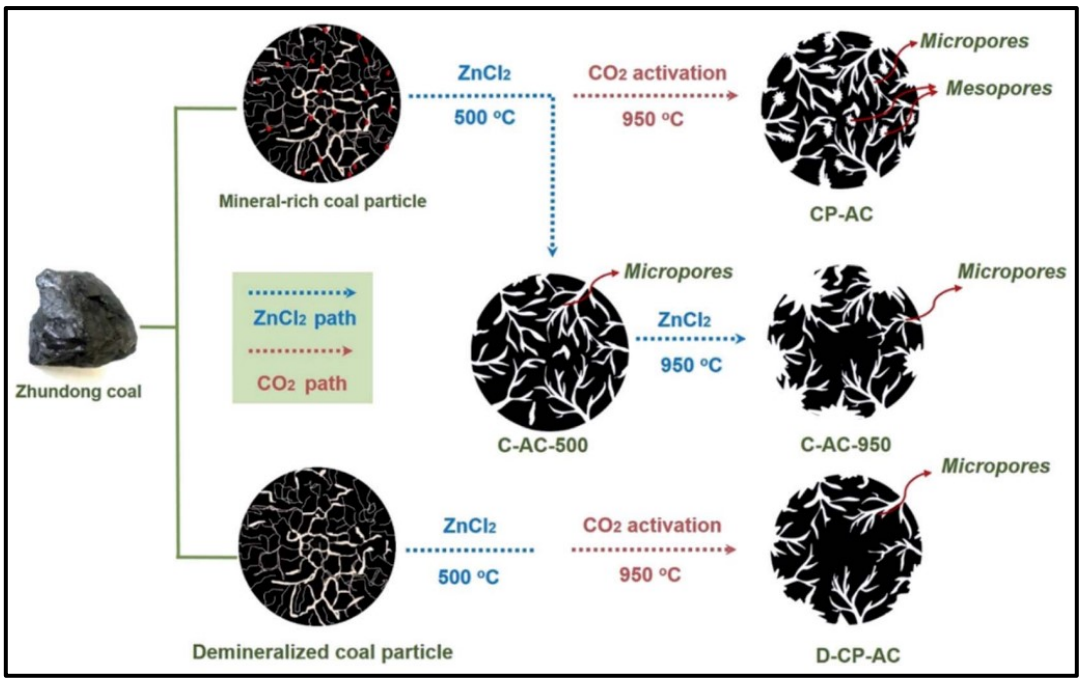


Figure 2.21: Schematic of charcoal activation using both chemical and gasification methods, reproduced from work by Li et al [129] under Creative Commons licensing.

Unlike zeolites, which have fixed aperture sizes based on the orientation of their building blocks, the distribution of pores within ACs is heterogenous and influenced by the activation conditions. Falco et al [130] found that, regardless of the precursor material, microporous AC could be produced by carefully controlling the hydrothermal carbonisation temperature- samples activated at 240 ºC had higher surface areas and pore volumes, while samples activated at 280 ºC had narrower pores. Another study on porous carbons by Okhovat et al [68] found increasing the impregnation ratio of chemical agents KOH or $ZnCl_2$ resulted in larger pore sizes and mesopore volumes. While AC is predominantly non-polar due to the prevalence of methyl groups on its surface, it often contains a number of functional groups which afford it some interactivity with polar molecules, the most common acidic and basic groups including carboxyls, hydroxyls, carbonyls, quinones, pyrones, and pyridines [131].

2.4.3. Porous silicas

The most ubiquitous form of porous silica is silica gel, which is used primarily as a desiccant for liquid or vapour phase water [64]. Silica gels are prepared by sol-gel polymerisation of silicon alkoxides

which, when hydrolysed in the presence of a solvent, produces silanols (or Si-OH groups) which then form longer chains via condensation reactions and bridging siloxane (Si-O-Si) groups. When sufficient siloxane groups form, they respond cooperatively as a colloidal solution which, over time, form a 3-dimensional network of condensed silica species which, following gelation, increases in viscosity to form a solid object in the shape of the mould. Depending on the method of solvent phase removal from the pore network, an aerogel or xerogel is formed [132].

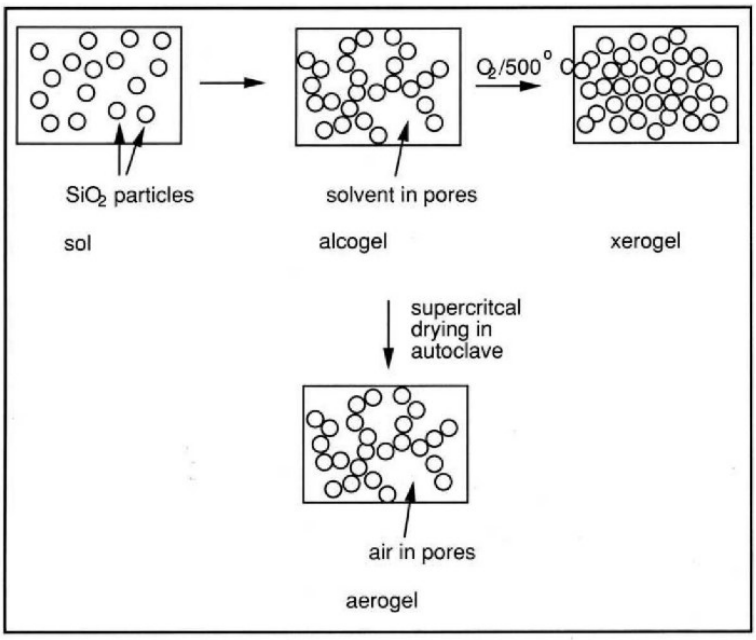


Figure 2.22: Illustration of silica xero- and aero-gel formation from a sol-gel solution, reproduced from work by Buckley and Greenblatt [132] with permission.

2.5. Metal-organic frameworks

The term ‘metal-organic framework’, often shortened to ‘MOF’, was coined by Yaghi et al [133], with a layered Co-based trimesate that was able to reversibly adsorb solvent molecules, even showing selectivity towards aromatics over linear compounds. The first example of room temperature gas sorption in 3D MOFs was by Kondo et al in 1997 [134], showing the ability of these synthetic frameworks to interact with light gases including nitrogen, oxygen, and methane. Since their discovery,

thousands of studies have been carried out on synthesising and applying metal-organic frameworks to gas adsorption applications [135].

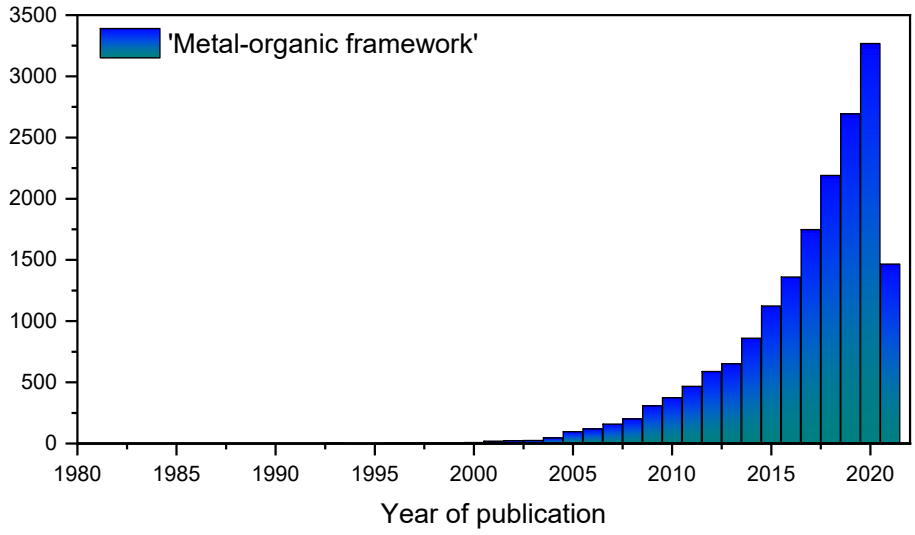


Figure 2.23: Number of publications using the term 'Metal-organic framework', found using Pubmed. Date of search: 17th May 2021.

2.5.1. Structural flexibility

The nature of metal-linker bonding within many MOFs affords them a certain degree of flexibility within their structure, leading to their definition as a third-generation 'soft porous crystal' [136]. Soft porous crystals are defined as porous solids possessing a structure which is both highly ordered and transformable, and are generally described by three categories: first-generation, where porosity collapses irreversibly upon guest molecule removal (i.e. no permanent porosity); second-generation, in which the framework of the material is stable and robust, analogous to zeolites; and third generation, where the porous framework responds reversible to external chemical or physical stimuli. Certain MOFs, often termed 'breathing' MOFs, exhibit a drastic change in unit cell volume when exposed to certain stimuli, resulting in changes to pore size and volume. The two most common transitions are between closed-to-open pore, and between narrow-to-large pore forms, although both transitions can be categorised by the mechanism by which the unit cell volume changes:

1. Swelling, characterised by a gradual enlargement of the unit cell volume with no change in unit cell shape, the extent of which depends on the nature of the guest molecule. For example, work by Mellot-Draznieks et al. [137] found the unit cell volume of evacuated fumaric acid-based MIL-88 increased from 1135 $Å^3$ to 1840, 1970, 2090 and 2110 $Å^3$ following immersion in liquid n-butanol, ethanol, methanol, and water respectively. A similar effect to swelling can also occur via thermal expansion and shrinking, which do not require the presence of guest molecules.
2. Breathing, in which unit cell volume changes are accompanied by changes in the characteristic distances and angles of the unit cell. This results in the framework structure distorting and a corresponding increase or decrease in the accessible aperture size.
3. Linker rotation, defined as a continuous transition where the special alignment of a linker molecule changes by turning around a rotational axis. This rotation can be tuned to occur in the presence of guest molecules with certain chemistry, creating selectively 'gating' pore apertures. An example of this effect was demonstrated by Seo et al [138] using a cadmium-based coordination polymer containing pyridyl linkers capable of interacting with each other via -OH groups. Polar molecules, such as water and methanol, could interact with the metal centres of the framework, resulting in selective adsorption.
4. Subnetwork displacement, a phenomenon only applicable to systems with individual frameworks weakly linked via van der Waals interactions. These separate frameworks can drift and relocate about each other, resulting in flexibility via catenation or layer stacking.

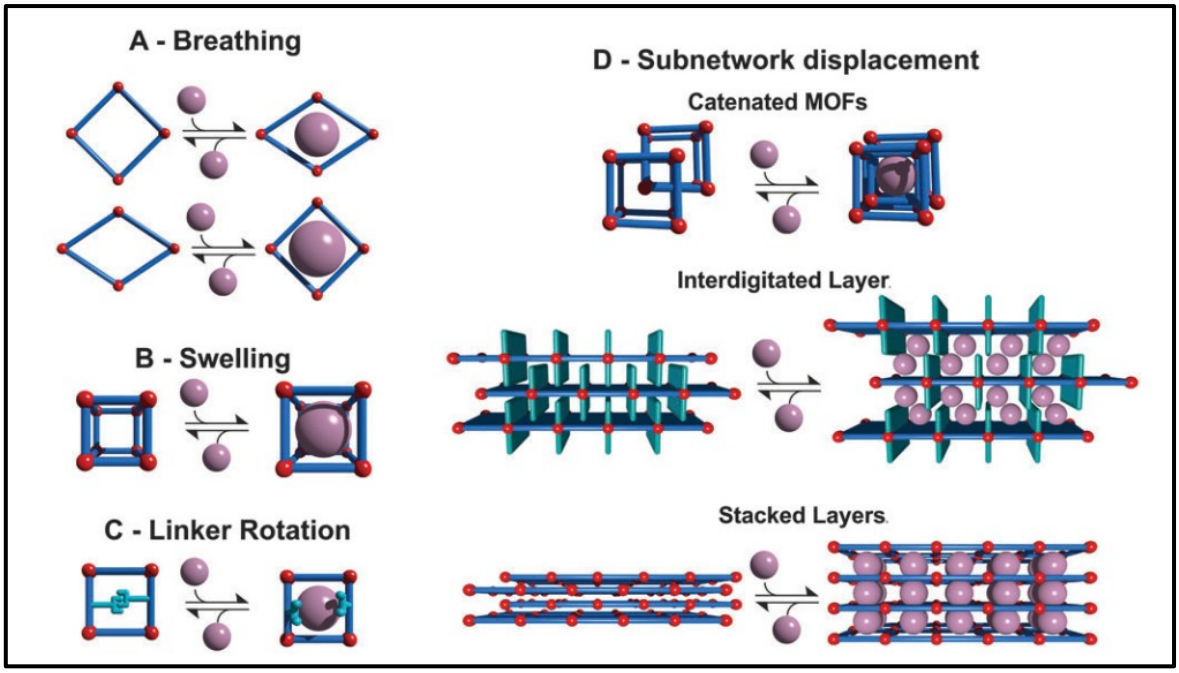


Figure 2.24: Mechanisms of framework flexibility due to inclusion or displacement of guest molecules, reproduced from work by Schneemann et al [139] under Creative Commons licensing.

This flexibility has been experimentally proven using several techniques. Work by Mellot-Draznieks et al. on MIL-88 [137] collected powder X-ray diffraction data for the MOF under different conditions. As-synthesised MIL-88 possessed three low-angle peaks at 2θ values of approximately 9º, 11º, and 12º. With exposure to solvents, the peaks at 9º and 11º shifted to lower angles, while the peak at 12º shifted to higher angles, with the extent of these changes increasing with smaller, more polar solvents. These peak shifts were used to calculate the changes in unit cell parameters and the effect of guest molecules on unit cell volume. In addition to solvents increasing the unit cell volume, high temperature drying resulted in the unit cell volume decreasing compared to samples dried at room temperature. Similar work by Kondo et al [140] found the (200) peaks of ELM-13, associated with the stacking direction, shifted to lower angles upon adsorbing acetone vapour, indicating an expansion in the interlayer spacing. On the other hand, the (020) and (021) peaks did not show any shift upon adsorption, meaning the 2D layer structure was likely negligibly affected. Raman spectroscopy has also been used in identifying changes in bond configurations in flexible porous solids [141], although these are typically

combined with diffraction techniques to confirm changes in unit cell parameters. The stretching of framework windows due to the presence of a certain adsorbate driving force can result in adsorption of molecules that would be considered too large to enter a rigid window of the same size [142]. These features make MOFs an interesting candidate for highly selective adsorbents, depending on their framework's response to certain stimuli.

2.5.2. Zeolitic imidazolate frameworks

Zeolitic imidazolate frameworks, or 'ZIFs', are a subcategory of metal-organic frameworks in which the metal ions are linked via imidazolate bridges. The angle of 145º formed by the metal centres and linker molecules is analogous to the bridging angle of Si-O-Si bonds in zeolites, giving ZIFs a zeolite-like topology [143].

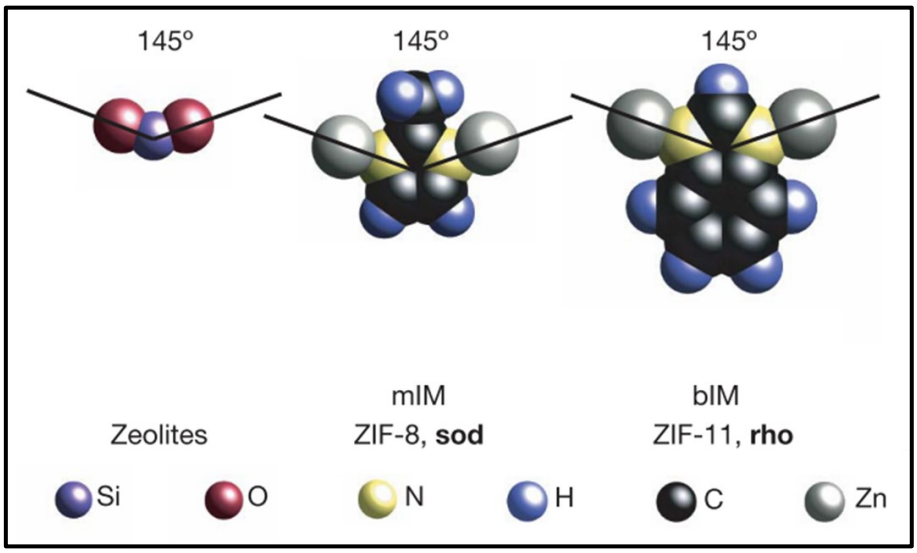


Figure 2.25: Illustration of the bridging angle in zeolites (left), sodalite-like ZIF-8 (middle), and RHO-like ZIF-11 (right), the latter two synthesised using 2-methylimidazole and benzimidazole, respectively. Adapted from work by Wang et al [144] with permission.

Similar to zeolites, ZIFs typically have a homogeneous micropore size distribution, dictated by their building blocks and synthesis conditions, although they have been shown to possess some degree of flexibility in their framework. This allows the ingress of fluid molecules larger than what might be

expected from theoretical calculations or crystalline aperture data [145]. Over 100 ZIF structures have been discovered over the years [146], with a wide range of surface areas: from sub-50 m^2/g [147] to several thousand m^2/g [144], [148]. Their high surface areas and microporosity make many ZIFs popular for gas-phase applications including adsorption [144], [145] and catalysis [149]. The general structural formula for a ZIF is TL_2 where T is a tetrahedral divalent metal ion (such as Zn^{2+} or Co^{2+}) and L is an imidazolate species [146]. Several factors influence the final structure of the ZIF: the imidazolate, due to their chemistry and steric profile; the metal ion, due to its size, coordination bond strength and electron configurations; and the reaction conditions, with factors such as temperature and pH resulting in different chemical reaction pathways.

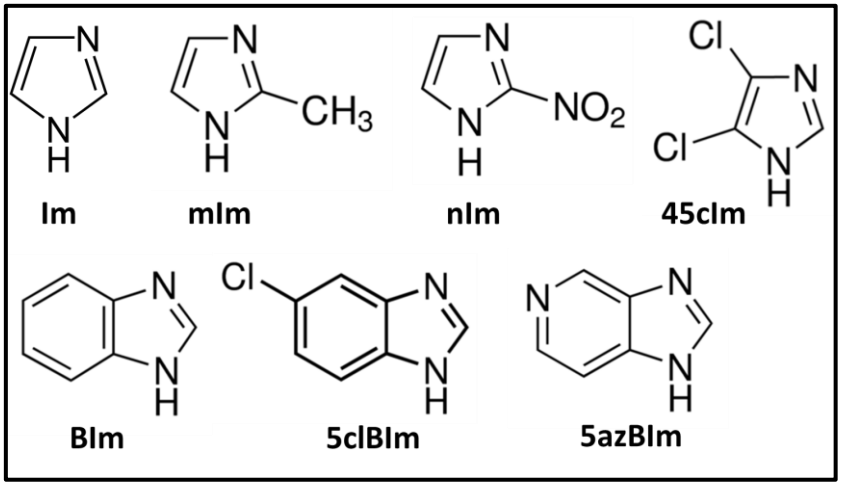


Figure 2.26: Examples of imidazolate linkers used in the synthesis of zeolitic imidazole frameworks

2.5.2.1. ZIF-8

The most ubiquitous metal ions for synthesis of ZIFs are Zn, followed by Co and Cd, with ZIF-8 being the most commonly researched [148]. ZIF-8 consists of zinc ions linked by 2-methylimidazole (mIm) molecules, with the bulky methyl groups within the linker resulting in a sodalite-like topology. Similar to sodalite and faujasite zeolites, ZIF-8 has two framework apertures, with the smaller leading into the larger [150]. The size of these apertures depends on the method of characterisation due to their tendency to expand upon gas intrusion via linker rotation [151], but have been determined to be approximately 3.4 and 11.6 Å based on the van der Waals radii of the constituent atoms [147] and derivations from the

planar spacing using X-ray diffraction [145]. The flexibility of ZIF-8's pores has been confirmed via X-ray diffraction methods and vapour adsorption by Ueda et al [151], who found that bulkier molecules such as carbon tetrachloride and benzene shifted ZIF-8's (110) plane to lower angles, indicating an increase in unit cell volume (i.e. expansion of the aperture)- as shown in **Figure 2.27**. This, combined with significantly reduced diffusion coefficients, allowed for adsorption activation energies to be plotted as a function of adsorbate kinetic diameter- concluding that xylene molecules had a significantly increased driving forces required for adsorption compared to smaller aromatics.

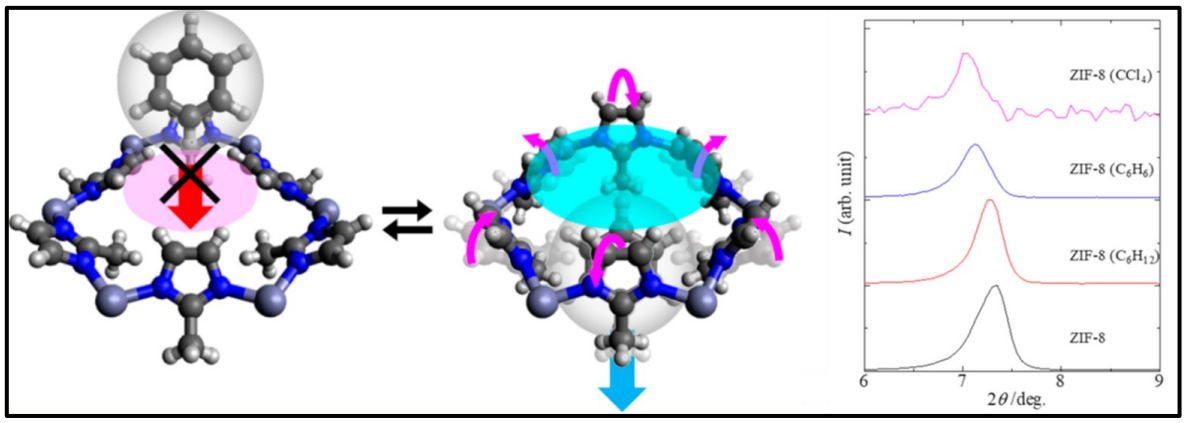


Figure 2.27: Schematic of ZIF-8 flexibility via linker rotation (left) and shift in low-angle XRD peak (right) upon exposure to bulky molecule. Reproduced from work by Ueda et al [151] under Creative Commons licensing.

However, the so-called 'limiting aperture' for ZIF-8 in terms of its adsorption of fluid molecules has been debated in multiple publications, but it is generally accepted that the diffusion of vapour-phase aromatics is noticeably lower than that of linear aliphatics [145], with the latter being found to be selectively adsorbed over branched isomers of the same carbon number [150]. In addition to its ability to selectively adsorb molecules based on their kinetic diameter, the methyl groups in ZIF-8's framework leads to low capacity for water vapour, and a Type V isotherm when exposed to alcohol [145] vapours, similar to high-silica zeolite Y [100].

Due to its high surface area, low pore size, and ability to be synthesised at room temperature using solvothermal conditions, ZIF-8 is commonly studied in adsorption and catalysis applications, as well as its cousin ZIF-67, which is synthesised using cobalt as a metal source in place of zinc. This change in metal has been found to result in changes to the material properties, with one study [152] finding the stiffer bonding between Co and adjacent N atoms resulted in lower swelling amplitude than that of ZIF-8, which may affect its kinetic-based selectivity. ZIF-67 has also been found to have improved catalytic ability over ZIF-8 in reactions such as the cycloaddition of CO_2 to epichlorohydrin [153]. However, ZIF-67 has been found to be unstable in aqueous conditions, with hydrolysis occurring due to the breaking of weak cobalt-imidazolate bonds [154], resulting in losses in crystallinity. Despite this instability, ZIF-67 exposed to liquid water for prolonged periods has still been found to possess a high capacity for CO_2 [153], meaning the surface area and porosity of the material may only be partially impacted by the hydrolysis reaction.

2.5.3. Structured and monolithic MOFs

Whilst many particulate adsorbents possess good molecular adsorption kinetics [155], several operational difficulties exist when integrating fine particulates into adsorption processes including large pressure drops in adsorbent packed columns as well as challenges with adsorbent recovery and recycling. Structured monolithic adsorbents with their intrinsically larger and better defined physical dimensions, have several advantages including greater mechanical stability, reduced pressure drop, higher heat transfer, and higher volumetric efficiency [156]. The most common methods of creating structured adsorbents is through compaction of particulate adsorbents. For any affective compaction process, the aim is to reduce the void volume between the grains of the powder, without destroying the microporous structure of the active adsorbent, such as a zeolite or MOF. For MOFs, the point at which mechanical structure collapse occurs depends on the nature of the metal-linker bonds and its subsequent rigidity. For example, Bambalaza et al [157] studied the hydraulic compaction of UiO-66 and found that even at the highest applied pressure of 665 MPa the BET surface area of the final material only decreased from 1737 to 1707 m^2/g compared to the powder and, as a result of the density increasing almost threefold, the pelletized UiO-66 had a substantially increased volumetric hydrogen capacity. On

the other hand, compaction of HKUST-1 using only 70 MPa resulted in a material with approximately 50% lower BET surface area [158]. UiO-66 is considered one of the most 'rigid' MOFs due to its high degree of coordination between zirconium secondary building units (SBUs) and organic linkers, totalling twelve coordination bonds per Zr cluster, whereas the SBUs in HKUST-1 are coordinated by one water molecule and four oxygens via organic linkers, resulting in the latter possessing a shear modulus an entire order of magnitude lower [159]. Another method for producing macro-scale adsorbents is combining the active adsorbent with a binder or monolithic support structure. The addition of binding materials is commonplace for zeolite adsorbents, with compounds such as clay and alumina, although the impact these binders have on porosity can be variable. Charkhi et al [160] found that the addition of bentonite clay to NaY zeolite led to a reduction in its BET surface area and strontium ion removal efficiency, with these quantities decreasing more as binder content increased, while the mechanical stability of the 2:3 binder: zeolite material was found to be almost 1200% higher than that of the binder-free material. Similar work on zeolite beta [161] found the addition of 30 wt% bentonite binder reduced the specific surface area from 454 m^2/g, compared to 681 m^2/g for the powdered zeolite.

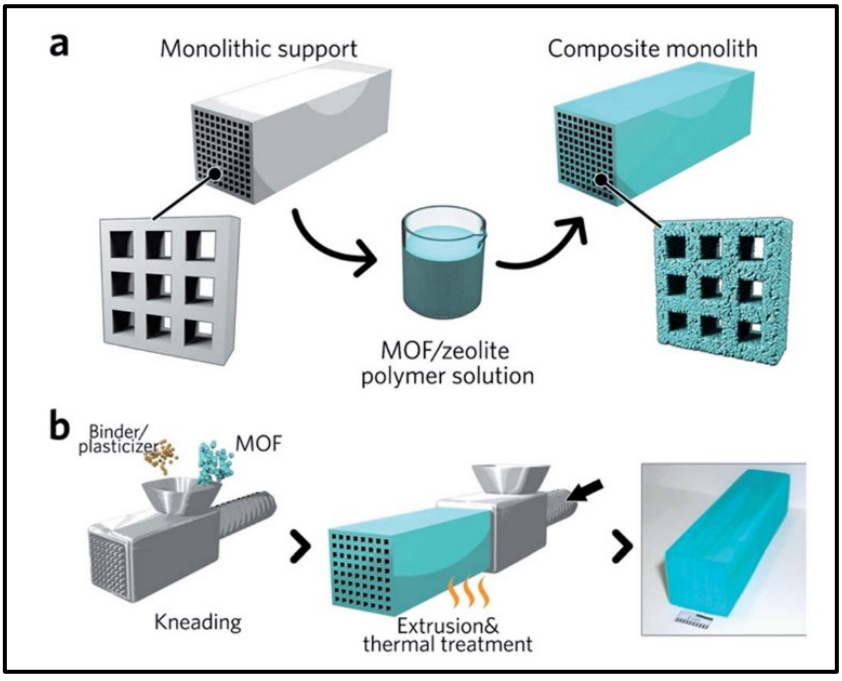


Figure 2.28: Strategies for producing monolithic MOF composites through depositing on monolithic supports (a) and extrusion of composites consisting of active MOF materials and binder. Reproduced from work by Hou et al [159] under Creative Commons licensing.

2.6. Adsorption of volatile organic compounds

Unlike nitrogen and many other light gases, volatile organic compounds have additional complexities in their physical and chemical structure that make them a unique target for adsorbents. In the case of non-polar adsorbates, such as aliphatic hydrocarbons, the size of the molecule in terms of its kinetic diameter and presence of branching chains will determine whether it can be adsorbed by porous materials or excluded based on size selectivity. However, because of the large size of VOC molecules, the magnitude of dispersive interactions between surface and molecule allow for high adsorption capacities in materials with sufficient porosity. Jia et al [162] found that the electron acceptor ability and dispersive force of the VOCs played major roles in their adsorption. These conclusions, reached by fitting of experimental equilibrium data with both Dubinin-Radushkevich and Linear Solvation Energy Relationship models, were consistent for VOCs with a wide range of chemistries including ketones, alkanes, alcohols, halogenated, and aromatic hydrocarbons. In the case of polar VOCs, reduced adsorption capacity comes about as the hydrophobicity of the adsorbent increases although this effect can sometimes be neglected as the driving force for adsorption, partial pressure, increases and the electrostatic barrier for entry is overcome [100].

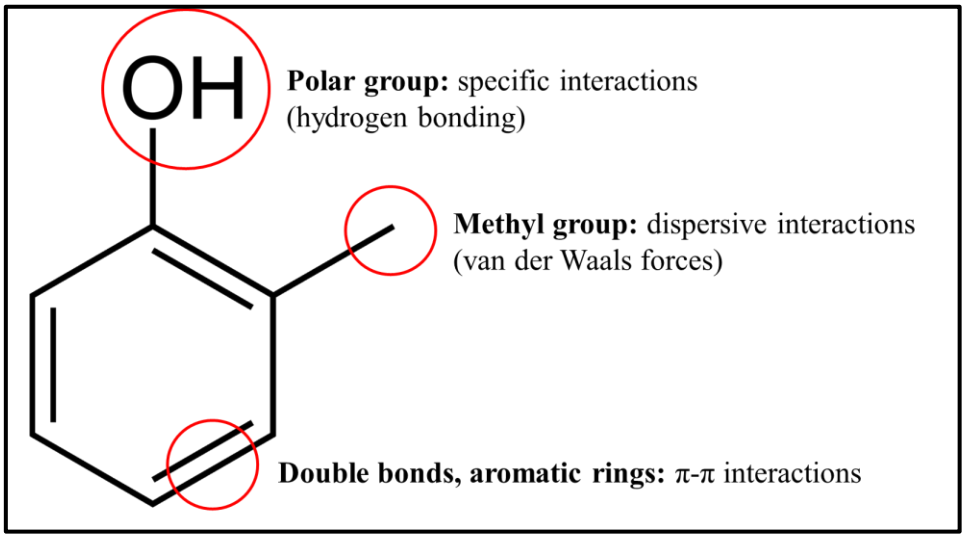


Figure 2.29: Examples of functional groups and subsequent bonding and interaction types in VOCs with multiple chemistries, in this example ortho-cresol.

To be considered an effective VOC adsorbent, the material must be competitive with commercial options. Activated charcoal fibres (ACF) are commonly utilised for ventilation applications in indoor spaces, due to their low cost, low pressure drop, and ease of integration into cloth filters. A study by Sidheswaran et al [163] tested the performance of ACF cloth filter (Zorflex FM 10) for adsorbing several VOC species simultaneously at part-per-billion concentration levels and at 30 % relative humidity. The work found the filter's capacity for VOCs varied between 2.6 to 48.2 mg/g depending on the nature of the species, with a combined capacity of 90.7 mg/g.

The number of adsorption sites within a porous material is limited, and selectivity for harmful VOCs is required due to the concentration of water vapour exceeding that of volatile species by several orders of magnitude. Therefore, adsorption hydrophobicity is a must-have property in any porous material being applied to trapping volatiles in the presence of even trace amounts of humidity. Minimising the number of hydrophilic adsorption sites while leaving sufficient sites for VOCs to interact with is perhaps the chief challenge of porous material design. Of course, there are no perfectly hydrophobic materials as most surfaces will possess some quantity of hydrophilic adsorption sites, whether this is due to defects, impurities, or additives. Generally, the adsorption of water vapour at low RHs in porous materials follows one of four isotherm trends, which can be used to describe four kinds of hydrophilic/ phobic adsorbents, as shown in **Figure 2.30.**

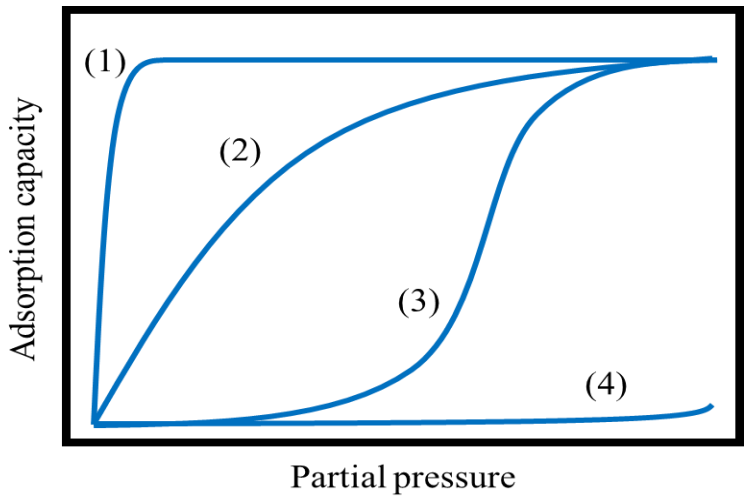


Figure 2.30: Isotherms of the four most common behaviours of hydrophilic/ hydrophobic adsorbents, assuming the materials have similar pore volumes and surface areas.

Adsorbent 1 has greater hydrophilicity than adsorbent 2 due to the steepness of the Type I isotherm, but both can still adsorb water without the need of significant driving force. The Type V shape of adsorbent 3 shows some hydrophobicity at lower RH, with adsorption driving forces required to fill the pores of the material. However, as RH or water partial pressure increases past a critical point, the material adsorbs a similar quantity to adsorbents 1 and 2. Finally, adsorbent 4 can be described as highly hydrophobic as it adsorbs low, often negligible, quantities of water vapour at all RHs studied. At the highest RHs, many materials containing mesopores will adsorb greater quantities of water vapour due to a higher density of surface defects [44], [164]. While this may not give an indication to the overall hydrophobicity of the pristine material, in applications at higher humidity the adsorption of water vapour in mesopores may still be an important consideration. In the subsequent sections, the adsorption of non-polar and polar VOCs onto porous adsorbents, both industrial as well as synthetic, will be discussed. In addition, the impact of water adsorption on the overall effectiveness of materials to adsorb VOCs will be discussed.

2.6.1. Adsorption by zeolites

As mentioned before, the pore size distribution of zeolites depends on the type of building blocks used during synthesis, and their orientation within the framework. These factors dictate the maximum size of VOC molecule that can be adsorbed into the micropores of the zeolite. A-type/ LTA zeolites have been mentioned previously for their molecular sieving properties, which they excel at thanks to their homogeneous pores with sizes small enough to exclude adsorption of larger molecules. Zeolites in this family have been shown good performance in adsorbing small molecules in ambient air such as water and CO_2 [165], as well as toxic compounds including SO_2 and NO [166]. Faujasite zeolites have similar structure to LTA, although the arrangement of sodalite cages in FAU leads to two homogeneous aperture sizes 2-3 times the size of A-type zeolites. This structure allows a much wider range of molecules, in terms of both size and shape, to be adsorbed and captured by faujasite zeolites. In a study on benzene decomposition [167], the reactor containing X-type zeolite was able to complete remove benzene, with its kinetic diameter of 0.59 nm, from the effluent gas, while A-type types could only partially decrease the benzene concentration due to their insufficient pore size.

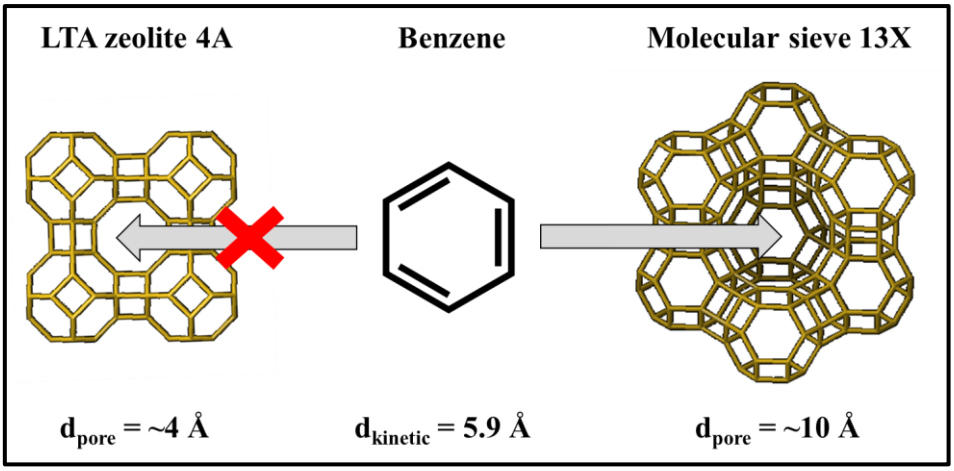


Figure 2.31: Illustration of molecular sieving of benzene by smaller pore zeolite LTA 4A compared to molecular sieve 13X.

Faujasites typically have increased pore volumes and wider pore size distributions than LTA, improving both the kinetics and quantities of gases adsorbed [166]. Zeolite X has been shown to be capable of adsorbing large molecules with both polar and non-polar chemistries, such as triplal fragrance [110] and alkylated aromatic [168] molecules respectively. ZSM-5 zeolites have narrower pores than faujasite, with the former's pentasil units having apertures in the range of 0.51-0.56 nm [169], leading to more restrictions in the size of molecules that can be adsorbed. However, a calorimetric study by Dunne et al [169] found that non-polar vapours had greater heats of adsorption in narrow-pore ZSM-5 than wide pore zeolite X. This difference was credited to an increase in dispersion forces with decreasing pore size, which are the dominating adsorption energies for non-polar molecules, which may be due to the overlapping dispersive interaction energies of the micropore walls [170]. Therefore, for a given chemical structure, narrower pores result in stronger adsorbate-adsorbent interactions, which may be a consideration for systems in which molecular sieving of the VOCs is an unlikely occurrence.

A study by Kim & Ahn [52] compared the performance of several zeolites, including high- and low-silica faujasites, in adsorbing high concentrations of harmful vapours with different polarities. In this work, the high-silica Y zeolite (USY) and zeolite X (MS13X) had almost identical surface areas and pore sizes due to their crystal structures, and adsorbed similar quantities of non-polar aromatics

including benzene, toluene, and xylene isomers. However, when polar VOCs were studied, the hydrophobicity of USY led to reduced performances due to its lower number of hydrophilic, or high energy, adsorption sites. The extent of this hydrophobicity can be seen in a study by Halasz et al [100] in which the adsorption of methanol onto USY generated a Type V isotherm. Type V isotherms have been discussed previously and represent highly non-preferential adsorption phenomena. In this system, the initially low adsorption capacity of methanol is hypothesised to be due to purely surface interactions around the pore apertures of the hydrophobic zeolite. The authors state the repulsive force field of the oxygen ions within the zeolite framework may act as a barrier to polar molecules attempting to enter the pores, resulting in these polar molecules occupying sites around the micropore without filling it until a particular driving force is met. This effect is most pronounced for water vapour, which has a consistently low adsorption capacity at all partial pressures or humidity values, only being able to adsorb onto surface defects and inside the mesopores of the zeolite. In the case of non-polar molecules, such as hydrocarbons, no such resistance is encountered and the molecule is able to fill the pores of the zeolite even at low concentrations [171]. For compounds with polar and non-polar bonding, such as alcohols, pore filling occurs at intermediate partial pressures, resulting in an inflection point in the Type V isotherm.

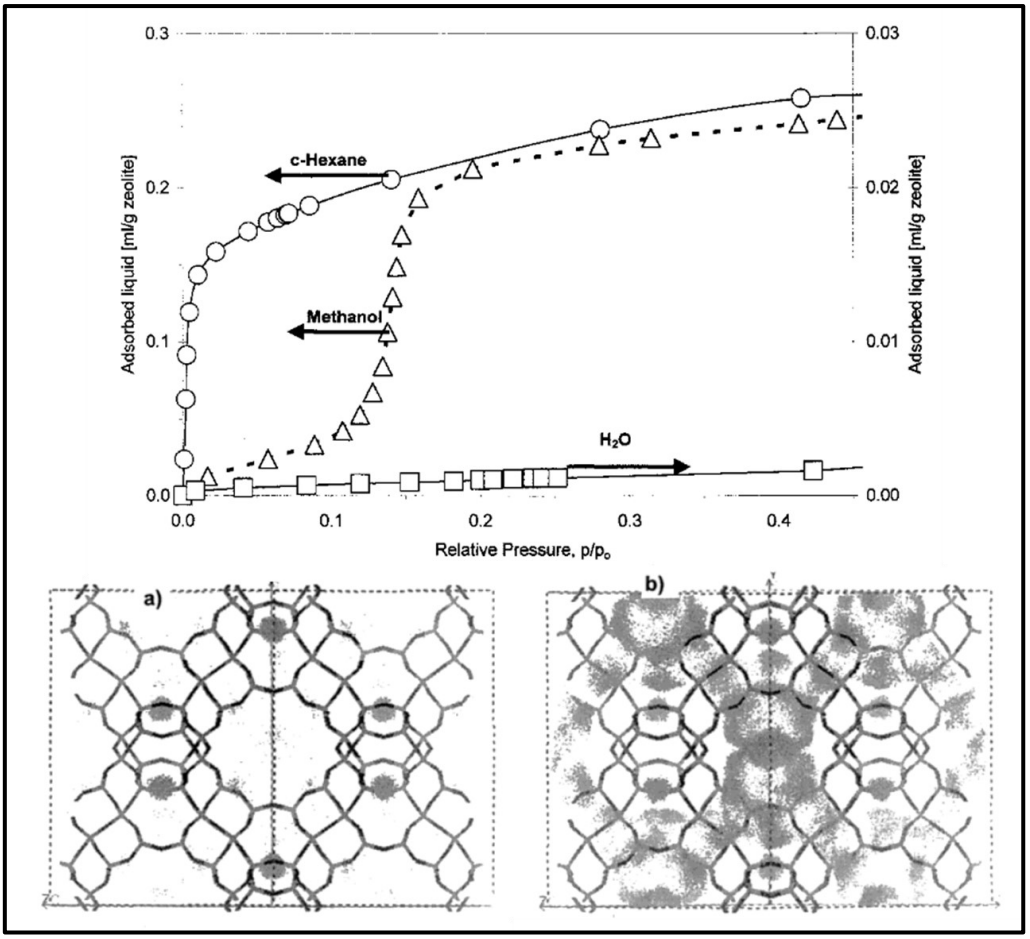


Figure 2.32: Adsorption of vapours onto high-silica zeolite Y (top), and mass dispersion maps of methanol vapour on/ in the surface and pores of the hydrophobic zeolite at a concentration below (left) and above (right) the Type V inflection point. Reproduced from work by Halasz et al [172] with permission.

2.6.1.1. Impact of water vapour on adsorption in zeolites

VOC-water selectivity within zeolites is largely dictated by the hydrophobicity of the surface and pore framework of the material, which in turn depends on its ion composition. The negative charge of alumina, or $[AlO_4]^-$, tetrahedrons increases the electronegativity of the zeolite framework, increasing its acidity and its ability to adsorb water, hydrophilic molecules, and cations [173]. This ability to interact strongly with hydrophilic molecules has been shown in zeolite 13X and 3A, which displayed Type I isotherms when exposed to water vapour in a study by Kim et al. [174]. The same study found that

high-silica zeolite Y, or 'ultra-stable zeolite Y' or 'USY' had negligible uptake of water vapour up until the highest RHs, leading to a Type III isotherm due to multilayer adsorption and condensation in mesopores. For this reason, USY is more commonly chosen for applications where hydrophobic VOCs are the adsorbate of interest.

This influence of silica content on hydrophobicity also affects the ability of zeolites to adsorb under humid conditions. Tao et al [73] found the adsorption capacity for benzene, acetone, and methanol on molecular sieve 13X (zeolite X), whilst high under dry conditions, was negatively impacted when water vapour was present in the feed stream, with reductions in breakthrough times of up to 62.5%. This effect was exacerbated when the zeolite was pre-conditioned under the effect of humidity, as all active sites within the material, whether hydrophilic or hydrophobic, became saturated with water molecules. Similarly, low-silica A-type zeolites adsorb water preferentially over harmful non-polar compounds, reducing their effectiveness as adsorbents for air treatment. Multicomponent breakthrough curves of a mixture of light gases on LTA [175] found that water vapour displaced all other compounds including H_2S, CO_2, N_2 and CH_4. This hydrophilicity in low-silica zeolites makes them popular materials for water recovery, either in gas stream drying or solvent purification [176], but less effective in applications where VOCs are in competition with water vapour. An extensive study by Kraus et al [177] confirmed that 13X and LTA-type zeolites adsorbed negligible quantities of toluene when exposed to a mixture of toluene and water vapour, while USY and high-silica ZSM-5 zeolites retained up to 75% of their capacity compared to dry conditions. Breakthrough curves in Kraus's study confirmed that the mechanism of competition in low-silica zeolites such as zeolite 13X was displacement of pre-adsorbed toluene molecules by water due to the hydrophilic nature of the zeolite. As shown in **Figure 2.33**, the outlet flux of toluene vapour in the zeolite 13X column exceeded the inlet, indicating the competitive displacement of that molecule and increased saturation of the outlet stream.

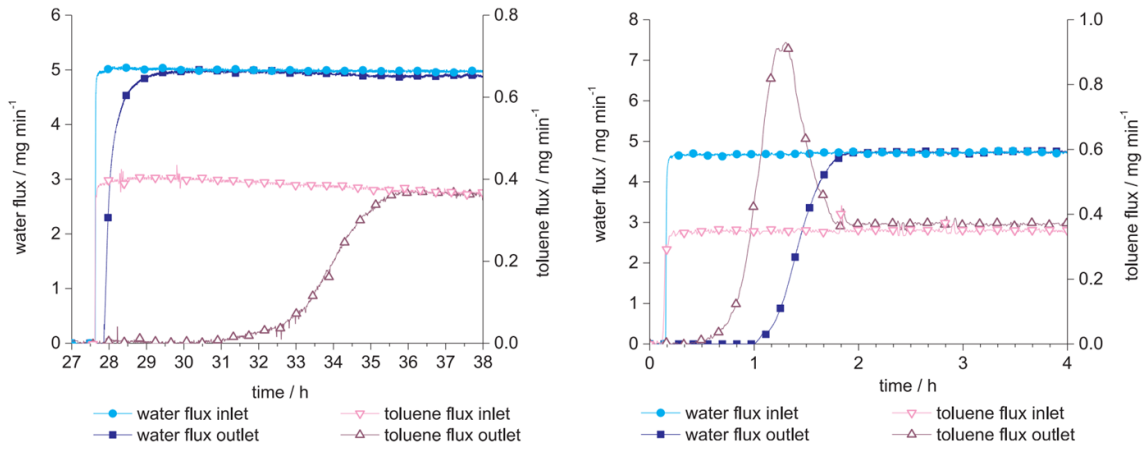


Figure 2.33: Breakthrough curves of toluene and water vapour, exposed to adsorbents HiSiv1000 (left) and zeolite 13X (right) simultaneously. Note the outlet toluene flux exceeding the inlet flux in the zeolite 13X system due to displacement of toluene molecules by water. Reproduced from work by Kraus et al [177] with permission.

The extra-framework cation content is also an important consideration for multicomponent adsorption in zeolites. Meininghaus & Prins [178] studied high-silica ZSM-5 zeolites in which the extra-framework Na+ ions had been replaced by H+ ions, commonly through reaction with ammonium salts. Despite having the same Si:Al ratio, the sodium form adsorbed significantly greater quantities of water, methanol, and 2-butanone than its acidified form. This difference implies the sorption of water is dominated by its interaction with charge-balancing cations, such as sodium. For hydrophobic zeolites, water's sorption is therefore influenced strongly by adsorbate-adsorbate interactions, which are unfavourable compared to the stronger adsorbate-adsorbent interactions between non-polar species and the zeolite. On the other hand, studies on non-polar interactions with Na- and H- forms of zeolites [169] found no correlation between non-polar adsorption energy and cation content.

From these studies, reducing the number of polar adsorption sites can be accomplished in two ways: increasing the silica to alumina ratio, due to the contribution of alumina tetrahedrons to acidity; and reducing the amount of framework and extra-framework cations. Both of these methods are commonly

carried out post-synthetically [42][120], improving hydrophobicity by altering the content of functional groups within the zeolite's structure.

2.6.2. Adsorption by activated carbons

Activated carbon (AC) is ubiquitous in adsorption applications, including those associated with harmful or unwanted volatile species, with hundreds of studies being published over the years. Among these, AC has been found to be particularly effective at adsorbing non-polar hydrocarbons such as alkanes, alkenes, and aromatics. In general, the adsorption of VOCs onto AC is controlled by five potential interactions- hydrophobic effect, π-π bonds, hydrogen bonds, vdW interactions, and covalent and electrostatic interactions [131]. In the case of non-polar hydrocarbons, vdW interactions are particularly important and can describe many of the trends seen in selectivity for alkanes of a particular size. A multicomponent study [179] on VOC adsorption on beaded AC found that n-decane adsorbed favourably over n-hexane in two-component breakthrough studies. This difference was theorised to be due to the adsorbent having higher affinity for longer chain alkanes. This conclusion is supported by inverse gas chromatography experiments [82] which reported that the adsorption enthalpy increased linearly with chain length for C5-C8 molecules interacting with charcoal. Similar findings have been reported for aromatic VOCs: Shin et al [180] found that capacities for aromatics followed the trend ethyl benzene > toluene > benzene in both dry and wet conditions; while Lillo-Rodenas et al [181] reported displacement of benzene molecules by heavier toluene molecules on the surface of charcoal when the adsorbent was exposed to a mixture of the two vapours. London dispersion forces, which are dominant in physisorption, increase with molecular weight leading to stronger adsorbent-adsorbate interactions [182]. However, exposing adsorbents to longer chain alkanes increases the difficulty of their regeneration, due to the slower diffusion of larger molecules into and out of the micropores of the charcoal, with a review study by Pui, Yusoff, & Aroua [183] recommending charcoal mesopores 2-3 times the kinetic diameter of the adsorbed VOC in order to avoid diffusive hindrance. Wu et al [170] found that the desorption efficiency of linear C5-C7 alkanes decreased noticeably with increasing chain length, with this effect being more pronounced in AC than a hydrophobic cross-linked polymer resin. This superior desorption performance was accredited to the lower micropore volume of the resin, as

smaller pores possess greater adsorption energies due to the overlapping of adsorption forces from opposite walls of the micropore. The shape and size profile of the molecule also has an impact on the strength of interaction between it and the adsorbent surface. Lai et al [184] found that C6 molecules with smaller steric profiles adsorbed more readily onto charcoal surfaces compared to those with branched or cyclic structures- as the number of branching groups increased, steric hindrance led to a reduced capacity on the adsorbent. The extent to which adsorbate shape influences capacity depends on the pore size distribution of the adsorbent. Activated charcoal, unlike microporous zeolites, has heterogeneously shaped and sized pores in the nanometre range, allowing it to adsorb branched species with diameters larger than its smallest apertures. However, activated charcoal is unable to tolerate high temperatures in the same manner that zeolites can, and so difficulties exist when regenerating the material for re-use in VOC or hazardous gas adsorption applications [185].

The non-polar nature of ACs results in limitations to their ability to adsorb and interact strongly with hydrophilic molecules at low concentrations. Tefera et al [179] conducted an 8 component breakthrough curve study on activated charcoal, exposing it to VOCs with a range of chemistries including aromatics, aliphatic, ketones, aldehydes and alcohols. The study found that all polar compounds (n-butanol, n-butyl acetate, 2-heptanone, and 2-butoxyethanol) were displaced from the charcoal adsorbent by more strongly interacting non-polar aromatics and aliphatics.

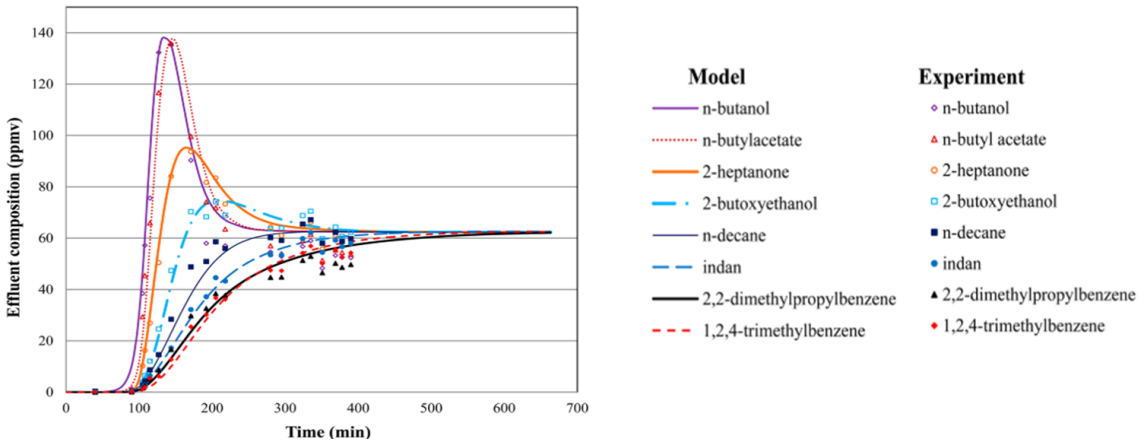


Figure 2.34: Experimental and modelled breakthrough curves of a mixture of VOCs in a column of activated carbon. Reproduced from work by Tefera et al [179] with permission.

The acidic and basic functional groups present on AC's surface afford some measure of interaction with hydrophilic adsorbates. For example, the presence of both oxygen and sulphur containing in activated charcoals was found by Petit et al [186] to contribute to enhanced adsorption of ammonia, with converted sulphate groups in particularly reacting with ammonia to form salts more easily retained by the micropores of the adsorbent. These groups, especially those containing oxygen and nitrogen, contribute towards the polar bonding AC can achieve with VOCs, although the presence of surface oxygen may inhibit specific interactions between hydrophobic VOCs and π-electron rich regions of the AC. A study by Lillo-Ródenas [187] found that the removal of surface oxygen groups from ACs through thermal treatment improved their adsorption capacity for benzene and toluene vapours at low concentrations, although the porosity of the charcoal was deemed to be a more important factor than surface oxygen content. Unlike hydrophobic zeolites, the heterogeneous nature of activated charcoal's apertures results in little change to the classification of the isotherm shape, i.e. no shift from type I/II to type III/V. Instead, the steepness of the adsorption isotherm and the subsequent adsorption capacity decreases as the polarity of the adsorbing molecule increases, as shown by a study by Lai et al [184], who found that VOCs with ketone chemistry were adsorbed less favourably than linear or branched alkanes. While many VOCs prominent within indoor environments possess polar bonding groups, such as ketones, alcohols and acids [188], the reduced capacity of charcoals for these compounds is often a necessary trade-off in order to limit its interactions with water vapour.

2.6.2.1. Impact of water vapour on adsorption in activated carbons

Activated charcoal's uptake of water vapour typically follows a Type V isotherm shape, with a steep increase in adsorbed amounts at higher RHs, despite the hydrophobic nature of charcoal's surface. A study by Pei & Zhang [189] on toluene adsorption in activated charcoal found the most significant performance reduction occurred when increasing the RH to 80 %, which was credited to the increased 'critical radius' that water molecules could fill as RH increases. However, the Kelvin equation is only valid in pores with diameters of 2 nm or more [50], and the study by Pei & Zhang extrapolates its hypothesis to pores in the range of 0.3 nm. Dubinin & Serpinsky [164] hypothesised this phenomena of increased water uptake to be due to surface chemical species or defects present on the surface around

which water vapour molecules condense as their pressure approaches saturation, similar to previous reports on zeolite framework defects.

The impact of humidity also appears to be affected by the chemistry of the VOC, with non-polar adsorbates being less negatively affected by the presence of water vapour. A study by Cao et al [190] conducted at a concentration of ~2000 ppm of VOC found the capacity for acetone in AC dropped by 19.5 % when RH was increased from 20-40 %, compared to a drop of only 9.4 % for toluene under the same conditions. However, under the most extreme conditions, the drop in performance between 20-80 % RH was similar for acetone and toluene, at 47.4 % and 41.2 % respectively. On the other hand, a study by Laskar et al [191] found that at an RH of 55 % only negligible changes in VOC breakthrough curve shape or capacity were observed, due to AC's affinity towards VOCs over water vapour. However, upon reaching 95 % RH, noticeable performance decreases were measured for 2-propanol, acetone, n-butanol, and even toluene vapour, although the highly dispersive 1,2,4-trimethylbenzene appeared to be unaffected by even the highest levels of water vapour. A sudden increase in competition at the highest humidities, matches what is seen in the material's type V water isotherm, possessing an inflection point around 55-60 % humidity. This behaviour was also seen for the adsorption of benzene on activated charcoal cloth by Cal et al [192], who observed that significant decreases in acetone and benzene adsorption capacity were observed at RHs above 60 %, which corresponded to the exponential growth portion of the water isotherm. This behaviour is probably due to water vapour condensing within the mesopores of the charcoal at higher RH, making them unavailable for VOC adsorption. This reduction in performance was more noticeable for VOCs with a concentration of 500 ppmv than 1000 ppmv, which may be due to a reduced driving force for VOC molecules to remain adsorbed on the surface of the charcoal. In contrast to other studies, the study on activated charcoal cloth found that acetone was the least impacted by the presence of water vapour, which was thought to be due to acetone being infinitely soluble within condensed water, whereas benzene is hydrophobic and insoluble. Rodriguez-Mirasol et al [193] reported similar trends, with the co-sorption capacities of vapour phase water-methanol mixture far exceeding water-MEK and water-benzene mixtures, which was ascribed to the complete solubility of methanol in water, while MEK is only 24 % soluble, and benzene has almost

negligible solubility at room temperature. However, both Cal and Rodriguez-Mirasol used gravimetric methods for measuring the multicomponent capacity of AC. As explained earlier in this review, gravimetric methods struggle to fully quantify the separate capacities for each species when an adsorbent is exposed to a mixture of gases or vapours. Therefore, any conclusions regarding the selectivity of the AC samples in those studies, or the nature of the adsorption when several components are present, can only be considered semi-quantitative.

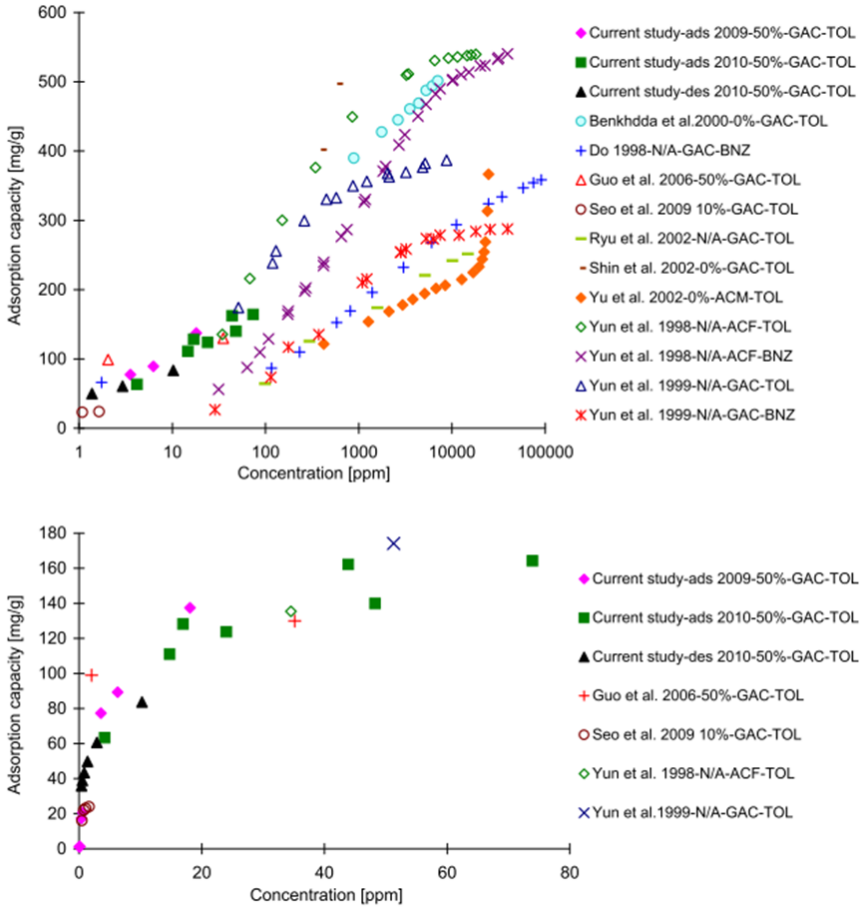


Figure 2.35: Summary of adsorption capacities of toluene (TOL) and benzene (BNZ) vapours onto activated charcoal at a wide range of concentrations (top), and a focus towards lower concentrations (bottom). Legend format: reference-relative humidity of measurement- material- vapour; GAS- granular activated carbon; ACF- activated carbon fibre; ACM- activated carbon monolith; N/A- relative humidity not reported in reference. Reproduced from work by Pei & Zhang [189] with permission.

2.6.3. Adsorption by porous silicas

Commercial silica gel, while possessing high surface are, does not possess large quantities of micropores and is almost entirely mesoporous [194]. Adsorption isotherms of aromatics in industrial adsorbents by Wang et al [195] found the steepness of the isotherm, often used as a measure for microporosity, to be significantly greater in activated charcoal than silica gel. In addition, despite its large pore apertures, silica gel still exhibited molecular sieving when exposed to *p*-xylene, credited to two factors: the molecule's symmetric structure, resulting in a lower molecular polarity; and the molecule's larger kinetic diameter compared to other BTEX chemicals. For molecules with smaller diameters than the minimum silica aperture size, the capacity appeared to increase with molecular weight, with silica adsorbing greater quantities of *o/m*-xylene and toluene than benzene at equivalent partial pressures. However, the surface of silica gel is predominantly polar and exerts poor interactivity with non-polar vapours, as shown by gas titration experiments by Biliński [196] which found that the isoteric heat of adsorption for n-octane was relatively low compared to benzene. Octane is a non-polar vapour and therefore interacts with the polar silica surface only through nonspecific forces, while the electron-donor properties of benzene afford it increased interactivity with the electron-acceptor character of the silica surface. This character also explains the relatively poor adsorption of chloroform vapour, which itself only has electron acceptor and nonspecific components of its surface tension. One method of reducing adsorbent hydrophilicity is post-synthetic modification. Huang et al [194] modified commercial silica gel using trimethylchlorosilane under microwave exposure, with the resulting solid having a water vapour capacity 7 times lower than that of the unmodified gel although the process also reduced the surface area of the gel from 462 m^2/g to 431 m^2/g and its n-hexane capacity from 0.36 to 0.31 g/g. These n-hexane adsorption experiments were carried out at a concentration of 0.8 g/L, or around 227,000 ppm. This level far exceeds any reasonable concentration for VOC adsorption in indoor spaces but may provide useful information for applications like industrial vapour recovery.

2.6.3.1. Impact of water vapour on adsorption in porous silicas

Silica gel adsorbs significant quantities of water vapour due to its surface chemistry and high mesopore volume, leading to its common use as a desiccant. Mikhail and Shebl [64] hypothesised that silica gels

contained surface sites with both hydrophilic and hydrophobic surface chemistry, but that the adsorption of water vapour at higher pressures predominantly involved polar interactions. However, due to its low cost and ease of regeneration, silica gel has been studied for its use in air cleaning applications. Ge et al [197] tested a desiccant wheel for the control of both total VOCs (TVOCs) and moisture, finding that silica gel had a TVOC removal efficiency of approximately 0.8 when exposed to a contaminant concentration of 0.91 mg/m^3 and an RH of 45 %, representative of indoor levels. This efficiency decreased with increasing humidity, to a minimum of ~0.5 at 85 % RH, as well as decreasing at higher TVOC levels, indicating a saturated state for silica gel that may make it unsuitable for more extreme environments. In addition, the regeneration temperature had a noticeable impact on the effectiveness of the filter, with the removal efficiency ranging from 0.62 to 0.94 when the sample was activated at temperatures between 60-100˚C. Similar results were found by Sheng et al [198] when analysing a silica gel rotor, with removal efficiencies decreasing by 5-15% when regeneration air temperature was decreased by 10˚C. The mechanism of competition occurring between VOCs and water vapour was explored through toluene breakthrough studies by Lu et al [199], finding that pure silica gel exhibits a BTC indicative of VOC displacement by adsorbing water, with outlet concentrations exceeding inlet concentrations at an elevated RH of 80 %, as shown below in **Figure 2.36**. This study investigated the impact of a composite's carbon: silica ratio on VOC adsorption performance, finding that carbon content improved the composite's resistance to humidity, as well as increasing its saturation capacity for a variety of VOC molecules.

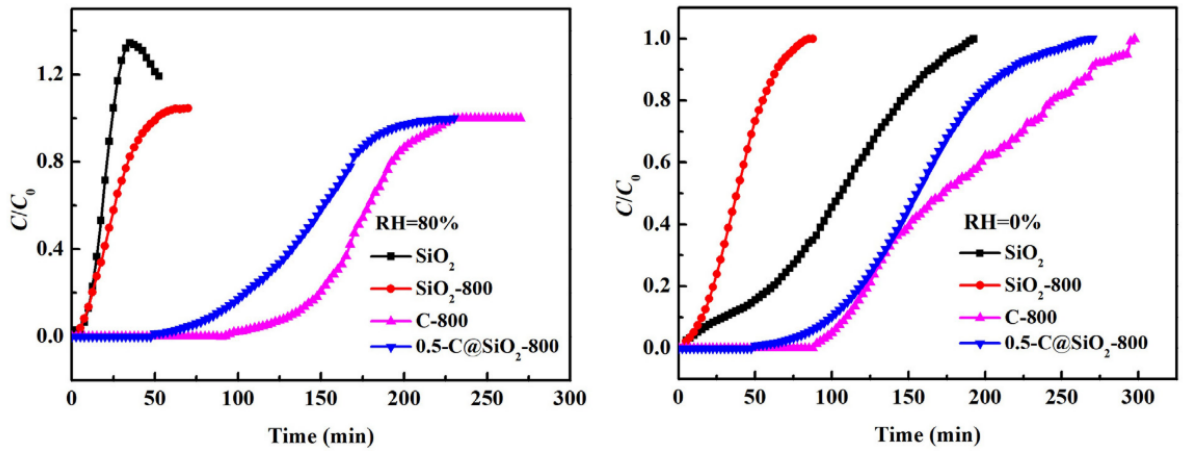


Figure 2.36: Breakthrough curves of toluene vapour on silica and carbon adsorbents, carried out at relative humidities of 80 % (left) and 0 % (left). Reproduced from work by Lu et al [199] with permission.

This effect was most noticeable for non-polar VOCs such as toluene and n-hexane as silica can only interact with these species through weaker dispersion forces, while the hydrophilic chemistry of the silica benefits its adsorption of polar species such as acetone, ethyl acetate, and ethanol. Sheng et al [198] found this hydrophilic chemistry benefited the filtration performance of silica gel for formaldehyde, acetone and ethanol, even in the presence of humidity due to their water solubility. Silica gel's inability to effectively adsorb non-polar VOCs was thought to be solvable by combining silica gel with another active component such as a metal organic framework.

2.6.4. Adsorption by metal-organic-frameworks

Many framework materials, particularly metal-organic-frameworks and their derivatives, have been designed specifically to act as effective adsorbents. This functionality is typically achieved by synthesising materials with high surface areas, porosities, and beneficial surface chemistry. One example of the influence of surface area on performance is Yang et al [200], who synthesised MIL-101 with a BET surface area of almost 4000 m^2/g, and achieved a benzene adsorption capacity of 1291 mg/g at $P/P_0 = 0.55$, almost double that of activated charcoal, and over seven times that of ZSM-5 zeolite under similar conditions. MIL-type MOFs are very common in VOC applications due to their high pore

volume and surface area but, like porous silicas, their large aperture size can make them unsuitable for VOC adsorption at dilute levels. Trung et al [201] investigated the adsorption of linear C5-C9 alkanes in MIL-100 and MIL-101, which have minimum aperture sizes of ~5.0 and ~11.7 Angstroms respectively.

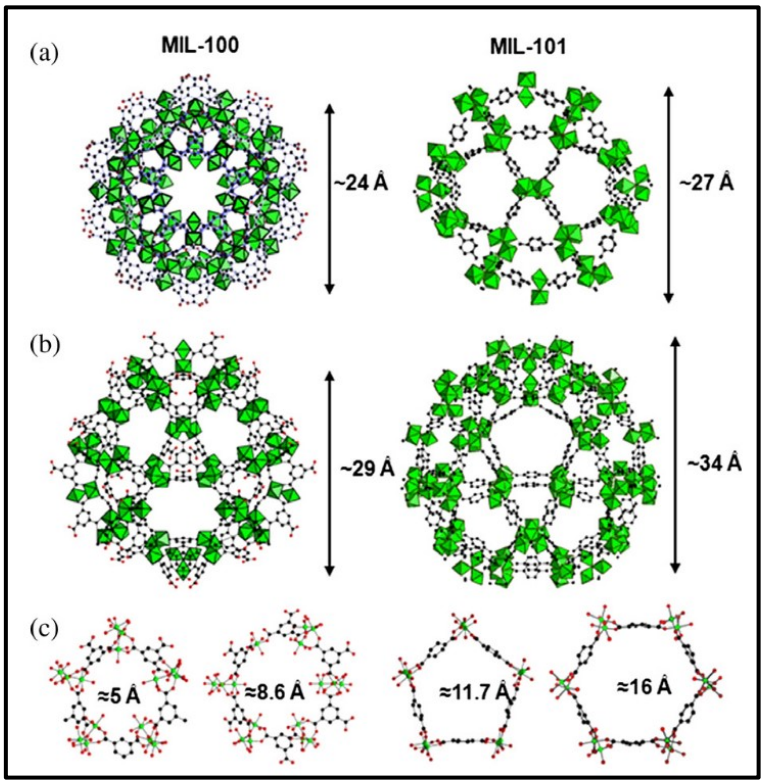


Figure 2.37: Sizes of small cages (a), large cages (b), and pentagonal and hexagonal windows in MIL-100 and MIL-101. Reproduced from work by Trung et al [201] with permission.

Differences in the pore sizes and surface areas of these MIL-type MOFs resulted in two observations, both of which can be seen in **Figure 2.38**:

1. Superior adsorption of alkanes at high partial pressures in MIL-101, due to higher Langmuir surface area and total pore volume.
2. Superior adsorption of alkanes at low partial pressures in MIL-100, compared to a stepped isotherm shape in MIL-101, the latter due to higher concentrations being required to fill the larger pores.

This study suggests the strength of interaction between adsorbing linear alkane vapours and MIL adsorbents is governed by two properties: the pore size distribution of the adsorbent, with smaller apertures being filled at lower pressures and resulting in a steeper adsorption isotherm; the size of the alkane molecule, which itself has two competing influences, kinetic and thermodynamic. Kinetically, the larger alkanes have reduced diffusion into the adsorbent's pore structure which may result in reductions in adsorption capacity. Thermodynamically, the capacity for alkanes increases with molecular weight due to stronger dispersion forces.

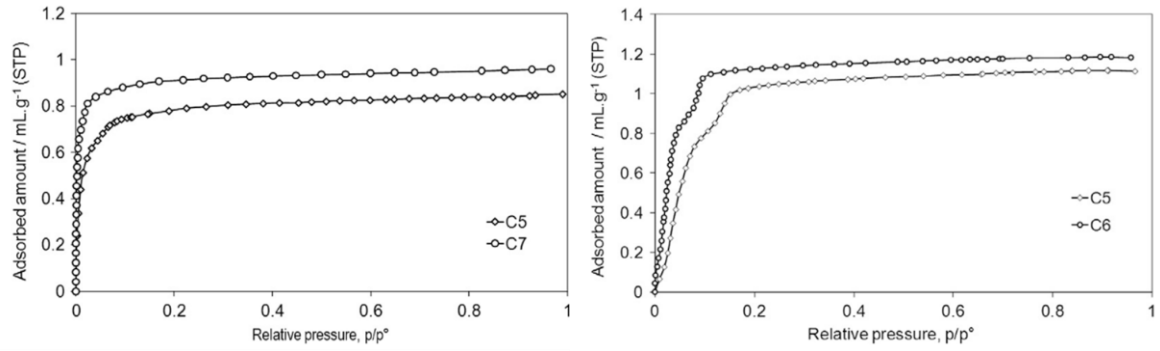


Figure 2.38: Vapour isotherms of n-pentane and n-heptane in MIL-100 (left) and MIL-101 (right), measured at 303 K. Reproduced from work by Trung et al [201] with permission.

This thermodynamic effect was observed not only in single component isotherms, but also multicomponent experiments by Wang [202] in which MIL-101's capacity followed the trend ethylbenzene > toluene > benzene. These datasets largely match with previous trends for carbon [179] and zeolite [170] adsorbents. MIL-100 and MIL-101, when exposed to methanol vapour [203], [204], produced an isotherm with multiple inflection points indicating unfavourable interactions, similar to hydrophobic zeolite Y [100]. These points precede large increases in capacity due to sufficient driving force to induce pore filling of the small and large MIL-100 cages. Compared to water vapour, these condensation steps shift towards lower pressures for methanol due to the electrostatic sieving effect of the MOFs pore aperture, with initial water adsorption occurring due to cluster formation around hydrophilic metal sites in large cages [204]. This effect is also seen in micro-mesoporous DUT-67 [205], which itself has multiple distinctly sized pore apertures in the range of 5-15 Å. Water adsorbed

in a three-step isotherm, with RHs of 5, 30, and 35 % leading to pore filling through condensation in progressively larger pores. In methanol only two distinct adsorption steps are visible, and the adsorption of heavier alcohols resulted in a type I isotherm. However, even these heavier alcohols reached equilibrium at higher partial pressures than non-polar molecules such as hexane and toluene, i.e. hydrophobic adsorbates have initially steeper isotherms, further emphasising the hydrophobicity of the pore apertures.

ZIF-8 has been found to adsorb significant quantities of non-polar vapours, with a study by Zhang et al [145] measuring type I isotherms for a range of species including linear aliphatics, branched aliphatics, and aromatic hydrocarbons. ZIF-67, with its almost identical structure to ZIF-8, also possesses strong interactivity for hydrophobic vapours. Vellingiri et al [206] found that ZIF-67 possessed the highest enthalpy of toluene adsorption, at least 24.8 % higher compared to MOF-199, UiO-66, and 4A zeolite. On the other hand, polar vapours do not interact strongly with ZIF-8/67, resulting in type V isotherms similar to MIL-100- methanol systems, although the inflection point for ZIF-8 and methanol exists at higher partial pressures due to the increased driving force required [207]. Like MIL-100 and zeolite Y, the inflection point for pore filling exists at lower partial pressures for adsorbates with increasing components of dispersive surface tensions, i.e. heavier alcohols.

One of the primary limitations of ZIF-8 and ZIF-67 is their small aperture size which, whilst flexible, limits the size of molecules that can be incorporated into their micropores, and reduces diffusion kinetics and subsequently the adsorption rate for larger molecules [145]. The flexibility of the ZIF-8 pore aperture allows molecules larger than the ‘atomistic aperture size’ [147] to be adsorbed, with a recent study by Ueda et al [151] ascribing this behaviour to a flipping motion of the imidazolate linkers. This motion requires a certain amount of ‘driving force’ to happen and the extent of this motion increases with adsorbate kinetic diameter. The study expressed the activation barrier of molecules passing through the aperture as a function of their size, with molecules exceeding a kinetic diameter of 0.6 nm (p-, o-, and m-xylene in particular) having a sharp increase in the energy requirement. Without sufficient driving force, these bulkier molecules struggled to be adsorbed by ZIF-8, with adsorption times in the range of 10^4 seconds, or almost half a day.

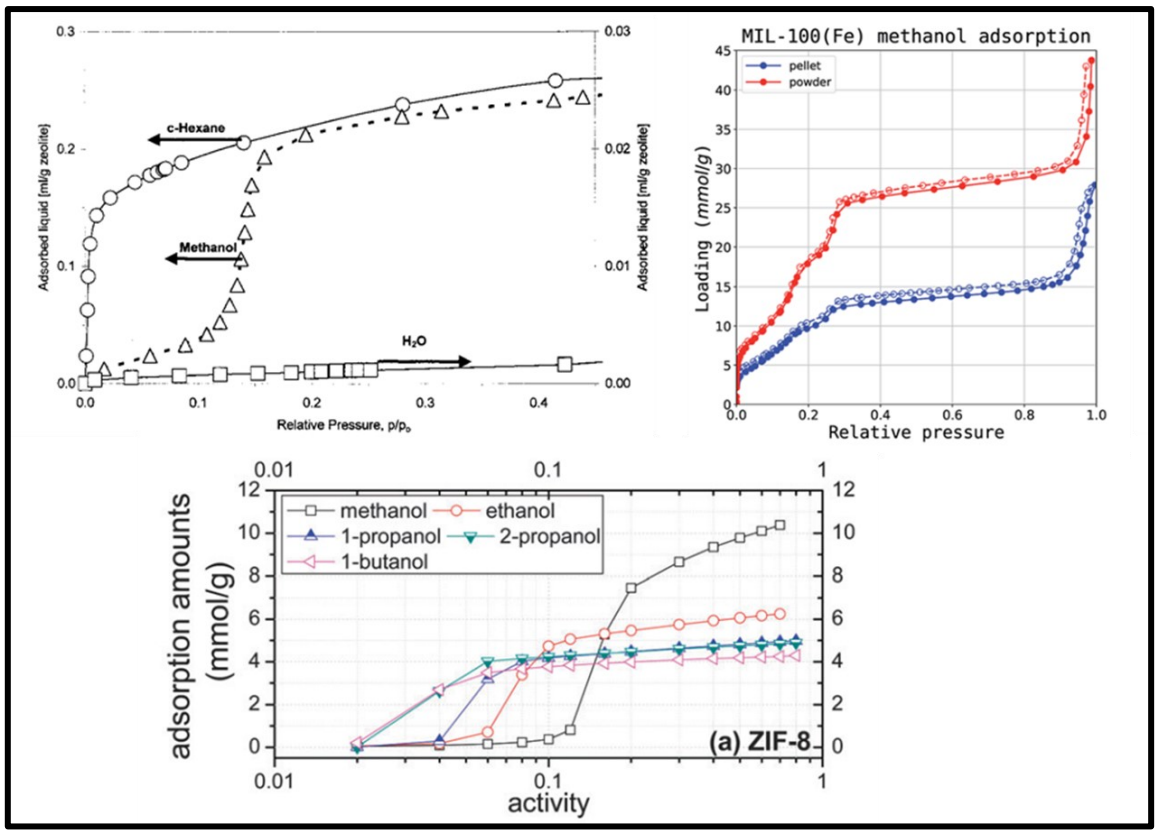


Figure 2.39: Stepped isotherms of high-silica zeolite Y (left), MIL-100 (Fe) (right), and ZIF-8 (bottom) when exposed to methanol vapour, showing hydrophobic screening effect. Reproduced from work by Halasz et al [172], Iacomi et al [203], and Zhang et al [207], with permission.

2.6.4.1. Impact of water vapour on adsorption by metal-organic frameworks

Water adsorption in MOFs typically occurs via three potential mechanisms. The first is chemisorption with the metal centres of the framework, sometimes leading to structural degradation. Low et al [208] proposed two primary mechanisms for water-induced degradation: ligand displacement, inserting the water molecule into the metal-oxygen bond between metal and linker, leading to the formation of a hydrated metal cation weakly bonded to the free ligand; and hydrolysis, where the metal-ligand bond is broken and water dissociates to form a hydroxylated cation and a free protonated ligand.

$$M^{n+} - L^{n-} \; + \; H_2O \rightarrow M^{n+} - (OH_2) \cdots L^{n-} \tag{2.36}$$

$$M^{n+} - L^{n-} \; + \; H_2O \rightarrow M^{n+} - (OH)^- \; + \; HL^{(n-1)-} \tag{2.37}$$

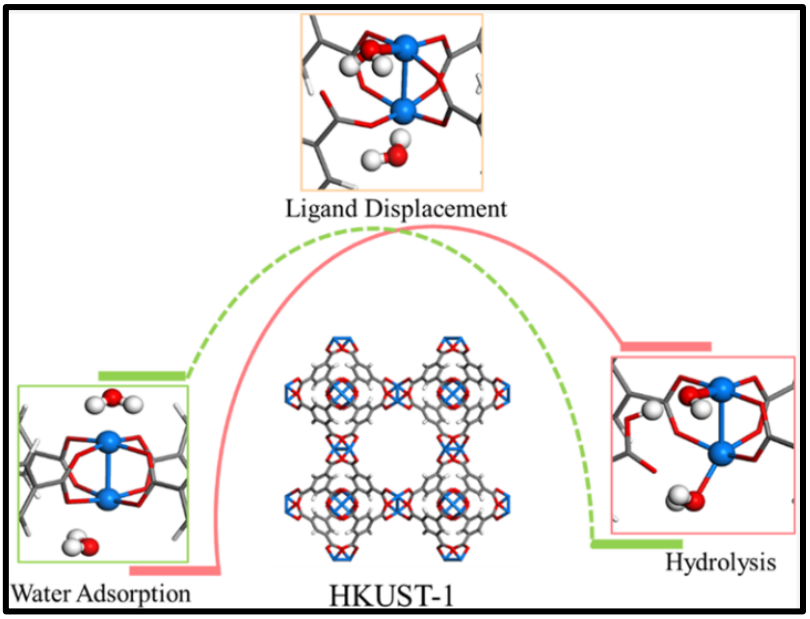


Figure 2.40: Theoretical degradation mechanisms of $Cu_3(BTC)_2$, HKUST-1, by ligand displacement or hydrolysis in the presence of water. Reproduced from work by Xue et al [209] with permission.

While trends for MOF stability in water are acknowledged, they are largely qualitative. Stability typically depends on the interaction strength between water molecules and the metal centres of the MOF compared to the metal-linker bond, as shown by the water instability of ZIF-67 compared to ZIF-8. Despite having almost identical structures, containing the same linker molecule and sodalite-like topology, the cobalt in ZIF-67 forms strong bonds with water molecules leading to a reduction in crystallinity when exposed to liquid water [153]. The second and third water adsorption mechanisms, specifically reversible layer and cluster adsorption, and irreversible capillary condensation, are typical in commercial porous materials, and have been discussed in previous sections. A review paper by Canivet et al [210] summarised the water uptake of over 30 different MOFs, and found that ZIF-8 had by far the lowest capacity at only 0.01-0.02 cm^3/g at an RH of 80 %, at least 20 times lower than that of other MOFs studied at similar RH levels. This 'hyperhydrophobicity' is likely a combination of methylated linker groups and small apertures, leading to a high density of polar-repelling functional groups [211], exhibiting low water uptake even at pressures approaching the saturation vapour pressure of water. While many MOFs exhibit stepped isotherms when exposed to water, MOF-74 is one

exception [212], which possesses a single ~11 Å aperture, and contains metals bridged by 2,5-dihydroxyterephthalate, which itself contains hydrophilic -OH groups. It is likely that the presence of a single, large pore aperture with hydrophilic bonding chemistry allows a MOF to produce a type I isotherm when exposed to water vapour, similar to molecular sieve 13X [174].

Multicomponent breakthrough experiments by Xian et al [99] found MIL-101's capacity for benzene vapour adsorption dropped from 0.319 mmol/g to 0.125 mmol/g when the RH was increased from 5 to 80 %, with similar trends exhibited for dichloroethane and ethyl acetate. A loss in capacity was also measured when RH was increased just to 40%, although the extent of competition was much lower. MIL-101's inflection point for water uptake occurs at a 40 % RH, resulting in a fourfold increase in water adsorption capacity between 40-80 % RH. Calculated desorption activation energies at intermediate partial pressures in the range of P/P_0 = 0.05-0.1 followed the trend water > dichloroethane > ethyl acetate > benzene, with polar molecules interacting more strongly with surface of MIL-101. Water's desorption activation energy was calculated as 72.96 kJ/mol, at least 54 % higher than any other VOC, which may account for the significant competition for adsorption by water vapour. The reduction in MOF performance with humidity is exacerbated at low concentrations, as shown by a 2017 study by Vellingiri et al [206]. This work tested a wide variety of MOFs including UiO-66, ZIF-67, and MOF-199 in adsorbing toluene at a partial pressure of 0.0026- around 20 times lower than that of the work by Xian. The work studied the impact of RH up to 50%, finding that all adsorbents' capacities decreased by at least a factor of 2, with MOF-199's interaction with water being strong enough to displace pre-adsorbed toluene molecules. Vellingiri's earlier work in 2016 [213] studied the removal of several classes of volatile and semi-volatile compounds (aromatics, volatile fatty acids, phenols, and indoles) by both MOFs and industrial adsorbents, specifically activated charcoals and Tenax TA. While the humidity was 34 % in all measurements, the concentration of the VOC species was representative of those in indoor air, at ~100 parts per billion. High surface area activated charcoal was found to have the highest removal capacity for non-polar species, specifically volatile fatty acids and aromatics. MOF-199 was the highest performing adsorbent when exposed to phenols and indoles which, after conducting DFT calculations, was credited to two effects: π-π interactions between the benzene rings and C=C

bonds of the MOF linkers and the aromatic chemistry of the vapours; and specific interactions between the polar groups of the guest molecules and the copper ions of the MOF-199. The study emphasises the importance of MOF chemistry for adsorption of species at ultra-low concentrations representative of those in indoor air.

Compared to MOFs in general, datasets on competition adsorption of VOCs and water on ZIF-8 or ZIF-67 are few and far between, and many of the studies possess unusual datasets when compared to single-component studies. For example, a comparative study by Xie et al [214] measured negligible uptake of benzene by ZIF-8 at a level of 10 ppmv in the presence of humidity, but also reported remarkably low adsorption capacity in dry conditions, with ZIF-8 producing an almost Type V isotherm. This contrasts with the steep type I behaviour of ZIF-8 when exposed to non-polar vapours noted in previous studies [145]. Breakthrough studies for a toluene- ZIF-8 system by Jafari et al [215] at 1000 ppmv found that ZIF-8's performance was heavily impacted by its activation conditions, with its capacity increasing almost eightfold when pre-treatment temperature was increased from 150˚C to 300˚C. In addition, the toluene breakthrough times were negligibly affected by an increase in RH from 40-60 %, although the adsorption capacity from noted to drop dramatically as RH was increased higher, from 410 mg/g to 203.3 mg/g at 40 and 80 % RH respectively. Vellingiri et al [206] found that ZIF-67's capacities for toluene at ~180 ppm were 224, 185, and 63.1 mg/g at RHs of 0, 25, and 50 % respectively. There are clearly noticeable disparities in the reported adsorption performance of ZIF-8 and ZIF-67 for VOCs in the presence of humidity, with some studies failing to include full characterisation results such as X-ray diffraction or nitrogen isotherms, making accurate assessment of crystallinity or porosity difficult. While ZIF-8 and -67 possess incredible adsorption hydrophobicity, the effect of reduced driving force at low VOC concentrations must be investigated, as it is likely to have a negative impact on the ability for ZIF-8/67 to accommodate aromatic VOCs at dilution levels approaching those found in indoor spaces. Whether this effect is more prevalent in linear alkanes, which are also an important and harmful VOC present in air pollution [216], and are a key emission from transport sources [217], also requires further study.

2.6.4.2. Adsorption by modified MOFs and composites

A common motivation for modifying MOFs is to improve its selectivity or interaction strength with a species. One example of this is the addition of graphene oxide (GO) into a ZIF-8 reaction mixture by Chu et al [218] which, despite producing a composite with lower BET surface area, improved the final material's adsorption capacity for toluene vapour in both dry and humid conditions by up to 20 %. This improvement was credited to π-π interactions between the aromatic ring of toluene and the GO layers, the latter of which contain significant quantities of C=C bonds. The recyclability of the composite was promising, with negligible losses in toluene capacity after multiple cycles. The presence of GO in the reaction mixture did not appear to affect the nucleation and growth of ZIF-8 crystals, but still possessed significant interactivity with those crystals, as shown by the distortion of characteristic ZIF-8 peaks in the PXRD pattern at elevated GO contents.

While some additives directly interface with adsorbates to improve or reduce interactivity, some have a structure-directing effect on the final synthesised material, as shown in work by Zhang et al [219] on PVP-modified UiO-66. At certain loading levels in the initial reaction mixture, specifically at a 2:1 molar ratio of zirconium to PVP, the composite was found to possess improved capacity for toluene in dry and humid conditions despite a 17 % reduction in pore volume. Rather than PVP-adsorbate interactions, enhanced heats of toluene adsorption were ascribed to interactions between the molecule's aromatic ring and missing-linker defects present in the structure-directed PVP MOF. The reason for the material's improved hydrophobicity was not investigated in depth, although may be related to the presence of surface active PVP molecules. While PVP, like other surfactants, contains both hydrophilic and hydrophobic groups, it is possible that the hydrophilic group (C=O) is shielded from the surface due to interactions with the zirconium metal centres. This viewpoint is supported by the presence of missing-linker defect sites where the metal-surfactant interactions surpassed metal-linker, and the ratio-dependent nature of the hydrophobicity: at low concentrations of PVP the influence of the surfactant on surface chemistry is less significant and outweighed by the hydrophilic bonding of UiO-66; whilst at high concentrations there is likely an excess of PVP present, leading to the hydrophilic 'heads' of the surfactant being exposed and allowed to interact with water vapour. However, this excess of surfactant

may be removed during activation, as the thermogravimetry profile of the modified samples show noticeable mass loss in temperatures between 25-100˚C, which was credited to loss of solvent molecules. However, without post-activation FTIR or spectrometric analysis of the outlet of the thermogravimetry equipment, this influence of surface PVP on functionality cannot be neglected. UiO-66 has also been modified through the addition of alkylphosphonic acids, coordinating to the Zr metal ion via metal-oxygen-phosphorus bonds [220]. The post-synthetic addition of octadecylphosphonic acid was found to provide a low energy, hydrophobic surface chemistry which allowed the modified MOF to become non-wetting in liquid water. This modification, while negligibly altering surface area, improved the MOFs ability to absorb liquid-phase solvents such as acetone, methanol, and toluene. However, the impact that these acids had on vapour adsorption in MOFs was not investigated.

2.7. Conclusions

From these reviewed studies, it should be apparent that while many porous materials possess high surface areas, micropore volumes, and excellent single-component capacities for VOCs, the assessment of these materials for VOC capture must be carried out under realistic conditions. High levels of VOC dilution and the presence of relative humidity have both been found to significantly reduce the effectiveness of many classes of adsorbents including zeolites, charcoals, and MOFs. By analysing these impacts and how certain materials behave in realistic air cleaning environments, several properties become apparent as desirable for effective adsorbents:

- High surface area and micropore volume, providing a larger number of adsorption sites
- Hierarchical porosity to improve diffusion, adsorption kinetics, and allowing for effective adsorbent regeneration
- Sufficiently small pore size to facilitate adsorption of adsorbates at low concentrations
- Sufficiently large pore size to allow adsorption and desorption of branched, aromatic, or otherwise large molecules, and to not restrict diffusion into the pores
- Hydrophobic adsorption chemistry, to improve selectivity for volatile organic compounds over water vapour, especially in processes involving high levels of humidity

- Strong interactivity between adsorbent and VOC, either through dispersive surface chemistry or, in the case of aromatic VOCs, the addition of π bonding functionality.

Finding or synthesising materials with these properties, while also considering practical limitations such as cost, availability and, in the case of synthetic materials, ease of manufacturing, is a key challenge for researchers in the field of adsorption science. Despite many adsorbents being described as 'hydrophobic' in the literature, those with hydrophobic pore apertures, such as high-silica zeolite Y, MIL-100, and ZIF-8, appeared to have particularly low interactivity with polar species, providing their critical pore-filling partial pressure was not met. However, the impact that pore filling by water vapour has on the extent or mechanism of competition was not a focus of any literature studies, with many simply crediting a material's high performance on an abstract 'hydrophobicity'.

A distinction should also be made between two different modes of competition adsorption characterisation where one species is water vapour. In 'wet adsorbent' experiments, the solid material is pre-exposed to water vapour prior to exposure to the adsorbate of interest [101], while in 'wet adsorbate' experiments the gas or vapour stream is humidified and the adsorbent is exposed to all adsorbate species simultaneously [177]. In the former mode, water vapour does not need to initially compete for adsorption sites, reducing the relative impact of displacement on the final saturation capacity of the material. Comparisons between these two modes, measured using gravimetric and fixed-bed adsorption are largely non-existent in the literature.

Based on this gap in literature, and to supplement existing experimental assets, the design and construction of apparatus for assessing adsorbent materials in fixed-bed conditions will be carried out. Focus should be placed on tight control over operational parameters, and the ability to independently measure gas and vapour concentrations at a wide range of levels to quantitatively measure the impact of humidity on performance. Breakthrough curve analysis will not only allow for quantitative performance determination but could also provide insight into the mechanisms of competition occurring, and how these may differ depending on the chemistry and porosity of the adsorbent, or the level of relative humidity.

Chapter 3: Methodology

The initial stages of this project focused on characterising the physical and chemical properties of industrial porous materials, and how these properties may influence their adsorption and selectivity for volatile organic compounds. One conclusion from the early stages of the work was the need for additional experimentation to probe the multicomponent interactions between the adsorbent and adsorbate molecules when a mixture of vapours was present, and how these vapours may compete for adsorption sites. To this end, a bench-top breakthrough analyser was designed and built for testing the interactions of solids with gas-water, vapour-water, and gas-vapour-water mixtures. To better understand the nature of adsorbent-adsorbate interactions, both in single/ multicomponent as well as gravimetric/ fixed bed modes of adsorption, fitting of experimental adsorption data using empirical and first principles models was carried out.

To encompass the variety of techniques and methods used in this project, this Chapter will be divided into 5 sections:

1. Materials used for synthesis and measurements
2. Physical and chemical characterisation of materials
3. Adsorption characterisation of materials
4. Development of bench-top breakthrough curve analyser
5. Fitting of experimental adsorption data, standard deviations, and repeat measurements

3.1. Materials, chemicals, and standard synthesis procedures

3.1.1. Materials

3.1.1.1. Industrial adsorbents

The initial stages of this project functioned as a case study for VOC adsorption by porous materials, stemming from an industrial collaboration with Procter & Gamble Co. USA. The materials tested during this initial stage were chosen based on three factors: recommendations from the industrial collaborator, based on their own internal findings; commonly utilised adsorbent samples found in literature, to verify

equipment and measurement accuracy; and samples that allow for a range of porosities and surface chemistries to be tested.

Powder activated charcoal (Supelco 05105, AC) and granular activated charcoal (C2764, GAC) were acquired from Sigma Aldrich, UK. High-silica zeolite Y (Advera 88Y, A88Y) and high-silica ZSM-5 (Advera 14Z, A14Z) were acquired from PQ Corporation, UK as extruded pellets. Molecular sieve 13X (Supelco 20304, 45-60 mesh, MS13X) was acquired from Sigma Aldrich, UK. Amorphous silica gel powder (Zeofree 91, AS) was acquired from Huber Engineered Materials, USA. All materials were analysed in their as-received form with no modifications, except for drying, activation, and grinding of pelletized samples for X-ray diffraction and fluorescence, and water contact angle measurements.

3.1.1.2. Solvents and synthesis reagents

All organic solvents used for vapour generation and synthesis were ordered with a minimum of 98 % purity: methanol (CAS: 67-56-1), 2-propanol (67-63-0), and n-hexane (110-54-3) were acquired from VWR International, UK; ethanol (64-17-5) was acquired from Sigma Aldrich, UK; toluene (108-88-3) and 2-butanone (78-93-3) were acquired from Thermo Fisher Scientific (UK). In-house de-ionised water was used for water vapour measurements and humidity pre-conditioning.

All reagents for ZIF-8 and ZIF-67 synthesis were ordered with a minimum of 97 % purity. Zinc nitrate hexahydrate (10196-18-6), zinc acetate dihydrate (5970-45-6), zinc bromide anhydrous (7699-45-8), cobalt nitrate hexahydrate (10026-22-9), and 2-methylimidazole (693-98-1) were acquired from Sigma Aldrich, UK. Modulating ligands n-butylamine (109-73-9) and 1-methylimidazole (616-47-7) were acquired from Sigma Aldrich, UK.

All reagents for MIL-100 synthesis were ordered with a minimum of 97 % purity. Iron nitrate nonahydrate (7782-61-8) and trimesic acid (554-94-0) were acquired from Sigma Aldrich, UK. Decylphosphonic acid (6874-60-8) and octadecylphosphonic acid (4724-47-4) were acquired from Sigma Aldrich, UK.

3.1.2. Synthesis of metal-organic frameworks

To test their applicability in VOC adsorption, and to investigate the influence of water pore filling on adsorption competition, ZIF-8/ 67 and MIL-100 were synthesised. In this chapter the general procedures for synthesizing these materials will be outlined, although specific information about optimisation and sol-gel formation will be included in Chapter 5 & 6. For analysis, all MOF powders are ground to fine powders and sieved using 180-250μm meshes.

3.1.2.1. Synthesis of powder ZIF-8 and ZIF-67

Synthesis procedures were developed based on the methods by Cravillon et al [221] For the synthesis of ZIF-8 and ZIF-67 powders, 0.745 g (~2.5 mmol) of zinc nitrate hexahydrate or 0.720 g (~2.5 mmol) of cobalt nitrate hexahydrate, respectively, was dissolved in 50 mL of methanol. A second solution was prepared by dissolving 1.642 g (~20 mmol) of 2-methylimidazole in 50 mL of methanol, which was combined with the first solution under magnetic bar stirring until solutions were well mixed. After 24 hours the resulting precipitate was centrifuged and washed with methanol 3 times before drying at 150 mbar at room temperature overnight. ZIF-8 and ZIF-67 powders prepared in this way were denoted as ZIF-8 and ZIF-67, respectively.

3.1.2.2. Synthesis of monolithic ZIF-8 and ZIF-67

The monolithic samples are prepared almost identically to the powders, apart from the addition of between 0.99/ 1.98/ 3.96 mL (~10/20/40 mmol) of *n*-butylamine or 0.80/1.59/3.19 mL (~10/20/40 mmol) of 1-methylimidazole to the solution containing 2-methylimidazole. This resulted in a metal: linker: modulator molar ratios between 1:8:4-1:8:16. In addition, the cleaned sol-gel product was allowed to air dry under ambient temperature and pressure (i.e. instead of vacuum drying) for a period of 72 hours.

To test the effects of a mixture of modulating ligands on monolith formation, a mixture of 0.80 mL (~10 mmol) of 1-methylimidazole and 0.99 mL (~10 mmol) of *n*-butylamine was added to the solution containing 2-methylimidazole. The precipitates were then treated in an identical manner to the previous procedure.

3.1.2.3. Synthesis of powder and monolithic MIL-100

Synthesis procedures were developed for iron-based MIL-100 in both powder and monolithic form. The powder synthesis was based on a procedure reported by Kyong-Seo et al [222] and work by a fellow research, Luqman Hakim Mohn Azmi. A solution containing 20 mL of D.I. water, 8.016 g (~20 mmol) of iron nitrate nonahydrate, 2.752 g (~13 mmol) of trimesic acid and, for the monolith, 1.29 mL (~13 mmol) of n-butylamine were combined in a 25 mL Teflon-lined stainless-steel reactor and stirred until well mixed. The reactor was then sealed and placed in a synthesis oven at a temperature of 160˚C for a period of 12 hours before being cooled to room temperature. The slurry was recovered, cleaned, and centrifuged once using hot D.I. water followed by cleaning and centrifuging with ethanol three times, before a final wash with room temperature ethanol for the powder, or either D.I. water, ethanol, or methanol for the monolith. The slurry was dried at room temperature and pressure for a period of at least 1 week until a dry powder or monolith formed, followed by drying at 150 mbar and 120˚C overnight.

3.2. Physical and chemical material characterisation

For most characterisation techniques, solid samples were degassed under two different sets of conditions:

1. Regular degassing, in which industrial and MOF samples are degassed at 300˚C and 120˚C without the presence of vacuum. These conditions are used for characterisation techniques in which the samples are not required to be completely dry or clean for analysis.
2. Intense degassing, in which industrial and MOF samples are degassed at 300˚C and 200˚C in the presence of vacuum of 150 mbar. These conditions are used for techniques in which the presence of contaminants will influence the interactions of probe molecules, such as gas pycnometry and gas or vapour adsorption analysis, or the presence of adsorbed vapours and gases will significantly reduce the quality of collected images, in the case of scanning electron microscopy.

In subsequent sections, references will be made to ‘regular’ and ‘intense’ degassing. In both conditions, a drying time of 3 hours is used unless specified otherwise.

3.2.1. X-ray diffraction

X-ray diffraction, or XRD, uses the constructive interference of X-rays scattered by the atoms of a material to determine the structure of that material, typically the presence of certain crystalline phases and the nature of those crystal lattices. When the X-rays from a given source reach the atoms of the studied material, the electrons absorb and re-emit X-rays with the same energy as whatever reached them in a process called elastic scattering. These ‘diffracted’ X-rays interfere with one another- the nature of which depends on how the waves ‘line up’ with one another: when the waves are in alignment, the signal is amplified resulting in ‘cosntructive interference’; when the waves are out of alignment, the net signal is reduced resulting in ‘destructive alignment’- with the most extreme case being when the waves are half a wavelength, or 180˚, out of alignment- resulting in a net signal of zero. In crystalline materials, the constituent atoms form distinct planes with set distances between them- this allows the diffracted X-rays to constructively interfere with one another at certain incident X-ray angles.

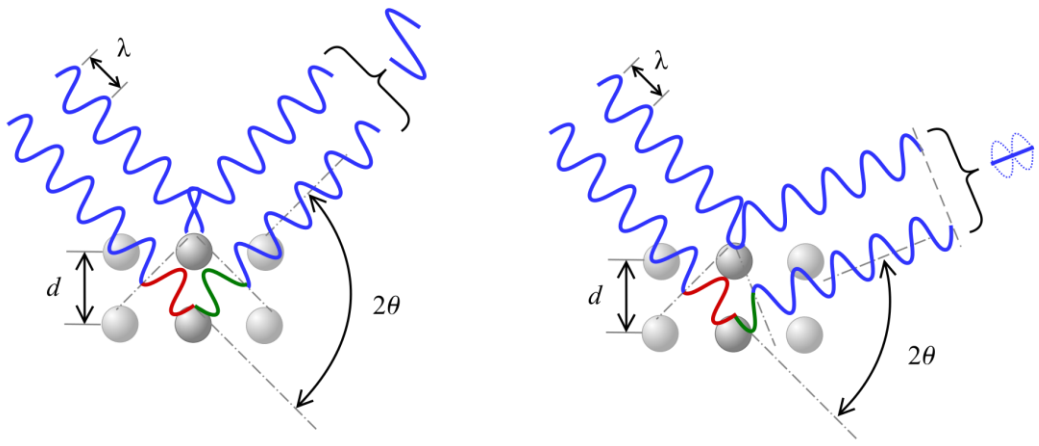


Figure 3.1: Illustration of X-ray diffraction in a crystalline material. Blue circles and black lines represent atoms and X-rays respectively. The left image represents an incidence angle resulting in constructive interference of diffractive X-rays, while the right image shows destructive interference of diffractive X-rays. Reproduced from Wikipedia [223] under Creative Commons licensing.

This constructive interference and amplification of the signal is seen during X-ray diffraction experiments as a 'peak' in the spectra and is assigned to a 2θ value equal to the angle between the incident and scattered X-ray beams. For a particular atomic spacing, the incident angle which will result in constructive interference is defined in Bragg's law [224]:

$$n\lambda = 2 \cdot d \cdot \sin(\theta) \tag{3.1}$$

Where n is a positive integer, λ is the wavelength of the incident X-ray wave, d is the distance between the lattice planes, and θ is angle of incidence of the X-ray beam relative to the lattice plane. X-ray diffraction patterns are largely specific to each compound, allowing them to be used as markers for specific phases and used for identifying the composition of a sample. For example, titanium dioxide can contain several different crystalline phases depending on its source- X-ray diffraction can help to identify which phases are present in a particular sample [225].

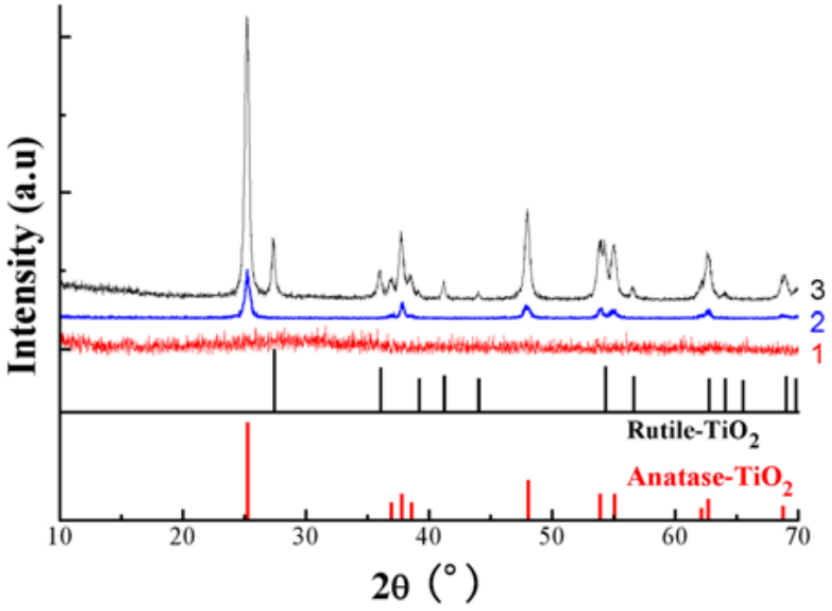


Figure 3.2: Powder X-ray diffraction spectra for TiO_2 nanoparticles (1, 2, and 3) alongside characteristic peaks for rutile- and anatase-phase TiO_2. Reproduced from work by Wang et al [225] through Creative Commons licensing.

Powder XRD patterns were collected using an X'Pert Pro X-ray diffractometer (Malvern Panalytical, UK) with the following operating conditions: Cu-Kα radiation at 40 kV and 20 mA, in a 2θ scan range of 4º-60º, using a step size of 0.03º. Samples are dried using regular degassing conditions. Drying accomplishes two goals: reducing agglomeration of particles due to moisture, allowing a finer powder to be prepared; removal of potential crystalline hydrates or alternative phases due to excess moisture. In the case of monolithic, structured, or pelletised adsorbents, the samples are ground to a fine powder prior to measurement for ease of preparation. A small quantity, typically around 100 mg depending on sample density, is placed onto the XRD sample holder which containers a circular indentation. The powder sample is then pressed into this groove using a clean glass slide to produce a uniform flat surface for diffraction, ensuring the powder sample height is homogeneous.

3.2.2. Thermogravimetric analysis

Thermogravimetric analysis (TGA) measures the change in mass of a sample when exposed to certain temperature profiles. By increasing the temperature of the sample linearly at a particular heating rate, the stability of that sample can be measured as a function of temperature. In this work, TGA is primarily used for measuring the temperature-induced structural degradation of the sample, allowing activation conditions to be determined that will sufficiently degas the sample without damaging it. For modified samples, TGA can also provide information about the strength or stability of a modification or coating on the sample. TGA can be combined with other analytical techniques to gain deeper understanding of the phase transitions and mass loss events, although these were not investigated in-depth in this work. Differential scanning calorimetry (DSC) measures the difference in the quantity of heat required to increase the temperature of the sample as a function of temperature and can give information regarding phase changes such as glass transitions, crystallisation, and dehydration. Mass spectrometry (MS), when combined with TGA, can help to identify the composition of any species produced during the heating of the sample, whether that be trapped water, solvents, or the combustion of the material itself.

Thermogravimetry profiles were determined using an STA 449 F5 Jupiter (NETZSCH, Germany). Sample temperatures were raised from 50 to 1000ºC at a rate of 5ºC/ min in all experiments for consistency. In terms of experimental preparation, 15-30 mg of sample is weighed and placed into a

ceramic holder which is then placed into the TGA equipment. Samples are not dried before analysis, as the experiment itself can be used as a method of determining trapped moisture, contaminants or, in the case of synthetic MOFs, remaining reaction solvent or linker molecules. Measurements using both oxygenated (dry air) and inert (nitrogen) carrier gases was carried out, with the gas used in TGA plots being specified.

3.2.3. Fourier transform infrared spectroscopy

Infrared spectroscopy operates by measuring the absorption, or transmittance of infrared light by the chemical bonds within a sample with different bonds absorbing infrared radiation at specific wavelengths. Therefore, by altering the wavelength of infrared light across a sample and measuring the absorbance or transmittance of that light, the presence of different bonding groups within the material can be determined. This absorbance not only applies to the solid material itself, but also any molecules present on its surface or within the bulk, such as trapped moisture or contaminants.

The infrared spectra for each sample were collected using a Cary 630 FTIR (Agilent, USA), in transmittance mode in a wavenumber range of 500-4000 cm^{-1} using a diamond tip and attenuated total reflectance (ATR) method. No sample grinding was carried out. As FTIR can give an indication to the water content of the material, and by extension its hydrophobicity, scans of each sample are taken without pre-drying of the sample. If certain bonding groups could be obscured by the broad peak of water around 3200 cm^{-1} [226], samples are re-analysed using regular degassing conditions.

3.2.4. Gas and solid-medium pycnometry

Pycnometry uses the known volume of a sample holder and the volume of a particular intruding fluid or fluid-like medium to measure the total volume of sample present during an experiment. The nature of the fluid determines what type of density is measured, as different media can penetrate different sized spaces and apertures within a sample. For example, while a gas can enter the small pores of a sample and in between constituent particles or crystals in a structured material, a dry flow medium like glass beads may only be able to identify external void volume. For this work, two definitions of density are experimentally determined: true density, determined using helium pycnometry, measuring the

material's volume, excluding closed (blind) pores; and bulk density, determined using dry flow medium (glass beads), measuring the material's volume including interstitial spaces and external voids, but not pore volume.

The main operation of a gas pycnometer consists of two chambers, one for containing the sample and one for expansion of gas, both of which are well understood in terms of their volume. These chambers are linked to a gas inlet and outlet and to each other via valves, and a pressure gauge is connected to the sample chamber for monitoring of the system pressure. Initially the system is flushed with the analysis gas, typically helium, to degas the sample and remove any moisture or contaminants from the system- during this time all valves are open. The expansion and vent valves are then closed, the sample chamber is filled to a certain pressure, P_1, and the system is allowed to equilibrate via monitoring of the pressure gauge. The fill valve is then closed, and the expansion valve is opened- allowing the system to equilibrate to a new pressure P_2. This process is then repeated multiple times, each time measuring the values of P_1 and P_2.

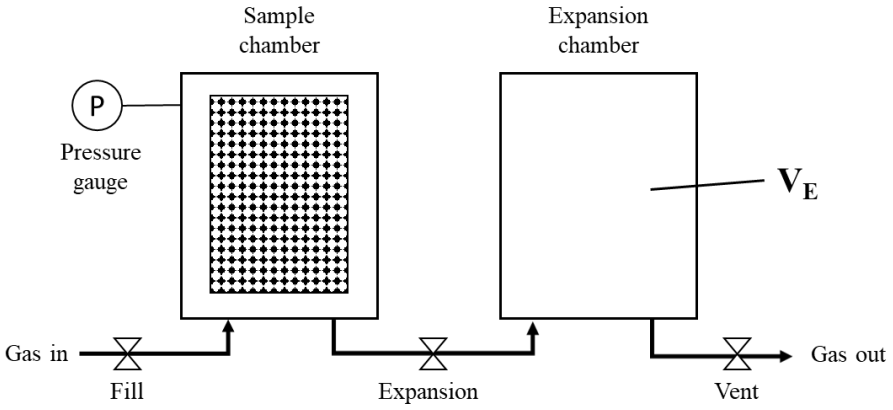


Figure 3.3: Schematic of gas pycnometry equipment, including chambers, valves and pressure gauge.

As the total sample chamber volume (i.e. without sample), expansion chamber volume, and pressure differences are all known, the volume and density of sample can be calculated using the following equations [227]:

$$V_S = V_C - \frac{V_E}{\frac{P_1}{P_2} - 1} \tag{3.2}$$

$$\rho_S = \frac{m_S}{V_S} \tag{3.3}$$

V_S, V_C, and V_E are the sample volume, empty sample chamber volume, and expansion chamber volume, P_1 and P_2 are the system pressures before and after the expansion valve is opened, ρ_S is the absolute density of the sample, and m_S is the mass of the sample.

For determination of bulk density the displacement a dry-flow medium such as small glass beads is measured following the addition of the sample. These beads can penetrate into external voids in the sample (i.e. between large particles), but not into the pores or smaller apertures. The volume of flow medium is measured using the depression of a plunger through a glass cylinder filled with the medium. This method allows the reference volume to be calculated using the distance moved by the plunger and the internal diameter of the cylinder. The sample is then added to the flow medium and mixed before the plunger is depressed again, measuring the new total volume- the volume of sample can then be calculated by subtracting the volume of flow medium. During the plunger depression the cylinder is rotated to ensure good mixing of the sample and/ or flow medium.

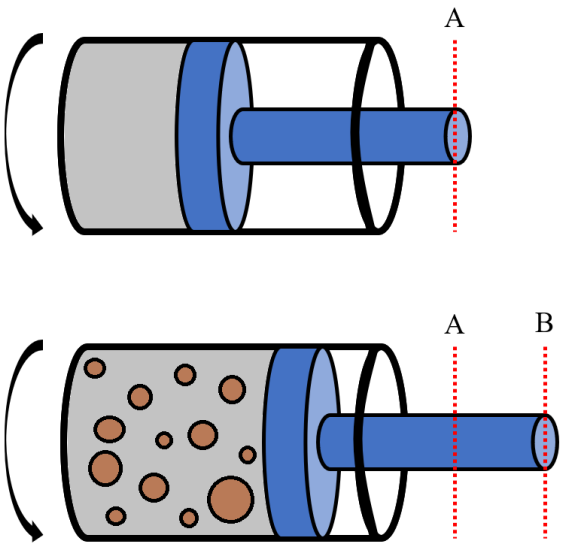


Figure 3.4: Schematic of bulk density measurement using dry flow medium. Points A and B represent the plunger position without (top) and with (bottom) the addition of sample respectively.

The density of adsorbent samples was measured via pycnometry using an Accupyc II 1340 (Micromeritics, USA) with Helium gas as the probe molecule, and solid-phase compression using a GeoPyc 1360 (Micromeritics, USA) and glass beads as the compression medium. The Accupyc was temperature-controlled to 25˚C, while the GeoPyc did not contain any temperature control and experiments were carried out at the laboratory temperature. Samples were dried using intense degassing conditions, as detailed at the start of **Section 3.2**. More intense degassing conditions were deemed necessary as sufficient degassing is required to remove any adsorbed gases that may affect the pressure readings for helium pycnometry and ensures the sample is dry and easy to mix with the dry flow medium for bulk measurements. No sample grinding was carried out.

3.2.5. Contact angle

The contact angle is the angle where a liquid-vapour interface meets a solid surface and quantifies the wettability of that solid. The measurement of this angle is most commonly carried out using water as the liquid, which then allows for the liquid-phase hydrophobicity of the solid to be measured- increased wetting is indicative of a stronger interaction, and therefore a more hydrophilic surface.

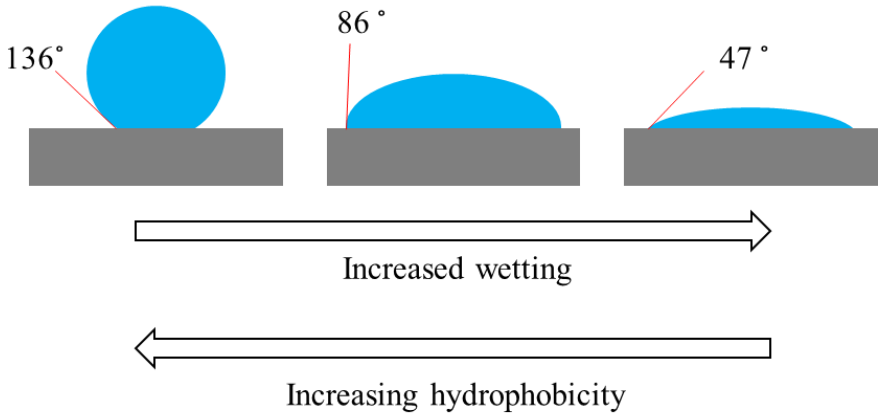


Figure 3.5: Illustration of water contact angles on more (left) and less (right) hydrophobic solid surfaces.

For water contact angle measurements, a fixed volume droplet of water is formed using an automatic syringe and allowed to wet the solid surface, with the process recorded using a high-speed camera. The

individual image frames can then be analysed to measure the solid-liquid-vapour angle. In the case of the advancing angle, the process is repeated by progressively adding more volume to the droplet- with the advancing angle defined as the highest contact angle measured prior to an angle decrease.

Water contact angles were measured using a Krüss DSA25 (Krüss Scientific, Germany). Samples were prepared by initially drying under regular degassing conditions, following by grinding to a fine powder and sticking to a glass slide using double-sided tape. This approach allowed a uniform, flat surface of the material to be prepared. An initial droplet volume of 20 μL is generated, with additions of 5 μL being made progressively to determine the advancing angle. If the droplet moves away from the camera or has difficulty being suspended on the sample, a video is recorded of the formation and suspension of the droplet on the surface. Stills from the video are analysed to calculate the final contact angle- in these cases the advancing angle cannot be calculated due to the inability to add additional volume to the droplet. Measurements were carried out at room temperature.

3.2.6. Scanning electron microscopy

Scanning electron microscopy (SEM) is a technique for imaging of solid samples at high magnifications, often to analyse features in the micrometre- nanometre size range. This is accomplished by focusing a high-energy beam of electrons onto the surface of a sample. When these electrons reach the surface, they interact in several ways- producing secondary electrons, backscattered electrons, and characteristic X-rays. Secondary electrons originate from the surface or near-surface regions are of a relatively low energy- these are the electrons used for imaging the topography and physical structure of samples. Backscattered electrons originate from a much broader region of the sample and are due to elastic collisions of electrons with atoms, altering the former's trajectory. The larger the atom, the stronger the scattering effect and the higher the resulting signal. This allows imaging of a sample while being able to identify different sample phases due to differences in elemental composition.

Scanning electron microscopy can be combined with energy dispersive X-ray spectroscopy, or EDS, in order to identify the elements present in a sample. In EDS, a beam of electrons is focused on the sample, leading to the emission of X-rays at a characteristic energy value depending on the elements present.

For example, the beam may excite an electron in the inner shell of a particular elemental atom, ejecting it from the shell while leaving behind an electron hole to be filled by an electron in a higher energy, outer shell. The difference in energy level between these higher and lower energy shell electrons may be released as an X-ray, which is specific to the atomic structure of the emitting element, and therefore allows the composition to be measured. In some cases, electrons from several shells (denoted by letters K, L, M, N, and O) may be ejected leading to multiple peaks at different energy levels. The amount of energy required to excite electrons depends on what elements or shells are present. The characteristic X-rays for K and L shells of elements in the periodic table, measured in keV, are typically supplied by SEM or EDS manufacturers. For example, the characteristic Kα X-rays for argon and krypton are 2.957 and 12.631 keV respectively, which require a minimum accelerating beam voltage of 5 kV or 15 kV respectively [228]. However, as the energy of the incident beam increases, sample degradation becomes more likely due to effects such as heating, atomic displacement, and electrostatic charging [229].

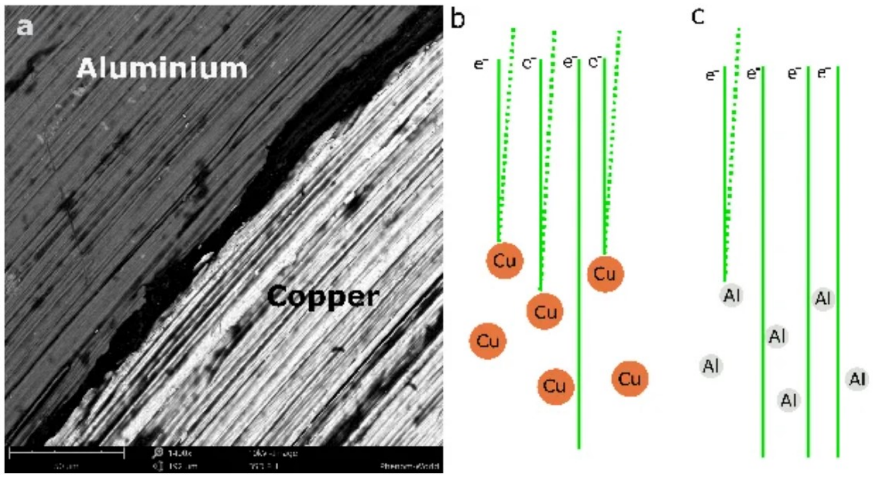


Figure 3.6: Illustration of back scattering analysis of samples: SEM images of sample containing aluminium and copper (a); schematics for scattering potential of larger Cu atoms (b), and smaller Al atoms (c). Reproduced from whitepaper article by AZO Materials and Thermo Fisher Scientific [230] with permission.

SEM and EDS experiments were carried out using a LEO Gemini 1525 (Zeiss, Germany) and an INCA (Oxford Instruments, UK) with silicon drift detector respectively. In typical experiments, samples are

coated with 15 nm of chromium prior to measurement in order to provide a conductive surface for SEM analysis. Prior to coating, samples were dried using intense degassing conditions to remove moisture and contaminants and prevent 'charging'- where the electrons of the beam are repelled by other electrons. Details of this intense degassing can be found at the beginning of **Section 3.2**. This phenomenon leads to the image appearing to move or blur and makes image collection difficult. For SEM analysis, an accelerating voltage of 5 kV is used to minimise sample degradation. For EDS analysis, accelerating voltages between 5-15 kV are used to collect spectra of all possible elements present. When analysing SEM data, ImageJ is used for measuring feature sizes such as crystals, and the contrast and brightness are altered to improve the final image quality.

3.2.7. Low-temperature nitrogen sorption

Gas adsorption is typically used for calculating surface area, pore volume, and pore size distribution data of porous solid materials by measuring the quantity of an inert gas, typically nitrogen, adsorbed by the material as a function of pressure. As with volumetric adsorption techniques mentioned in the literature review, low-temperature nitrogen adsorption uses the difference in gas pressure to measure the equilibrium capacities. When utilising nitrogen, an inert non-polar gas, the measurement is typically carried out at a temperature at or below the boiling point of the gas (-196˚C) which allows the adsorbate to condense freely onto the surface and inside the pores and spaces of the material. This condensation, for the purposes of calculating the BET surface area, is assumed to occur onto the surface in a monolayer which allows the calculation of the available area as the properties of the gas are known. The sorption isotherm of the nitrogen can be used to calculate several structural properties related to the surface area and pore volume of the sample, which were expanded upon in the literature review of the properties of porous materials.

Gas sorption experiments were carried out on a 3-Flex Physisorption (Micromeritics, USA). Sample preparation is key for gas sorption analysis as the samples must be completed degassed to provide accurate data for surface area and porosity. After measuring the mass of the sample tube and combined sample and tube mass, intense degassing is carried out overnight under a vacuum of 0.15 mbar using a VacPrep 061 (Micromeritics, USA). The tubes are then re-measured, giving the final dry sample mass

by subtracting the mass of tube. These samples are then loaded into the equipment and degassed in-situ at 0.067 mbar for a further 2 hours at a temperature 20˚C lower than the original degassing. These more intense degassing conditions reflect the sensitivity of the gas adsorption equipment

3.2.7.1. Analysis of nitrogen sorption data

To accurately determine the adsorbed quantity of gas by the sample, the 'empty' volume of sample tube must be known. For this reason, it is recommended that the sample tube volume is measured after analysis to prevent any additional degassing of the sample from nitrogen intrusion affecting the results, and to ensure the empty measurement and sorption measurements are carried out at the same temperature.

Surface areas were calculated using the BET method, following the Rouquerol criteria [39]:

1. A positive value for the BET constant c. An example of this is shown in **Figure 3.7**.
2. Data points in which the gradient of the Rouquerol plot (n_{ads}*(1-P/P_0) vs P/P_0) is positive.

This generally corresponded to a nitrogen partial pressure range of 0.02-0.08. Any deviation from this range will be discussed in subsequent chapters.

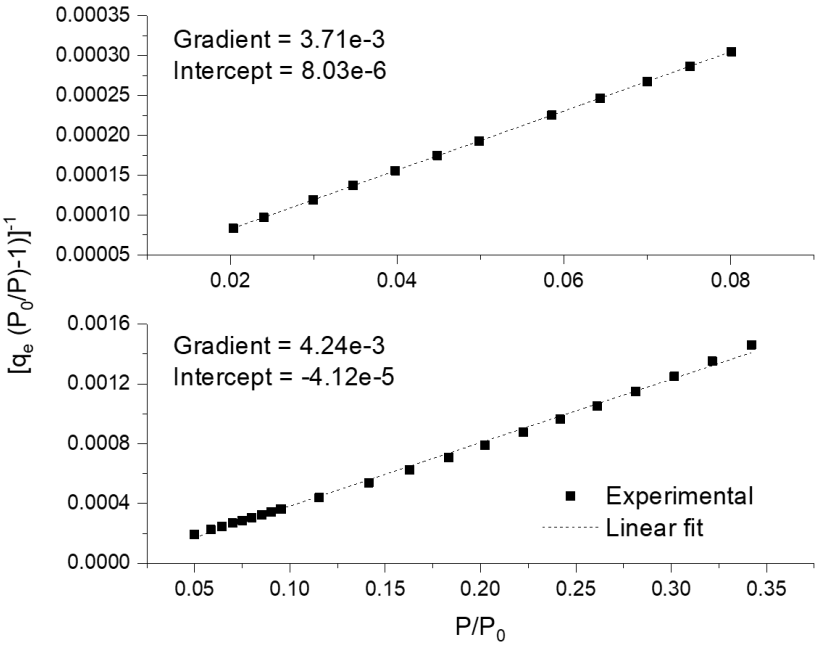


Figure 3.7: Linear fits of BET plots for activated charcoal, using the Rouquerol (top) and standard BET (bottom) partial pressure ranges. Note the negative intercept when fitting the standard BET range.

Micropore volume was determined using the t-plot method using the Harkins & Jura estimation for thickness of adsorbed film. This method has been used extensively for assessing the microporosity of zeolites [66], charcoals [231][65], and MOFs [153]. Discussion of micropore volume determination is elaborated on in **Section 2.2.3.1.**

The total pore volume of samples was calculated using the uptake of nitrogen at the plateau region of the isotherm at a partial pressure exceeding $P/P_0 > 0.97$. If no plateau region formed, i.e. the sample contains significant macroporosity, the total pore volume cannot be accurately determined via nitrogen sorption as the gas cannot be assumed to be adsorbed in a state close to its bulk liquid form [40]. Instead, a volume determined at a partial pressure before this steep inflection point, typically P/P_0 ~0.9-0.95, will be reported.

The pore size distribution of samples was determined using non-local density functional theory, specifically using the Tarazona DFT model in the Micromeritics model library. This particular model has been used in characterising the pore size distributions of zeolites [232], charcoals [233], and MOFs [234].

3.2.8. X-ray fluorescence

X-ray fluorescence, or XRF, uses the emission of fluorescent (or secondary) X-rays from a sample to determine its elemental composition. When an atom is exposed to short-wavelength X-rays with sufficient energy, an electron from one of its inner orbital shells can be dislodged. For the atom to remain stable, the valency left behind by the dislodged electron is filled from an electron at a higher energy orbital shell. As this electron drops to a lower energy state, it releases a fluorescent X-ray unique to that element. The position of these peaks and their intensity/ height can be related to the element present and its concentration respectively.

XRF was used for determining the Si:Al ratios and metal composites of industrial zeolites and silica samples. Experiments were carried out using an Epsilon 3 XLE X-ray fluorescence spectrometer

(Malvern Panalytical, UK) with the following operating conditions: Ag anode with maximum settings 50 kV, 3 mA and 15 V; Cu tube filter; Si drift detector, 145 eV @ 5.9 keV/ 1000 cps. Before analysis, samples were ground and dried using regular degassing conditions, detailed at the beginning of **Section 3.**2, to reduce caking due to moisture, and the powder was evenly spread within the XRF sample holder before analysis.

3.3. Measurement of material sorption properties using dynamic vapour sorption

Dynamic vapour sorption, or DVS, is a gravimetric adsorption technique typically used for analysing the uptake of gases and vapours, particularly water vapour, by solid materials. The DVS apparatus used in the project are the DVS Resolution and DVS Endeavour produced by Surface Measurement Systems, UK. The fundamentals of gravimetric adsorption characterisation can be found in **Section 2.3.1.1.** DVS uses a series of mass flow controllers and solvent bubbling units to control the partial pressure of solvent or water vapour solid samples are exposed to. The DVS apparatus used can control the adsorption temperature in the range of 10-70˚C with fluctuations of ~0.1˚C at 25˚C, and the partial pressure in the range of 0.005-0.95 (i.e. 0.5-95 % of the solvent's vapour pressure) [235]. These vapours are generated via bubbling units, where the carrier gas is passed through liquid solvent to produce a vapour stream at the vapour pressure of that solvent. Additionally, DVS can generate vapours for two solvents (typically water and a VOC) simultaneously, which allows for additional experimental flexibility and semi-quantitative multicomponent experiments- these are discussed later in this section.

When a sample is exposed to a particular environment, the mass of the sample is recorded using high-sensitivity mass balances with an advertised precision of 0.1 μg [235]. This approach has two benefits: precise determination of both the adsorption capacity and kinetics; and allowing for small sample sizes to be used for adsorption measurements, which is particularly useful for synthetic or high cost samples such as MOFs. In the case of the DVS Endeavour, the equipment uses five balances which are exposed to a shared absorbate environment, allowing large quantities of data to be collected simultaneously. The DVS software uses methods and sequences, which expose samples to a set series of conditions without manual input. This methodology is commonly used for generating adsorption isotherms: the sample

dries in the instrument, with the final mass recorded as a ‘dry mass’; the sample is then exposed to a particular vapour concentration, and the equipment measures the mass profile of the sample until a defined ‘equilibrium’ is reached; this process is then repeated for a new vapour concentration until a full adsorption/ desorption isotherm is generated. These datasets, containing potentially tens of thousands of mass, time, and partial pressure values, can be used to calculate the sorption kinetics and equilibria of the vapour-solid system.

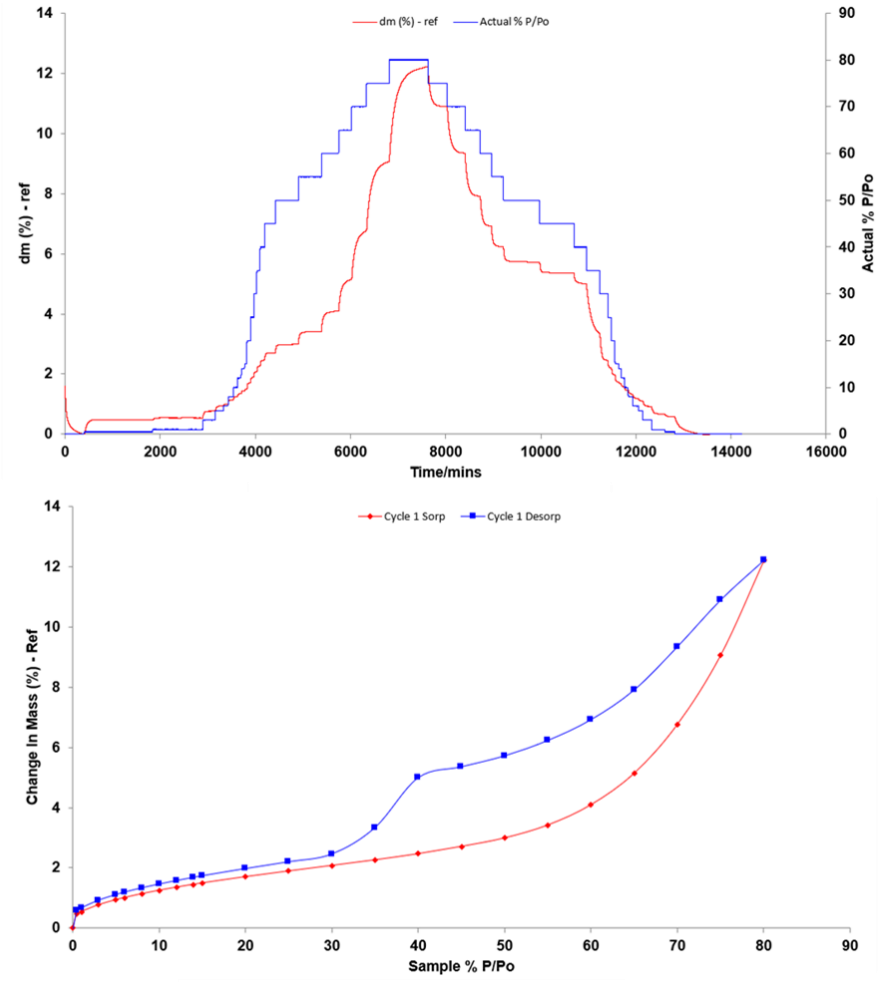


Figure 3.8: Kinetic mass profile (top) and corresponding sorption isotherm (bottom) of water vapour interacting with zeolite Y, measured using DVS Endeavour at 25˚C.

3.3.1. Design of dynamic vapour sorption methods

By creating different DVS methods and sequences, many experiments can be carried out. This section will detail the general procedure for developing different methods. All methods, regardless of the type of data being collected, must consider the mass equilibrium condition required for the software to move to the next stage of the method, i.e. when should the instrument move to the next partial pressure? This can be decided in two ways:

1. Fixed-time method: the method will move to the next stage of the experiments after an allotted amount of time has been reached, e.g. after 200 minutes of being exposed to 10 % humidity, the sample will then be exposed to 20 % humidity for a further 400 minutes. Each stage of the method can have individual time allotments, which may be important for adsorption steps at higher pressures that occur more slowly.
2. dm/dt method: the method will move to the next stage of the experiments after the sample reaches a defined level of 'mass equilibrium', or the percentage change in mass of the sample (relative to dry mass) per minute, e.g. a dm/dt value of 0.0015 mass %/ min means the experiment will not move forward until the sample mass changes by less than 0.0015 % of the dry mass per minute, either increasing or decreasing. With the dm/dt method, additional parameters for the averaging time range (i.e. over how many minutes is the dm/dt value averaged), the stability duration (i.e. how many minutes must the dm/dt be below the required value for until deemed 'at equilibrium'), and the maximum time allowed for each method step before the next step begins regardless of the dm/dt value. The maximum time allowed is often determined by trial-and-error during initial adsorbent tests but can be overestimated with little issue due to the method only moving forward to the next set of conditions after a sufficiently low dm/dt method has been reached. The advantage of the dm/dt method is that it allows a consistent value of equilibrium to be defined between samples, making comparisons of capacity more reproducible. In situations where the kinetics are unknown, the dm/dt method can often provide a shorter experimental timeframe as there is no 'unnecessary' time spent after the sample has already reached equilibrium.

An important note for the DVS Endeavour- as all five samples are exposed to a shared environment, i.e. the same temperature and partial pressure, all five samples must reach equilibrium before the method moves forward. For all adsorption measurements, each step of the method has a required dm/dt value of 0.00075 mass%/min, an averaging time range of 10 minutes and a stability duration of 20 minutes. The maximum step time varies between solid-vapour systems, but is generally either 24 or 48 hours, the latter of which is used for particularly slowly adsorbing/ desorbing systems.

3.3.1.1. Single-component isotherm method

The analysis method for generating a sorption isotherm is relatively simple. First, the sample(s) are dried in-situ under air flow. Although samples are pre-dried at elevated temperature and reduced pressure, it is likely they will adsorb some moisture while being transferred to the DVS. This initial drying step ensures any surface moisture is removed prior to measurement. Then, progressively higher partial pressures of vapour are generated, with the sample(s) reaching equilibrium with each partial pressure before moving to the next. Once the maximum partial pressure is reached, normally 0.9-0.95, the process can be repeated in reverse, with progressively lower and lower pressures used. This allows the adsorption hysteresis to be measured.

For VOC isotherms, greater focus is placed on the low-pressure isotherm points as this range better represents concentrations in vapour recovery or air cleaning applications. Partial pressure 'steps' will typically be between 1-3 % in the range of 0-30 % P/P_0, and around 5 % in the range of 30-90 % P/P_0. On the other hand, the isotherms for water vapour are typically measured using pressure steps of 5 % for the entire range of 0-90 % P/P_0.

3.3.1.2. Single-component cycling method

In a cycling method, the sample is exposed to a certain partial pressure and allowed to reach equilibrium. The sample is then exposed to some form of in-situ drying before re-adsorbing the species of interest. The form of drying can vary depending on the nature of the experiment- the DVS Endeavour has the limitation of only drying via the incubator temperature range of 10-70˚C, while the single-sample DVS Resolution can have a heating jacket installed to activate samples at temperatures up to 200˚C [236].

This process can be repeated any number of times to test the reusability of an adsorbent over multiple adsorption-desorption cycles.

3.3.1.3. Two-component competitive adsorption method

In a two-component experiment, the same is first exposed to one of the solvent vapours and allowed to reach equilibrium. Then, while maintaining the same level of the first vapour, the sample is exposed to a step change in partial pressure of the second vapour. The capacity for the second vapour can be measured by subtracting the capacity of the first vapour from the total capacity. This method represents the 'wet adsorbent' mode of competitive adsorption, where the volatile species bond to unoccupied sites, or attempt to displace pre-adsorbed water present on the material. A study by Fletcher, Benham & Thomas [101] combined gravimetric two-component measurements with mass spectrometry to measure the competitive capacity of activated charcoal for n-octane and water at respective partial pressures of 0.1 and 0.6. The hypothesised that the two species do not share any potential adsorption sites. In all experiments reported in this work, the relative partial pressure of water exceeded that of the VOC by at least 20 times to reduce the overlap in accessible adsorption sites due to partial pressure. As gravimetric analysis of a two-component vapour stream only allows the total amount of sorption to be quantified, any measurements of humid performance must consider this limitation and be considered only semi-quantitative, even when reproducible. By that, it is effectively assumed that the second solute does not displace the first adsorbed solute. The validity of this assumption was tested by carrying out 'reversed' two-component experiments where water was exposed following pre-exposure to toluene, shown in **Figure A.1** of the Appendix. For adsorbents with low water uptake (powder activated charcoal), the mass reached a fixed plateau after water exposure, while more hydrophilic adsorbents (ZSM-5 zeolite) displayed a negative gradient after the initial increase in mass- indicating some degree of displacement. This emphasises the limitations of this technique as a fully quantitative measure of selectivity, especially for adsorbents with favourable interactivity for the second exposed vapour. However, due to the omnipresence of humidity in industrial processes, including manufacturing, water vapour exposure is almost guaranteed prior to any application of an adsorbent, and the 'worst-case

scenario' of humidity pre-exposure still provides a useful metric when screening potential adsorbent materials.

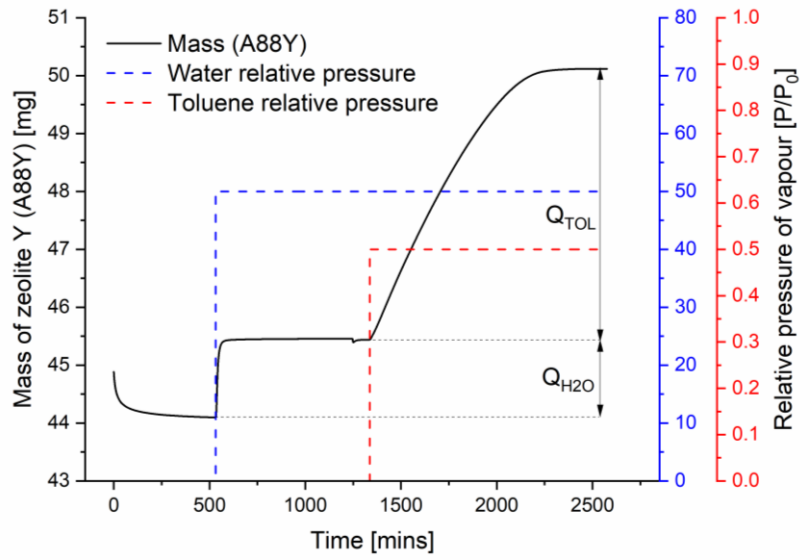


Figure 3.9: Mass profiles of zeolite Y in a two-component adsorption experiment, in which the sample is pre-exposed to water vapour following an initial drying step, and then exposed to a step change in toluene vapour concentration. Q represents the adsorption capacity of the material for a particular adsorbate. Measurement carried out using DVS Endeavour, T = 25˚C.

The two-component mode of the DVS equipment can also be used for 'humid cycling' experiments, where the cycling adsorption-desorption of a vapour is carried out while the humidity of the system is maintained. For applications where humidity is present, the reusability of a material constantly exposed to water vapour is an important design consideration.

3.3.2. Sample preparation for dynamic vapour sorption

Like nitrogen gas sorption, DVS requires the analysed samples to be fully activated in order for their adsorption capacity for water vapour and/ or VOCs to be determined accurately. Samples are activated using intense degassing conditions, i.e. around 300˚C for industrial materials and 200˚C for MOFs, under reduced pressures around 150 mbar. Between 20-50 mg of sample are then transferred to the DVS sample pans before being allowed to dry under dry air flow until their change in mass is reduced below

0.00075 mass %/ min. DVS does not require samples to be in any particular physical state or shape for analysis, so samples are typically analysed as-received or as-synthesised, i.e. monoliths and extruded powders are not ground to fine powders.

3.3.3. Analysis of dynamic vapour sorption data

Raw mass data is converted to adsorption capacity by dividing by the dry mass of sample, typically defined as the lowest mass observed at a partial pressure of 0 % (i.e. the drying step), with the difference from unity defined as the capacity in g/g- typically multiplied by 1000 to units of mg/g:

$$Q_x \left[\frac{mg}{g}\right] = \left(\frac{m_{sample}(t)\ [g]}{m_{dry}\ [g]} - 1\right) * 1000\ \left[\frac{mg}{g}\right] \tag{3.4}$$

Isotherms are constructed by using the final equilibrium capacity a material has at each partial pressure step. Importantly, the 'actual' measured partial pressure is used for constructing isotherms, rather than the 'target' partial pressure specified in the software method, as these values can differ depending on the reliability of the generation method (e.g. a target of 90 % may only yield 89.5 % if leaks are present). Isotherms are fitted using a variety of adsorption models, which will be elaborated on later in this Chapter. For analysing kinetic data, the adsorption capacity versus time datasets are taken for particular partial pressure steps and fitted using pseudo-first order or pseudo-second order models, which will be described later in this Chapter.

3.3.3.1. Humidity-dependant hydrophobicity indexes

Single component adsorption data was used to assess the relative hydrophobicity of each adsorbent through the calculation of hydrophobicity indexes (H.I.s) [237]. Several methods for measuring H.I.s exist for both gas and liquid phase adsorption processes, including chemistry, which are summarised in **Table 3.1**. Methods typically involve the use of probe molecules, either in liquid or gas phase, to assess the extent of interactivity that probe has with the solid surface. This may be assessed using a contact angle, adsorption capacity, or a retention time, all of which provide some amount of insight on how favourable the fluid-solid interaction is.

Table 3.1: Summary of literature methods for determining adsorbent hydrophobicity.

Method of determining material hydrophobicity	Reference
Comparing liquid-phase uptake of non-polar and polar solvents, measured using ^{1}H NMR spectroscopy. $$Surface\ polarity\ index, P_i = \frac{Q_{nHEX} - Q_{DMF}}{Q_{nHEX} + Q_{DMF}}\ [\frac{mg}{mg}]$$	[238]
Determining dispersive and specific components of material's surface free energy via the retention time of non-polar and polar gas probe molecules, measured using inverse gas chromatography	[239]
Comparing wettability of water and toluene solvents onto solid material using contact angle measurements.	[240]
Comparing single-component adsorption capacities for non-polar and polar species, using volumetric adsorption equipment. $$Hydrophobicity\ index, H.I. = \frac{Q_{nHEX}}{Q_{H2O}}\ [\frac{mg}{mg}]$$	[100]
Comparing adsorption capacities for non-polar and polar species during multi-component experiments, measured using breakthrough curve analysis equipment.	[177]

In applications where pre-exposure to humidity is likely, such as passive adsorption processes without the use of active regeneration or a continuous process stream, the additional considerations of dynamic H.I.s (i.e. selectivity based on adsorption kinetics) may not be as pertinent. In this study, a new method of calculating H.I.s was developed using static adsorption data as a function of process humidity to better understand how humid performance might be linked to the concentration of water vapour. This represents the 'wet adsorbent' mode of competitive adsorption with water, where the solid phase is exposed to water vapour prior to VOC adsorption, compared to the 'wet adsorbate' mode where water vapour is present in the VOC concentration front as a mixture. This current study defines the hydrophobicity indexes in each system as:

$$H.I._{static}\ (x) = \frac{Q_{Toluene,0.005}\ \left[\frac{mmol}{g}\right]}{Q_{Water,x}\ \left[\frac{mmol}{g}\right]} \tag{3.5}$$

$H.I._{static}(x)$ is the material's static molar hydrophobicity index at a particular RH x, $Q_{Toluene,0.005}$ [mmol/ g] is the molar toluene quantity adsorbed by the material at a partial pressure of $P/P_0 = 0.005$, and $Q_{Water,x}$ [mmol/ g] is the same quantity for water vapour, at an RH of *x.* In this work, the partial pressure of water (or relative humidity) used was varied to ascertain how the H.I. value for each adsorbent changed with process humidity.

3.4. Design and construction of bench-top breakthrough analyser

As previously mentioned, the performance of adsorbent materials can be measured in several different ways, with the most common being gravimetric and volumetric instruments. For applications where the adsorbent is acting under a particular set of constraints, breakthrough curve analysis (BCA) is a popular tool for analysing its capacity, regeneration, and selectivity. BCA equipment is typically made up of three sections:

1. Generation, where the desired test fluid (typically gas) is prepared, using mixing of several gas streams, or the addition of water or volatile vapour through solvent bubbling.
2. Adsorption, where a bed of the adsorbent material is packed inside of a column before being exposed to the analysis gas. This column element will often be heated in order to allow in-situ regeneration.
3. Detection, where the eluted gas exits from the adsorption column, analysed, and its composition determined. This information, alongside various process conditions, is used to determine the adsorption performance of the material.

Each of these sections will be discussed, as robust control, measurement, and understanding of each is required to collect accurate data. An illustration of these three sections can be found in **Figure 3.10.**

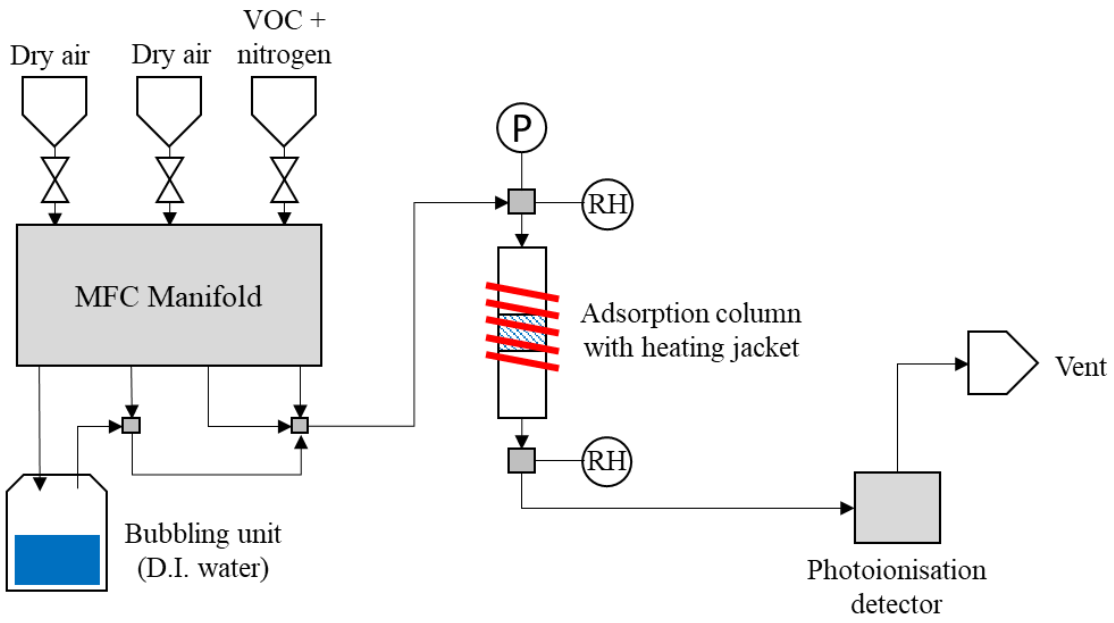


Figure 3.10: Schematic for breakthrough curve analyser, including: mass flow controller manifold and bubbling unit (generation); adsorption column with heating jacket (adsorption); and relative humidity (RH), pressure (P), and photoionisation detector (PID) sensors (detection).

3.4.1. Construction materials

The materials listed below will include the materials of construction in the gas manifold, the sensor components, and the source of 3rd party components such as mass flow controllers (MFCs), bubbling units, and heaters.

3.4.1.1. Building materials

Three kinds of tubing were used for the construction of the breakthrough analyser: 1/8-inch 316 stainless steel flexible tubing; 1/4-inch 316 stainless-steel rigid tubing; and 1/4-inch corrugated 316 stainless-steel tubing. All valves and standard fittings were made of stainless steel (Swagelok, USA). Bespoke sensor fittings and heating coil housing were constructed from stainless steel and copper respectively. Heating insulation was accomplished using Supelco 20411 glass wool (Fisher Scientific, USA).

3.4.1.2. Generation of concentration and temperature

The MFC manifolds were adapted from those in a DVS Resolution (Surface Measurement Systems, UK). Mass flow controllers MFC 2252 (Axetris, Switzerland) were calibrated for nitrogen and air up to a maximum flowrate each of 50 mL/min. Bubbling units were similarly adapted from the DVS Resolution, using 50 mL glass bottles containing deionised water or the solvent of interest. Maintenance of 25˚C is carried out using the incubator of a DVS Advantage (Surface Measurement Systems, UK). High-temperature heating was accomplished using a custom-built heating jacket, with the details described later. Type K thermocouples were ordered from RS Components, UK. Dual-element heating tapes, with specifications of 240 V and 0.02 W/ mm^2, were ordered from Omega, USA.

3.4.1.3. Sensory components

Temperature and relative humidity were measured using Rotronic HC2-CO5 compact probes (Rotronic, UK). Concentrations of volatiles were measured at two different concentration levels, both using humidity- resistant photoionisation detectors (Ionscience, UK): for low levels, 1-50,000 ppbv, a PID 2 PPB was used; for high levels, 0.1-4000 ppmv, a PID 2 PPM was used. For the pre-heater, temperature was monitored using an RS PRO Type K thermocouple (RS Components, UK). Column pressure and pressure drop were measured using a Wika DS-10-S digital pressure gauge (Wika, UK).

Note: plans were in place for the use of a Voice 200 Ultra SIFT-MS (Syft Technologies, New Zealand), located at a Procter & Gamble Co. research site in Reading, UK. However, due to the COVID-19 pandemic, it was deemed unfeasible to carry out the integration of the breakthrough curve analyser with P&G assets on-site. For this reason, multi-VOC breakthrough experiments were not carried out.

3.4.1.4. Testing materials

For testing the accuracy of the breakthrough analyser, adsorption experiments were carried out on industrial adsorbents. Specialty cylinders for nitrogen and dilute volatile vapours in nitrogen were ordered from BOC (BOC Ltd, UK). In-house deionised water was used for generating humidity, while in-house dry air was used as a carrier gas for VOC and water breakthrough curves.

3.4.2. Construction of the breakthrough analyser

3.4.2.1. Gas inlets

The MFC manifold allowed for three gas inlets, which were typically dictated by the experiment being carried out. For VOC and water experiments, dry air was used as the primary carrier gas alongside the specialist gas cylinder containing nitrogen and dilute concentrations of the vapour of interest, e.g. 100 ppmv of toluene vapour in nitrogen. All gas was piped from the laboratory's air supply or cylinder array using 1/4-inch stainless steel gas line piping, with the connection to the regulator of the cylinders made using 1/4-inch corrugated stainless-steel piping, or 1/4-inch flexible fluorinated ethylene propylene propylene (FEP).

3.4.2.2. Mass flow controller manifold

The MFCs are arranged into a manifold based on the DVS Resolution. This configuration allows for semi-independent control of four of the five gas outlets, and completely independent control of the fifth. The first four are linked into two pairs, which share the same bubbling system, and are labelled 'A' and 'B'. In a DVS these are associated with two different types vapours, with A being used for water vapour only, and B being used for solvent vapours. The relationship between the three inlet and five outlets is shown in **Figure 3.11**.

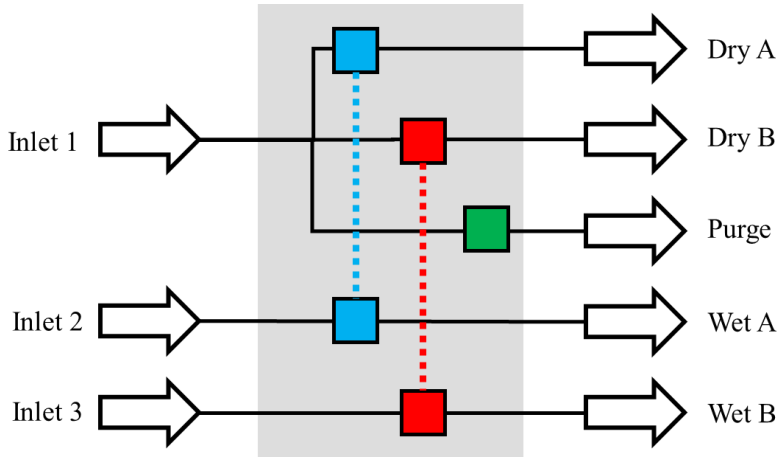


Figure 3.11: Schematic of mass flow controller manifold. Solid black lines show gas flow between inlet and outlet valves. Coloured boxes and dotted lines show dependence links between MFCs (e.g. Dry B and Wet B, red, have flowrates and control systems dependant on one other).

Flowrate is controlled through two means: setting the 'total' flowrate of a linked pair, such as Dry + Wet A; and setting the ratio of 'wet' to 'dry' in that total flow. For example, if the control of humidity was assigned to 'A', and the user wanted 40 mL/min of gas flow with a relative humidity of 40% they would set the total, that is Dry + Wet, flowrate to 40 mL/min and the fraction of 'wet' flowrate to be 0.4. A and B can be controlled independently of each other, as can the 'Purge' line. This purge line is typically used for clearing the system in between experiments and can also be used as a separate concentration delivery stream if needed.

3.4.2.3. Concentration generation

Concentration is controlled via the mixing of 'wet' and 'dry' flows, as detailed in the previous section. In the case of gases and solvent vapours at low concentration, the 'wet' flow is provided via the use of specialty gas cylinders. For high concentration solvent vapours and water vapour, a bubbling system is utilised where gas is passed through liquid solvent, creating a headspace with the vapour pressure of the liquid. This is then mixed with the 'dry' flow to reach the desired relative humidity or partial pressure of vapour. Unlike the DVS equipment, the concentration was only maintained via open-loop controls. While the concentration of gas components can be measured, it was not used as a feedback closed-loop control due to the complexity of the electronics and programming required. This meant that additional concentration testing and calibration was required, which is detailed later in this Chapter.

To reduce dead time, 1/8-inch tubing was used to connect the MFC manifold and the bubbling/ mixing units. Compared to 1/4-inch tubing, the same length of 1/8-inch tubing reduces dead volume, and by extension dead time, by a factor of 4.

3.4.2.4. Packed-bed column and pre-heater

After gas streams pass through the inlet sensory housing, the gas reaches a three-way valve with two options: the gas can be redirected through a bypass, used for measuring initial concentrations and leak testing; or through the column itself. The bypass is a standard piece of 1/4-inch stainless steel tubing connected the three-way valves at either end of the column section. A pressure gauge is placed in a Swagelok T-joint before the packed bed to measure any pressure drop due to the packing of the column.

The columns themselves are 3mm I.D. borosilicate glass columns with a length of approximately 17 cm. Before samples are packed, a small slug of glass wool is placed into the tube to prevent the bed from dropping down, with another slug being placed on top after packing the adsorbent. This glass wool, considering its low surface area relative to the adsorbents, is unlikely to have a impact on the breakthrough curve or subsequent calculated capacity or kinetic parameters [241].

The pre-heater was designed to heat samples up to temperatures of 300˚C in order to activate them in-situ and allow for continuous remote testing and regeneration of samples. The heating jacket consists of several component:

1. A type K thermocouple to monitor and control pre-heater temperature via a feedback loop.
2. A copper tube with an internal diameter of ~3/8 inch to allow housing of both the adsorption column and thermocouple. Copper was chosen based on its high thermal conductivity.
3. Two heating coils, consisting of dual-element heating tapes, wrapped around the copper tube to provide heating up to 300˚C.
4. Glass wool surrounding the heating coil to provide insulation and prevent the jacket's outer surface from overheating and affecting the other components of the breakthrough analyser.
5. A large stainless-steel cylinder surrounding the glass wool, to prevent inhalation or direct physical handling of the glass wool. Screw caps were fitted at both ends and 1/2-inch holes were drilled into the centres to allow easy access to the column inside.

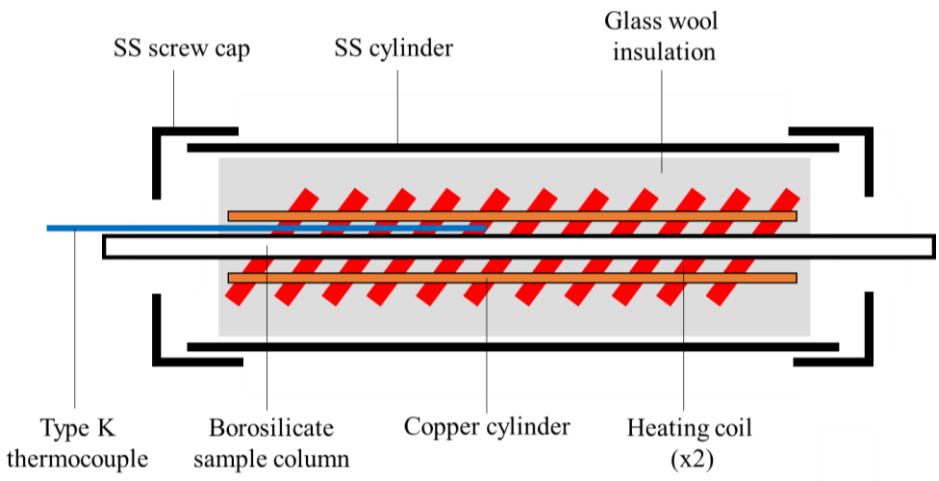


Figure 3.12: Simplified schematic of pre-heater setup for fixed-bed sample analysis column.

3.4.2.5. Sensory components

Bespoke housing units were designed and constructed in the Department's student machine workshop out of stainless steel. These units, shown in **Figure 3.13**, had four apertures: two for the gas inlet and outlet, standard 1/4-inch Swagelok; one for the combined temperature and humidity probe, also using a 1/4-inch Swagelok fitting, with space for the sensor bored ~1 inch deep into the unit; and one for a CO2 probe (not utilised in this work), using an M23x1 thread that replicates the plastic filter cap for the sensor. These housing units were placed before and after the column/ bypass array to have a constant measurement of the initial concentration, as well as acting as checks between the sensors to ensure both are working correctly.



Figure 3.13: Photograph of the sensory housing unit. Connections from top clockwise: gas inlet; gas outlet; CO2 probe; and combined temperature and humidity probe.

3.4.2.6. Photoionization detector

Unlike the CO_2, temperature, and humidity probes, the PID required separate housing due to the size and nature of the probe. The probe itself is connected to a circuit board, which in turn is connected to a separate circuit board which has the appropriate connections for power input and communication with a computer via USB cable. This format makes the PID setup much larger than that of the compact CO2 and humidity probes. For this reason, the outlet of the sensor housing described previously is connected to the gas delivery hood of the PID, which itself is stored inside a temperature-controlled miniature storage unit. The temperature of the unit is maintained at 30˚C to prevent condensation of water or solvent vapours in the gas stream.

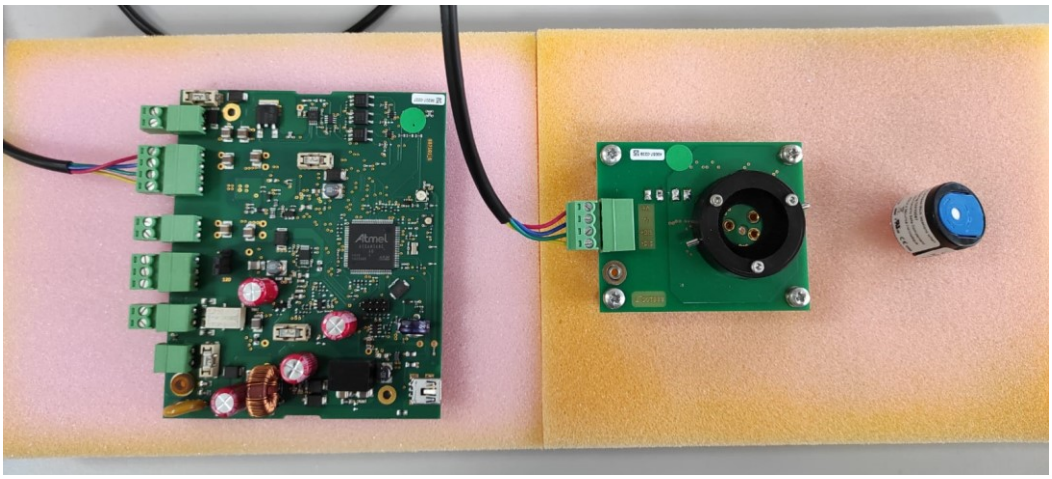


Figure 3.14: Photograph of integration board (left), sensor control board (middle), and photoionization detector (right).

3.4.2.7. Experimental operation and controls

Control of the breakthrough analyser was accomplished using a modified form of the control program for the DVS Resolution. This software allows the setting of maximum flowrates, wet and dry ratios, and the temperature of the incubator. In addition, the base form of the software can measure and record the levels of relative humidity in two locations (i.e. before and after the column), as well as options for a pre-heater module, in which the temperature and ramping rate can be specified. The primary

modification made was to allow the Vaisala CO_2 sensors to communicate with the DVS hardware and software to allow the CO_2 concentration to be monitored in the same program that monitors humidity and temperature. Due to the lack of an open-source software library for the PID, VOC concentrations were measured using a separate program developed by IonScience.

3.4.2.8. Operation of photoionisation detector

Photoionisation detectors, or PIDs, operate through the ionisation of molecules through photons, typically from high-energy ultraviolet (UV) radiation. A typical PID will use a UV lamp to bombard incoming gas-phase molecules with photons to dislodge electrons and form cations, which then form an electric current. This current is measured and, alongside calibration data relating signals and concentrations, will output a measurement for the gas-phase species' concentration.

3.4.3. Leak tests

Leak tests were carried out using Snoop (Swagelok, UK) soap solution. The liquid was sprayed onto joints and areas with seals. In the case of a leak, bubbles would form, and the joint would either be re-tightened or disconnected and re-aligned before tightening. Flowrates were measured using an Agilent ADM 2000 flowmeter (Agilent, USA) at various points on the apparatus to measure any potential losses in flow between components. As with many construction projects, new leaks arose during the course of building and re-piping the equipment. Most leak issues appeared around the breakthrough column itself, as the PTFE ferrules used resulted in a less 'tight' connection than with stainless steel. However, cutting the glass columns to the correct length and careful packing of the material to reduce pressure drop resulted in the flow sensor post-column detecting flowrates between 99.5-100 mL/min out of a possible 100 mL/min, which was deemed acceptable.

3.4.4. Sensor testing and calibration

Breakthrough curves use integrated concentration versus time profiles to calculate capacity. Therefore, the concentration detected by the sensor has a direct impact on how performance will be measured by altering the y axis of the curve. Similarly, the time taken for the sensor to detect a species will impact

the integral of the breakthrough curve through the x axis. The calculation of a ‘dead time’ or ‘dead volume’ is required to correct each experimental breakthrough curve and ensure the results are accurate.

3.4.4.1. Humidity sensor calibration

Humidity sensors were calibrated by altering the relative ‘wet’ and ‘dry’ flowrates in the generation stage of the DVS Endeavour and the breakthrough analyser, the former of which has a humidity sensor calibrated via independent salt deliquescence experiments. Assuming no leaks or loss in flowrate, the same ‘wet’ and ‘dry’ flowrate fractions in both machines will yield equal values for relative humidity. Flowrate fractions between 0.05 and 0.9 were tested and used to calibrate the humidity sensors.

3.4.4.2. Photoionization detector (PID) calibration

To ensure that experiments and calculations were completed accurately, several PID calibration experiments were carried out to test the ‘actual’ VOC concentrations delivered by the BCA flow controller manifold. Beforehand, three calibration points for the photoionisation detector were measured:

1. A ‘zero’, taken as the signal generated after 10 minutes of exposure to 100 mL/min dry air.
2. A ‘low span’, measured under the same conditions using a calibration cylinder containing air with 10 ppmv of toluene vapour.
3. A ‘high span’, measured under the same conditions using a calibration cylinder containing air with 25 ppmv of toluene vapour.

These tests were repeated using flowrates of 10, 20, and 50 mL/min to ensure that the device’s readings were independent of gas flowrate. Following the calibration of the PID, the concentration of toluene vapour was increased to 5 and 10 ppmv through the mixing of two gas streams containing either dry air or 100 ppmv of toluene vapour in a balance of nitrogen.

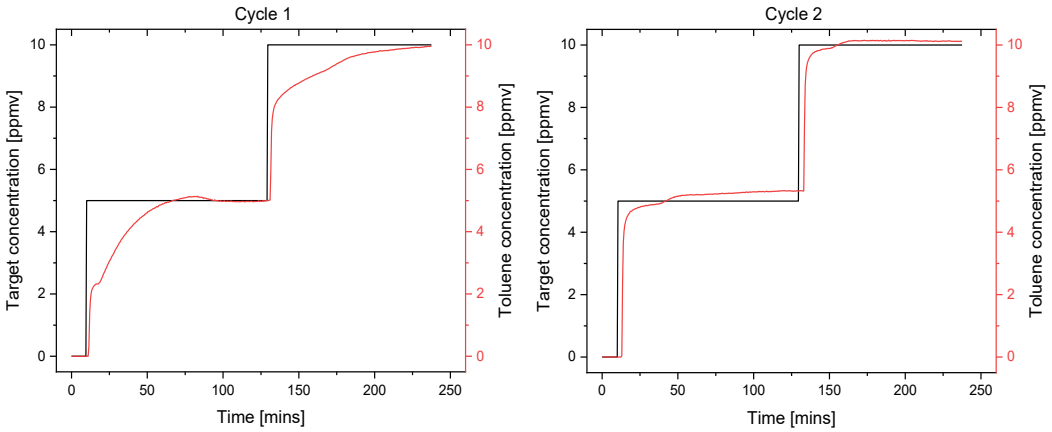


Figure 3.15: Target and actual toluene concentrations in the breakthrough analyser over two cycles, as a function of time for cycle 1 (left) and cycle 2 (right). Experiments were carried out at T = 25˚C and a total flowrate through the column of 100 mL/min.

As shown by **Figure 3.15** (left)**,** the PID sensor had an atypical profile when initially measuring incoming toluene concentrations. This effect was not present during the second cycle and is hypothesised to be due to the sensor 'warming up' or becoming acclimated to the measurement environment. Future single-step experiments showed the same results, with the initial jumps in concentration being slower than later ones. For this reason, each series of breakthrough experiments was preceded by an initial step change in concentration through the bypass lasting at least 5 hours.

3.4.5. Dead time determination

The time taken to measure step-changes in concentration through an empty borosilicate column were carried out for both humidity and PID sensors, as they are located at different distances from the adsorption column. The variation of these response times with concentration and flowrate was also tested.

3.4.5.1. Dead time of humidity sensors

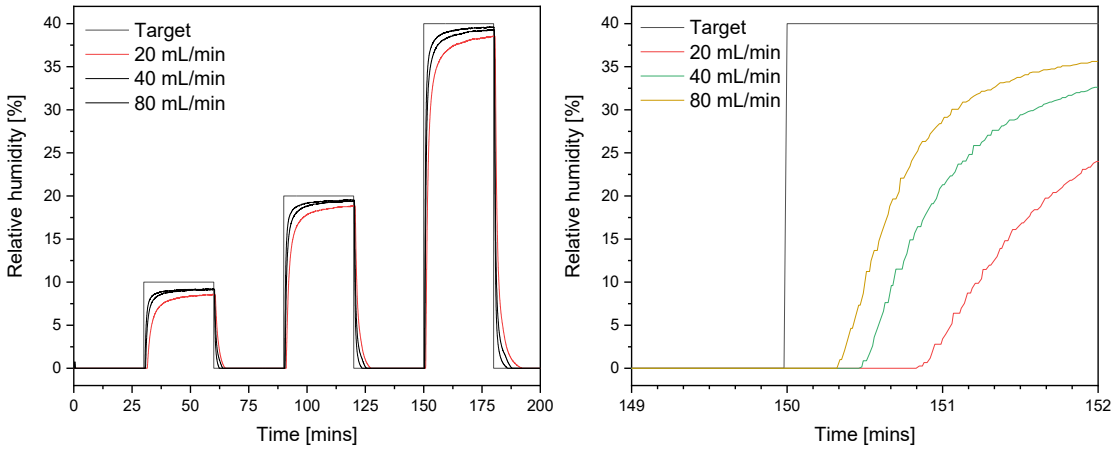


Figure 3.16: Target and actual relative humidities measured by the pre-column humidity sensor for flowrates between 20-80 mL/min. Right plot shows close-up of 0-40 % RH step. T = 25˚C.

As expected, the dead time of the pre- and post-column sensors was found to decrease drastically as the flowrate was increased from 20-40-80 mL/min. For example, between 20-80 mL/min at 20 % RH the pre-column dead time changes by a factor of 2.9 (64 and 22 seconds). However, this change was not observed to be linear, e.g. the change in dead time should be a factor of 4 to match the flowrate. This is due to the sensor response time, quoted by the supplier as < 15 seconds [242], which is likely not linearly affected by the flowrate of the gas, if at all. Assuming the response time is unaffected by flowrate, it can be manually calculated using the following equation:

$$Response\ time = \frac{Dead\ time_{flowrate=x\frac{mL}{min}}[s] - Dead\ time_{flowrate=y\frac{mL}{min}}[s]}{\frac{x\ \left[\frac{mL}{min}\right]}{y\ \left[\frac{mL}{min}\right]} - 1} \quad (3.6)$$

Where x and y are the carrier gas flowrates. For example, at 20 % RH, the pre-column dead times for 80 mL/min and 20 mL/min are 22 and 64 seconds respectively. Therefore, the calculated response time would be approximately 42/3 = 14 seconds. This method results in calculated response times between

8-29 seconds, except when using the first pre-column dataset for 20 mL/min and 10 % RH, which is noticeably longer than expected- credited to the sensor 'warming up'.

The level of relative humidity was also found to have an effect on the dead time, with pre- and post-column dead times consistently decreasing as humidity increased. Initially this was credited to the sensor responding to the larger change in humidity faster. However, the difference between pre- and post-column also was found to decrease with increasing humidity- despite the fact that any change in sensor response time should be identical for both sensors. For this reason, dead time measurements were carried out prior to each measurement at the exact conditions expected for the breakthrough curve.

Multiplying the dead times by the carrier gas flowrate in their respective experiment resulted in pre- and post-column dead volumes between 17-41 mL and 29-57 mL, with an average difference of ~ 14.3 mL. Assuming identical sensor response times for pre- and post-column probes, the average column dead volume measured was approximately 14 mL.

Table 3.2: Dead times of pre- and post-column humidity sensors, measured at relative humidities between 10-40 % RH, and carrier gas flowrates between 20-80 mL/min. T =25˚C.

Flowrate [mL/min]	**Sensor location**	**Dead time [s] [a] (equivalent volume [b] [mL])**		
		10 % RH	**20 % RH**	**40 % RH**
20	*Pre-column*	91 (30)	64 (21)	51 (17)
	Post-column	148 (49)	107 (36)	88 (29)
40	*Pre-column*	46 (31)	35 (23)	28 (19)
	Post-column	68 (45)	56 (37)	47 (31)
80	*Pre-column*	31 (41)	22 (29)	20 (27)
	Post-column	43 (57)	32 (43)	29 (39)

[a] Uncertainty in time measurements is ~0.02 minutes, or ~1 second.

[b] Calculated by multiplying dead time by carrier gas flowrate.

3.4.5.2. Dead time of PID

Increases in flowrate resulted in reductions in the measured dead time, as expected by an increase in the velocity of the carrier gas. Similar to the humidity probe, this reduction was not entirely linear due to the response time of the PID likely being flowrate independent. Based on **equation 3.6**, PID response

times between 5-20 seconds were calculated. Column dead volumes could not be calculated as the PID was located only post-column, outside of the main incubator, due to the size of the integration board and wiring required. Total dead volumes between 80- 93 mL were calculated. When accounting for an average PID response time of 8.3 seconds, total dead volumes between 77-82 mL were calculated. These values were significantly higher than those of the pre- and post-column humidity probes. However, the PID was located in separate housing connected to the main column incubator using 1/8 inch O.D. piping, making any further reduction in dead volume difficult.

Table 3.3: Dead times of PID sensor, measured at toluene concentrations between 5-50 ppmv, and carrier gas flowrates between 20-80 mL/min. T =25˚C.

Flowrate	**Dead time [s] [a] (equivalent volume [b] [mL])**			
[mL/min]	**5 ppmv**	**10 ppmv**	**25 ppmv**	**50 ppmv**
20	255 (85)	245 (81)	240 (80)	246 (82)
40	133 (88)	125 (83)	128 (85)	127 (84)
80	70 (93)	67 (89)	67 (89)	66 (88)

[a] Uncertainty in time measurements is 1 second.

[b] Calculated by multiplying dead time by carrier gas flowrate.

At concentrations exceeding 10 ppmv, the PID concentration profile was noticeably less steep, taking much longer to reach the final equilibrium concentration. In addition, steps exceeding 25 ppmv (> 30 ppmv) could not be determined by the PID, due to exceeding the operating range of the sensor. Sensors with a wider range of detectable concentrations have a trade-off of smaller resolution, making accurate determination of dilute BTCs difficult. In addition, while the concentration of 50 ppmv could not be detected by the PID, the humidity probe had a noticeable jump to approximately 0.9 % RH when exposed to 50 ppmv of toluene vapour. This suggests that elevated levels of VOCs may affect or damage the polymer lining of the humidity probe. For this reason, concentrations were not allowed to exceed 10 ppmv in regular BTC experiments.

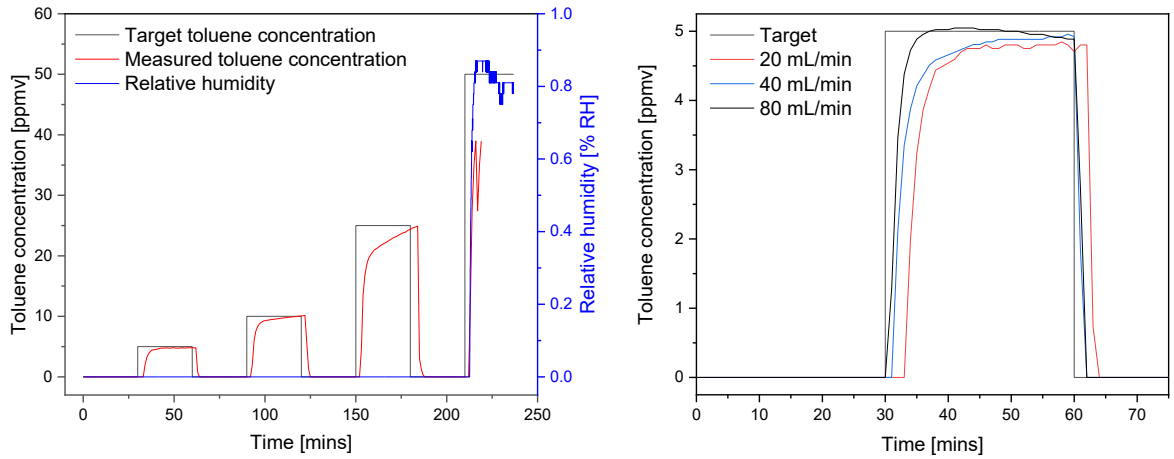


Figure 3.17: Target and actual toluene concentrations measured by the photoionization detector for flowrates between 20-80 mL/min. Right plot shows close-up of 5ppmv step. T = 25˚C.

3.4.5.3. Comparisons between dead volume and sample volume

Dead volumes between 17-41 mL and 29-57 mL for the pre- and post-column humidity sensors, and 77-82 mL for the PID sensor were calculated. In most experiments, samples were packed into columns to form a bed with dimensions of 2 cm x 0.3 cm (height x diameter), resulting in a bed volume of approximately 0.14 mL. While this volume is significantly lower than the dead volume, it is important to consider the length of time taken for a breakthrough curve experiment and how that relates to the time taken for the probes to measure a particular concentration.

Based on data for **Figure 3.16** and **Figure 3.17**, the humidity and PID sensors have a dead time of approximately 2.5 and 9.1 minutes before reaching 95 % of their final value at 40 mL/min. However, when the equivalent dead time at 40 mL/min (i.e. the time taken for the sensor to first detect water or a VOC) is subtracted, the time taken from ‘detection’ to ‘saturation’ is only 1.7 minutes for the humidity probe and 6.5 minutes for the PID.

For comparison- during a typical experiment, the toluene breakthrough profile in a fixed bed, i.e. from the point is it detected by the PID until the concentration reaches a final plateau after full bed saturation, took at least 120 minutes to complete, with most high-capacity systems taking several hundred minutes. Due to the relatively poor mass transfer of toluene through a packed bed of porous material, the influence of sensor response time is negligible compared to the breakthrough profile of the bed.

Therefore, the subtraction of the equivalent dead time of the system is sufficient in 'correcting' any breakthrough profiles generated for VOCs in porous materials.

In the case of water vapour, the breakthrough profiles followed one of three trends:

1. Immediate breakthrough, making any accurate determination of capacity impossible regardless of sensor response time.
2. Long 'breakthrough' times followed by fast saturation, as observed in **Figure 3.18**. In these cases, the vast majority (> 95 %) of water is adsorbed pre-breakthrough, reducing the impact of sensor response time on calculated adsorbed quantity.
3. Short 'breakthrough' times followed by slow saturation taking at least 30 minutes. In these cases, the breakthrough profile timeframe is at least 10 times larger than the sensor response time, minimising its impact on the shape and final calculated adsorbed quantity.

Only trend 1 presents a case for inaccurate water breakthroughs and was only observed for ZIF adsorbents, which is elaborated on in **Chapter 7.** For trends 2 and 3, a subtraction of the equivalent dead time of the system is sufficient in 'correcting' water breakthrough curves in porous materials.

3.4.6. Testing of column pre-heater

Rather than an analytical approach, the tuning of the pre-heater control loop was carried out in a trial-and-error basis, using different combinations of P, I, and D terms to lead to minimal heating fluctuations. For the purposes of indoor air cleaning, ambient pressure and temperature were used for all adsorption experiments- therefore, the pre-heater was only used for the purposes of activating porous samples. While minor temperature fluctuations were present, the pre-heater was found to be able to activate samples at temperatures up to 250˚C before the magnitude of fluctuations exceeded 10 % of the regeneration temperature.

3.4.7. Measurement of fixed bed pressure drop

The pressure increase in the column was measured using a digital pressure gauge (Wika, UK) located in a T-joint before the fixed-bed column. Pressure drops, shown below in **Table 3.4**, were highest for fine powders but were negligible for large particulates.

Table 3.4: Measured pressure drop for adsorbent beds during dynamic breakthrough adsorption experiments, measured at two different gas flowrates. Temperature in all experiments was 25ºC. Adsorbent bed length and diameter were 2 cm and 0.4 cm respectively.

Sample	**Pressure drop (bar)**	
	Flowrate = 50 mL/min	**Flowrate = 100 mL/min**
Activated carbon (fine powder)	0.72	> 1.00
Activated carbon (granules)	< 0.01 [a]	< 0.01 [a]
Molecular sieve 13X (pellets)	0.02	0.04
Zeolite Y (pellets)	< 0.01 [a]	< 0.01 [a]

[a] No pressure drop detected by gauge

[b] Pressure drop exceeded safe operating conditions of equipment and gas flow was halted

3.4.8. Validation of adsorption capacity of porous materials

To cross-validate the measured total capacity through breakthrough curve analysis, calculated adsorbed quantities were compared to measured adsorbed quantities obtained through gravimetric means. Tests were conducted at a target water partial pressure of $P/P_0 = 0.5$ (50 % RH) using a flowrate of 10 mL/min in order to maximise the residence time of water vapour in the bed [94]. Generation of toluene adsorption data at 10 ppmv for DVS could not be carried out due to the slow adsorption kinetics being on a similar magnitude to the drift and vibrations present in the DVS apparatus, making any meaningful assessment of equilibrium or saturation capacity impossible.

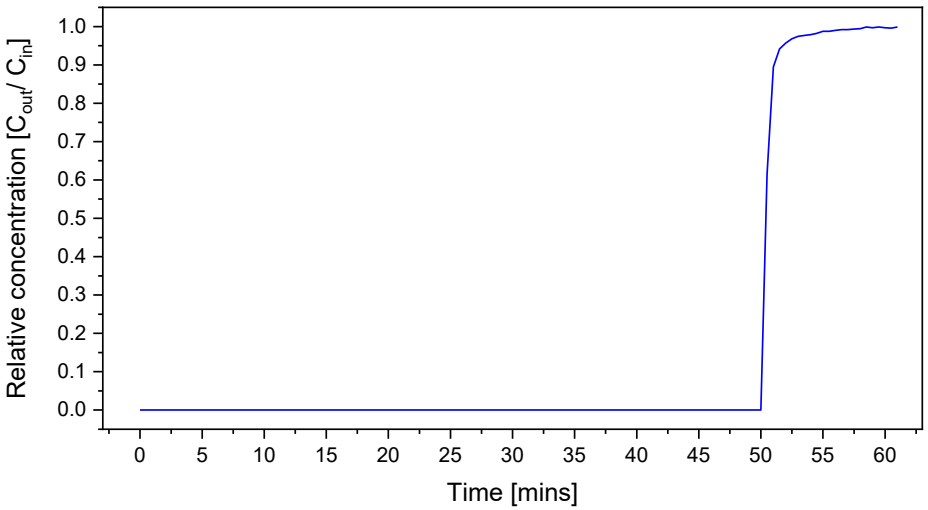


Figure 3.18: Breakthrough curve of water vapour on MS13X, carried out at a flowrate of 10 mL/min, relative humidity of 49.5 % and a temperature of 25˚C.

After subtracting the equivalent capacity from dead time, the adsorption capacity of MS13X in the breakthrough experiment were calculated to be 212.4 ± 8.1 mg/g at a relative humidity value of 49.5 ± 0.8 %. Compared to the gravimetric capacity of 223.0 ± 5.4 mg/g, measured at 50.0 ± 0.05 %, these breakthrough values are in good agreement based on 95 % confidence intervals, only differing from by around 4.8 %. The breakthrough capacity being lower than the gravimetric capacity may be due to the aforementioned effects of fixed-bed residence time.

3.4.9. Generation of experimental breakthrough curve datasets

All non-powder samples, including extruded zeolite pellets and granulated activated charcoal, were roughly ground before being sieved- leaving particles with sizes between 180 and 250 µm. For dilute volatile adsorption experiments, specialised gas cylinders containing ppm levels of VOCs in a balance of nitrogen were ordered from BOC (UK).

Samples were packed into 3mm I.D. borosilicate columns to a bed height of approximately 2.5 cm in order to keep this process variable consistent as well as ensuring the bed length is at least 3 times that of the bed diameter [80]. Larger sample granules or monoliths were ground and sieved to sizes of approximately 250 µm, in order to have a column diameter: particle size ratio of at least 10 [80].

Silanised wool slugs were placed above and below the packed bed to prevent particles falling through. Sample masses before and after activation were recorded to calculate the dry bed mass in each experiment. Samples are heated to their activation temperature, 300˚C for industrial adsorbents and 200˚C for MOF adsorbents, for 4 hours prior to each measurement under nitrogen flow. Data is collected following a step-change in humidity, VOC concentration, or a combination of the two. Concentrations are monitored via humidity probes (Rotronic, UK) and a photoionisation detector (IonScience, UK) located post-column. Experiments are stopped once the C_{out}:C_{in} ratio has a value of unity for at least 10 minutes. The breakthrough point in experiments is defined as the time taken to reach an outlet concentration equal to 5 % of the inlet, i.e. a C_{out}/ C_{in} value of 0.05. Useable capacities were calculated using the integrated area up to this time value. To better compare the performance of different materials under the same conditions, the x-axis in comparative plots has been normalised both by multiplying by carrier gas flowrate and dividing by dry sample mass, resulting in units of mL/mg.

Note: the majority of BTCs were generated in triplicate (N=3), with standard deviations reflecting that. In addition, useability values were calculated for each individual BTC and then averaged to give the value and standard deviation quoted in text or tables. Therefore, the 'average' useable and total capacity will not necessarily result in the 'average' useability.

3.5. Dataset fitting, standard deviations, significance, and repeat measurements

3.5.1. Isotherm models

To better understand and describe experimental isotherms, mathematically models can be used to determine various parameters related to capacity, adsorption heterogeneity, and interaction strength. A review of common mathematical models is explored and discussed to select which models will best describe the datasets in this work.

3.5.1.1. Langmuir

One of the simplest and most widely used isotherm models is the Langmuir model, expressed in **equation 2.4** in **Section 2.1.2.1.** [243]: The main assumptions of the Langmuir model are [244]:

1. The materials surface and active sites are homogenous in terms of their energy level
2. No adsorbate-adsorbate interactions occur on the surface
3. The maximum uptake is defined by the monolayer capacity of the adsorbent, i.e. pore filling and multilayer adsorption are not considered

The Langmuir equation has been used in previous studies to fit type I isotherms, such as ethanol adsorption in silicalite MFI zeolite [245] or o-xylene onto modified clay [246]. The Langmuir model reduces to the Henry's law equation at low pressures, making the model thermodynamically consistent at low coverages or loadings. However, the assumptions of the model are rarely valid for materials with heterogeneous adsorption sites, e.g. hydrophilic versus hydrophobic, narrow versus wide pores, or high degrees of microporosity.

3.5.1.2. Freundlich

While the Langmuir model has a theoretical basis, the Freundlich equation is purely empirical and designed to fit isotherm data regardless of the mechanism of adsorption [243], [244], [247]:

$$q_{Freu} = K_F \cdot \left(\frac{P}{P_0}\right)^{\frac{1}{n}} \tag{3.7}$$

Where q is the amount adsorbed, P is the pressure of adsorbate in the gas phase, and K_F and n are constants specific to the Freundlich equation representing the strength of interaction and the heterogeneity of the surface respectively. The model has been found to be unsuitable for modelling high-pressure monolayer adsorption due to the model's tendency to continuously increase the adsorbed gas quantity. In addition, the model does not match the Henry's law equation at low pressures, leading to poorer fitting at low coverages. Therefore, while the model is simple to use and often provides good fitting of datasets at intermediate pressure ranges, the lack of theoretical basis limits the insight that can be drawn from such successful fitting.

3.5.1.3. Combined Langmuir-Freundlich models

To overcome the limitations of the two simpler models, the Freundlich and Langmuir models are commonly combined in various forms including the Sips and Toth equations. The Sips equation is a

combination of the Langmuir and Freundlich models, introducing a finite adsorption limit, q_m, which offsets the continuous increase in adsorbed quantities in the Freundlich model. The two other variables, a_s and n, are the Sips constant and heterogeneity factor of the system. The model reduces to the Langmuir equation when n is equal to 1, i.e. a completely heterogeneous surface, matching the assumption of the Langmuir model [243], [244].

$$q_{Sips} = \frac{q_m \cdot a_s \cdot \left(\frac{P}{P_0}\right)^{\frac{1}{n}}}{1 - a_S \cdot \left(\frac{P}{P_0}\right)^{\frac{1}{n}}} \tag{3.8}$$

The Sips model has been used extensively in modelling adsorption of light gases onto activated charcoal [248], although only in pressure ranges where monolayer adsorption is expected [249]. Additionally, the Sips model has been found to be capable of modelling sigmoidal curves and may be suitable for adsorption systems presenting Type IV or V isotherms [250]. The Toth equation is another empirical modification for the Langmuir equation, accounting for heterogeneity present in adsorption systems. The Toth equation assumes a quasi-Gaussian distribution of adsorption site energies which is asymmetrical [243]. The constants in the equation are similar to those in the Sips model, with q_m, K_T, and n representing the maximum adsorption amount, the Toth constant, and the heterogeneity of the adsorption sites. Similarly, when n = 1 (i.e. complete heterogeneity) the equation reduces to the Langmuir equation.

$$q_{Toth} = \frac{q_m \cdot K_T \cdot \frac{P}{P_0}}{(1 + (K_T \cdot P)^n)^{\frac{1}{n}}} \tag{3.9}$$

The Toth equation has been successfully used to fit isotherm data of alkyl and aromatic hydrocarbons, including gasoline vapours, onto hydrophobic faujasite zeolites [239], [251]. The choice of the Toth equation by Kondor & Dallos [239] was based on two factors: the heterogeneity of adsorption sites, measured using surface energy analysis by inverse gas chromatography; and the thermodynamic consistency of the Toth equation in the Henry's law pressure region, compared to empirical correlations by Freundlich, Sips, and the Dubinin models.

3.5.1.4. Brunauer-Emmett-Teller

The BET model, developed by Brunauer, Emmett, and Teller, assumes that only surface adsorption occurs, building up to an infinite number of layers as the experimental pressure approaches the adsorbate's saturation pressure [252]. The model, the expression of which can be found as **equation 2.5** in **Section 2.1.2.2.**, has an obvious advantage over Langmuir as it can describe multilayer adsorption onto surfaces. This attribute is useful for describing the adsorption behaviour of materials lacking porosity, i.e. only adsorbing species onto their external surface, and for adsorbent-adsorbate pairs that have unfavourable interactions, e.g. hydrophobic zeolites or activated carbons adsorbing water vapour. Despite the model's supposed ability to model the formation of an infinite number of adsorbate layers, it is typically only used to describe the formation of a single adsorbate layer, resulting in a limited application range of partial pressures typically between 0.05-0.35 [252], [253].

3.5.1.5. Guggenheim-Anderson-de Boer

A modification of the BET equation was proposed individually by Guggenheim, Anderson and de Boer at separate times [252], which introduces an additional constant, K_{GAB}, as a correction factor for the properties of the multilayer [254]:

$$q_{GAB} = \frac{q_m \cdot C_{GAB} \cdot K_{GAB} \cdot \frac{P}{P_0}}{\left(1 - K_{GAB}\frac{P}{P_0}\right) \cdot \left(1 - \left(K_{GAB} \cdot \left(\frac{P}{P_0}\right)\right) + \left(C_{BET} \cdot K_{BET} \cdot \left(\frac{P}{P_0}\right)\right)\right)} \tag{3.10}$$

This new constant creates a limit to the formation of the multilayers, providing a finite value for the adsorption capacity to reach at the highest partial pressures, allowing the GAB model to be used in a wider range of partial pressures than the BET model, up to water activities of 0.9 (i.e. 90 % RH) [252]. Both the BET and GAB equations are commonly used for modelling the interactions of water vapour onto non-porous [30] and porous materials [255], due to their ability to accurately fit isotherms with inflection points such as Type II, III, IV, and V [250].

3.5.1.6. Dubinin Radushkevich and Dubinin Astakhov models

The Dubinin-Radushkevich model is based on the potential theory of Polanyi, which considers that adsorption forces act at distances exceeding the dimensions of a single molecule and are only partly shielded by the previously adsorbed layer(s) [33]. The potential theory depends upon the adsorption potential of the system, and the volume of the adsorbed layer. Dubinin and Radushkevich then proposed an empirical, micropore filling theory based on the work by Polanyi [31], the expression of which can be found in **equation 2.8** of **Section 2.1.3.1.**

Dubinin and Astakhov formed a more general expressed by replacing the exponent of 2 in **equation 2.8** by a constant n, which has been linked to the degree of heterogeneity of the micropore system (i.e. the broadness of the pore size distribution) [34]. These equations are only capable of modelling adsorption in intermediate pressure ranges, due to their thermodynamic inconsistency in the low pressure Henry's law region [256], although this inconsistency has been found to be reduced in the DA model due to the added flexibility from its n parameter [253]. Both models have a strong thermodynamic basis and can provide insight into the adsorption mechanism as well as the properties of the adsorbent material itself. For example, Cheng & Hu [257] used the DA model to successfully predicted the surface area of MOF-5, ZIF-8, HKUST-1 and MIL-53 based on their adsorption of acetylene. The DA and DR equations have both had extensive use in the modelling of adsorption of volatile organic compounds in microporous solids including activated charcoal [34], zeolites [258], and metal-organic frameworks [257].

3.5.2. Fitting experimental adsorption kinetics

As discussed in Chapter 2, several methods for quantifying adsorption kinetics exist, with pseudo first order (PFO) and pseudo second order (PSO) being some of the most common. These two equations, found in **Section 2.3.2.1.**, were used for fitting kinetic data in this work.

3.5.3. Fitting experimental breakthrough curves

As discussed in Chapter 2, many of the commonly used mathematically models for describing breakthrough curves (Thomas, Yoon-Nelson, Bohart-Adams) are mathematically identical and can be described by the logistic equation [92], the exact form of which can be found in **equation 2.32**.

The meaning of parameters *a* and *b* depend on the model used. For this project, the Bohart-Adams model was used to describe the breakthrough curves of the majority of adsorbent-adsorbate pairs due to its relative simplicity, as the parameter *b* can be directly linked to the rate constants k_{BA} which describes the ease of mass transfer in the packed bed [92]. To emphasise the use of the logistic equation, the model will be referred to as the Bohart-Adams Logistic model, or BAL model.

3.5.3.1. Fitting adsorbate 'rollover' in competitive breakthrough curves

To describe BTCs with rollover present, i.e. in the case of significant adsorption competition leading to displacement, an alternative model was required. To this end, a combination of the Boltzmann and exponential modified Gaussian (EMG) equations was utilised, based on a study by Shu-Jiang et al [259] who used this method to describe the breakthrough curve of xenon sampling dynamics in a carbon molecular sieve column. The combined equation is the following:

$$y = (kA_2 + D_1) + k\frac{A_1 - A_2}{1 + e^{\frac{t-x1}{dx}}} + \frac{D_2}{D_3\sqrt{\frac{\pi}{2}}}e^{\frac{-2(t-x_2)^2}{D_3^2}} \tag{3.11}$$

Where y and t are the relative outlet concentration and time respectively, $A_{1\text{-}2}$ are Boltzmann constants related to the initial and final y values of the system, x_1 is the time value at the mid-point of the breakthrough, and dx is a constant related to the steepness of the BTC. $D_{1\text{-}3}$ are constants related to the initial and final y values and the height of the peak, and x_2 is the time value for the maxima of the peak. Illustrations of these constants and their meaning are shown below.

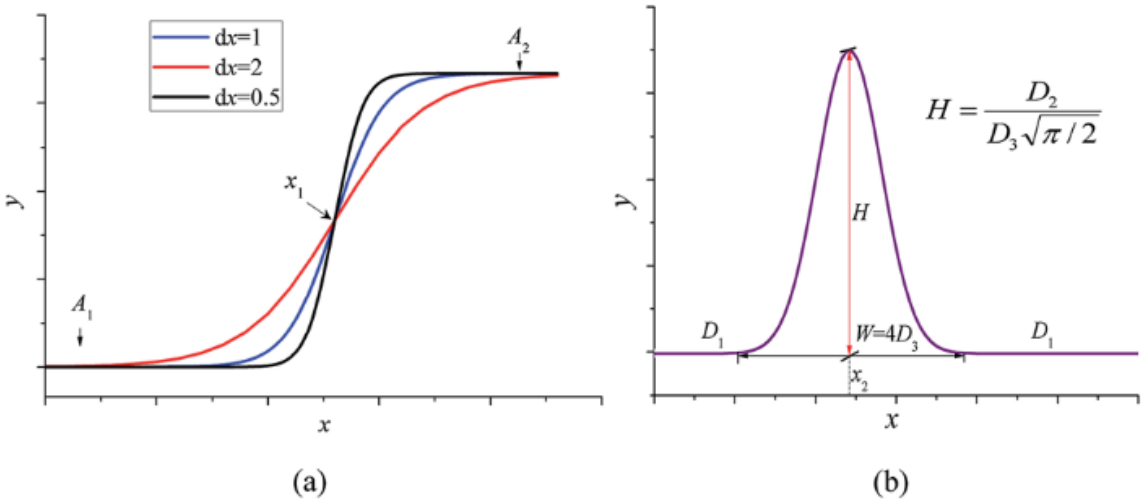


Figure 3.19: Illustration of constants for the Boltzmann (a) and EMG (b) equations, reproduced from work by Shu-Jiang et al [259] with permission.

3.5.4. Methodology for fitting of experimental datasets

Single-component organic solvent vapour isotherms, collected using DVS apparatus, were fitted using the Langmuir, Freundlich, Sips, and Dubinin-Astakhov models. This selection allows a mixture of empirical, theoretical, 2-, and 3-parameter models to be utilised and assessed for their ability to describe preferential and non-preferential adsorption onto solid adsorbents. For water vapour isotherms, the BET and GAB models will be used due to their ability to describe type III and type V isotherms. In addition, the Langmuir and Freundlich isotherms were tested for their ability to fit water isotherms, depending on the shape of the water isotherm- i.e. for hydrophobic MOFs the type III isotherm would not be well described by Langmuir, so Freundlich was chosen. For VOCs the models were assessed in at low partial pressures, typically below $P/P_0 = 0.3$, to reflect the importance of low-mid concentrations in volatile removal. For water the models were assessed in the full isotherm data range to represent the range of humidity present in these applications. Fitting was carried out by minimisation of the Marquadt's percent standard deviation (MPSD) [260], a popular error function in isotherm fitting studies [261]:

$$MPSD = 100\sqrt{\frac{1}{n-p}\sum_{i=1}^{n}\left(\frac{q_{i,calc}-q_{i,meas}}{q_{i,meas}}\right)^2} \quad (3.12)$$

Gravimetric adsorption kinetics data, collected using DVS apparatus, were fitted using the pseudo first order and pseudo second order models. As mentioned previously experimental data fits will be carried out for uptake ranges of 0-1 q_{max} and 0-0.85 q_{max} to test the effect of near-equilibrium data on PSO bias. In both data ranges, fitting will be assessed by the maximisation of the adjusted coefficient of determination (adj. R^2) in OriginPro, which considers the number of variables used for fitting:

$$R^2_{adj} = 1 - \frac{(1 - R^2)(n - 1)}{n - k - 1} \tag{3.13}$$

Where R^2 is the coefficient of determination, n is the number of data points, and k is the number of variables in the fitting model- discouraging the addition of variables with little to no theoretical or empirical meaning to simply improve fitting, as this action will result in lower adjusted R^2 values.

Breakthrough curves were fitted either using the Bohart-Adams Logistic equation (BAL) or the Boltzmann-EMG equation, depending on whether adsorbate rollover is present. To test the accuracy of breakthrough curve fitting, two criteria will be assessed: the adjusted coefficient of determination (adj. R^2) value in OriginPro; and the calculated values for useable capacity, total capacity, and useability for the fitted curve.

3.5.5. Standard deviation and repeat measurements

For experimental data plots containing error bars, these represent the standard deviation (SD) around the average result:

$$SD = \sqrt{\frac{\sum(x - \bar{x})}{n}} \tag{3.14}$$

Where x is one experimental result, $\bar{x}$ is the average result, and n is the total number of results. For the majority of experiments, n= 3. However, any divergence from this number, higher or lower, will be noted in the description of the figure or table. When finding the standard deviation of calculated values, e.g. an equation z = x* y, the SD is calculated in the following way:

$$\frac{SD_z}{z} = \sqrt{\left(\frac{SD_x}{x}\right)^2 + \left(\frac{SD_y}{y}\right)^2} \quad (3.15)$$

Where SD_z, SD_x, and SD_y are the standard deviations of average values z, x, and y.

3.7. Conclusions

This Chapter outlined the methodology for carrying out physical and chemical characterisation, gravimetric adsorption, and fixed-bed adsorption. The background for many of these techniques and the procedure in which they are carried out are based on literature studies on similar materials as, user experience over the course of the project, and the advice and guidance of fellow researchers at the institution.

For the purposes of better understanding multicomponent adsorption interactions, a bench-top breakthrough curve analyser was designed and developed. In the initial design stages, focus was placed on a modular design for the sensory components allowing the equipment to be used in a range of applications. The control of flow rates, and by extension concentrations, was accomplished using a modified form of the mass flow controller manifold of a DVS Resolution. This allowed the control of relative humidity in the range of 0-90 % and, with the use of specialised gas cylinders, the control of VOC concentrations in the range of 500 ppbv- 20 ppmv. Re-purposed incubator housing was used for adsorption measurements carried out at temperatures between 20-50˚C. A custom-built heating jacket was developed for in-situ regeneration up to a temperature of 300˚C, allowing continuous testing of adsorbent beds remotely during the COVID-19 lockdown phase. Multiple gas sensors, including those for relative humidity, carbon dioxide, and volatile organic compounds, were integrated into the equipment to allow continuous monitoring of post-column concentrations. To ensure accurate collection of adsorbate concentration data, significant time was spent on the calibration of sensory elements, including the recording and of empty-column experiments to allow system dead times and volumes to be calculated. Finally, validation experiments were carried out for the adsorption of water vapour onto molecular sieve 13X- with calculated fixed-bed saturation capacities within 5 % of those calculated using industry gravimetric equipment.

Chapter 4: Characterisation of porous materials for solvent vapour removal

4.1. Introduction

As discussed in the literature review, porous materials are a common method for adsorbing volatile organic compounds, thereby reducing their concentration in indoor or outdoor spaces. In this Chapter, several industrial porous adsorbents were investigated for their effectiveness in adsorbing volatile organic compounds. The adsorbents included microporous, mesoporous, hydrophilic, and hydrophobic materials, some of which were recommended by the industrial sponsor of this work, Procter & Gamble Co. USA, for their potential utilisation in odour abatement. The industrial application field of malodour removal shares many similarities with VOC removal as both require materials with a high numbers of active adsorption sites, typically achieved through surface area or porosity, combined with a selectivity for harmful or malodourous vapours over water vapour.

The physical and chemical properties of these adsorbents were tested using standard analytical methods including gas adsorption, thermogravimetric analysis, and infrared spectroscopy. These not only allowed the relevant physicochemical properties of each material to be determined but, as each material is commonly utilised in adsorption fields and somewhat well characterised in the literature, this analysis would indirectly validate the accuracy of the analytical equipment, and the methods used.

The adsorption performance of each of the selected materials for a series of VOCs with varying chemistries was tested, alongside that of water vapour, to determine the materials' adsorption capacity and hydrophobicity. Single-component data was used to determine molar hydrophobicity indexes as a function of humidity, to better represent how the performance and selectivity of a material for removing non-polar vapours may change as the relative humidity is increased. Adsorption selectivity was further evaluated by carrying out dual-solvent multicomponent adsorption experiments, where samples were pre-exposed with different levels of water vapour before introducing a volatile vapour. This 'wet adsorbent' mode of competitive provided a benchmark not only for material selection, but also to guide further material development and preparation, as well as necessitating the design of new adsorption equipment to more quantitatively assess the impact of water vapour on VOC adsorption performance.

The experimental adsorption isotherms and adsorption kinetics profiles were fitted using a range of mathematical models in order to provide additional information regarding the mechanism of adsorption, as well as better quantify the timeframe in which vapours were adsorbed by the porous materials, and how this could be impacted by the presence of water vapour. The influence of near-equilibrium data on the quality of data fitting by the pseudo first and second order models was investigated, to determine whether bias existed for systems in which equilibrium is reached relative slowly. Finally, to better encapsulate the need for both high adsorption kinetics and capacity in multicomponent experiments, a definition of kinetic productivity was developed based on the parameters of the pseudo first order model. The effect of several properties including adsorbate size and chemistry, adsorbate partial pressure, material properties, and the level of relative humidity, were investigated for their effect on modelled kinetic parameters.

4.2. Results and discussion

4.2.1. X-ray diffraction

X-ray diffraction (XRD) patterns for MS13X, A88Y, and A14Z, shown in **Figure 4.1**, all matched well with zeolitic reference patterns from the X'Pert HighScore Plus database and from the literature [119], [262], indicating that these samples consisted of a single highly crystalline phase. The similar diffraction patterns of MS13X and A88Y are due to the two zeolites having the same faujasite crystal structure, although the two differing in terms of their chemical functionality, with A88Y having a higher framework silica to alumina ratio. Patterns for activated charcoal (AC) and amorphous silica (AS) produced broad peaks and lacked definition due to these materials' amorphous nature.

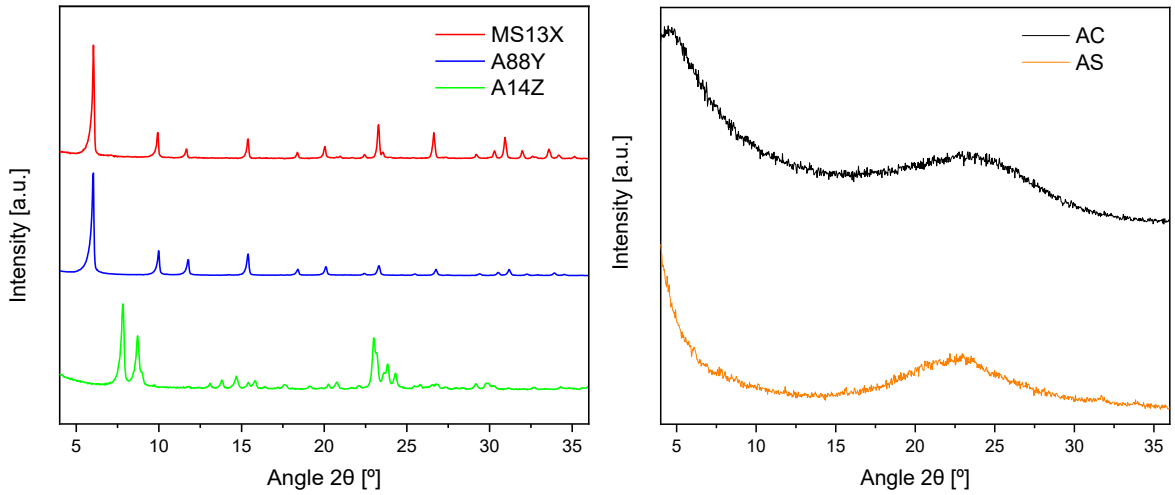


Figure 4.1: X-ray diffraction patterns for industrial adsorbents: molecular sieve 13X, MS13X; zeolite Y, A88Y; ZSM-5 zeolite, A14Z; activated charcoal, AC; amorphous silica, AS.

4.2.2. X-ray fluorescence

MS13X, A88Y, and A14Z were found to have SiO_2:Al_2O_3 ratios of 1.9, 35.8, and 29.7 respectively according to the data collected by X-ray fluorescence. Molecular sieve 13X's silica: alumina ratio of 1.9 is slightly higher than the theoretical range of 1-1.5 typical in X-type zeolites [109], which may be explained by the presence of a binding material to aid with forming homogenous MS13X pellets. A common binding agent for zeolite X in kaolin [263], which itself contains a high proportion of silica. However, no diffraction peaks for kaolinite, or any other binders, were distinctly visible in MS13X's spectra [264], meaning any binder present is either at low enough levels to not be detected, or the binder is non-crystalline. For the high-silica zeolites, this value is lower than the ratio given by the supplier (PQ Corporation, USA), and is likely due to the presence of extra-framework aluminium or binding agents [44]. AS was found to be over 98.8 mol% SiO_2, with trace amounts of Al, Na, and K ions.

Table 4.1: Metal compositions of adsorbents: molecular sieve 13X, MS13X; zeolite Y, A88Y; ZSM-5 zeolite, A14Z; activated charcoal, AC; amorphous silica, AS. Measured by X-ray fluorescence.

Abundance [mol %]	**AC** [a]	**AS**	**MS13X**	**A88Y**	**A14Z**
SiO_2	--	98.9 ± 0.1	54.5 ± 0.3	96.6 ± 0.5	94.9 ± 0.6
Al_2O_3	--	0.3 ± 0.1	29.4 ± 0.7	2.7 ± 0.1	3.2 ± 0.1
Na_2O	--	0.1 [b]	9.0 ± 0.3	< 0.1 [b]	< 0.1 [b]
CaO	--	0.1 [b]	1.0 ± 0.1	< 0.1 [b]	< 0.1 [b]
TiO_2	--	< 0.1 [b]	0.3 [b]	0.5 ± 0.1	< 0.1 [b]
Fe_2O_3	--	< 0.1 [b]	2.3 ± 0.2	0.4 [b]	< 0.1 [b]
SiO_2:Al_2O_3 [mol:mol]	--	> 300	1.9 ± 0.1	35.8 ± 1.3	29.7 ± 0.9

[a] Due to carbonaceous nature, sample could not be analysed by XRF

[b] Measured standard deviation < 0.1 mol %.

4.2.3. Fourier-transform infrared spectroscopy

FTIR spectra for the five studied adsorbents are shown in **Figure 4.2**. AC's FTIR spectra consisted of a largely noisy signal with no discernible peaks- likely due to overlapping of bonds and stretching modes between carbon, hydrogen, oxygen, and nitrogen atoms [189]. The peaks in silica's spectra at 806 and 1065 cm^{-1} likely correspond to the characteristic anti-symmetric and symmetric stretching modes of the Si-O-Si bridge, while the shoulder observed around 976 cm^{-1} has previously been allocated to the Si-OH stretching mode [265]. Peaks between 650-1200 cm^{-1} in zeolites are typically associated with stretching modes between silicon, aluminium, and oxygen atoms. The peaks around 750-800 cm^{-1} likely correspond to the stretching of Al-O vibrations, while the peaks at higher wavenumbers are associated with Si-O, Si-O-Si, and Si-O-Al [266], [267]. Notably, the vibration regions for the high-silica zeolites appears to be shifted to higher wavenumbers compared to unmodified zeolite X (MS13X). This effect has been noted by Miessner et al [268] for zeolite Y and ZSM-20 zeolites, and is hypothesised to be due to the dealumination process undergone by high-silica, or ultra-stable, forms of

zeolite frameworks. MS13X's peak at 675 cm^{-1} can be attributed to the Si-O-M bridges, where M is an exchangeable metal ion- in this case it is likely Na^{+}. This peak appears, albeit with lower intensity, in the A88Y sample, which matches well with the results from XRF showing the significantly lower sodium content of the hydrophobically-modified faujasite. The presence of this peak in A88Y but not A14Z can be explained via XRF: A88Y was found to have a detectable quantity of titania and ferrous ions, leading to a Si-O-M peak; while A14Z was found to consist entirely of silica and alumina, resulting in no discernible peak in the wavenumber region of 675 cm^{-1}. A88Y was also found to possess a small peak between 3640-3670 cm^{-1}- work by Shaikh et al [269] on high-silica ZSM-5 assigned this peak to extra-framework $Al(OH)_x$ species. However, this peak was only weakly visible and was not present at all in the A14Z sample, suggesting low levels of extra-framework species, despite both samples undergoing industrial dealumination [44].

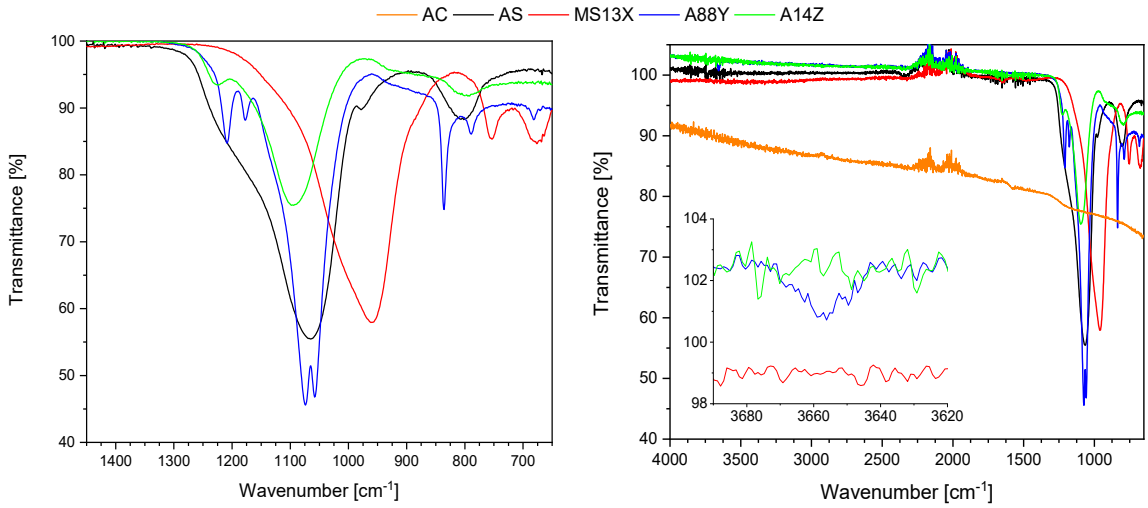


Figure 4.2: FTIR spectra for industrial adsorbents, in wavenumber ranges of 650-1450 cm^{-1} (left), and 650-4000 cm^{-1} (right). Inset graph shows zeolite samples in 3620-3690 cm^{-1} region. AC not shown on left graph due to broad peaks and to improve clarity.

4.2.4. Thermogravimetric analysis

Following initial mass loss in the range T < 200ºC due to surface-bound water and contaminants, all samples were thermally stable up to temperatures around 600˚C in air, confirming that thermal activation in air could be carried out at any temperature below this point. Above this temperature, activated charcoal began to thermally degrade, whereas amorphous silica and all zeolites studied were stable until temperatures approaching 900-1000ºC. The thermogravimetric mass loss profiles in air for the adsorbent materials are shown in **Figure A.3.** in the Appendix.

4.2.5. Density of industrial adsorbents

The absolute densities of the industrial samples were all found to exceed 2 g/cm^3, similar to published work on industrial zeolites, silicas, and charcoals [270] although absolute densities for each individual sample could not be found. The absolute densities, in g/cm^3, followed the trend A14Z (2.34 ± 0.02) > A88Y (2.24 ± 0.03), AS (2.22 ± 0.03) > MS13X (2.20 ± 0.01) > AC (2.08 ± 0.04). The bulk densities of industrial samples, in g/cm^3, followed the trend A14Z (1.22 ± 0.01), A88Y (0.83 ± 0.01), MS13X (0.63 ± 0.02), AS (0.56 ± 0.01), AC (0.34 ± 0.02). Ground powder forms of A88Y and A14Z, denoted A88Y(G) and A14Z(G), were found to have bulk densities of 0.74 ± 0.03 g/cm^3 and 0.87 ± 0.04 g/cm^3. AC's bulk density was found to be well within the literature range of 0.32-0.38 g/cm^3 [271], while AS appeared to have noticeably lower density than the commonly values in literature > 0.7 g/cm^3 [272]. However, the bulk density of silica is known to vary greatly depending on the total porosity of the material, making exact comparisons difficult [273]. The bulk densities for zeolites appeared to vary greatly depending on the study, with the binder content of the material appearing to have a significant impact on the bulk density of the composite [274]. In general, bulk densities between 0.6 [275] to 0.97 [276] g/cm^3 were found for powders, with extruded powders consistently having higher densities, typically above 1 g/cm^3 [274].

4.2.6. Surface area and pore volume measurements

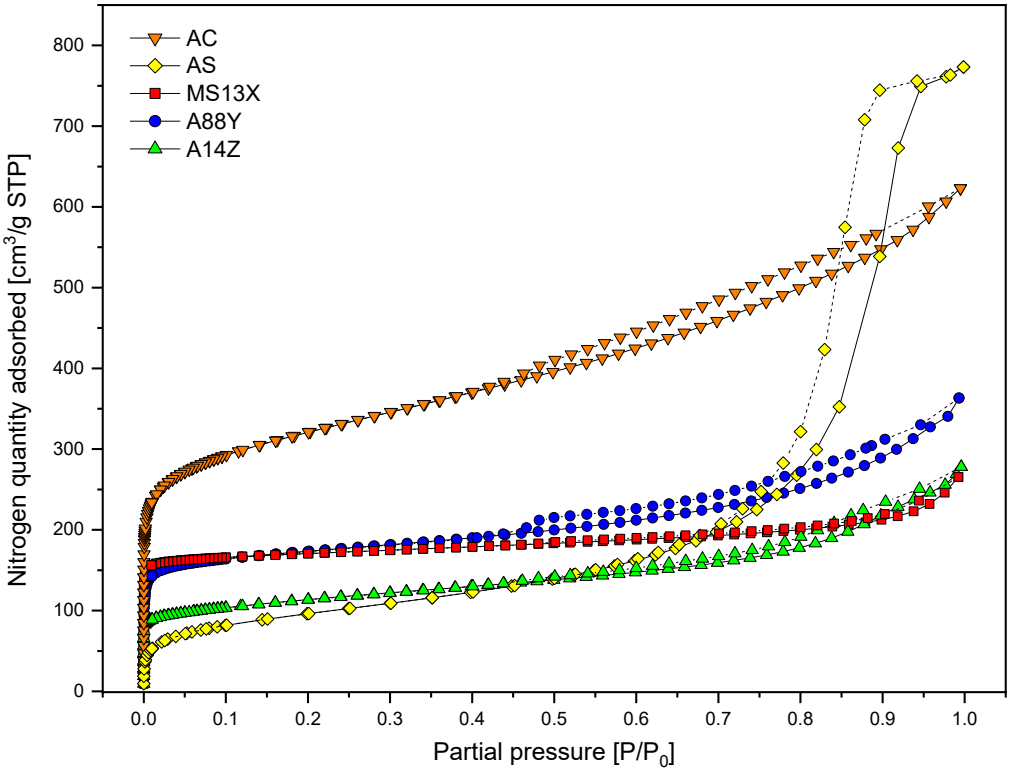


Figure 4.3: Nitrogen isotherms for adsorbent samples: activated charcoal, AC; amorphous silica, AS; molecular sieve 13X, MS13X; zeolite Y, A88Y; ZSM-5 zeolite, A14Z. Solid and dashed lines correspond to adsorption and desorption points respectively. T = -196˚C.

The nitrogen isotherms for all samples are shown in **Figure 4.3**. All samples were shown to be highly porous, with steep initial isotherm gradients at low partial pressures. All samples except MS13X displayed hysteresis loops at higher partial pressures, suggesting some degree of wide-pore mesoporosity. AC's gradual increase in N_2 uptake at intermediate partial pressures reflects the hierarchical network of pore apertures in its structure, which is also seen to a lesser extent in zeolite samples A88Y and A14Z. AS adsorbed the majority of N_2 at high partial pressures exceeding P/P_0 = 0.5, likely due to mesoporous nature.

Table 4.2: BET surface areas, micropore volumes, and total pore volumes of industrial adsorbents, determined using N_2 gas adsorption data at -196ºC.

Sample	BET Surface Area[1] [$m^2\ g^{-1}$]	Micropore Volume[2] [$cm^3\ g^{-1}$]	Total Pore Volume[3] [$cm^3\ g^{-1}$]
AC	1245 ± 62	0.209 ± 0.010	1.149 ± 0.105
AS	338 ± 2	0.008 ± 0.005	1.187 ± 0.011
MS13X	666 ± 31	0.209 ± 0.008	0.346 ± 0.030
A88Y	658 ± 3	0.175 ± 0.005	0.542 ± 0.011
A14Z	413 ± 3	0.076 ± 0.006	0.444 ± 0.058

[1] Calculated using linear fit of adsorption data in pressure range of $0.02 < P/P_0 < 0.08$

[2] Calculated using t-plot analysis

[3] Total gas adsorption volume determined at gas partial pressure of $P/P_0 > 0.99$

Table 4.2 shows the measure surface areas, micropore volumes and total pore volumes of the industrial adsorbents. AC was found to have the highest surface area of 1245 m^2/g as well being tied for highest micropore volume alongside MS13X with a value of 0.209 cm^3/g. Despite similar surface areas, faujasites MS13X and A88Y had noticeable disparities in their proportion of volume in the mesopore region. The dealumination process carried out on these zeolites has been shown to create mesopores within the structure of the material [44], which accounts for their comparatively wide hysteresis loops. BET surface areas, micropore volumes, and total pore volumes of MS13X and A88Y compared well to zeolite X and high-silica zeolite Y adsorbents studied by Kim & Ahn [52]. A14Z was found to have similar BET surface area to unmodified H-ZSM-5 in work by da Silva et al [277] although the latter had noticeably higher micropore volume but lower mesopore volume. This difference may be explained by the dealumination process undergone by A14Z, which can lead to the collapse of microporous structure to form additional mesopores [44]. Amorphous silica differed from the other sorbents due to its relative lack of micropores, with over 99% of its pore volume located in pores 2 nm or larger. The charcoal in this study differed from many in literature due to its high content of mesopores and relatively small percentage of microporosity (~18 %). Lillo-Ródenas et al [187] studied 10 activated carbons for benzene and toluene adsorption- surface areas between 656-2746 m^2/g were observed, but all samples contained at least 62 % of their pore volume within micropores. These materials all produced standard

type I isotherms when analysed via nitrogen sorption and did not possess the gradual increase in pressure at medium to high partial pressures that this study's AC did. However, the synthesis conditions of activated carbons strongly influence its final properties and, being such a ubiquitous material, each study likely has a charcoal with a different porous structure- making any direct comparison difficult. Based on a thorough review of literature, no studies could be found in which the surface area of the specific charcoal used in this work (Supelco 05105, Sigma Aldrich) was measured, and the manufacturers did not specify a surface area value. Carbon samples with similar isotherm shapes to this work's AC, i.e. with hierarchical micro-meso porosity, by Rordriguez-Mirasol et al [193], who found that carbon with a burn-off weight percentage of 63 % was found to have a BET surface area, micropore volume, and total pore volume of 1348 m^2/g, ~0.4 cm^3/g, and ~1.2 cm^3/g, resulting in a microporosity of approximately 33 %. Work by Pak & Jeon [278] studied the impact of vacuum regeneration on VOC removal performance by AC, with the material studied having a BET surface area, micropore volume, and total pore volume of 1067 m^2/g, 0.14 cm^3/g, and 0.58 cm^3/g. Therefore, the values for surface area and porosity in this work are well within the range of micro-mesoporous charcoals in literature, although it is important to consider the. Amorphous silica's BET surface area, micropore volume, and total pore volume match silica gel in a literature study by Bilinski [196].

Based on NLDFT calculations, all samples contained pores in suitable size range for adsorbing the volatile species in this study (i.e. above 0.5 nm), as shown in **Figure A.4** in the Appendix. AC and AS possessed a series of heterogeneously sized pores in the micro- and meso- size regimes. AC had a large amount of pore volume in pores 2 nm and less, while AS had its highest amount of pore volume in pores 2 nm and larger- confirming its mesoporous nature. When assuming cylindrical pore geometry, all zeolites had homogenous micropores < 1.5 nm matching those of literature pore size distributions [109], [113], with the high-silica zeolites having noticeably increased mesopore volumes compared to MS13X due to the formers' aforementioned dealumination procedure [44]. In addition, A88Y appeared to have additional peak broadening around the 1 nm diameter range, which may indicate some expansion or collapse of microporous structure, linked to the increased mesoporosity of high-silica zeolites.

Table 4.3: Comparison of experimental and literature values for surface area, micropore, and total pore volumes of adsorbents. Standard deviations for values in this work can be found in **Table 4.2**.

		AC	AS	MS13X	A88Y	A14Z
BET SSA [m^2/g]	*Current*	1245	338	666	658	413
	Literature	1348 [193]	468 [196]	582 [52]	591 [52]	344 [277]
Micropore volume [cm^3/g]	*Current*	0.209	0.008	0.209	0.175	0.076
	Literature	~0.4 [193]	0.009 [196]	0.199 [52]	0.188 [52]	0.11 [277]
Total pore volume [cm^3/g]	*Current*	1.149	1.187	0.346	0.542	0.444
	Literature	~1.2 [193]	1.1 [196]	0.215 [52]	0.298 [52]	0.21 [277]

4.2.7. Advancing contact angles and surface hydrophobicity

When analysing AS, MS13X, and A14Z water droplets were found to wet the surface immediately, giving contact angles < 5 ˚ that could not be accurately measured. AC and A88Y's advancing water contact angles were measured as 37.7 ± 1.7˚ and 72.5 ± 5.2˚, both of which were below the threshold of 90˚ to qualify their surface as being hydrophobic. Number of repeat measurements, N = 5.

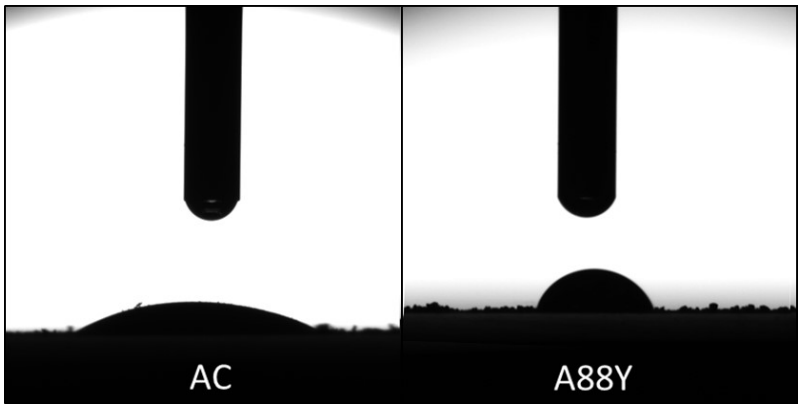


Figure 4.4: Advancing contact angles: activated charcoal, AC (left); and ground zeolite Y, A88Y (right)

4.2.8. Single-component vapour adsorption performance

Figure 4.5 (a) shows the water adsorption isotherms for the five studied samples, with the performance of each appearing to depend on both surface chemistry as well as the porosity of the adsorbent. The interaction of adsorbent materials with water molecules is important for indoor air applications due to water vapour's prevalence in these environments. MS13X was found to be most sensitive to the presence of low levels of humidity which is most likely due to its high surface area and number of sodium and aluminium ions, both of which contribute towards its acidity and ability to interact strongly with water vapour. Amorphous silica, despite its low surface area, adsorbed greater quantities of water than both the high-silica zeolites A14Z and A88Y, and AC especially at mid-to-high humidities. AS's use as a desiccant is attributed to its high water uptake in these humidity ranges, and matches well to literature data for wide-pore silica [64], reflecting its high mesopore volume and high density of hydrophilic silanol (Si-OH) groups. Despite their similar crystal structures, faujasites MS13X and A88Y had notable disparities in their adsorption behaviour with water vapour. A88Y and A14Z are designed to have reduced aluminium and sodium cation content, both of which have been attributed to an increase in hydrophobicity in various zeolites [116], [119], and are reflected in their water uptake in previous studies [177]. However, both zeolites were still found to possess some quantity of water capacity at low partial pressures, noticeably higher than AC- this may be due to some amount of surface extra-framework alumina species which have been found to act as a Lewis acid [124], or defect sites within the dealuminated framework. AC had the lowest water uptake initially, followed by an increase at RHs exceeding 50 % due to the mesoporous nature of the adsorbent, matching well with the trends and absolute quantities reported previously [279]. Higher humidity levels above 0.5 (i.e. > 50 % RH), and corresponding moisture uptakes, are important for adsorption processes in built environments, as adsorption processes within these locations will typically occur at similar relative humidity levels [280].

The adsorption isotherms of toluene and n-hexane shown in **Figure 4.5 (b)-(c)** are best described by type I or type II isotherms, both of which describe rapid micropore filling and/ or surface adsorption at low adsorbate concentrations [40]. The BET surface area appeared to be a good determinant for the low-pressure adsorption of non-polar species [73], whereas the quantity adsorbed at higher pressures

was dependant on the total pore volume of the adsorbents. When exposed to 0.005 P/P_0 of toluene, AC was found to possess the highest capacity (264.1 ± 4.2 mg/g), almost double that of the second-best performer MS13X (144.3 ± 1.6 mg/g) likely due to the former's higher surface area. Good agreement with literature values for low-concentration toluene adsorption was found for both AC [181], AS [195], and all zeolites samples [177].

The adsorption of polar species, similarly to water, seemed to be dependent on both the physical and chemical properties of the adsorbent materials. Activated charcoals traditionally have been found to more readily adsorb non-polar or weakly polar species due to their dispersive bonding chemistry [184]. 2-butanone, 2-propanol, and ethanol are relatively polar molecules compared to toluene and n-hexane [28] and so, like water, will interact strongly with adsorbents with hydrophilic bonding chemistry such as low-silica molecular sieves [281]. This effect is seen by studying the steepness of the initial stages of the isotherms in **Figure 4.5 (d)-(f)** for AC and A88Y, which decreased noticeably as molecular polarity increases.

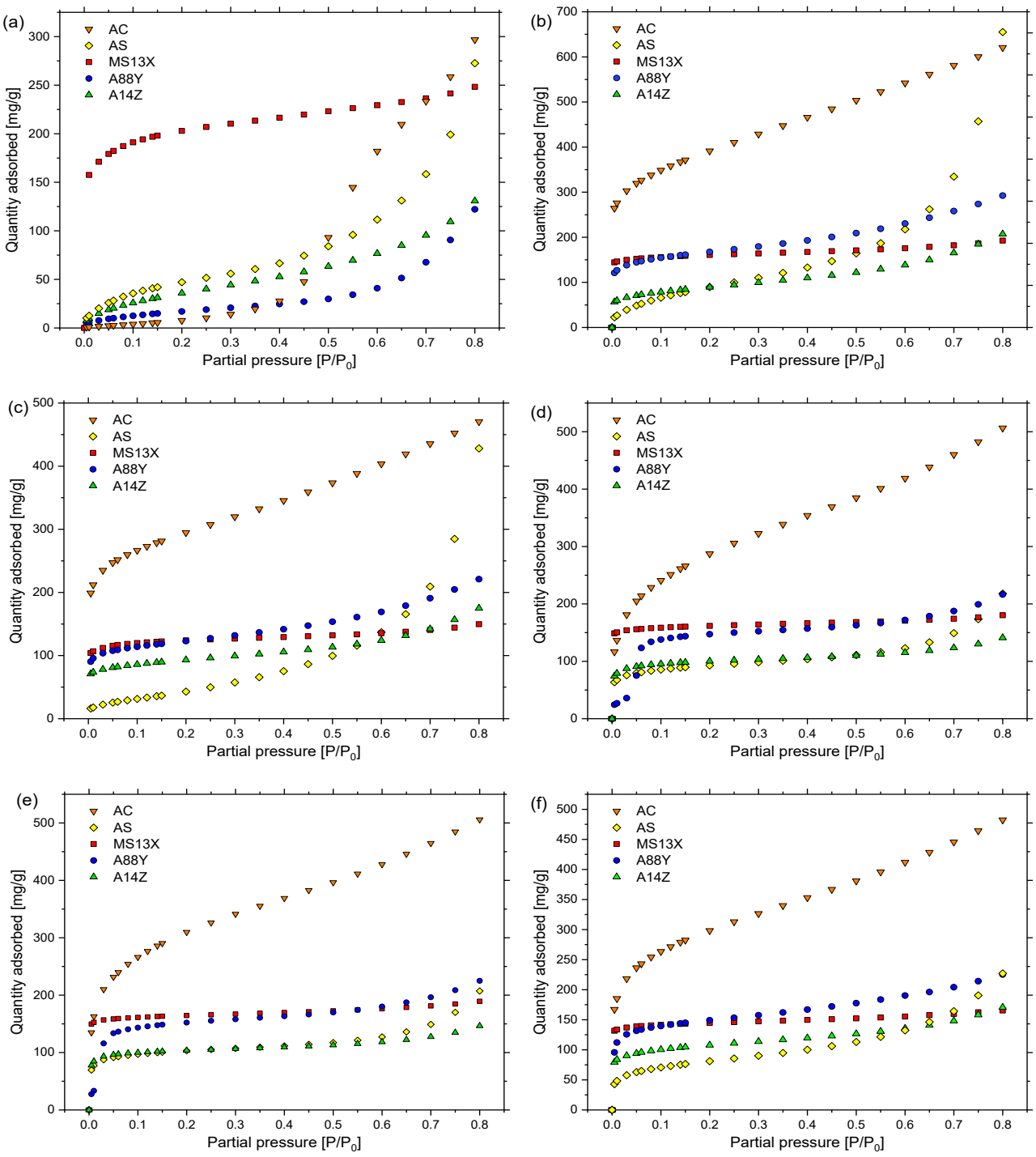


Figure 4.5: Vapour adsorption isotherms of water (a), toluene (b), n-hexane (c), ethanol (d), 2-propanol (e), and 2-butanone (f). Adsorbents studied: activated charcoal, AC; amorphous silica, AS; molecular sieve 13X, MS13X; zeolite Y, A88Y; ZSM-5 zeolite, A14Z. T = 25˚C.

Table 4.4: Summary of literature comparisons for single-component water and toluene capacities of adsorbents.

		AC	AS	MS13X[3]	A88Y[3]	A14Z[3]
Water capacity [mg/g][1]	*This study*	93.2 ± 2.6	94.1 ± 2.1	223.2 ± 2.2	29.9 ± 1.4	63.5 ± 1.3
	Literature	100 [279]	50-110 [64]	220-280	25-60	20
Toluene capacity [mg/g][2]	*This study*	264.1 ± 4.2	21.2 ± 0.9	145.4 ± 1.6	120.6 ± 1.5	57.4 ± 0.4
	Literature	250-310 [181]	37 [195]	120-210	90-130	60-80

[1] Measured at 50 % RH.

[2] Measured at partial pressure of toluene vapour, $P/P_0 = 0.005$

[3] Literature values for capacity of zeolite samples reproduced from work by Kraus et al. [177]

4.2.8.1. Unusual isotherm of zeolite Y and polar adsorbates

A88Y exhibited a stepped type V isotherm when exposed to ethanol and 2-propanol vapours, indicating an unfavourable interaction at lower partial pressures. A previous study [100] on methanol and dealuminated zeolites credited this behaviour to the difficulty of the polar molecule overcoming the electrostatic adsorption barrier of the zeolite Y pores. Measurements carried out on low molecular weight alcohols, shown in **Figure 4.6**, found that the inflection point at which pore filling commences occurs at higher partial pressures in more polar species, indicating the repulsion is likely dependant on the electrostatic properties of the adsorbates. The adsorption of toluene and water onto A88Y provide the two extremes of this interaction: the capacity for toluene, due to ease of micropore filling, increased rapidly at low pressure; whereas water was seemingly unable to penetrate this barrier, and is limited to adsorption on the surface and inside the mesopores of A88Y.

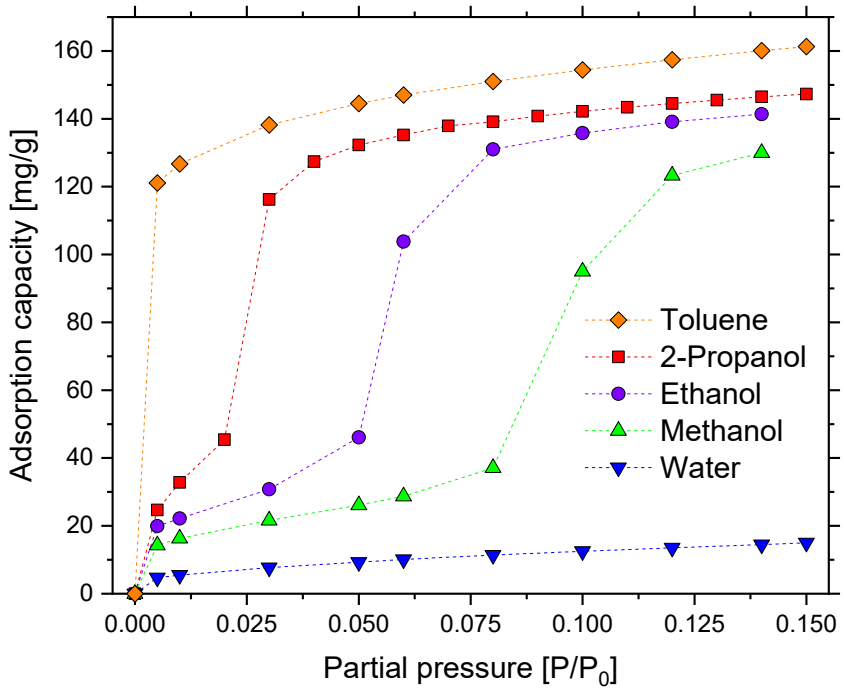


Figure 4.6: Isotherms of polar and non-polar vapours on high-silica zeolite Y, A88Y. T = 25˚C.

This reduced capacity for non-polar species due to surface chemistry is a key design constraint for removing VOCs from humidified environments. An ideal adsorbent would have sufficient hydrophobicity to minimise water adsorption but still allow the capture of VOCs with polar bonding chemistries. Despite this hydrophobicity, A88Y was still found to adsorb greater quantities of water vapour than AC at low RHs. As discussed earlier, the higher than expected aluminium content in A88Y determined via XRF may be due to extra-framework aluminium which can be generated during the dealumination process [44]. Extra-framework, or non-framework aluminium has been found to increase the hydrophilicity of high-silica zeolite Y due to its Lewis acidity, or ability to donate protons [124]. Therefore, extra-framework aluminium acts as a sort of hydrophilic defect site, allowing the adsorption of water onto the surface of the high-silica zeolite Y while being unable to fill its micropores.

4.2.8.2. Hydrophobicity indexes

Single component toluene and water adsorption data was used was varied to ascertain how the H.I. value for each adsorbent changed with process humidity, as shown in **Figure 4.7.**

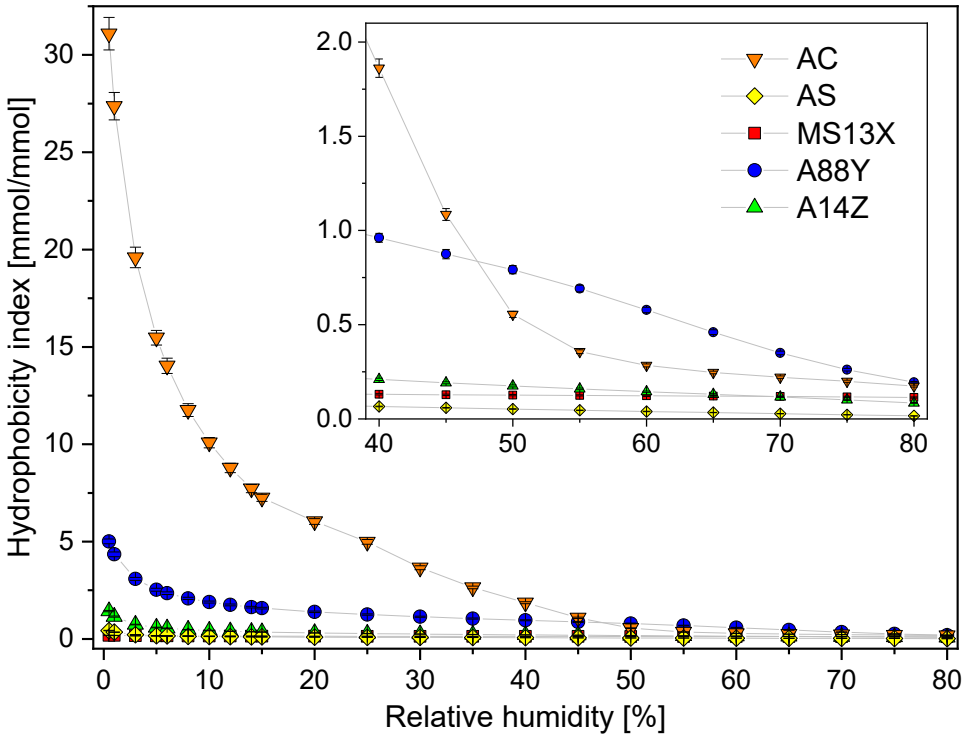


Figure 4.7: Molar hydrophobicity indexes (H.I.s) calculated as a function of RH for adsorbent samples: activated charcoal, AC; amorphous silica, AS; molecular sieve 13X, MS13X; zeolite Y, A88Y; ZSM-5 zeolite, A14Z. $(P/P_0)_{toluene} = 0.005$, T = 25˚C.

At low RHs, AC possessed the highest H.I. values, followed by high silica zeolites, and finally AS and MS13X. However, when calculated using an RH of 50 % and above, which more accurately represents the relative water and volatile concentrations in indoor air, the H.I. value of A88Y was found to be highest. As shown in **Figure 4.5**, AC's high mesopore volume leads to an increase in water adsorption when RHs exceeded 40 %, contributing to a steep reduction in its hydrophobicity index in **Figure 4.7**. In the case of A88Y, water's interactions are restricted to bonding sites on the surface of the material, due to the hydrophobic nature of the adsorbent's pore openings [100]. These indexes, calculated using single-component adsorption data, may be useful indicators of the performance of adsorbents in the presence of water vapour.

Table 4.5: Metrics of hydrophobicity for industrial porous materials. Water capacities and hydrophobicity indexes calculated using an RH of 70 %. T = 25˚C.

Adsorbent	Water capacity [mg/g]	Hydrophobicity Index [mmol/mmol]	Water contact angle [˚]
AC	233.4 ± 8.2	0.247 ± 0.08	37.7 ± 1.7
AS	158.3 ± 6.2	0.034 ± 0.01	0 [1]
MS13X	236.5 ± 2.7	0.119 ± 0.01	0 [1]
A88Y	67.6 ± 1.9	0.261 ± 0.08	72.5 ± 5.2
A14Z	95.5 ± 1.8	0.131 ± 0.02	0 [1]

[1] Water contact angles could not be determined as surface became fully wetted

Considering the varied techniques for calculating hydrophobicity, as well as some broadness in how the term 'hydrophobicity' is defined, there is some value in clarifying the use of this term in this work. The general term 'hydrophobicity' will be used when referring to a material's ability to not adsorb polar species in the vapour phase such as alcohols and water, i.e. the 'adsorption hydrophobicity'. As seen in the trends for H.I., a material's adsorption hydrophobicity is a function of the relative humidity it is exposed to, as the adsorption sites water vapour can access and occupy change depending on its driving force. Therefore, the hydrophobicity of a material is not a set or immutable property and will depend largely on its application. For example, when analysing the water vapour uptake AC may be considered hydrophobic at an RH of 10 %, but it cannot be considered hydrophobic at an RH of 80 % as its uptake exceeds all other adsorbents bar AS at this RH level. When considering the H.I. indexes, the trends in adsorption hydrophobicity also change with RH- with A88Y overtaking AC at RH values > 45 %. When referring to an adsorbent's 'surface hydrophobicity', this will be related to the advancing water contact angle the material displays which, barring a change in temperature or surface roughness, is a relatively fixed quantity. How a material's 'surface hydrophobicity' and 'adsorption hydrophobicity' relate to one another will be discussed in subsequent sections and Chapters.

4.2.9. Two-component vapour adsorption performance

Samples were equilibrated with water vapour in the range of 0-70 % RH to represent both low and high humidity conditions for built environments. **Figure 4.8** shows the capacity for toluene and ethanol vapour of adsorbent samples following pre-exposure to different levels of humidity.

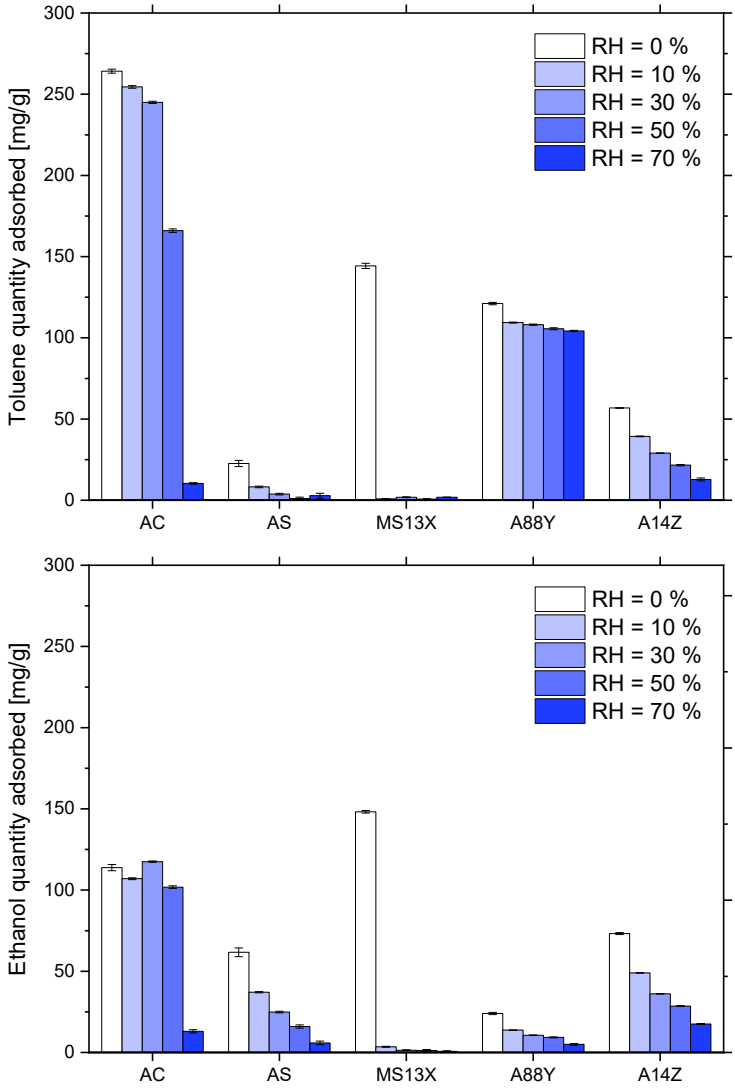


Figure 4.8: Two-component adsorption capacities of toluene (top) and ethanol (bottom) after pre-exposure to different levels of RH. Adsorbent samples studied: activated charcoal, AC; amorphous silica, AS; molecular sieve 13X, MS13X; zeolite Y, A88Y; ZSM-5 zeolite, A14Z. T = 25˚C.

Two component capacities, shown in **Figure 4.8**, were found to depend strongly on the hydrophobicity and relative water uptake of the adsorbent. In general, two-component adsorption interactions can be divided into two phenomena: co-adsorption, where the species interact with different adsorption sites; and competitive adsorption, where they occupy and compete for the same adsorption sites. MS13X is the best example for competitive adsorption, as its capacity for both toluene and ethanol dropped to negligible levels following exposure to even the lowest quantities of water vapour. On the other hand, A88Y was found to retain a relatively high adsorption capacity for toluene at all humidity values studied. The initial drop in capacity from 0-10 % humidity is likely due to toluene interacting with extra-framework aluminium defects located on the external surface of the zeolite [100], [177] which, due to their Bronsted acidity [124], interacts strongly with water vapour. In addition, as shown by **Figure 4.6**, water is unable to enter the micropores of zeolite Y, providing different bonding sites for the two molecules to co-adsorb. Despite A88Y's selectivity for toluene over water, its low capacity for dry ethanol led to similarly low removal in humid conditions. AC's interactions with water and volatile vapour depend on the concentration of water vapour it is exposed to, as predicted by the hydrophobicity indexes calculated previously. At all but the highest humidity, AC maintained a high capacity for both toluene and ethanol despite the presence of water vapour, but its performance was found to decrease noticeably at an RH of 70 %. A study by Pei & Zhang [189] on toluene adsorption in activated charcoal found the most significant performance reduction occurred when increasing the relative humidity from 50- 80%. This effect was credited to the increased 'critical radius' that water molecules could fill as RH increases. However, the Kelvin equation is only valid in pores with diameters of 2 nm or more, and the study extrapolates its hypothesis to pores in the range of 0.34 nm. The increased interactivity with water vapour at high RH may instead be due to the presence of surface or mesopore defects increasing the hydrophilicity of AC, which become more important at high RH as larger pores are filled [164].

For the adsorption of ethanol, the capacity for A14Z and AS with increasing humidity decreased less severely than for toluene. The polar nature of ethanol could have led to it occupying higher energy adsorption sites unfilled by water molecules. The adsorbed quantity of ethanol for AC appeared to increase at 30 % RH, which may indicate beneficial adsorbate-adsorbate interactions between pre-

adsorbed water molecules and the adsorbing ethanol molecules [282]. This interaction likely requires a balance between sufficient surface wetting and limited pore blocking as the ethanol capacity was found to decrease at all other humidity values studied. The data collected in single-component measurements appears to offer insight into the performance losses of studied adsorbents. As shown by **Figure 4.5**, AC's interactions with water vapour begin the transition from type III to type V at RHs exceeding 50 %, marked by a sudden increase in water capacity. This point also appears to mark the transition from co-adsorption into competitive adsorption of water vapour and volatiles in **Figure 4.8**, due to the lack of selectivity in the adsorption sites of the studied adsorbent. This decrease in capacity is mirrored in the hydrophobicity indexes plotted in **Figure 4.7**, emphasising the potential use of single-component data in predicting humid adsorption performance.

4.2.9.1. Relationship between hydrophobicity indexes and two-component capacities

To assess the effectiveness of single-component data in informing the multicomponent performance of adsorbents, humid toluene capacities were compared to H.I. values calculated at corresponding humidity values. From the data in **Figure 4.9**, H.I.s appeared to be a poor determinant of performance in hydrophilic samples AS and MS13X, with the latter having no trend between single- and two-component data. AC and A14Z's performance were well described by semi-logarithmic trends with R^2 values of 0.884 and 0.989 respectively, while A88Y's performance/ H.I. plot followed a largely linear trend with an R^2 of 0.934. H.I. indexes in this work were calculated as a function of humidity and are not simply a material property ascribed regardless of process conditions. This may be a useful indictor of the humid adsorption performance of hydrophobic materials for non-polar vapours.

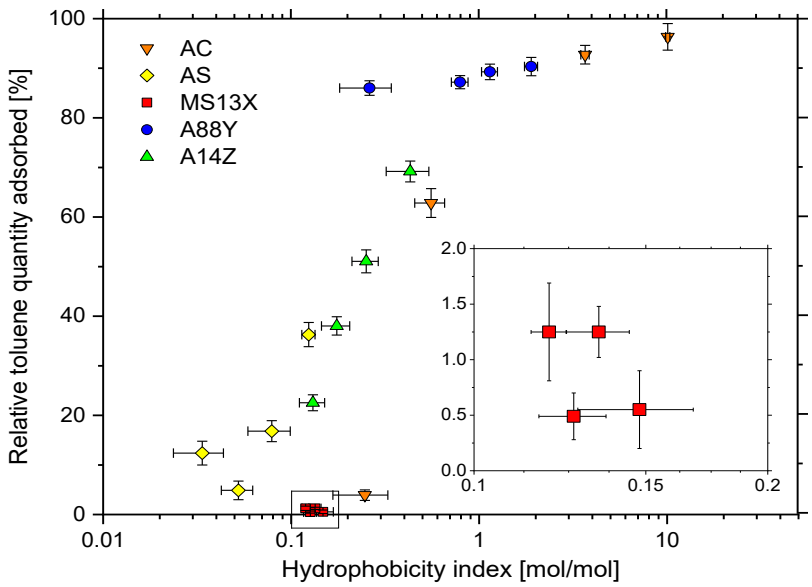


Figure 4.9: Relationship between hydrophobicity indexes and relative toluene capacities, measured using single- and two- component adsorption data respectively. Adsorbent samples studied: activated charcoal, AC; amorphous silica, AS; molecular sieve 13X, MS13X; zeolite Y, A88Y; ZSM-5 zeolite, A14Z. T = 25˚C.

4.2.10: Cycling performance of adsorbents

As seen in **Figure 4.10**, adsorption capacity in dry cycling dropped noticeably for AC, MS13X and A14Z in the second cycle before either remaining largely constant or dropping slightly in future cycles. This decrease is likely due to the minimum pore sizes of these materials being on a similar scale to the kinetic diameter of toluene, leading to restricted diffusion of the molecule out of the pores in the desorption steps. On the other hand, AS and A88Y did not show any significant drop in productivity with cycle number. In the case of AS, its mesoporous nature and large pore apertures make it unlikely for toluene molecules to become trapped. A88Y, despite having the same pore size as MS13X of ~0.9 nm, also has a noticeable amount of micropore volume in an aperture with a size of ~1.1-1.2 nm. This, combined with its hierarchical mesoporosity from dealumination, may create an easier path for toluene to travel in and out of the micropores. The drop in performance was most noticeable in AC, which had its capacity decrease by around 35 %, from 264.2 mg/g to 174.3 mg/g, although this was still noticeably higher than the other adsorbents studied in dry conditions. Regeneration studies on activated charcoal

have shown decreases in adsorption capacity with increasing cycle time due to pore blockage, and often utilize high temperature or vacuum conditions for regeneration [278]. In the case of A88Y, the quantity of toluene adsorbed dropped by around 5 % before remaining constant. A similar study on ultra-stable (high silica) zeolite Y [283] found its capacity for toluene drop by around 10 % in cycling experiments. With the introduction of 50 % RH, the toluene amount adsorbed in the first cycle dropped to those values shown in **Figure 4.8**. AC's relative performance was found to drop by 35 %, identical to that of the dry cycling experiments. A14Z had a drop in performance of around 57 %, greater than the drop of ~20 % in dry conditions. A88Y maintained a relative performance of over 98 % in all studied cycles, allowing it to adsorb quantities of toluene similar to AC under these conditions. The trends observed suggest the role of water vapour in regeneration and adsorption cycling behavior likely depends on the adsorbent's surface chemistry and pore structure, as well as the preferred bonding sites of water and toluene molecules. The negligible amount of toluene adsorbed by AS and MS13X in humid cycling experiments made any accurate analysis difficult.

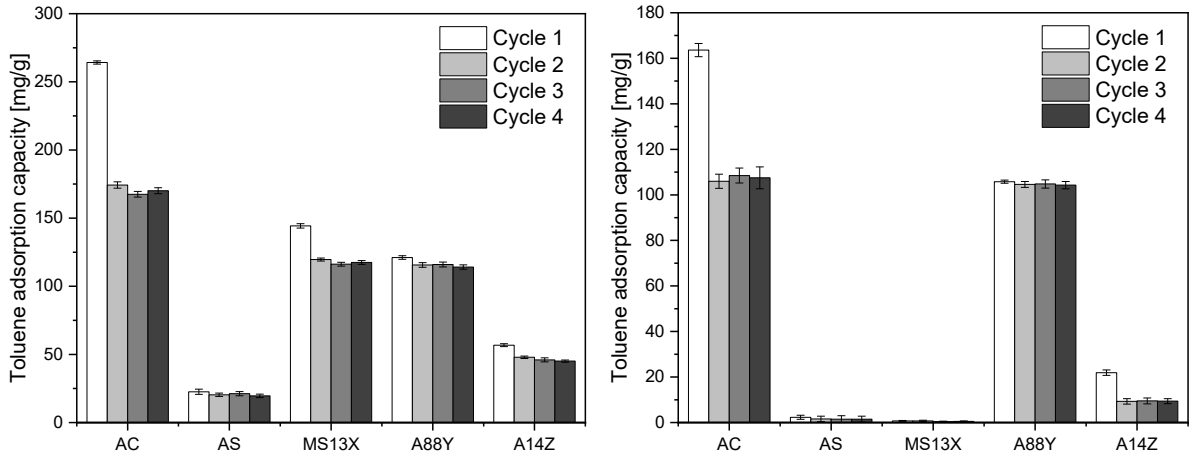


Figure 4.10: Quantities of toluene adsorbed as a function of cycle number, under dry (left) and humid (right) conditions. Samples studied: activated charcoal, AC; amorphous silica, AS; molecular sieve 13X, MS13X; zeolite Y, A88Y; ZSM-5 zeolite, A14Z. Partial pressure of toluene in all cycling experiments, $P/P_0 = 0.005$. RH in humid experiments = 50 %. Desorption carried out under 200 mL/min of dry air flow, T = 25˚C.

4.2.10.1. Estimated productivity of toluene adsorption

The productivity of an adsorption column can be defined as the quantity of vapour adsorbed per unit mass of adsorbent per hour [284][285]. Using the kinetic adsorption data (i.e. mass uptake versus time) from the cycling experiments, an approximation for productivity can be calculated as a function of cycle number and relative humidity. As all five samples were exposed to the same conditions in the same instrument, the time taken for adsorption was not dictated by the step time, which depends solely on the slowest adsorbent, but the mass equilibrium of each individual sample. The time elapsed was defined as the time taken to reach an adsorption gradient value of 0.00075% dry mass per minute. AS had noticeably higher productivity than all adsorbents bar AC, due to its exceptional adsorption kinetics for toluene, with its large pore apertures leading to negligible size-induced diffusion limitations for the aromatic molecule. Similarly, the hierarchical porosity of A88Y leads to improved adsorption kinetics in dry conditions compared to MS13X despite the latter's greater toluene capacity. The trends in dry and wet conditions for cycle number largely follow the trends for capacity in **Figure 4.10.** One noticeable discrepancy is the increase in humid toluene productivity with higher cycle numbers for AC, increasing by approximately 17%. Although the extent of this improvement varied slightly during repeat experiments, the same trend was seen in every case. This implies that the presence of humidity significantly affects the adsorption kinetics in the first cycle of toluene adsorption but less in the second cycle. Due to the drop in capacity in dry conditions, it can be assumed that the 'trapped' toluene is located predominantly in smaller micropores while 'released' toluene is adsorbed inside of larger micropores and the surface of the charcoal. In the second cycle the 're-adsorbed' toluene is likely located in/ on these larger micropores, the kinetics for which may be less affected by the presence of water molecules on the surface. Regardless, the superior adsorption kinetics of AC over A88Y allow it to outperform all other industrial adsorbents in this study in terms of productivity in dry or humid conditions. The plots for productivity in dry and humid conditions can be found in **Figure A.7** in the Appendix.

Table 4.6: Toluene adsorption capacities and estimated productivities of adsorbents during the 4th performance cycle in dry and humid conditions. All experiments carried out using a toluene partial pressure of 0.005, humid experiments used 50 % RH for both pre-exposure and regeneration.

Adsorbent	4th Cycle Capacity		4th Cycle Productivity [10^{-3} kg/ kg h]	
	Dry	Humid	Dry	Humid
AC	170.1 ± 2.2	107.5 ± 4.8	13.79 ± 0.25	12.76 ± 0.43
AS	19.6 ± 1.3	1.5 ± 1.3	9.59 ± 0.24	2.95 ± 0.07
MS13X	117.5 ± 1.4	0.5 ± 0.2	6.03 ± 0.2	N/A[1]
A88Y	114.1 ± 1.6	104.3 ± 1.6	8.95 ± 0.11	7.11 ± 0.11
A14Z	45.1 ± 0.8	9.4 ± 1.1	5.31 ± 0.15	1.41 ± 0.15

[1] Due to highly competitive sorption profile, exact time taken for adsorption step to occur could not be determined accurately. Therefore, productivity could not be calculated.

4.2.12: Fitting of adsorption kinetics

All kinetic parameters, and associated R^2 values, are included in **Tables A.10- A.22** in the Appendix. The two kinetic models, pseudo first order (PFO) and pseudo second order (PSO), were tested using an uptake range of 0-1 q_{max}. In addition, the range of 0-0.85 q_{max} was tested to discern whether the kinetic profiles of the VOC or water uptake naturally aligned with the linear region of PSO, leading to inaccurate determination of the best-fitted model, as recommended by Simonin [88]. Lack of convergence was most observed for systems with low adsorption capacity, leading to similar magnitudes to the DVS microbalance's drift and benchtop vibrations, or the competitive kinetic profiles of less hydrophobic adsorbents exposed to a mixture of water and toluene vapours.

4.2.12.1: Investigation of Simonin data range

Due to the low driving force for adsorption to occur in VOC experiments, i.e. a low partial pressure of only 0.005, the kinetics curves for each adsorbent were linear until reaching high q/q_{max} values, typically above 0.9-0.95, as shown in **Figure 4.11**. This resulted in the Simonin range of 0-0.85 q_{max} fitting an almost entirely linear uptake curve and different trends in kinetic parameters compared to the standard range of 0-1 q_{max}.

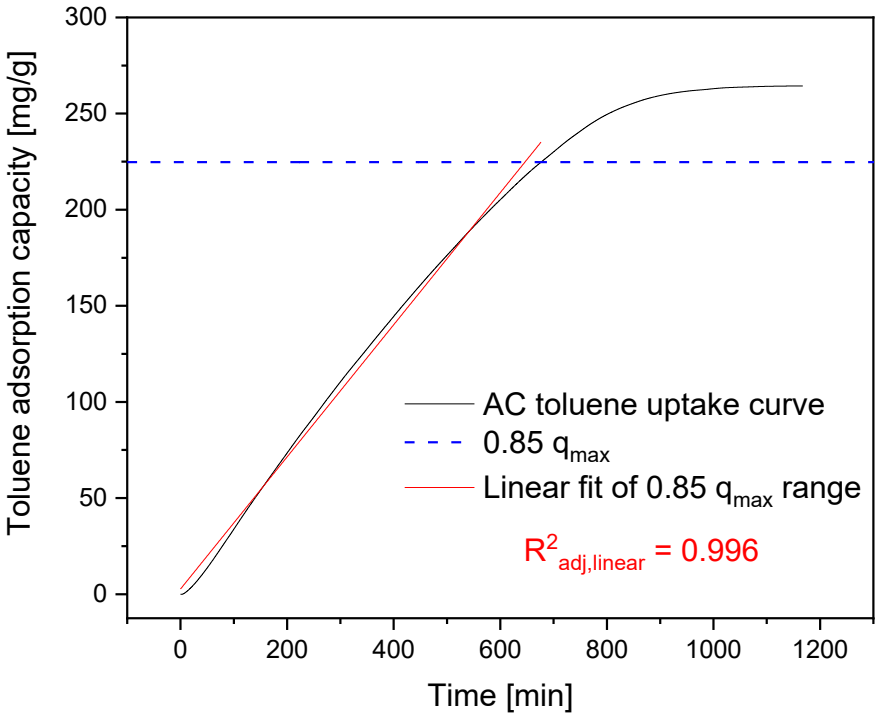


Figure 4.11: Toluene adsorption kinetics curve for AC, showing Simonin uptake limit, and linear fitting of kinetics data within this range of 0-0.85 q_{max}. $P/P_{0,TOL}$ = 0.005, T = 25˚C.

However, the Simonin data range did appear to alter which models fitted the experimental data best. When using a q_{max} data range of 0-1, out of a possible 65 adsorbent-adsorbate pairs, 56 (86 %) datasets were best fit by PFO, 7 (11 %) datasets by PSO, and 2 (3 %) datasets were fitted equally by both. When using the Simonin q_{max} data range of 0-0.85, 8 (12 %) datasets were best fit by PFO, 7 (11 %) datasets by PSO, and 50 (77 %) datasets were fitted equally by both. The similar fits for experimental data in the Simonin range is likely due to the quasi-linear dataset at lower capacities. For adsorption processes with low driving forces, i.e. at low adsorbate concentrations or partial pressures, the initial rate of adsorption is predominantly linear and the process occurs relatively slowly- this linear range can be easily described using either a first or second order fitting model. The kinetics curve in this work do not match those reviewed and analysed in Simonin's work, which may explain the lack of bias towards PSO. Fits using the PSO were found to have lower adjusted R^2 values than PFO, although the difference

in R^2 values decreased upon application of Simonin's limit as both models were essentially fitting a linear profile.

4.2.12.2: Adsorption rate constant trends of adsorbent-adsorbate pairs

For the adsorption of n-hexane, the trend in PFO rate constants was AS > A14Z > A88Y > MS13X > AC. This trend was almost identical for toluene, except for AC outperforming MS13X. However, the PFO rate constants for toluene were noticeably lower than for n-hexane- decreasing by a factor between 2.2 and 4.9. This is likely due to the higher kinetic diameter of toluene compared to n-hexane, which has been credited to reduce the permeability of gas-solid systems, as well as increase the diffusion activation energy [286][151].

Interestingly, the A88Y had the highest k_{PFO} values for the adsorption of ethanol, 2-propanol, and water vapour at all humidity values except 10 % RH, where AC outperformed by almost a factor of 2. Considering the high hydrophobicity of high-silica zeolite Y's pores, fast kinetics may be explained by the mechanism of adsorption. For polar species below their 'critical' driving force partial pressure, i.e. where the inflection point of the Type V isotherm occurs, the molecules can only settle on surface sites around the aperture openings of high-silica zeolite Y [100]. To test the effect of pore filling vs surface filling on kinetics, data fitting was carried out on two different regions of the zeolite Y- ethanol isotherm: initial surface filling at a partial pressure of 0.005, below the 'critical' driving force; and micropore filling at a partial pressure of 0.06, at or exceeding the 'critical' driving force in the Type V isotherm, as shown in **Figure 4.6**. The PFO kinetic rate constants for A88Y-ethanol were calculated to be 0.00920 min^{-1} during surface filling and 0.00398 min^{-1} for micropore filling, with the latter being approximately 2.3 times smaller. It is important to note that the equilibrium capacity of zeolite Y for ethanol at a partial pressure of 0.06 is 5 times higher than the same capacity at a partial pressure of 0.005, 123.3 mg/g and 24.5 mg/g respectively. However, for the sake of understanding kinetic or diffusion parameters the final adsorbed quantity is irrelevant- definitions of diffusivity or kinetic rate constants use the fractional uptake as a function of time [89][90]. These findings, i.e. that adsorption mechanisms dominated by pore filling are slower than those involving purely surface adsorption, may

indicate that the diffusion of molecules into zeolite Y's pores is the step most affecting the overall kinetics of adsorption.

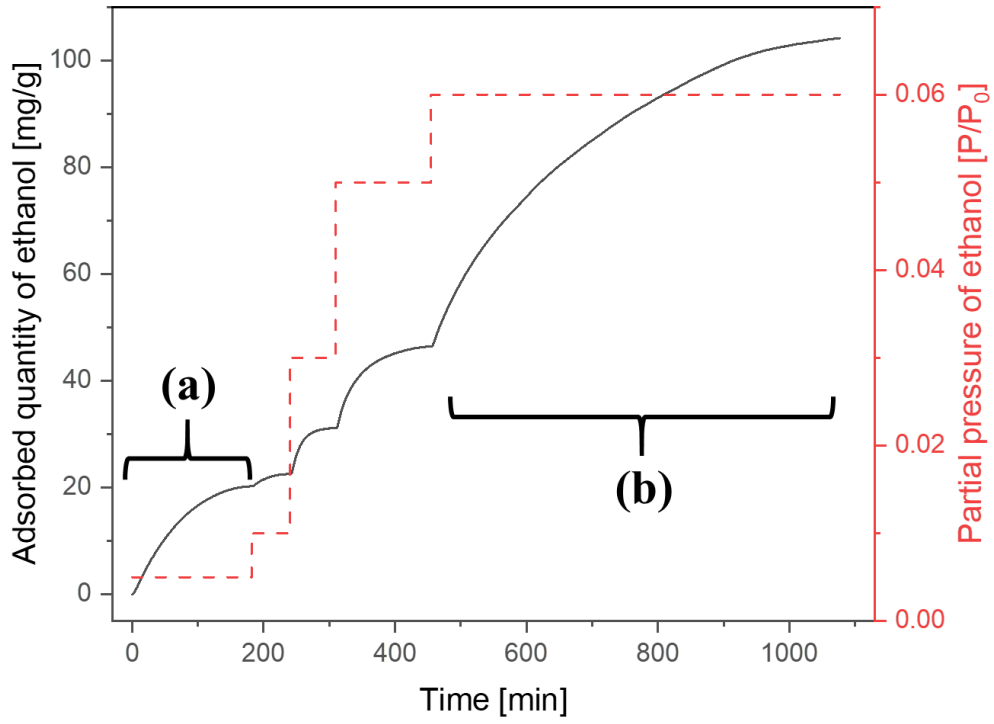


Figure 4.12: Ethanol uptake profiles by zeolite Y (A88Y), highlighting two mechanisms of adsorption occurring at two different partial pressures- surface filling (a) and micropore filling (b).

Studies by Wang et al [287] on toluene adsorption by activated charcoal and Gong et al [288] on CO_2 adsorption by chabazite zeolite both hypothesised pore diffusion to be the rate limiting step for adsorption kinetics due to the superior fitting of the Bangham kinetic model equation compared to pseudo first order, pseudo second order, and Elovich models. However, the Bangham equation contains 3 parameters compared to the other models' 2 parameters, which will inherently improve its ability to fit and describe experimental datasets. Unlike literature findings, this study uses reproducible experimental datasets described by a consistent kinetic fitting model to discern between adsorption kinetics pre- and post- pore filling. The hypothesis of superior kinetics in adsorption predominantly onto the surface is also supported by the higher ethanol k_{PFO} values for A14Z and AS compared to microporous MS13X. While all 3 materials possess high surface areas between 300-700 m^2/g, A14Z

and AS have most of their pore volume, at least 95 %, in large mesopores, while MS13X is predominantly (60 %) microporous. However, as the surface chemistry and hydrophobicity of these materials is not consistent these parameters cannot be neglected as contributors to the adsorption kinetics or diffusion process. The adsorption rate, according to the Langmuir kinetic equation [289], is proportional to the adsorbate concentration and the proportion of available adsorption sites. Therefore, for two materials with identical pore size distributions and surface areas but differing surface chemistries, the one with greater hydrophobicity will contain a lower number of polar adsorption sites- reducing the adsorption kinetics of polar species. This effect will become less noticeable as the species' polarity decreases, as polar adsorption sites are still capable of interacting with adsorbate species via London dispersion forces. In addition, the Langmuir rate equation assumes adsorption only occurs on these surface sites and is therefore less valid for materials with high degrees of microporosity- such as zeolites and activated carbons. In addition, the equation assumes that the enthalpy of adsorption is independent of coverage- while in porous materials the enthalpy of adsorption is typically found to decrease with coverage as the higher energy adsorption sites, e.g. in smaller pores, are filled first followed by lower energy sites in larger pores and on the surface. This further emphasises the importance of using reproducible experimental datasets to describe or attempt to explain adsorption phenomena alongside fitting and description of limited datasets using theoretical or empirical models.

The adsorption of water vapour, as mentioned previously, resulted in superior PFO rate constants for hydrophobic AC and A88Y. However, as humidity increased, AC was found to have poorer kinetics while MS13X began to overtake other samples with regards to the rate constant- the final trend at 70% RH was found to be A88Y > MS13X > A14Z > AS > AC. As humidity or partial pressure increases, the size of pores the molecules try to fill also increases- at the highest partial pressures, mesoporous materials will undergo capillary condensation with adsorbing gas and vapour molecules. Here it is likely that the process of filling mesopores through capillary condensation has an impact on the adsorption kinetics- while MS13X adsorbs water molecules predominantly through micropore filling or surface adsorption, the latter of which will be dominant at the highest pressures.

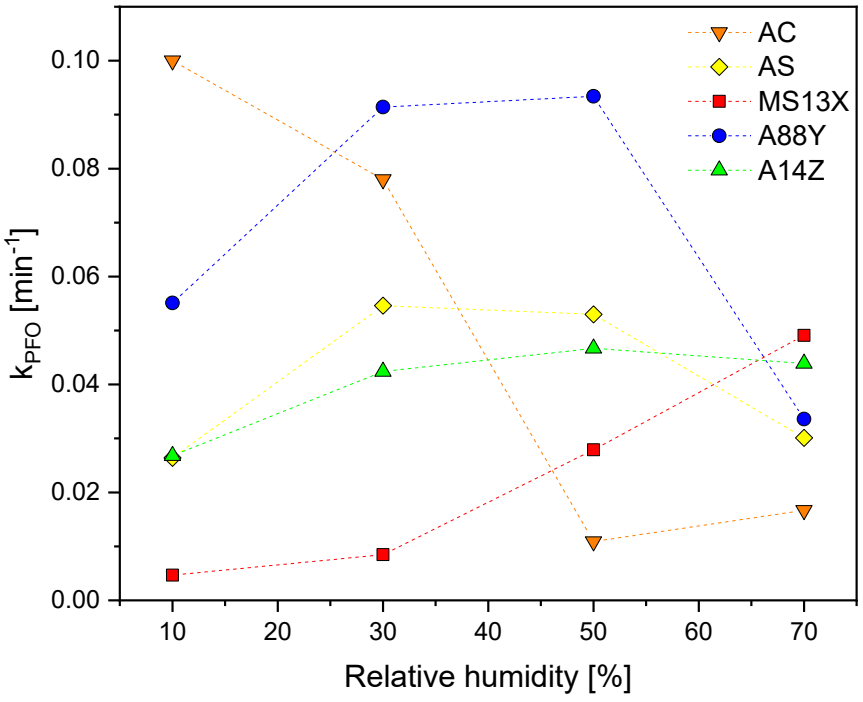


Figure 4.13: PFO adsorption rate constants for water adsorption as a function of relative humidity, for all industrial adsorbents studied. Kinetic model fitting in the uptake range of 0-1 q_{max}. T = 25˚C. Calculated error for parameters smaller than symbols.

The impact of relative humidity (RH) on kinetics appeared to follow one of three trends:

- A decrease in kinetics with RH, as observed in AC. This is likely due to the mechanism of adsorption shifting from surface adsorption, to micropore filling, and finally mesopore filling and capillary condensation.
- An increase in kinetics with RH, as observed in MS13X. This is likely due to the aforementioned consistent mechanism of water uptake, i.e. micropore filling and surface adsorption. As the mechanism remains consistent, but the driving force for adsorption to occur increases, the process will occur faster.
- An initial increase with RH due to increased driving force followed by plateauing or decreasing. This effect was present in AS, A88Y, and A14Z, which possess significant differences in their

microporosity, hydrophobicity, and pore size. This makes any accurate analysis of the trend, and assessing the role of adsorption mechanism changes, difficult.

Even though the trends in water rate constants are not clear between samples, it does appear that the mechanism of adsorption plays an important role in the speed at which adsorption and saturation occur.

4.2.12.3: Impact of humidity on toluene adsorption kinetic rate constants

By assessing only the rate constants of toluene adsorption after pre-exposure to humidity, the impact that this environment has on the capacity of the material, and thereby its overall performance or productivity, is lost. For this reason, two datasets were plotted against RH: the kinetic rate constants for toluene adsorption, using the PFO model; and the product of the aforementioned rate constant and the equilibrium toluene capacity, which will be denoted as the 'kinetic productivity'. This parameter is a measured of time-referenced adsorption capacity.

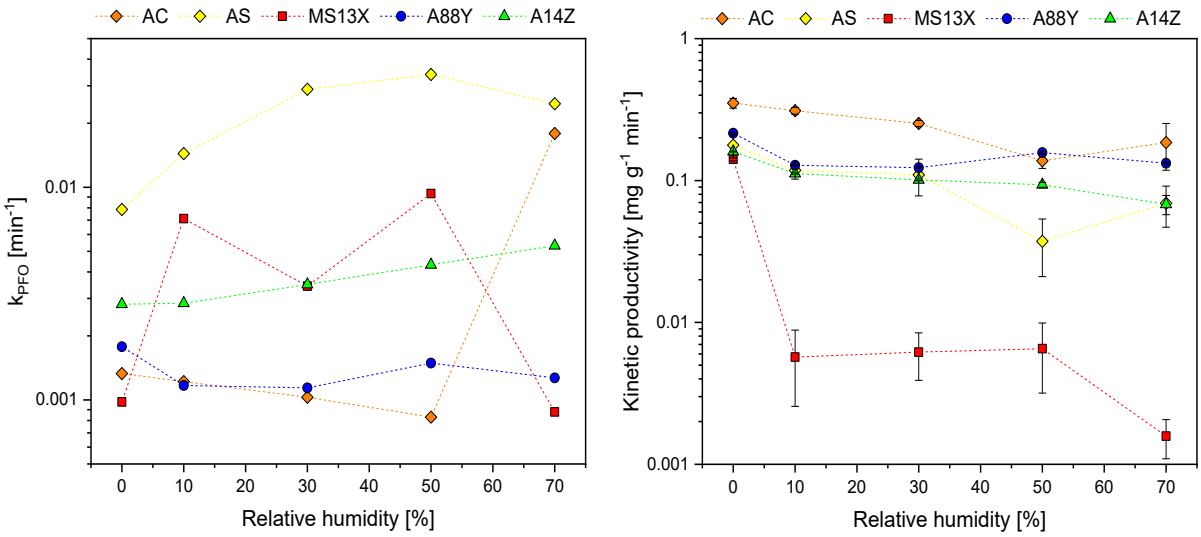


Figure 4.14: PFO adsorption rate constants (left) and the kinetic productivities (right) for toluene adsorption as a function of pre-exposure relative humidity, for all industrial adsorbents studied. Kinetic model fitting in the uptake range of 0-1 q_{max}. T = 25˚C.

The trend between humidity pre-exposure level and PFO rate constant varied significantly between samples: A88Y had an initial decrease before fluctuating around the same level; AC decreased gradually

before a significant increase at a humidity level of 70 % RH; A14Z consistently increased at every increment in humidity, AS appeared to increase, plateau, and then fall as humidity increased; and MS13X had no discernible trend whatsoever. When capacity was taken into account, different trends for the kinetic productivity emerge: AS and A14Z exhibit gradually decreasing performance with increasing humidity; MS13X has a sharp decrease, likely due to the significant competition between water vapour and toluene; A88Y, similar to trends in k_{PFO} decreases before fluctuating slightly around the same level; and AC, similar to k_{PFO}, has a gradual decrease before rapidly increasing to above dry levels at a humidity of 70 % RH. This indicates that despite the significantly reduced capacity AC possesses for toluene after pre-exposure to extreme humidity, it appears to possess superior adsorption kinetics rate constants compared to zeolite samples, both hydrophilic and hydrophobic. Whether this toluene is located on hydrophobic sites on the surface, within micropores, or both, cannot be determined using these experiments, making analysis of the effect of adsorption mechanism on kinetics difficult.

Table 4.7: Summary of pseudo first order kinetic rate constants for each adsorbent for different VOC molecules and water vapour. T = 25˚C. Red numbers indicate fits that did not converge.

Adsorbate species		**k_{PFO} [min^{-1}]**				
		AC	**AS**	**MS13X**	**A88Y**	**A14Z**
n-Hexane [a]		0.0037	0.0267	0.0048	0.0048	0.0062
Ethanol [a]		0.0040	0.0039	0.0017	0.0092	0.0033
2-Propanol [a]		0.0013	0.0020	0.0007	0.0044	0.0016
2-Butanone [a]		0.0040	0.0111	0.0021	0.0025	0.0043
Toluene [1]	0% RH	0.0013	0.0077	0.0010	0.0018	0.0028
	10% RH	0.0012	0.0144	0.0071	0.0012	0.0029
	30% RH	0.0010	0.0289	0.0034	0.0011	0.0035
	50% RH	0.0008	0.0339	0.0093	0.0015	0.0043
	70% RH	0.0179	0.0247	0.0009	0.0013	0.0053
Water [2]	10% RH	0.1170	0.0264	0.0047	0.0551	0.0268
	30% RH	0.0780	0.0546	0.0085	0.0914	0.0424
	50% RH	0.0109	0.0530	0.0279	0.0934	0.0467
	70% RH	0.0167	0.0301	0.0491	0.0336	0.0439

[1] Partial pressure of VOCs in all experiments = 0.005.

[2] RH varied between 10-70 %.

4.3. Conclusions

Industrial porous materials were investigated for the adsorption of volatile organic compounds, specifically silica gel, activated charcoal, and high- and low-silica zeolites. For zeolite samples A88Y and A14Z, the process of dealumination was initially detected via FTIR, and their increased silica: alumina ratio was confirmed quantitatively via X-ray fluorescence. Nitrogen sorption measurements confirmed that all samples exhibited BET surface areas of at least 300 m^2/g, while only AC, A88Y, and MS13X displayed significant microporosity. All samples were found to have pore volumes, surface areas and, in the case of zeolite samples, pore size distributions matching those of literature.

Isotherms of n-hexane and toluene vapours largely followed similar trends to those of nitrogen, while more polar molecules were found to be adsorbed lass favourably by AC and A88Y due to their hydrophobicity. The adsorption isotherms for A88Y were found to change significantly with adsorbate polarity- non-polar species produced type I, with a shift to type V for light alcohols, and finally type II/III for water vapour. This phenomenon is credited to the hydrophobic apertures of A88Y selectively adsorbing molecules depending on polarity [100]. To better illustrate this adsorption selectivity, single-component hydrophobicity indexes were calculated as a function of relative humidity, allowing the humidity-dependent nature of selectivity to be ascertained. AC's and A88Y's hydrophobicity was observed to extend to liquid system, resulting in contact angles of 37.7˚ and 72.5˚ respectively, while all other water-adsorbent systems resulted in full surface wetting and contact angles < 5˚.

The adsorption of toluene and ethanol after pre-exposure to relative humidity was studied using dual-solvent gravimetric methods. Hydrophilic adsorbents MS13X and AS were found to have significantly reduced humid capacity for VOCs as water was able to occupy all active sites and, due to its polar chemistry and strong interactivity with the surface of the adsorbent, could not be displaced by more non-polar solvent vapours. AC's performance appeared to inversely follow the trend of its water isotherm, with significant reductions in toluene and ethanol capacity as humidity increased above 50 %. Only A88Y maintained a high adsorption capacity for toluene at all RHs studied, although its hydrophobic apertures prevented any significant adsorption of ethanol. These two-component results were well described by the single-component H.I.s in hydrophobic adsorbents AC, A88Y, and A14Z,

but the sudden drop-off in removal efficiency of hydrophilic MS13X and AS could not be accounted for by single-component measurements. Cycling experiments found that zeolite and silica adsorbents had stable adsorption capacities for toluene for up to 4 cycles, likely due to their pore apertures exceeding the kinetic diameter of toluene. AC, with its narrower and more heterogenous apertures, had a reduction in performance of around 35 %. These losses were exacerbated when cycling was carried out in the presence of humidity and, similarly to single-pass experiments, only A88Y had stable toluene capacities throughout all cycles.

For the fitting of adsorption kinetics, the pseudo first order model provided superior fits compared to the pseudo second order model. The impact of RH on water uptake kinetics provided additional information regarding the changing mechanism of adsorption at different stages of the adsorption isotherm- with pore filling mechanisms presenting significantly lower PFO rate constants. This was supported by the superior adsorption kinetics for ethanol onto A88Y compared to other adsorbents, which can be explained by its hydrophobic pore apertures preventing pore filling by the alcohol molecules.

This Chapter confirms that high microporosity and adsorption hydrophobicity are desirable qualities in a VOC adsorbent. Zeolite Y's exceptional humid performance was credited to the polarity-dependant molecular sieving of its micropore apertures. The role that these apertures have on performance and the mechanism by which VOCs and water vapour compete in multicomponent systems, warrants further study. Investigations into adsorbents with 'hyperhydrophobicity' could provide additional information about the role of hydrophobic apertures on performance. Conversely, adsorbents with stepped water isotherms could provide insight on the role of water pore filling on competition mechanisms.

Chapter 5: Synthesis of metal-organic frameworks possessing hydrophobic apertures

5.1. Introduction

Vapour adsorption studies on industrial adsorbents found that high surface area and microporosity were desirable properties for adsorbing non-polar VOCs, while hydrophobic micropore apertures improved VOC removal efficiency in the presence of humidity. An advantage of metal-organic frameworks (MOFs) is the variety of organic linkers available to form their porous framework, and the variety of adsorption chemistries they can impart. Alkylated functional groups, such as ZIF-8's 2-methylimidazole or MAF-6's 2-ethylimidazole linker molecules [290], can result in significant increases to the adsorption hydrophobicity of the MOF. In applications where humidity plays a competitive role, such as VOC adsorption, the wide variety of functionalities and surface chemistries available in MOFs make them a promising adsorbent technology.

Based on literature vapour adsorption data for a range of metal-organic-frameworks, ZIF-8 was found to have the lowest capacity for water vapour [207] while adsorbing high quantities of non-polar vapours such as alkanes and aromatics [145]. Synthesis procedures for ZIF-8 vary greatly in terms of their zinc source, linker content, and reaction environment [291]–[293]. To this end, the optimisation of ZIF-8 synthesis conditions was carried out with the goal of optimising several performance metrics: BET surface area and microporosity from nitrogen adsorption; dry VOC uptake, at multiple partial pressures; and humid VOC uptake at low concentrations, following pre-exposure to water vapour. The effect of these synthesis conditions on product yield, relative crystallinity and crystal size and shape was also investigated using standard analytical techniques such as X-ray diffraction and electron microscopy. Importantly, the trends observed for changing synthesis conditions were compared to literature studies investigating the same phenomena- not only to confirm the synthesis procedure is successful for ZIF-8, but to gain better insight on the mechanisms of crystal formation and how these can impact the final performance of the material. The cobalt analogue of ZIF-8, ZIF-67, was also synthesised due to the relative lack of VOC adsorption data or comparisons between them despite their similar pore structure and surface area [153], and its relatively similar synthesis procedure.

However, this 'hyperhydrophobicity' has one drawback for this work- the lack of a pore filling event by water vapour makes investigating the impact of these events on adsorption competition impossible. Some MOFs of the 'MIL' family, such as MIL-125, MIL-100 and MIL-101, produce multi-step isotherms when exposed to water vapour [210]. In the case of MIL-100/101, this is due to a progressive filling of the MOFs' mesopore cages, which can only be accessed through smaller micropore apertures, containing hydrophobic surface chemistry due to their benzene tri- and di-carboxylic acid linkers respectively. Distinct pore filling events by water vapour, 1 for MIL-101 and 2 for MIL-100, can be measured and determined via water isotherm measurements. MIL-100 (Fe) will be used to investigate the role of relative humidity on the hydrophobicity of an adsorbent, and the limitations of defining it as purely a material property. In addition, the impact of water pore filling events on adsorption competition and performance will be studied.

5.2. Experimental methods

5.2.1. Optimisation of ZIF-8 synthesis

The standard procedure for synthesising powder ZIF-8 and ZIF-67 can be found in **Section 3.1.2.1.** Variations were made in the choice of solvent, the metal: linker ratio, and zinc salt to find the optimum conditions to produce crystalline ZIF powders with high surface area and microporosity. A summary of these variations is shown in **Table 5.1**. For the synthesis of ZIF-67 powder, the same procedure was carried out using cobalt nitrate hexahydrate instead of the zinc salt while using the conditions that produced the best performing ZIF-8 sample.

5.2.2. Synthesis of MIL-100

The synthesis procedure, seen in **Section 3.1.2.3.**, will be based on the previous work of a fellow researcher within the group, Luqman Hakim Mohn Azmi. This procedure has already been optimised to produce highly microporous MIL-100.

Table 5.1: Summary of ZIF synthesis conditions, all carried out at room temperature.

Experiment	Reaction solvent	Metal: linker: solvent [mol: mol: mol]	Metal source and amount [mmol]
1	Water	1:8:5500	Zinc nitrate hexahydrate, 2.5
2	Methanol	1:8:2500	Zinc nitrate hexahydrate, 2.5
3	Ethanol	1:8:1725	Zinc nitrate hexahydrate, 2.5
4	Methanol	1:1:2500	Zinc nitrate hexahydrate, 2.5
5	Methanol	1:2:2500	Zinc nitrate hexahydrate, 2.5
6	Methanol	1:4:2500	Zinc nitrate hexahydrate, 2.5
7	Methanol	1:6:2500	Zinc nitrate hexahydrate, 2.5
8	Methanol	1:8:2500	Zinc nitrate hexahydrate, 2.5
9	Methanol	1:16:2500	Zinc nitrate hexahydrate, 2.5
10	Methanol	1:8:2500	Zinc acetate dihydrate, 2.5
11	Methanol	1:8:2500	Zinc bromide anhydrous, 2.5
12	Methanol	1:8:2500	Cobalt nitrate hexahydrate, 2.5

5.3. Results and discussion

5.3.1. Synthesis of MOF powders

Following mixing of the salt and linker solutions, the reaction mixture for ZIF-8 powders began to cloud after ~5-10 minutes of reaction time. After cleaning, centrifuging, and drying, all ZIF-8 samples formed fine white powders, while the ZIF-67 sample formed a fine purple powder. MIL-100 formed a coarse, brown-orange powder following high temperature drying, as shown in **Figure 5.1**.

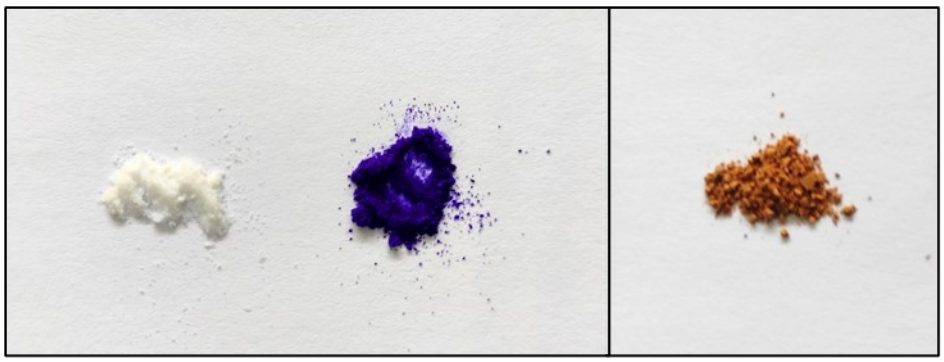


Figure 5.1: ZIF-8 (left) and ZIF-67 (middle) and MIL-100 (right) powders following cleaning, centrifuging and drying.

5.3.2. Initial screening of ZIF powders

Due to the time investment and limited availability of certain techniques and equipment, screening of ZIF powders was carried out to focus work on samples with the highest likelihood of functioning well as VOC adsorbents. Product yield, relative crystallinity, and toluene adsorption capacities were used as deciding factors for which samples would be deemed acceptable and undergo in-depth analysis.

5.3.2.1. Product yield

Three reaction media were tested for ZIF synthesis: water, methanol, and ethanol. Whilst both methanol and ethanol produced recoverable quantities of precipitate after 24 h of reaction time, the reaction mixture containing water did not. Even after centrifuging for several cycles at 8400 rpm, no observable precipitate could be recovered. In ZIF-8 formation, deprotonated 2-methylimidazole ions (mIm^-) are required to bridge solvated zinc ions, which forms the building units of the framework. Water, due to its high pK_a value and ability to function as a Lewis acid, was hypothesised by Jian et al [294] to donate protons to mIm in hydrolysis reactions, forming $HmIm^+$ ions which are unable to coordinate with solvated zinc ions. The same study found that an excess of mIm in solution can function as a moderate deprotonation agent, as its deprotonation constant is higher than the intermediate zinc-mIm coordinated ion compound. Based on nitrogen isotherms, Zn: mIm ratios of at least 20 were required to form porous products, although ratios as high as 70 only produced ZIF-8 with a surface area of 1126 m^2/g, far below methanol-based synthesis procedures using the same zinc salts [293].

The yields, based on the starting mass of zinc salt, for reactions using methanol and ethanol were approximately 68 % and 35 % respectively (i.e. for every 1g of zinc nitrate hexahydrate, ~680mg and ~350mg of ZIF-8 powder would be produced respectively). When adjusting the ratio of zinc nitrate hexahydrate: 2-methylimidazole (Zn:mIm), all ratios produced recoverable quantities of precipitate, although the yield for ZIF-8 appeared to reach a maximum of 68 % at a ratio of 1:8, although this value was not statistically significant compared to ratios of 1:6 and 1:16 based on a 95 % confidence interval, equivalent to two standard deviations [295], [296]. Using zinc acetate and zinc bromide as reactants produced significantly lower yields of sample compared to those using nitrate salt, with values of 28 %

and 37 % respectively. ZIF-67 differed from ZIF-8 reactions in that a precipitate was observable after only a couple of hours, as well as an instantaneous colour change upon mixing of the two reactants. The yield of ZIF-67 powder was measured to be ~58 % by mass.

5.3.2.2. Product crystallinity

Samples synthesised in methanol and ethanol were both found to have good crystallinity based on their PXRD patterns, with characteristic peaks at 7.4º, 10.4º, 12.8º, 14.8º, 16.5º, 18.1º, 22.2º, 24.6º, 26.7º and 29.7º [297]. Despite ZIF-8/67 having a formation metal: linker ratio of 1:2, i.e. $Zn(mIm)_2$, Ta et al [298] found that synthesis metal: linker ratios with this value resulted in only the formation of ZnO, with no ZIF-8 peaks observed in the diffraction spectra. However, the 'minimum' ratio required for ZIF-8 crystal formation is disputed. Studies by Lim et al [299] and Zhang et al [292], carried out using the same temperature and solvent conditions, have found ZIF-8 crystals can form and grow using Zn: mIm ratios as low as 1:1. This work confirms that synthesis at a Zn: mIm ratio of 1:1 in methanol and 25˚C is sufficient to form a crystalline product.

Relative crystallinities were calculated by integrating the peak areas of the characteristic peaks at 2θ values equal to or below 18.1º and comparing to the sample with the highest peak area. Increasing the metal: linker ratio from 1:1 to 1:8 led to an increase in product crystallinity, implying a ratio higher than the final material (i.e. repeating units of 1 metal ion coordinated to 2 imidazole bridges) is required to form a fully crystalline phase. However, increasing the ratio to 1:16 led to a noticeable decrease in crystallinity. Zhang et al. [292] observed a similar trend, hypothesising this decrease to be due to excess imidazole coating the crystals during synthesis and preventing further growth. Their work also found a metal: linker ratio of 1:8 was optimal for crystallinity.

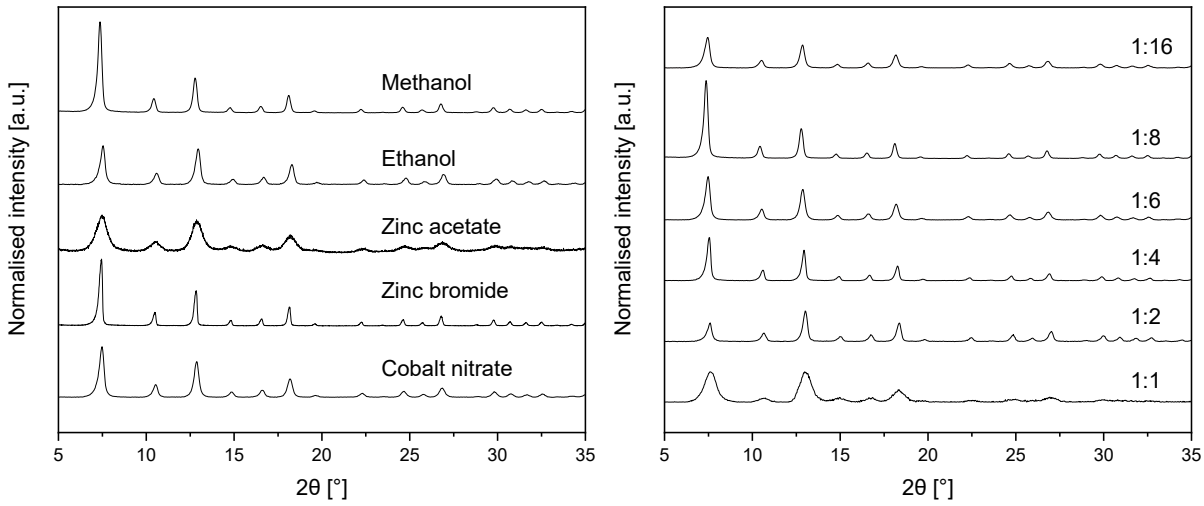


Figure 5.2: PXRD patterns for ZIFs synthesised under different salt and solvent conditions (left) and synthesised using different molar ratios of zinc nitrate and 2-methylimidazole (right).

5.3.2.3. Adsorption performance for toluene vapour

After exposing both samples to toluene vapour at a partial pressure of P/P_0 = 0.005, the samples synthesised in methanol and ethanol adsorbed 263.1 mg/g and 192.7 mg/g respectively. Zn: mIm ratios of 1:4, 1:6, and 1:8 were found to have similar capacities between 256.5 mg/g to 263.1 mg/g. These samples were found to have significantly higher capacities than those synthesised with ratios of 1:1, 1:2, and 1:16, based on 95 % confidence intervals of the samples. ZIF-8 samples synthesised using zinc acetate and zinc bromide had toluene capacities of 244.0 mg/g and 248.9 mg/g, similar to samples using zinc nitrate as a reactant. Importantly, samples with largely different relative crystallinities were found to possess similar capacities for toluene vapour, and likely similar porosities. Therefore, the crystallinity of the ZIFs cannot be directly linked to performance, insofar as the final material possesses the characteristic peaks and features of ZIF-8/67.

5.3.2.4. Summary of screening of ZIF synthesis methods

Table 5.2: Summary of yield, crystallinity, and toluene capacities for synthesised ZIF samples

Sample	Yield [%]	Relative crystallinity [%]	Toluene adsorption capacity [mg/g]
1	None recoverable	--	--
2	67 ± 3.1	N.D.	263.1 ± 3.8
3	35 ± 3.2	59.3 ± 3.8	192.7 ± 3.1
4	16 ± 1.9	10.6 ± 3.1	72.6 ± 6.2
5	34 ± 2.8	42.2 ± 4.4	120.5 ± 5.5
6	55 ± 3.6	51.2 ± 5.9	263.1 ± 4.2
7	62 ± 4.4	68.6 ± 6.7	256.5 ± 4.8
8	68 ± 4.2	100	262.7 ± 3.9
9	60 ± 3.9	58.1 ± 6.6	175.5 ± 3.6
10	28 ± 2.8	13.4 ± 4.2	244.0 ± 6.0
11	37 ± 2.2	60.9 ± 5.3	248.9 ± 4.3
12	58 ± 4.1	46.9 ± 6.1	266.8 ± 3.7

Number of repeat measurements (N) for yield, relative crystallinity and toluene capacity = 5, 5, and 2 respectively.

From measurements of yield, crystallinity, and toluene uptake, two sets of ZIF-8 samples were chosen to be analysed further, both of which used methanol as a reaction solvent: ZIF-8 with a metal: linker ratio of 1:8, using three different zinc salts (zinc nitrate, zinc acetate, and zinc bromide); and ZIF-8 using zinc nitrate as a metal source, using three different metal: linker ratios (1:4, 1:6, 1:8). Finally, ZIF-67 using cobalt nitrate as the metal source, methanol as the reaction medium, and a metal: linker ratio of 1:8 was chosen as a comparator to the ZIF-8 samples. These samples displayed the highest values for yield, crystallinity, and toluene uptake.

It is important to note that the measurement of relative crystallinity appeared to be strongly dependant on the sample preparation and even spreading of the powders onto the XRD sample holder. Repeat experiments on the same sample with different degrees of grinding, i.e. producing finer powders with a more homogenous sample height, resulted in large disparities in peak intensity and by extension relative crystallinity. Despite ZIF-8 produced using zinc nitrate and a metal: linker ratio of 1:8 consistently

having the highest relative crystallinity, it was decided that toluene uptake, probing the characteristically high porosity and surface area of the ZIF samples, was a better screening criterion for synthesis procedures. For example, ZIF-8 produced using zinc acetate adsorbed similar quantities of toluene vapour to samples produced using zinc nitrate (244 mg/g and 263 mg/g respectively) despite the former having significant noise in its XRD spectra and subsequently lower relative crystallinity.

Graphs of average values and 95 % confidence intervals for yield and toluene capacity can be found in **Figure A.13** of the Appendix. Due to the dependant nature of relative crystallinity, and its inability to describe or account for changes in capacity, confidence intervals for relative crystallinity were not included in the plot.

5.3.3. Crystallinity and yield of MIL-100 powder

The XRD pattern of MIL-100 (Fe) can be found in **Figure A.14.** in the Appendix. Compared to ZIF samples, MIL-100 showed noticeably more noise in its patterns, although characteristic peaks at 6.0˚, 6.4˚, 10.5˚, 10.6˚, 11.1˚, 11.3˚ and 20.3˚ could still be seen [222], [300], [301]. Following cleaning, centrifuging, and drying, the mass yield of MIL-100, measured relative to the iron nitrate nonahydrate, was approximately 60 ± 11.5 %. The high standard deviation was likely due to the sludge-like consistency of the MOF solution post-reaction, and difficulties in recovery of the solid into cleaning vessels.

5.3.4. Influence of ZIF-8 reaction conditions on crystal size

SEM images collected showed that all zinc nitrate-based syntheses produced clearly defined ZIF-8 crystals with sizes typically below 100 nm in diameter. Average crystal sizes were determined based on the diameters of 20 crystals. The average diameters of crystals produced using ratios of 1:4, 1:6, and 1:8 were 83.9 ± 14.2 nm, 61.6 ± 8.9 nm, and 60.1 ± 8.5 nm respectively. This reduction in crystal size with increasing linker reactant ratio confirms findings in literature [292], [298] which suggests that greater initial linker amount results in higher rates of nucleation and a resultant larger number of crystals with smaller diameters.

When analysing ZIF-8 samples using zinc acetate and zinc bromide, well-defined crystals were found with rhombic dodecahedral shape, with diameters of 512.6 ± 62.6 nm and 612.1 ± 67.7 nm respectively. Work by Schejn et al. [293] found that salt counterions that formed 'softer' bases (i.e. containing larger, relatively polarisable donor atoms) resulted in a lower density of nuclei forming and higher average crystal size. These zinc precursors, such as zinc bromide, have lower reactivity (i.e. soft Zn^{2+} acid and soft Br^- base) and result in a lower quantity of Zn^{2+} ions available to coordinate with mIm. These fewer nucleation points are therefore afforded greater quantities of linker to coordinate with each, resulting in larger crystals.

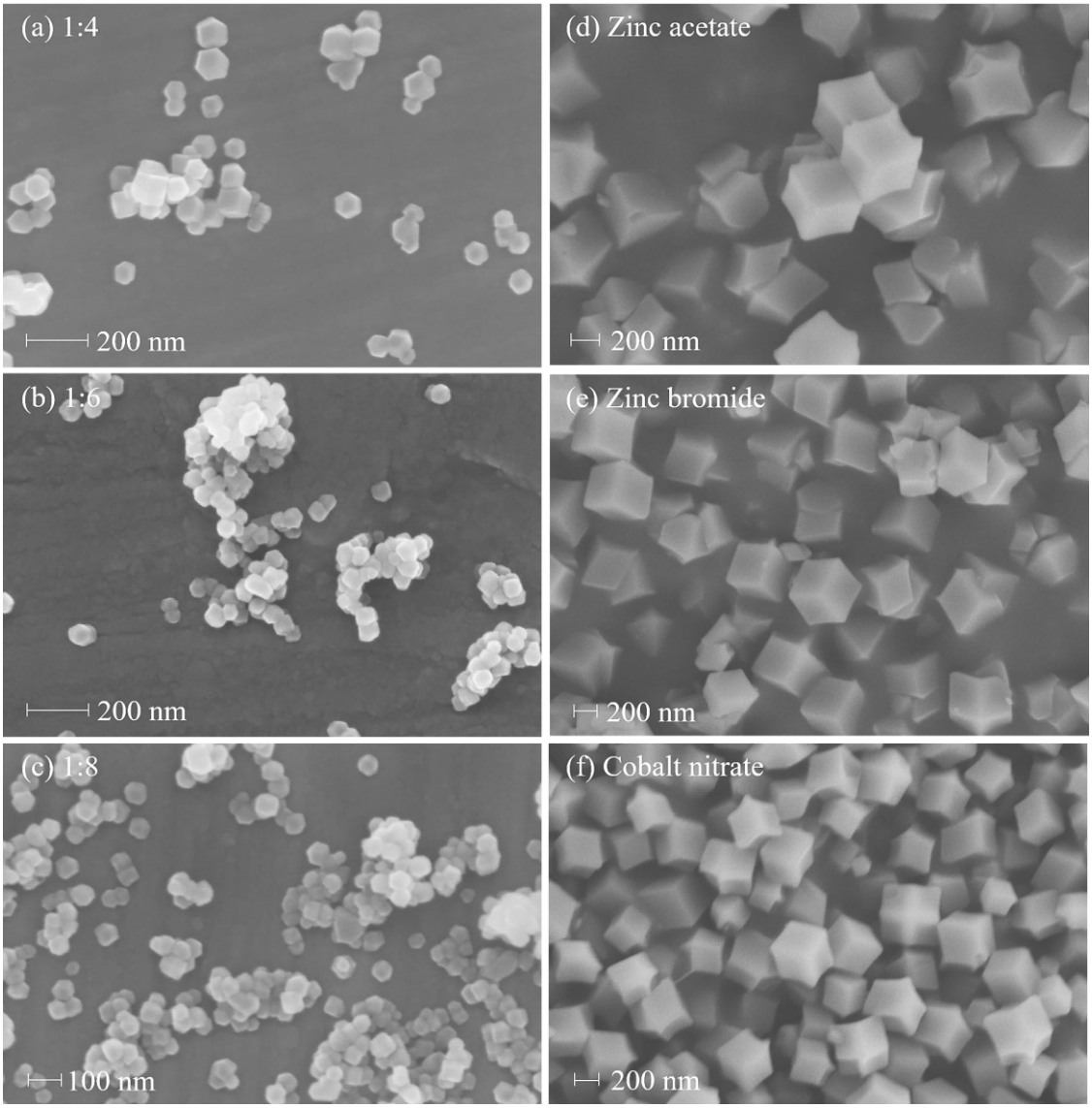


Figure 5.3: Scanning electron microscopy images collected for ZIF samples: zinc: linker ratios of 1:4 (a), 1:6 (b), 1:8 (c); zinc acetate (d) and bromide (e) salts; and ZIF-67 using cobalt nitrate (f).

ZIF-67 had a crystal size of approximately 466 ± 85 nm, matching literature values synthesised under similar conditions [153]. Substituting cobalt for zinc in ZIF-8/67 synthesis has consistently produced larger crystals [153], [302], although the exact reasoning for this size difference is often not explored. Öztürk et al [303] synthesised ZIF-8 and ZIF-67 thin films under a variety of synthesis conditions:

- Increases in linker content induced a higher nucleation rate, resulting in a larger number of smaller crystals.
- Increases in temperature were found to not affect the nucleation rate, but instead were hypothesised to help overcome the activation energy of the oligomerisation of metal-linker pairs to form frameworks. Therefore, the 'growth' of crystals was found to improve with higher temperatures, increasing particle size.
- The higher electronegativity/ reactivity of Co^{2+} compared to Zn^{2+} resulted in faster nucleation and growth according to atomic force microscopy results. Raman spectra found that the nitrogen-metal-nitrogen vibrations were shifted to higher wavenumbers in the ZIF-67 system, implying a stronger/ stiffer bond between imidazole linker molecules and cobalt compared to zinc.

These findings suggest that the higher reactivity of cobalt ions, and their stronger interactions with mIm promote both nucleation and growth processes, resulting in a high number of larger crystals. In addition, the cobalt system appears to follow similar trends to zinc, with work by Guo et al [304] finding that the use of 'softer' bases such as sulphate (SO_4^{2-}) and acetate ($CH_3O_2^-$) resulted in lower cobalt source reactivity, fewer nucleation sites, and larger final crystals. Several shapes were observed for the ZIF crystals including cubic and rhombic dodecahedron, as well as intermediate shapes, although many of the particles were aggregates of several crystals with no clearly defined shape. The same work by Schejn [293] found that systems that had larger final crystal sizes also had improved isotropy, or uniformity in shape. This mirrors the results in this work, with the zinc acetate, bromide, and cobalt nitrate ZIF adsorbents producing crystals with clearly defined edges and facets.

5.3.5. Thermal stability of ZIF-8/67 and MIL-100 adsorbents

ZIF samples with different metal: linker ratios were all found to be thermally stable to temperatures around 300˚C in nitrogen and showed negligible differences in TG profiles. Similarly, ZIF-8 synthesised using zinc nitrate, acetate, and bromide were all found to have similar thermal stabilities. Schejn et al [293] found that ZIF-8 synthesised using acetate and bromide salts had greater thermal stability than those using nitrate salts due to large differences in their crystal sizes. However, the crystals synthesised in Schejn's work were noticeably larger than those in this work, making direct comparison difficult. For clarity, only a single ZIF-8 sample was plotted in **Figure A.15** in the Appendix. ZIF-67 was found to have a thermal stability around 20˚C lower than that of ZIF-67 [305], with both samples studied losing approximately 63-64 % of their mass upon reaching 1000 ˚C, matching previous studies on the thermal decomposition of ZIF adsorbents [293], [306].

MIL-100 powder was found to have noticeable mass loss events in the temperature range of 50-120˚C, which are likely due to the evaporation and loss of trapped solvents such as water or ethanol from the cleaning process. The powder was stable in nitrogen to temperatures up to 250-300˚C, past which the acid linker begins to degrade [222]. The total mass loss of MIL-100 was estimated at ~74 % as shown in **Figure A.15**.

5.3.6. Surface area and pore volume of powder MOFs

When exposed to nitrogen, all ZIF samples produced isotherms with initially steep gradients that plateaued at low pressure, well described by IUPAC as a type I isotherm [40], followed by an upswing in uptake at higher partial pressures- indicating all samples possessed some meso/macropores with large diameters but no hierarchical micro/mesoporosity. **Figure 5.4** shows the isotherm of ZIF-8 (1:8), while the isotherms for other ZIF-8/67 samples can be found inn **Figure A.16**. A thin hysteresis loop was observed for ZIF samples in the high partial pressure region, which suggests the extent of capillary condensation, which results in large differences between capacities in the adsorption and desorption branches, is low. A small hysteresis loop was also present in the partial pressure range of $0.01 < P/P_0 < 0.03$, which has been observed to occur for N_2, Ar, CO, and O_2 adsorption by Casco et al [307]. Inelastic

neutron scattering experiments found no changes in the rotational or vibrational modes of the ZIF-8 structure when Ar and O_2 gases were introduced- these gases only exhibited two low-pressure isotherm steps: the first related to the interactions of quadrupole/ dipole moment of the adsorbate and ZIF-8; and the second in which hysteresis occurs. A third step is found in N_2 and CO systems and, due to changes in rotational modes, is ascribed to a linker swinging motion. The lack of this step for Ar and O_2 adsorption, and the lack of rotational/ vibrational mode changes, indicates that the hysteresis loop cannot be due to linker rotation, and is instead associated with unit cell expansion.

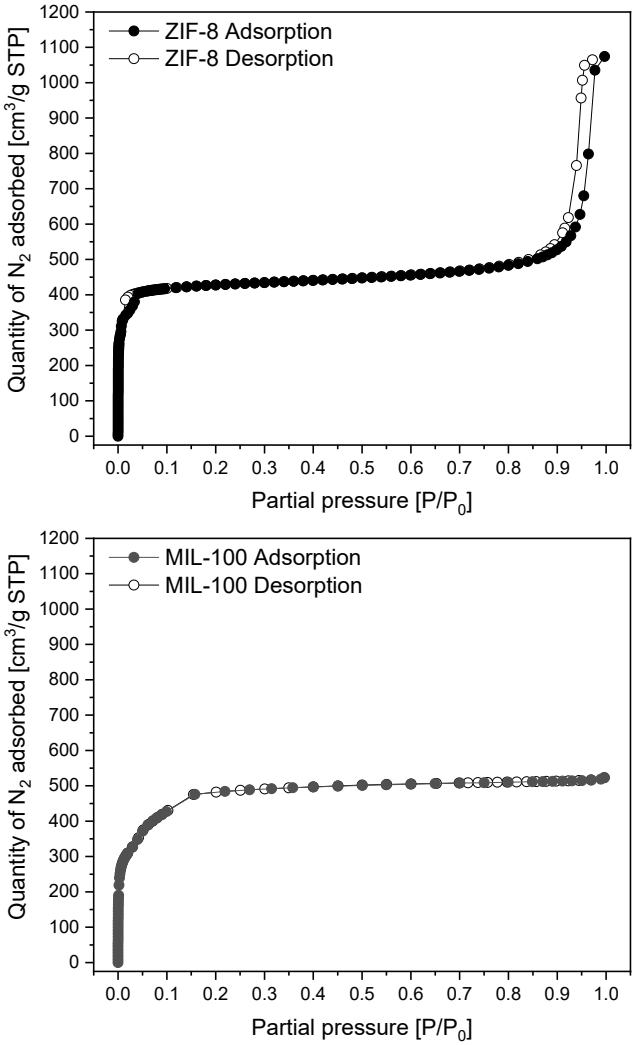


Figure 5.4: Nitrogen sorption isotherms for MOF adsorbents: ZIF-8, synthesised using a metal: linker ratio of 1:8 and zinc nitrate as the metal source (top); and MIL-100 (bottom). T = -196˚C.

The isotherm of MIL-100 appears to be type I (b), indicating a broader distribution of micropores within its structure compared to ZIF-8. MIL-100 possesses both micropores and mesopores as part of its framework, which likely accounts for the 'softer' gradient at partial pressures between ~0.005-0.15 as the mesopore cages are gradually filled by nitrogen accessing MIL-100's microporous windows. MIL-100 did not possess the noticeable upswing in capacity at high partial pressures, suggesting considerably fewer large mesopores or macroporosity compared to ZIF-8 despite similar grinding procedures. MIL-100 also possessed almost no hysteresis at any partial pressure, implying a lack of capillary condensation occurring.

Table 5.3: BET surface areas, micropore volumes, and total pore volumes of ZIF adsorbents, determined using N_2 gas adsorption data at -196ºC.

Sample	BET Surface Area [1] [m^2 g^{-1}]	Micropore Volume [2] [cm^3 g^{-1}]	Total Pore Volume [3] [cm^3 g^{-1}]
ZIF-8 (1:4)	1728 ± 24	0.579 ± 0.035	0.754 ± 0.016
ZIF-8 (1:6)	1783 ± 15	0.558 ± 0.044	0.822 ± 0.012
ZIF-8 (1:8)	1801 ± 20	0.546 ± 0.038	0.831 ± 0.016
ZIF-8 (acetate)	1755 ± 36	0.467 ± 0.081	0.740 ± 0.021
ZIF-8 (bromide)	1814 ± 21	0.495 ± 0.057	0.765 ± 0.018
ZIF-67	1753 ± 27	0.583 ± 0.029	0.838 ± 0.011
MIL-100	2007 ± 83	0.688 ± 0.035	0.810 ± 0.060 [4]

[1] Calculated using linear fit of adsorption data in pressure range of $0.02 < P/P_0 < 0.08$

[2] Calculated using t-plot analysis

[3] Total gas adsorption volume determined at partial pressure of $P/P_0 \sim 0.90$

[4] Total gas adsorption volume determined at partial pressure of $P/P_0 \sim 0.95$

All ZIF samples were shown to possess considerable BET surface areas, micropore, and total pore volumes above 1700 m^2/g, 0.40 cm^3/g, and 0.70 cm^3/g respectively. The degree of macroporosity at high partial pressures made the typical estimation of total pore volume via the Gurvitsch rule difficult [40]. For this reason, total pore volumes were estimated using a lower partial pressure of P/P_0 ~0.90. Samples synthesised using zinc nitrate and zinc bromide had similar BET surface areas to those synthesised by Schejn et al (1700 ± 30 m^2/g and 1713 ± 45 m^2/g) [293], although the same study found

samples synthesised using zinc acetate had noticeably lower surface areas (1477 ± 36 m^2/g), which was not an observation in this work. The BET surface area of ZIF-8 samples using different metal: linker ratios did not appear to be change significantly based on 95 % confidence intervals, with all values differing by no more than ~100 m^2/g (~6 % of the average). Varying the zinc salt did not appear to significantly impact the surface area or pore volume distribution of the ZIF-8 samples, with all samples having at least 60 % of their pore volume being present within micropores and surface areas around 1700-1800 m^2/g. ZIF-67 had a calculated surface area of 1753 m^2/g, only 2.7 % less than that of zinc-nitrate based ZIF-8 synthesised using the same metal: linker ratio of 1:8. ZIF-67 was found to possess a micropore volume of 0.583 cm^3/g, similar to that of ZIF-8 made using a metal: linker ratio of 1:4. Zhang et al's study on the influence of metal: linker ratio on ZIF-8 synthesis [292] found similar values for micropore volume using the t-plot method, between 0.59 and 0.62 cm^3/g for metal: linker ratios of 1:4 and 1:8 respectively. Similarly, Tsai & Langner [308] measured t-plot micropore volumes of 0.474 cm^3/g for ZIF-8 synthesised using zinc nitrate and 2-methylimidazole at a ratio of 1:8. MIL-100 exceeded all ZIF-8/67 samples in BET surface area and micropore volume. As it contained a similar total pore volume, its overall microporosity was estimated at ~85 %. However, the distribution of this micropore volume is important to consider in applications at dilute concentration levels.

5.3.6.1. Pore size distributions of powder MOFs

Based on Tarazona NLDFT calculations, all ZIF samples were found to have similar sized micropore apertures of 9 and 17 Å for the small and large pore respectively. Pore size distributions for ZIF-8 in literature have been found to vary significantly- with some disparity even for the number of pore apertures present below 2 nm. The presence of a second micropore (i.e. the large pore) could be linked to the stepped isotherm and potential hysteresis loop in the nitrogen isotherm between $0.01 < P/P_0 < 0.03$ mentioned previously. For example, work by Hadi et al [309] measured a single pore aperture in the micropore range and no low-pressure isotherm step loop, while ZIF-8 synthesised by Bose et al [310] possessed both- although the lack of description in these studies related to the method of PSD determination prevents any accurate hypothesis to be drawn. In addition, the exact size of these apertures according to nitrogen isotherms is also unclear based purely on literature- with apertures sizes

varying greatly between 5 [309] to 10 Å [311]. Most literature studies did not specify their method of determining the pore size distribution. However, in the example study by Hadi [309] the BJH method was specified which, as it is based on the methodology and assumptions of the Kelvin equation, is invalid for pore sizes < 2 nm for nitrogen, and may influence not only the size but also the number of pores predicted by the model. The method used in this study, i.e. Tarazona NLDFT assuming cylindrical pore geometry, has resulted in literature-accurate determinations of zeolite Y, ZSM-5, and molecular sieve 13X. However, the flexible nature of ZIF-8's pores may make accurate determination of the pore size distribution difficult.

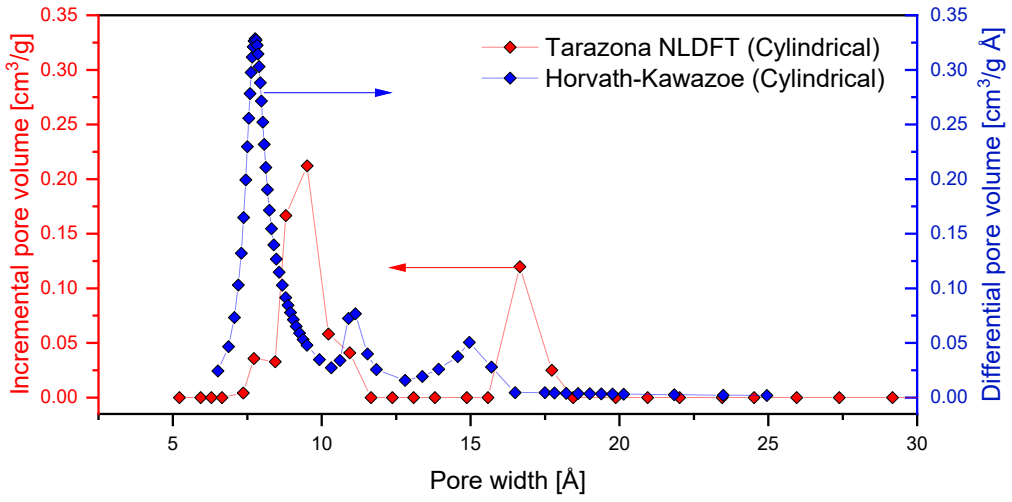


Figure 5.5: Comparison of Tarazona NLDFT and Horvath-Kawazoe models, both assuming cylindrical pore geometry, in predicting the pore size distribution of ZIF-8 synthesised using zinc nitrate and a metal: linker ratio of 1:8. Calculated using nitrogen sorption data at T = 196˚C.

As shown in **Figure 5.5**, the use of different models can have a strong impact on the calculated pore size distribution. Tarazona NLDFT and Horvath-Kawazoe [312], both commonly utilised models available in the Micromeritics isotherm analysis package [60], result in minimum micropore sizes of ~9.5 Å and ~7.8 Å respectively. Additionally, the use of the Horvath-Kawazoe method results in three apertures being predicted, while the Tarazona NLDFT method predicts two. Therefore, without clarification on the exact method of pore size distribution determination, like-for-like comparisons

between the pore sizes in this work and in the literature are difficult. Regardless of this complication, this work's findings of two pore apertures (one small, one large) below 2 nm match with literature studies on ZIF-8. In addition, when using the same PSD model, all samples were found to possess pore apertures in the range of 9-10 and 17-18 Å, indicating the synthesis procedures are successful in producing both crystalline and characteristically porous ZIF-8/67.

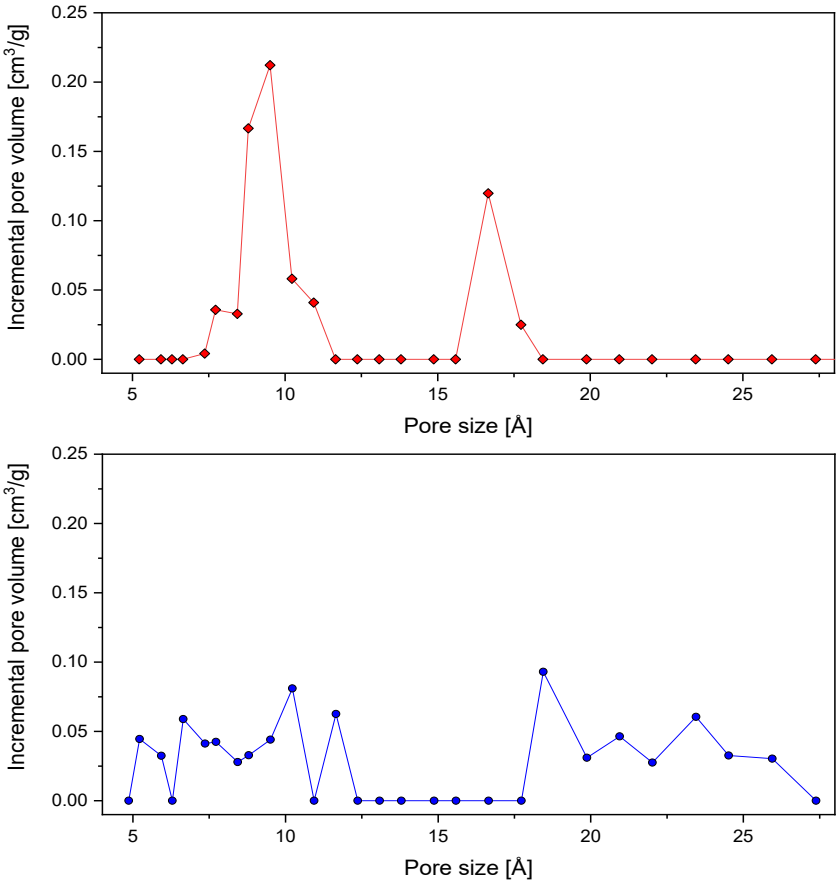


Figure 5.6: Pore size distributions of powder ZIF-8 (top) and MIL-100 (bottom), calculated using Tarazona NLDFT model assuming cylindrical pore geometry, using nitrogen sorption data at T = 196˚C.

Pore size distributions of MIL-100 powder, shown in **Figure 5.6**, exhibited two broad pore sizes in the range of 5-13 and 18-27 Å: the first distribution likely corresponds to the diameter of the pentagonal and hexagonal windows; while the second distribution corresponds to the diameters of the small and large cages in the framework [201]. Both the size of these apertures and the broadness of the pore volume distributions match literature studies on Fe-based MIL-100 [313], [314]. The significant amount

of pore volume located in large micropores/ small mesopores explains the relatively gentle nitrogen sorption slope and may reduce MIL-100's effectiveness at adsorbing species at particularly dilute concentrations, where its framework pore volume may not be completely utilised.

5.3.7. Adsorption of VOCs and water vapour by MOFs

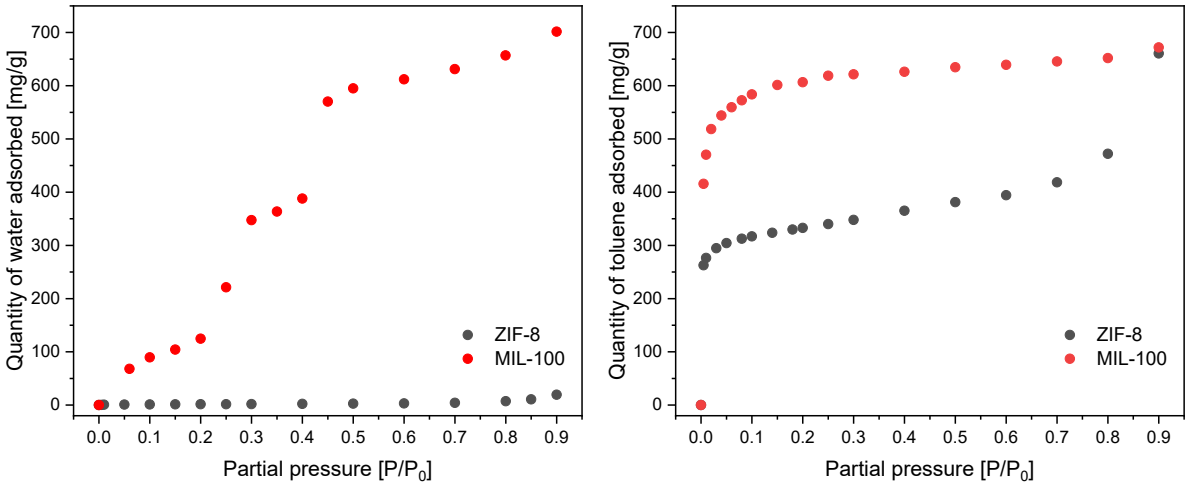


Figure 5.7: Water (left) and toluene (right) adsorption isotherms for ZIF-8 and MIL-100. T = 25˚C.

The adsorption of toluene followed a similar trend to nitrogen sorption, with all ZIFs having high capacities for the vapour at low pressures, $P/P_0 = 0.005$, of at least 240 mg/g, similar to the measured capacities of ZIF-8 for aromatics in work by Zhang et al [145]. The isotherm shape appears to be a combination of Type I, with steep initial gradient, and Type II, with an uptake in capacity at the highest pressures. All ZIF samples had almost identical isotherm shapes and capacities, as seen in **Figure A.17**. MIL-100 adsorbed significantly greater quantities of toluene compared to ZIF-8 at all partial pressures below $P/P_0 = 0.9$, at which the macroporosity of the ZIF-8 powder enabled it to adsorb similar quantities to MIL-100. However, MIL-100's toluene isotherm had a much gentler initial slope, further suggesting that its pore volume may not be fully accessible by toluene at lower concentrations. This behaviour has been credited previously to the presence of a step at low partial pressures due to the presence of two hydrophobic cages, large and small, in the MIL-100 framework [201]. These cages will fill at different partial pressures by virtue of molecules accessing the pentagonal and hexagonal windows that lead into

the larger cages, resulting in a stepped isotherm that becomes more prevalent as adsorbate polarity increases. MIL-100 powder adsorbed approximately 670 mg/g of toluene at the highest partial pressure. Previous work on MIL-100 and MIL-101 found the former was capable of adsorbing ~655 mg/g (~1.0 mL/g) of n-octane vapour at a partial pressure of 0.9 and a temperature of 40˚C, and the adsorption process also produced a type I isotherm with a similarly gentle slope.

ZIF-8 showed exceptionally low affinity for water vapour, displaying type III isotherms with maximum uptakes below 51 mg/g at 90 % RH for all samples. The maximum uptake of water vapour increased with higher total pore volume, with ZIF-8 (1:4) having the lowest capacity, and ZIFs synthesised using alternative salts and larger crystal size (cobalt nitrate, zinc acetate and zinc bromide) also appeared to have noticeably higher water uptake. MIL-100 displayed its characteristic water isotherm, with multiple steps present. These regions of the isotherm can be ascribed to three water adsorption mechanisms:

- P/P_0 = 0-0.25: Adsorption on the external surface of MIL-100, due to uncoordinated Fe ions present. This includes some clustering around the pentagonal and hexagonal micropore apertures.
- P/P_0 = 0.3-0.4: Filling of the smaller mesopore cage via pentagonal window.
- P/P_0 > 0.4-0.45: Filling of the larger mesopore cage via hexagonal window.

Similar to zeolite Y and ZIF-8, the hydrophobic apertures of MIL-100 require a certain driving force of water vapour in order to overcome the electrostatic barrier and induce pore filling. Despite the smaller pores likely having a stronger repulsion effect, as observed previously by ZIF-8's micropores being filled by methanol at a higher partial pressure than zeolite Y, simulation studies by Mileo et al [315] contend that the most confined environment corresponds to the preferential region for the water to adsorb onto/ into. This hypothesis is consistent with the Kelvin equation which asserts that larger pores require greater driving forces to be filled than smaller pores.

ZIF-8/67 were also found to produce a type V isotherm when exposed to methanol vapour, with micropore filling occurring at partial pressures exceeding P/P_0 = 0.1, as seen in **Figure A.18**. This isotherm inflection point was the same for all studied ZIFs, implying that the synthesis procedure did

not impact the hydrophobicity of the aperture itself and the hydrophobic framework of ZIF-8/67 was present in all cases. This phenomenon is similar to the 'gatekeeping' effect of zeolite Y in Chapter 4, which required a partial pressure of 0.08 P/P_0 before methanol began to fill the micropores of its framework. This indicates a similar, perhaps slightly stronger, hydrophobic aperture effect in ZIF-8/67 compared to high-silica zeolite Y.

5.3.7.1. Hydrophobicity indexes of MOF adsorbents

ZIF-8 was found to have significantly greater hydrophobicity indexes than industrial adsorbents at all relative humidity values studied, emphasising its hyperhydrophobicity and lack of affinity towards polar molecules. On the other hand, the high porosity of MIL-100 and its high capacity for water vapour at low pressures, due to uncoordinated Fe ion defects, displayed much lower H.I.s than ZIF-8, zeolite Y, and activated charcoal. for example, at an RH of 50 %, the order of H.I.s follows the trend ZIF-8 (15.17) > zeolite Y (0.79) > powder activated charcoal (0.56) > MIL-100 (0.14).

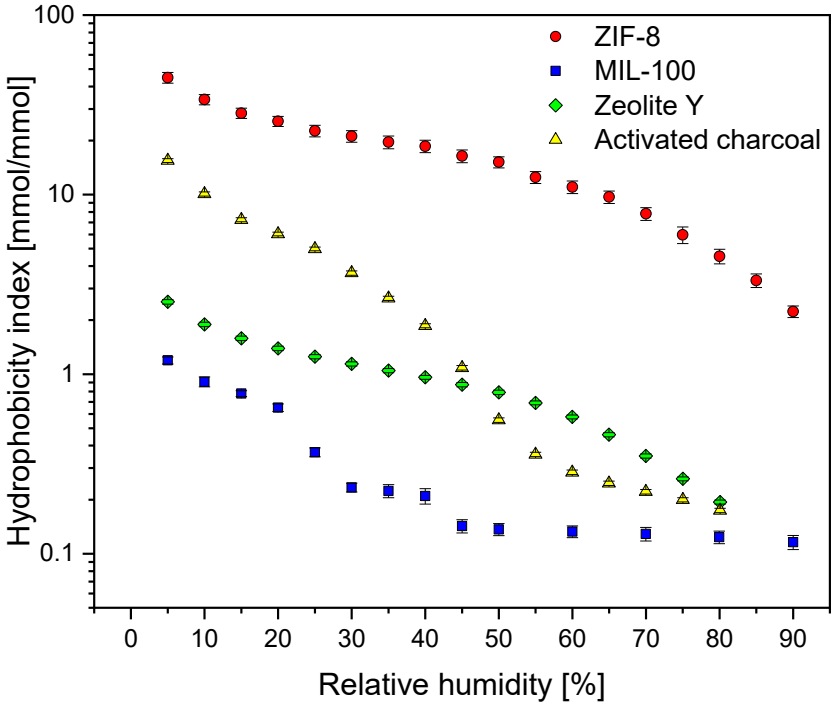


Figure 5.8: Molar hydrophobicity indexes (H.I.s) calculated as a function of RH for ZIF-8, synthesised using zinc nitrate and a metal: linker ratio of 1:8, and MIL-100. Plots for zeolite Y and activated charcoal shown for comparison. $(P/P_0)_{toluene}$ = 0.005, T = 25˚C.

5.3.7.2. Influence of VOC diameter and crystal size on ZIF-8 adsorption kinetics

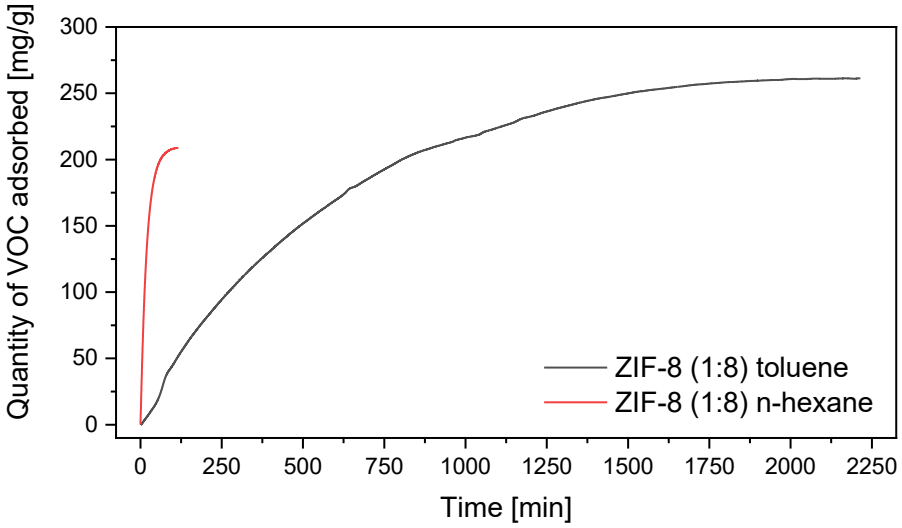


Figure 5.9: Adsorption kinetics curves for toluene and n-hexane vapour on ZIF-8 (1:8). Partial pressure of vapour in all experiments is $P/P_0 = 0.005$. T = 25˚C.

Despite exhibiting lower capacity, as seen in **Figure A.17**, the adsorption of n-hexane was found to occur significantly faster than for toluene. As shown in **Figure 5.9**, the kinetics curve for n-hexane was noticeably steeper than that of toluene with ZIF-8 and led to equilibrium being reached approximately 1900 minutes (1.3 days) sooner. Ueda et al [151] found that bulkier xylene isomers had significantly greater diffusion activation energies, calculated using the Arrhenius relationship for multi-temperature diffusivities, than both benzene and toluene molecules. However, there was also a large disparity in the activation energies for different xylene isomers, despite almost identical van der Waals radii- which was credited to the shape selectivity of the ZIF-8 framework and that maximum molecular diameter was a better representative scale to compare. Diffusion experiments by Zhang [145] found that the corrected diffusivity of ZIF-8 for n-hexane was almost 2 orders of magnitude greater than that of the smallest aromatic compound, benzene. In addition, the diffusion activation energies for VOC molecules were found to increase almost linearly with the kinetic diameter of those molecules. It is likely that, while flexible enough to accommodate large molecules, the limiting aperture size of ZIF-8 reduces their diffusion into the framework cages due to linker motion being required, with the extent of motion

increasing with the molecule's kinetic diameter. Comparisons for the kinetic rate parameters for VOC adsorption by ZIF-8 and MIL-100 powders will be carried out later in this Chapter.

5.3.8. Impact of humidity on toluene adsorption by ZIF-8/67 and MIL-100

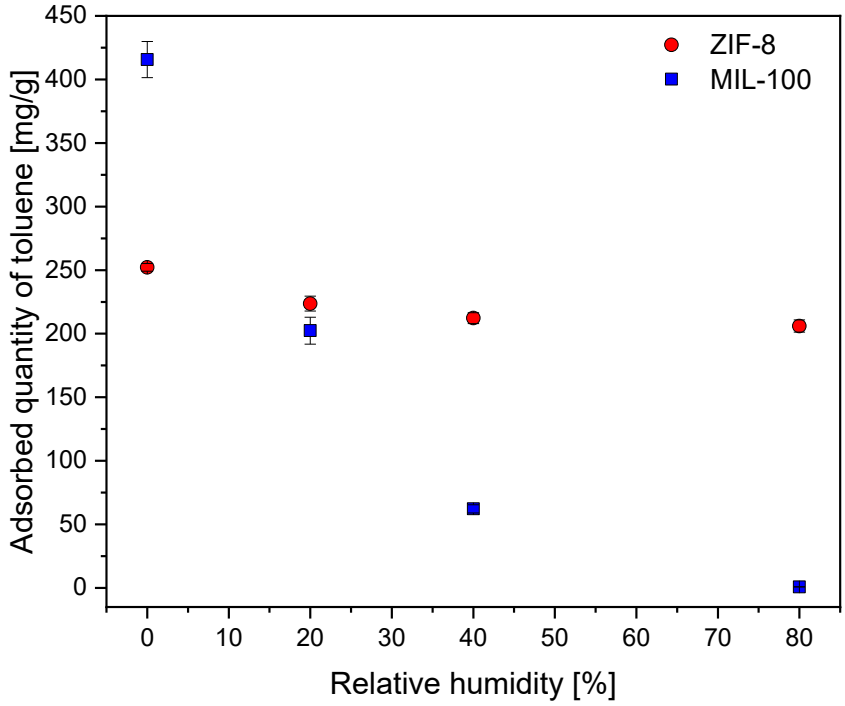


Figure 5.10: Toluene adsorption capacities for ZIF-8 and MIL-100 as a function of pre-exposure relative humidity. $P/P_{0,\ toluene}$ = 0.005, T = 25˚C.

Similar to zeolite Y in Chapter 4, ZIF-8 adsorbed high quantities of toluene vapour at all RH values, at least 80 % that of dry conditions. On the other hand, the capacity of MIL-100 for toluene depends strongly on the level of humidity it is pre-exposed to- all levels were noted to decrease the capacity of the adsorbents compared to the previous level, and no plateau effect was observed to occur, a notable feature of both hydrophobic adsorbents like zeolite Y in Chapter 4 and ZIF-8. It is possible that each RH corresponds to a different mechanism of adsorption occurring and the following rationale can be proposed [316]:

- 20 % RH: As observed in **Figure 5.7**, water primarily adsorbs onto the surface of MIL-100 while not accessing either its small or large micropore windows (i.e. to fill its small and large

mesopores), which have hydrophobic chemistry, based on the first plateau of MIL-100's water isotherm. This results in restricting the number of adsorption sites for toluene on the surface but not inside the pores. This led to an approximately 30 % reduction in capacity, which may reflect the number of shared adsorption sites between water and toluene at their respective partial pressures. At this level, MIL-100 adsorbs similar quantities of toluene to ZIF-8 under the same conditions.

- 40 % RH: At this point, filling of MIL-100's small mesopore has occurred via overcoming the electrostatic barrier of the smaller pentagonal micropore window, but the larger aperture still does not contain any water vapour. This is reflected by a significant drop in capacity of around 85 %. However, sites are likely still available for toluene molecules within this larger pore.
- 80 % RH: At this point, all sites within MIL-100 have been saturated with water vapour, as noted by the final plateau region in **Figure 5.7** and **Figure 5.10**. This explains the negligible quantity of toluene adsorbed following this level of pre-exposure.

These findings further emphasise the importance of evaluating the hydrophobicity of adsorbents at multiple levels of relative humidity, and not presenting 'hydrophobicity' as a material property. In addition, the process of pore filling by water vapour appears to have a significant impact on the performance of adsorbents, supported by both MIL-100 in this Chapter, and molecular sieve 13X in Chapter 4.

5.4. Conclusions

In this Chapter the synthesis of ZIF-8, ZIF-67, and MIL-100 adsorbents was carried out. All recoverable samples were found to possess their characteristic diffraction peaks based on theoretical and literature patterns. However, the screening metric of relative crystallinity was found to be insufficient to discern between high- and low-porosity ZIF samples, likely due to a diffraction pattern's intensity being dependent on sample preparation and particle size.

Nitrogen sorption confirmed the significant surface area (>1700 m^2/g) and microporosity (>0.4 cm^3/g) of all ZIF samples synthesised using a metal: linker ratio between 1:4 and 1:8, regardless of the metal

source. All synthesised MOFs were found to have superior textural properties, with the exception of total pore volume, compared to industrial adsorbents. NLDFT methods confirmed the presence of two micropore apertures in ZIF-8 around 9 and 17 Å, while MIL-100 possessed broad pore volume distributions at 5-13 and 18-27 Å that were ascribed to its microporous windows, and the mesoporous cages they lead into respectively- both MOFs had similar distributions to literature studies.

MIL-100's broader pore size distribution resulted in a much gentler nitrogen isotherm slope for nitrogen and toluene. However, due to its higher surface area and microporosity, MIL-100 adsorbed approximately 65 % more toluene than ZIF-8 at a partial pressure of 0.005. MIL-100's distinct pore structure also produced a characteristic stepped isotherm when exposed to water vapour, with regions corresponding to surface, small mesopore, and large mesopore filling. On the other hand, ZIF-8 and ZIF-67 were both found to adsorb negligible quantities of water vapour (< 60 mg/g) even at RH levels of 90 %. This resulted in ZIF adsorbents having hydrophobicity indexes far exceeding those of MIL-100 or industrial adsorbents and possessing a type V isotherm similar to zeolite Y when exposed to alcohol vapours, confirming the electrostatic repulsion effect of its micropore aperture.

Humid toluene adsorption experiments found that ZIF adsorbents largely followed the same trends as zeolite Y, likely due to their exceptionally hydrophobic pore apertures providing sites for toluene to adsorb, with ZIF-8's performance not dropping below 80 % compared to dry conditions. MIL-100's performance varied drastically based on the mechanism of adsorption- water adsorbing on the external surface, in the small mesopore, and in the large mesopore resulted in toluene capacities being reduced by 30, 85, and 100 % compared to dry conditions. This confirms that the mechanism of water adsorption can lead to significant changes in the selectivity of a porous for non-polar species, and may have an influence on the mechanism of competition. This also reaffirms that hydrophobicity should not be considered a purely material property, and that materials possessing hydrophobic pore apertures can still possess high capacities for water vapour if sufficient driving force is met.

Chapter 6. Modulator-based synthesis of high-density monolithic MOF adsorbents

6.1. Introduction

As discussed in **Section 2.5.3**, structured or monolithic adsorbents have several advantages over their powder equivalents, including greater mechanical stability, reduced pressure drop, and higher density [156]. However, the most common methods for producing these monoliths are post-synthetic, requiring the synthesis of a powdered adsorbent before carrying out some form of modification, whether that be through compaction or combination with binders- both of which can significantly reduce the final porosity of the material. Synthetic pathways to 'pure' monoliths, containing only the active adsorbent component, are highly sought after, especially if these can be carried out using a single reaction step. The synthesis of metal-organic frameworks via sol-gel methods has gained traction in recent years, due to their ease of production, the ability to introduce new pore size regimes into the material [317], and their subsequent processing into monoliths [318]. The gelation mechanism of MOFs typically involves three steps [319]: metal-ligand coordination to form MOF chains; the aggregation of these MOF chains, forming MOF particles; aggregation of these MOF particles to construct hierarchical structures supported partially by the solvent molecules. Extensive crystallisation or precipitation events could affect the formation of these hierarchical structures, and several methods have been explored to suppress crystallisation and promote gelation. Including the addition of competing metal centres [319], acids [234], and changes in the reaction conditions [320]. Gels of ZIF-8 have been prepared through the use of modulating ligands [221] in order to investigate the effect of modulating linkers on crystal size, but the use of these gels for monolith production has not been investigated.

The initial interest in monolithic MOFs in this work began when n-butylamine was investigated for its effect on crystal size [221]. It was noted that the addition of n-butylamine resulted in the crystallisation reaction occurring much faster, within less than an hour, and the final product was a sol-gel rather than a settled powder. One of these sol-gels was left to dry at room temperature over a weekend and was discovered to have formed large, glassy particles. From this serendipitous observation, the formation of monoliths using various modulating ligands was systematically investigated, as well as the physical, chemical, and adsorption properties of the final products. While powdered ZIF-8 was found to have

high adsorption capacity and hydrophobicity as noted in the previous Chapter, the particulate state of the material makes it difficult for applications where fixed-bed adsorption is the mechanism of pollutant removal, such as filtration systems. Monolithic materials, with their improved density and higher particle size, can be utilised and recovered much more easily than fine powders, making them of particular industrial interest.

In this Chapter the synthesis of ZIF-8 and ZIF-67 monoliths was investigated through the addition of modulating ligands n-butylamine, 1-methylimidazole, or a combination of the two. In addition, expansion of this method to the synthesis of monolithic MIL-100 was tested. The effect of modulators and monolith formation on crystallinity and crystal structure was investigated via X-ray diffraction and scanning electron microscopy. The final porosity and surface area of samples was measuring using low-temperature nitrogen adsorption and expressed in terms of the volume of the sample by carrying out bulk density measurements using dry flow medium compression. The use of bulk density and subsequently volume-relative properties and performance of each material helped to better contextualise the findings within filtration applications, as the amount of adsorption per unit volume of a filter is likely a more important operating parameter than the total mass. Surface and adsorption hydrophobicity were measured using water contact angle and vapour measurements, and the adsorption of volatile species with and without the presence of humidity was investigated using dynamic vapour sorption experiments. Finally, due to the ability to introduce particles and reagents into the MOF's sol-gel post-synthesis, modifications to the hydrophobicity of MIL-100 were carried out via the addition of alkyl phosphonic acids, based on a procedure by Sun et al [220]. Modified forms of UiO-66 were found to have largely unchanged porosity but increased the material's water contact angle from hydrophilic (19˚) to hydrophobic (160˚) levels. This Chapter will expand upon that study by investigating the impact on water vapour adsorption, and whether the pore-filling by water vapour can be shifted to higher partial pressures or removed entirely- both of which could have significant impacts on its selectivity in VOC adsorption.

6.2. Experimental methods

Synthesis procedures for powder and monolithic MOFs can be found in **Section 3.1.2**.

6.2.1. Hydrophobic modification of MIL-100

To improve the hydrophobicity of MIL-100 as an adsorbent, alkyl phosphonic acids were used to alter the surface chemistry of the final material. The powders were modified based on a procedure by Sun et al [220] used for UiO-66- 500 mg of MIL-100 powder was immersed in 500 mL of ethanol solution containing either 836 mg of octadecylphosphonic acid (OPA) or 556 mg of decylphosphonic acid (DPA), equivalent to ~5 mM concentration of acid. The solution was stirred at room temperature for 24 hours, with the final solid being washed with ethanol three times to remove excess acid and dried at 150 mbar at room temperature for 24 hours followed by 120˚C for a further 24 hours. For the monolithic MIL-100, 50 mL of the 5 mM acid solutions in ethanol were added to 50 mL of ethanol containing 50 mg of monolith in slurry form, after cleaning and centrifuging with ethanol three times. This amount was determined using the dry product yields for the unmodified monolith for a single centrifugation tube, followed by portioning off a fraction of the sol-gel solution into a separate vessel to achieve a similar ratio of MOF to acid between powder and monolith. The final solution containing both sol-gel and acid was stirred continuously for 24 hours at room temperature. The mixture was then centrifuged and cleaned using water, with the final wet gel allowed to dry under the same conditions as the unmodified MIL-100 monoliths. The loading of acids post-modification was determined by weighing dried unmodified and modified forms of the powder/ monolith that contained the same initial quantity of MOF, i.e. the same starting mass of sol-gel solution in the case of monoliths.

6.3. Results and discussion

6.3.1. Synthesis of monolithic MOFs

6.3.1.1. Monolithic ZIF-8 and ZIF-67

Upon combining the metal and linker/modulator solutions, the latter containing n-butylamine, the mixture immediately became cloudy with white or purple-pink colouration, for ZIF-8 and ZIF-67 syntheses respectively, significantly faster than the synthesis of powder ZIFs. As shown in **Figure 6.1**,

the sol-gel had formed into a separate layer from the methanol in the span of around 30 minutes, compared to the powder which took several hours.

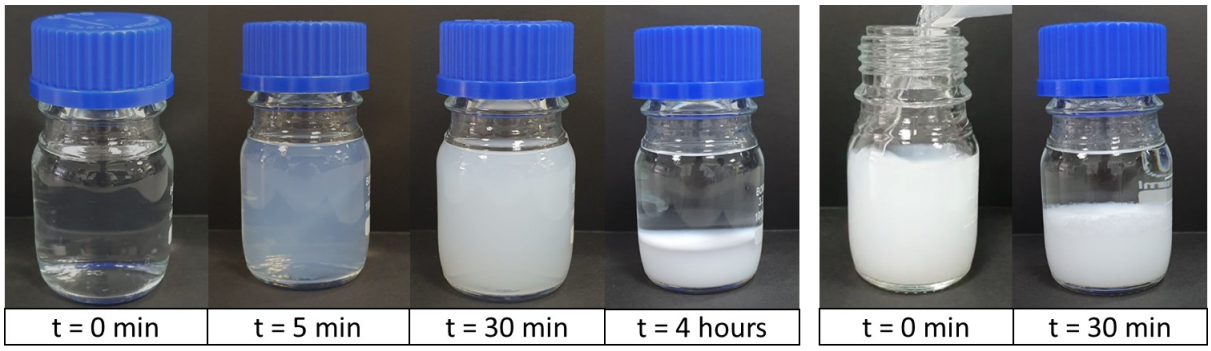


Figure 6.1: State of ZIF-8 synthesis at different time periods without (left) and with (right) addition of n-butylamine. All reactions carried out in a fume hood at room temperature.

Whether or not monoliths formed depended strongly on the quantity of modulator(s) in the reaction mixture, and the modulator(s) used. In the case of n-butylamine, modulator contents lower than 20 mmol produced what appeared to be 'packed powders' which quickly broke upon any application of pressure. The monoliths that did form had a glassy appearance and diameters in the range of a few millimetres, with either clear or purple colouration for ZIF-8 and ZIF-67 respectively. These monoliths were denoted ZIF-8 (NB-1:x) and ZIF-67 (NB-1:x) where x is the mmol of n-butylamine in the synthesis mixture for every mmol of 2-methylimidazole, either 1 or 2. Reactions using a 1:1 mixture of modulators resulted in monoliths with similar size and appearance to those using only butylamine and were denoted as ZIF-8 (ML) and ZIF-67 (ML). Reactions using solely 1-methylimidazole as a modulator produced significantly lower quantities of precipitate, with mixtures using 1-methylimidazole amounts greater than 10 mmol producing no observable quantity of precipitate. The samples that did produce precipitate did not form monoliths upon drying and instead produced fine powders, labelled ZIF-8 (1M-0.5) and ZIF-67 (1M-0.5). All monoliths possessed some degree of hardness and required significant mechanical effort to grind for characterisation techniques.

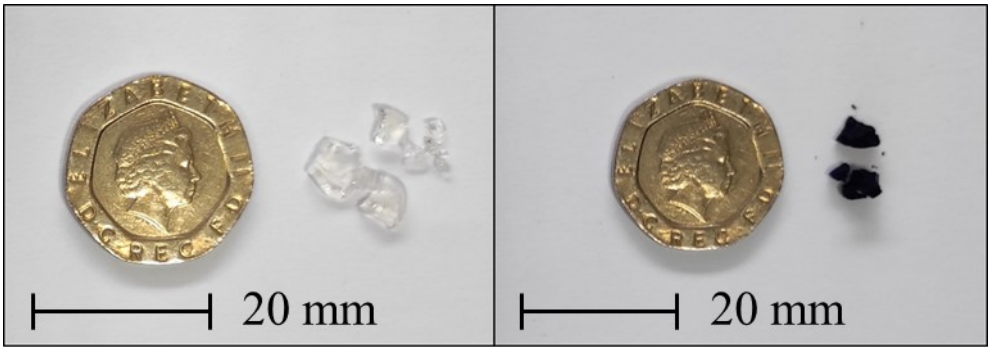


Figure 6.2: Photographs of ZIF-8 (NB-1) (left) and ZIF-67 (NB-1) (right) monoliths. British 20 pence coin shown for scale.

6.3.1.2. Monolithic MIL-100

The choice of final cleaning solvent had a significant impact on the formation of MIL-100 (NB), with only water forming monolithic products. The higher vapour pressure of ethanol and methanol when compared to water resulted in much faster drying rates than when water was used.

The selection of optimal drying conditions for monolith production from sol-gels is essential. Literature studies have found that slow evaporation of the solvent enables the densification of primary particles, as well as continued particle interactions during the drying process, improving porosity and density of the final product [317]. On the other hand, elevated drying rates may lead to the destruction of the gel's macrostructure and result in a powdered MOF producs, as the MOF particles' mobility is significantly slower than the replacement of solvent with air [317], [320]. Using water as the final cleaning solvent appeared to produce monoliths with sizes between 5-20 mm displaying significant hardness and resistance to grinding via mortar and pestle, although the drying process took between 7-10 days to complete. The acid modified MIL-100 powders appeared to have darker orange/ brown colouration, becoming more noticeable in the OPA sample compared to DPA. MIL-100 (NB)/ DPA and MIL-100 (NB)/ OPA both formed monolithic solids in the same time period as MIL-100 (NB) and did not have any discernible changes in colour or hardness compared to the unmodified monolith.

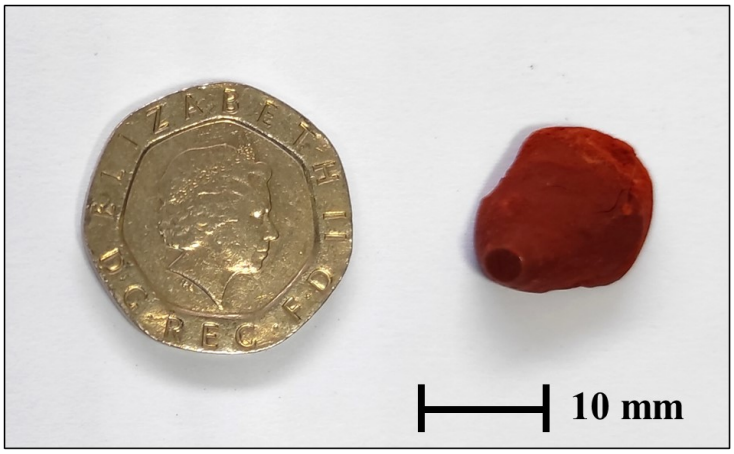


Figure 6.3: Photograph of MIL-100 (NB) monolith. British 20 pence coin shown for scale.

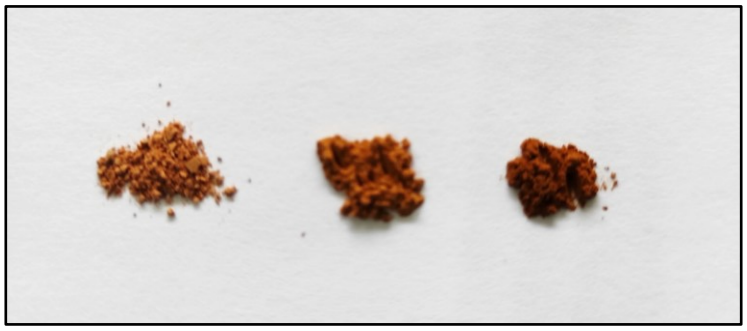


Figure 6.4: Photograph of MIL-100 powders: unmodified (left); DPA-modified (middle); and OPA-modified (right).

6.3.1.3. Loading of acids on powder and monolithic MIL-100

Based on dry masses of unmodified and modified forms of MIL-100, the loadings of DPA and OPA in the powder MIL-100 were 2.4 ± 0.3 % and 2.2 ± 0.2 % respectively, while the loading of DPA and OPA in the monolithic MIL-100 were 7.5 ± 1.3 % and 9.9 ± 1.7 % respectively. Clearly, the introduction of the acid molecules into the sol-gel of MIL-100 (NB) increases the loading of the acid molecules, possibly due to the acids being trapped within the gel's macrostructure as it dries to form the final monolith, while they may only interact with the external surface of the MIL-100 powder particles.

6.3.2. Impact of monolith formation on crystallinity

Powder samples of ZIF-8 and ZIF-67 were found to have high crystallinity, matching well with literature reference patterns [153] displaying characteristic peaks at 2θ = 7.4˚, 10.4˚, 12.8˚, 14.8˚, 16.6˚

and 18.1˚. The zinc and cobalt ZIFs formed using the modulator 1-methylimidazole displayed reduced crystallinity, 39 % and 50 % respectively, although all characteristic peaks were present. The presence of noise and the peak broadening within the diffraction patterns of the modulated synthesis samples is likely due to the presence of amorphous content [321], with all relative crystallinities for monoliths below 33 %. Doubling the ratio of n-butylamine modulator in the reaction mixture reduced the relative crystallinity of zinc- and cobalt- based monoliths by 6 % and 9 % respectively. ZIF-8 (ML) was found to be almost entirely amorphous, with peaks only observable at 2θ = 12.8˚ and 18.1˚ resulting in a relative crystallinity of < 1%.

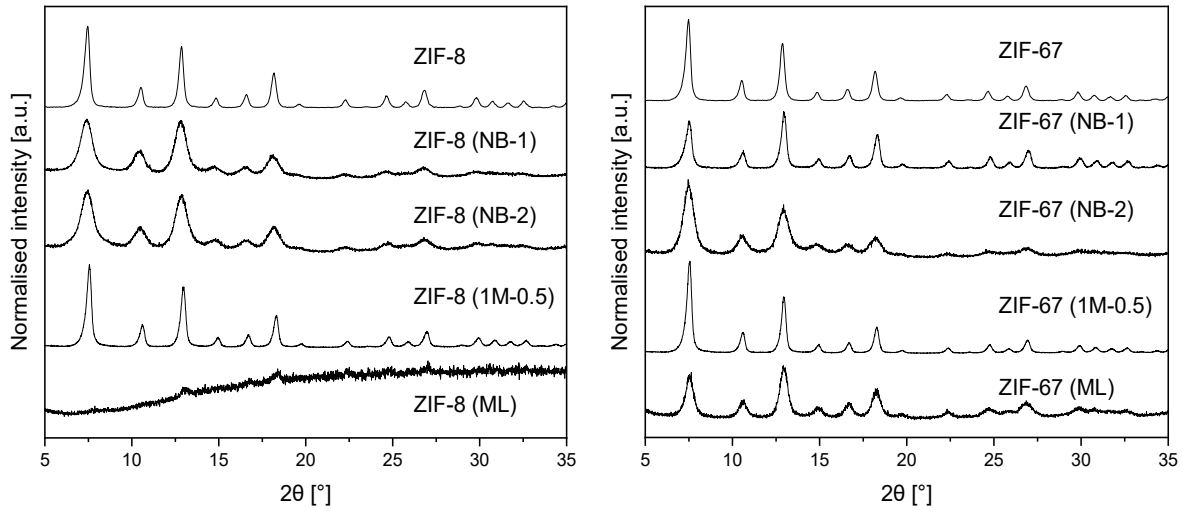


Figure 6.5: PXRD patterns for zinc- (left) and cobalt- (right) based ZIFs synthesised using different types and amounts of modulating ligands.

This highly amorphous product may be due to extensive monodentate linkages formed between zinc and cobalt ions and the modulating ligands of *n*-butylamine and 1-methylimidazole [299]. Previous studies on ZIF-8 modulation by *n*-butylamine and 1-methylimidazole separately found distinct crystals could be formed [221], albeit with a reduced size. The results in this work suggest a mixture of these ligands produces unfavourable conditions for ZIF-8 crystal growth, enough to inhibit formation of a fully crystalline phase. On the other hand, ZIF-67 still appears to be able to form products with some degree of crystallinity even with multiple modulating ligands present.

The addition of n-butylamine to form monolithic MIL-100 led to significant noise in the PXRD patterns of the sample, likely due to an increased amorphous content, although both contained several of the characteristic diffraction peaks of MIL-100 [222]. This effect is similar to that of ZIF monoliths, where the presence of monodentate linkages between Fe and n-butylamine may produce a non-crystalline solid phase.

6.3.2.1. Impact of acid modification on crystallinity

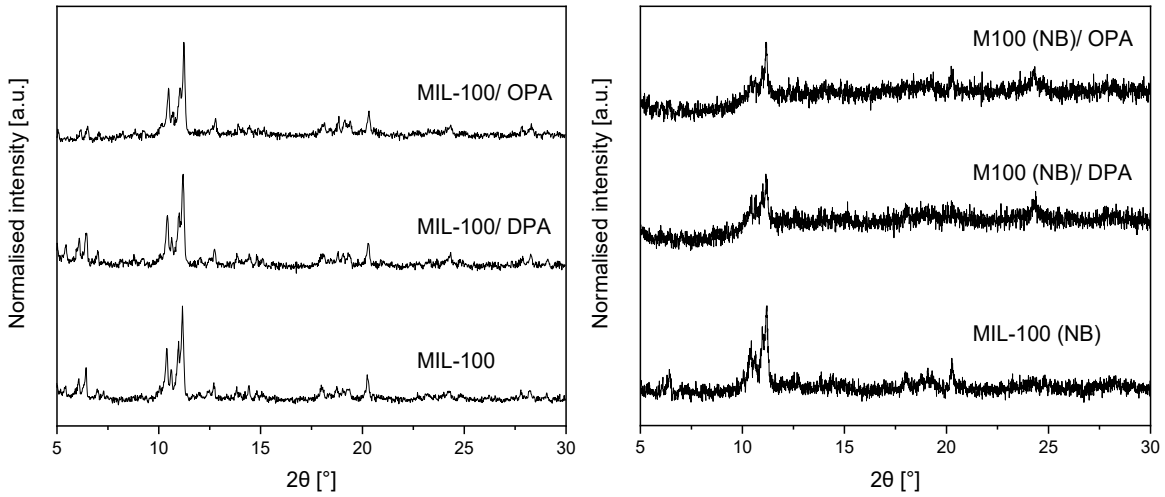


Figure 6.6: PXRD patterns for unmodified and acid-modified MIL-100 powders (left) and monoliths (right) formed using n-butylamine as a modulating ligand.

The patterns for powder MIL-100 did not appear to change significantly with the addition of DPA, although the intensity of some low angle peaks did decrease for the sample containing OPA. A similar effect has been seen in MOF-5, with samples dried at higher temperatures having higher intensities of low angle peaks due to the removal of solvent molecules within the pores [322]. The presence of larger OPA molecules trapped within MIL-100's pores may therefore result in reductions in peak intensity, particularly at lower angles. In the case of MIL-100 monoliths, the addition of DPA and OPA led to obscuring of the low angle peaks. This may indicate that the acid molecules interact more strongly with the monolith than the powder, or that a greater proportion of acid is trapped within the monolith structure- which is supported by the mass loadings calculated. However, due to the significant amount

of noise in monolithic samples from the increased amorphous content, it is difficult to accurately assess the impact of acid modification on MIL-100 crystallinity.

6.3.3. FTIR of monolithic MOFs

No distinct differences between the FTIR spectra of powder and monolithic ZIF-8 or ZIF-67 were observed. The peaks around 1580 cm^{-1} and the collection of peaks between 1375-1500 cm^{-1} are associated with the C=N and ring stretching modes of the imidazole unit respectively. Peaks in the region of 900-1375 cm^{-1} and below 800 cm^{-1} can be assigned to the in- and out- of plane bending of the imidazole ring [323]. Spectra for ZIF samples can be found in **Figure A.20** in the Appendix.

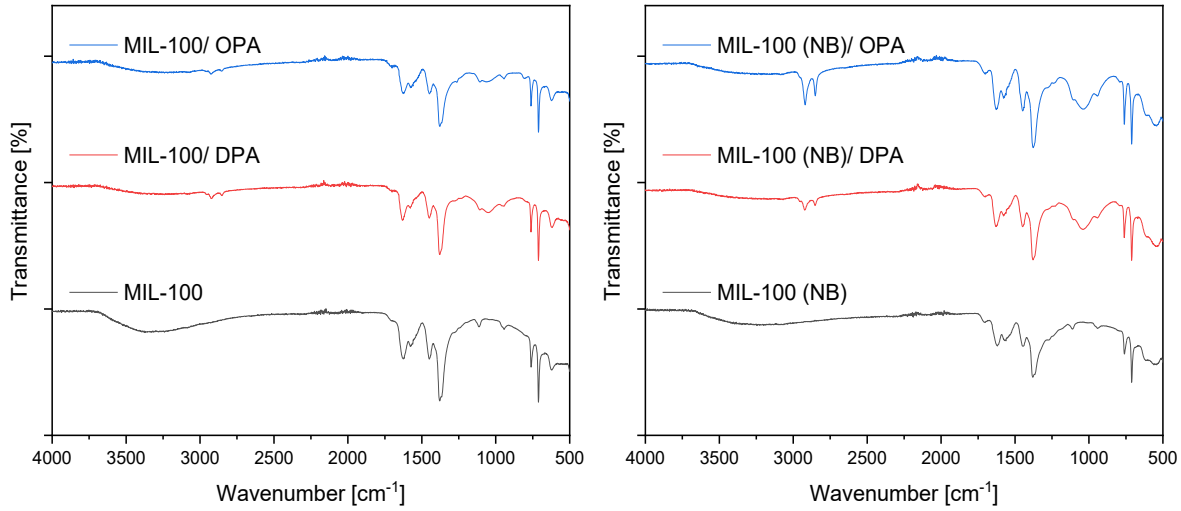


Figure 6.7: FTIR spectra for powder (left) and monolithic (right) MIL-100 samples

Monolithic and powder MIL-100 had similar FTIR spectra. The presence of DPA and OPA could be seen in the spectra for modified samples- noticeable peaks at wavenumbers 2920 cm^{-1} and 2850 cm^{-1} can be assigned to symmetric C-H stretching vibrations of $-CH_2$ groups, whilst 2960 cm^{-1} shoulder can be assigned to the asymmetric stretching of the terminal $-CH_2$ group. The additional broad peak around ~1050 cm^{-1} likely corresponds to the phosphate-oxygen stretching vibrations. These peaks were found to have much lower transmittance values for powder MIL-100 compared to MIL-100 monoliths- this

may be due to better attachment of the acids to the monolith constituent particles, or trapped DPA and OPA molecules within the monoliths macrostructure as they were added prior to drying.

6.3.4. Thermogravimetric analysis of monolithic MOFs

The thermogravimetry profiles of these materials can be found in **Figure A.21** in the Appendix. ZIF-8 and ZIF-8 (NB-1) were found to be thermally stable up to temperatures of 350-400ºC and lost approximately 64-65% of their mass once reaching equilibrium at 1000ºC. ZIF-8 (ML)'s lack of crystallinity and amorphous structure conferred it approximately 200ºC of additional thermal stability compared to ZIF-8, with mass loss events at 600, 800, and 1000ºC. ZIF-67 and ZIF-67 (NB-1) also appeared to be stable up to approximately 350-400ºC, although the latter was found to have a much steeper drop in mass. ZIF-67 (ML) exhibited a mass loss of 17% below 200ºC, which is hypothesised to be due to loss of trapped unreacted 1-methylimidazole. The lack of noticeable mass loss for this temperature range in ZIF-67 (NB) implies that residual *n*-butylamine is insufficient to contribute to the mass loss of the studied monolithic ZIF-67 samples. The final mass loss of ZIF-67, ZIF-67 (NB-1) and ZIF-67 (ML) was found to be 64, 66, and 69% respectively at 1000ºC.

MIL-100 powders were found to have noticeable mass loss events in the temperature range of 50-120˚C, which are likely due to the evaporation and loss of trapped solvents such as water or ethanol from the cleaning process. Despite the supposed hydrophobic modification of the MIL-100 by the alkyl acids, similar quantities of solvent were removed. All powder samples were found to be stable in nitrogen to temperatures up to 250-300˚C, past which the BTC linker begins to degrade [222], although the acid-modified samples did appear to have a less steep loss in mass post-500˚C which may be due to contributions from the vaporisation of the decyl- and octadecyl-phosphonic acids, or possible strong interactions between the acid molecules and iron centres [220], as previous studies have shown that alkyl phosphonic acids are capable of displacing carboxylate linker molecules in MOFs [324].

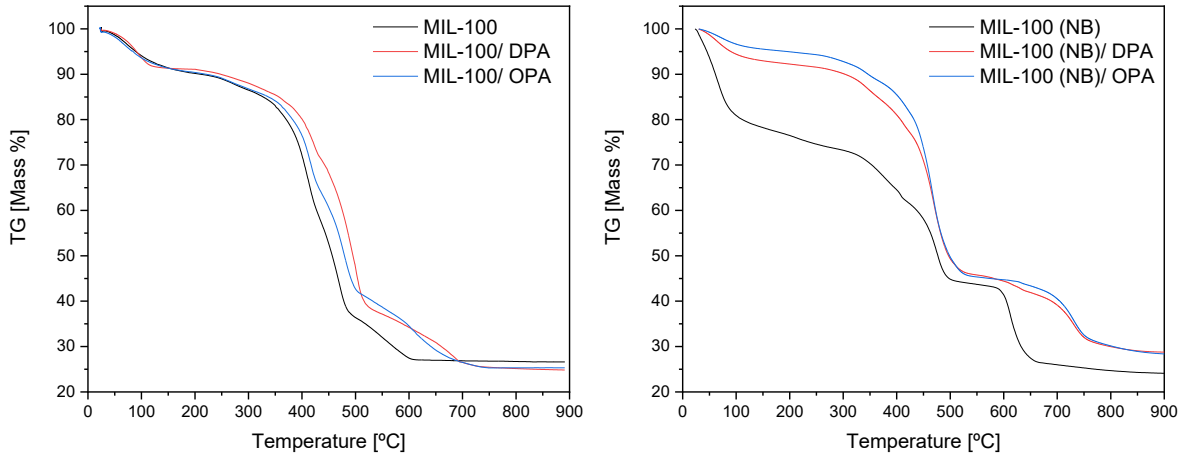


Figure 6.8: Thermogravimetry profiles for powder (left) and monolithic (right) MIL-100 in N_2.

The monolithic MIL-100 (NB) exhibited a mass loss event in the temperature range of 20-120˚C, far exceeding that of the powder samples. This loss event is likely due to vaporization of excess *n*-butylamine as well as trapped water molecules leftover from drying. The absence of this event in the acid-modified forms of MIL-100 (NB), which were similarly synthesised using *n*-butylamine, lends to the hypothesis that the loss of mass in this temperature region is due to trapped water from the drying process. The imparted hydrophobicity and, as shown later, reduced porosity of the modified MIL-100 monoliths likely led to fewer trapped water molecules to be released during heating. The plateau region from 500-600˚C in MIL-100 (NB) matches well with the TG profile of the linker trimesic acid [325], or H_3BTC ligand, and may be due to the thermal degradation of trapped ligand or reactant within the monolithic structure. The final mass plateau region appears to occur at higher temperatures for both DPA and OPA monoliths, similar to the modified powder samples. The TG profile of DPA in nitrogen, in a study by Phan et al [326], shows a gradual mass loss event in the region of 600-800˚C, which may explain the seemingly improved thermal stability of the modified sample. The final mass of the unmodified MIL-100 monolith is noticeably lower than the acid-modified forms, likely due to the aforementioned trapped water.

6.3.5. Comparisons between powder and monolith density

ZIF-8 and ZIF-67 powders were found to have true densities of approximately 0.95 g/cm^3, although their bulk densities were significantly lower- around 0.39 ± and 0.38 ± g/cm^3, slightly above literature values for commercial ZIF-8 [327]. All monolithic ZIFs were found to have enhanced bulk densities between 1.04-1.28 g/cm^3, with those synthesised using a mixture of ligands, ZIF-8 (ML) and ZIF-67 (ML) found to have the highest densities of 1.25 ± 0.05 and 1.28 ± 0.03 g/cm^3 respectively. These bulk densities are higher than the skeletal density of the ZIF-8/67 framework. Previous work on monolithic ZIF-8 credited this difference to insufficient activation or the presence of impurities [327], the latter of which is supported in this work due to the reduced crystallinity of the monolithic samples compared to the powders. ZIF-8 (1M-0.5) and ZIF-67 (1M-0.5) powders were found to have similar bulk densities to their unmodulated forms. Studies by Mehta et al [328] and Tian et al [327] were able to synthesise ZIF-8 monoliths with bulk densities of 1.05 g/cm^3, using a sol-gel based approach, and 1.19 g/cm^3, through an extended reaction approach, respectively. These densities match well with those in this work. However, it is important to note that both these studies use mercury as a flow medium for determining the bulk density of their monoliths, while this work used small glass beads. Glass beads, even with small diameters, will not be able to penetrate spaces as small as those penetrated by mercury, especially when pressure is applied. Therefore, the measured volumes of sample, and by extension the calculated bulk densities, between this study and those in literature may be different by virtue of the displacement mediums used.

Powder MIL-100 had a bulk density of 0.38 ± 0.02 g/cm^3, slightly above literature values (0.16-0.35 g/cm^3) for commercial MIL-100 powder [329]. The addition of DPA and OPA to the powder appeared to slightly increase the bulk density, although this modification is not statistically significant due to the standard deviation present between samples. Monolithic MIL-100 (NB) had a bulk density of 0.73 ± 0.04 g/cm^3, an increase of around 92 % compared to the powder. The addition of acids to the MIL-100 (NB) sol-gel prior to drying also appeared to increase the density of the final material, perhaps due to increased agglomeration of particles when coated with surfactant molecules or the presence of the acids in the spaces between constituent MOF particles.

6.3.6. Surface area and pore volume of ZIF and MIL monoliths

Based on nitrogen adsorption data, ZIF-8 and ZIF-67 were found to have similar surface areas of 1812 and 1810 m^2/g respectively, although the latter was found to have superior micropore and total pore volume. In all cases, the porosity distributions of the monolithic samples were found to differ greatly from their powdered forms. As shown **in Figure 6.9** and **Figure A.22**, monoliths synthesised using *n*-butylamine were found to have hierarchical porosity and showed an increased isotherm gradient in the P/P_0 = 0.1-0.8 region, which has been observed previously for ZIF-8 powders synthesised in the presence of *n*-butylamine [221], whereas unmodulated ZIF-8 and ZIF-67 were found to plateau in uptake following micropore filling. This hierarchical porosity may be due to the introduction of interstitial voids between the primary particles [317], leading to a network of heterogeneously sized apertures. Monolithic samples also produced a plateau region at high pressures, indicating a lack of macroporosity observable in powder samples. Larger amounts of *n*-butylamine in the synthesis mixture appeared to result in further decreases in microporosity and total pore volume, although there were no statistically significant differences in BET surface area between (NB-1) and (NB-2) samples. ZIF-67 (ML) was found to be predominantly microporous, lacking the increase in adsorption at the highest partial pressures, with around 80% of its pore volume being found in apertures with diameters of 2 nm or less, suggesting that a mixture of *n*-butylamine and 1-methylimidazole may lead to minimal formation of inter-particle space, or that alternative drying conditions are required to form these spaces in this material. Samples synthesised using 1-methylimidazole as the only modulator produced isotherm shapes almost identical to those of the unmodulated powders, albeit with lower surface areas and porosities. Several studies report on the synthesis of zeolitic imidazolate framework monolithic adsorbents. Tian et al [327] achieved monolith formation by two methods: room temperature drying of ZIF-8 crystals produced using standard reaction conditions in ethanol; and the extended reaction of ZIF-8 crystals with further mIm linkers in ethanol solution. Mehta et al [328] also synthesised ZIF-8 monoliths without the addition of acids or competing linkers, and were also able to incorporate tin nanoparticles into these monoliths. In both cases, the monoliths were found to have lower BET surface areas, ~1400 m^2/g, than powdered samples, but improved volumetric efficiency on account of their

density. BET surface areas and total pore volumes of monoliths in this work were found to exceed the values measured for monolithic ZIF-8 in these works. However, the monoliths in this work were found to have reduced micropore volume compared to literature, with the exception of ZIF-67 (ML).

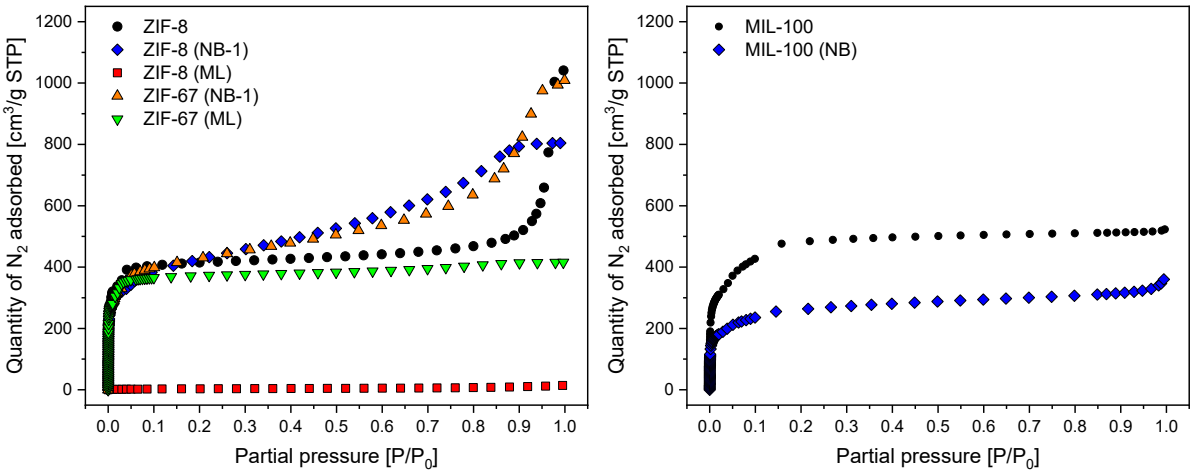


Figure 6.9: Nitrogen adsorption isotherms for ZIF (left) and MIL (right) powder and monolithic adsorbents. T = -196˚C.

ZIF-8 (ML) was the only ZIF sample studied that was found to be functionally non-porous, with measured surface area and total pore volume of only 11 m^2/g and 0.004 cm^3/g. The higher density of the monolithic samples is reflected in their volume-relative surface areas which, apart from ZIF-8 (ML), exceeded their powder counterparts. ZIF-8 (NB), ZIF-67 (NB) and ZIF-67 (ML) were all found to have similar volumetric surface areas in the range of 1850-2050 m^2/cm^3. ZIF-67 (ML) and ZIF-67 (NB) were found to have the highest volumetric micropore volume and total pore volume, at 0.673 cm^3/cm^3 and 1.810 cm^3/cm^3 respectively.

Monolithic MIL-100 was found to have significantly reduced BET surface area compared to its powder form, at 1084 and 2007 m^2/g respectively, with similar reductions in micro- and total porosity observed. Like the ZIF-8 and ZIF-67 monoliths, however, the improved density of MIL-100 (NB) resulted in a similar volumetric BET surface area to the powder, at 791 and 763 m^2/g respectively. The addition of the modulating ligand likely reduces the overall quantity of pore volume in the final material, similar

to the ZIF monolith system, either through generation of non-porous amorphous content, or by reducing the crystallinity of the framework and restricting the formation of characteristic porosity. Despite MIL-100 and MIL-100 (NB) possessing almost identical nitrogen isotherm shapes at low pressures, the latter was found to have a steeper isotherm gradient at intermediate partial pressures and a noticeable upswing in uptake at the $P/P_0 > 0.9$. This trend mirrors the results of ZIF monoliths synthesised using *n*-butylamine, with the hierarchical porosity likely due to interstitial spaces forming between the MOF particles- although the lack of plateau in the MIL-100 isotherms suggests macroporosity. When accounting for this sudden increase in uptake at high partial pressures, the application of the Gurvisch rule for total pore volume determination may not be accurate- similar to ZIF powders. Total pore volumes at P/P_0 ~0.9 were found to be 15-30 % lower than those at 0.99 for monolithic samples, while being similar for powder samples (within 5 %).

Table 6.1: Bulk densities, surface areas, and porosities of powder and monolithic adsorbents, determined using dry medium displacement at 25˚C, and nitrogen sorption at -196˚C respectively.

Adsorbent	Bulk density [g/cm^3]	SSA_{BET} [m^2/g] [1]	V_{micro} [cm^3/g] [2]	V_{total} [cm^3/g] [3]
ZIF-8	0.39 ± 0.02	1812 ± 36	0.521 ± 0.042	0.873 ± 0.019 [4]
ZIF-8 (NB-1)	1.17 ± 0.08	1766 ± 54	0.386 ± 0.038	1.289 ± 0.059
ZIF-8 (NB-2)	1.13 ± 0.11	1676 ± 103	0.331 ± 0.039	1.148 ± 0.077
ZIF-8 (1M-0.5)	0.37 ± 0.02	1694 ± 39	0.415 ± 0.036	0.792 ± 0.021 [4]
ZIF-8 (ML)	1.25 ± 0.05	11 [6]	-- [5]	0.004 [6]
ZIF-67	0.38 ± 0.02	1810 ± 58	0.584 ± 0.031	0.891 ± 0.027 [4]
ZIF-67 (NB-1)	1.11 ± 0.08	1787 ± 24	0.410 ± 0.035	1.631 ± 0.057
ZIF-67 (NB-2)	1.14 ± 0.10	1764 ± 64	0.389 ± 0.039	1.161 ± 0.103
ZIF-67 (1M-0.5)	0.36 ± 0.04	1666 ± 27	0.430 ± 0.028	0.887 ± 0.018 [4]
ZIF-67 (ML)	1.28 ± 0.03	1644 ± 34	0.526 ± 0.046	0.672 ± 0.040
MIL-100	0.38 ± 0.02	2007 ± 83	0.688 ± 0.035	0.810 ± 0.060
MIL-100 (NB)	0.73 ± 0.04	1084 ± 44	0.339 ± 0.021	0.489 ± 0.028 [4]

[1] Calculated using the Rouquerol partial pressure range of 0.02-0.08

[2] Calculated using t-plot method, encompassing both micropore size ranges.

[3] Calculated using single-point nitrogen sorption capacity at a partial pressure > 0.99

[4] Calculated using single-point nitrogen sorption capacity at a partial pressure > 0.9

[5] Due to non-porous nature of sample, no micropore volume could be determined

[6] Standard deviations of surface area and pore volume were < 1 m^2/g and < 0.001 cm^3/g

6.3.6.1. Pore size distributions of monolithic ZIFs

All porous ZIF samples were found to have similar sized pores, around 9 and 17 Å for small and large pores respectively, matching the characteristic pores of the powder, as shown by the calculated pore size distributions in **Figure 6.10**. In the case of ZIF-8 samples synthesised using n-butylamine, micropores with sizes between 12-13 Å can also be seen. Two possible explanations for this are:

- Partial blocking of a portion of the 17 Å apertures, possibly due to modulating ligands. This may account for the lower volume located in these larger apertures compared to other samples.
- The generation of inter-particle spaces from the addition of *n*-butylamine, although these spaces are typically generated in the mesopore size range.

These NB-type monoliths were also found to possess a great deal of pore volume located in apertures with diameters > 20 Å, showing similar patterns to charcoal and silica studied in Chapter 4. This further confirms that the addition of n-butylamine produced macroscopic monoliths with hierarchical porosity. Comparatively, ZIF-67 (ML) had little discernible mesoporosity based on NLDFT calculations. ZIF-8 (ML)'s lack of porosity was also confirmed in its pore size distribution.

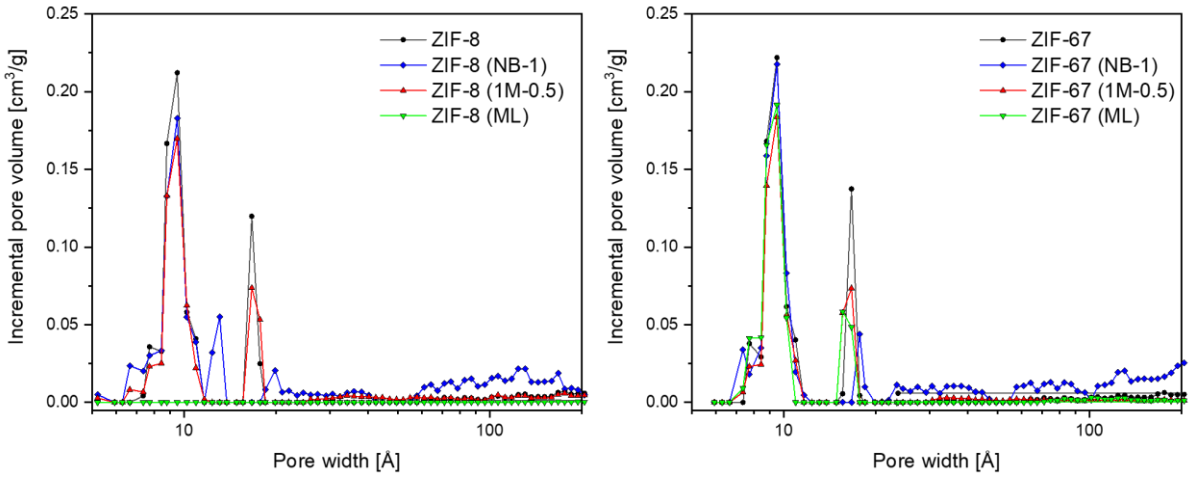


Figure 6.10: Pore size distributions of zinc (left) and cobalt (right) ZIFs, calculated using Tarazona NLDFT model assuming cylindrical pore geometry, using nitrogen sorption data at T = 196˚C.

Note: Because of their reduced yield, surface areas, pore volumes, and bulk densities, further analysis of ZIF samples synthesised using solely 1-methylimidazole as a modulating linker was not carried out.

6.3.6.2. Impact of acid modification on surface area and pore volume of MIL-100

The post-synthetic addition of DPA and OPA to powder MIL-100 powder was found to reduce the surface area by approximately 13 % and 21 % respectively, although the large standard deviation in these values results in no statistical significance between the two acid-modified samples. This decrease may be due to the long alkyl chains either blocking or obstructing the apertures of the MOF framework. Sun et al [220] found the addition of OPA to UiO-66 had little to no impact on the pore volume of the MOF, and calculated similar surface areas for modified and unmodified materials. Based on pore volume distributions from Sun's study, the OPA did not enter the pores of the UiO-66 and therefore did not inhibit the pore volume available for molecules such as nitrogen to adsorb.

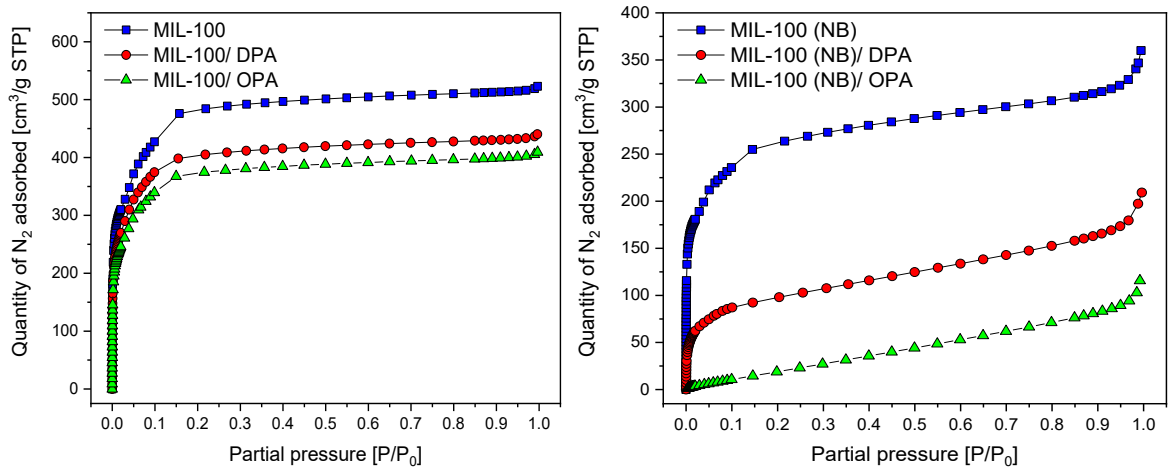


Figure 6.11: Nitrogen adsorption isotherms for modified powder (left) and monolithic (right) MIL-100 adsorbents. T = -196˚C.

The addition of acids to MIL-100 (NB) had a much more significant impact on surface area and porosity- with DPA and OPA reducing surface area by 63 % and 89 % respectively, and the latter possessing negligible microporosity. There are several explanations for this:

- Higher mass loading of acids in the monolith (7.5 ± 1.3 - 9.9 ± 1.7 %) compared to the powder (2.2 ± 0.2 -2.4 ± 0.3 %). This directly reduces the total amount of porous material within the sample on a mass basis.
- Due to higher loading, the degree of pore blocking within the monolithic sample is greater.
- As the acids were added before drying of the sol-gel, the trapped acid may block or inhibit the formation of free space in between the MIL-100 particles.

Regardless of the reasoning, this significant reduction in porosity may make modifications through sol-gel incorporation disadvantageous, depending on the extent it affects hydrophobicity.

Table 6.2: Densities, surface areas, and porosities of MIL-100 adsorbents, determined using dry medium displacement at 25˚C, and nitrogen sorption at -196˚C.

Adsorbent	Bulk density [g/cm^3]	SSA_{BET} [m^2/g] [1]	V_{micro} [cm^3/g] [2]	V_{total} [cm^3/g]
MIL-100/ DPA	0.39 ± 0.02	1747 ± 116	0.568 ± 0.053	0.682 ± 0.061 [3]
MIL-100/ OPA	0.40 ± 0.03	1582 ± 122	0.529 ± 0.051	0.634 ± 0.051 [3]
MIL-100 (NB)/ DPA	0.79 ± 0.03	407 ± 40	0.078 ± 0.016	0.256 ± 0.021 [4]
MIL-100 (NB)/ OPA	0.83 ± 0.04	125 ± 17	-- [5]	0.129 ± 0.015 [4]

[1] Calculated using the Rouquerol partial pressure range of 0.02-0.08, with the exception of MIL-100 (NB)/ OPA, which used the standard BET partial pressure range of 0.05-0.35.

[2] Calculated using t-plot method, encompassing both micropore size ranges.

[3] Calculated using single-point nitrogen sorption capacity at a partial pressure > 0.99

[4] Calculated using single-point nitrogen sorption capacity at a partial pressure ~0.9.

[5] Due to low porosity nature of sample, no micropore volume could be determined

Monolithic MIL-100 samples possessed similar pore distributions to the powder, in the range of 5-13 Å and 18-27 Å nm. This confirms that, despite reductions in crystallinity, the framework of the MOF still contains the characteristic apertures of MIL-100 (Fe) [313], [314]. In addition, all monolithic MIL-100 samples were found to possess noticeable heterogeneous mesoporosity, while pore size distributions for the powders showed no porosity beyond the characteristic apertures.

The DPA- and OPA-modified MIL-100 powders possessed almost identical pore size distributions, albeit with reduced pore volume located in each of the regimes, signifying that the reduction in porosity

and surface area is due to some amount of alkyl acids located within the cages of the MOF. The effect of acid modification on the porosity of the monolithic samples was much more pronounced, with addition of DPA and OPA resulting in reductions in micropore volume of 75 % and 100 % respectively. The nitrogen isotherm of MIL-100 (NB)/ OPA follows a Type III trend, and displaying severely reduced BET surface area, micropore, and mesopore volumes. The volume located within the small- and large-pores was significantly reduced in MIL-100 (NB)/ DPA, with this effect more noticeable in the larger aperture. For MIL-100 (NB)/ OPA, no pore volume in any pores with a diameter < 2.5 nm were predicted based on NLDFT calculations.

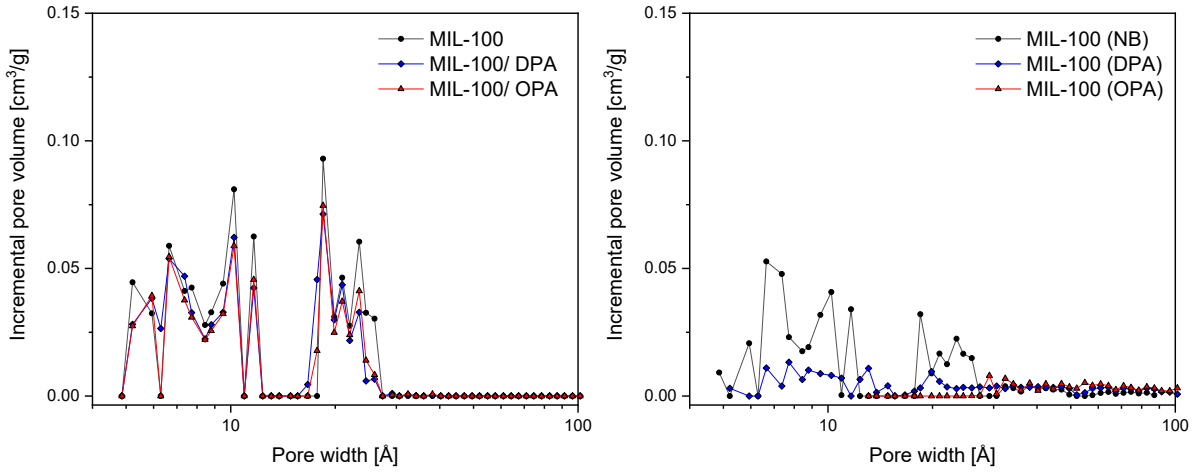


Figure 6.12: Pore size distributions of powder (left) and monolithic (right) MIL-100 with and without acid modification, calculated using Tarazona NLDFT model assuming cylindrical pore geometry, using nitrogen sorption data at T = 196˚C.

6.3.7. Scanning electron microscopy of monolithic MOFs

ZIF-8 (NB-1) and ZIF-67 (NB-1) were found to consist largely of densely packed particles with an average diameter of 35.0 ± 5.7 and 69.6 ± 9.7 nm respectively, although only the latter appeared to possess a distinct shape, with ZIF-8 (NB-1)'s particles being largely spherical and possessing few facets. ZIF-67 (NB-2) was also found to possess distinct crystals with a similar size to monoliths produced with half the amount of n-butylamine, at 56.2 ± 11.3 nm. Additionally, many of the crystalline

particles appear to be agglomerated with what is assumed to be amorphous material. ZIF-8 (NB-2), ZIF-8 (ML) and ZIF-67 (ML) were found to lack any distinct or well-defined nanoparticles, and crystal size distributions could not be determined.

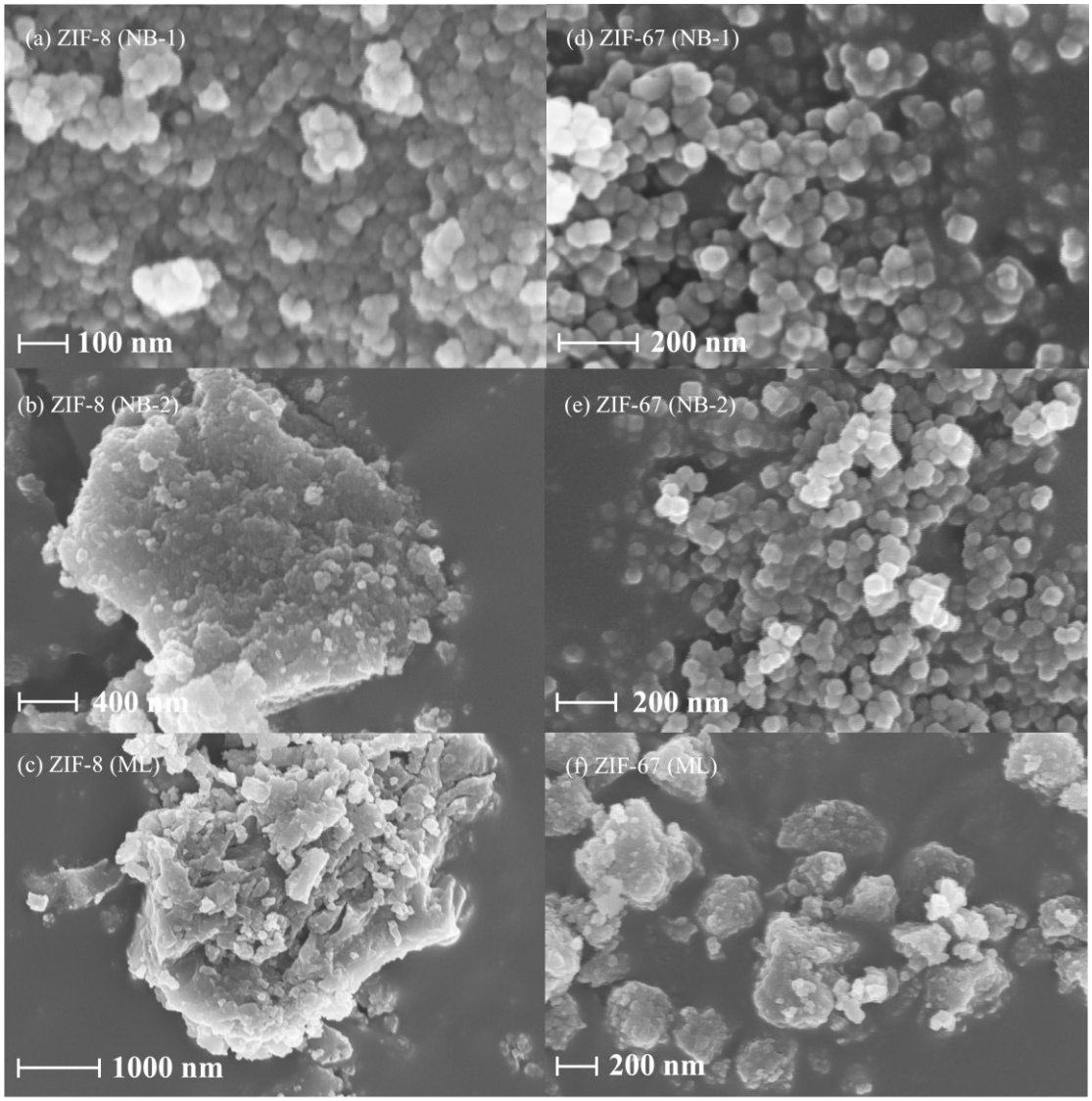


Figure 6.13: Scanning electron microscopy images of ZIF monoliths, including scale bars.

MIL-100 was found to be formed of distinct particles with diameters in the range of several hundred nanometres. The sizes and shapes of these particles are heterogenous, with an average diameter of 221 nm and a standard deviation of 96 nm, over 43 % of the diameter- similar to that of the study this work's synthesis procedure was adapted from [222]. MIL-100 (NB) appeared to consist of heterogenous

particles with a range of sizes and shapes making any average size difficult to determine accurately. The particles in MIL-100 (NB) were distinct compared to those of ZIF monoliths, suggesting they may form some macrostructure during the creation of the monolith from the sol-gel, but that the constituent particles are still large enough to be imaged and are not instead agglomerated with amorphous content.

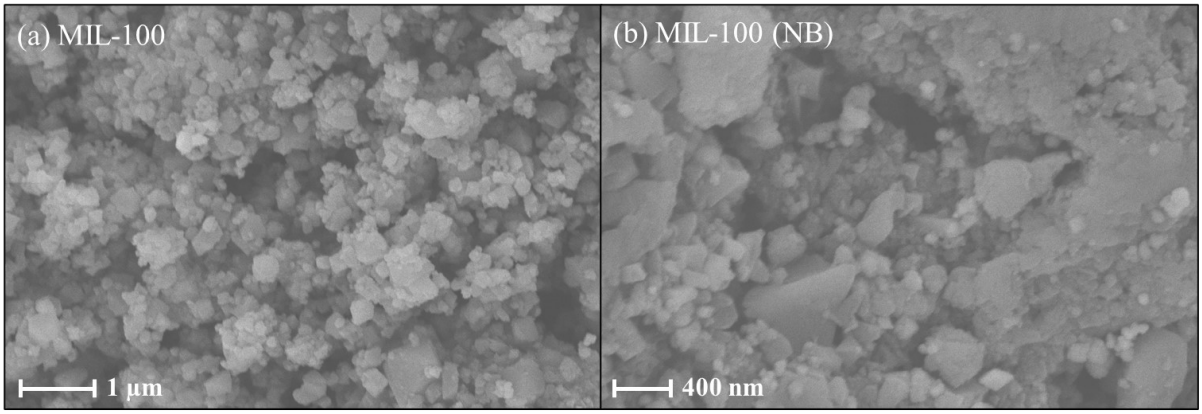


Figure 6.14: Scanning electron microscopy of MIL-100 powder (left) and monolith (right).

6.3.8. Advancing water contact angles of powder and monolithic MOFs

All ZIF samples were found to possess advancing contact angles in the range of 114-136˚, qualifying them as 'hydrophobic' but not 'superhydrophobic' materials [330]. Monolithic samples were consistently found to possess higher water contact angles than their respective powders, although the increase in apparent contact angle due to changes in substrate surface roughness cannot be neglected. As a material's roughness increases, the wettability caused by the chemistry of the surface will be enhanced- i.e. hydrophilic materials will become more hydrophilic and hydrophobic materials will become more hydrophobic when roughness is added [331], [332]. The adsorption hydrophobicity of the powder and monolithic adsorbents will be discussed directly later in this Chapter.

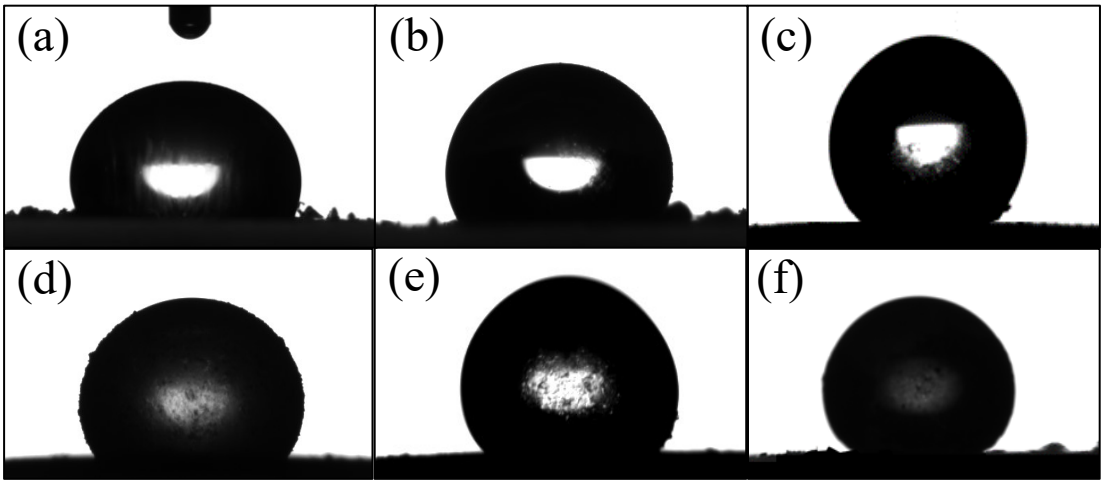


Figure 6.15: Advancing contact angles of ZIF samples: ZIF-8, (a); ZIF-8 (NB-1), (b); ZIF-8 (ML), (c); ZIF-67, (d); ZIF-67 (NB-1), (e); ZIF-67 (ML), (f). N = 5.

Similar to ZIF samples, monolithic MIL-100 (NB) was found to possess a superior contact angle compared to its powder form, at 86.8 ± 3.1˚ and 41.0 ± 1.1˚. As before, the contributions of surface chemistry and surface roughness on contact angle must both be considered, although the increase in water contact angle for MIL-100 monoliths is much more significant than for ZIFs. The addition of DPA and OPA were both found to increase the hydrophobicity of the MIL-100's surface, leading to far superior water contact angles, all above 120˚. The addition of DPA and OPA to MIL-100 powder increased the contact angle by 235 % and 228 % respectively, while the addition of DPA and OPA to MIL-100 (NB) increased the contact angle by 43 % and 60 % respectively. This drastic increase has been observed previously in the work by Sun et al [220], who found the contact angle of UiO-66 increase from 19˚ to 160˚, i.e. from hydrophilic to superhydrophobic, upon the addition of OPA. The non-polar chemistry of the acid's alkyl chains reduces the material's interactions with liquid water, resulting in reduced surface wetting.

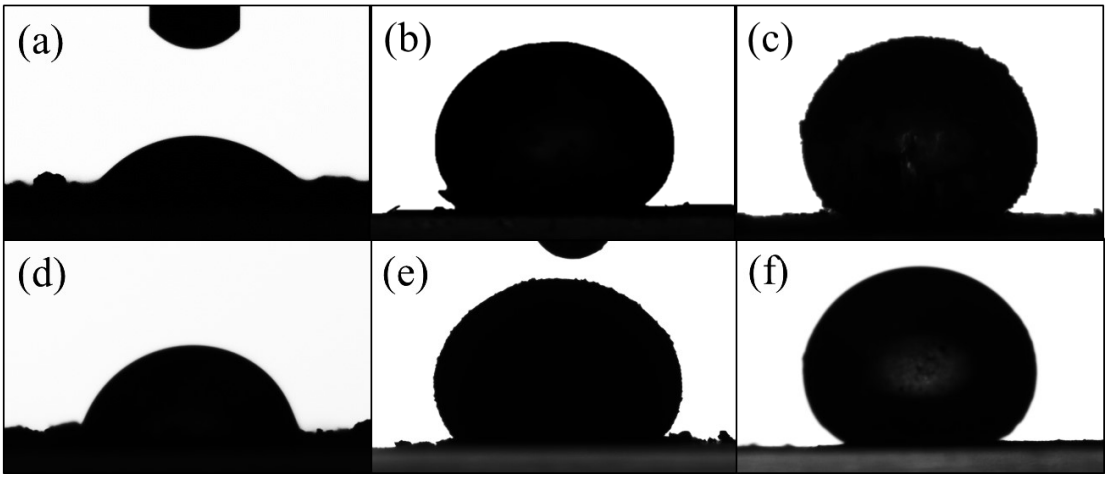


Figure 6.16: Advancing contact angles of MIL-100 samples: MIL-100, (a); MIL-100/ DPA, (b); MIL-100/ OPA, (c); MIL-100 (NB), (d); MIL-100 (NB)/ DPA, (e); MIL-100 (NB)/ OPA, (f).

6.3.9. Single-component VOC adsorption by monolithic ZIFs

Vapour adsorption isotherms for the six studied materials are shown in **Figure 6.17**. All samples were found to have high adsorption hydrophobicity based on their low water vapour uptake, best described as Type III isotherms [40]. Monolithic samples, except for ZIF-8 (ML), were all found to have higher water uptake than their powder counterparts, with capacities between 48 and 84 mg/g at the highest studied RH of 90 %. This suggests that monolithic ZIF samples reported here differ slightly in their water adsorption behaviour compared to powders, perhaps due to the former's amorphous content. Activated charcoal and zeolite Y studied in Chapter 4, were found to adsorb 297 and 122 mg/g of water vapour 80 % RH, emphasising the adsorption hydrophobicity of the ZIFs in this Chapter. The adsorption of toluene appeared to follow the same trend as nitrogen adsorption. While powder samples had the greatest uptake of toluene at the lowest studied concentrations due to their higher surface areas, their uptakes plateaued afterwards, resembling Type I isotherms [40] and only noticeably increased at the highest concentrations. ZIF-8 (NB-1) and ZIF-67 (NB-1), due to their hierarchical pore structure, do not possess this flat plateau region and adsorb greater quantities of toluene vapour in the P/P_0 = 0.2- 0.9 region, with their isotherm shapes more closely described by Type II or Type IV [40]. ZIF-8 (NB-1) and ZIF-67 (NB-1) adsorbed 826.3 mg/g and 1030.9 mg/g of toluene vapour at the highest partial

pressure studied, outperforming their powder counterparts by 29.8 % and 38.6 % respectively. When expressed in volume-relative terms, considering the materials' densities, ZIF-8 and -67 monoliths outperform their powder forms by 289 % and 305 % respectively, further emphasising their advantages in industrial applications for vapour adsorption. ZIF-8 (ML) had no noticeable uptake of any VOCs or water vapour, similar to nitrogen experiments. The adsorption of methanol vapour was best described by Type V isotherms for all porous samples studied. All porous samples appeared to have an inflection point around P/P_0 = 0.08-0.1, after which cage-filling occurred. This effect has been observed previously when adsorbing alcohol molecules on both hydrophobic zeolites [172], [333], as well as ZIF-8 powders [145]. Monolithic samples adsorbed slightly greater quantities of methanol pre-inflection despite their lower BET specific surface area, suggesting that the monolith formation may affect the ZIF materials' affinity towards polar molecules. There are several possible explanations for this:

- The formation of the monolith contributes to hierarchical mesoporosity and external surface area within the final material, which polar molecules can better interact with due to the lower density of hydrophobic linker groups.
- The possible presence of amine groups from the modulating linker may improve the material's ability to interact via hydrogen bonding, further improving its interactivity with polar molecules. However, the presence of primary amine groups could not be confirmed via FTIR, and the N-H wag for primary and secondary amines was detected in all ZIF samples, including the powder.
- The reduced crystallinity of the sample inherently reduces the degree of order of the ZIF framework. As the framework itself has significant hydrophobic chemistry, disorder or defects within the framework may have lower hydrophobicity. This is similar to defect sites in hydrophobic zeolites, such as those caused by dealumination [44].

Despite the small increases in the uptake of methanol and water, monolithic ZIFs can still be considered to possess the characteristic hyperhydrophobicity of the powders.

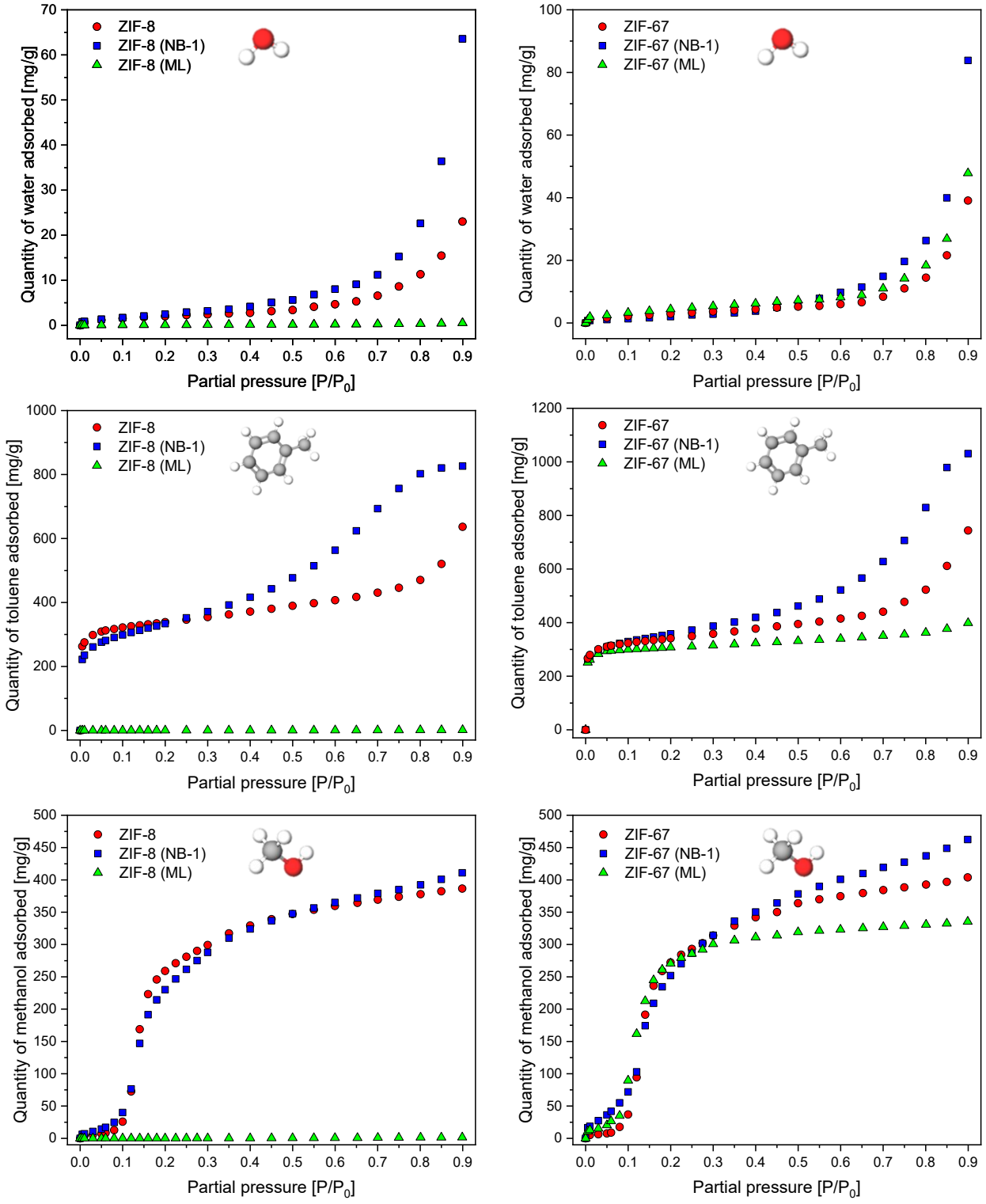


Figure 6.17: Vapour adsorption isotherms for zinc (left) and cobalt (right) ZIF samples. From top to bottom, vapours studied are water, toluene, and methanol. All measurements carried out at 25ºC.

6.3.10. Single-component VOC adsorption by monolithic MIL-100

Similar to nitrogen sorption, MIL-100 (NB) adsorbed lower quantities of toluene vapour compared to its powder form due to lower surface area and porosity. However, when the density of the adsorbents is considered they adsorbed similar amounts of toluene at $P/P_0 = 0.005$- powder and monolith uptake were 158 and 164 mg/g respectively. Monolithic MIL-100 appeared to have a much steeper gradient in its initial water isotherm while possessing the characteristic pore filling events at partial pressures around 0.25 and 0.45. This steeper initial gradient suggests the monolith contains a greater proportion of uncoordinated iron sites on its external surface, which has been hypothesised to account for water uptake of MIL-100 pre-pore filling [315]. This further supports the hypothesis that the reduction in crystallinity during sol-gel and monolith formation likely influences the hydrophilicity of the material.

The loss of capacity for toluene in acid-modified MIL-100 powders and monoliths followed a trend almost exactly like that of the nitrogen sorption: in powder form the addition of DPA and OPA led to similar reductions; while in monolithic MIL-100 OPA much more drastically reduced the MOFs performance for toluene removal- despite the two acids having similar mass loading in the modified monolith. The water uptake of the DPA- and OPA-modified MIL-100 powders are similar in both trend and magnitude, although the latter was found to adsorb slightly less water at all partial pressures studied. This effect could be due to two phenomena:

- Improved hydrophobicity of the final material due to the longer chain length of OPA (18) compared to DPA (10), resulting in additional dispersive surface chemistry while reducing the number of high-energy polar adsorption sites.
- Increased pore blocking by the OPA molecules compared to DPA. This assertion is supported by the reduced surface area and pore volumes of the OPA-modified sample determined via nitrogen sorption, as well as the slight reduction in toluene adsorption capacity.

The reduced adsorption of both toluene and nitrogen suggests that both DPA and OPA can have a significant effect on the adsorption behaviour of MIL-100 powder, and this modification appears to be stable even when regenerated at elevated temperature and reduced pressure.

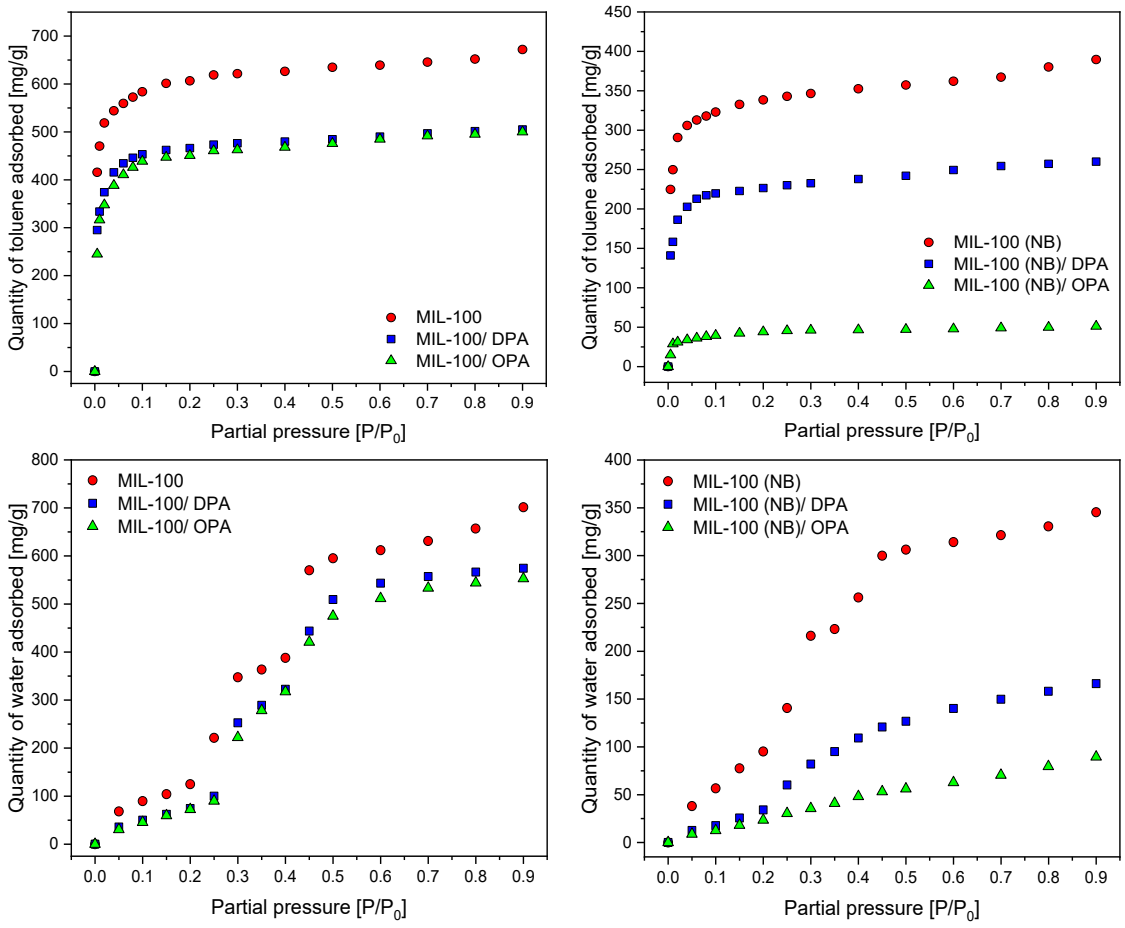


Figure 6.18: Vapour adsorption isotherms for powder (left) and monolithic (right) MIL-100 samples. Vapours studied are toluene (top) and water (bottom). All measurements carried out at 25ºC.

6.3.11. Comparing hydrophobicity indexes of powder and monolithic MOFs

Molar hydrophobicity indexes (H.I.s), using methods described in Chapter 4, were calculated using the adsorbed molar quantity of toluene at a partial pressure of 0.005 and water at several RHs. Hydrophobic adsorbents from Chapter 4 were included in these plots to compare the MOFs samples in this study to standard industrial materials.

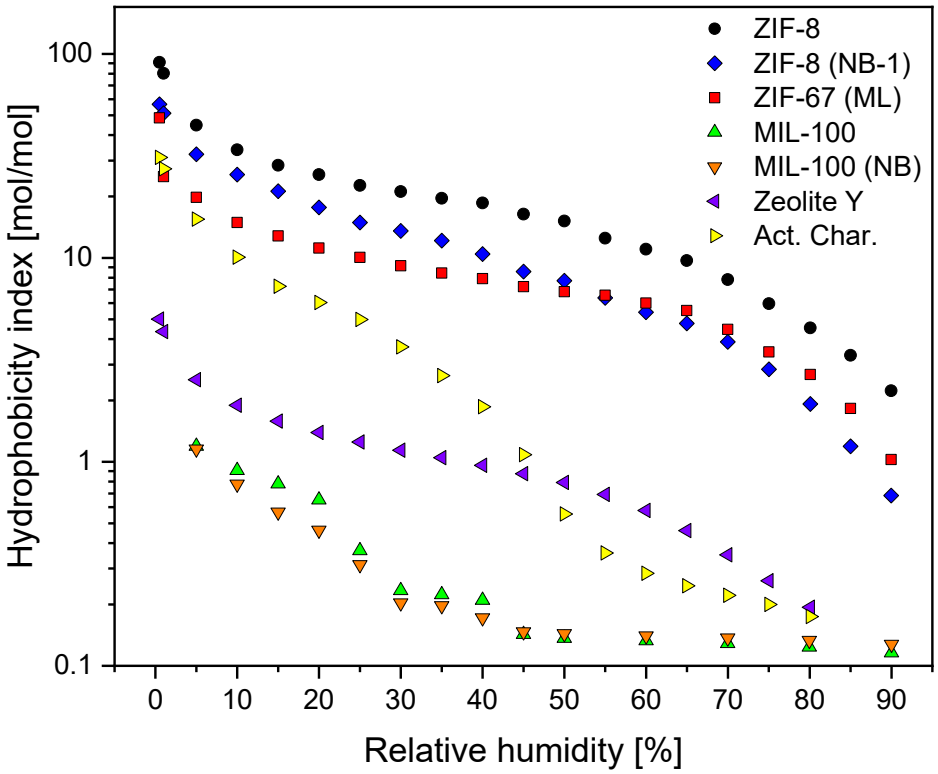


Figure 6.19: Molar hydrophobicity indexes for powder and monolithic MOFs, including industrial adsorbents for comparison. All measurements carried out at 25ºC.

All porous ZIF samples in this study were found to possess higher H.I. values than the industrial adsorbents at the highest RHs studied, while MIL-100 adsorbents displayed lower H.I.s than all other adsorbents. Despite having significantly higher toluene uptake than other adsorbents, MIL-100's high water capacity at RHs < 20 % due to surface uncoordinated iron results in much lower indexes. These indexes are reduced even further as partial pressures increase past 20 % and water begins to fill the mesopores of the MOF framework. As shown in **Table A.1** in the Appendix, despite having higher surface hydrophobicity (i.e. higher contact angles), monolithic MOFs possessed similar or smaller molar hydrophobicity indexes and appeared to interact more favourably with water molecules than their powder counterparts. This increased adsorption hydrophilicity is likely due to the additional amorphous content, while added surface roughness from the size of the ground particles may contribute to the increased contact angle, as discussed in previous sections. This observation also provides an important consideration that adsorption hydrophobicity cannot always be directly informed by the water contact

angle of the adsorbent, and direct adsorption measurements are required to determine how the material will interact with gas- or vapour-phase molecules.

6.3.11.1. Impact of acid modification on hydrophobicity indexes of MIL-100

At low RHs, acid-modified MIL-100 powders had similar molar hydrophobicity indexes to the unmodified form. This suggests that the modification lowers the material's capacity for toluene and water to similar degrees. Therefore, while the non-polar nature of the alkyl acids may contribute to the surface hydrophobicity of the material, the impact of pore blocking on performance appears to be universal regardless of adsorbate chemistry. Similar to unmodified powders and monoliths, this suggests that surface hydrophobicity measured via water contact angles cannot be used as an indicator for adsorption hydrophobicity for modified MIL-100 powders. For monolithic samples, the addition of DPA appeared to reduce the uptake of water more significantly than the uptake of toluene, leading to an improvement in hydrophobicity index. As the DPA molecules are added to the sol-gel MOF, it is possible that the drying process traps the acids between MOF particles as the monolith forms, or within the framework apertures. The mass loading of the acids onto the monolith was noticeably higher than the powder, potentially leading to a stronger hydrophobic effect. This hypothesis is supported by the pore size distributions of the DPA-modified monolith, with significantly reduced volume located in both apertures of the MIL-100 framework. However, zeolite Y and activated charcoal were found to possess superior molar hydrophobicity indexes compared to all MIL-100 samples studied, although these values approached those of MIL-100 (NB) and MIL-100 (NB)/ DPA as the humidity increases to above 70 % as the industrial samples adsorbed greater quantities of water into their mesopores.

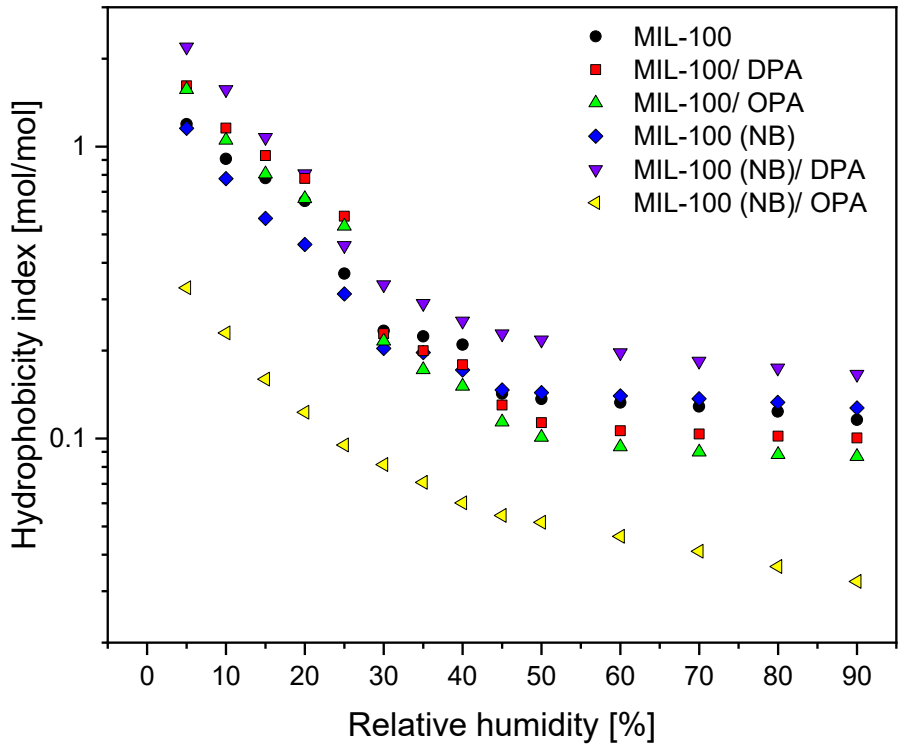


Figure 6.20: Molar hydrophobicity indexes for acid modified MIL-100 in powder and monolithic form. All measurements carried out at 25ºC.

6.3.12. Impact of humidity on toluene adsorption by monolithic MOFs

For multi-component studies, ZIF-8 (ML) was not tested due to its lack of surface area and porosity. Due to the inflection point in MIL-100 water isotherms, RHs of 20, 40, and 80 % were tested to determine whether pore filling by the water molecules had a noticeable impact on toluene adsorption.

ZIF-8 and ZIF-67 powders adsorbed almost identical quantities of toluene at all water pre-exposure levels, with overlapping data within standard deviation bars. The loss of porosity in ZIF-8 (NB-1) led to a reduction in toluene adsorption performance in dry conditions and a slightly higher reduction in capacity- as RH increased from 0-20 % ZIF-8 (NB-1) lost 15.0 % capacity compared to ZIF-8 powder which only decreased by 11.3 %- although, based on 95 % confidence intervals this difference was not statistically significant. The impact of humidity appeared to follow the ZIF's trends in water isotherm, with the magnitude of the water uptake at high pressures matching subsequent losses in performance,

i.e. a larger reduction for samples synthesised using n-butylamine. Possible explanations for increases in water uptake by monoliths, and by extension increases in adsorption competition, have been discussed in previous sections of this Chapter. At the highest water concentrations, the formation of a liquid-like water layer may create a barrier of entry for toluene molecules adsorbing on the outer surface of the MOF. Despite this, all ZIF adsorbents were found to have exceptional adsorption performance for toluene at all pre-exposure levels studied, far exceeding those of activated charcoal and zeolite Y measured under the same conditions.

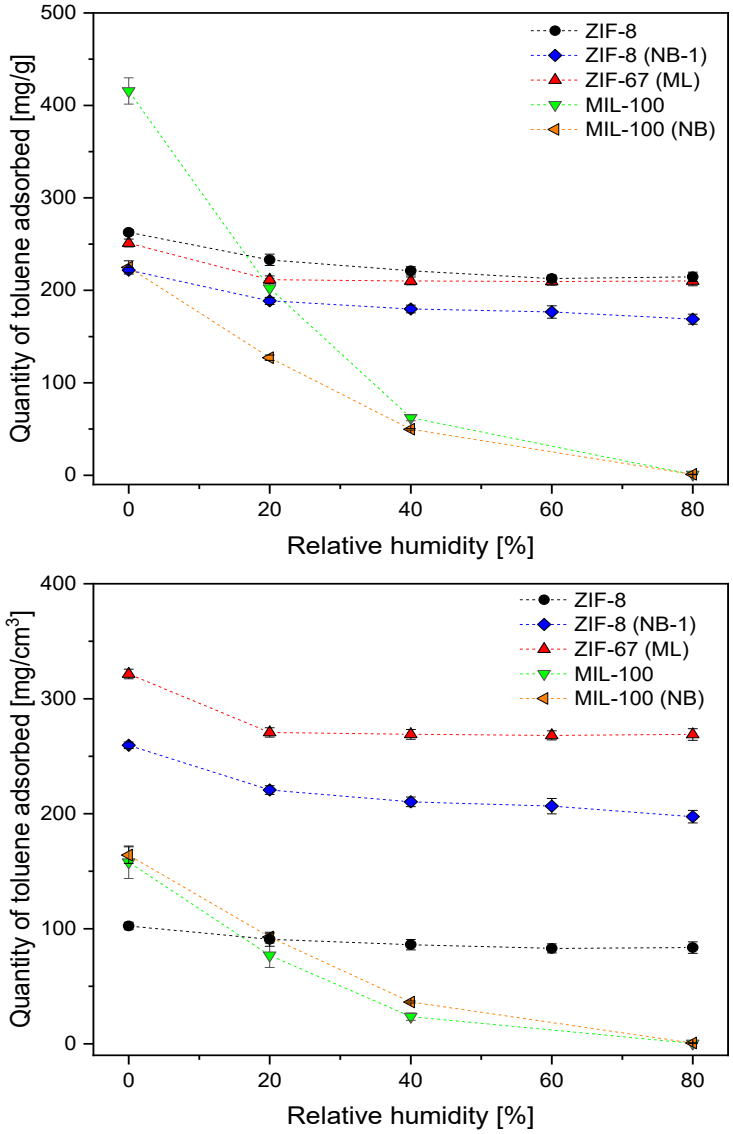


Figure 6.21: Adsorption of toluene vapour following pre-exposure of water vapour at different humidity levels for MOF adsorbents, expressed in mass- (top) and volume- (bottom) relative terms. Partial pressure of toluene in all experiments, $P/P_0 = 0.005$. T = 25˚C.

MIL-100 (NB) had a similar trend in toluene uptake as MIL-100, with drastic drops in performance at 20, 40, and 80 % RH- which can be credited to the different mechanisms of water adsorption outlined in Chapter 5 for the powder sample. Therefore, monolithic MOFs in this work not only possess the characteristic pore sizes of their respective powders, but also their characteristic pore hydrophobicity and humid toluene adsorption trends. These results are summarised in **Table 6.3**.

Table 6.3: Dry and humid capacities for toluene at a partial pressure of 0.005, expressed in volume-relative terms, for MOF adsorbents, with zeolite Y and activated charcoal shown for comparison. T = 25˚C.

Adsorbent	Dry (0 % RH) [mg/g]	Humid (40 % RH) [mg/g]	Humid (80 % RH) [mg/g]
ZIF-8	262.7 ± 3.2	221.1 ± 4.5	214.6 ± 5.0
ZIF-8 (NB-1)	221.9 ± 2.8	179.8 ± 4.2	168.8 ± 5.4
ZIF-67	266.8 ± 3.1	218.5 ± 4.3	213.5 ± 3.1
ZIF-67 (NB-1)	259.6 ± 2.9	217.8 ± 2.4	198.5 ± 2.4
ZIF-67 (ML)	251.2 ± 4.2	210.2 ± 4.2	210.1 ± 5.1
MIL-100	415.6 ± 14.2	62.2 ± 3.2	0.8 ± 0.1
MIL-100 (NB)	224.8 ± 7.2	49.8 ± 0.9	0.9 ± 0.2
Activated charcoal	264.2 ± 1.2	212.4 ± 4.9	9.3 ± 0.7
Zeolite Y	121.1 ± 0.7	107.3 ± 2.5	100.9 ± 1.1

When expressed in volume-relative terms, monolithic ZIF samples adsorbed between 153-217 % more toluene than their powder counterparts in dry conditions, and between 136-232 % more toluene than their powder counterparts in high humidity (80 % RH) conditions. However, the drastic loss in porosity for MIL-100 (NB) resulted in it adsorbing similar volume-relative quantities of toluene to the powder. The trend in volumetric uptakes in dry conditions followed the trend ZIF-67 (ML) > ZIF-67 (NB-1) > ZIF-8 (NB-1) > MIL-100 (NB) = MIL-100 > ZIF-8 = ZIF-67 = Zeolite Y > activated charcoal. A similar trend is observed at medium (40 %) and high (80 %) RHs, except for MIL-100 samples which adsorb the least of any adsorbents studied. It appears that the volumetric capacities for MOF monoliths follow the trend in density, as these were found to vary significantly between samples, from 0.73- 1.28 g/cm^3. Volume-relative capacities can be found in **Table A.2** in the Appendix.

6.3.12.1. Impact of acid modification on humid toluene adsorption performance of MIL-100

For MIL-100 samples, MIL-100 (NB)/ OPA was not tested as it was found to be functionally non-microporous. The presence of water vapour at an RH of 20 % led to noticeable drops in toluene capacity, at least a 30 % reduction in performance, for all samples. The DPA-modified powder and monolith samples appeared to adversely affect their humid capacity of toluene at this level, with reductions of 60 % and 49 % respectively. Even the addition of OPA to the powder, while possessing the smallest loss in performance at 20 % RH, did not lead to any relative improvement in effectiveness as humidity increased. This data is summarised in **Figure A.27** and **Table A.3** in the Appendix. This further emphasises the limitations in predicting adsorption hydrophobicity using surface hydrophobicity measurements. The modification of MIL-100 using alkyl phosphoric acids, while improving the MOFs' water contact angle significantly, did not have any impact on the relative water uptake or selectivity for non-polar VOC species.

6.3.13. Fitting of experimental adsorption kinetics

Kinetic fitting parameters for ZIF adsorbents using pseudo first order and pseudo second order models can be found in **Tables A.27-A.37** in the Appendix, and for MIL-100 adsorbents in **Tables A.40-A.46**. Out of a combined 92 systems, 58 (63 %) were best fit by the PFO model, 29 (32 %) were best fit by the PSO model, and 5 (5 %) were fitted equally by both. As the kinetics of adsorption are slow due to low driving force, similar to the kinetic analysis in Chapter 4, no bias towards the PSO model was found. While all kinetic data was fitted successfully for non-polar species, several fits did not converge when analysing polar water and methanol adsorption onto ZIFs. This lack of convergence may be due to the relatively noisy mass versus time profiles, as the uptake of the polar vapours was of a similar magnitude to the DVS microbalance drift and small jumps present due to benchtop vibrations and disturbances, resulting in poorer fitting.

The rate parameters for the adsorption of each vapour by ZIFs vary noticeably, largely following the trend of water > methanol > n-hexane > toluene. The fast adsorption of water and methanol is likely due to the mechanism of adsorption being surface site filling, as neither of these species were found to

fill the pores of the ZIFs at these partial pressures. According to **Figure 6.18**, methanol requires a partial pressure of around 0.08-0.1 P/P_0 to begin the transition to pore filling- i.e. the second inflection point of the type V isotherm. On the other hand, water is never observed to fill the pores of ZIF-8 or ZIF-67, with its type III isotherm implying predominantly surface monolayer and multilayer formation, although adsorption into the mesopores at high partial pressures cannot be ruled out. This supports previous assertions in Chapter 4 that some information regarding the mechanism of adsorption can be determined based on the kinetics of adsorption, providing no size-based molecular sieving occurs. On that note, despite their similar polarity and likely combination of surface and pore filling, n-hexane was found to have significantly higher kinetic rate constants than toluene. For example, for ZIF-8 and ZIF-67 powder the values of k_{PFO} for n-hexane were found to be 31 and 8 times greater than the same values for toluene. Toluene's kinetic diameter is of a similar magnitude to the flexible aperture of ZIF-8 and ZIF-67, the exact size of which has been debated in literature, leading to significantly reduced diffusion into the pores [151]. While not completely sieving the molecule, and still allowing its adsorption, the significantly reduced kinetics may result in kinetics-based selectivity for smaller molecules over aromatics.

ZIF-8 powder was found to possess k_{PFO} values noticeably higher than ZIF-67 powder for dry n-hexane, toluene, and methanol adsorption. Gas adsorption experiments determined that while the two materials possessed similar pore size distributions, ZIF-67 was found to have greater BET surface area, micro-, and total-pore volume- which may typically be associated with superior uptake kinetics. However, ZIF-67 was found to possess crystals almost 8 times larger than its zinc-based counterpart based on SEM experiments. Tanaka et al [334] found that increasing the crystal size of ZIF-8 from 60 nm to 470 nm, very closely matching the disparity in size in this work, resulted in equilibrium being reached 2.5 times slower. For systems in which uptake is controlled by diffusion into the pore network, the adsorption time was found to vary with the square of the crystal size, while this relationship was found to be directly proportional for surface-barrier limited adsorption. Torad et al [335] found that nanoporous carbons produced from small-size ZIF-8 crystals had faster equilibration times when exposed to toluene vapour compared to those produced from large-size crystals. Work by Uehara et al [336] on porous

coordination polymers found similar trends- as crystal size increases, the diffusion pathway into the pores and adsorption sites increases with it, leading to poorer kinetics. This effect was much more pronounced at low concentrations, whereas the nature of the analyte, which in the study by Uehara was n-hexane and methanol, appeared to be the dominant influencer of kinetics.

In terms of dry toluene adsorption, all MIL-100 materials were found to have rate constants in the range of 8.56 e-04 to 6.00 e-4 min^{-1}, between the ranges of industrial and ZIF adsorbents. Their sufficiently large pore apertures circumvent the limitations of the flexible but narrow apertures of ZIF-8/67, but they still appear to adsorb more slowly than charcoals and high-silica zeolites. Comparing between MIL-100 adsorbents, the modified monoliths appeared to have the highest dry toluene rate constants. As mentioned previously, the addition of DPA and OPA to the sol-gel of MIL-100 (NB) prior to drying led to noticeably reductions in the final materials pore volume due to blocking of the apertures by the acid molecules. However, the final materials still have sufficient surface areas (> 100 m^2/g) to adsorb volatile species. As micropore volume decreased, a greater proportion of the adsorption occurs via surface filling, this is supported by MIL-100 (NB)/ OPA having the highest rate constant of all while also possessing negligible microporosity. For water adsorption, all MIL adsorbents showed significant decreases in rate constant as RH increased from 20-40 %, compared to consistent increases at all other RH intervals. Based on isotherm and literature studies [315], adsorption at 20 and 40 % RH occurs via surface filling and a combination of surface and mesopore filling respectively. Comparisons between adsorption at 20 and 80 % RH also show the former to have a higher rate constant, even as driving force increases fourfold. These observations further support that the mechanism of adsorption may have an impact on adsorption kinetics, alongside environmental factors such as humidity or concentration driving force.

6.3.13.1. Impact of humidity on toluene kinetics

Exposing samples to water vapour prior to toluene adsorption was found to not only reduce their capacity, but also the adsorption kinetics. PFO rate constants were found to decrease by between 37-66 % when RH was increased from 0-20 %. No clear trend was found to occur as humidity was increased

further, with all samples' PFO rate constants found to fluctuate at values below that of the dry adsorption experiment.

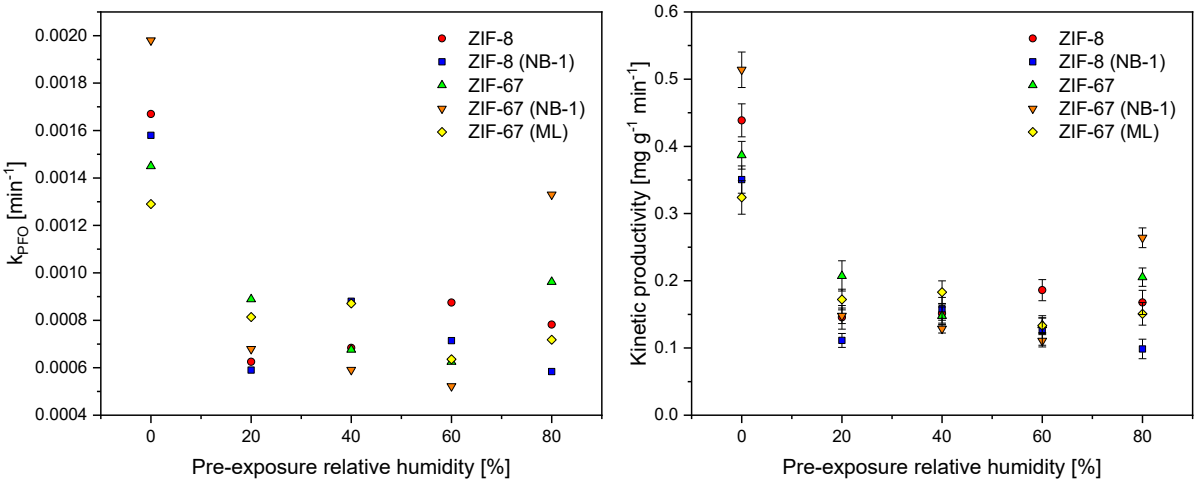


Figure 6.22: Impact of water vapour pre-exposure on pseudo-first order model kinetic parameters (left) and kinetic productivities (right) for toluene adsorption. T = 25˚C, $P/P_{0,\ toluene}$ = 0.005.

This behaviour is likely due to the stable adsorption capacity for toluene, which did not change significantly as pre-exposure humidity was increased from 20-80 %. This is supported by the plots of kinetic productivity as a function of RH in **Figure 6.22**, which followed almost identical trends to the adsorption rate constants. For reference, the kinetic productivities of ZIF-8/67 at 80 % RH pre-exposure are between 0.13-0.33 mg/g min, while kinetic productivities for AC and A88Y at 70 % RH pre-exposure were calculated at 0.54 and 0.13 mg/g min. However, this level of exposure did lead to a > 95 % reduction in capacity for activated charcoal compared to dry conditions- 10.4 mg/g compared to 264.2 mg/g. For this reason, kinetic productivity may not be an altogether reliable method of determining the effectiveness of VOC adsorbents.

Table 6.4: Summary of pseudo first order kinetic rate constants for each adsorbent for different VOC molecules and water vapour. T = 25˚C. Red numbers indicate fits that did not converge.

Adsorbate species		k_{PFO} [min^{-1}]				
		ZIF-8 (Powder)	**ZIF-8 (NB-1)**	**ZIF-67 (Powder)**	**ZIF-67 (NB-1)**	**ZIF-67 (ML)**
n-Hexane [1]		0.0512	0.0456	0.0049	0.0121	0.0057
Methanol [1]		0.0946	0.0214	0.0672	0.0386	0.006
Toluene [1]	0% RH	0.0017	0.0016	0.0015	0.0020	0.0013
	20% RH	0.0006	0.0006	0.0009	0.0007	0.0008
	40% RH	0.0007	0.0009	0.0007	0.0006	0.0009
	60% RH	0.0009	0.0007	0.0006	0.0005	0.0006
	80% RH	0.0008	0.0006	0.001	0.0013	0.0007
Water [2]	20% RH	0.156	0.194	0.088	0.248	0.006
	40% RH	0.184	0.158	0.077	0.165	0.097
	60% RH	0.194	0.063	0.033	0.026	0.105
	80% RH	0.218	0.109	0.159	0.148	0.147

[1] Partial pressure of VOCs in all experiments = 0.005.

[2] Relative humidity varied between 20-80 %.

For MIL-100 adsorbents, the pre-exposure of water vapour at 20 % RH had different effects on toluene adsorption rate constants depending on the material- monolithic samples showing a decrease while powders had an increase in kinetics. All materials were found to have reduced capacities as water vapour adsorbed onto surface sites that could otherwise be occupied by toluene, but the exact mechanism by which this affected kinetics is not clear. As pre-exposure RH increased from 20 to 40 %, the adsorption rate constants for toluene were found to increase in all materials, as shown in **Figure A.30**. This may relate to the filling of the smaller aperture of MIL-100. As these pores can no longer be filled by toluene molecules, the adsorption capacity of the MIL-100 adsorbents decreases- leading to a larger proportion of the adsorption capacity being due to surface filling. This results in changes to the average rate constant for toluene adsorption. No clear trend in water adsorption rate constants with changing relative humidity was found for any sample. MIL-100 presents an interesting case study for kinetics, as different adsorption mechanisms can clearly be defined by the water isotherm of the material- i.e. surface adsorption, large pore filling, small pore filling. Many of these adsorption regions overlap or occur

simultaneously, especially as humidity increases, making accurate assessment difficult as several effects will have an impact on the overall speed at which water is adsorbed, e.g. pore size, pore hydrophobicity, driving force, adsorption mechanism, surface chemistry.

Table 6.5: Summary of pseudo first order kinetic rate constants for all microporous MIL-100 adsorbents for toluene and water vapour. T = 25˚C.

Adsorbate species		**k_{PFO} [min^{-1}]**				
		MIL-100	**MIL-100/ DPA**	**MIL-100/ OPA**	**MIL-100 (NB)**	**MIL-100 (NB)/ DPA**
Toluene [1]	0% RH	0.0009	0.0014	0.0010	0.0012	0.0037
	20% RH	0.0010	0.0020	0.0018	0.0008	0.0022
	40% RH	0.0031	0.0037	0.0039	0.0014	0.0035
Water [2]	5% RH	0.01898	0.0335	0.0204	0.0067	0.0097
	20% RH	0.03198	0.0332	0.0350	0.0112	0.0231
	40% RH	0.00824	0.0071	0.0078	0.0033	0.0070
	80% RH	0.01425	0.0196	0.0147	0.0038	0.0163

[1] Partial pressure of VOCs in all experiments = 0.005.

[2] RH varied between 20-80 %.

6.4. Conclusions

This Chapter explored a modulator-based sol-gel approach for producing ZIF-8, ZIF-67, and MIL-100 monoliths, the first reported procedure based on a review of recent literature. The addition of modulating ligands to the reaction mixtures of ZIF-8 and ZIF-67 was found to reduce the synthesis time noticeably, while producing a sol-gel product that, when dried under ambient pressure, resulted in millimetre to centimetre scale monoliths. MIL-100 monoliths were found to be much larger, in the range of several centimetres, although took significantly longer to form due to the necessity of water as the final cleaning solvent. X-ray diffraction found that while monoliths possessed several of the low-angle characteristic peaks of the base MOF, they had significantly lower crystallinity compared to their powder forms. Scanning electron microscopy confirmed the presence of amorphous material within the monoliths and, in some cases, the lack of any visible crystalline facets.

Despite their reduced crystallinity and the presence of amorphous content, gas adsorption measurements confirmed most monoliths were found to possess surface areas above 900 m^2/g and the characteristic micropore size distributions of ZIF-8/67 or MIL-100. In the case of ZIF-8/67, reductions in the monoliths' calculated surface areas and micropore volumes were offset by their superior bulk density, at least threefold that of ZIF powders, resulting in improved volume-relative surface areas and porosities. The choice of modulating linker(s) also resulted in final materials with differences in pore size distributions. For example, ZIF-67 synthesised using only n-butylamine produced a material with hierarchical porosity, while monoliths synthesised using a combination of n-butylamine and 1-methylimidazole were almost entirely microporous. This ability to tune the pore size distribution of the final monolith by altering the composition of the reaction mixture, and without any necessary post-synthetic modifications, is of particular interest in adsorption fields. On the other hand, MIL-100 (NB) monoliths had a ~50 % reduction in porosity, and a bulk density almost twice that of the powder-resulting in similar volume-relative textural properties between the two forms of the MOF. The addition of alkyl phosphonic acids was also found to reduce the porosity and surface area of the MOF samples, with the addition of DPA and OPA to the sol-gel of MIL-100 (NB) resulting in a much more significant loss in surface area and pore volume compared to the modified powder.

The acid modification of MIL-100 resulted in a significant increase to water contact angle, as did the formation of the monolith- raising the MIL-100 samples' surface wetting to similar levels to ZIF samples, qualifying them as 'hydrophobic'. Water vapour adsorption measurements confirmed the characteristic hydrophobicity of the ZIF and MIL monoliths, with the former adsorbing < 90 mg/g at even the highest RH, and the latter possessing pore filling isotherm steps at similar RHs to the powder. Acid modification, while reducing the water capacity of the MIL samples, also reduced the toluene capacity by a similar extent. This suggests that while improvements could be made to surface hydrophobicity, adsorption hydrophobicity was unaffected, and adsorption was instead impacted by pore blocking or surface area loss from the acid modification.

The reduced surface area and porosity of the monoliths resulted in reduced adsorption capacities for toluene vapour, although the ZIFs' high adsorption hydrophobicity resulted in high efficiency in adsorbing toluene following humidity pre-exposure. Humid capacities were found to exceed 76 % of dry capacities in all cases, further emphasising the application of monolithic ZIFs in indoor air capture. In the case of monolithic adsorbents, their high density resulted in volume-relative capacities between 2.3-3.3 times higher than their respective powder forms. However, the restrictive pore size of ZIF-8/67 resulted in significantly reduced adsorption kinetics for toluene, with fitted kinetics rate constants between 3-30 times lower than for n-hexane. The competitive adsorption of toluene by MIL-100 was found to be strongly dependant on the humidity pre-exposure level, and acid modification was found to not improve the adsorption capacity in two-component experiments. Significant losses in powder and monolith toluene capacity at 20, 40, and 80 % RH were ascribed to pre-exposed water saturating surface, small mesopore, and large mesopore adsorption sites respectively- restricting the number of available sites for toluene. This supports previous assertions that 'hydrophobicity' is not an immutable quality and depends strongly on the material as well as its environment. In addition, the mechanism of adsorption for water vapours appears to influence the extent of competition with toluene observed- although the exact mechanism of this competition will be elucidated in the following Chapter.

Chapter 7: Multicomponent fixed-bed adsorption of dilute VOCs on porous materials

7.1. Introduction

Previously in this thesis, adsorption characterisation had been carried out through gravimetric means, typically using Dynamic Vapour Sorption (Surface Measurement Systems, UK) equipment. This apparatus allows the generation of adsorption isotherms and direct determination of both capacity and kinetic data. The shape of these isotherms can also be used to inform the nature of the interaction between the vapour and solid:

- Strong interactivity, resulting in a steep initial slope and high capacity, e.g. the adsorption of toluene vapour onto activated charcoal.
- Weak interactivity, resulting in low uptake and a type III or IV isotherm due to defects within the mesopores or multilayer surface adsorption, e.g. water vapour adsorption onto ZIF-8.
- Driving force-dependent interactivity, resulting in a type V isotherm caused by the filling of micro- or mesopores by molecules that would typically be repulsed but can be accommodated when a particular driving force or pressure is reached, e.g. the adsorption of light alcohols on zeolite Y or ZIF-8, or the adsorption of water vapour onto MIL-100.

The DVS apparatus allowed for the option of introducing two vapours to the sample simultaneously, which was utilised to pre-expose samples to humidity before a step change in VOC concentration- allowing 'humid capacities' to be determined. However, due to the semi-quantitative nature of multicomponent gravimetric adsorption, the mechanism of adsorption competition could not be determined. In addition, the minimum concentrations reachable using standard DVS equipment was approximately 0.005 P/P_0 which, for toluene vapour, equals a concentration of ~180 ppmv. While these levels well within the maximum short- and long-term limits for workplace VOC exposure [5], they are far higher than WHO-recommended indoor exposure limits [7] or typical elevated concentrations in dwellings [1], typically in the range of 10s-1000s of parts-per-billion.

Breakthrough curve (BTC) analysis is a commonly utilised tool in adsorption science for studying the competitive adsorption of species onto a packed bed of adsorbent, most commonly in solid phase. For

example, Kraus et al [177] used BTC analysis to measure the adsorption capacity of 22 zeolites for toluene vapour with and without the presence of water vapour. This study was accomplished by measuring the outlet toluene and water concentrations via a nondispersive infrared (NDIR) sensor and humidity probe respectively, which allowed the concentrations of each molecule to be determined independently. Walgraeve et al [337] were able to study the adsorption of VOCs onto particulate matter at concentrations below 1 ppm by using selected ion flow tube mass spectrometry (SIFT-MS), a technique known for its high sensitivity to VOC molecules. The methods of concentration determination, i.e. the sensors used in the BTC analyser, not only dictate the species that can be detected, but also what concentration range the technique is applicable to.

Fixed-bed adsorption using pre-diluted VOC gases allows for adsorption data to be collected quickly and at low concentrations. To this end, a bench-top breakthrough analyser was designed and built with the help of Surface Measurement Systems, repurposing equipment and parts from out-of-production DVS equipment as well as developing customisable sensor housing, heating jacket and breakthrough column piping. VOC and water vapour concentrations were detected independently by using a photoionisation detector (PID) and humidity probe respectively in single- and multi-component adsorbate streams. More details about the design and construction of this equipment, as well as sensor testing and adsorption capacity validation experiments, can be found in Chapter 3.

In this Chapter, the bench-top breakthrough analyser (BCA) was used to determine the capacity of industrial and synthesised adsorbents for several vapours at concentrations of 10 ppmv. This not only included the total/ equilibrium/ saturation capacity, comparable to that of DVS, but also the useable capacity which relates to the unused bed length and efficiency of the column. The impact of carrier gas flowrate was investigated to determine an ‘ideal’ condition for maximising mass transfer as well as experimental throughput, using total and useable capacity as metrics. The impact of water vapour on dilute VOC adsorption was determined using the ‘wet adsorbate’ mode, where the VOC and water are combined in vapour phase before being eluted to the sample, in contrast to the ‘wet adsorbent’ mode in gravimetric experiments. The shape of the resultant BTCs allowed for quantitative determination of the total and useable capacities of adsorbents for VOCs in the presence of humidity, and the nature of

competition present. Finally, mathematical models were used to fit experimental BTC datasets to determine parameters related to the capacity and mass transfer within the fixed-bed adsorption process.

7.2. Results and discussion

Experimental BTCs of dilute volatiles were collected for both industrial and synthetic porous adsorbents. These were used to determine the low-concentration adsorption capacity and useability in each vapour-solid system. The impact of relative humidity and cycling on adsorption performance and selectivity was also investigated. Finally, these experimental datasets were fitted to several fixed-bed adsorption models in order to quantify the kinetics and mass transfer effects through the column.

7.2.1. Choice of flowrate for fixed-bed adsorption measurements

To assess adsorbents under consistent process conditions, the flowrate of the carrier gas must be chosen. Due to limitations in the mass flow controller (MFC) manifold, MFCs are only semi-independent. For experiments using a flowrate of 100 mL/min, 50 mL/min from MFC pair 1 (controlling humidity) and 50 mL/min from MFC pair 2 (controlling VOC concentration), the maximum relative humidity possible is 50 %. On the other hand, if a humidity of 80 % is required, the maximum flowrate of pair 2 must be lowered to 10 mL/min, resulting in a total flowrate of 60 mL/min, 50 mL/min of which can be saturated with humidity, resulting in a maximum RH of 83.3 %. However, the flowrate of the carrier gas affects the residence time of the adsorbable phase, e.g. toluene vapour, in the adsorbent bed and may influence the useable and total adsorption capacities depending on the extent of the change to diffusion or mass transfer. Two systems were analysed to test the effect of residence time on BTCs: molecular sieve 13X and water vapour at 50 % RH, where the concentration of adsorbate is high leading to reduced kinetic limitations; and molecular sieve 13X with 10 ppmv of toluene, where kinetic limitations will be apparent. Higher flowrates were used for the toluene experiments (i.e. at least 40 mL/min), due to the relative length of the experiments.

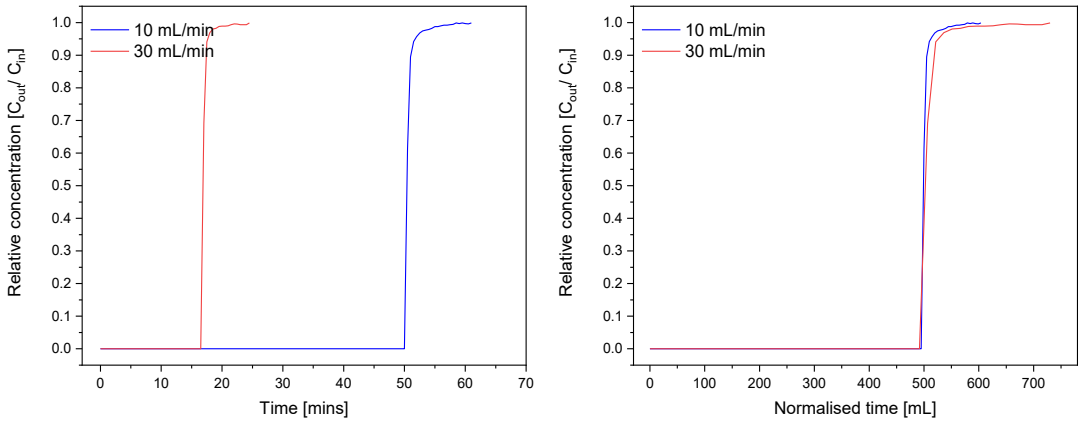


Figure 7.1: Breakthrough curves of water vapour on molecular sieve 13X using carrier gas flowrates of 10 and 30 mL/min. T = 25˚C. Left plot uses standard time axis, right plot normalises axis by flowrate.

When the carrier gas flowrate was increased from 10 to 30 mL/min, the breakthrough time decreased by almost exactly a factor of 3, from 50.5 minutes to 17 minutes. This is due to the increased flowrate, decreased residence time, and faster saturation of the packed bed. However, as seen in the rightmost plot in **Figure 7.1**, the threefold increase in carrier gas flowrate resulted in almost no observable changes in the shape of the water BTC when the axis was normalised by flowrate- although the measured 'useability' of the column was found to decrease from 0.982 to 0.956.

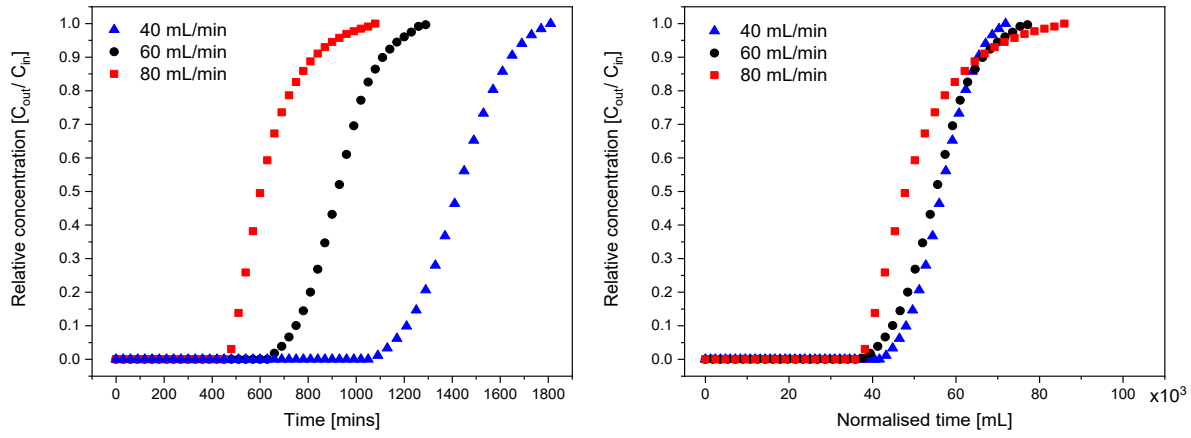


Figure 7.2: Breakthrough curves of 10 ppmv toluene vapour on molecular sieve 13X using carrier gas flowrates of 40, 60, and 80 mL/min. T = 25˚C. Left plot uses standard time axis, right plot normalises axis by flowrate.

Contrastingly, BTCs of toluene vapour were found to vary significantly between flowrates of 60 and 80 mL/min, with the latter having a noticeably gentler slope post-breakthrough and taking much longer than other flowrates to reach a final saturation point when measured using normalised time. This may be due to the system not reaching equilibrium fully, which is supported by the BTCs of 40 and 60 mL/min being almost identical. As flowrate had little impact on the overall shape of the BTCs, as well as the values for useability and capacity, a flowrate of 60 or 40 mL/min is sufficient for the bed to reach equilibrium with the inlet concentration stream.

The 'useability', or fraction of VOC adsorbed pre-breakthrough point compared to the total, of molecular sieve exposed to 40, 60, and 80 mL/min was 0.736, 0.695, and 0.667 respectively. As flowrate increases, the residence time of toluene molecules in the column decreases and the amount of time an adsorbate species has to interact with the porous bed is reduced [77], [338]. While this may result in the bed being saturated more quickly, it also has a negative effect on the column useability. This effect has been observed previously by Pandey et al [338] who found the unused bed length, related to the adsorption occurring post-breakthrough, increased with liquid flowrate. Interestingly, the total capacity, also called the 'saturation' or 'equilibrium' capacity, of the bed was also found to decrease at flowrates of 80 mL/min, which is unusual since the total capacity of a material is expected to be constant for a particular concentration and temperature. However, the same observations were made by Pandey's study and liquid-phase work by López-Cervantes et al [339] who found the total (i.e. saturation) capacity of the adsorbent bed decreased as flowrate was increased. This was credited to a reduced amount of time for the adsorbent to interact with the incoming species. Jafari et al [215] found this effect to occur in gas-phase applications as well, with the adsorption capacity of ZIF-8 for toluene vapour decreasing from 104 mg/g to 47 mg/g as flowrate was increased from 20-50 mL/min. Therefore, unlike passive adsorption in DVS, the residence time of adsorbate molecules at low concentration appears to strongly influence the final capacity. The reason this effect is more prevalent for toluene at low concentrations than water vapour at high concentrations is likely related to the exceptional mass transfer and diffusion for water vapour at these levels. A relative humidity of 50 % is equivalent to around 11.52 $\mu g/cm^3$ of water, whereas 10 ppmv of toluene is equivalent to 0.04 $\mu g/cm^3$ of toluene, 300

times lower than the former. Therefore, residence time is likely a more important factor for adsorption at lower concentration levels. Little difference in saturation capacity was measured for experiments at 40 and 60 mL/min, and useability differed by only 6%. Based on these results, a flowrate of 60 mL/min was chosen for all BTC experiments as this would allow for a humidity up to 83 % to be achieved, while reducing the amount of time taken for the bed to become saturated and therefore increase the experimental throughput of the machine.

Table 7.1: Impact of carrier gas flowrate on breakthrough time and capacities of molecular sieve 13X when exposed to water vapour or toluene at fixed concentrations. T = 25˚C.

System	Inlet concentration	Flowrate [mL/min]	t_B [1] [min]	Useable capacity [2] [mg/g]	Total capacity [mg/g]	Useability
Water	*49.5 ± 0.2*	9.9 ± 0.1	17 ± 0.1	208.6 ± 3.2	212.4 ± 8.1	0.981 ± 0.004
[% RH]	*49.4 ± 0.2*	29.8 ± 0.1	50.5 ± 0.5	203.7 ± 3.3	213.1 ± 7.3	0.960 ± 0.008
Toluene [ppmv]	*10.06 ± 0.10*	39.9 ± 0.1	1170 ± 55	60.3 ± 3.5	81.9 ± 4.2	0.736 ± 0.027
	10.09 ± 0.09	59.8 ± 0.2	720 ± 40	55.2 ± 3.6	79.6 ± 3.9	0.695 ± 0.028
	10.04 ± 0.11	79.6 ± 0.2	480 ± 35	47.8 ± 3.8	72.2 ± 5.3	0.667 ± 0.012

[1] Defined as the time taken for the outlet concentration to reach 5 % of the inlet.

[2] Calculated using time values between 0-t_B

7.2.2. Dilute toluene adsorption by industrial porous materials

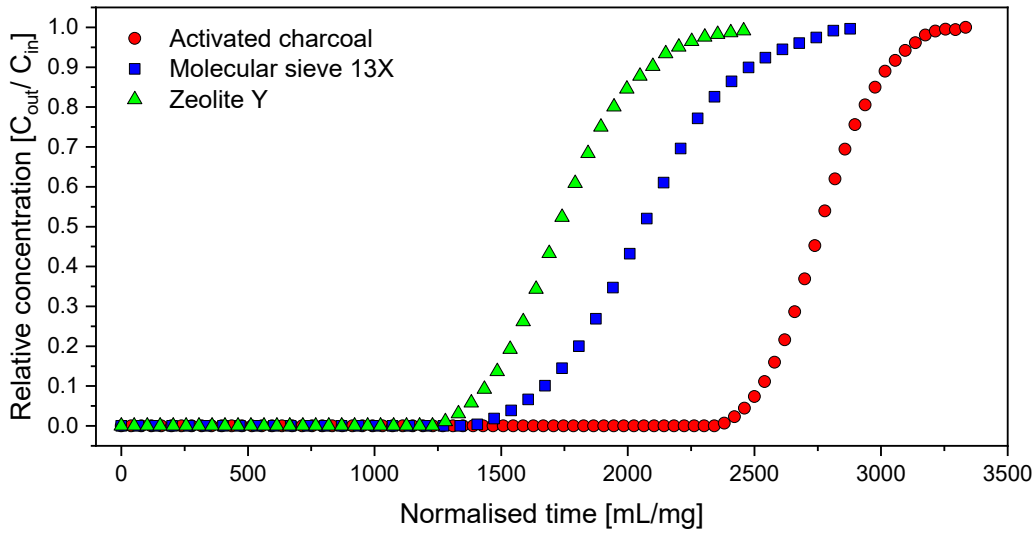


Figure 7.3: Toluene breakthrough curves for industrial adsorbents. Gas flowrate = 60 mL/min. C_{in} = 10 ppmv, T = 25˚C.

As shown by **Figure 7.3**, the breakthrough times for adsorbents followed the trend granulated activated charcoal (GAC) > molecular sieve 13X (MS13X) > zeolite Y (A88Y), with the same trend in total adsorbed quantities of toluene. Despite similar BET surface areas, MS13X exceeded A88Y's total capacity by almost 20 %, which may be linked to the former's greater degree of microporosity. As concentration decreases, the size of pores that can be filled also decreases, making microporous materials more suitable for dilute adsorption. The process that removes framework aluminium from A88Y has also been found to collapse microporous structure, producing additional mesoporosity. However, MS13X's BTC possessed a gentler slope following toluene breakthrough, which is typically associated with poorer kinetics of adsorption in the bed, or a wider mass transfer area through the column. Studies on adsorption of aromatic VOCs by mesoporous ZSM-5 zeolite [340] have found that the presence of mesopores improved the diffusion of bulky molecules into the pores of the material. This may explain the relatively steep slopes of AC and A88Y, despite the latter's poorer total capacity. Therefore, a balancing act is required when considering adsorbents:

- Sufficient microporosity to accommodate large quantities of VOC at dilute levels

- Hierarchical pore structure to facilitate diffusion of molecules into the pores

GAC was found to possess a capacity approximately 33 % higher than MS13X, despite both materials having similar t-plot micropore volumes, 0.214 and 0.209 cm^3/g respectively. One possible explanation for this discrepancy is the superior surface area of GAC (1168 m^2/g) compared to MS13X (666 m^2/g), which would provide a greater number of surface sites to be filled by toluene molecules despite the low concentration. In addition, while MS13X possesses a single micropore aperture in the size range of 0.8-0.9 nm according to NLDFT, granulated GAC possesses heterogenous micropores in the range of 0.5-2 nm. At a concentration of 10 ppmv, pore sizes of > 0.8 nm may only be partially filled, while those < 0.8 nm can utilise their entire volume to accommodate toluene molecules. Finally, as residence time and mass transfer have found to affect the total capacity of the material, the series of heterogenous apertures in activated charcoal may improve the mass transfer and diffusion of incoming molecules onto the adsorption sites of the bed- further increasing capacity. All materials possessed similar bulk densities, between 0.64-0.76 g/cm^3, although the increased density of A88Y was noted to improve its volumetric capacity to a similar level to MS13X.

Table 7.2: Fixed-bed toluene capacities for industrial materials. Flowrate in all experiments set to 60 mL/min. C_{in} = 10 ppmv. T = 25˚C.

Sample	Capacity [mg/g]		Capacity [mg/cm^3] [1]		Useability
	Useable	Total	Useable	Total	
Granular activated charcoal [2]	93.7 ± 4.4	105.9 ± 5.0	71.2 ± 3.8	80.5 ± 4.4	0.886 ± 0.019
Zeolite Y	52.3 ± 2.2	66.8 ± 2.5	38.7 ± 2.3	49.4 ± 2.7	0.789 ± 0.014
Molecular sieve 13X	59.9 ± 3.9	79.5 ± 4.2	37.7 ± 2.7	50.1 ± 3.1	0.751 ± 0.013

[1] Calculated by multiplying capacity by bulk density

[2] Bulk density of GAC determined to be 0.76 ± 0.02 g/cm^3 based on solid-medium displacement

Literature values for granular activated charcoal at concentrations at or below 10 ppm vary between 60-100 mg/g based on a review by Pei & Zhang [189], although many of these experiments were carried out in the presence of between 0-50 % relative humidity which, as noted in previous Chapters and literature, has a negative impact on activated charcoal's capacity for VOCs. Based on these findings,

GAC's calculated total capacity of 105.9 mg/g appears reasonable. No literature data could be found on the capacity of faujasites for toluene at dilute concentrations (i.e. < 50 ppm). However, Shiau et al [341] found that a fixed bed of molecular sieve 10A adsorbed 126.6 mg/g of isopropanol vapour at a concentration of 20 ppm. Therefore, capacities in the range of 50-100 mg/g at dilute toluene levels also appear reasonable for zeolites with sufficiently large pores.

7.2.2.1. Impact of humidity on toluene adsorption by industrial porous materials

To assess the industrial materials under realistic conditions, the packed beds were exposed to a mixture of 10 ppmv of toluene vapour and an RH of either 40 or 80 %. Unlike previous measurements in this project using DVS, this represents the 'wet adsorbate' mode of competitive adsorption, compared to the 'wet adsorbent' mode where samples as pre-exposed to water before adsorbing a VOC.

Water vapour was found to break through almost immediately during the experiment, with breakthrough times of under a minute measured for both 40 and 80 % relative humidity, after subtracting the appropriate dead time for the system. While the experiment at 40 % RH reached saturation quickly, a much gentler slope was measured at 80 %, likely indicating that the higher uptake of GAC at RHs exceeding 50 % (i.e. during the exponential growth region of GAC's type III/V isotherm) is much slower in nature that the initial surface adsorption. As this uptake is often hypothesised to be due to the presence of defects on the surface or within GAC's mesopores [164], the adsorption kinetics for this mechanism may differ from molecules adsorbing through surface adsorption.

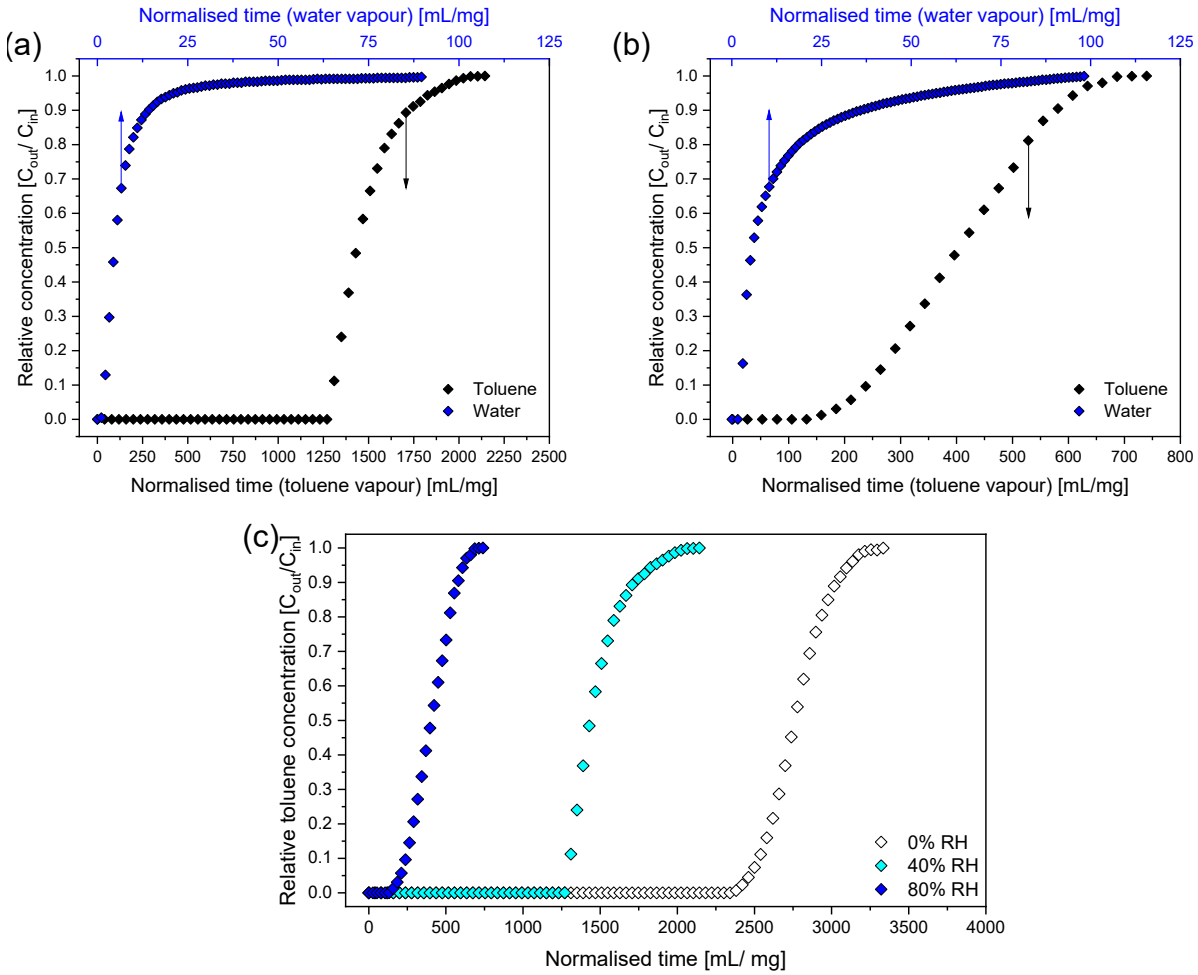


Figure 7.4: Multicomponent breakthrough curves for toluene and water vapour on granular activated charcoal, at concentrations of 10 ppmv and 40 % (a) or 80 % (b) RH. A combined plot of the three toluene vapour breakthrough curves (c) is shown for comparison. Flowrate = 60 mL/min, T = 25˚C.

The BTCs of toluene were found to shift significantly towards smaller times as the relative humidity is increased, resulting in reductions in the total and useable capacities of GAC. The total capacity of GAC was measured at 105.9, 57.0, and 11.2 mg/g at 0, 40 and 80 % RH, or a drop in performance of 46.2 and 89.4 % respectively. The useability of the material appeared to be relative stable between 0-40 % RH (0.886 and 0.861) but dropped to 0.665 as humidity was increased to 80 % RH. This implies that the presence of large quantities of water vapour may hinder the diffusion or transport of toluene molecules into the micropores of the GAC. This mirrors the sharp decrease in pseudo first order kinetic rate parameters for toluene adsorption as humidity increased in Chapter 4, although this was carried out

in the ‘wet adsorbent’ mode- i.e. the worst case scenario where toluene is adsorbed following saturation of water vapour. While the simultaneous exposure of water and toluene affords toluene better opportunity to adsorb than when it is eluted following pre-exposure of water vapour, its driving force in fixed-bed experiments is almost 20 times lower than in gravimetric, which may exacerbate any impact of water vapour on adsorption or diffusion. Interestingly no ‘rollover’ was present in the high-humidity GAC adsorption experiments, despite significant loss in performance. This may be due to water vapour eluting through the column significantly faster than toluene, as seen in the water breakthrough times at 40 and 80 % RH being under 10 mL/mg, while toluene takes at least 100 mL/mg to breakthrough regardless of humidity. As water elutes much faster, toluene is unable to occupy a significant number of adsorption sites during this time, preventing any pre-adsorbed molecules from being displaced.

A88Y was found to have a similar change in water breakthrough profile to GAC when moving from 40 to 80 % relative humidity, resulting in the water capacity useability decreasing from 0.769 to 0.536. Similar to GAC, A88Y begins to adsorb greater quantities of water vapour at higher RHs due to the presence of mesopores with more hydrophilic surface chemistry than the framework’s micropores. Similar to Chapter 4, A88Y was found to have a reduction in performance as humidity was increased from 0 to 40 %, total capacity decreased from 66.8 mg/g to 54.5 mg/g, but remained largely constant from 40 to 80 % RH, only decreasing to 52.7 mg/g. A88Y’s hydrophobic micropores prevent the ingress of water molecules, resulting in adsorption sites only accessible by non-polar species such as toluene. The initial drop in performance may be due to some toluene adsorbing onto surface sites that water can access, or that framework defects allow for some water to adsorb in or close-to the micropores of the zeolite. The dealumination process, which improves the hydrophobicity of the final material by removing framework aluminium, results in the collapsing of micropores to form hierarchical porosity, and can introduce extra-framework alumina and amorphous silica-alumina [44], both of which can interact more strongly with water vapour. However, this effect appears to only be present as humidity is initially increasing, implying that the majority of toluene molecules are located within defect-free

micropores. Similar to GAC, the lack of rollover can likely be explained by the relatively fast elution of water through the zeolite bed compared to toluene.

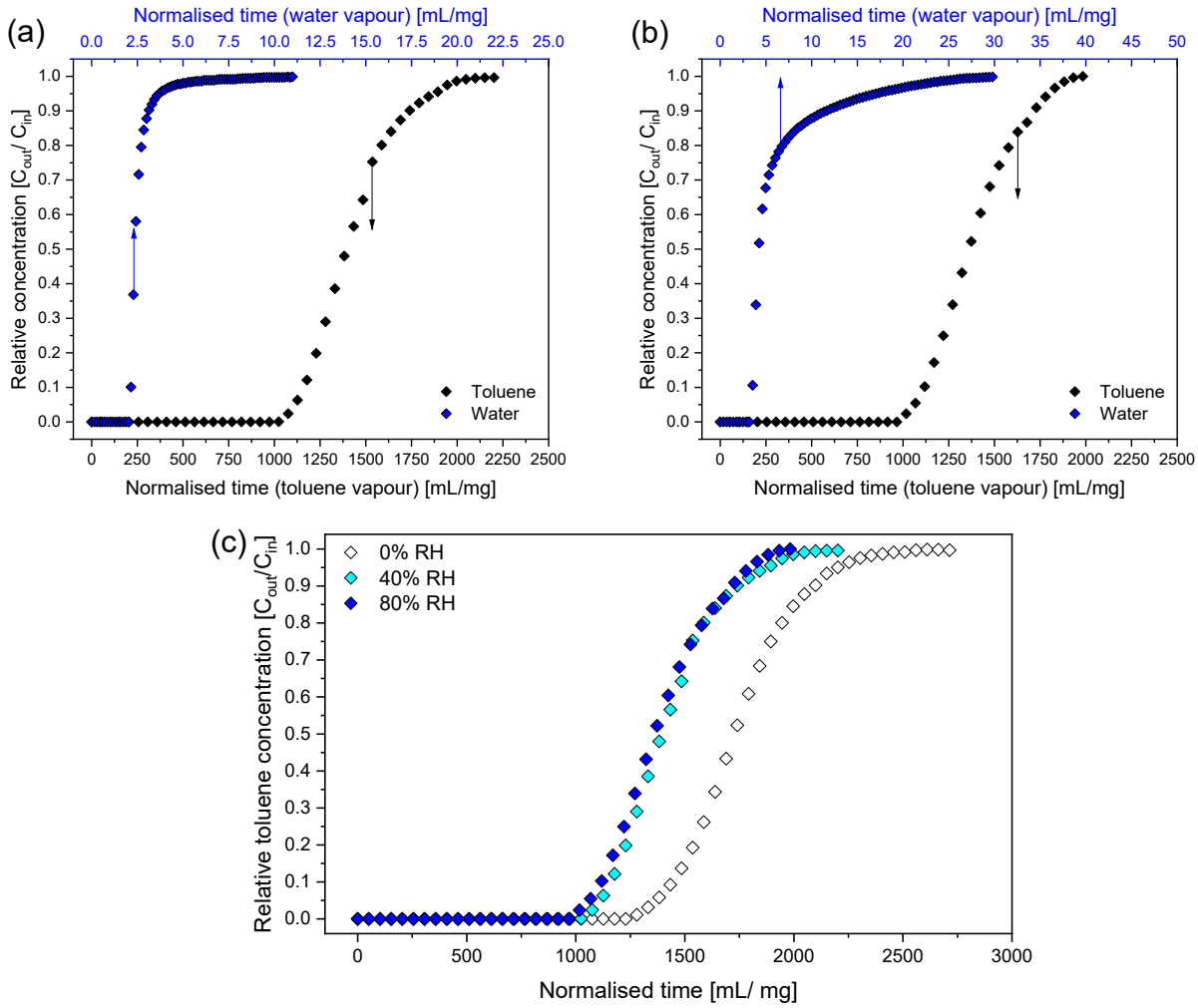


Figure 7.5: Multicomponent breakthrough curves for toluene and water vapour on zeolite Y, at concentrations of 10 ppmv and 40 % (a) or 80 % (b) RH. A combined plot of the three toluene vapour breakthrough curves (c) is shown for comparison. Flowrate = 60 mL/min, T = 25˚C.

MS13X present the most interesting humid BTCs, with the outlet toluene concentration increasing above that of the inlet. This 'rollover' effect can be described by the water vapour interacting more strongly with the adsorbent surface compared to toluene, leading to the latter being displaced from their adsorption sites. These outgoing toluene molecules combine with those from the inlet, resulting in an increase in concentration above what would be expected. This phenomenon has been observed in

several adsorption systems where adsorption selectivity for one compound is significant, either based on size [78] or chemistry [342]. Similar behaviour by molecular sieve 13X has been observed by Kraus et al [177] at a toluene concentration of 216 ppmv and a relative humidity of 64 %, resulting in a total adsorption capacity of below 2.5 mg/g. In this work the capacity for toluene by MS13X was measured to be 79.5 mg/g and 0.26 mg/g at 0 and 40 % RH, the latter of which was calculated by integrating the BTC around the C_{out}/ C_{in} line of 1, i.e. adding any area under the line and subtracting any area above it. As no information regarding how much of the displaced toluene was pre- or post-breakthrough, no accurate determination for useability could be made.

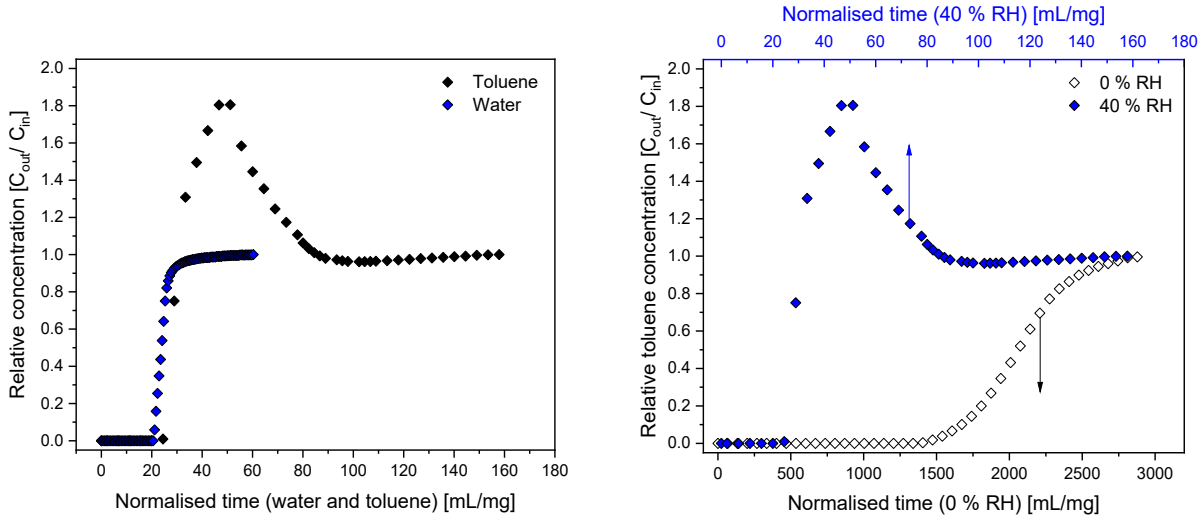


Figure 7.6: Multicomponent breakthrough curves for toluene and water vapour on molecular sieve 13X, at concentrations of 10 ppmv and 40 % RH (left). A combined plot of the toluene vapour breakthrough curves (right) is shown for comparison. Flowrate = 60 mL/min, T = 25˚C.

When accounting for the density of the adsorbents, few changes were observed in the performance trends as A88Y and GAC possessed similar capacities for toluene at 40 % RH while also possessing similar bulk densities. In addition, the significant losses in performance of GAC and MS13X at 80 and 40 % RH respectively could not be offset by the sample density. Interestingly, the trends in uptake largely follow those found in Chapter 4 in dual-solvent gravimetric experiments, despite the lower concentration in the BTC experiments.

Table 7.3: Fixed-bed capacities for toluene vapour for multicomponent vapour mixtures on industrial adsorbents. Experiments carried out in 'wet adsorbate' mode where toluene and water vapour were eluted simultaneously through the adsorbent bed. Flowrate = 60 mL/min. C_{in} = 10 ppmv. T = 25˚C.

Sample	Humidity [% RH]	Capacity [mg/g]		Useability
		Useable	Total	
Granular activated charcoal	0	93.7 ± 4.4	105.9 ± 5.0	0.886 ± 0.019
	39.5 ± 0.3	49.2 ± 2.9	57 ± 4.3	0.861 ± 0.023
	79.4 ± 0.5	7.5 ± 0.9	11.2 ± 1.1	0.665 ± 0.024
Zeolite Y	0	52.3 ± 2.2	66.8 ± 2.5	0.789 ± 0.014
	39.7 ± 0.2	42.5 ± 1.8	54.5 ± 2.1	0.784 ± 0.009
	79.5 ± 0.4	40 ± 1.7	52.7 ± 2.4	0.758 ± 0.010
Molecular sieve 13X	0	59.9 ± 3.9	79.5 ± 4.2	0.751 ± 0.013
	39.8 ± 0.2	0.9 ± 0.1	0.3 ± 0.1 (0.9 ± 0.1 [1])	N/A [2]

[1] Quantity of toluene displaced during multicomponent experiment

[2] Could not be determined due to significant rollover in BTC

7.2.3. Dilute toluene adsorption by powder and monolithic ZIFs

Monolithic and powder ZIFs were found to have similar BTC profiles, with a gentle slope post-breakthrough before reaching saturation. This led to much lower useability than industrial adsorbents, all below 0.55. Despite this, all ZIFs were found to have exceptional total toluene capacities of at least 72 mg/g. BTCs of toluene vapour on ZIF-8 by Jafari et al [215] found similarly low useability in the adsorbents, with higher flowrates resulting in faster breakthrough times and a reduction in the useable capacity of the adsorbent. The highest adsorption capacity measured, for a toluene concentration of 100 ppmv and a flowrate of 50 mL/min, was approximately 47 mg/g- noticeably lower than the results of this work. However, an important distinction is the nature of the ZIF-8 adsorbent in Jafari's work- the BET surface area and total pore volume of the powder ZIF-8 was calculated as 847 m^2/g and 0.32 cm^3/g. The surface area of the ZIF-8 powder studied here is 1812 m^2/g, 114 % higher than that of Jafari, and the total pore volume is 1.667 cm^3/g, a 421 % increase. However, the ZIF-8 in Jafari's work showed no increase in nitrogen capacity at high pressures, suggesting it is entirely microporous. Even when using

only the micropore volume of the ZIF-8 in this work, 0.521 cm^3/g, it still exceeds that of Jafari's by 63 %. Therefore, direct comparisons between the adsorbents are difficult to make. In addition, while the ZIF-8 in Jafari's work had a noticeably lower useability, the material's lack of mesopores, overall lower porosity and surface area, and significantly higher crystal size (~ 2 µm compared to < 100 nm crystals in this work) may have led to reduced mass transfer into the pores [42].

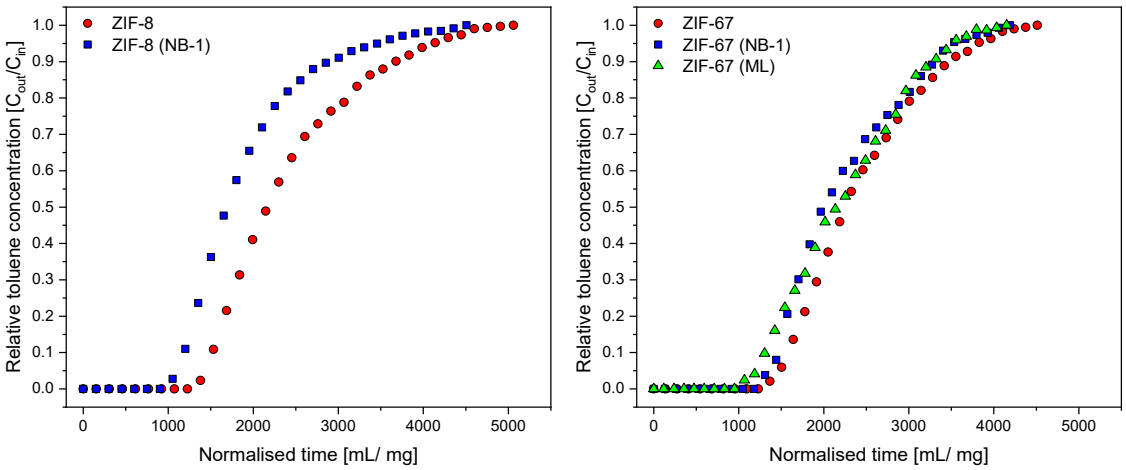


Figure 7.7: Toluene breakthrough curves for zinc (left) and cobalt (right) ZIF adsorbents at 10 ppmv. Flowrate = 60 mL/min, T = 25˚C.

The ZIF monoliths formed using n-butylamine were found to have lower total and useable capacity than their respective powders, although possessing similar fractional useability- i.e. ZIF-8 and ZIF-8 (NB-1) had useabilities of 0.604 and 0.586 respectively, while ZIF-67 powder and ZIF-67 (NB-1) had useabilities of 0.607 and 0.601 respectively. This suggests similar mass transfer of toluene into the pores of the monolithic ZIFs compared to the powders, despite the introduction of hierarchical porosity into the former. It is possible that while the monoliths have a network of random pores, their reduced microporosity and presence of amorphous content may offset any increase in accessibility to the micropores by the hierarchical nature of their pore volume. This is supported by ZIF-67 (ML) with its lower useability of 0.520- this material has been found to have noticeably lower crystallinity and, despite possessing a high degree of microporosity, contained negligible amounts of mesoporosity, hierarchical or otherwise. ZIF-67 therefore presents an interesting case study for how amorphous

content in modulator-derived monoliths affects the mass transfer of adsorbate species into their micropores.

When accounting for the density of the ZIF adsorbents, the advantages of the synthesised monoliths becomes more apparent- with at least a 140 % increase in total capacity measured for all ZIF systems. The highest total capacity measured was ZIF-67 (ML) at 110.0 mg/cm^3, exceeding all industrial adsorbents as well as ZIFs. The highest useable capacity was ZIF-67 (ML) at 57.8 mg/cm^3 which, while higher than industrial zeolites, was approximately 20 % lower than GAC. This suggests that while monolithic ZIFs can be effective for gradually reducing the concentration of aromatic VOCs, they have poorer column efficiency than industrial charcoals due to their poorer mass transfer.

Table 7.4: Fixed-bed toluene capacities for ZIF materials. Flowrate = 60 mL/min. C_{in} = 10 ppmv, T = 25˚C.

Sample	Capacity [mg/g]		Capacity [mg/cm^3] [1]		Useability
	Useable	Total	Useable	Total	
ZIF-8	54.5 ± 3.7	90.6 ± 5.4	21.2 ± 1.8	35.3 ± 2.8	0.604 ± 0.024
ZIF-8 (NB-1)	42.2 ± 3.6	72.5 ± 4.0	49.4 ± 5.4	84.8 ± 7.5	0.586 ± 0.019
ZIF-67 [2]	55.5 ± 4.9	91.6 ± 6.6	21.1 ± 2.2	34.8 ± 3.1	0.607 ± 0.029
ZIF-67 (NB-1) [2]	50.9 ± 3.7	84.8 ± 5.0	56.6 ± 5.8	94.1 ± 8.8	0.601 ± 0.016
ZIF-67 (ML)	45.1 ± 3.2	85.9 ± 5.8	57.8 ± 4.3	110.0 ± 7.9	0.520 ± 0.021

[1] Calculated by multiplying capacity by bulk density

[2] Number of repeat measurements, N =2

7.2.3.1. Comparison of n-hexane and toluene breakthrough curves

As shown in the kinetic analysis of VOCs in Chapter 6, n-hexane was found to be adsorbed much faster by ZIF-8 and ZIF-67 than toluene vapour was, credited to the former's smaller kinetic diameter and ease of passage into the flexible pores of the ZIF framework. To investigate whether this effect is observable in fixed-bed systems at dilute concentrations, BTC experiments were carried out for n-hexane vapour at the same concentration of 10 ppmv.

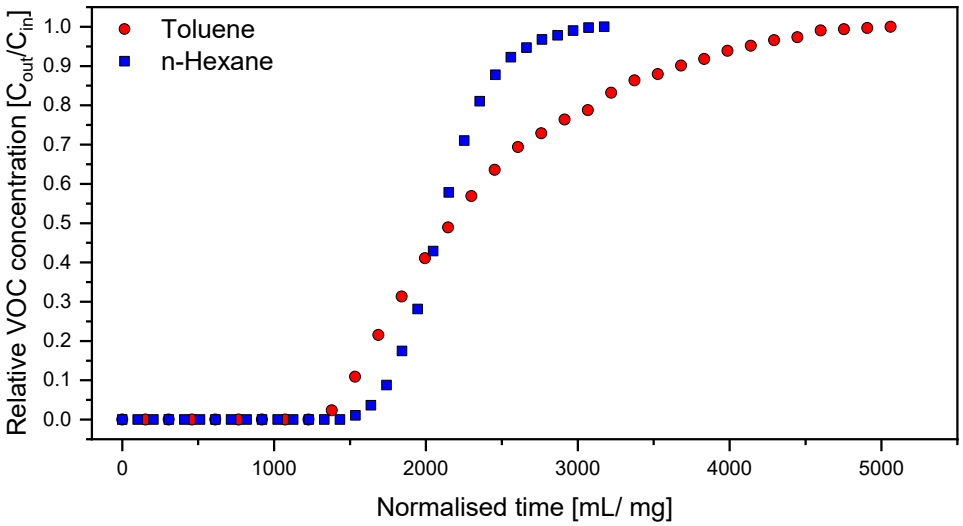


Figure 7.8: Breakthrough curves for toluene and n-hexane on ZIF-8 powder, carried out in separate single-component experiments at 10 ppmv. Flowrate = 60 mL/min, T = 25˚C.

While the total capacity at saturation for n-hexane was measured to be 74.5 ± 2.1 mg/g, around 18 % lower than the same quantity for toluene, the useable capacity was approximately 9 % higher, at 59.4 ± 1.8 mg/g. The reduction in saturation capacity can be explained by the lower molecular weight of n-hexane compared to toluene, 86 g/mol and 92 g/mol respectively, resulting in a lower magnitude of London dispersion forces available for non-polar adsorption interactions [182], the primary means of interaction for ZIF-8 due to its hydrophobic nature. The higher useable capacity, and by extension the higher useability of 0.799 ± 0.023, supports the hypothesis that the pore aperture of ZIF-8 and ZIF-67, while flexible, limits the adsorption kinetics of bulkier molecules into the micropores. Molecules with sufficiently small kinetic diameters, such as n-hexane, have improved mass transfer into the pore volume of the material and results in higher column efficiency, similar to that of industrial zeolites adsorbing toluene.

7.2.3.2. Impact of humidity on toluene adsorption by ZIF adsorbents

Due to the similar hydrophobicity of powder and monolithic adsorbents, only ZIF-8, ZIF-8 (NB-1) and ZIF-67 (ML) were investigated for the effect of modulating ligand on humid performance. In addition, based on similar humid toluene adsorption efficiencies at mid and high levels of humidity, ZIF-8 (NB-1) and ZIF-67 (ML) toluene adsorption experiments were only carried out at the most extreme condition of 80 % RH.

Water BTCs could not be accurately determined for ZIF-8, ZIF-8 (NB-1), or ZIF-67 (ML) at either 40 or 80 % relative humidity. Due to the incredibly hydrophobic nature of the adsorbents, adsorption capacities in the range of 2-20 mg/g result in breakthrough times < 1 minute for all samples. This breakthrough time is of the same magnitude as the estimated dead time of the humidity probe, between 30-60 seconds depending on flowrate and humidity- this led to significant standard deviations in measured water capacities in the range of 50-120 % of the value. It is estimated that approximately 800 mg of sample would be required to collect an accurate breakthrough of water vapour on ZIF-8/ 67, which has two drawbacks:

- A high quantity of sample is required, leading to significant pressure drop in powder samples
- The length of the toluene breakthrough experiment would be extended by ~20-40 times, resulting in a timeframe of several weeks per experiment, which is unfeasible

For these reasons, and that the important data is the impact of water on the toluene BTC, rather than the water BTC, the mass of sample was kept the same as dry experiments and only the outlet concentration data for toluene vapour is shown in multicomponent ZIF plots.

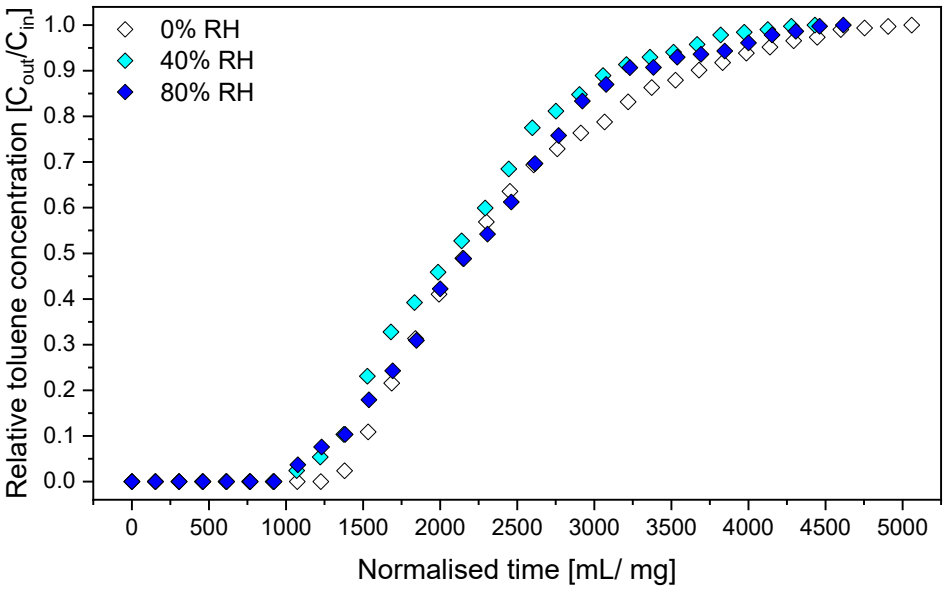


Figure 7.9: Multicomponent breakthrough curves for toluene and water vapour on ZIF-8 powder, at concentrations of 10 ppmv and 40 % or 80 % RH. Flowrate = 60 mL/min, T = 25˚C.

As shown in **Figure 7.9**, water vapour was found to have minimal impact on the BTCs of toluene vapour on ZIF-8 powder, with similarly gentle slopes following breakthrough. Humidified experiments were found to break through approximately an hour faster than those in dry conditions, resulting in a reduction in useable capacity- however, the overall loss in total saturation capacity was only 9.2 and 10.3 % for 40 % and 80 % RH respectively. Losses in total capacity from dry to humid may be due to similar phenomena in the zeolite Y system, i.e. loss of surface hydrophilic sites that water may occupy over toluene, the presence of defect sites, or the surface-bound water preventing some ingress of water molecules. The former two effects do not appear to be exacerbated upon increasing the relative humidity from 40-80 %, as the total capacity only drops from 82.3 mg/g to 81.3 mg/g. However, the useability did drop considerably from 0.570 to 0.465. This may indicate that the presence of large amounts of water vapour adsorbed on surface sites reduces the mass transfer of toluene molecules into the micropores of the ZIF framework. Water isotherms on ZIF adsorbents show a marked increase at higher pressures, typical of type III isotherms, likely due to water forming multilayers on the surface- this

sudden increase in surface water content may exacerbate any mass transfer limitations the flexible ZIF pores impose on adsorbing toluene molecules.

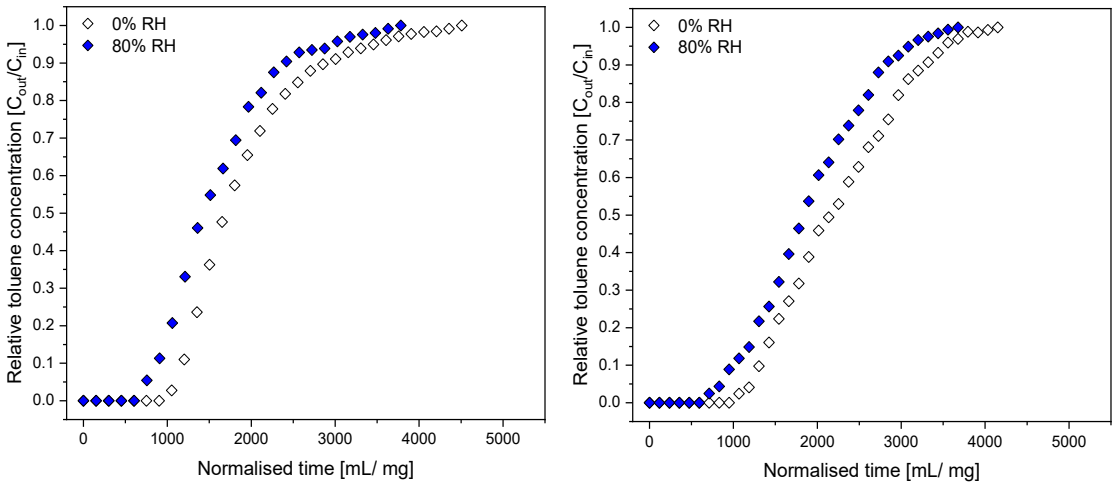


Figure 7.10: Multicomponent breakthrough curves for toluene and water vapour on ZIF-8 (NB-1) (left) and ZIF-67 (ML) (right), at a toluene concentration of 10 ppmv and 0 and 80 % RH. Flowrate = 60 mL/min. C_{in} = 10 ppmv, T = 25˚C.

More significant losses in performance were measured for ZIF-8 (NB-1) and ZIF-67 (ML) monoliths, with their respective total adsorption capacities decreasing to 60.4 mg/g (-16.7 %) and 73.1 mg/g (-14.9 %). This is likely due to the reduced crystallinity of these materials and a greater quantity of framework defects due to monodentate linkages between zinc and either n-butylamine or 1-methylimidazole. Therefore, while water vapour is not able to enter the micropores of the ZIF-8/67, these surface defects can accommodate their polar interactions. ZIF-8 (NB-1) and ZIF-67 (ML) had useability values of 0.465 (-20.6 %) and 0.453 (-13.7 %), further supporting that the adsorption of water vapour at higher RHs likely has an impact on the mass transfer of toluene molecules into the ZIFs' micropores. ZIF-67 (ML), despite possessing almost no mesoporosity, presents both a type III water isotherm and a loss in useability at high humidities- it can be inferred from this that the impact of water vapour on toluene mass transfer from multilayer surface adsorption is significant.

Table 7.5: Fixed-bed capacities for toluene vapour for multicomponent vapour mixtures on ZIF adsorbents. Experiments carried out in 'wet adsorbate' mode where toluene and water vapour were eluted simultaneously through the adsorbent bed. Flowrate = 60 mL/min. C_{in} = 10 ppmv. T = 25˚C.

Sample	Humidity [% RH]	Capacity [mg/g]		Useability
		Useable	Total	
ZIF-8	0	54.5 ± 3.7	90.6 ± 5.4	0.604 ± 0.024
	39.8 ± 0.2	47.1 ± 2.6	82.3 ± 3.8	0.570 ± 0.021
	79.7 ± 0.4	37.7 ± 1.9	81.3 ± 2.8	0.465 ± 0.018
ZIF-8 (NB-1)	0	42.2 ± 3.6	72.5 ± 4.0	0.586 ± 0.019
	79.5 ± 0.3	28.3 ± 1.2	60.4 ± 2.4	0.465 ± 0.017
ZIF-67 (ML)	0	45.1 ± 3.2	85.9 ± 5.8	0.525 ± 0.021
	79.8 ± 0.3	33.2 ± 1.9	73.0 ± 2.5	0.453 ± 0.030

Again, when the density of the materials was considered, the volume-relative toluene capacities for monolithic samples were found to far exceed that of the powders. At 80 % RH, the total adsorption capacities of ZIF-8, ZIF-8 (NB-1) and ZIF-67 (ML) were calculated to be 31.7, 70.7, and 93.6 mg/cm^3.

7.2.4. Dilute toluene adsorption by MIL-100

MIL-100 powder was found to be much coarser than ZIF powders, and had no measurable pressure drop when exposed to a carrier gas flowrate of 60 mL/min. MIL-100 powder was determined to have useable and total toluene adsorption capacities of 59.6 and 81.6 mg/g respectively, and an average fractional useability of 0.732 ± 0.011. The BCA profile of MIL-100 was similar to those of industrial adsorbents, with a much less extended mass transfer area compared to ZIF adsorbents and had a total toluene capacity of MIL-100 similar to that of MS13X. This is despite MIL-100's BET surface area and micropore volume (2007 m^2/g and 0.688 cm^3/g) being 3 and 3.3 times greater than that of MS13X (666 m^2/g and 0.209 cm^3/g) respectively. This may be due to incomplete filling of MIL-100's pores- whilst the two micropore windows have sizes between 5-13 Å, the mesopores have a much higher diameter (18- 27 Å) than the single aperture of molecular sieve 13X (0.9 Å). MIL-100 was also found to have a much broader distribution of pore volume in its pores compared to MS13X. Under-utilisation of the pore volume in MIL-100 would lead to a performance lower than expected by its total pore volume.

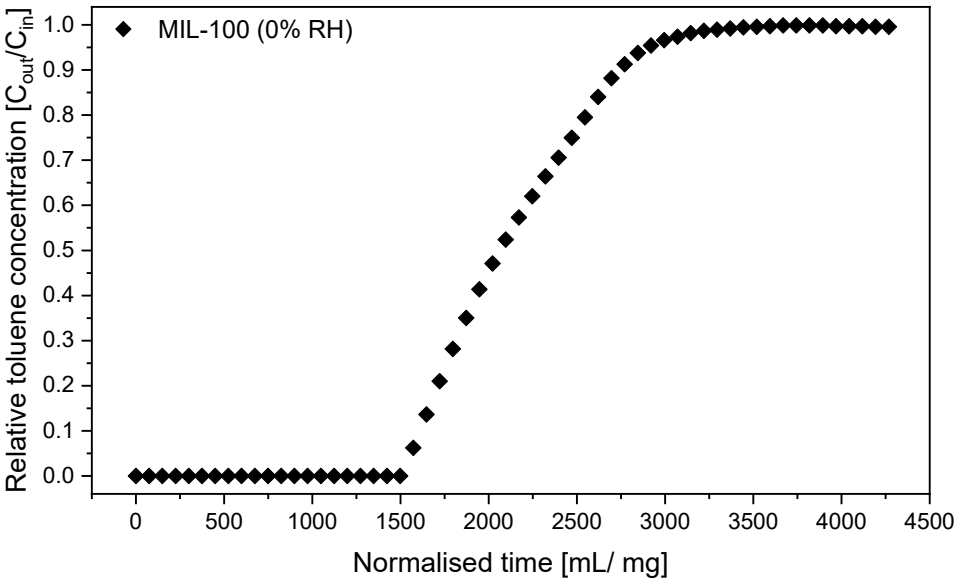


Figure 7.11: Toluene breakthrough curves for MIL-100 powder at 10 ppmv. Flowrate = 60 mL/min, T = 25˚C.

After a thorough review of the literature, no low-concentration VOC adsorption studies could be found for MIL-100. However, dilute adsorption of aromatic vapours in both dry and humid conditions has been studied on MIL-101. To understand how the capacities of MIL-101 and MIL-100 for dilute VOCs compare, literature studies on their VOC adsorption performance at higher concentrations must be considered. MIL-101 has been found to possess lower adsorption capacity for of VOCs compared to MIL-100 as concentration decreases, due to the difficulty of filling the larger micropores of MIL-101 [201]. MIL-101's micropore windows have diameters of ~12 and ~16 Å compared to MIL-100's ~5 and ~9 Å, according to molecular simulations [201]. Trung et al's work [201] found that these larger pores resulted in a noticeable 'step' in the isotherms of even linear alkanes as partial pressure decreases below 0.2 (at a temperature of 30˚C). Therefore, while the Langmuir surface area of MIL-100 is lower than that of MIL-101, 3000 m^2/g and 4800 m^2/g respectively, MIL-100 may have comparable capacity for aromatic molecules in dilute conditions due to the ease of filling its micropores compared to MIL-101. A BTC study by Zhu et al [343] measured the capacity of MIL-101(Cr) and a novel MIL adsorbent, MIL-Z1 (Cr) for benzene vapour at a concentration of 25.6 x 10^{-6} mmol/mL, or ~ 2 ppm, at relative

humidity values of 5, 40, and 60 % RH. An important note is that the novel MIL adsorbent had a minimum pore size of approximately 7 Å, in-between that of MIL-100 and MIL-101. At the lowest humidity of 5 %, MIL-101 and MIL-Z1 adsorbed approximately 262 and 254 mg/g respectively. However, single-component adsorption experiments on MIL-101 by Zhao et al [344] measured capacities in the range of 100-200 mg/g at significantly higher concentrations, i.e. $0.005 < P/P_0 < 0.01$.

There appear to be large disparities in the literature for the VOC adsorption capacity of MOFs, especially at dilute concentrations. However, a calculated total capacity of 81.6 mg/g for MIL-100 can be considered reasonable and does not appear to be overestimated compared to the literature. The lower capacity of MIL-100 for toluene compared to MIL-101 for benzene may be due to steric limitations of the toluene molecule into the pores of MIL-100 at lower concentrations, or the higher specific surface area of MIL-101 resulting in a greater adsorption capacity.

7.2.4.1. Impact of humidity on toluene adsorption by MIL-100

MIL-100 has a unique isotherm shape when exposed to water vapour, due to the filling of its small and large pores at different RHs. The pores of MIL-100, while hydrophobic, are not able to completely repel water vapour molecules with significant enough driving forces. At 25˚C The filling of MIL-100's small and large pores occur at RHs between 25-30 % and 40-45 % respectively. For this reason, the adsorption capacity of MIL-100 for toluene vapour was assessed at 3 humidity values:

- 20 % RH, before water can access the smaller pentagonal window and only adsorbs via interacting with surface defects Fe sites and pre-adsorbed water molecules.
- 40 % RH, after the filling of the smaller mesopore via pentagonal windows but before the filling of the larger mesopore.
- 80 % RH, after the filling of all mesopores and when water can access all aperture windows.

The BTCs of water vapour on MIL-100 at 40 and 80 % RH were found to have a distinct shape compared to BTCs at 20 % RH, possessing a visible 'step' in the profile. This extension of the breakthrough curve has been observed in a study by Bozbiyik et al [345] in which an aluminium fumarate MOF with similar water isotherm shape to MIL-100 was analysed. The water BTC at 14 %

RH followed the same trend as MIL-100 at 20 % RH, while BTCs at 39 and 75 % RH possessed a similar step. This step is likely due to the filling of the smaller aperture of MIL-100, as it occurs at a partial pressure above the critical filling pressure for water on MIL-100. Similarly, the step in at 80 % RH likely is linked to the filling of both mesoporous apertures in MIL-100.

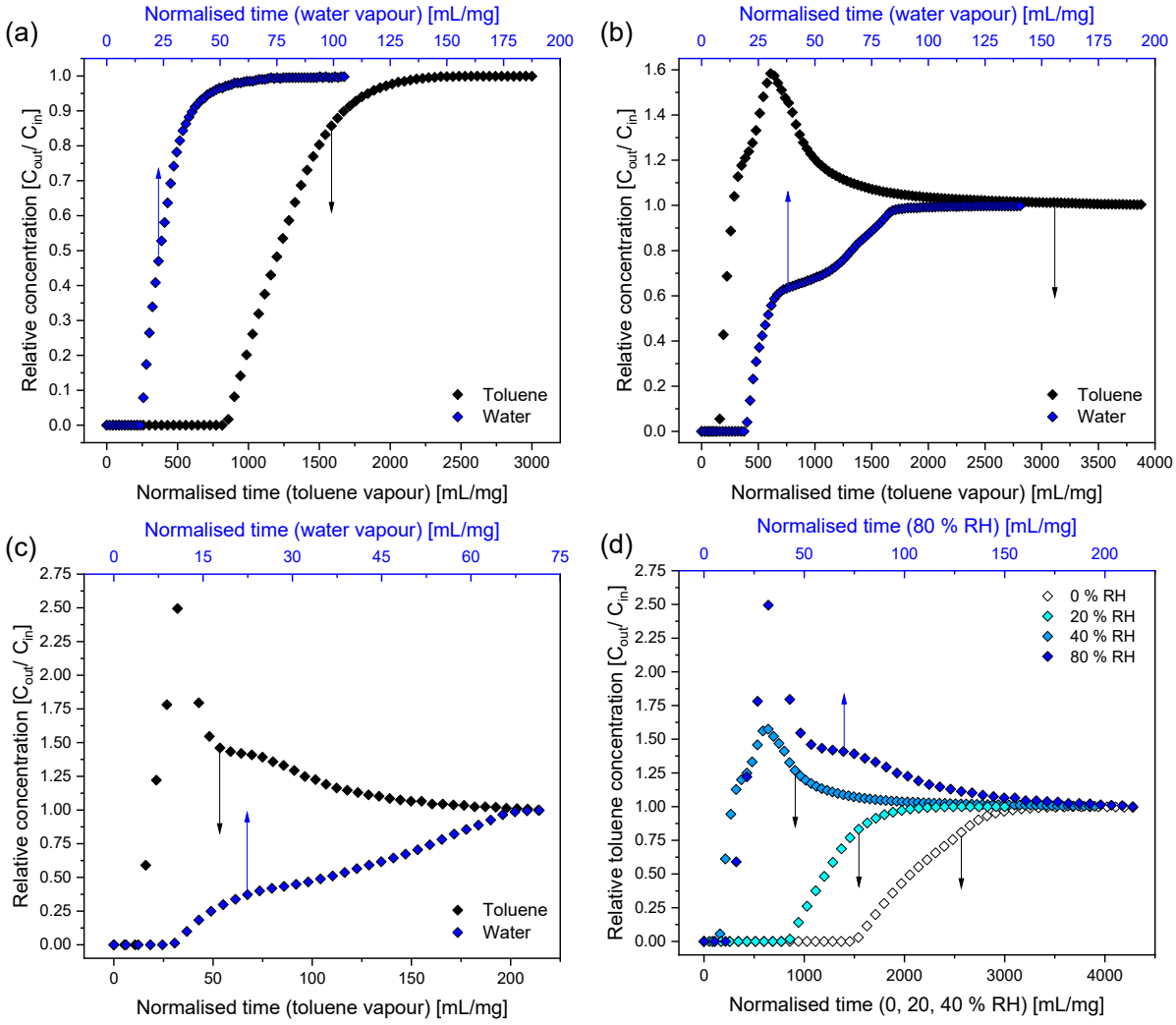


Figure 7.12: Multicomponent breakthrough curves for toluene and water vapour on MIL-100, at concentrations of 10 ppmv and 20 % (a), 40 % (b), and 80 % (c) RH. A combined plot of the four toluene vapour breakthrough curves (d) is shown for comparison. Flowrate = 60 mL/min. T = 25˚C.

The mechanism of competition between water and toluene molecules in MIL-100 appeared to be humidity dependant. Increasing the humidity from 0-20 % RH resulted in the total capacity decreasing

from 81.6 mg/g to 47.9 mg/g, or a reduction of 41.3 %. Based on MIL-100's water isotherm, an RH of 20 % results in water molecules adsorbing onto the external surface of the framework but not filling either of its pores. The loss of toluene capacity implies that some toluene molecules reside on the surface of the MOF, the sites of which were at least partially saturated with water molecules, resulted in a lower number of surface-adsorbed toluene. The fractional useability of MIL-100 at 20 % RH was calculated as 0.711, only 3 % lower than that of MIL-100 in dry conditions. If surface water molecules did inhibit toluene molecule's ability to enter the micropores, this would likely lead to poorer mass transfer into those pores, and a reduction in useability- a decrease of only 3 % likely reflects that the loss of surface toluene sites is a greater contributor to capacity loss than pore filling inhibition.

Increasing the humidity from 20-40 % or 20-80 % resulted in the mechanism of competition shifting to a displacement process, with significant rollover of toluene visible at both humidity values. This resulted in net total capacities of approximately 7.8 mg/g and 0.6 mg/g at 40 and 80 % RH respectively, or a decrease of 92.3 % and > 99 % respectively. As mentioned previously, humidity values of 40 and 80 % RH result in the filling of at least one or both framework apertures by water vapour. The displacement of toluene at these humidities implies that a significant quantity of toluene was adsorbed into these pores, and that the interaction strength between MIL-100's framework apertures and toluene was weaker than the interaction of the apertures with water vapour. Therefore, while the accessible microporous windows may have largely dispersive character, resulting in a particular driving force being required to penetrate them, the internal chemistry of the mesopores appears to have at least some polar character at elevated RHs. Compared to the results in Chapter 5, the impact of humidity is much more significant in these dilute conditions, as MIL-100 retained approximately 15 % of its dry capacity at 40 % RH. This disparity could be due to the higher concentration of toluene, resulting in toluene molecules occupying a larger proportion of sites in the larger aperture of MIL-100, which is not filled by water vapour at 40 % RH. However, both gravimetric and BTC experiments show that MIL-100 adsorbs negligible quantities of toluene at a relative humidity of 80 %. Interestingly, the quantity of 'displaced' toluene at 80 % appeared to be lower than at 40 %, 2.0 mg/g and 14.1 mg/g respectively. This suggests that a greater proportion of the competition occurred via water occupying toluene sites

prior to toluene attempting to adsorb, i.e. that water was able to reach and interact with these sites faster than toluene. With the concentration of water increasing by a factor of two, the mass transfer to the micropores of MIL-100 is likely to be higher due to increased driving force, while the driving force for toluene to reach these micropores is unchanged at 10 ppmv.

Table 7.6: Fixed-bed capacities for toluene vapour for multicomponent vapour mixtures on MIL-100. Experiments carried out in 'wet adsorbate' mode where toluene and water vapour were eluted simultaneously through the adsorbent bed. Flowrate = 60 mL/min. C_{in} = 10 ppmv. T = 25˚C.

Sample	Humidity [% RH]	Capacity [mg/g]		Useability
		Useable	Total	
MIL-100	0	59.6 ± 4.2	81.6 ± 5.6	0.732 ± 0.011
	19.9 ± 0.1	34.0 ± 2.3	47.9 ± 2.9	0.711 ± 0.013
	39.5 ± 0.2	6.2 ± 0.9	7.8 ± 1.1 (14.1 ± 1.2 [1])	N/A [2]
	79.6 ± 0.3	0.4 ± 0.1	0.6 ± 0.1 (2.0 ± 0.2 [1])	N/A [2]

[1] Quantity of toluene displaced during multicomponent experiment

[2] Could not be determined due to significant rollover in BTC

7.2.5. Fitting of experimental breakthrough curves

Model parameters and fitted useable and total capacities are shown in **Tables A.44-A.56** in the Appendix. The Bohart-Adams Logistic (BAL) model was used to fit toluene and n-hexane BTCs for all materials except for MS13X at 40 % relative humidity, and MIL-100 at 40 and 80 % relative humidity. Due to the significant rollover in these systems, the Boltzmann-EMG model was used. The Bolztmann-EMG equation was also tested for its applicability to the stepped water vapour BTCs of MIL-100 at 40 and 80 % RH.

7.2.5.1. Fitting of experimental BTCs for industrial adsorbents

All toluene BTCs were found to be well described by the BAL model according to their adjusted R^2 values, all above 0.99. Similarly, all water BTCs were fitted with adj. R^2 values of at least 0.94 using the BAL model, except for GAC at 80 % RH- this is likely due to the almost immediate breakthrough followed by long saturation time. The inability of the BAL model to describe fast breakthroughs is more notable in **Table A.51** where the modelled curve had a useable capacity of 0 for GAC at both 40 and

80 % RH. The fitted BTCs were found to begin at C_{out}/ C_{in} values above 0, as shown in **Figure 7.13**, which could be ascribed to water vapour eluting immediately through the column and only weakly interacting with the GAC bed.

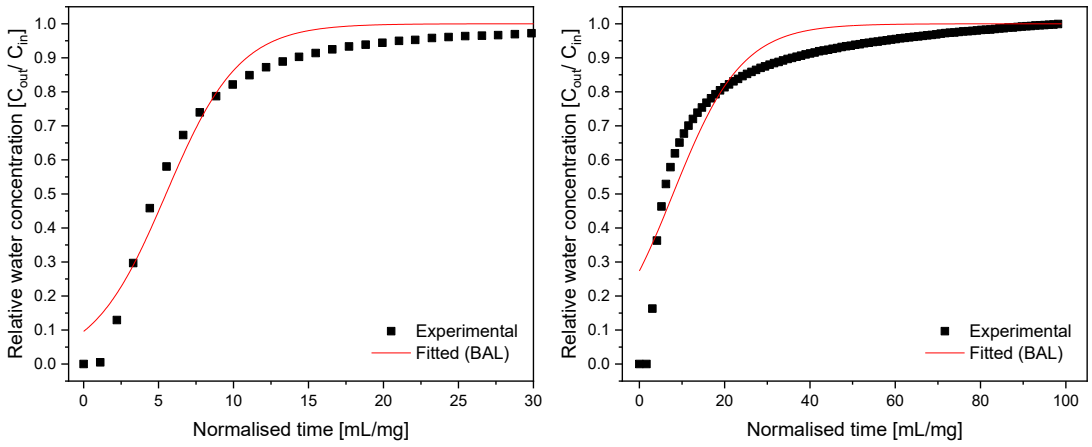


Figure 7.13: Comparison of experimental and fitted water BTCs for GAC at 40 % (left) and 80 % (right) relative humidity. Fitting carried out using Bohart-Adams Logistic model. Flowrate = 60 mL/min. T= 25˚C.

The BAL model appeared to generate fits that had total capacities matching well with experimental values, except for GAC (80) where the capacity was overestimated by 37.5 %. With the same exception, the BAL fits resulted in useability values below experimental in all cases- this is due to the gentler initial profile predicted by the model pre-breakthrough, whereas many of the experimental BTCs were found to possess very few points in the data range of $0 < C_{out}/ C_{in} < 0.05$. As illustrated in **Figure 7.14 (left),** the additional integrated area underneath the fitted curve can be seen clearly when plotted together with experimental data. The Boltmann-EMG model was found to fit the competitive BTC of toluene well for MS13X at 40 % RH, with an adjusted R^2 of 0.994. The parameters of A1 and D1, related to the initial y value, are both equal to zero, and the values for x_1 and x_2 appear to correctly match the normalised time values related to the mid-point of the BTC (assuming no rollover) and the mid-point of the rollover peak respectively. Using the Boltzmann-EMG model, the fitted values for

useable, total, and displaced toluene capacities differed from experimental values by -15.2 %, 7.7 %, and 4.7 % respectively.

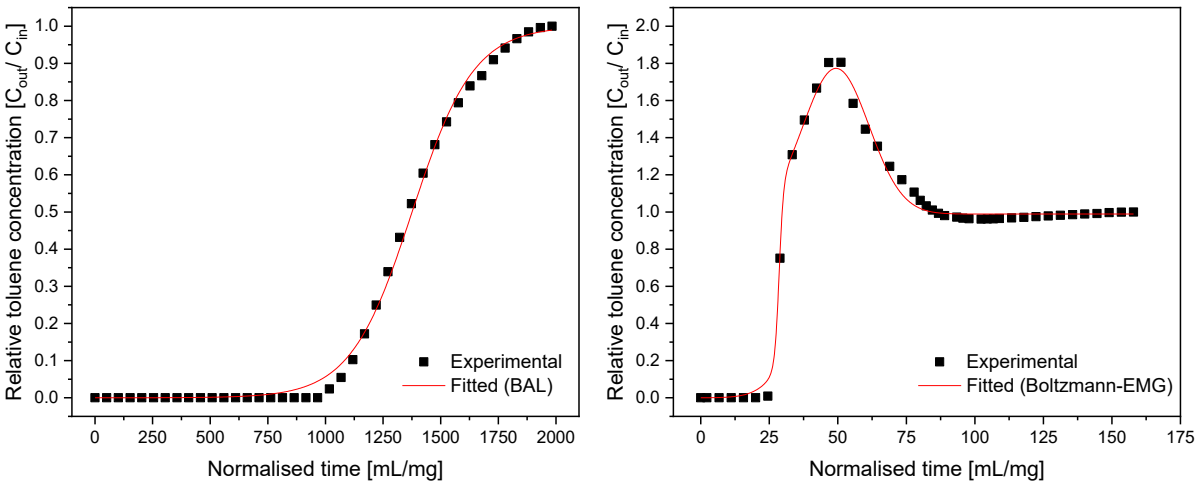


Figure 7.14: Comparison of experimental and fitted toluene BTCs for zeolite Y at 80 % RH (left) and MS13X at 40 % RH (right). Fitting carried out using Bohart-Adams Logistic and Boltzmann-EMG models. Flowrate = 60 mL/min. T= 25˚C.

In dry conditions, the fixed-bed adsorption rate constants were found to follow the trend GAC (0.01023 mg/mL) > A88Y (0.00703 mg/mL) > MS13X (0.00555 mg/mL), matching the trend in useability. However, no clear relationship was found between the rate constant and useability when extended over the enter dry and humid dataset. The introduction of 40 % relative humidity was found to increase k_{BA} for both GAC and A88Y, by 11 % and 13 % respectively despite reductions in their total and useable capacities. Increases in the adsorption rate constant with humidity have been observed on AC by Wang et al [346] and high-silica zeolite Y by Xu et al [283] although the reasoning behind this effect was not explored in their work. One possible explanation is the filling of certain adsorption sites by water results in a more homogeneous distribution of hydrophobic sites for toluene to interact with. This effect combined with the reduced number of available sites and therefore the reduction in interaction between adsorbate and adsorbent, would result in the VOC breaking through earlier and the bed becoming saturated much faster. However, the exact impact this would have on mass transfer is uncertain, and the trends in k_{BA} are not clear enough to draw conclusions from. For example, while increasing the humidity

to humidity to 80 % further increases the k_{BA} of GAC to 0.0126 mg/mL, the k_{BA} of A88Y decreases to 0.00748 mg/mL, between the values for 0 and 40 % RH. No rate constant is defined in the Boltzmann-EMG model, so comparisons could not be made between dry and humid MS13X toluene profiles.

Water BTCs were found to have k_{BA} values at least an order of magnitude greater than toluene BTCs for all studied materials, indicating superior mass transfer through the packed bed. This is likely due to the majority of adsorption at lower RHs occurring via surface filling. This is supported by the reduced water k_{BA} values at higher RHs for GAC and A88Y, where mesopore filling will be the primary mechanism of water adsorption. In Chapter 4 the same conclusions were reached based on the reduction in k_{PFO} values for water adsorption at higher RHs, above the inflection points of the type V and type IV isotherms of AC and A88Y.

7.2.5.2. Fitting of experimental BTCs for MOF adsorbents

Similar to industrial adsorbents, the BAL model appeared to describe the experimental data of ZIF BTCs well based on the coefficient of determination, with adj. R^2 values all above 0.98, with the best fitted being ZIF-8 powder and n-hexane with an adj. R^2 approaching 1 (0.9996). This ease of fitting by the BAL model is surprising due to the gentle slope of the ZIF toluene BTCs and their relatively low fractional useability. Similar to industrial systems, the BAL model was found to underestimate the useable capacity and useability of the adsorbents in all dry and humid systems. This is likely due to the BAL curves following a more traditional BTC shape with an initially slow increase in outlet concentration, extending the mass transfer zone, as shown in **Figure 7.15**. However, the BAL model appeared to produce total capacities similar to experimental, with an average difference of only 3.2 ± 1.8 % from experimental values, with the largest difference being 5.7 % for ZIF-8 (NB-1) (0), and the lowest being only 0.40 % ZIF-8 (0) n-HEX. This, combined with its high R^2, implies that the BAL model is particularly effective at fitting and predicting capacities for systems in which more typical BTCs are produced as shown in the rightmost plot of **Figure 7.15**, i.e. with minimal mass transfer limitations. However, the model was found to be sufficient for fitting all ZIF-VOC systems.

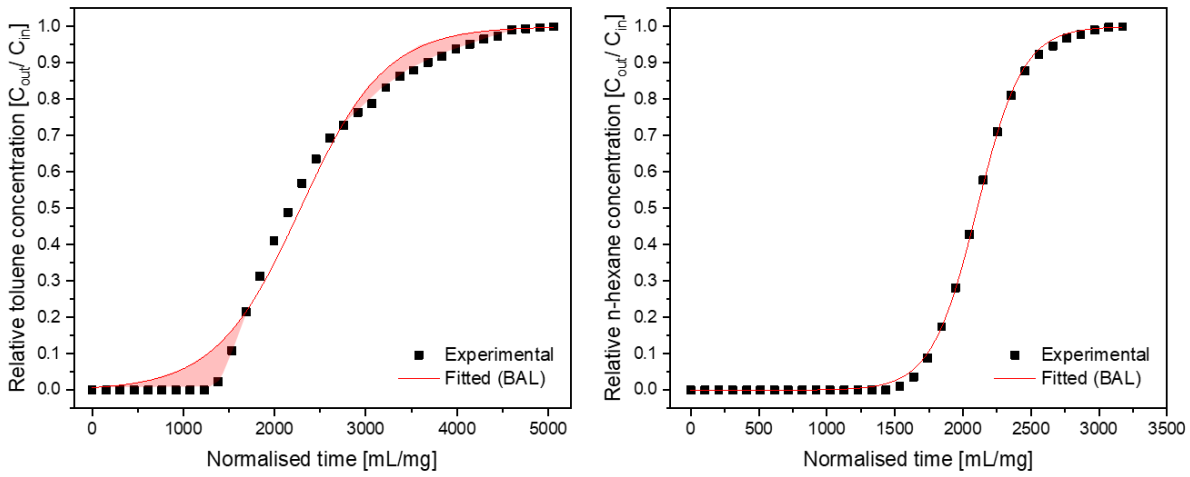


Figure 7.15: Comparison of experimental and fitted BTCs for toluene (left) and n-hexane (right) on ZIF-8 powder at 0 % RH. Shaded region on toluene curve indicates 'lost' capacity due to traditional breakthrough curve symmetry. Fitting carried out using Bohart-Adams Logistic model. Flowrate = 60 mL/min. T= 25˚C.

In terms of the k_{BA} rate constants, MOF's values were typically much lower than those for industrial adsorbents, with the exception of ZIF-8 powder with n-hexane which was above dry toluene on MS13X, 0.00596 and 0.00555 mg/mL respectively. With this exception, the reduced rate constants can be ascribed to poorer mass transfer of toluene in ZIF systems than industrial zeolites and charcoals. These observations match those in gravimetric kinetics studies, with ZIF-8 and ZIF-67 requiring over a day to reach equilibrium with toluene vapour at a partial pressure of 0.005 P/P_0, while industrial materials reached saturation in noticeably shorter time periods. The findings in this Chapter suggest that this phenomenon, likely due to the aperture size expansion of ZIF-8/67 required to accommodate toluene molecules, is present in dilute fixed-bed systems as well as passive adsorption systems. Similar to industrial materials, no clear trend in carrier gas humidity and toluene k_{BA} values were found- with ZIF-8 (NB-1) and ZIF-67 (ML) having increased rate constants from 0-80 % RH, while the rate constants for ZIF-8 powder followed the trend 40 % RH > 80% RH > 0 % RH. Work by Jafari et al [347] found the Thomas model rate constant for fixed-bed toluene adsorption by ZIF-8 increased from 2.62 to 3.10 when humidity was increased from 40-60 %, but decreased to 2.21 at 80 % RH. Multiple effects likely

contribute to these changes in rate constant: reduction in capacity resulting in faster breakthrough; filling of higher energy active sites, increasing hydrophobic site homogeneity; and modification of mass transfer due to adsorbed water molecules.

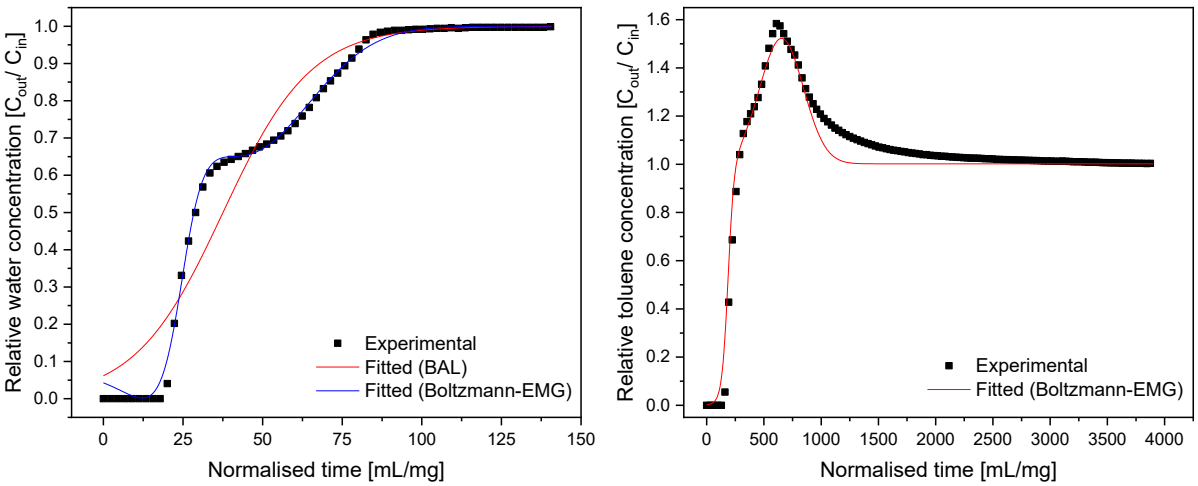


Figure 7.16: Comparison of experimental and fitted water (left) and toluene (right) BTCs for MIL-100 at 40 % RH. Fitting carried out using Bohart-Adams Logistic and Boltzmann-EMG models. Flowrate = 60 mL/min. T= 25˚C.

MIL-100's toluene and water BTCs at 20 % RH and below could be well described by the BAL model, with adj. R^2 values above 0.993. The k_{BA} rate constant for toluene BTCs at 0 and 20 % RH were calculated as 0.00370 and 0.00582 respectively, in-between those of ZIF and hydrophobic industrial adsorbents studied under similar conditions. MIL-100 presented atypical toluene and water BTCs in multicomponent experiments at 40 and 80 % RH. The rollover of the toluene BTC was well described by the Boltzmann-EMG model. The step in the water BTC could not be fitted by the BAL model, while the Boltzmann-EMG model produced a fit with a non-zero initial outlet water concentration. The empirical nature of the Boltzmann-EMG and the large number of variables within the equation allow it to fit most datasets successfully, including the 4 inflection points of MIL-100's water BTC. Despite this, the adj. R^2 for the BAL and Boltzmann-EMG models were similar, at 0.946 and 0.998 respectively.

Table 7.7: Experimental and fitted values for capacity and useability of adsorbents for toluene. Values calculated by integrating BTCs generated using the Bohart-Adams Logistic or Boltzmann-EMG models. Flowrate = 60 mL/min. C_{in} = 10 ppmv, T = 25˚C.

Material	Experimental			Fitted		
	Useable capacity [mg/g]	Total capacity [mg/g]	Useability	Useable capacity [mg/g]	Total capacity [mg/g]	Useability
GAC (0)	93.8	105.9	0.886	94.6	105.7	0.895
GAC (40)	49.2	57.0	0.861	46.0	56.1	0.819
GAC (80)	7.5	11.2	0.665	6.4	15.4	0.417
A88Y (0)	52.3	66.8	0.789	50.0	66.3	0.755
A88Y (40)	42.5	54.5	0.784	39.4	53.9	0.731
A88Y (80)	40	52.7	0.758	37.0	52.2	0.709
MS13X (0)	59.9	79.5	0.751	58.5	79.2	0.738
MS13X (40) [1]	0.9	0.3 (0.9 [2])	N/A [3]	0.8	0.2 (0.8 [2])	N/A [3]
ZIF-8 (0)	54.5	90.6	0.604	34.0	86.5	0.393
ZIF-8 (40)	47.1	82.3	0.570	32.8	80.4	0.409
ZIF-8 (80)	37.7	81.3	0.465	34.5	84.8	0.407
ZIF-8 (0) n-HEX [4]	59.4	74.5	0.799	59.3	74.8	0.792
ZIF-8 (NB-1) (0)	42.2	72.5	0.586	27.4	68.6	0.400
ZIF-8 (NB-1) (80)	28.3	60.4	0.465	17.9	57.3	0.313
ZIF-67 (0)	55.5	91.6	0.607	40.2	88.7	0.453
ZIF-67 (NB-1) (0)	50.9	84.8	0.601	32.6	82.1	0.396
ZIF-67 (ML) (0)	45.1	85.9	0.520	31.1	84.6	0.367
ZIF-67 (ML) (80)	33.2	73.0	0.453	24.3	72.0	0.338
MIL-100 (0)	59.6	81.6	0.732	53.5	86.1	0.621
MIL-100 (20)	34	47.9	0.711	29.5	50.2	0.588
MIL-100 (40) [1]	6.2	6.3 (14.1 [2])	N/A [c]	4.1	6.9 (9.5 [2])	N/A [3]
MIL-100 (80) [1]	0.4	0.6 (2.0 [2])	N/A [c]	0.3	0.6 (1.6 [2])	N/A [3]

[1] Fitting carried out using the Boltzmann-EMG model

[2] Quantity of toluene displaced during multicomponent experiment

[3] Could not be determined due to significant rollover in BTC

[4] Parameters for n-Hexane breakthrough

7.4. Conclusions

In this Chapter, the adsorption capacity of porous materials for toluene vapour was determined at dilute concentrations representing real-world conditions, i.e. 10 part-per-million by volume, as well quantifying the effect of water vapour on this capacity. These measurements were carried out using a bench-top breakthrough curve analyser, designed and built as part of this project. The device independently monitors the post-column levels of water and toluene vapour using a humidity probe and photoionization detector respectively. Multicomponent measurements were carried out in the 'wet adsorbate' mode, i.e. where the gas phase containing the VOC species also contains water vapour and both are eluted through the sample simultaneously.

Industrial adsorbents zeolite Y, molecular sieve 13X, and granular activated charcoal were found to possess high toluene adsorption capacities in the range of 66-106 mg/g due to their surface area and microporosity, similar to the total VOC capacity of the commercial charcoal cloth adsorbent Zorflex FM 10 [163]. The 'useability' of the materials, often related to the ease of mass transfer through the bed, appeared to increase with the hierarchical porosity of the adsorbent, with almost entirely microporous MS13X having the lowest industrial useability of 0.751 while GAC had a useability of 0.886. Synthetic ZIF-8 and ZIF-67 adsorbents, both power and monoliths, were found to have significantly poorer mass transfer, with fractional useability values between 0.520-0.607, matching gravimetric toluene adsorption profiles in Chapter 5 and 6. Experiments with n-hexane confirmed that ZIF-8's narrow aperture size restricts the adsorption of larger molecules like toluene. Despite this, ZIF adsorbents were found to possess high total capacities for toluene and, when accounting for packed adsorbent density, monolithic ZIF-8 and ZIF-67 had superior volume-relative total capacities compared to industrial adsorbents. MIL-100 possessed similar mass-relative total toluene capacity to ZIF-8 and ZIF-67 powders but, due to its larger pore apertures, had a higher useability of 0.732. The useability of an adsorbent bed is an important property, as low useability equates to essentially 'unused' or 'wasted' packed bed length in applications where particularly noxious compounds are being removed, and only a certain concentration limit can be tolerated.

The most interesting data was collected during multicomponent experiments, where the packed bed was exposed to water and toluene simultaneously. Results for hydrophobic industrial adsorbents A88Y and GAC followed gravimetric trends for similar materials in Chapter 4, with A88Y possessing high efficacy for toluene removal at all studied humidity values, while GAC had noticeable losses in performance at both 40 and 80 % RH. The lack of displacement in GAC and A88Y humid BTCs indicates that water was able to occupy sites that toluene would otherwise adsorb onto faster than toluene could access them, which is supported by the almost immediate breakthrough of water vapour in these columns, and their significant faster equilibration compared to toluene vapour. ZIF-8 and ZIF-67, with their similar pore structures and improved hydrophobicity over A88Y, possessed similar trends with their total capacity only decreasing by up to 17 % under the most extreme conditions of 80 % RH. All reductions in capacity for industrial hydrophobic materials and ZIF adsorbents appeared to be due to water occupying adsorption sites prior to toluene or accessing sites toluene could not, as shown by the shift of toluene BTCs to lower time values. However, the more extreme case of competition adsorption, i.e. displacement of adsorbed toluene molecules, was observed in MS13X and MIL-100. MS13X, due to its high adsorption hydrophilicity displayed a 'rollover' effect in the toluene BTC at 40 % RH, in which the outlet concentration exceeded the inlet. This displacement resulted in a total capacity of < 1 mg/g which matched the negligible quantities of toluene adsorbed in 'wet adsorbent' DVS experiments in Chapter 4. However, the breakthrough curve experiments in this Chapter elucidate the different mechanisms of competition in toluene-water-adsorbent systems. MIL-100 appeared to illustrate these mechanisms best, due to its humidity-dependant adsorption mechanism for water vapour. At low humidity (20 % RH), MIL-100 has a noticeable ~41 % reduction in toluene capacity due to water adsorbing onto surface sites around the framework's micropores. When humidity is increased to 40 and 80 % RH, where filling of the small and large mesopores occurs according to adsorption isotherms in Chapter 5, MIL-100's ability to adsorb toluene is reduced by ~92 % and > 99 % respectively. Pores normally accessible only to the non-polar species, toluene, due to their polarity-based molecular sieving, can accommodate water molecules via pore filling when sufficient driving

force is supplied. The filling of these pores by water vapour, and the resulting displacement of toluene molecules, suggests that while the openings of these pores is hydrophobic, hydrophilic sites exist within the apertures which interact favourably with water over toluene. These results further emphasise the importance of hydrophobic pore apertures in maintaining adsorption selectivity for non-polar molecules in high humidity conditions, as well as the necessity to test adsorbents in the presence of water vapour. The high density of ZIF monolith samples ZIF-8 (NB-1) and ZIF-67 (ML) resulted in these samples possessing the highest volume-relative useable and total toluene adsorption capacities at an RH value of 80 %.

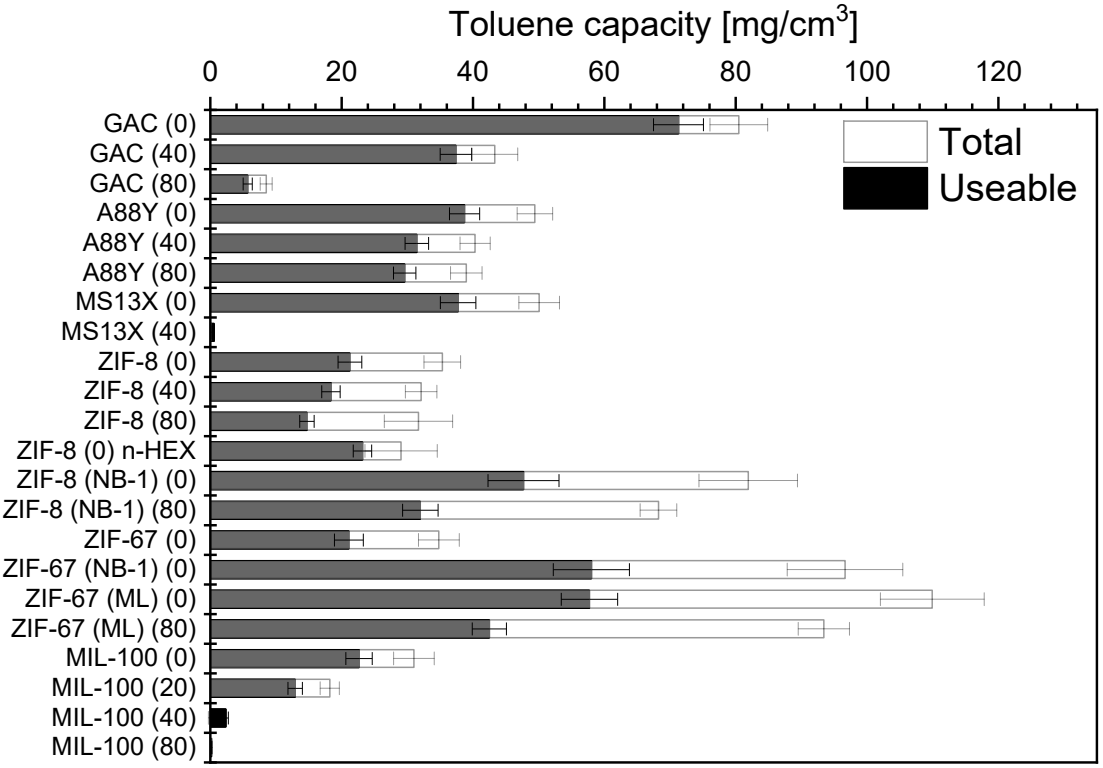


Figure 7.17: Fixed-bed total and useable toluene capacities expressed in volume-relative terms, measured at 10 ppmv and an RH equal to the bracket, between 0-80 %. T = 25˚C.

Fitting of experimental datasets was carried out using the Bohart-Adams Logistic (BAL) model, and the Boltzmann-EMG model, the latter of which was utilised for systems with additional inflection points

due to rollover or stepped BTCs. The BAL model gave good fits for the majority of vapour-solid systems, although tended to underestimate useable and total adsorption capacity as it assumed a much more ‘ideal’ or ‘gentle’ BTC shape. The Boltzmann-EMG model gave good fits for toluene BTCs in which displacement was present, i.e. MS13X and MIL-100, although its empirical nature and large number of variables means these fits can provide no physical insights into the adsorption processes. Contrastingly, the Bohart-Adams rate constant k_{BA} appeared to have a semi-proportional relationship with the useability of the material. This allowed for a more quantitative description of mass transfer limitations within a packed bed, highlighted by ZIF-8 powders adsorption rate constants for toluene (0.00216 mg/mL) being almost 3 times lower than its constant for n-hexane (0.00596 mg/mL).

Despite the limitations of gravimetric apparatus and the semi-quantitative nature of its two-component adsorption experiments, many of the trends in this Chapter match well with previously observed trends for pre-exposure humid toluene adsorption studies. Therefore, ‘wet adsorbent’ and ‘wet adsorbate’ datasets relate remarkable well to each other. However, the importance of breakthrough curve analysis in measuring low-concentration adsorption data in significantly smaller timeframes cannot be undervalued, especially when this data can be used to decipher the mechanisms behind single- and multicomponent VOC capture.

Chapter 8: Conclusions and future work

8.1. Summary

This project focused on researching methods of characterising the adsorption performance of porous materials for volatile organic compounds (VOCs), and how the physicochemical properties of the materials can influence this performance. Past studies in this area made several parameters desirable for potential VOC adsorbents:

- High surface area and micropore volume, with hierarchical porosity to improve mass transfer.
- A pore size suitable for adsorbing large molecules at low concentrations.
- Hydrophobic surface and adsorption chemistry.

During the project, several research questions and aims became apparent which related to understanding the structure-property-performance relationships of porous adsorbents, and how these relationships can be defined or determined. In order to address these research aims, extensive reviewing of existing literature and reproducible and accurate experimentation was carried out.

8.1.1. Adsorption hydrophobicity

As mentioned previously, 'hydrophobicity' is a commonly cited property of effective VOC adsorbents. As VOCs exist together with comparatively high levels of water vapour due to ambient relative humidity, adsorbents must have high selectivity for VOCs over water. This is one of the primary reasons why zeolites and charcoals are commonly employed commercially due to their selective adsorption of non-polar species, providing they have sufficiently high surface area and dispersive interaction potential.

Adsorption experiments in Chapter 4 confirmed literature findings, with zeolite Y and activated charcoal powder having high non-polar VOC adsorption capacities, while adsorbing minimal amounts of water vapour at low to medium humidity. Pre-exposure at these humidity levels also resulted in minimal losses in toluene adsorption performance, while more hydrophilic adsorbents like molecular

sieve 13X showed minimal capacity at any pre-exposure level. However, activated charcoal's capacity dropped significantly as humidity increased to 50 % and above, matching the inflection point in the charcoal's water isotherm. In literature the term 'hydrophobicity' is often used as a catch-all term and often the distinctions between 'surface' and 'adsorption' hydrophobicity are not discussed or elaborated upon and is often quoted as a purely material property. The findings in Chapter 4 suggest that adsorption hydrophobicity is dependant on both material and environmental factors, especially the level of relative humidity. Calculating single-component hydrophobicity indexes as a function of relative humidity, while not computationally complex, provided a novel method of illustrating this dependency, and appeared to be a good predictor for 'wet adsorbent' toluene capacity in hydrophobic materials [333].

The relatively high performance of high-silica zeolite Y compared to charcoal was ascribed to its hydrophobic micropore apertures [172], which prevented the ingress of polar molecules until a particular driving forces was met. This retention of adsorption hydrophobicity at extreme humidities was present in ZIF-8 and ZIF-67 samples synthesised in Chapter 5 and 6, which possessed similarly hydrophobic framework apertures as well as significantly higher surface areas and pore volumes compared to the zeolite. The micro-mesoporous MIL-100 had the most interesting illustration of pore hydrophobicity, with mesopore cages being accessible through hydrophobic micropore windows. These cages could be filled by water vapour at specific RH values, around 25 and 45 % at 25˚C for the small and large cages respectively [315]. These filling events not only significantly affected the hydrophobicity index of MIL-100, but also its selectivity towards toluene. Another important observation was that water contact angles provided little information regarding a material's response to water vapour. Modification of MIL-100 using hydrophobic acids in Chapter 6, while significantly increasing their surface hydrophobicity, resulted in no improvement to adsorption hydrophobicity. These findings further emphasise the importance of assessing adsorption hydrophobicity at a wide range of humidity values, as it is a function of both the material's surface chemistry, pore structure, and the environment in which it is being applied.

8.1.2. Monolithic metal-organic frameworks

One unintended research outcome from the synthesis of metal-organic frameworks was the development of a modulator-based procedure for forming sol-gels of MOFs and, by gradual drying, high-density MOF monoliths [348]. Single-step procedures, like those explored in Chapter 6, are highly sought after in literature, as it does not require the addition of binding agents, or compaction of the final adsorbent- both of which can have a significant impact on porosity and surface chemistry [159]. Characterisation of ZIF-8, ZIF-67, and MIL-100 monoliths confirmed they possessed the characteristic diffraction peaks, micropore size distributions, and adsorption hydrophobicity of their respective base powders. The generation of amorphous content within the monoliths, either through reduced crystallisation or monodentate linkages with the modulating ligands, resulted in poorer porosity and surface area compared to powder materials. However, the significantly increased density resulted in improved performance for the ZIF monoliths- with volume-relative toluene capacities up to 230 % higher than powder equivalents in humid conditions. MIL-100, due to a much more significant loss in porosity, had similar volume-relative properties and performance between its powder and monolith forms.

These monolith MOFs had an additional advantage in fixed-bed adsorption measurements, bypassing the significant pressure drop present for packed beds of powder adsorbents. Alongside extruded and granulated industrial zeolites and charcoals, structured ZIFs presented excellent volume-relative toluene capacities in dilute conditions. Monolithic ZIFs, due to their retention of characteristic pore hydrophobicity, outperformed all other industrial adsorbents in high humidity (80 % RH) conditions, with total toluene capacities as high as 93.6 mg/cm^3 in dilute conditions (10 ppmv). In applications where volume is an important design criterion, e.g. for filtration columns with space limitations, high-density structured adsorbents have a clear advantage over powders.

8.1.3. Competitive adsorption of VOCs in humidified environments

The initial stages of this project used two-component gravimetric experiments to semi-quantitatively assess the performance of VOC adsorbents in humid conditions by pre-exposing them to fixed levels of relative humidity. This 'wet adsorbent' illustrated the importance of adsorption hydrophobicity when screening for effective adsorbents, and how this hydrophobicity changes with humidity.

To measure VOC adsorption performance in conditions that better represent real-world environments, a breakthrough curve analyser was developed capable of measuring volatile concentrations at part-per-million levels in the presence of high levels of water vapour. Dilute toluene adsorption experiments, carried out in 'wet adsorbate' mode at 10 ppmv of toluene, confirmed many of the trends of gravimetric studies, while elucidating the mechanisms of competitive adsorption occurring. In granulated charcoal, zeolite Y, and ZIF-8/67, competition appeared to occur via water eluting through the packed bed quickly, occupying shared adsorption sites which toluene would otherwise access. On the other hand, hydrophilic molecular sieve 13X showed significant rollover in its breakthrough profile in humidified toluene experiments- ascribed to displacement of toluene molecules by water vapour, suggesting strong selectivity for polar compounds. This 'extreme' level of competition indicates a potentially unsuitable adsorbent due to its inability to adsorb high quantities of toluene in the presence of humidity. MIL-100 was found to transition towards more extreme competition as humidity increased- at 20 % RH, no displacement of toluene was observed, while above this value significant rollover was present. This phenomenon is likely due to the gradual filling of mesopore cages by water molecules at particular RH values, as described in MIL-100's water isotherm. These findings suggests that the humidity-dependant adsorption hydrophobicity does not only inform the extent of adsorption competition and selectivity, but also the mechanism by which water and non-polar VOCs compete. Together with observations regarding the humidity-dependant nature of VOC selectivity, these findings emphasise **pore** hydrophobicity as a desirable property compared to simply **adsorption** or **surface** hydrophobicity, alongside physical characteristics such as high levels of microporosity, surface area, and bulk density.

8.2. Future work

During this project, several potential areas of research were made apparent that either did not fit the theme of the project, were not possible with the current experimental apparatus, or were too time consuming to complete, the latter of which was exacerbated by the COVID-19 pandemic and the temporary shutdown of the laboratory at Imperial College London. This section will provide an overview of these research topics.

8.2.1. Investigation of adsorption enthalpy and multi-temperature breakthrough curves

During the early stages of this work, several experiments were carried out investigating the effect of temperature on adsorption capacity for hydrophobic adsorbents. By generating adsorption isotherms of toluene at multiple temperatures, the adsorption enthalpy could be determining using the Clausius-Clapeyron equation. This method requires accurate fitting of the isotherms using suitable isotherm models to determine the temperature dependence of the pressure required to reach a certain adsorbate loading. However, the isotherms of polar molecules onto hydrophobic adsorbents often result in Type III, Type V, or more unusual multi-stepped isotherms, e.g. water onto MIL-100. For this reason, generation of multi-temperature isotherm plots, and accurate fitting of these datasets to mathematical or empirical models requires dedicated time and research. By understanding how the adsorption enthalpy of a vapour-solid system may change between surface- and pore-filling mechanisms, a better understanding of the strength of these interactions can be elucidated. While the temperature of the breakthrough analyser can be kept stable at 25˚C to within 0.1˚C, any deviation from this temperature leads to noticeable oscillations, making the current apparatus unsuitable for multi-temperature fixed-bed adsorption. However, in the event that the incubator heater design is improved, multi-temperature breakthrough curves could provide information regarding how bed mass transfer is affected by an increase or decrease in temperature. In addition, if the adsorption column could be fitted with one or more high-sensitivity temperature probes, efforts could be made to track the change in bed temperature

as adsorption occurred over the course of the experiment, allowing the heats of adsorption to be qualitatively or quantitatively determined.

8.2.2. Effect of ZIF-8 pore expansion on toluene adsorption kinetics

In the later stages of this work, a review of the pore size distributions of ZIF-8 found a 2012 study by Karagiaridi et al [149] in which the 2-methylimidazole linker of ZIF-8 was post-synthetically replaced with the imidazole molecule. This resulted in a larger minimum pore size and allowed the new material, SALEM-2, to adsorb greater quantities of n-hexane, cyclohexane, and toluene. However, vapour adsorption measurements for this material were not carried out, despite its BET surface area being only 20 % lower than the base ZIF-8. The primary structural limitation of ZIF-8 as a VOC filtration media based on experimental work in this project is the restricted diffusion of bulky molecules, such as aromatics, into its micropores. Carrying out isotherm and fixed-bed adsorption studies on SALEM-2 to determine its selectivity, hydrophobicity, and adsorption kinetics for aromatic molecules could provide a potential alternative route for ZIF adsorbents.

8.2.3. Palladium-doped ZIF-8 monoliths

Alongside monolithic synthesis, the synthesis of TiO_2- and palladium-doped ZIF-8 monoliths was carried out successfully, with the presence of the catalytic particles confirmed via X-ray diffraction and energy dispersive X-ray spectroscopy combined with scanning electron microscopy (SEM-EDS). Diffraction patterns also found that in regular ZIF-8 monolith synthesis conditions, palladium acetate readily dissociated and aggregated to form palladium black, or Pd(0). The addition of acetic acid prevented this aggregation, but the final composite was found to possess diffraction peaks matching theoretical peaks of palladium nitrate. It was hypothesised that varying the choice of zinc salt may allow the tuning of the final state of palladium catalyst within the composite, which could provide significant benefits for the field of catalysis where certain palladium sources may be required. Initial catalytic tests for the transfer hydrogenation of levulinc acid to form gamma-valerolactone were successful in batch mode, although continuous mode produced unusual cyclic by-products, some of which possessed

nitrogen-containing groups- indicating that the n-butylamine present within the monoliths may contribute to the products of the reaction. In summary, ZIF-8 monoliths may provide a unique support structure for catalytic particles, and the influence of their synthesis conditions on the final catalytic material is cause for investigation.

8.2.4. Photocatalytic oxidation of VOCs using breakthrough analyser

Similar to the work on palladium composites, TiO_2 particles were successfully combined with ZIF-8 monoliths in a single step synthesis process. TiO_2 has been utilised in the photocatalytic oxidation of VOCs into carbon dioxide [349], and the development of the bench-top breakthrough analyser in this project could allow for photocatalytic measurements to be carried out. The fixed-bed columns are constructed from borosilicate glass, which can be highly transparent to UV radiation- allowing a suitable UV source to easily irradiate the adsorbent, or in this case catalytic, bed. While not discussed extensively in this thesis, the breakthrough curve analyser in the project was designed with modular sensors include an infrared CO_2 sensor (Vaisala, Finland) which has allowed for measurement of single- and multi-component breakthrough curves of carbon dioxide and water. By utilising all three sensors (humidity probe, infrared CO_2 sensor, and photoionisation detector), a mixture of VOC and water could be eluted through a packed bed of TiO_2 or TiO_2/ ZIF-8 composite while the bed is irradiated with suitable UV light. Measuring the outlet profiles of water vapour, dilute VOC and CO_2 would allow the user to quantify the activity of the catalyst to oxidize the VOC, e.g. n-hexane or toluene, into CO_2.

References

[1] J. Shuai *et al.*, "Health risk assessment of volatile organic compounds exposure near Daegu dyeing industrial complex in South Korea," *BMC Public Health*, vol. 18, pp. 1–13, 2018.

[2] A. Steinemann, "Volatile emissions from common consumer products," *Air Qual. Atmos. Heal.*, vol. 8, no. 3, pp. 273–281, 2015.

[3] P. Wolkoff, "Impact of air velocity, temperature, humidity, and air on long-term VOC emissions from building products," *Atmos. Environ.*, vol. 32, no. 14–15, pp. 2659–2668, 1998.

[4] M. Hodgson, "Indoor Environmental Exposures and Symptoms," *Environ. Health Perspect.*, vol. 110, no. 4, pp. 663–667, 2002.

[5] UK Health and Safety Executive, "EH40/2005 Workplace exposure limits (4th Edition)," 2020. [Online]. Available: https://www.hse.gov.uk/pubns/books/eh40.htm. [Accessed: 20-May-2021].

[6] J. Seo, S. Kato, Y. Ataka, and S. Chino, "Performance test for evaluating the reduction of VOCs in rooms and evaluating the lifetime of sorptive building materials," *Build. Environ.*, vol. 44, no. 1, pp. 207–215, 2009.

[7] P. Guo *et al.*, "Sick building syndrome by indoor air pollution in Dalian, China," *Int. J. Environ. Res. Public Health*, vol. 10, no. 4, pp. 1489–1504, 2013.

[8] R. Tong, L. Zhang, X. Yang, J. Liu, P. Zhou, and J. Li, "Emission characteristics and probabilistic health risk of volatile organic compounds from solvents in wooden furniture manufacturing," *J. Clean. Prod.*, vol. 208, pp. 1096–1108, 2019.

[9] M. I. Khoder, "Formaldehyde and aromatic volatile hydrocarbons in the indoor air of Egyptian office buildings," *Indoor Built Environ.*, vol. 15, no. 4, pp. 379–387, 2006.

[10] F. I. Khan and A. Kr. Ghoshal, "Removal of Volatile Organic Compounds from Polluted Air,"

J. Loss Prev. Process Ind., vol. 13, no. 6, pp. 527–545, 2000.

[11] S. W. Blocki, "Hydrophobic zeolite adsorbent: A proven advancement in solvent separation technology," *Environ. Prog.*, vol. 12, no. 3, pp. 226–230, Aug. 1993.

[12] B. De Lacy Costello *et al.*, "A review of the volatiles from the healthy human body," *J. Breath Res.*, vol. 8, no. 1, 2014.

[13] M. Noguchi, S. Tanaka, K. Watanabe, and A. Yamasaki, "Correlation between odor concentration and volatile organic compounds (VOC) composition of environmental tobacco smoke (ETS)," *Int. J. Environ. Res. Public Health*, vol. 13, no. 10, 2016.

[14] D. Bourdin, P. Mocho, V. Desauziers, and H. Plaisance, "Formaldehyde emission behavior of building materials: On-site measurements and modeling approach to predict indoor air pollution," *J. Hazard. Mater.*, vol. 280, pp. 164–173, 2014.

[15] J. Williams and A. Ringsdorf, "Human odour thresholds are tuned to atmospheric chemical lifetimes," *Philos. Trans. R. Soc. B Biol. Sci.*, vol. 375, no. 1800, 2020.

[16] H. Swenson and N. P. Stadie, "Langmuir's Theory of Adsorption: A Centennial Review," *Langmuir*, vol. 35, pp. 5409–5426, 2019.

[17] C. Erkey, "Chapter 4 - Thermodynamics and Dynamics of Adsorption of Metal Complexes on Surfaces from Supercritical Solutions," in *Supercritical Fluids and Organometallic Compounds*, vol. 1, C. Erkey, Ed. Oxford, UK: Elsevier Science, 2011, pp. 41–77.

[18] F. L. Leite, C. C. Bueno, A. L. Da Róz, E. C. Ziemath, and O. N. Oliveira, "Theoretical models for surface forces and adhesion and their measurement using atomic force microscopy," *Int. J. Mol. Sci.*, vol. 13, no. 10, pp. 12773–12856, 2012.

[19] J. B. Adams, "Bonding Energy Models," in *Encyclopedia of Materials: Science and Technology*, K. H. J. Buschow, R. W. Cahn, M. C. Flemings, B. Ilschner, E. J. Kramer, S. Mahajan, and P. Veyssière, Eds. Oxford, UK: Elsevier, 2001, pp. 763–767.

[20] S. J. Park and M. K. Seo, “Chapter 4: Solid-Solid Interfaces,” in *Interface Science and Composites*, vol. 18, Amsterdam: Elsevier, 2011, pp. 253–331.

[21] E. B. Uvarov, D. R. Chapman, and A. Isaac, *The Penguin Dictionary of Science*. New York: Schocken Books, 1972.

[22] E. Arunan *et al.*, “Defining the hydrogen bond: An account (IUPAC Technical Report),” *Pure Appl. Chem.*, vol. 83, no. 8, pp. 1619–1636, 2011.

[23] S. Suzuki, P. G. Green, R. E. Bumgarner, S. Dasgupta, W. A. Goddard, and G. A. Blake, “Benzene Forms Hydrogen Bonds with Water,” *Science*, vol. 257, no. 5072, pp. 1990–1993, 1992.

[24] T. Steiner and G. R. Desiraju, “Distinction between the weak hydrogen bond and the van der Waals interaction,” *Chem. Commun.*, vol. 8, pp. 891–892, 1998.

[25] University of Washington, “Non-Covalent Short Range Interactions,” in *Nanoscience on the Tip: A workshop in Scanning Probe Microscopy*, 2009, pp. 1–14.

[26] C. T. Chiou, “Chapter 4: Fundamentals of the Adsorption Theory,” in *Partition and Adsorption of Organic Contaminants in Environmental Systems*, C. T. Chiou, Ed. Hoboken: John Wiley & Sons, Ltd, 2002, pp. 39–52.

[27] A. V. Kiselev, “Non-specific and specific interactions of molecules of different electronic structures with solid surfaces,” *Discuss. Faraday Soc.*, vol. 40, pp. 205–218, 1965.

[28] S. Rohani, S. Horne, and K. Murthy, “Control of Product Quality in Batch Crystallization of Pharmaceuticals and Fine Chemicals. Part 1: Design of the Crystallization Process and the Effect of Solvent,” *Org. Process Res. Dev.*, vol. 9, no. 6, pp. 858–872, 2005.

[29] S. Brunauer, P. Emmett, and E. Teller, “Adsorption of gases in multimolecular layers,” *J. Am. Chem. Soc.*, vol. 60, no. 2, pp. 309–319, Jan. 1938.

[30] M. S. Alamri, A. A. Mohamed, S. Hussain, M. A. Ibraheem, and A. A. Abdo Qasem, "Determination of Moisture Sorption Isotherm of Crosslinked Millet Flour and Oxirane Using GAB and BET," *J. Chem.*, vol. 2018, pp. 1–8, 2018.

[31] M. M. Dubinin, "The potential theory of adsorption of gases and vapors for adsorbents with energetically nonuniform surfaces," *Chem. Rev.*, vol. 60, no. 2, pp. 235–241, 1960.

[32] O. Kadlec, "The History and Present State of Dubinin's Theory of Adsorption of Vapours and Gases on Microporous Solids," *Adsorpt. Sci. Technol.*, vol. 19, no. 1, pp. 1–24, 2001.

[33] A. Gil and P. Grange, "Application of the Dubinin-Radushkevich and Dubinin-Astakhov equations in the characterization of microporous solids," *Colloids Surfaces A Physicochem. Eng. Asp.*, vol. 113, no. 1–2, pp. 39–50, 1996.

[34] D. Burevski, "The application of the Dubinin-Astakhov equation to the characterization of microporous carbons," *Colloid Polym. Sci.*, vol. 260, no. 6, pp. 623–627, 1982.

[35] N. D. Hutson and R. T. Yang, "Theoretical basis for the Dubinin-Radushkevitch (D-R) adsorption isotherm equation," *Adsorption*, vol. 3, no. 3, pp. 189–195, 1997.

[36] W. Radzinski and D. Everett, *Adsorption of Gases on Heterogeneous Surfaces*. Cambridge, USA: Academic Press, 1991.

[37] P. S. Liu and G. F. Chen, "General Introduction to Porous Materials," in *Porous Materials: Processing and Applications*, Oxford, UK: Butterworth-Heinemann, 2014, pp. 1–20.

[38] S. Mondal and P. Sibanda, "Computational study on convective flows in presence of chemical reaction and thermal radiation in porous/non-porous cavities," *Glob. J. Pure Appl. Math.*, vol. 12, no. 4, pp. 3641–3671, 2016.

[39] J. Rouquerol, P. Llewellyn, and F. Rouquerol, "Is the BET equation applicable to microporous adsorbents?," in *Characterization of Porous Solids VII: Studies in Surface Science and Catalysis*, 2007, vol. 160, pp. 49–56.

[40] M. Thommes *et al.*, “Physisorption of gases, with special reference to the evaluation of surface area and pore size distribution (IUPAC Technical Report),” *Pure Appl. Chem.*, vol. 87, no. 9–10, pp. 1051–1069, 2015.

[41] V. Gómez-Serrano, C. M. González-García, and M. L. González-Martín, “Nitrogen adsorption isotherms on carbonaceous materials. Comparison of BET and Langmuir surface areas,” *Powder Technol.*, vol. 116, no. 1, pp. 103–108, 2001.

[42] D. Verboekend, G. Vilé, and J. Pérez-Ramírez, “Hierarchical Y and USY zeolites designed by post-synthetic strategies,” *Adv. Funct. Mater.*, vol. 22, no. 5, pp. 916–928, 2012.

[43] A. R. Mohamed, M. Mohammadi, and G. N. Darzi, “Preparation of carbon molecular sieve from lignocellulosic biomass: A review,” *Renew. Sustain. Energy Rev.*, vol. 14, no. 6, pp. 1591–1599, 2010.

[44] M. C. Silaghi, C. Chizallet, and P. Raybaud, “Challenges on molecular aspects of dealumination and desilication of zeolites,” *Microporous Mesoporous Mater.*, vol. 191, pp. 82–96, 2014.

[45] K. S. W. Gregg, S. J.; Sing, *Adsorption, Surface Area and Porosity*, 2nd ed. London, UK: Academic Press, 1982.

[46] A. Galarneau, F. Villemot, J. Rodriguez, F. Fajula, and B. Coasne, “Validity of the t-plot method to assess microporosity in hierarchical micro/mesoporous materials,” *Langmuir*, vol. 30, no. 44, pp. 13266–13274, 2014.

[47] M. Kruk and M. Jaroniec, “Determination of mesopore size distributions from argon adsorption data at 77 K,” *J. Phys. Chem. B*, vol. 106, no. 18, pp. 4732–4739, 2002.

[48] F. Villemot, A. Galarneau, and B. Coasne, “Adsorption-based characterization of hierarchical metal-organic frameworks,” *Adsorption*, vol. 20, no. 2–3, pp. 349–357, 2014.

[49] E. M. Voigt and R. H. Tomlinson, “The Determination of Pore Size Distribution and Surface Area From Adsorption Isotherms,” *Can. J. Chem.*, vol. 33, no. 2, pp. 215–231, 1955.

[50] T. Takei, M. Chikazawa, and T. Kanazawa, “Validity of the Kelvin equation in estimation of small pore size by nitrogen adsorption,” *Colloid Polym. Sci.*, vol. 275, no. 12, pp. 1156–1161, 1997.

[51] I. S. Khattab, F. Bandarkar, M. Khoubnasabjafari, and A. Jouyban, “Density, viscosity, surface tension, and molar volume of propylene glycol + water mixtures from 293 to 323 K and correlations by the Jouyban–Acree model,” *Arab. J. Chem.*, vol. 10, pp. S71–S75, 2017.

[52] K. J. Kim and H. G. Ahn, “The effect of pore structure of zeolite on the adsorption of VOCs and their desorption properties by microwave heating,” *Microporous Mesoporous Mater.*, vol. 152, pp. 78–83, 2012.

[53] D. Peralta, G. Chaplais, J. L. Paillaud, A. Simon-Masseron, K. Barthelet, and G. D. Pirngruber, “The separation of xylene isomers by ZIF-8: A demonstration of the extraordinary flexibility of the ZIF-8 framework,” *Microporous Mesoporous Mater.*, vol. 173, pp. 1–5, 2013.

[54] S. A. Moggach, M. T. Wharmby, P. A. Wright, S. Parsons, and T. Düren, “Framework Flexibility in ZIF-8 Explored by Experiments and Simulations (Supporting Information),” *J. Am. Chem. Soc.*, pp. 4–8, 2011.

[55] D. M. Ruthven, “Chapter 21: Diffusion in zeolite molecular sieves,” in *Studies in Surface Science and Catalysis: Introduction to Zeolite Science and Practice*, 3rd ed., J. Cejka, H. van Bekkum, A. Corma, and F. Schueth, Eds. Amsterdam, NL: Elsevier, 2007, pp. 737–785.

[56] D. H. Olson and W. O. Haag, “Structure-Selectivity Relationship in Xylene Isomerization and Selective Toluene Disproportionation,” in *Catalytic Materials: Relationship Between Structure and Reactivity (ACS Symposium Series)*, vol. 248, T. Whyte, R. Betta, E. Derouane, and R. Baker, Eds. Washington, USA: American Chemical Society, 1984, pp. 275–307.

[57] R. Bardestani, G. S. Patience, and S. Kaliaguine, “Experimental methods in chemical engineering: specific surface area and pore size distribution measurements—BET, BJH, and

DFT," *Can. J. Chem. Eng.*, vol. 97, no. 11, pp. 2781–2791, 2019.

[58] E. P. Barrett, L. G. Joyner, and P. P. Halenda, "The Determination of Pore Volume and Area Distributions in Porous Substances. I. Computations from Nitrogen Isotherms," *J. Am. Chem. Soc.*, vol. 73, no. 1, pp. 373–380, 1951.

[59] M. L. Ojeda, J. M. Esparza, A. Campero, S. Cordero, I. Kornhauser, and F. Rojas, "On comparing BJH and NLDFT pore-size distributions determined from N2 sorption on SBA-15 substrata," *Phys. Chem. Chem. Phys.*, vol. 5, no. 9, pp. 1859–1866, 2003.

[60] Micromeritics, "Micromeritics Whitepaper: An Introduction to NLDFT Models for Porosity Characterisation," *Micromeritics Whitepapers*, 2021. [Online]. Available: https://www.micromeritics.com/Repository/Files/WP_An_Introduction_to_NLDFT.pdf. [Accessed: 13-Mar-2021].

[61] J. Jagiello and Micromeritics, "Introduction to Characterization of Pore Structure of Materials Using NLDFT Models," *Micromeritics Whitepapers*, 2008. [Online]. Available: https://www.micromeritics.com/Repository/Files/WP_An_Introduction_to_NLDFT.pdf. [Accessed: 13-Mar-2021].

[62] International Organization for Standardization, "Pore size distribution and porosity of solid materials by mercury porosimetry and gas adsorption- Part 3: Analysis of micropores by gas adsorption," 2007.

[63] S. K. P. Veerapandian, N. De Geyter, J. M. Giraudon, J. F. Lamonier, and R. Morent, "The use of zeolites for VOCs abatement by combining non-thermal plasma, adsorption, and/or catalysis: A review," *Catalysts*, vol. 9, no. 1, pp. 98–138, 2019.

[64] R. S. Mikhail and F. A. Shebl, "Adsorption in relation to pore structures of silicas II. Water vapor adsorption on wide-pore and microporous silica gels," *J. Colloid Interface Sci.*, vol. 34, no. 1, pp. 65–75, 1970.

[65] J. Villarroel-Rocha, D. Barrera, A. G. Blanco, M. E. R. Jalil, and K. Sapag, “Importance of the αs-plot method in the characterization of nanoporous materials,” *Adsorpt. Sci. Technol.*, vol. 31, no. 2/3, pp. 165–183, 2013.

[66] K. Ramesh, K. S. Reddy, I. Rashmi, and A. K. Biswas, “Porosity Distribution, Surface Area, and Morphology of Synthetic Potassium Zeolites: A SEM and N2 Adsorption Study,” *Commun. Soil Sci. Plant Anal.*, vol. 45, no. 16, pp. 2171–2181, 2014.

[67] Z. Wan, W. Wu, W. Chen, H. Yang, and D. Zhang, “Direct synthesis of hierarchical ZSM-5 zeolite and its performance in catalyzing methanol to gasoline conversion,” *Ind. Eng. Chem. Res.*, vol. 53, no. 50, pp. 19471–19478, 2014.

[68] A. Okhovat, A. Ahmadpour, F. Ahmadpour, and Z. Khaki Yadegar, “Pore Size Distribution Analysis of Coal-Based Activated Carbons: Investigating the Effects of Activating Agent and Chemical Ratio,” *ISRN Chem. Eng.*, vol. 2012, pp. 1–10, 2012.

[69] M. Hajnos, J. Glinski, J. Horabik, and J. Lipiec, “Porosimetry,” in *Encyclopedia of Agrophysics*, vol. 1, Dordrecht, NL: Springer, 2011, pp. 941–942.

[70] S. P. Rigby and R. S. Fletcher, “Interfacing mercury porosimetry with nitrogen sorption,” *Part. Part. Syst. Charact.*, vol. 21, no. 2, pp. 138–148, 2004.

[71] W. C. Conner, J. F. Cevallos-Candau, E. L. Weist, J. Pajares, S. Mendioroz, and A. Cortes, “Characterization of Pore Structure: Porosimetry and Sorption,” *Langmuir*, vol. 2, no. 2, pp. 151–154, 1986.

[72] Y. Belmabkhout, M. Frère, and G. De Weireld, “High-pressure adsorption measurements. A comparative study of the volumetric and gravimetric methods,” *Meas. Sci. Technol.*, vol. 15, no. 5, pp. 848–858, 2004.

[73] W.-H. Tao, T. C.-K. Yang, Y.-N. Chang, L.-K. Chang, and T.-W. Chung, “Effect of Moisture on the Adsorption of Volatile Organic Compounds by Zeolite 13×,” *J. Environ. Eng.*, vol. 130,

no. 10, pp. 1210–1216, 2004.

[74] R. L. Hassel, N. D. Hesse, and TA Instruments, “Dynamic Vapor Sorption Characterization of Pharmaceutical Recrystallization,” 2007. [Online]. Available: http://www.tainstruments.com/pdf/literature/TA335 DVS Characterization of Recrystallization.pdf. [Accessed: 12-Dec-2020].

[75] A. Gabelman and Gabelman Process Solutions LLC, “Adsorption basics: Part 1,” *AiChE: Chemical Engineering Progress*, 2017. [Online]. Available: https://www.aiche.org/sites/default/files/docs/pages/adsorption_basics_part_1.pdf. [Accessed: 03-Nov-2019].

[76] Z. Z. Chowdhury, S. B. Abd Hamid, and S. M. Zain, “Evaluating design parameters for breakthrough curve analysis and kinetics of fixed bed columns for Cu(II) cations using lignocellulosic wastes,” *BioResources*, vol. 10, no. 1, pp. 732–749, 2015.

[77] H. Patel, “Fixed-bed column adsorption study: a comprehensive review,” *Appl. Water Sci.*, vol. 9, pp. 1–17, 2019.

[78] P. S. Bárcia, J. A. C. Silva, and A. E. Rodrigues, “Separation by Fixed-Bed Adsorption of Hexane Isomers in Zeolite BETA Pellets,” *Ind. Eng. Chem. Res.*, vol. 45, no. 12, pp. 4316–4328, 2006.

[79] I. C. C. Mantovaneli, E. C. Ferretti, M. R. Simões, and C. Ferreira Da Silva, “The effect of temperature and flow rate on the clarification of the aqueous stevia-extract in a fixed-bed column with zeolites,” *Brazilian J. Chem. Eng.*, vol. 21, no. 3, pp. 449–458, 2004.

[80] N. S. Wilkins, A. Rajendran, and S. Farooq, “Dynamic column breakthrough experiments for measurement of adsorption equilibrium and kinetics,” *Adsorption*, vol. 27, pp. 397–422, 2020.

[81] A. W. Heinen, J. A. Peters, and H. van Bekkum, “Competitive adsorption of water and toluene on modified activated carbon supports,” *Appl. Catal. A Gen.*, vol. 194–195, pp. 193–202, 2000.

[82] E. Díaz, S. Ordóñez, A. Vega, and J. Coca, “Adsorption characterisation of different volatile organic compounds over alumina, zeolites and activated carbon using inverse gas chromatography,” *J. Chromatogr. A*, vol. 1049, no. 1–2, pp. 139–146, 2004.

[83] J. Wang and X. Guo, “Adsorption kinetic models: Physical meanings, applications, and solving methods,” *J. Hazard. Mater.*, vol. 390, no. January, pp. 122156–122174, 2020.

[84] G. W. Kajjumba, S. Emik, A. Öngen, H. K. Özan, and S. Aydin, “Modelling of Adsorption Kinetic Processes- Errors, Theory and Application,” in *Advanced Sorption Process Applications*, S. Edebali, Ed. IntechOpen, 2018, p. Chapter 10.

[85] L. Largitte and R. Pasquier, “A review of the kinetics adsorption models and their application to the adsorption of lead by an activated carbon,” *Chem. Eng. Res. Des.*, vol. 109, pp. 495–504, 2016.

[86] X. J. Liu, Y. F. Shi, M. A. Kalbassi, R. Underwood, and Y. S. Liu, “Water vapor adsorption isotherm expressions based on capillary condensation,” *Sep. Purif. Technol.*, vol. 116, pp. 95–100, 2013.

[87] L. Giraldo, P. Rodriguez-Estupiñán, and J. C. Moreno-Piraján, “Isosteric heat: Comparative study between Clausius-Clapeyron, CSK and adsorption calorimetry methods,” *Processes*, vol. 7, no. 4, pp. 203–228, 2019.

[88] J. P. Simonin, “On the comparison of pseudo-first order and pseudo-second order rate laws in the modeling of adsorption kinetics,” *Chem. Eng. J.*, vol. 300, no. April, pp. 254–263, 2016.

[89] Y. S. Ho and G. McKay, “Pseudo-second order model for sorption processes,” *Process Biochem.*, vol. 34, pp. 451–465, 1999.

[90] R. M. Barrer and B. E. F. Fender, “The diffusion and sorption of water in zeolites- I. Sorption,” *J. Phys. Chem. Solids*, vol. 21, no. 1/2, pp. 1–11, 1961.

[91] Surface Measurement Systens, “DVS Advanced Analysis Suite v7.0- User Manual (Revision

2),” 2008.

[92] K. H. Chu, “Breakthrough curve analysis by simplistic models of fixed bed adsorption: In defense of the century-old Bohart-Adams model,” *Chem. Eng. J.*, vol. 380, no. June 2019, pp. 122513–122521, 2020.

[93] Y. H. Yoon and J. H. Nelson, “Application of gas adsorption kinetics. I. A theoretical model for respirator cartridge service life,” *Am. Ind. Hyg. Assoc. J.*, vol. 45, no. 8, pp. 509–516, Aug. 1984.

[94] S. S. Baral, N. Das, T. S. Ramulu, S. K. Sahoo, S. N. Das, and G. R. Chaudhury, “Removal of Cr(VI) by thermally activated weed Salvinia cucullata in a fixed-bed column,” *J. Hazard. Mater.*, vol. 161, no. 2–3, pp. 1427–1435, 2009.

[95] G. S. Bohart and E. Q. Adams, “Some aspects of the behavior of charcoal with respect to chlorine,” *J. Am. Chem. Soc.*, vol. 42, no. 3, pp. 523–544, 1920.

[96] A. Nuhnen and C. Janiak, “A practical guide to calculate the isosteric heat/enthalpy of adsorption via adsorption isotherms in metal-organic frameworks, MOFs,” *Dalt. Trans.*, vol. 49, no. 30, pp. 10295–10307, 2020.

[97] J. Pires, A. Carvalho, and M. B. De Carvalho, “Adsorption of volatile organic compounds in Y zeolites and pillared clays,” *Microporous Mesoporous Mater.*, vol. 43, pp. 277–287, 2001.

[98] R. Roque-Malherbe, “Chapter 12- Applications of natural zeolites in pollution abatement and industry,” in *Handbook of Surfaces and Interfaces of Materials*, H. S. B. T.-H. of S. and I. of M. Nalwa, Ed. Burlington: Academic Press, 2001, pp. 495–522.

[99] S. Xian *et al.*, “Competitive adsorption of water vapor with VOCs dichloroethane, ethyl acetate and benzene on MIL-101(Cr) in humid atmosphere,” *RSC Adv.*, vol. 5, no. 3, pp. 1827–1834, 2015.

[100] I. Halasz, S. Kim, and B. Marcus, “Hydrophilic and hydrophobic adsorption on Y zeolites,” *Mol. Phys.*, vol. 100, no. 19, pp. 3123–3132, 2002.

[101] A. J. Fletcher, M. J. Benham, and K. M. Thomas, “Multicomponent Vapor Sorption on Active Carbon by Combined Microgravimetry and Dynamic Sampling Mass Spectrometry,” *J. Phys. Chem. B*, vol. 106, pp. 7474–7482, 2002.

[102] Z. Zhao, S. Wang, Y. Yang, X. Li, J. Li, and Z. Li, “Competitive adsorption and selectivity of benzene and water vapor on the microporous metal organic frameworks (HKUST-1),” *Chem. Eng. J.*, vol. 259, pp. 79–89, 2015.

[103] M. Moshoeshoe, M. Silas Nadiye-Tabbiruka, and V. Obuseng, “A Review of the Chemistry, Structure, Properties and Applications of Zeolites,” *Am. J. Mater. Sci.*, vol. 7, no. 5, pp. 196–221, 2017.

[104] T. Armbruster and M. E. Gunter, “Crystal structures of natural zeolites,” *Rev. Mineral. Geochemistry*, vol. 45, no. 1, pp. 1–67, 2001.

[105] D. S. Coombs *et al.*, “Recommended nomenclature for zeolite minerals: report of the subcommittee on zeolites of the International Mineralogical Association, Commission on new Minerals and Mineral names,” *Can. Mineral.*, vol. 35, no. 6, pp. 1571–1606, 1997.

[106] U.S. Geological Survey, “Zeolites Statistics and Information,” *Mineral commodity summaries 2019: U.S. Geological Survey*, 2019. [Online]. Available: https://www.usgs.gov/centers/nmic/zeolites-statistics-and-information.

[107] A. Julbe and M. Drobek, “Zeolite A: Type,” in *Encyclopedia of Membranes*, E. Drioli and L. Giorno, Eds. Berlin, DE: Springer, 2016, pp. 2055–2056.

[108] ZEODET: Association of Detergent Zeolite Producers, “Zeolites for Detergents,” 2000. [Online]. Available: https://www.euzepa.eu/images/3.ZEODETbrochure.pdf. [Accessed: 27-Jan-2021].

[109] A. Julbe and M. Drobek, “Zeolite X: Type,” in *Encyclopedia of Membranes*, E. Drioli and L. Giorno, Eds. Berlin, DE: Springer, 2015, pp. 2059–2060.

[110] R. Tekin, N. Bac, J. Warzywoda, and A. Sacco, “Encapsulation of a fragrance molecule in zeolite X,” *Microporous Mesoporous Mater.*, vol. 215, pp. 51–57, 2015.

[111] A. Julbe and M. Drobek, “Zeoltie Y: Type,” in *Encyclopedia of Membranes*, E. Drioli and L. Giorno, Eds. Berlin, DE: Springer, 2016, pp. 2060–2061.

[112] A. Julbe and M. Drobek, “ZSM-5 Zeolite Membrane,” in *Encyclopedia of Membranes*, E. Drioli and L. Giorno, Eds. Berlin, DE: Springer, 2016, pp. 2069–2070.

[113] M. Pera-Titus, “Thermodynamic Analysis of Type VI Adsorption Isotherms in MFI Zeolites,” *J. Phys. Chem. C*, vol. 115, no. 8, pp. 3346–3357, 2011.

[114] L. B. McCusker and C. Baerlocher, “Chapter 2: Zeolite structures,” in *Studies in Surface Science and Catalysis: Introduction to Zeolite Science and Practice*, 3rd ed., J. Cejka, H. van Bekkum, A. Corma, and F. Schueth, Eds. Elsevier, 2007, pp. 13–37.

[115] C. Baerlocher and L. B. McCusker, “Database of Zeolite Structures,” 2021. [Online]. Available: http://www.iza-structure.org/databases/. [Accessed: 19-Apr-2021].

[116] N. Y. Chen, “Hydrophobic properties of zeolites,” *J. Phys. Chem.*, vol. 80, no. 1, pp. 60–64, 1976.

[117] J. C. Groen, L. A. A. Peffer, and J. Pérez-Ramírez, “Pore size determination in modified micro- and mesoporous materials. Pitfalls and limitations in gas adsorption data analysis,” *Microporous Mesoporous Mater.*, vol. 60, no. 1–3, pp. 1–17, 2003.

[118] K. Chen, J. Kelsey, J. L. White, L. Zhang, and D. Resasco, “Water Interactions in Zeolite Catalysts and Their Hydrophobically Modified Analogues,” *ACS Catal.*, vol. 5, no. 12, pp. 7480–7487, 2015.

[119] L. Shirazi, E. Jamshidi, and M. R. Ghasemi, “The effect of Si/Al ratio of ZSM-5 zeolite on its morphology, acidity and crystal size,” *Cryst. Res. Technol.*, vol. 43, no. 12, pp. 1300–1306, 2008.

[120] M. Müller, G. Harvey, and R. Prins, “Comparison of the dealumination of zeolites beta, mordenite, ZSM-5 and ferrierite by thermal treatment, leaching with oxalic acid and treatment with SiCl 4 by 1H, 29Si and 27Al MAS NMR,” *Microporous Mesoporous Mater.*, vol. 34, pp. 135–147, 2000.

[121] T. Kawai and K. Tsutsumi, “Evaluation of the Secondary Pore Structure of Hydrothermally- and Acid-treated Faujasite Type Zeolites,” *Adsorption*, vol. 4, no. 3–4, pp. 225–231, 1998.

[122] Y. Ni *et al.*, “Preparation of hierarchical mesoporous Zn/HZSM-5 catalyst and its application in MTG reaction,” *J. Nat. Gas Chem.*, vol. 20, no. 3, pp. 237–242, 2011.

[123] W. Lutz, “Zeolite Y: Synthesis, modification, and properties - A case revisited,” *Adv. Mater. Sci. Eng.*, vol. 2014, pp. 1–20, 2014.

[124] D. Coster, A. L. Blumenfeld, and J. J. Fripiat, “Lewis Acid Sites and Surface Aluminum in Aluminas and Zeolites: A High-Resolution NMR Study,” *J. Phys. Chem.*, vol. 98, pp. 6201–6211, 1994.

[125] M. R. Bonilla *et al.*, “Diffusion study by IR micro-imaging of molecular uptake and release on mesoporous zeolites of structure type CHA and LTA,” *Materials (Basel).*, vol. 6, no. 7, pp. 2662–2688, 2013.

[126] K. M. Horax, S. Bao, M. Wang, and Y. Li, “Analysis of graphene-like activated carbon derived from rice straw for application in supercapacitor,” *Chinese Chem. Lett.*, vol. 28, no. 12, pp. 2290–2294, 2017.

[127] K. Labus, S. Gryglewicz, and J. Machnikowski, “Granular KOH-activated carbons from coal-based cokes and their CO2 adsorption capacity,” *Fuel*, vol. 118, pp. 9–15, 2014.

[128] F. Rodríguez-Reinoso and M. Molina-Sabio, “Activated carbons from lignocellulosic materials by chemical and/or physical activation: an overview,” *Carbon*, vol. 30, no. 7, pp. 1111–1118, 1992.

[129] L. Li, F. Sun, J. Gao, L. Wang, X. Pi, and G. Zhao, “Broadening the pore size of coal-based activated carbon via a washing-free chem-physical activation method for high-capacity dye adsorption,” *RSC Adv.*, vol. 8, no. 26, pp. 14488–14499, 2018.

[130] C. Falco *et al.*, “Tailoring the porosity of chemically activated hydrothermal carbons: Influence of the precursor and hydrothermal carbonization temperature,” *Carbon*, vol. 62, pp. 346–355, 2013.

[131] X. Zhang, B. Gao, A. E. Creamer, C. Cao, and Y. Li, “Adsorption of VOCs onto engineered carbon materials: A review,” *J. Hazard. Mater.*, vol. 338, pp. 102–123, 2017.

[132] A. M. Buckley and M. Greenblatt, “The sol-gel preparation of silica gels,” *J. Chem. Educ.*, vol. 71, no. 7, pp. 599–602, 1994.

[133] O. M. . Yaghi, G. Li, and H. Li, “Selective binding and removal of guests in a microporous metal-organic framework,” *Nature*, vol. 378, no. December, pp. 703–706, 1995.

[134] M. Kondo, T. Yoshitomi, K. Seki, H. Matsuzaka, and S. Kitagawa, “Three-Dimensional Framework with Channeling Cavities for Small Molecules:,” *Science*, no. 16, pp. 357–358, 1997.

[135] N. Stock and S. Biswas, “Synthesis of Metal-Organic Frameworks (MOFs): Routes to Various MOF Topologies, Morphologies, and Composites,” *Chem. Rev.*, vol. 112, no. 2, pp. 933–969, 2012.

[136] S. Horike, S. Shimomura, and S. Kitagawa, “Soft porous crystals,” *Nat. Chem.*, vol. 1, no. 9, pp. 695–704, 2009.

[137] C. Mellot-Draznieks, C. Serre, S. Surblé, N. Audebrand, and G. Férey, “Very large swelling in hybrid frameworks: A combined computational and powder diffraction study,” *J. Am. Chem. Soc.*, vol. 127, no. 46, pp. 16273–16278, 2005.

[138] J. Seo, R. Matsuda, H. Sakamoto, C. Bonneau, and S. Kitagawa, “A pillared-layer coordination

polymer with a rotatable pillar acting as a molecular gate for guest molecules," *J. Am. Chem. Soc.*, vol. 131, no. 35, pp. 12792–12800, 2009.

[139] A. Schneemann, V. Bon, I. Schwedler, I. Senkovska, S. Kaskel, and R. A. Fischer, "Flexible metal-organic frameworks," *Chem. Soc. Rev.*, vol. 43, no. 16, pp. 6062–6096, 2014.

[140] A. Kondo, H. Kajiro, T. Nakagawa, H. Tanaka, and H. Kanoh, "A flexible two-dimensional layered metal-organic framework functionalized with (trifluoromethyl)trifluoroborate: Synthesis, crystal structure, and adsorption/separation properties," *Dalt. Trans.*, vol. 49, no. 12, pp. 3692–3699, 2020.

[141] J. Seo, C. Bonneau, R. Matsuda, M. Takata, and S. Kitagawa, "Soft secondary building unit: Dynamic bond rearrangement on multinuclear core of porous coordination polymers in gas media," *J. Am. Chem. Soc.*, vol. 133, no. 23, pp. 9005–9013, 2011.

[142] A. J. Fletcher, K. M. Thomas, and M. J. Rosseinsky, "Flexibility in metal-organic framework materials: Impact on sorption properties," *J. Solid State Chem.*, vol. 178, pp. 2491–2510, 2005.

[143] B. Chen, Z. Yang, Y. Zhu, and Y. Xia, "Zeolitic imidazolate framework materials: Recent progress in synthesis and applications," *J. Mater. Chem. A*, vol. 2, no. 40, pp. 16811–16831, 2014.

[144] B. Wang, A. P. Côté, H. Furukawa, M. O'Keeffe, and O. M. Yaghi, "Colossal cages in zeolitic imidazolate frameworks as selective carbon dioxide reservoirs," *Nature*, vol. 453, no. 7192, pp. 207–211, 2008.

[145] K. Zhang *et al.*, "Exploring the framework hydrophobicity and flexibility of ZIF-8: From biofuel recovery to hydrocarbon separations," *J. Phys. Chem. Lett.*, vol. 4, no. 21, pp. 3618–3622, 2013.

[146] K. Noh, J. Lee, and J. Kim, "Compositions and Structures of Zeolitic Imidazolate Frameworks," *Isr. J. Chem.*, vol. 58, no. 9, pp. 1075–1088, 2018.

[147] X. C. Huang, Y. Y. Lin, J. P. Zhang, and X. M. Chen, "Ligand-directed strategy for zeolite-type

metal-organic frameworks: Zinc(II) imidazolates with unusual zeolitic topologies," *Angew. Chemie - Int. Ed.*, vol. 45, no. 10, pp. 1557–1559, 2006.

[148] M.-S. Jang, H.-J. Kwon, W.-S. Ahn, Y.-R. Lee, H.-Y. Cho, and S. Kim, "ZIF-8: A comparison of synthesis methods," *Chem. Eng. J.*, vol. 271, pp. 276–280, 2015.

[149] O. Karagiaridi, M. B. Lalonde, W. Bury, A. A. Sarjeant, O. K. Farha, and J. T. Hupp, "Opening ZIF-8: A catalytically active zeolitic imidazolate framework of sodalite topology with unsubstituted linkers," *J. Am. Chem. Soc.*, vol. 134, no. 45, pp. 18790–18796, 2012.

[150] P. A. P. Mendes, A. E. Rodrigues, P. Horcajada, C. Serre, and J. A. C. Silva, "Single and multicomponent adsorption of hexane isomers in the microporous ZIF-8," *Microporous Mesoporous Mater.*, vol. 194, pp. 146–156, 2014.

[151] T. Ueda, T. Yamatani, and M. Okumura, "Dynamic Gate Opening of ZIF-8 for Bulky Molecule Adsorption as Studied by Vapor Adsorption Measurements and Computational Approach," *J. Phys. Chem. C*, vol. 123, pp. 27542–27553, 2019.

[152] P. Krokidas, M. Castier, and I. G. Economou, "Computational Study of ZIF-8 and ZIF-67 Performance for Separation of Gas Mixtures," *J. Phys. Chem. C*, vol. 121, no. 33, pp. 17999–18011, 2017.

[153] K. Zhou, B. Mousavi, Z. Luo, S. Phatanasri, S. Chaemchuen, and F. Verpoort, "Characterization and properties of Zn/Co zeolitic imidazolate frameworks vs. ZIF-8 and ZIF-67," *J. Mater. Chem. A*, vol. 5, no. 3, pp. 952–957, 2017.

[154] S. A. Ahmed, D. Bagchi, H. A. Katouah, M. N. Hasan, H. M. Altass, and S. K. Pal, "Enhanced Water Stability and Photoresponsivity in Metal-Organic Framework (MOF): A Potential Tool to Combat Drug-resistant Bacteria," *Sci. Rep.*, vol. 9, pp. 19372–19383, 2019.

[155] A. Elsayed, S. Mahmoud, R. Al-Dadah, J. Bowen, and W. Kaialy, "Experimental and numerical investigation of the effect of pellet size on the adsorption characteristics of activated

carbon/ethanol," *Energy Procedia*, vol. 61, pp. 2327–2330, 2014.

[156] F. Akhtar, L. Andersson, S. Ogunwumi, N. Hedin, and L. Bergström, "Structuring adsorbents and catalysts by processing of porous powders," *J. Eur. Ceram. Soc.*, vol. 34, no. 7, pp. 1643–1666, 2014.

[157] S. E. Bambalaza, H. W. Langmi, R. Mokaya, N. M. Musyoka, J. Ren, and L. E. Khotseng, "Compaction of a zirconium metal-organic framework (UiO-66) for high density hydrogen storage applications," *J. Mater. Chem. A*, vol. 6, no. 46, pp. 23569–23577, 2018.

[158] G. W. Peterson, J. B. Decoste, T. G. Glover, Y. Huang, H. Jasuja, and K. S. Walton, "Effects of pelletization pressure on the physical and chemical properties of the metal-organic frameworks Cu3(BTC)2 and UiO-66," *Microporous Mesoporous Mater.*, vol. 179, pp. 48–53, 2013.

[159] J. Hou, A. F. Sapnik, and T. D. Bennett, "Metal-organic framework gels and monoliths," *Chem. Sci.*, vol. 11, no. 2, pp. 310–323, 2020.

[160] A. Charkhi, M. Kazemeini, S. J. Ahmadi, and H. Kazemian, "Fabrication of granulated NaY zeolite nanoparticles using a new method and study the adsorption properties," *Powder Technol.*, vol. 231, pp. 1–6, 2012.

[161] Z. Vajglová *et al.*, "Effect of Binders on the Physicochemical and Catalytic Properties of Extrudate-Shaped Beta Zeolite Catalysts for Cyclization of Citronellal," *Org. Process Res. Dev.*, vol. 23, no. 11, pp. 2456–2463, 2019.

[162] L. Jia, J. Shi, C. Long, F. Lian, and B. Xing, "VOCs adsorption on activated carbon with initial water vapor contents: Adsorption mechanism and modified characteristic curves," *Sci. Total Environ.*, vol. 731, p. 139184, 2020.

[163] M. A. Sidheswaran, H. Destaillats, D. P. Sullivan, S. Cohn, and W. J. Fisk, "Energy efficient indoor VOC air cleaning with activated carbon fiber (ACF) filters," *Build. Environ.*, vol. 47, pp. 357–367, 2012.

[164] M. M. Dubinin and V. V. Serpinsky, “Isotherm equation for water vapor adsorption by microporous carbonaceous adsorbents,” *Carbon*, vol. 19, no. 5, pp. 402–403, 1981.

[165] E. Jaramillo and M. Chandross, “Adsorption of small molecules in LTA zeolites. 1. NH3, CO2, and H2O in zeolite 4A,” *J. Phys. Chem. B*, vol. 108, no. 52, pp. 20155–20159, 2004.

[166] H. Yi, H. Deng, X. Tang, Q. Yu, X. Zhou, and H. Liu, “Adsorption equilibrium and kinetics for SO2, NO, CO2 on zeolites FAU and LTA,” *J. Hazard. Mater.*, vol. 203–204, pp. 111–117, 2012.

[167] A. Ogata, D. Ito, K. Mizuno, S. Kushiyama, and T. Yamamoto, “Removal of dilute benzene using zeolite-hybrid plasma reactor,” in *Transactions on Industry Applications*, 2001, vol. 37, no. 4, pp. 959–964.

[168] D. M. Ruthven and B. K. Kaul, “Adsorption of Aromatic Hydrocarbons in NaX Zeolite. 1. Equilibrium,” *Ind. Eng. Chem. Res.*, vol. 32, no. 9, pp. 2047–2052, 1993.

[169] J. A. Dunne, M. Rao, S. Sircar, R. J. Gorte, and A. L. Myers, “Calorimetric Heats of Adsorption and Adsorption Isotherms. 2. O2, N2, Ar, CO2, CH4, C2H6, and SF6 on NaX, H-ZSM-5, and Na-ZSM-5 Zeolites,” *Langmuir*, vol. 7463, no. 26, pp. 5896–5904, 1996.

[170] J. Wu, L. Zhang, C. Long, and Q. Zhang, “Adsorption characteristics of pentane, hexane, and heptane: Comparison of hydrophobic hypercrosslinked polymeric adsorbent with activated carbon,” *J. Chem. Eng. Data*, vol. 57, no. 12, pp. 3426–3433, 2012.

[171] X. S. Zhao, Q. Ma, and G. Q. Lu, “VOC removal: Comparison of MCM-41 with hydrophobic zeolites and activated carbon,” *Energy & Fuels*, vol. 12, no. 6, pp. 1051–1054, 1998.

[172] I. Halasz, S. Kim, and B. Marcus, “Uncommon adsorption isotherm of methanol on a hydrophobic Y-zeolite,” *J. Phys. Chem. B*, vol. 105, no. 44, pp. 10788–10796, 2001.

[173] B. Jha and D. N. Singh, “Chapter 2: Basics of Zeolites,” in *Fly Ash Zeolites: Innovations, Applications, and Directions*, B. Jha and D. N. Singh, Eds. New York, USA: Springer, 2016.

[174] K. M. Kim, H. T. Oh, S. J. Lim, K. Ho, Y. Park, and C. H. Lee, "Adsorption Equilibria of Water Vapor on Zeolite 3A, Zeolite 13X, and Dealuminated Y Zeolite," *J. Chem. Eng. Data*, vol. 61, no. 4, pp. 1547–1554, 2016.

[175] W. Lutz, M. Suckow, and M. Bülow, "Adsorption of hydrogen sulphide on molecular sieves. No enrichment in the presence of carbon dioxide," *Gas Sep. Purif.*, vol. 4, no. 4, pp. 190–196, 1990.

[176] W. L. F. Armarego, "Chapter 1: Common Physical Techniques Used in Purification," in *Purification of Laboratory Chemicals*, 8th ed., W. Armarego, Ed. Oxford, UK: Butterworth-Heinemann, 2017, pp. 1–70.

[177] M. Kraus, U. Trommler, F. Holzer, F. D. Kopinke, and U. Roland, "Competing adsorption of toluene and water on various zeolites," *Chem. Eng. J.*, vol. 351, no. June, pp. 356–363, 2018.

[178] C. K. W. Meininghaus and R. Prins, "Sorption of volatile organic compounds on hydrophobic zeolites," *Microporous Mesoporous Mater.*, vol. 35, pp. 349–365, 2000.

[179] D. T. Tefera, Z. Hashisho, J. H. Philips, J. E. Anderson, and M. Nichols, "Modeling competitive adsorption of mixtures of volatile organic compounds in a fixed-bed of beaded activated carbon," *Environ. Sci. Technol.*, vol. 48, no. 9, pp. 5108–5117, 2014.

[180] H.-C. Shin, J.-W. Park, K. Park, and H.-C. Song, "Removal characteristics of trace compounds of landfill gas by activated carbon adsorption," *Environ. Pollut.*, vol. 119, no. 2, pp. 227–236, 2002.

[181] M. A. Lillo-Ródenas, A. J. Fletcher, K. M. Thomas, D. Cazorla-Amorós, and A. Linares-Solano, "Competitive adsorption of a benzene-toluene mixture on activated carbons at low concentration," *Carbon*, vol. 44, no. 8, pp. 1455–1463, 2006.

[182] B. A. De Moor, M.-F. Reyniers, and G. B. Marin, "Physisorption and chemisorption of alkanes and alkenes in H-FAU: a combined ab initio–statistical thermodynamics study," *Phys. Chem.*

Chem. Phys., vol. 11, pp. 2939–3958, 2009.

[183] W. K. Pui, R. Yusoff, and M. K. Aroua, "A review on activated carbon adsorption for volatile organic compounds (VOCs)," *Rev. Chem. Eng.*, vol. 35, no. 5, pp. 649–668, 2019.

[184] M.-H. Lai, R. Q. Chu, H.-C. Huang, S.-H. Shu, and T.-W. Chung, "Equilibrium Isotherms of Volatile Alkanes, Alkenes, and Ketones on Activated Carbon," *J. Chem. Eng. Data*, vol. 54, no. 8, pp. 2208–2215, 2009.

[185] F. Hussey and A. Gupta, "Removal of VOCs from industrial process exhaust with carbon and zeolite adsorbents," in *Air and Waste Management Association (AWMA) specialty conference on emerging solutions to VOC and air toxics control*, 1996.

[186] C. Petit, K. Kante, and T. J. Bandosz, "The role of sulfur-containing groups in ammonia retention on activated carbons," *Carbon*, vol. 48, no. 3, pp. 654–667, 2009.

[187] M. A. Lillo-Ródenas, D. Cazorla-Amorós, and A. Linares-Solano, "Behaviour of activated carbons with different pore size distributions and surface oxygen groups for benzene and toluene adsorption at low concentrations," *Carbon*, vol. 43, no. 8, pp. 1758–1767, 2005.

[188] J. M. . Logue, T. E. . McKone, M. H. . Sherman, and B. C. Singer, "Hazard assessment of chemical air contaminants measured in residences," *Indoor Air*, vol. 21, pp. 92–109, 2011.

[189] J. Pei and J. S. Zhang, "Determination of adsorption isotherm and diffusion coefficient of toluene on activated carbon at low concentrations," *Build. Environ.*, vol. 48, no. 1, pp. 66–76, 2012.

[190] L. Cao, X. Huang, F. Feng, and F. Ji, "Effect of relative humidity on adsorption capacity of organic vapors on activated carbon and prediction by the modified D-R equations," in *2010 International Conference on Digital Manufacturing and Automation*, 2010, vol. 1, pp. 608–611.

[191] I. I. Laskar, Z. Hashisho, J. H. Phillips, J. E. Anderson, and M. Nichols, "Modeling the Effect of Relative Humidity on Adsorption Dynamics of Volatile Organic Compound onto Activated Carbon," *Environ. Sci. Technol.*, vol. 53, no. 5, pp. 2647–2659, 2019.

[192] M. P. Cal, M. J. Rood, and S. M. Larson, “Removal of VOCs from humidified gas streams using activated carbon cloth,” *Gas Sep. Purif.*, vol. 10, no. 2, pp. 117–121, 1996.

[193] J. Rodriguez-Mirasol, J. Bedia, T. Cordero, and J. Rodriguez, “Influence of water vapor on the adsorption of VOCs on lignin-based activated carbons,” *Sep. Sci. Technol.*, vol. 40, no. 15, pp. 3113–3135, 2005.

[194] W. Huang, J. Xu, B. Tang, H. Wang, X. Tan, and A. Lv, “Adsorption performance of hydrophobically modified silica gel for the vapors of n-hexane and water,” *Adsorpt. Sci. Technol.*, vol. 36, no. 3–4, pp. 888–903, 2018.

[195] C. M. Wang, K. Sen Chang, T.-W. Chung, and H. Wu, “Adsorption equilibria of aromatic compounds on activated carbon, silica gel, and 13X zeolite,” *J. Chem. Eng. Data*, vol. 49, no. 3, pp. 527–531, 2004.

[196] B. Biliński, “High-temperature adsorption of n-octane, benzene, and chloroform onto silica gel surface,” *J. Colloid Interface Sci.*, vol. 225, no. 1, pp. 105–111, 2000.

[197] T. S. Ge, D. Qi, Y. J. Dai, and R. Z. Wang, “Experimental testing on contaminant and moisture removal performance of silica gel desiccant wheel,” *Energy Build.*, vol. 176, pp. 71–77, 2018.

[198] Y. Sheng, L. Zhang, Y. Wang, and L. Fang, “Explore energy saving operation strategy: Indoor VOCs removal performance of silica gel rotor in clean-air heat pump system at low regeneration air temperature,” *Energy Build.*, vol. 202, 2019.

[199] X. Lu *et al.*, “Preparation of hydrophobic hierarchical pore carbon–silica composite and its adsorption performance toward volatile organic compounds,” *J. Environ. Sci.*, vol. 87, pp. 39–48, 2020.

[200] K. Yang, Q. Sun, F. Xue, and D. Lin, “Adsorption of volatile organic compounds by metal-organic frameworks MIL-101: Influence of molecular size and shape,” *J. Hazard. Mater.*, vol. 195, pp. 124–131, 2011.

[201] T. K. Trung *et al.*, "Adsorption of C5-C9 hydrocarbons in microporous MOFs MIL-100(Cr) and MIL-101(Cr): A manometric study," *Microporous Mesoporous Mater.*, vol. 134, pp. 134–140, 2010.

[202] D. Wang *et al.*, "Study on the copper(II)-doped MIL-101(Cr) and its performance in VOCs adsorption," *Environ. Sci. Pollut. Res.*, vol. 25, no. 28, pp. 28109–28119, 2018.

[203] P. Iacomi, U. H. Lee, A. H. Valekar, J. S. Chang, and P. L. Llewellyn, "Investigating the effect of alumina shaping on the sorption properties of promising metal-organic frameworks," *RSC Adv.*, vol. 9, no. 13, pp. 7128–7135, 2019.

[204] M. F. De Lange *et al.*, "Understanding adsorption of highly polar vapors on mesoporous MIL-100(Cr) and MIL-101(Cr): Experiments and molecular simulations," *J. Phys. Chem. C*, vol. 117, no. 15, pp. 7613–7622, 2013.

[205] V. Bon, I. Senkovska, J. D. Evans, M. Wöllner, M. Hölzel, and S. Kaskel, "Insights into the water adsorption mechanism in the chemically stable zirconium-based MOF DUT-67- a prospective material for adsorption-driven heat transformations," *J. Mater. Chem. A*, vol. 7, no. 20, pp. 12681–12690, 2019.

[206] K. Vellingiri, P. Kumar, A. Deep, and K. H. Kim, "Metal-organic frameworks for the adsorption of gaseous toluene under ambient temperature and pressure," *Chem. Eng. J.*, vol. 307, pp. 1116–1126, 2017.

[207] K. Zhang *et al.*, "Alcohol and water adsorption in zeolitic imidazolate frameworks," *Chem. Commun.*, vol. 49, no. 31, pp. 3245–3247, 2013.

[208] J. J. Low, A. I. Benin, P. Jakubczak, J. F. Abrahamian, S. A. Faheem, and R. R. Willis, "Virtual high throughput screening confirmed experimentally: Porous coordination polymer hydration," *J. Am. Chem. Soc.*, vol. 131, no. 43, pp. 15834–15842, 2009.

[209] W. Xue, Z. Zhang, H. Huang, C. Zhong, and D. Mei, "Theoretical Insights into the Initial

Hydrolytic Breakdown of HKUST-1," *J. Phys. Chem. C*, vol. 124, pp. 1991–2001, 2020.

[210] J. Canivet, A. Fateeva, Y. Guo, B. Coasne, and D. Farrusseng, "Water adsorption in MOFs: Fundamentals and applications," *Chem. Soc. Rev.*, vol. 43, no. 16, pp. 5594–5617, 2014.

[211] A. U. Ortiz, A. P. Freitas, A. Boutin, A. H. Fuchs, and F. X. Coudert, "What makes zeolitic imidazolate frameworks hydrophobic or hydrophilic? The impact of geometry and functionalization on water adsorption," *Phys. Chem. Chem. Phys.*, vol. 16, no. 21, pp. 9940–9949, 2014.

[212] D. A. Yang, H. Y. Cho, J. Kim, S. T. Yang, and W. S. Ahn, "CO2 capture and conversion using Mg-MOF-74 prepared by a sonochemical method," *Energy Environ. Sci.*, vol. 5, no. 4, pp. 6465–6473, 2012.

[213] K. Vellingiri *et al.*, "Metal organic frameworks as sorption media for volatile and semi-volatile organic compounds at ambient conditions," *Sci. Rep.*, vol. 6, no. May, pp. 1–11, 2016.

[214] L. H. Xie, X. M. Liu, T. He, and J. R. Li, "Metal-Organic Frameworks for the Capture of Trace Aromatic Volatile Organic Compounds," *Chem*, vol. 4, no. 8, pp. 1911–1927, 2018.

[215] S. Jafari, Saeed; Ghorbani, Farshid; Bahrami, Abdorahman; Kazemian, Hossein; Yousefinejad, "Removal of Toluene from Air by Zeolitic Imidazolate Framework-8: Synthesis, Characterization, and Experimental Breakthrough Curve," *Int. J. Sci. Study*, vol. 5, no. 4, 2017.

[216] C. Cai, F. Geng, X. Tie, Q. Yu, and J. An, "Characteristics and source apportionment of VOCs measured in Shanghai, China," *Atmos. Environ.*, vol. 44, no. 38, pp. 5005–5014, 2010.

[217] G. Huang *et al.*, "Speciation of anthropogenic emissions of non-methane volatile organic compounds: a global gridded data set for 1970 – 2012," *Atmos. Chem. Phys.*, vol. 17, pp. 7683–7701, 2017.

[218] F. Chu, Y. Zheng, B. Wen, L. Zhou, J. Yan, and Y. Chen, "Adsorption of toluene with water on zeolitic imidazolate framework-8/graphene oxide hybrid nanocomposites in a humid

atmosphere," *RSC Adv.*, vol. 8, no. 5, pp. 2426–2432, 2018.

[219] X. Zhang, X. Lv, X. Shi, Y. Yang, and Y. Yang, "Enhanced hydrophobic UiO-66 (University of Oslo 66) metal-organic framework with high capacity and selectivity for toluene capture from high humid air," *J. Colloid Interface Sci.*, vol. 539, pp. 152–160, 2019.

[220] Y. Sun *et al.*, "A molecular-level superhydrophobic external surface to improve the stability of metal-organic frameworks," *J. Mater. Chem. A*, vol. 5, no. 35, pp. 18770–18776, 2017.

[221] J. Cravillon, R. Nayuk, S. Springer, A. Feldhoff, K. Huber, and M. Wiebcke, "Controlling zeolitic imidazolate framework nano- and microcrystal formation: Insight into crystal growth by time-resolved in situ static light scattering," *Chem. Mater.*, vol. 23, no. 8, pp. 2130–2141, 2011.

[222] Y. K. Seo *et al.*, "Large scale fluorine-free synthesis of hierarchically porous iron(III) trimesate MIL-100(Fe) with a zeolite MTN topology," *Microporous Mesoporous Mater.*, vol. 157, pp. 137–145, 2012.

[223] Wikipedia, "Bragg's law," *Wikipedia*, 2021. [Online]. Available: https://en.wikipedia.org/wiki/Bragg%27s_law. [Accessed: 04-Apr-2021].

[224] D. Stirling and J. Clark, "Chapter 5: Synthesis and Characterisation of Solid Sorbents," in *The Sulfur Problem: Cleaning up Industrial Feedstocks*, D. Stirling, Ed. Royal Society of Chemistry, 2000, pp. 39–66.

[225] J. Wang, J. Yu, X. Zhu, and X. Z. Kong, "Preparation of hollow TiO2 nanoparticles through TiO2 deposition on polystyrene latex particles and characterizations of their structure and photocatalytic activity," *Nanoscale Res. Lett.*, vol. 7, pp. 1–8, 2012.

[226] F. Cheng, Q. Cao, Y. Guan, H. Cheng, X. Wang, and J. D. Miller, "FTIR analysis of water structure and its influence on the flotation of arcanite (K2SO4) and epsomite (MgSO4· 7H2O)," *Int. J. Miner. Process.*, vol. 122, pp. 36–42, 2013.

[227] J. Malczyk and IntruQuest Inc, "Gas (Helium) Pycnometer Theory and Practice," 2019.

[Online]. Available: http://www.instruquest.com/files/GasPycnometerBasics.pdf. [Accessed: 27-Mar-2021].

[228] JEOL, "Periodic table for EDS analysis," *Periodic Tables for SEM, TEM, Mass Spec, and NMR*, 2019. [Online]. Available: https://www.jeolusa.com/RESOURCES/JEOL-Posters/lc/47251/lcv/s/jeoledsperiodictable. [Accessed: 12-Apr-2021].

[229] R. F. . Egerton, P. . Li, and M. . Malac, "Radiation damage in the TEM and SEM," *Micron*, vol. 35, no. 6, pp. 399–409, 2004.

[230] AZO Materials and Thermo Fisher Scientific Phenom-World BV, "Different Types of SEM Imaging – BSE and Secondary Electron Imaging," *AZO Materials*, 2017. [Online]. Available: https://www.azom.com/article.aspx?ArticleID=14309. [Accessed: 12-Feb-2021].

[231] Y. Yang, N. Burke, S. Ali, S. Huang, S. Lim, and Y. Zhu, "Experimental studies of hydrocarbon separation on zeolites, activated carbons and MOFs for applications in natural gas processing," *RSC Adv.*, vol. 7, no. 21, pp. 12629–12638, 2017.

[232] J. Kenvin *et al.*, "Quantifying the Complex Pore Architecture of Hierarchical Faujasite Zeolites and the Impact on Diffusion," *Adv. Funct. Mater.*, vol. 26, no. 31, pp. 5621–5630, 2016.

[233] C. Lastoskie, K. E. Gubbins, and N. Quirked, "Pore Size Distribution Analysis of Microporous Carbons: A Density Functional Theory Approach," *J. Phys. Chem.*, vol. 97, pp. 4786–4796, 1993.

[234] B. Bueken *et al.*, "Gel-based morphological design of zirconium metal-organic frameworks," *Chem. Sci.*, vol. 8, no. 5, pp. 3939–3948, 2017.

[235] Surface Measurement Systems, "DVS Endeavour," *Surface Measurement Systems- DVS Product Brochure*, 2020. [Online]. Available: https://www.surfacemeasurementsystems.com/wp-content/uploads/2020/09/DVS_Endeavour_E-Brochure.pdf. [Accessed: 21-Mar-2021].

[236] Surface Measurement Systems, “DVS Resolution,” *Surface Measurement Systems- DVS Product Brochure*, 2014. [Online]. Available: https://www.surfacemeasurementsystems.com/wp-content/uploads/2014/05/DVS-Resolution-brochure-v1.0.pdf. [Accessed: 21-Mar-2021].

[237] J. Weitkamp, P. Kleinschmit, A. Kiss, and C. H. Berke, “The hydrophobicity index – A valuable test for probing the surface properties of zeolitic adsorbents or catalysts,” in *Proceedings from the Ninth International Zeolite Conference*, 1993, pp. 79–87.

[238] M. Sin *et al.*, “Surface polarity estimation of metal-organic frameworks using liquid-phase mixture adsorption,” *Microporous Mesoporous Mater.*, vol. 251, pp. 129–134, 2017.

[239] A. Kondor and A. Dallos, “Adsorption isotherms of some alkyl aromatic hydrocarbons and surface energies on partially dealuminated Y faujasite zeolite by inverse gas chromatography,” *J. Chromatogr. A*, vol. 1362, pp. 250–261, 2014.

[240] G. P. Hao *et al.*, “Design of Hierarchically Porous Carbons with Interlinked Hydrophilic and Hydrophobic Surface and Their Capacitive Behavior,” *Chem. Mater.*, vol. 28, no. 23, pp. 8715–8725, 2016.

[241] E. Hadjittofis, G. G. Z. Zhang, and J. Y. Y. Heng, “Influence of sample preparation on IGC measurements: the cases of silanised glass wool and packing structure,” *RSC Adv.*, vol. 7, no. 20, pp. 12194–12200, 2017.

[242] Rotronic, “HC2-C04 / HC2-C05 Humidity Temperature Probe,” *Rotronic Product Overview*, 2020. [Online]. Available: https://www.rotronic.com/en-gb/hc2-c04-hc2-c05.html. [Accessed: 09-Nov-2020].

[243] M. A. Al-Ghouti and D. A. Da’ana, “Guidelines for the use and interpretation of adsorption isotherm models: A review,” *J. Hazard. Mater.*, vol. 393, no. January, p. 122383, 2020.

[244] N. Ayawei, A. N. Ebelegi, and D. Wankasi, “Modelling and Interpretation of Adsorption

Isotherms," *J. Chem.*, vol. 2017, pp. 1–11, 2017.

[245] K. Zhang *et al.*, "Adsorption of water and ethanol in MFI-type zeolites," *Langmuir*, vol. 28, no. 23, pp. 8664–8673, 2012.

[246] L. Gueudré, M. Milina, S. Mitchell, and J. Pérez-Ramírez, "Superior mass transfer properties of technical zeolite bodies with hierarchical porosity," *Adv. Funct. Mater.*, vol. 24, no. 2, pp. 209–219, 2014.

[247] D. A.O, "Langmuir, Freundlich, Temkin and Dubinin–Radushkevich Isotherms Studies of Equilibrium Sorption of Zn 2+ Unto Phosphoric Acid Modified Rice Husk," *IOSR J. Appl. Chem.*, vol. 3, no. 1, pp. 38–45, 2012.

[248] Y. J. Wu *et al.*, "Adsorption of Pure and Binary CO2, CH4, and N2 Gas Components on Activated Carbon Beads," *J. Chem. Eng. Data*, vol. 60, no. 9, pp. 2684–2693, 2015.

[249] N. Tzabar and H. J. M. ter Brake, "Adsorption isotherms and Sips models of nitrogen, methane, ethane, and propane on commercial activated carbons and polyvinylidene chloride," *Adsorption*, vol. 22, no. 7, pp. 901–914, 2016.

[250] C. Buttersack, "Modeling of type IV and V sigmoidal adsorption isotherms," *Phys. Chem. Chem. Phys.*, vol. 21, no. 10, pp. 5614–5626, 2019.

[251] Y. K. Ryu, J. W. Chang, S. Y. Jung, and C. H. Lee, "Adsorption isotherms of toluene and gasoline vapors on DAY zeolite," *J. Chem. Eng. Data*, vol. 47, no. 2, pp. 363–366, 2002.

[252] M. Caurie, "The derivation of the GAB adsorption equation from the BDDT adsorption theory," *Int. J. Food Sci. Technol.*, vol. 41, no. 2, pp. 173–179, 2006.

[253] I. I. Laskar and Z. Hashisho, "Insights into modeling adsorption equilibria of single and multicomponent systems of organic and water vapors," *Sep. Purif. Technol.*, vol. 241, no. January, p. 116681, 2020.

[254] J. Chirife, E. O. Timmerma, H. A. Iglesias, and R. Boquet, “Some features of the parameter k of the GAB equation as applied to sorption isotherms of selected food materials,” *J. food Eng.*, vol. 15, no. 1, p. 75—82, 1992.

[255] O. Vopička *et al.*, “Equilibrium and transient sorption of vapours and gases in the polymer of intrinsic microporosity PIM-1,” *J. Memb. Sci.*, vol. 434, pp. 148–160, 2013.

[256] A. Kapoor, J. A. Ritter, and R. T. Yang, “On the Dubinin—Radushkevich Equation for Adsorption in Microporous Solids in the Henry’s Law Region,” *Langmuir*, vol. 5, no. 4, pp. 1118–1121, 1989.

[257] P. Cheng and Y. H. Hu, “Dubinin-Astakhov model for acetylene adsorption on metal-organic frameworks,” *Appl. Surf. Sci.*, vol. 377, pp. 349–354, 2016.

[258] A. C. Fernandes and J. Pires, “Adsorption of Volatile Organic Compounds on Zeolite L,” *J. Chem. Eng. Data*, vol. 61, no. 11, pp. 3890–3896, 2016.

[259] L. Shu-Jiang *et al.*, “The breakthrough curve combination for xenon sampling dynamics in a carbon molecular sieve column,” *Analyst*, vol. 140, no. 2, pp. 428–433, 2015.

[260] D. W. . Marquardt, “An algorithm for least-squares estimation of nonlinear parameters,” *J. Soc. Ind. Appl. Math.*, vol. 11, no. 2, pp. 431–441, 1963.

[261] K. Y. Foo and B. H. Hameed, “Insights into the modeling of adsorption isotherm systems,” *Chem. Eng. J.*, vol. 156, no. 1, pp. 2–10, 2010.

[262] J. Zhao, G. Wang, L. Qin, H. Li, Y. Chen, and B. Liu, “Synthesis and catalytic cracking performance of mesoporous zeolite y,” *Catal. Commun.*, vol. 73, pp. 98–102, 2016.

[263] J. R. Ugal, M. Mustafa, and A. a Abdulhadi, “Preparation of Zeolite Type 13X from Locally Available Raw Materials,” *Iraqui J. Chem. Pet. Eng.*, vol. 9, no. 1, pp. 51–56, 2008.

[264] E. Klosek-Wawrzyn, J. Malolepszy, and P. Murzyn, “Sintering behavior of kaolin with calcite,”

Procedia Eng., vol. 57, no. May 2013, pp. 572–582, 2013.

[265] R. Antony, S. T. David Manickam, P. Kollu, P. V. Chandrasekar, K. Karuppasamy, and S. Balakumar, "Highly dispersed Cu(ii), Co(ii) and Ni(ii) catalysts covalently immobilized on imine-modified silica for cyclohexane oxidation with hydrogen peroxide," *RSC Adv.*, vol. 4, no. 47, pp. 24820–24830, 2014.

[266] D. Nibou, S. Amokrane, H. Mekatel, and N. Lebaili, "Elaboration and characterization of solid materials of types zeolite NaA and faujasite NaY exchanged by zinc metallic ions Zn(2+)," *Phys. Procedia*, vol. 2, no. 3, pp. 1433–1440, 2009.

[267] M. Safak Boroglu and M. Ali Gurkaynak, "Fabrication and characterization of silica modified polyimide-zeolite mixed matrix membranes for gas separation properties," *Polym. Bull.*, vol. 66, no. 4, pp. 463–478, 2011.

[268] H. Miessner, H. Kosslick, U. Lohse, B. Parlitz, and V. A. Tuan, "Characterization of highly dealuminated faujasite-type zeolites: Ultrastable zeolite Y and ZSM-20," *J. Phys. Chem.*, vol. 97, no. 38, pp. 9741–9748, 1993.

[269] I. R. Shaikh *et al.*, "H-ZSM-5 Zeolite Synthesis by Sourcing Silica from the Wheat Husk Ash: Characterization and Application as a Versatile Heterogeneous Catalyst in Organic Transformations including Some Multicomponent Reactions," *J. Catal.*, vol. 2015, pp. 1–14, 2015.

[270] H. G. T. Nguyen, J. C. Horn, M. Bleakney, D. W. Siderius, and L. Espinal, "Understanding material characteristics through signature traits from helium pycnometry," *Langmuir*, vol. 35, no. 6, pp. 2115–2122, 2019.

[271] O. A. Ekpete, A. C. Marcus, and V. Osi, "Preparation and Characterization of Activated Carbon Obtained from Plantain (Musa paradisiaca) Fruit Stem," *J. Chem.*, vol. 2017, 2017.

[272] H. T. Oh, S. J. Lim, J. H. Kim, and C. H. Lee, "Adsorption Equilibria of Water Vapor on an

Alumina/Zeolite 13X Composite and Silica Gel," *J. Chem. Eng. Data*, vol. 62, no. 2, pp. 804–811, 2017.

[273] The Editors of Encyclopaedia Britannica, "Silica gel," *Encyclopedia Britannica*, 2013. [Online]. Available: https://www.britannica.com/science/silica-gel. [Accessed: 15-Mar-2020].

[274] A. P. D. Almeida, C. Grande, R. Ribeiro, and J. P. B. Mota, "Formulation of ZSM-5 zeolite and UTSA-16 MOF by extrusion," Chemical and Biochemical Engineering, NOVA University of Lisbon, 2018.

[275] P. S. F. Mendes, J. M. Silva, M. F. Ribeiro, A. Daudin, and C. Bouchy, "From powder to extrudate zeolite-based bifunctional hydroisomerization catalysts: on preserving zeolite integrity and optimizing Pt location," *J. Ind. Eng. Chem.*, vol. 62, pp. 72–83, 2018.

[276] X. Cheng and X. T. Bi, "Modeling NOx adsorption onto Fe/ZSM-5 catalysts in a fixed bed reactor," *Int. J. Chem. React. Eng.*, vol. 11, no. 1, pp. 19–30, 2013.

[277] L. S. Da Silva, C. A. Araki, S. M. P. Marcucci, V. L. dos S. T. Da Silva, and P. A. Arroyo, "Desilication of ZSM-5 and ZSM-12 zeolites with different crystal sizes: Effect on acidity and mesoporous initiation," *Mater. Res.*, vol. 22, no. 2, 2019.

[278] S. H. Pak and Y. W. Jeon, "Effect of vacuum regeneration of activated carbon on volatile organic compound adsorption," *Environ. Eng. Res.*, vol. 22, no. 2, pp. 169–174, 2017.

[279] S. M. Taqvi, W. S. Appel, and M. D. LeVan, "Coadsorption of organic compounds and water vapor on BPL activated carbon. 4. Methanol, ethanol, propanol, butanol, and modeling," *Ind. Eng. Chem. Res.*, vol. 38, no. 1, pp. 240–250, 1999.

[280] A. V Arundel, E. M. Sterling, J. H. Biggin, and T. D. Sterling, "Indirect health effects of relative humidity in indoor environments," *Environ. Health Perspect.*, vol. 65, no. 3, pp. 351–361, 1986.

[281] C. M. Shen and W. M. Worek, "Cosorption characteristics of solid adsorbents," *Int. J. Heat Mass Transf.*, vol. 37, no. 14, pp. 2123–2129, 1994.

[282] W. Zou, B. Gao, Y. S. Ok, and L. Dong, “Integrated adsorption and photocatalytic degradation of volatile organic compounds (VOCs) using carbon-based nanocomposites: A critical review,” *Chemosphere*, vol. 218, pp. 845–859, 2019.

[283] L. Xu, Y. Li, J. Zhu, and Z. Liu, “Removal of Toluene by Adsorption/Desorption Using Ultra-stable Y Zeolite,” *Trans. Tianjin Univ.*, vol. 25, no. 4, pp. 312–321, 2019.

[284] J.-N. Kim, K.-T. Chue, S.-H. Cho, and J.-D. Kim, “Production of High-Purity Nitrogen from Air by Pressure Swing Adsorption on Zeolite X,” *Sep. Sci. Technol.*, vol. 30, no. 3, pp. 347–368, Feb. 1995.

[285] D. Danaci, P. A. Webley, and C. Petit, “Guidelines for Techno-Economic Analysis of Adsorption Processes,” *Front. Chem. Eng.*, vol. 2, no. January, pp. 1–11, 2021.

[286] A. B. Shelekhin, A. G. Dixon, and Y. H. Ma, “Theory of gas diffusion and permeation in inorganic molecular-sieve membranes,” *AIChE J.*, vol. 41, no. 1, pp. 58–67, 1995.

[287] Y. Wang, W. Chen, B. Zhao, H. Wang, L. Qin, and J. Han, “Preparation of high-performance toluene adsorbents by sugarcane bagasse carbonization combined with surface modification,” *RSC Adv.*, vol. 10, no. 40, pp. 23749–23758, 2020.

[288] H. Gong *et al.*, “In-situ synthesis of an excellent CO2 capture material chabazite,” *J. Taiwan Inst. Chem. Eng.*, vol. 103, pp. 160–166, 2019.

[289] A. W. Marczewski, “Analysis of Kinetic Langmuir Model. Part I: Integrated Kinetic Langmuir Equation (IKL): A New Complete Analytical Solution of the Langmuir Rate Equation,” *Langmuir*, vol. 26, no. 19, pp. 15229–15238, 2010.

[290] K. Jayaramulu *et al.*, “Hydrophobic Metal–Organic Frameworks,” *Adv. Mater.*, vol. 31, no. 32, pp. 1–31, 2019.

[291] E. L. Bustamante, J. L. Fernández, and J. M. Zamaro, “Influence of the solvent in the synthesis of zeolitic imidazolate framework-8 (ZIF-8) nanocrystals at room temperature,” *J. Colloid*

Interface Sci., vol. 424, pp. 37–43, 2014.

[292] Y. Zhang, Y. Jia, M. Li, and L. Hou, "Influence of the 2-methylimidazole/ zinc nitrate hexahydrate molar ratio on the synthesis of zeolitic imidazolate framework-8 crystals at room temperature," *Sci. Rep.*, vol. 8, pp. 9597–9604, 2018.

[293] A. Schejn, L. Balan, V. Falk, L. Aranda, G. Medjahdi, and R. Schneider, "Controlling ZIF-8 nano- and microcrystal formation and reactivity through zinc salt variations," *CrystEngComm*, vol. 16, no. 21, pp. 4493–4500, 2014.

[294] M. Jian, B. Liu, R. Liu, J. Qu, H. Wang, and X. Zhang, "Water-based synthesis of zeolitic imidazolate framework-8 with high morphology level at room temperature," *RSC Adv.*, vol. 5, no. 60, pp. 48433–48441, 2015.

[295] E. Sarti, T. Chenet, L. Pasti, A. Cavazzini, E. Rodeghero, and A. Martucci, "Effect of Silica Alumina Ratio and Thermal Treatment of Beta Zeolites on the Adsorption of Toluene from Aqueous Solutions," *Minerals*, vol. 7, no. 2, p. 22, 2017.

[296] X. Zhao, S. Villar-Rodil, A. J. Fletcher, and K. M. Thomas, "Kinetic isotope effect for H2 and D2 quantum molecular sieving in adsorption/desorption on porous carbon materials," *J. Phys. Chem. B*, vol. 110, no. 20, 2006.

[297] Y. Zhang, Y. Jia, and L. Hou, "Synthesis of zeolitic imidazolate framework-8 on polyester fiber for PM-2.5 removal," *RSC Adv.*, vol. 8, no. 55, pp. 31471–31477, 2018.

[298] D. N. Ta, H. K. D. Nguyen, B. X. Trinh, Q. T. N. Le, H. N. Ta, and H. T. Nguyen, "Preparation of nano-ZIF-8 in methanol with high yield," *Can. J. Chem. Eng.*, vol. 96, no. 7, pp. 1518–1531, 2018.

[299] I. H. Lim, W. Schrader, and F. Schüth, "Insights into the molecular assembly of zeolitic imidazolate frameworks by ESI-MS," *Chem. Mater.*, vol. 27, no. 8, pp. 3088–3095, 2015.

[300] M. A. Simon *et al.*, "Hydrothermal Synthesize of HF-Free MIL-100(Fe) for Isoniazid-Drug

Delivery," *Sci. Rep.*, vol. 9, no. 1, pp. 1–11, 2019.

[301] S. Huang, K. L. Yang, X. F. Liu, H. Pan, H. Zhang, and S. Yang, "MIL-100(Fe)-catalyzed efficient conversion of hexoses to lactic acid," *RSC Adv.*, vol. 7, no. 10, pp. 5621–5627, 2017.

[302] D. Saliba, M. Ammar, M. Rammal, M. Al-Ghoul, and M. Hmadeh, "Crystal Growth of ZIF-8, ZIF-67, and Their Mixed-Metal Derivatives," *J. Am. Chem. Soc.*, vol. 140, no. 5, pp. 1812–1823, 2018.

[303] Z. Öztürk, M. Filez, and B. M. Weckhuysen, "Decoding Nucleation and Growth of Zeolitic Imidazolate Framework Thin Films with Atomic Force Microscopy and Vibrational Spectroscopy," *Chem. - A Eur. J.*, vol. 23, no. 45, pp. 10915–10924, 2017.

[304] X. Guo, T. Xing, Y. Lou, and J. Chen, "Controlling ZIF-67 crystals formation through various cobalt sources in aqueous solution," *J. Solid State Chem.*, vol. 235, no. 3, pp. 107–112, 2016.

[305] M. Erkartal *et al.*, "From 2-methylimidazole to 1,2,3-triazole: a topological transformation of ZIF-8 and ZIF-67 by post-synthetic modification," *Chem. Commun.*, vol. 53, no. 12, pp. 2028–2031, 2017.

[306] C. Rösler *et al.*, "Hollow Zn/Co Zeolitic Imidazolate Framework (ZIF) and Yolk-Shell Metal@Zn/Co ZIF Nanostructures," *Chem. - A Eur. J.*, vol. 22, no. 10, pp. 3304–3311, 2016.

[307] M. E. Casco *et al.*, "Understanding ZIF-8 Performance upon Gas Adsorption by Means of Inelastic Neutron Scattering," *ChemistrySelect*, vol. 2, no. 9, pp. 2750–2753, 2017.

[308] C. W. Tsai and E. H. G. Langner, "The effect of synthesis temperature on the particle size of nano-ZIF-8," *Microporous Mesoporous Mater.*, vol. 221, pp. 8–13, 2016.

[309] A. Hadi, J. Karimi-Sabet, and A. Dastbaz, "Parametric study on the mixed solvent synthesis of ZIF-8 nano- and micro-particles for CO adsorption: A response surface study," *Front. Chem. Sci. Eng.*, vol. 14, no. 4, pp. 579–594, 2019.

[310] R. Bose, J. Ethiraj, P. Sridhar, J. J. Varghese, N. S. Kaisare, and P. Selvam, "Adsorption of hydrogen and carbon dioxide in zeolitic imidazolate framework structure with SOD topology: experimental and modelling studies," *Adsorption*, vol. 26, no. 7, pp. 1027–1038, 2020.

[311] S. Zhong, Q. Wang, and D. Cao, "ZIF-Derived Nitrogen-Doped Porous Carbons for Xe Adsorption and Separation," *Sci. Rep.*, vol. 6, no. January, pp. 14–19, 2016.

[312] S. U. Rege and R. T. Yang, "Corrected Horvath-Kawazoe Equations for Pore-Size Distribution," *AIChE J.*, vol. 46, no. 4, pp. 734–750, 2000.

[313] F. Tan *et al.*, "Facile synthesis of size-controlled MIL-100(Fe) with excellent adsorption capacity for methylene blue," *Chem. Eng. J.*, vol. 281, pp. 360–367, 2015.

[314] X. S. Wang, L. Li, J. Liang, Y. B. Huang, and R. Cao, "Boosting Oxidative Desulfurization of Model and Real Gasoline over Phosphotungstic Acid Encapsulated in Metal–Organic Frameworks: The Window Size Matters," *ChemCatChem*, vol. 9, no. 6, pp. 971–979, 2017.

[315] P. G. M. Mileo, K. Ho Cho, J. Park, S. Devautour-Vinot, J. S. Chang, and G. Maurin, "Unraveling the Water Adsorption Mechanism in the Mesoporous MIL-100(Fe) Metal-Organic Framework," *J. Phys. Chem. C*, vol. 123, no. 37, pp. 23014–23025, 2019.

[316] N. U. Qadir, S. A. M. Said, R. B. Mansour, K. Mezghani, and A. Ul-Hamid, "Synthesis, characterization, and water adsorption properties of a novel multi-walled carbon nanotube/MIL-100(Fe) composite," *Dalt. Trans.*, vol. 45, no. 39, pp. 15621–15633, 2016.

[317] B. M. Connolly *et al.*, "Tuning porosity in macroscopic monolithic metal-organic frameworks for exceptional natural gas storage," *Nat. Commun.*, vol. 10, pp. 2345–2356, 2019.

[318] K. Sumida, K. Liang, J. Reboul, I. A. Ibarra, S. Furukawa, and P. Falcaro, "Sol-Gel Processing of Metal-Organic Frameworks," *Chem. Mater.*, vol. 29, no. 7, pp. 2626–2645, 2017.

[319] A. Mahmood, W. Xia, N. Mahmood, Q. Wang, and R. Zou, "Hierarchical heteroaggregation of binary metal-organic gels with tunable porosity and mixed valence metal sites for removal of

dyes in water," *Sci. Rep.*, vol. 5, no. April, pp. 27–31, 2015.

[320] T. Tian *et al.*, "A sol-gel monolithic metal-organic framework with enhanced methane uptake," *Nat. Mater.*, vol. 17, no. 2, pp. 174–179, 2018.

[321] C. F. Holder and R. E. Schaak, "Tutorial on Powder X-ray Diffraction for Characterizing Nanoscale Materials," *ACS Nano*, vol. 13, no. 7, pp. 7359–7365, 2019.

[322] J. Hafizovic *et al.*, "The inconsistency in adsorption properties and powder XRD data of MOF-5 is rationalized by framework interpenetration and the presence of organic and inorganic species in the nanocavities," *J. Am. Chem. Soc.*, vol. 129, no. 12, pp. 3612–3620, 2007.

[323] B. Chen, Y. Zhu, and Y. Xia, "Controlled in situ synthesis of graphene oxide/zeolitic imidazolate framework composites with enhanced CO2 uptake capacity," *RSC Adv.*, vol. 5, no. 39, pp. 30464–30471, 2015.

[324] P. Deria *et al.*, "MOF functionalization via solvent-assisted ligand incorporation: Phosphonates vs carboxylates," *Inorg. Chem.*, vol. 54, no. 5, pp. 2185–2192, 2015.

[325] K. Guesh, C. A. D. Caiuby, Á. Mayoral, M. Díaz-García, I. Díaz, and M. Sanchez-Sanchez, "Sustainable Preparation of MIL-100(Fe) and Its Photocatalytic Behavior in the Degradation of Methyl Orange in Water," *Cryst. Growth Des.*, vol. 17, no. 4, pp. 1806–1813, 2017.

[326] T. A. Phan, F. X. Perrin, and L. Nguyen-Dinh, "Synthesis and characterization of decyl phosphonic acid, applications in emulsion polymerization and anti-corrosion coating," *Korean J. Chem. Eng.*, vol. 35, no. 6, pp. 1365–1372, 2018.

[327] T. Tian, J. Velazquez-Garcia, T. D. Bennett, and D. Fairen-Jimenez, "Mechanically and chemically robust ZIF-8 monoliths with high volumetric adsorption capacity," *J. Mater. Chem. A*, vol. 3, no. 6, pp. 2999–3005, 2015.

[328] J. P. Mehta *et al.*, "Sol–Gel Synthesis of Robust Metal–Organic Frameworks for Nanoparticle Encapsulation," *Adv. Funct. Mater.*, vol. 28, no. 8, 2018.

[329] A. Rezk, R. Al-Dadah, S. Mahmoud, and A. Elsayed, “Characterisation of metal organic frameworks for adsorption cooling,” *Int. J. Heat Mass Transf.*, vol. 55, no. 25–26, pp. 7366–7374, 2012.

[330] K. Y. Law, “Definitions for hydrophilicity, hydrophobicity, and superhydrophobicity: Getting the basics right,” *J. Phys. Chem. Lett.*, vol. 5, no. 4, pp. 686–688, 2014.

[331] R. N. . Wenzel, “Resistance of Solid Surfaces to Wetting by Water,” *Ind. Eng. Chem.*, vol. 28, no. 8, pp. 988–994, 1936.

[332] Biolin Scientific, “Technology note 7: Influence of surface roughness on contact angle and wettability,” *Biolin Scietific Academic: Attension*, 2018. .

[333] E. Hunter-Sellars, J. J. Tee, I. P. Parkin, and D. R. Williams, “Adsorption of volatile organic compounds by industrial porous materials : Impact of relative humidity,” *Microporous Mesoporous Mater.*, vol. 298, p. 110090, 2020.

[334] S. Tanaka *et al.*, “Adsorption and Diffusion Phenomena in Crystal Size Engineered ZIF-8 MOF,” *J. Phys. Chem. C*, vol. 119, no. 51, pp. 28430–28439, 2015.

[335] N. L. Torad *et al.*, “Facile synthesis of nanoporous carbons with controlled particle sizes by direct carbonization of monodispersed ZIF-8 crystals,” *Chem. Commun.*, vol. 49, no. 25, pp. 2521–2523, 2013.

[336] H. Uehara *et al.*, “Porous coordination polymer hybrid device with quartz oscillator: Effect of crystal size on sorption kinetics,” *J. Am. Chem. Soc.*, vol. 133, no. 31, pp. 11932–11935, 2011.

[337] C. Walgraeve *et al.*, “Sorption behaviour of targeted volatile organic compounds on airborne particulate matter using selected ion flow tube mass spectrometry,” *Biosyst. Eng.*, vol. 131, pp. 84–94, 2015.

[338] N. K. Pandey, P. Velavendan, R. Geetha, M. K. Ahmed, and S. B. Koganti, “Adsorption kinetics and breakthrough behaviour of Tri-n-butyl Phosphate on amberlite XAD-4 resin,” *J. Nucl. Sci.*

Technol., vol. 35, no. 5, pp. 370–378, 1998.

[339] J. López-Cervantes, D. I. Sánchez-Machado, R. G. Sánchez-Duarte, and M. A. Correa-Murrieta, "Study of a fixed-bed column in the adsorption of an azo dye from an aqueous medium using a chitosan–glutaraldehyde biosorbent," *Adsorpt. Sci. Technol.*, vol. 36, no. 1–2, pp. 215–232, 2018.

[340] L. Bu, M. R. Nimlos, D. J. Robichaud, and S. Kim, "Diffusion of aromatic hydrocarbons in hierarchical mesoporous H-ZSM-5 zeolite," *Catal. Today*, vol. 312, no. November 2017, pp. 73–81, 2018.

[341] C. H. Shiau, K. L. Pan, S. J. Yu, S. Y. Yan, and M. B. Chang, "Desorption of isopropyl alcohol from adsorbent with non-thermal plasma," *Environ. Technol.*, vol. 38, no. 18, pp. 2314–2323, 2017.

[342] R. Gong and T. C. Keener, "A Qualitative Analysis of the Effects of Water Vapor on Multi-Component Vapor-Phase Carbon Adsorption," *Air Waste*, vol. 43, no. 6, pp. 864–872, 1993.

[343] M. Zhu, P. Hu, Z. Tong, Z. Zhao, and Z. Zhao, "Enhanced hydrophobic MIL(Cr) metal-organic framework with high capacity and selectivity for benzene VOCs capture from high humid air," *Chem. Eng. J.*, vol. 313, pp. 1122–1131, 2017.

[344] Z. Zhao, X. Li, S. Huang, Q. Xia, and Z. Li, "Adsorption and Diffusion of Benzene on Chromium-Based Metal Organic Framework MIL-101 Synthesized by Microwave Irradiation," *Ind. Eng. Chem. Res.*, vol. 50, no. 4, pp. 2254–2261, 2011.

[345] B. Bozbiyik, T. Van Assche, J. Lannoeye, D. E. De Vos, G. V. Baron, and J. F. M. Denayer, "Stepped water isotherm and breakthrough curves on aluminium fumarate metal–organic framework: experimental and modelling study," *Adsorption*, vol. 23, no. 1, pp. 185–192, 2017.

[346] J. Wang, G. Wang, W. Wang, Z. Zhang, Z. Liu, and Z. Hao, "Hydrophobic conjugated microporous polymer as a novel adsorbent for removal of volatile organic compounds," *J.*

Mater. Chem. A, vol. 2, no. 34, pp. 14028–14037, 2014.

[347] S. Jafari, F. Ghorbani-Shahna, A. Bahrami, and H. Kazemian, "Effects of Post-Synthesis Activation and Relative Humidity on Adsorption Performance of ZIF-8 for Capturing Toluene from a Gas Phase in a Continuous Mode," *Appl. Sci.*, vol. 8, no. 2, p. 310, 2018.

[348] E. Hunter-Sellars, P. A. Saenz-Cavazos, A. R. Houghton, S. R. McIntyre, I. P. Parkin, and D. R. Williams, "Sol–Gel Synthesis of High-Density Zeolitic Imidazolate Framework Monoliths via Ligand Assisted Methods: Exceptional Porosity, Hydrophobicity, and Applications in Vapor Adsorption," *Adv. Funct. Mater.*, 2020.

[349] Y. Huang *et al.*, "Removal of indoor volatile organic compounds via photocatalytic oxidation: A short review and prospect," *Molecules*, vol. 21, no. 1, 2016.

Appendix

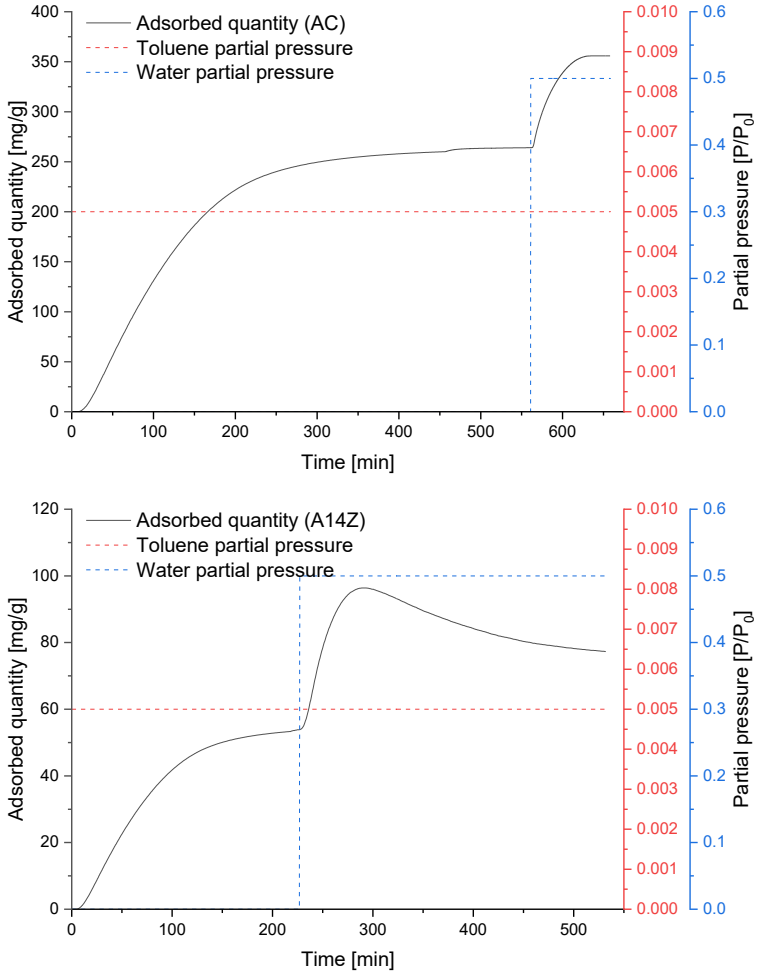


Figure A.1: Reverse pre-exposure multicomponent DVS experiments on powder activated charcoal (top) and ZSM-5 zeolite (bottom), T = 25˚C. Plots illustrate the limitation of two-component gravimetric data in determining quantitative selectivity for adsorbents with more hydrophilic chemistry, as shown by displacement curve for ZSM-5 zeolite.

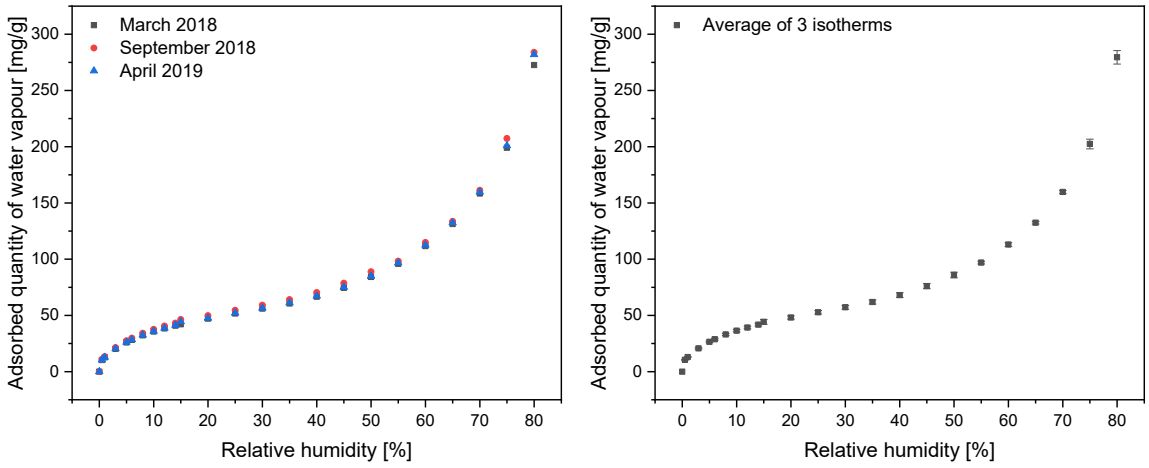


Figure A.2: Water adsorption isotherms of Zeofree 91 silica gel, carried out in ~6 month intervals to test the reproducibility and reliability of gravimetric adsorption experiments over the course of the project. Flowrate = 200 mL/min, mass of sample = 35-45 mg, T = 25 ˚C.

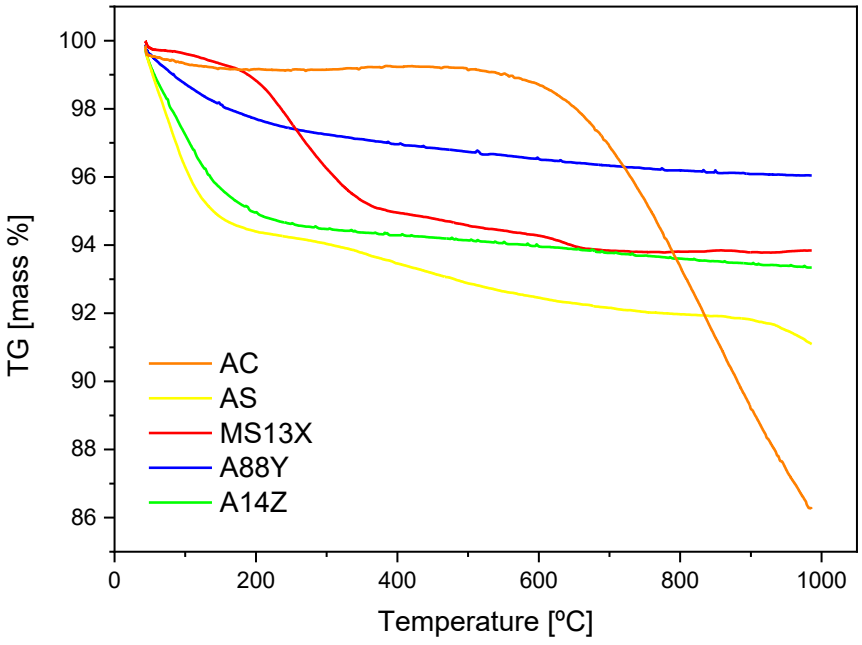


Figure A.3: Thermogravimetric profiles for adsorbents: molecular sieve 13X, MS13X; zeolite Y, A88Y; ZSM-5 zeolite, A14Z; activated charcoal, AC; amorphous silica, AS. Carried out under dry air flow.

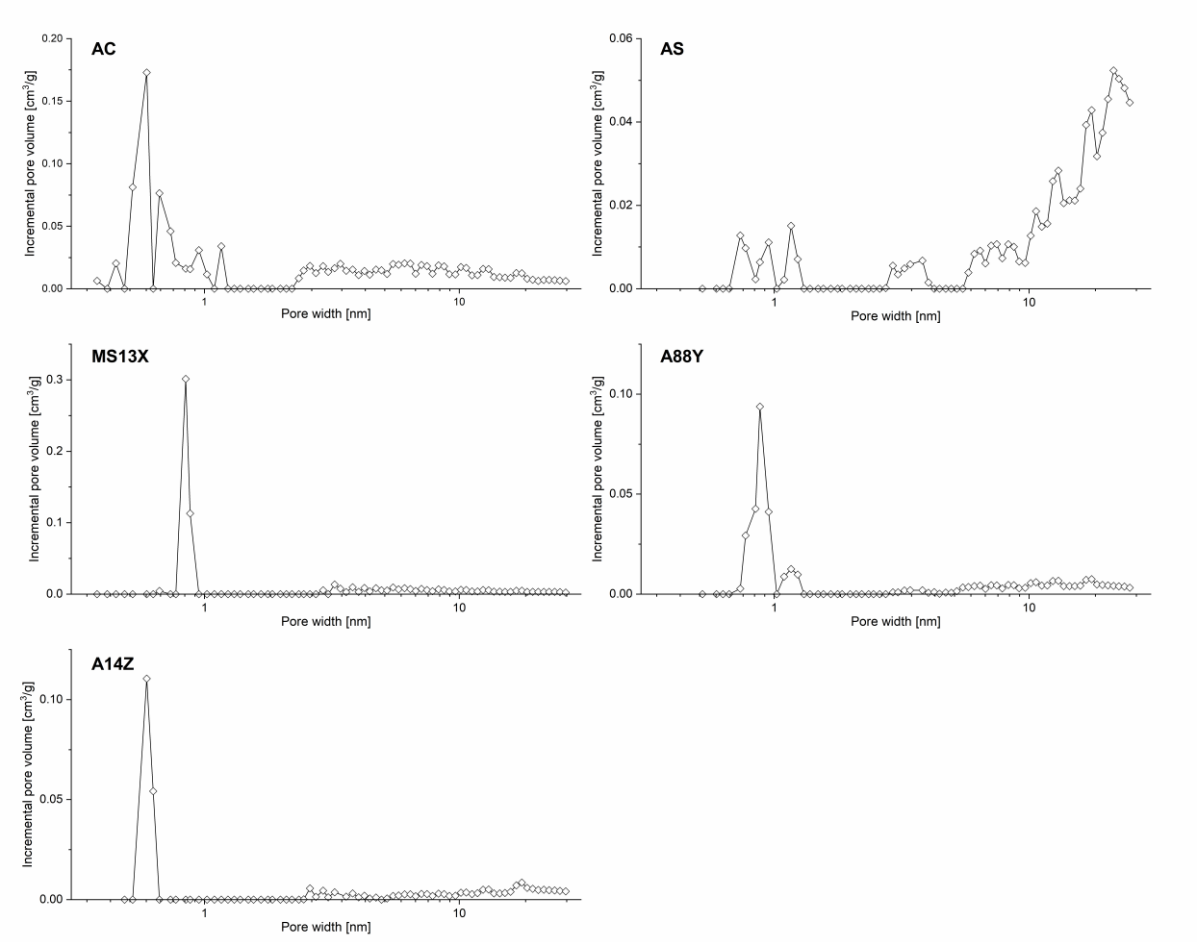


Figure A.4: Pore size distributions for adsorbents: molecular sieve 13X, MS13X; zeolite Y, A88Y; ZSM-5 zeolite, A14Z; activated charcoal, AC; amorphous silica, AS. Determined using experimental nitrogen adsorption data combined with NLDFT, assuming cylindrical pore geometry, T = -196˚C.

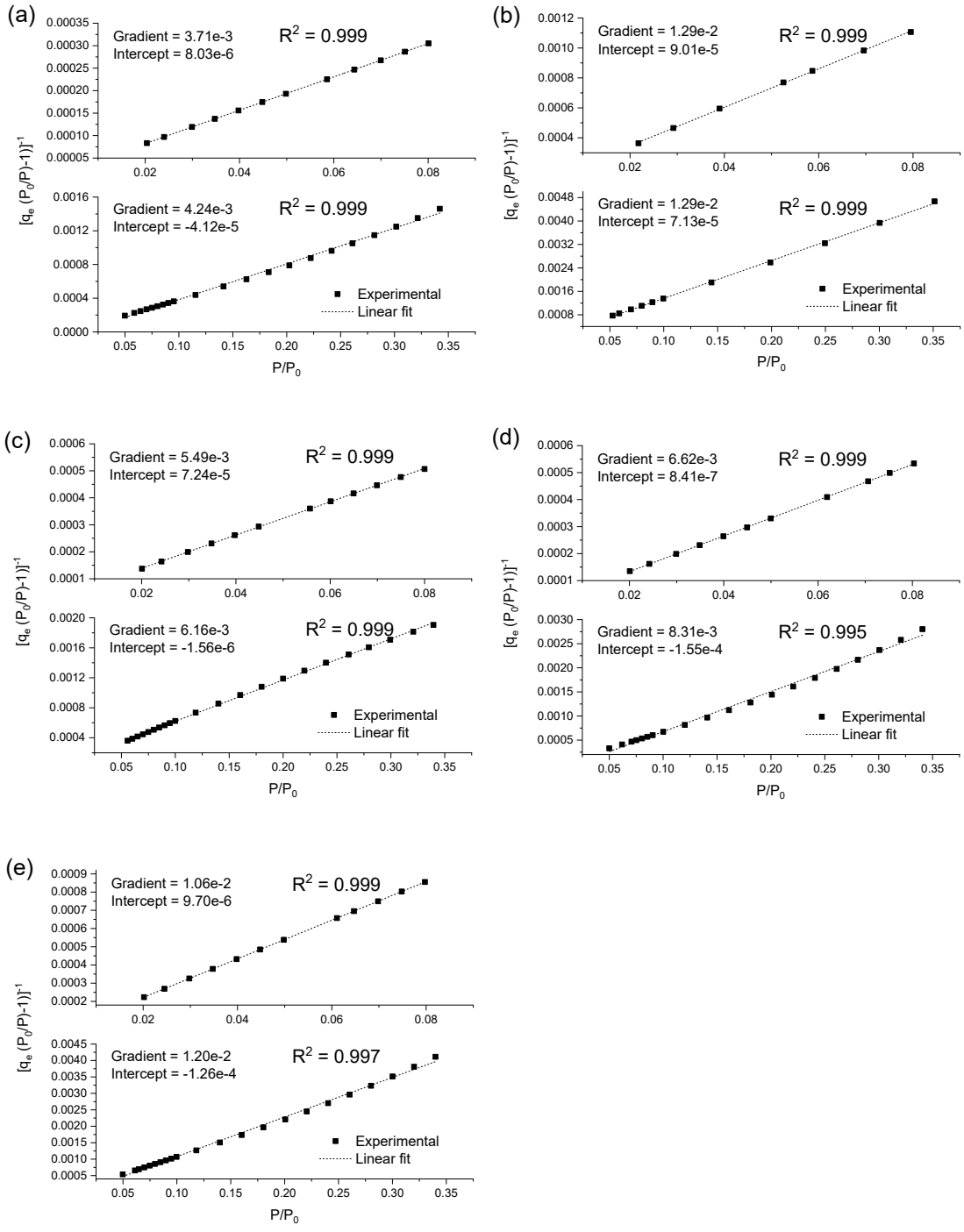


Figure A.5: Comparisons between Rouquerol (upper plots) and BET (lower plots) partial pressure ranges for determination of specific surface area. Adsorbents studied: activated charcoal, AC (a); amorphous silica, AS (b); molecular sieve 13X, MS13X (c); zeolite Y, A88Y (d); and ZSM-5 zeolite, A14Z (e). Based on nitrogen adsorption data, T = -196 ˚C.

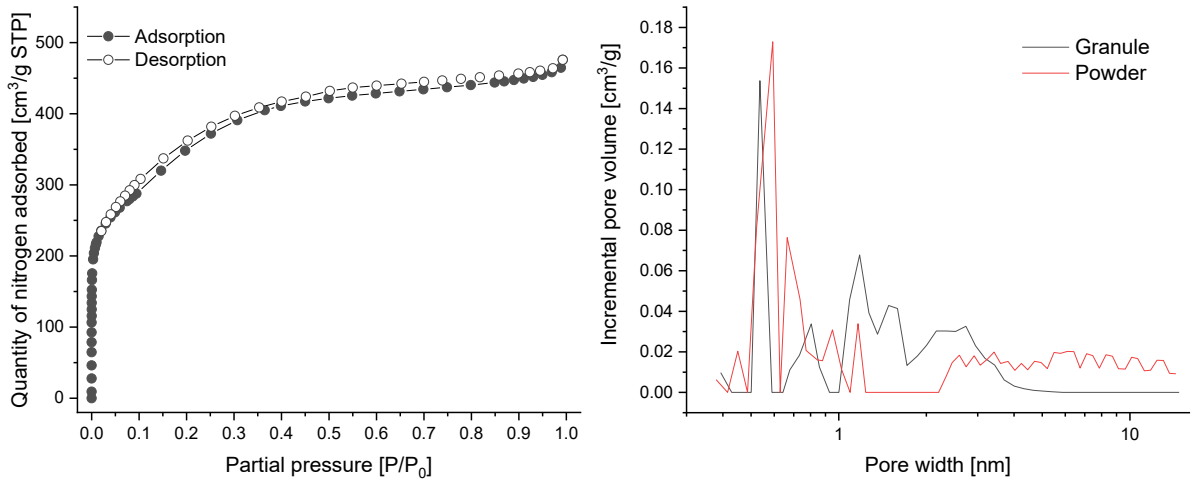


Figure A.6: Nitrogen isotherms (left) and pore size distribution (right) of granular activated charcoal. PSDs determined using NLDFT assuming cylindrical pore geometry with powder activated charcoal included for comparison. T = -196 ˚C.

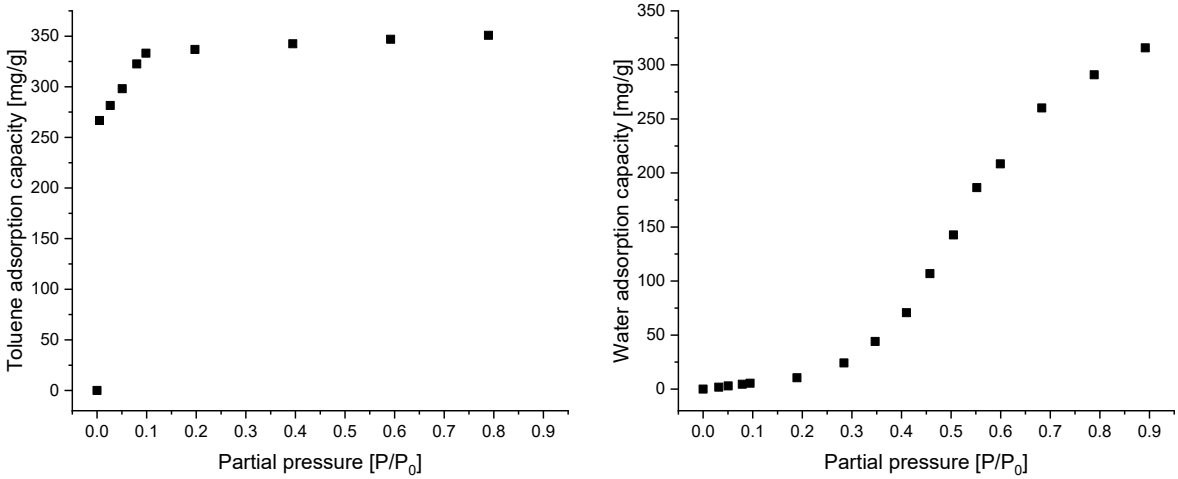


Figure A.7: Toluene (left) and water (right) isotherms of granular activated charcoal. T = 25˚C.

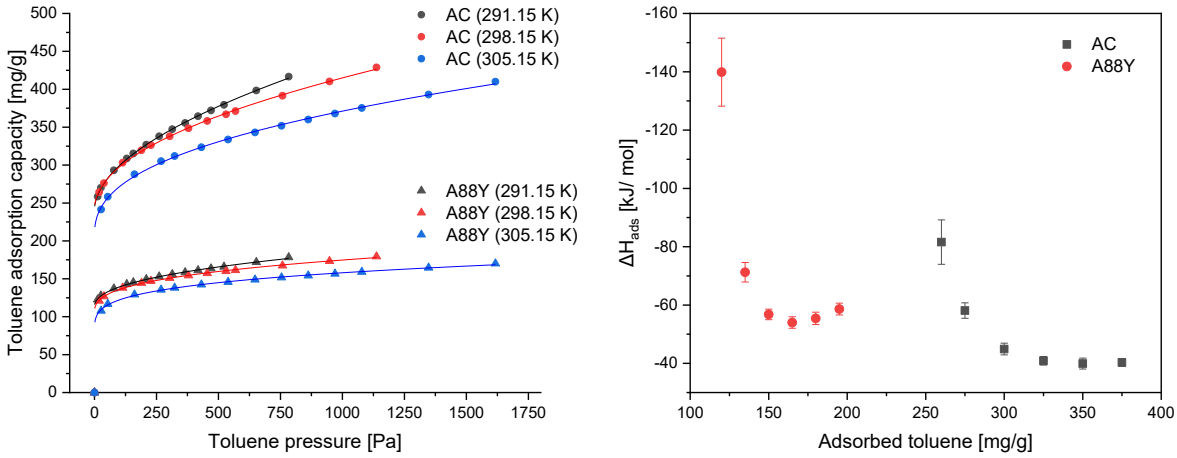


Figure A.8: Multi-temperature toluene isotherms (left) and enthalpies of adsorption as a function of toluene uptake (right) for powder activated charcoal and zeolite Y. Heats of adsorption determined by the Clausius-Clapeyron equation using fitted isotherms from the Dubinin-Astakhov model (solid lines). T = 18˚C, 25˚C, 32˚C.

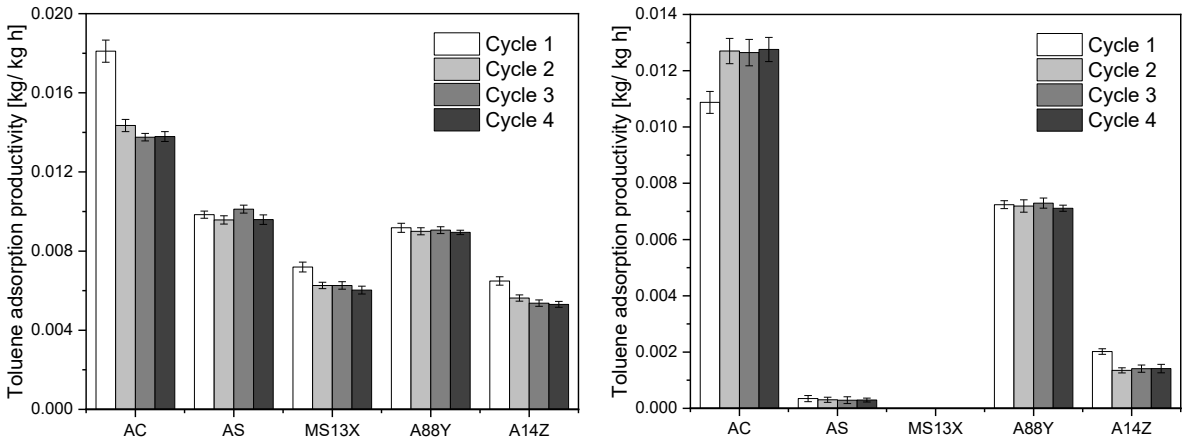


Figure A.9: Toluene adsorption productivities as a function of cycle number, under dry (left) and humid (right) conditions. Samples studied: activated charcoal, AC; amorphous silica, AS; molecular sieve 13X, MS13X; zeolite Y, A88Y; ZSM-5 zeolite, A14Z. Partial pressure of toluene in all cycling experiments, $P/P_0 = 0.005$. RH in humid experiments = 50 %. Desorption carried out under 200 mL/min of dry air flow, T = 25˚C.

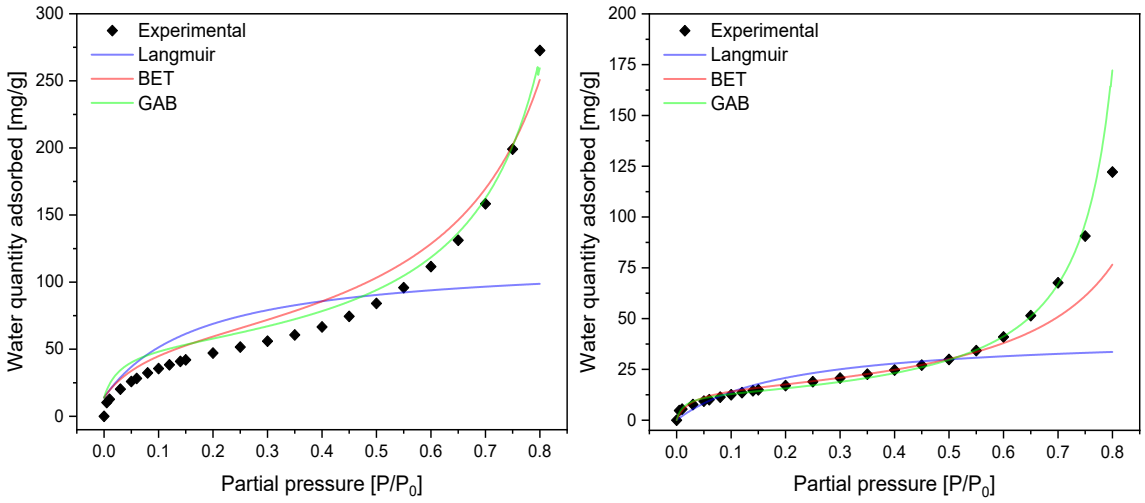


Figure A.10: Fitting of water adsorption isotherms of AS (left) and A88Y (right), T = 25˚C.

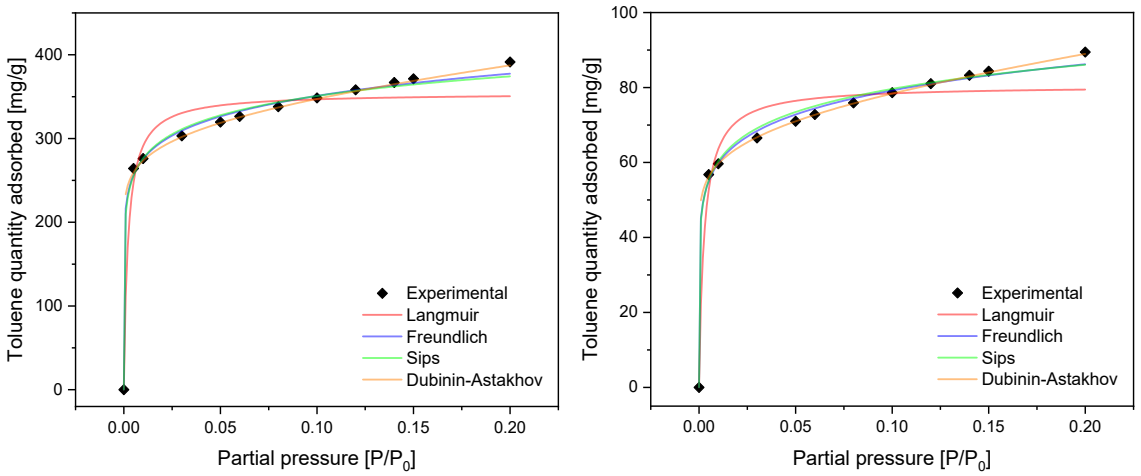


Figure A.11: Fitting of toluene adsorption isotherms of AC (left) and A14Z (right), T = 25˚C.

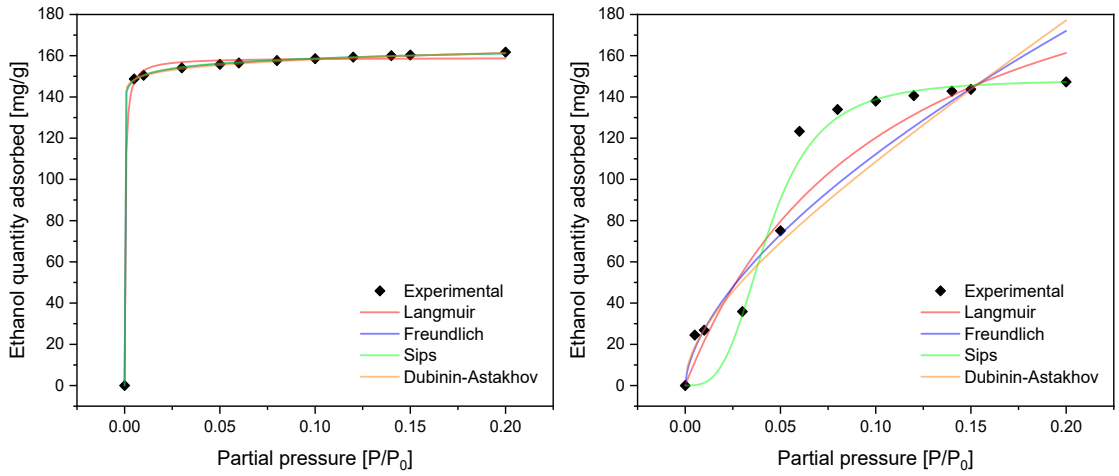


Figure A.12: Fitting of ethanol adsorption isotherms of MS13X (left) and A88Y (right), T = 25˚C.

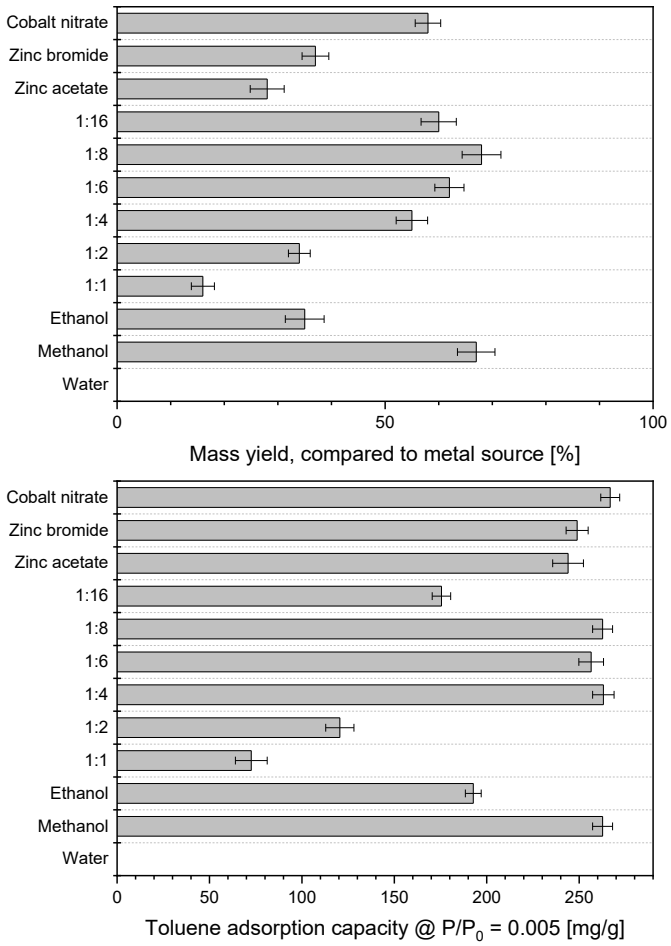


Figure A.13: Average values and 95 % confidence intervals for mass yield (top) and toluene adsorption capacity (bottom) for ZIF-8/67 synthesised using different reaction conditions.

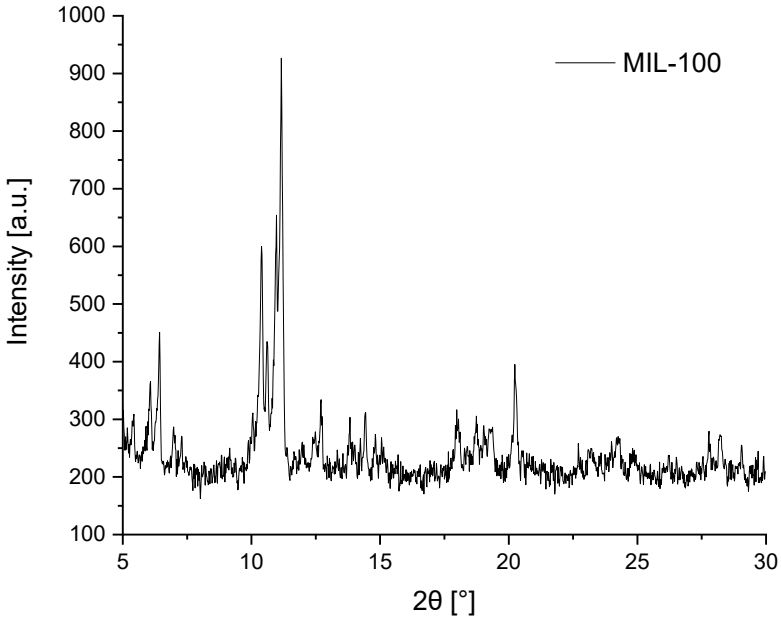


Figure A.14: Powder X-ray diffraction pattern for MIL-100 (Fe) powder.

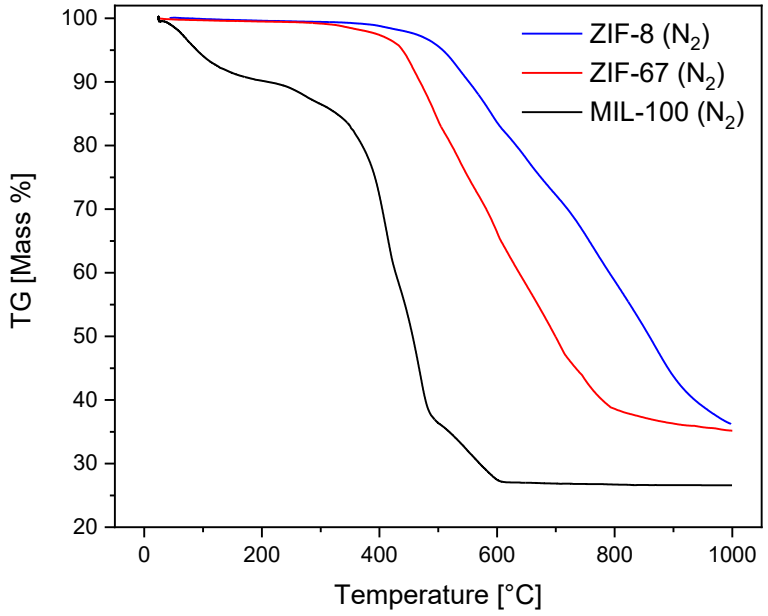


Figure A.15: Thermogravimetry profiles for ZIF-8, ZIF-67, and MIL-100 in an inert atmosphere of nitrogen. ZIF samples were synthesised using nitrate salts and a metal: linker ratio of 1:8.

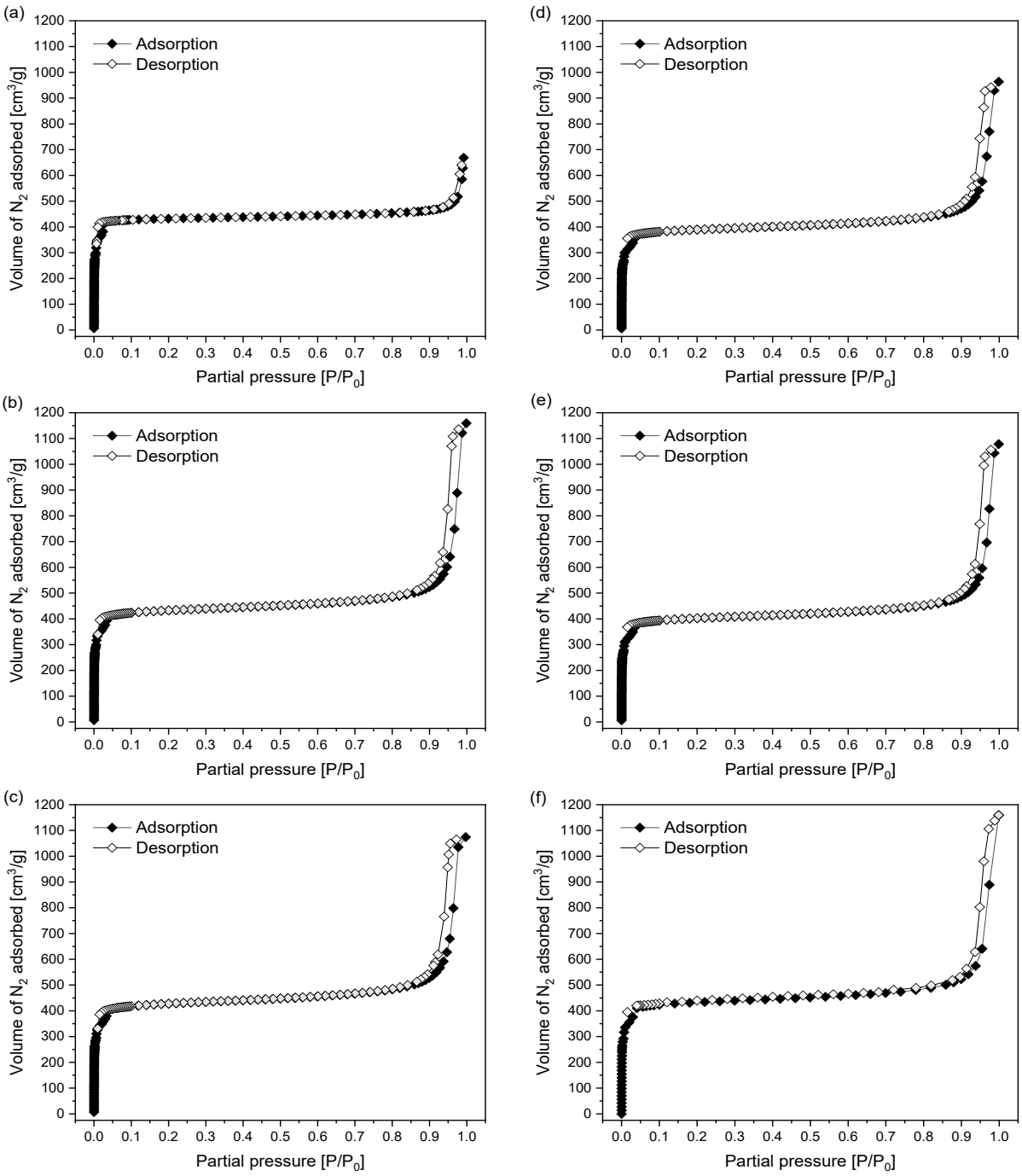


Figure A.16: Nitrogen isotherms for ZIF samples: zinc: linker ratios of 1:4 (a), 1:6 (b), 1:8 (c); zinc acetate (d) and bromide (e) salts of zinc; and ZIF-67 using cobalt nitrate (f). T = -196˚C.

Note: due to the long experimental times for generating adsorption isotherms, only toluene and water isotherms were generated for all ZIF samples in order to assess their non-polar adsorption capacity and kinetics, and their hydrophobicity. Methanol and n-hexane adsorption isotherm experiments were only carried out for ZIF-8 (1:4), ZIF-8 (1:8), and ZIF-67.

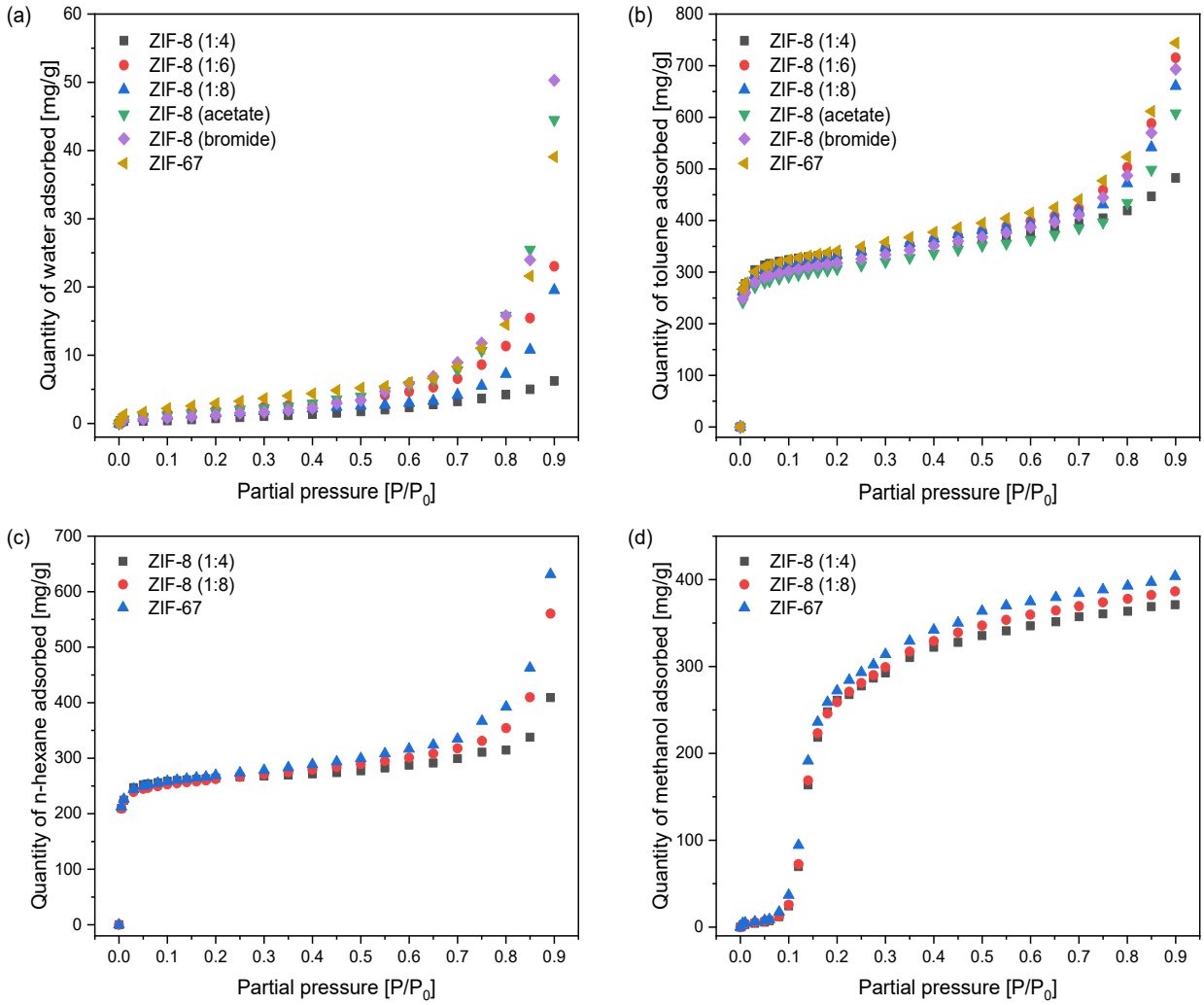


Figure A.17: Vapour adsorption isotherms for water (a), toluene (b), n-hexane (c), and methanol (d) on ZIF adsorbents. T = 25˚C.

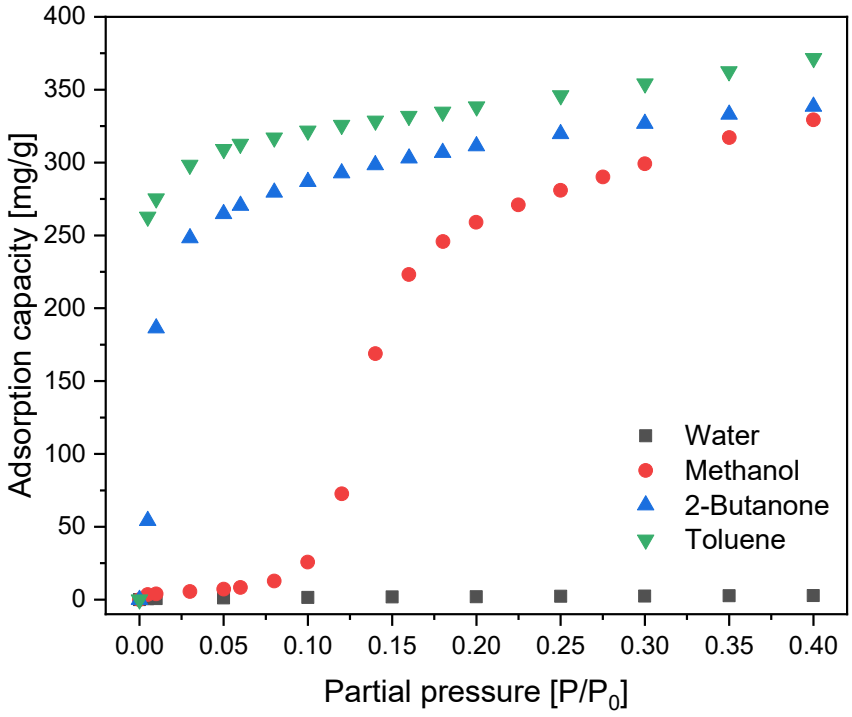


Figure A.18: Vapour isotherms of water, methanol, 2-butanone and toluene on ZIF-8 powder, synthesised with zinc nitrate and a metal: linker ratio of 8. T = 25˚C.

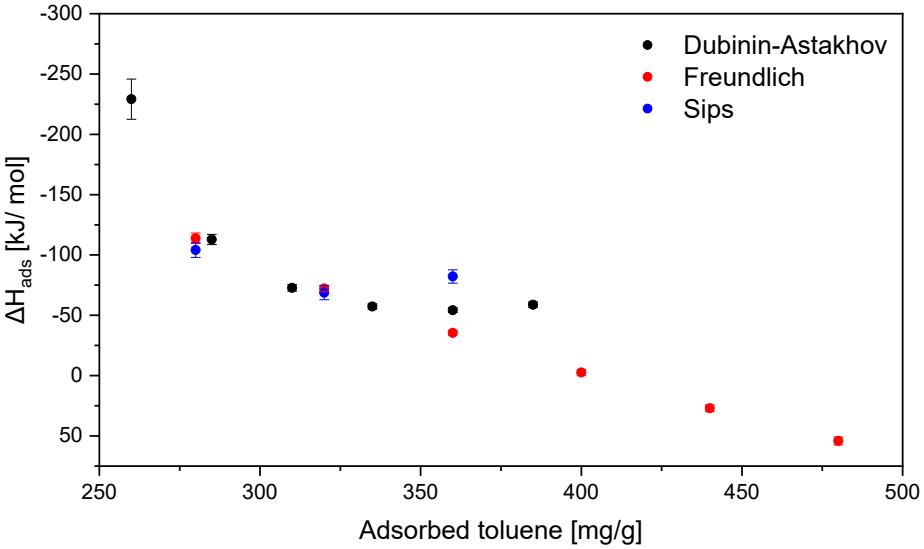


Figure A.19: Comparison of enthalpy of adsorption profiles when fitting with different isotherm models, for ZIF-8 synthesised with zinc nitrate and a metal: linker ratio of 8. Heats of adsorption determined by the Clausius-Clapeyron equation using several fitted isotherms. T = 18-32˚C.

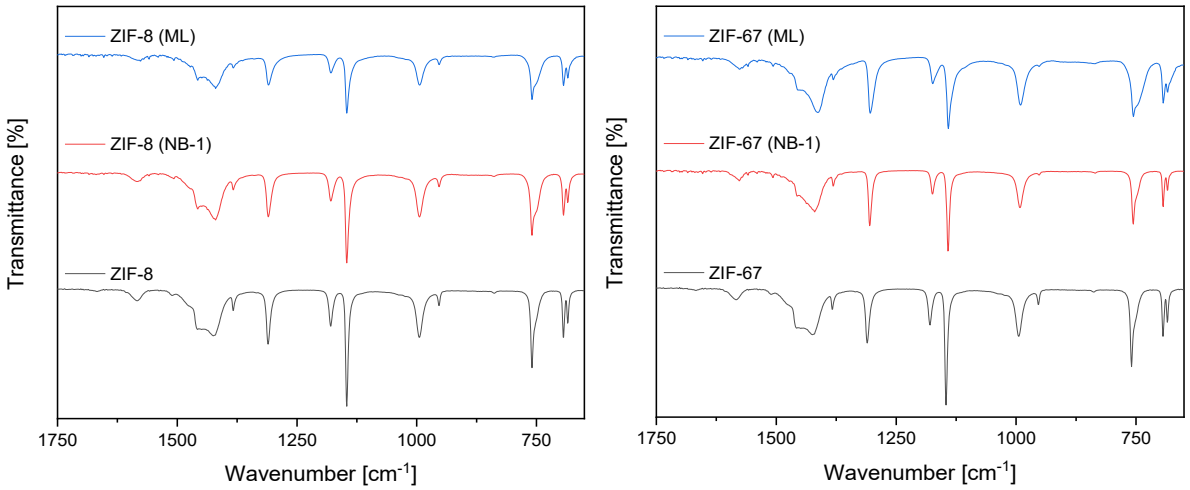


Figure A.20: FTIR spectra for powder and monolithic zinc-based (left) and cobalt-based (right) ZIFs

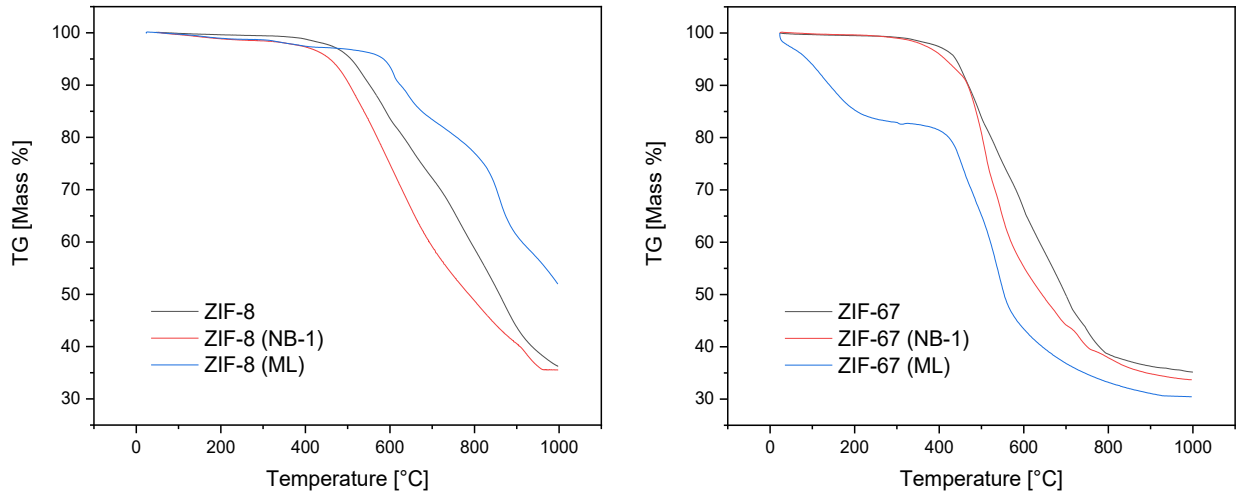


Figure A.21: Thermogravimetry profiles for zinc (left) and cobalt (right) based adsorbents in N_2

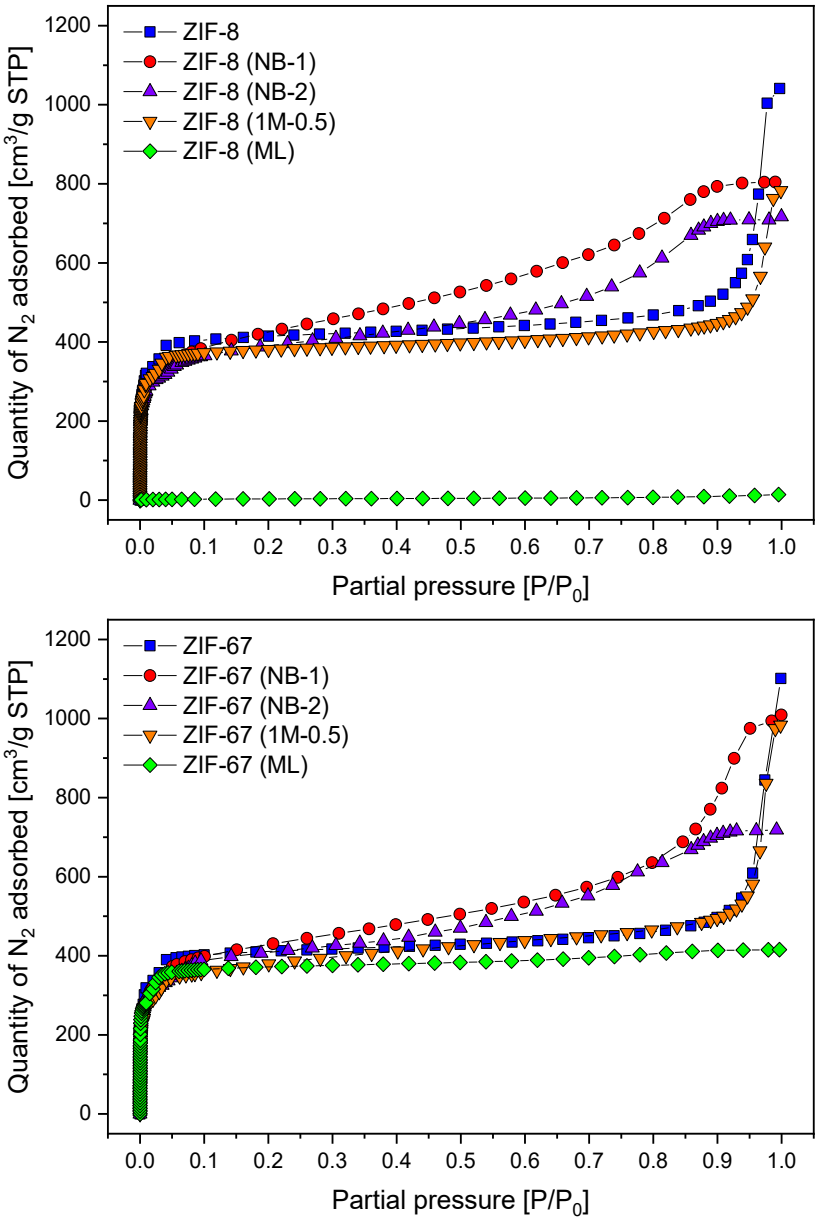


Figure A.22: Nitrogen adsorption isotherms for zinc (top) and cobalt (bottom) ZIF powder and monolithic adsorbents. T = -196˚C.

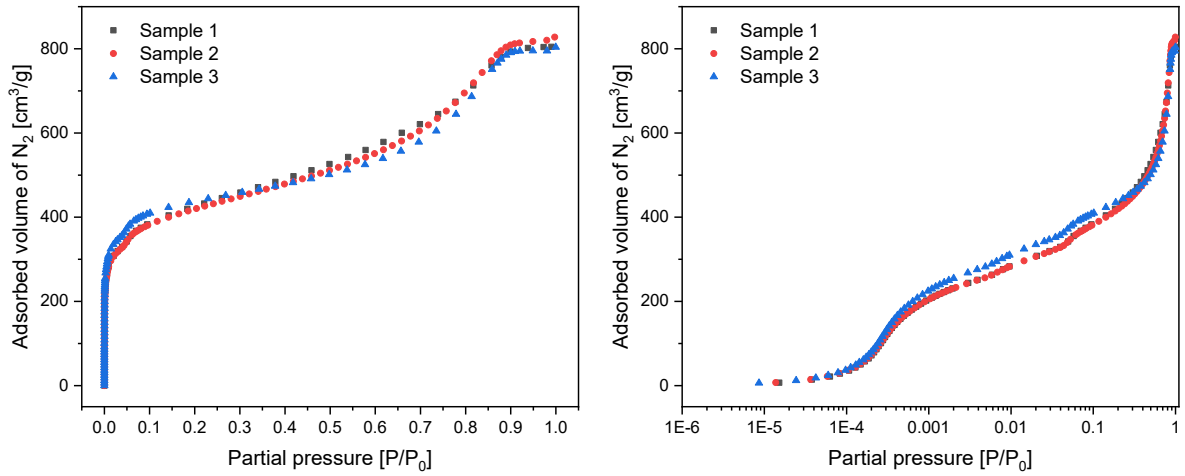


Figure A.23: Low-temperature N_2 isotherms of ZIF-8 (NB-1) samples synthesized in three separate batches, ran simultaneously using a 3-Flex Physisorption (Micromeritics, USA), illustrating reproducibility of monolith synthesis procedure. Plots shown using linear (left) and logarithmic (right) pressure axes to show similarities in overall isotherm shape and microporosity respectively. T = -196˚C.

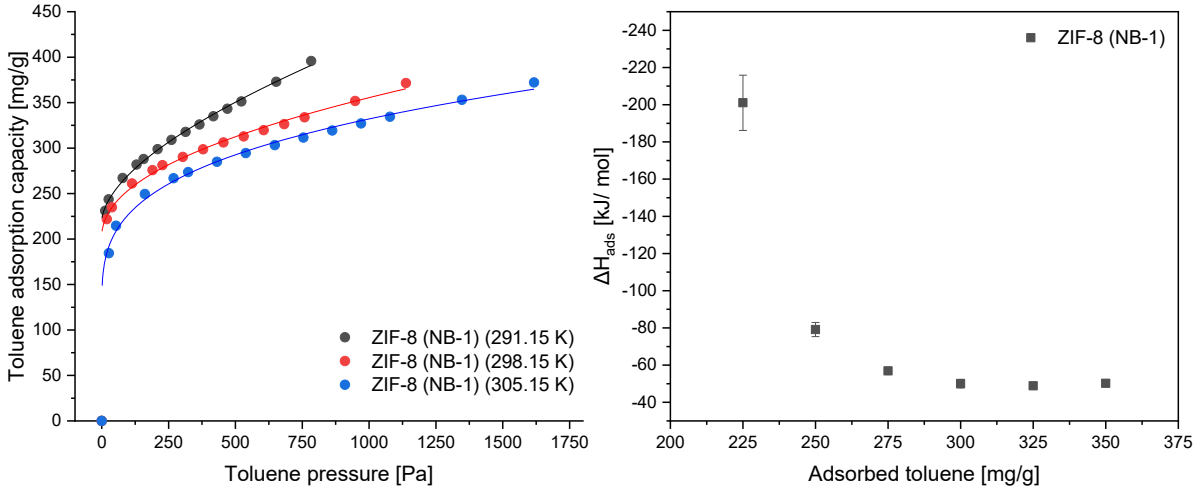


Figure A.24: Multi-temperature toluene isotherms (left) and heats of adsorption as a function of toluene uptake (right) for ZIF-8 (NB-1). Heats of adsorption determined by the Clausius-Clapeyron equation using fitted isotherms from the Dubinin-Astakhov model (solid lines). T = 18˚C, 25˚C, 32˚C.

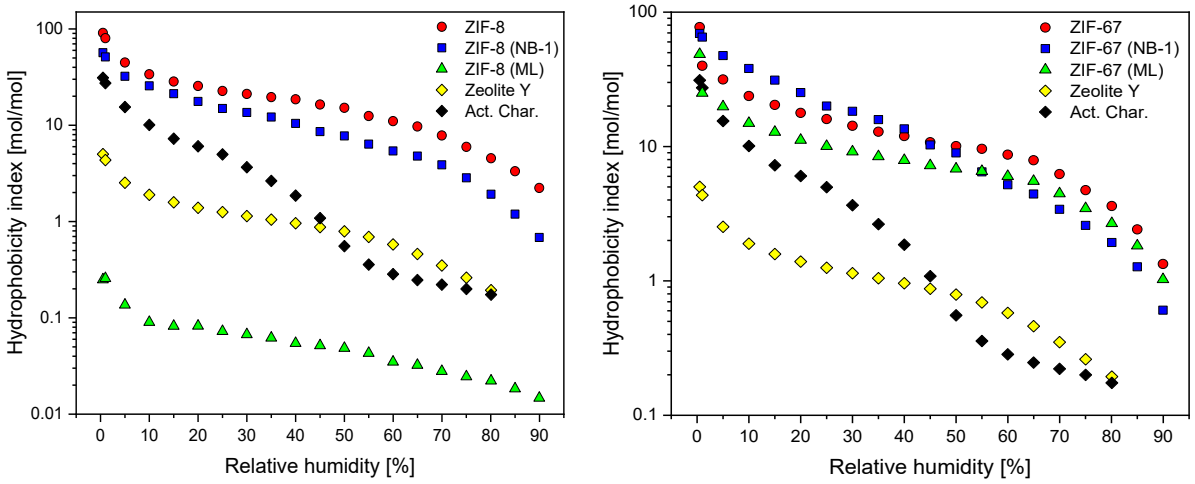


Figure A.25: Hydrophobicity indexes plotted as a function of humidity, for zinc (left) and cobalt (right) ZIF samples. Plots for dealuminated zeolite Y and activated charcoal are included for comparison. All measurements carried out at 25ºC.

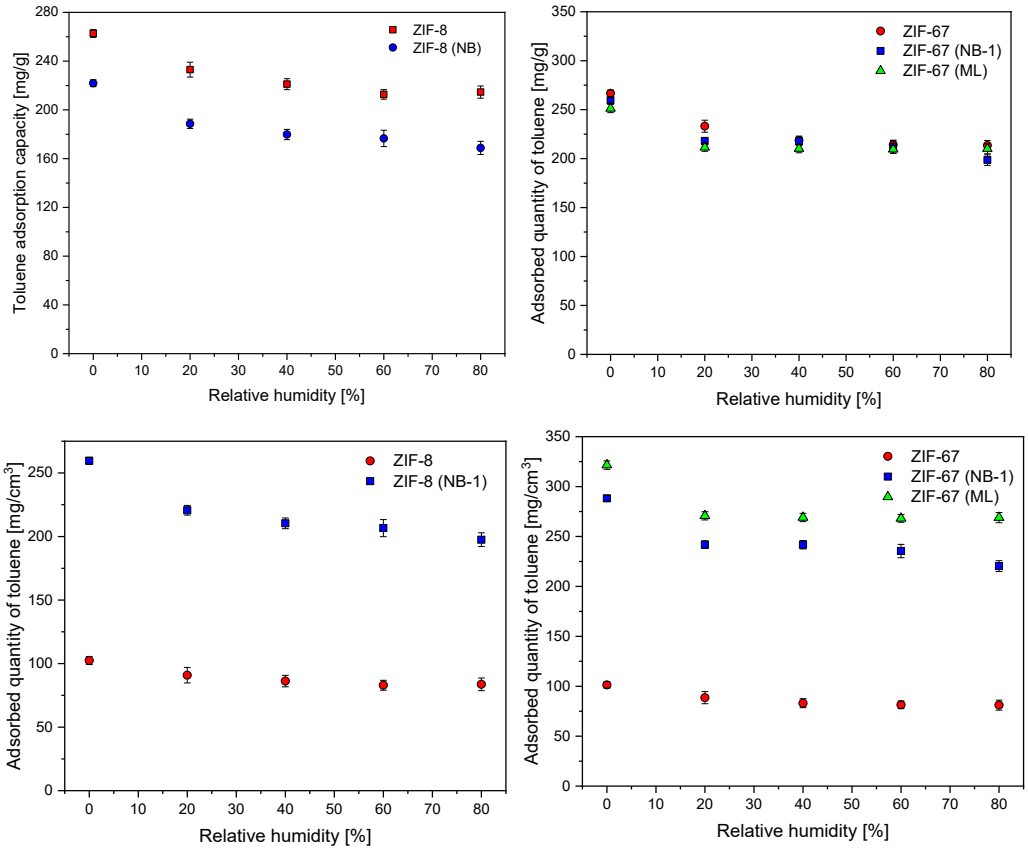


Figure A.26: Adsorption of toluene vapour following pre-exposure of water vapour at different humidity levels for zinc (left) and cobalt (right) ZIFs. Expressed in mass-relative (top) and volume-relative (bottom) terms. Partial pressure of toluene in all experiments, $P/P_0 = 0.005$. T = 25˚C.

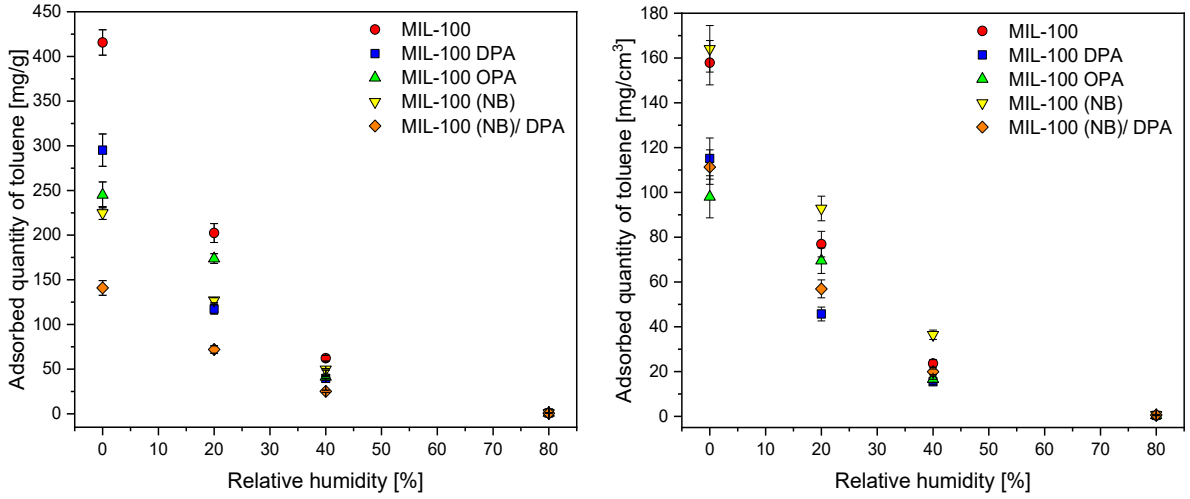


Figure A.27: Adsorption of toluene vapour following pre-exposure of water vapour at different humidity levels. Expressed in mass-relative (left) and volume-relative (right) terms. Partial pressure of toluene in all experiments, $P/P_0 = 0.005$. T = 25˚C. Number of repeat measurements, N = 2.

Table A.1: Summary of adsorption and surface hydrophobicity of porous MOF samples. Water capacity and H.I. values are quoted for medium (50 %) and high (90 %) relative humidity. All measurements carried out at 25ºC.

Adsorbent	Water vapour capacity [mg/g]		Hydrophobicity index [a] [mol/mol]		Advancing contact angle [b] [º]
	RH = 50 %	RH = 90 %	RH = 50 %	RH = 90 %	
ZIF-8	3.38 ± 0.12	23.02 ± 1.23	15.17 ± 0.57 [b]	2.23 ± 0.12	112.6 ± 2.8
ZIF-8 (NB-1)	5.61 ± 0.34	63.54 ± 2.57	7.74 ± 0.48 [b]	0.68 ± 0.03	124.0 ± 2.0
ZIF-67	5.19 ± 0.18	39.06 ± 2.01	10.07 ± 0.37 [b]	1.34 ± 0.07	114.8 ± 2.2
ZIF-67 (NB-1)	5.68 ± 0.44	83.83 ± 6.75	8.95 ± 0.70 [b]	0.61 ± 0.05	123.3 ± 1.9
ZIF-67 (ML)	7.20 ± 0.31	47.85 ± 3.19	6.83 ± 0.32 [b]	1.03 ± 0.07	122.0 ± 3.6
MIL-100	595.1 ± 18.2	701.5 ± 20.4	0.14 ± 0.01	0.12 ± 0.01	41.0 ± 1.1
MIL-100/ DPA	509.3 ± 17.8	574.4 ± 20.3	0.11 ± 0.01	0.10 ± 0.01	137.4 ± 5.9
MIL-100/ OPA	474.9 ± 16.9	552.9 ± 20.2	0.10 ± 0.01	0.09 ± 0.01	135.5 ± 6.1
MIL-100 (NB)	306.2 ± 18.1	345.3 ± 22.6	0.14 ± 0.02	0.13 ± 0.02	86.8 ± 3.1
MIL-100 (NB)/ DPA	126.7 ± 12.2	166.1 ± 14.5	0.22 ± 0.04	0.17 ± 0.03	124.1 ± 11.5
MIL-100 (NB)/ OPA	56.2 ± 3.9	89.5 ± 5.8	0.05 ± 0.01	0.03 ± 0.01	138.9 ± 12.2

[a] Calculated as molar capacity for toluene vapour at $P/P_0 = 0.005$ divided by molar capacity of water vapour at different RHs.

Table A.2: Dry and humid capacities for toluene at a partial pressure of 0.005, expressed in volume-relative terms, for MOF adsorbents, with zeolite Y and activated charcoal shown for comparison. T = 25˚C.

Adsorbent	Dry (0 % RH) [mg/cm^3] [1]	Humid (40 % RH) [mg/cm^3] [1]	Humid (80 % RH) [mg/cm^3] [1]
ZIF-8	102.5 ± 5.4	86.2 ± 4.8	83.7 ± 4.7
ZIF-8 (NB-1)	259.6 ± 18.1	210.4 ± 15.2	197.9 ± 14.9
ZIF-67	101.4 ± 5.5	83.0 ± 4.7	81.1 ± 4.4
ZIF-67 (NB-1)	288.2 ± 21.0	241.8 ± 17.6	220.3 ± 16.1
ZIF-67 (ML)	321.5 ± 9.3	269.1 ± 8.3	268.9 ± 9.1
MIL-100	157.9 ± 9.9	23.6 ± 1.8	0.3 ± 0.1
MIL-100 (NB)	164.1 ± 10.4	36.4 ± 2.1	0.7 ± 0.2
Activated charcoal	89.8 ± 5.3	72.2 ± 1.9	3.2 ± 0.3
Zeolite Y	100.5 ± 1.3	89.1 ± 5.6	83.7 ± 1.4

[1] Calculated by multiplying mass-relative capacity by bulk density.

Table A.3: Dry and humid capacities for toluene at a partial pressure of 0.005, expressed in volume-relative terms, for modified MIL-100 adsorbents. T = 25˚C.

Adsorbent	Dry (0 % RH) [mg/g]	Humid (40 % RH) [mg/g]	Humid (80 % RH) [mg/g]
MIL-100/ DPA	295.1 ± 18.1	39.6 ± 2.0	1.0 ± 0.1
MIL-100/ OPA	245.1 ± 14.5	41.4 ± 1.8	1.1 ± 0.2
MIL-100 (NB)/ DPA	140.9 ± 8.2	25.2 ± 1.2	0.7 ± 0.1
		[mg/cm^3] [1]	
MIL-100/ DPA	115.1 ± 9.2	15.4 ± 1.1	0.4 ± 0.1
MIL-100/ OPA	98.0 ± 9.4	16.6 ± 1.4	0.4 ± 0.1
MIL-100 (NB)/ DPA	117.0 ± 8.8	20.9 ± 1.4	0.6 ± 0.1

[1] Calculated by multiplying mass-relative capacity by bulk density.

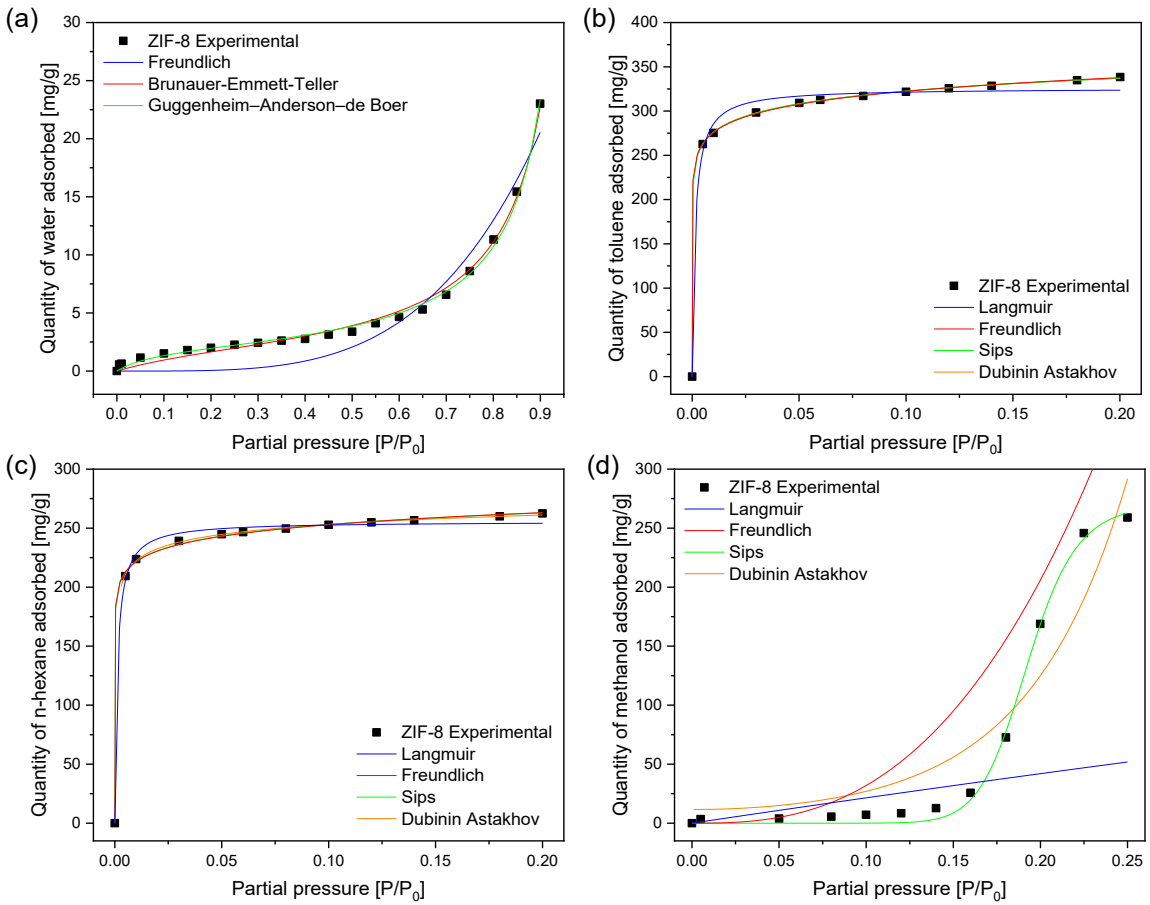


Figure A.28: Example fitting of experimental isotherm data for water (a), toluene (b), n-hexane (c) and methanol (d) on ZIF-8 powder. T = 25˚C.

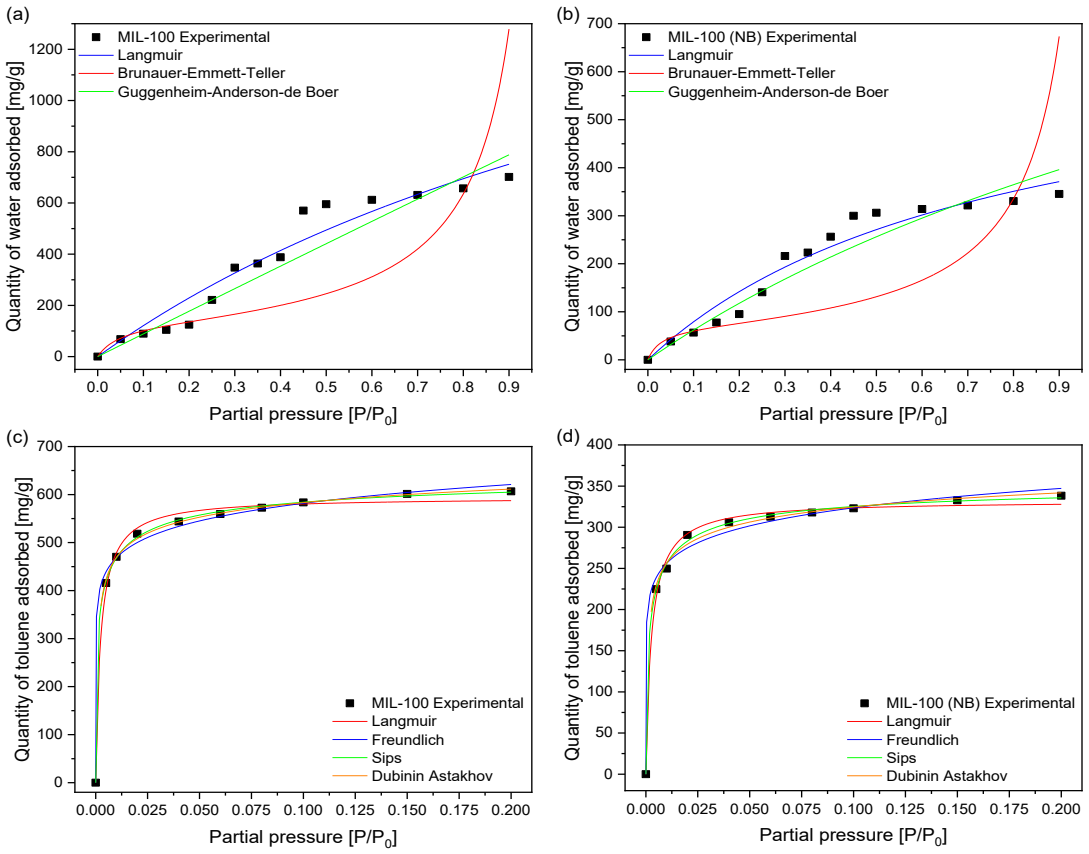


Figure A.29: Example fitting of experimental isotherm data for water on MIL-100 (a) and MIL-100 (NB) (b), and toluene on MIL-100 (c) and MIL-100 (NB) (d). T = 25˚C.

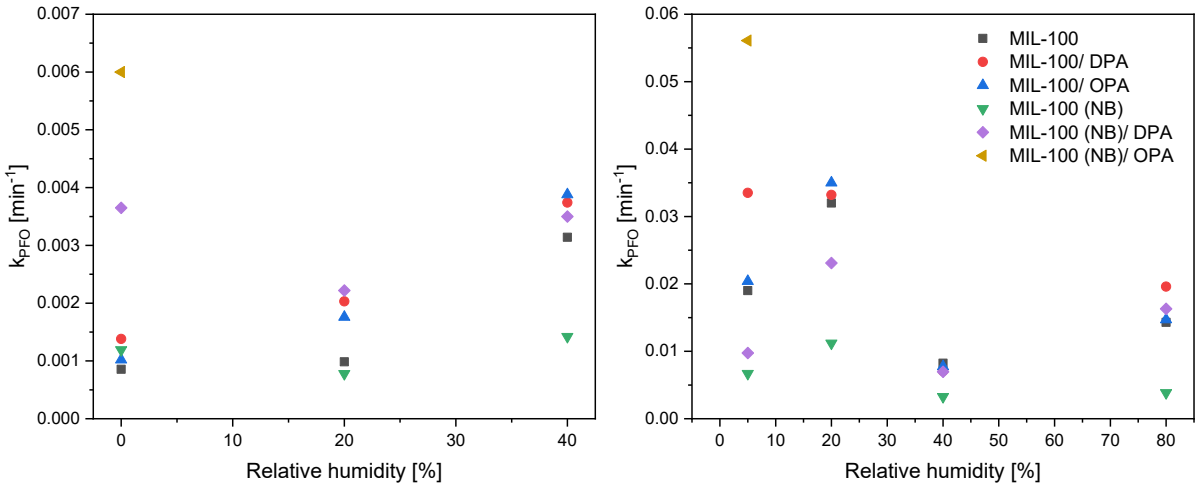


Figure A.30: Pseudo first order rate constants for toluene adsorption (left) and water adsorption (right) during single- and multi-component DVS experiments. T = 25˚C.

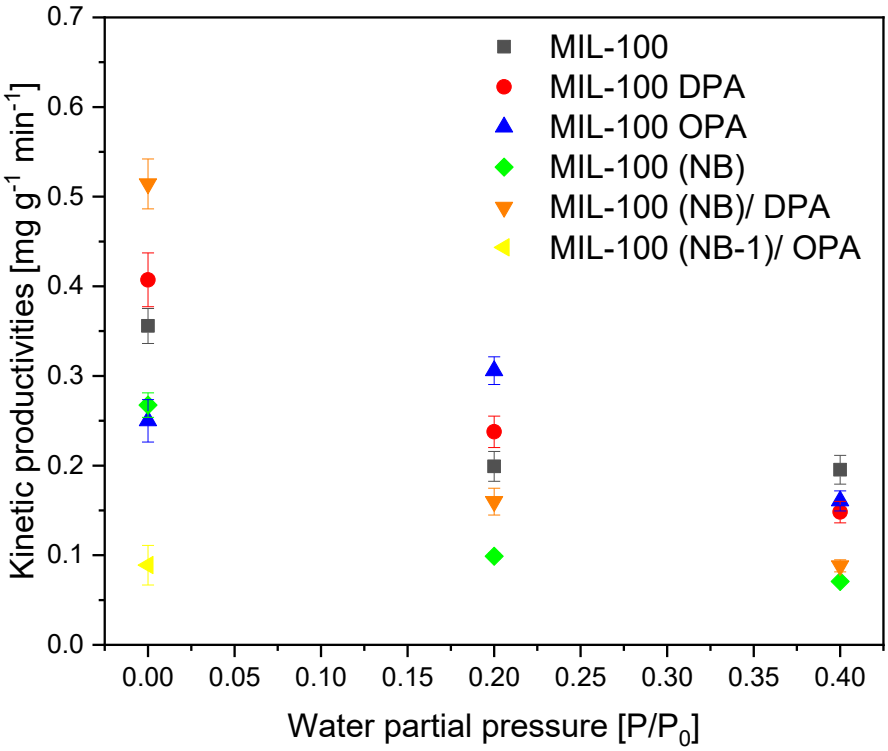


Figure A.31: Impact of water vapour pre-exposure on kinetic productivities for toluene adsorption for MIL-100 adsorbents. Productivities calculated as the product of pseudo first order rate constant and experimental adsorption capacity. T = 25˚C, $P/P_{0,\,toluene}$ = 0.005. N = 2.

Adsorption fitting parameters

Table A.4: Isotherm fitting parameters for water adsorption onto porous materials. T = 25ºC. Numbers in red represent fits that did not converge.

Sample	Langmuir			BET			GAB			
	Q_{max} [mg/g]	K [a.u.]	MPSD [%]	Q_{max} [mg/g]	C [a.u.]	MPSD [%]	Q_{max} [mg/g]	C [a.u.]	K [a.u.]	MPSD [%]
AC	5798.5	8.2e-3	84.90	187.6	0.17	54.2	224.1	0.13	1.04	55.44
AS	108.6	5.66	50.91	50.7	12.19	18.5	40.6	31.57	1.06	12.99
MS13X	216.8	170	11.81	96.9	3.9e7	68.0	189.9	1416.23	0.30	2.66
A88Y	42.2	4.85	56.17	15.4	41.10	28.0	12.6	66.20	1.16	15.37
A14Z	88.4	4.81	43.52	29.5	45.16	17.2	29.5	44.40	1.01	17.67

Table A.5: Isotherm fitting parameters for toluene adsorption onto porous materials. T = 25ºC. Numbers in red represent fits that did not converge.

Sample	Langmuir			Freundlich			Sips				Dubinin-Astakhov			
	Q_{max} [mg/g]	K [a.u.]	MPSD [%]	Q_{max} [mg/g]	n [a.u.]	MPSD [%]	Q_{max} [mg/g]	K [a.u.]	N [a.u.]	MPSD [%]	Q_{max} [mg/g]	E [kJ/ mol]	n [a.u.]	MPSD [%]
AC	354.3	459.7	6.63	446.9	0.105	2.09	797.4	2.436	0.171	2.68	256.4	19.8	2.12	0.35
AS	76.8	54.7	16.38	159.1	0.384	4.07	1742.0	0.003	0.394	4.56	17.2	9.5	1.56	1.04
MS13X	156.7	1947.1	1.88	167.0	0.029	0.53	491.2	3.65e-6	0.051	1.02	142.9	38.2	2.01	0.06
A88Y	156.4	556.5	4.88	189.3	0.087	0.96	431.7	0.11	0.129	1.25	114.6	24.3	1.59	0.21
A14Z	80.5	376.3	7.58	104.9	0.122	2.30	256.0	0.083	0.166	2.38	54.5	18.6	2.06	0.24

Table A.6: Isotherm fitting parameters for n-hexane adsorption onto porous materials. T = 25ºC. Numbers in red represent fits that did not converge.

Sample	Langmuir			Freundlich			Sips				Dubinin-Astakhov			
	Q_{max} [mg/g]	K [a.u.]	MPSD [%]	Q_{max} [mg/g]	n [a.u.]	MPSD [%]	Q_{max} [mg/g]	K [a.u.]	N [a.u.]	MPSD [%]	Q_{max} [mg/g]	E [kJ/ mol]	n [a.u.]	MPSD [%]
AC	271.6	118.4	5.6	296.6	0.104	1.09	630.7	0.429	0.166	1.57	177.1	24.4	1.75	0.47
AS	33.4	34.6	15.08	41.0	0.254	5.82	151.2	0.032	0.301	6.97	14.7	16.2	2.81	1.34
MS13X	120.4	280.9	2.65	125.6	0.049	0.35	183.5	3.88e2	0.127	0.59	95.9	41.9	1.44	0.21
A88Y	115.6	159.6	4.19	123.8	0.080	0.74	270.5	0.246	0.131	1.01	80.7	29.2	1.54	0.52
A14Z	86.9	192.0	4.59	92.7	0.071	1.45	211.6	0.101	0.114	1.74	68.8	26.2	2.58	0.28

Table A.7: Isotherm fitting parameters for ethanol adsorption onto porous materials. T = 25ºC. Numbers in red represent fits that did not converge.

Sample	Langmuir			Freundlich			Sips				Dubinin-Astakhov			
	Q_{max} [mg/g]	K [a.u.]	MPSD [%]	Q_{max} [mg/g]	n [a.u.]	MPSD [%]	Q_{max} [mg/g]	K [a.u.]	N [a.u.]	MPSD [%]	Q_{max} [mg/g]	E [kJ/ mol]	n [a.u.]	MPSD [%]
AC	257.5	129.5	9.56	423.5	0.244	0.49	18728.9	5.30e-7	0.256	6.14	77.4	10	0.98	0.51
AS	87.0	443.6	5.10	108.7	0.103	0.48	255.8	0.094	0.146	0.78	56.6	23.5	1.22	0.22
MS13X	159.0	2450.0	1.31	167.2	0.023	0.22	324.8	3.432	0.043	0.27	146.4	59.6	1.53	0.04
A88Y	245.3	9.6	29.12	464.4	0.617	25.35	148.3	22.940	3.222	49.41	4.1	2.7	0.84	27.6
A14Z	96.7	567.8	3.26	115.0	0.081	0.62	264.3	0.091	0.121	0.45	56.2	31.9	0.62	0.19

Table A.8: Isotherm fitting parameters for 2-propanol adsorption onto porous materials. T = 25ºC. Numbers in red represent fits that did not converge.

Sample	Langmuir			Freundlich			Sips				Dubinin-Astakhov			
	Q_{max} [mg/g]	K [a.u.]	MPSD [%]	Q_{max} [mg/g]	n [a.u.]	MPSD [%]	Q_{max} [mg/g]	K [a.u.]	N [a.u.]	MPSD [%]	Q_{max} [mg/g]	E [kJ/ mol]	n [a.u.]	MPSD [%]
AC	282.4	40.3	7.83	330.8	0.220	1.30	756.7	0.371	0.306	0.87	38.8	5.1	0.62	0.71
AS	99.0	110.6	3.52	107.3	0.103	1.30	133.2	73.430	0.300	0.47	19.6	3.4	0.32	0.49
MS13X	161.9	559.9	1.22	165.4	0.025	0.13	178.5	1.10e5	0.212	0.35	142.1	77.4	1.24	0.15
A88Y	194.8	10.6	15.83	217.9	0.509	22.52	172.1	10.459	1.213	14.92	8.1	5.8	1.08	24.48
A14Z	101.5	157.3	2.16	107.6	0.075	1.48	114.4	353.711	0.400	0.25	22.3	2.9	0.25	0.77

Table A.9: Isotherm fitting parameters for 2-butanone adsorption onto porous materials. T = 25ºC. Numbers in red represent fits that did not converge.

Sample	Langmuir			Freundlich			Sips				Dubinin-Astakhov			
	Q_{max} [mg/g]	K [a.u.]	MPSD [%]	Q_{max} [mg/g]	n [a.u.]	MPSD [%]	Q_{max} [mg/g]	K [a.u.]	N [a.u.]	MPSD [%]	Q_{max} [mg/g]	E [kJ/ mol]	n [a.u.]	MPSD [%]
AC	271.6	259.0	7.23	377.9	0.155	0.60	994.1	0.062	0.12	1.08	139.4	16.7	1.18	0.3
AS	73.3	229.3	7.69	105.0	0.169	0.65	275.4	0.077	0.216	1.16	34.9	15.4	1.15	0.46
MS13X	142.1	2150.8	1.44	150.3	0.026	0.23	1728.9	2.20e-6	0.154	14.21	129.2	57.5	1.48	0.07
A88Y	133.3	377.0	3.17	180.9	0.112	2.32	419.2	0.128	0.159	2.19	26.9	1.4	0.24	1.16
A14Z	101.5	598.7	4.50	121.4	0.082	0.84	279.2	0.089	0.121	1.1	75.4	25.7	1.53	0.31

Table A.10: Kinetic fitting parameters for n-hexane adsorption onto industrial porous materials. P/P_0 = 0.005, T = 25˚C. Numbers in red represent fits that did not converge.

Sample	$Q_{max, exp}$ [mg g^{-1}]	Uptake range: 0-1 q_{max}						Uptake range: 0-0.85 q_{max}					
		Pseudo first order			Pseudo second order			Pseudo first order			Pseudo second order		
		Q_{max} [mg g^{-1}]	K [min^{-1}]	Adj. R^2	Q_{max} [mg g^{-1}]	K [mg g^{-1} min^{-1}]	Adj. R^2	Q_{max} [mg g^{-1}]	K [min^{-1}]	Adj. R^2	Q_{max} [mg g^{-1}]	K [mg g^{-1} min^{-1}]	Adj. R^2
AC	197.6	311.2	0.00369	0.996	517.6	4.40E-06	0.995	502.8	0.00205	0.999	932.4	1.19E-06	0.999
AS	16.6	21.5	0.0267	0.993	33.2	5.49E-04	0.989	33.3	0.0139	0.998	64.4	1.19E-04	0.998
MS13X	103.3	157.4	0.00478	0.993	259.0	1.15E-05	0.991	345.3	0.00186	0.999	655.0	1.50E-06	0.999
A88Y	90.2	132.7	0.00478	0.993	216.0	1.40E-05	0.991	262.7	0.00207	0.999	493.5	2.24E-06	0.999
A14Z	70.9	99.1	0.00622	0.994	158.4	2.55E-05	0.992	184.4	0.00305	0.999	322.6	5.13E-06	0.999

Table A.11: Kinetic fitting parameters for ethanol adsorption onto industrial porous materials. $P/P_0 = 0.005$, T = 25˚C. Numbers in red represent fits that did not converge.

Sample	$Q_{max, exp}$ [mg g^{-1}]	Uptake range: 0-1 q_{max}						Uptake range: 0-0.85 q_{max}					
		Pseudo first order			Pseudo second order			Pseudo first order			Pseudo second order		
		Q_{max} [mg g^{-1}]	K [min^{-1}]	Adj. R^2	Q_{max} [mg g^{-1}]	K [mg g^{-1} min^{-1}]	Adj. R^2	Q_{max} [mg g^{-1}]	K [min^{-1}]	Adj. R^2	Q_{max} [mg g^{-1}]	K [mg g^{-1} min^{-1}]	Adj. R^2
AC	115.8	133.3	0.00398	0.989	192.3	1.57E-05	0.983	238.0	0.00181	0.994	435.7	2.27E-06	0.994
AS	64.2	91.7	0.00389	0.992	148.4	1.67E-05	0.989	212.2	0.00141	0.996	406.1	1.81E-06	0.996
MS13X	148.8	225.7	0.00167	0.993	371.4	2.80E-06	0.991	472.6	6.82E-04	0.998	897.6	4.01E-07	0.998
A88Y	24.7	29.5	0.0092	0.973	43.4	1.55E-04	0.963	17000	1.09E-05	0.991	2300	3.54E-08	0.991
A14Z	73.9	89.4	0.00334	0.993	133.3	1.81E-05	0.989	132.5	0.00194	0.996	236.7	4.63E-06	0.996

Table A.12: Kinetic fitting parameters for 2-propanol adsorption onto industrial porous materials. $P/P_0 = 0.005$, T = 25˚C. Numbers in red represent fits that did not converge.

Sample	$Q_{max, exp}$ [mg g^{-1}]	Uptake range: 0-1 q_{max}						Uptake range: 0-0.85 q_{max}					
		Pseudo first order			Pseudo second order			Pseudo first order			Pseudo second order		
		Q_{max} [mg g^{-1}]	K [min^{-1}]	Adj. R^2	Q_{max} [mg g^{-1}]	K [mg g^{-1} min^{-1}]	Adj. R^2	Q_{max} [mg g^{-1}]	K [min^{-1}]	Adj. R^2	Q_{max} [mg g^{-1}]	K [mg g^{-1} min^{-1}]	Adj. R^2
AC	137.9	182.6	0.00125	0.992	286.3	2.91E-06	0.989	322.2	6.02E-04	0.995	597.1	5.45E-07	0.995
AS	72.1	91.4	0.00197	0.994	139.7	9.80E-06	0.991	138.4	0.00113	0.998	248.6	2.55E-06	0.998
MS13X	149.6	247.5	6.63E-04	0.996	418.1	9.57E-07	0.995	411.6	3.60E-04	0.998	770.6	2.50E-07	0.998
A88Y	28.5	35.2	0.00439	0.985	53.0	5.85E-05	0.98	97.8	0.00122	0.994	188.3	3.37E-06	0.994
A14Z	78.9	96.6	0.00155	0.998	145.2	7.62E-06	0.996	108.7	1.30E-03	0.999	182.7	4.33E-06	0.999

Table A.13: Kinetic fitting parameters for 2-butanone adsorption onto industrial porous materials. P/P_0 = 0.005, T = 25˚C. Numbers in red represent fits that did not converge.

Sample	$Q_{max, exp}$ [mg g^{-1}]	Uptake range: 0-1 q_{max}						Uptake range: 0-0.85 q_{max}					
		Pseudo first order			Pseudo second order			Pseudo first order			Pseudo second order		
		Q_{max} [mg g^{-1}]	K [min^{-1}]	Adj. R^2	Q_{max} [mg g^{-1}]	K [mg g^{-1} min^{-1}]	Adj. R^2	Q_{max} [mg g^{-1}]	K [min^{-1}]	Adj. R^2	Q_{max} [mg g^{-1}]	K [mg g^{-1} min^{-1}]	Adj. R^2
AC	157.9	190.1	0.00395	0.985	280.7	1.03E-05	0.978	497.7	0.00116	0.998	942.9	6.48E-07	0.998
AS	37.3	48.8	0.0111	0.99	76.0	9.82E-05	0.986	113.6	0.00386	0.998	214.6	9.53E-06	0.998
MS13X	124.5	192.1	0.00212	0.995	317.6	4.14E-06	0.993	338.6	0.00106	0.998	633.9	8.96E-07	0.998
A88Y	95.6	100.8	0.00252	0.999	136.1	1.60E-05	0.998	98.4	0.00262	0.999	148.5	1.25E-05	0.999
A14Z	71.3	94.4	0.00429	0.989	147.5	1.95E-05	0.986	218.3	0.00151	0.997	414.5	1.92E-06	0.997

Table A.14: Kinetic fitting parameters for toluene adsorption onto industrial porous materials. P/P_0 = 0.005, T = 25˚C, pre-exposure RH of 0 %. Numbers in red represent fits that did not converge.

Sample	$Q_{max, exp}$ [mg g^{-1}]	Uptake range: 0-1 q_{max}						Uptake range: 0-0.85 q_{max}					
		Pseudo first order			Pseudo second order			Pseudo first order			Pseudo second order		
		Q_{max} [mg g^{-1}]	K [min^{-1}]	Adj. R^2	Q_{max} [mg g^{-1}]	K [mg g^{-1} min^{-1}]	Adj. R^2	Q_{max} [mg g^{-1}]	K [min^{-1}]	Adj. R^2	Q_{max} [mg g^{-1}]	K [mg g^{-1} min^{-1}]	Adj. R^2
AC	264.4	362.1	1.33E-03	0.988	572.7	1.52E-06	0.985	928.3	4.18E-04	0.999	1768	1.24E-07	0.999
AS	23.6	30.5	7.86E-03	0.983	47.2	1.13E-04	0.978	278.4	6.35E-04	0.997	558.6	5.67E-07	0.997
MS13X	144	214.3	9.78E-04	0.998	350.0	1.77E-06	0.998	262.1	7.54E-04	0.999	465.3	9.22E-07	0.999
A88Y	121.3	150.1	1.78E-03	0.983	224.6	5.66E-06	0.976	398.6	5.14E-04	0.999	754.8	3.60E-07	0.999
A14Z	57	72.0	2.82E-03	0.993	109.5	1.80E-05	0.989	112.1	1.55E-03	0.998	202.3	4.29E-06	0.998

Table A.15: Kinetic fitting parameters for toluene adsorption onto industrial porous materials. P/P_0 = 0.005, T = 25˚C, pre-exposure RH of 10 %. Numbers in red represent fits that did not converge.

Sample	$Q_{max, exp}$ [mg g^{-1}]	Uptake range: 0-1 q_{max}						Uptake range: 0-0.85 q_{max}					
		Pseudo first order			Pseudo second order			Pseudo first order			Pseudo second order		
		Q_{max} [mg g^{-1}]	K [min^{-1}]	Adj. R^2	Q_{max} [mg g^{-1}]	K [mg g^{-1} min^{-1}]	Adj. R^2	Q_{max} [mg g^{-1}]	K [min^{-1}]	Adj. R^2	Q_{max} [mg g^{-1}]	K [mg g^{-1} min^{-1}]	Adj. R^2
AC	254.5	352.6	0.00122	0.993	560	1.43E-06	0.991	592.9	6.29E-04	0.999	1087.8	3.17E-07	0.999
AS	8.9	9.3	0.0144	0.994	12.5	0.00101	0.983	12.3	0.00927	0.998	20.8	2.67E-04	0.998
MS13X	1.2	1.1	0.00712	0.681	1.2	0.00920	0.84	0.93	0.0165	0.642	1.0	0.0260	0.828
A88Y	109.4	162.7	0.00117	0.995	265.4	2.78E-06	0.994	258.8	6.54E-04	0.999	475.3	7.53E-07	0.999
A14Z	39.6	48.0	0.00285	0.997	71.5	2.89E-05	0.993	60.2	0.00206	0.999	103.4	1.18E-05	0.999

Table A.16: Kinetic fitting parameters for toluene adsorption onto industrial porous materials. P/P_0 = 0.005, T = 25˚C, pre-exposure RH of 30 %. Numbers in red represent fits that did not converge.

Sample	$Q_{max, exp}$ [mg g^{-1}]	Uptake range: 0-1 q_{max}						Uptake range: 0-0.85 q_{max}					
		Pseudo first order			Pseudo second order			Pseudo first order			Pseudo second order		
		Q_{max} [mg g^{-1}]	K [min^{-1}]	Adj. R^2	Q_{max} [mg g^{-1}]	K [mg g^{-1} min^{-1}]	Adj. R^2	Q_{max} [mg g^{-1}]	K [min^{-1}]	Adj. R^2	Q_{max} [mg g^{-1}]	K [mg g^{-1} min^{-1}]	Adj. R^2
AC	244.9	361.6	0.00103	0.994	588.6	1.11E-06	0.992	638.9	5.07E-04	0.999	1185.6	2.31E-07	0.999
AS	3.5	4.0	0.0289	0.994	5.8	0.00376	0.989	5.3	0.0192	0.994	9.2	0.00122	0.994
MS13X	1.2	1.3	0.00343	0.983	1.7	0.00171	0.99	1.1	0.00438	0.981	1.6	0.00233	0.987
A88Y	108.2	165.5	0.00114	0.995	272.6	2.60E-06	0.993	299.7	5.50E-04	0.999	559.5	5.28E-07	0.999
A14Z	29.1	33.9	0.00349	0.997	49.1	5.39E-05	0.993	40.3	0.00269	0.999	67.6	2.43E-05	0.999

Table A.17: Kinetic fitting parameters for toluene adsorption onto industrial porous materials. P/P_0 = 0.005, T = 25˚C, pre-exposure RH of 50 %. Numbers in red represent fits that did not converge.

Sample	$Q_{max, exp}$ [mg g^{-1}]	Uptake range: 0-1 q_{max}						Uptake range: 0-0.85 q_{max}					
		Pseudo first order			Pseudo second order			Pseudo first order			Pseudo second order		
		Q_{max} [mg g^{-1}]	K [min^{-1}]	Adj. R^2	Q_{max} [mg g^{-1}]	K [mg g^{-1} min^{-1}]	Adj. R^2	Q_{max} [mg g^{-1}]	K [min^{-1}]	Adj. R^2	Q_{max} [mg g^{-1}]	K [mg g^{-1} min^{-1}]	Adj. R^2
AC	172.5	284.9	8.30E-04	0.997	477.0	1.06E-06	0.996	378.2	5.81E-04	0.999	682.8	4.75E-07	0.999
AS	2.5	3.4	0.0339	0.985	5.4	0.00408	0.981	12.7	0.00713	0.989	25.2	1.43E-04	0.989
MS13X	0.3	0.4	0.00934	0.89	0.5	0.0169	0.905	0.3	0.0144	0.859	0.4	0.0385	0.884
A88Y	106.1	140.9	0.00149	0.992	219.5	4.57E-06	0.989	238.5	7.49E-04	0.999	435.6	9.47E-07	0.999
A14Z	22.5	25.6	0.00432	0.998	36.5	9.22E-05	0.994	29	0.00355	0.999	47.7	4.65E-05	0.999

Table A.18: Kinetic fitting parameters for toluene adsorption onto industrial porous materials. P/P_0 = 0.005, T = 25˚C, pre-exposure RH of 70 %. Numbers in red represent fits that did not converge.

Sample	$Q_{max, exp}$ [mg g^{-1}]	Uptake range: 0-1 q_{max}						Uptake range: 0-0.85 q_{max}					
		Pseudo first order			Pseudo second order			Pseudo first order			Pseudo second order		
		Q_{max} [mg g^{-1}]	K [min^{-1}]	Adj. R^2	Q_{max} [mg g^{-1}]	K [mg g^{-1} min^{-1}]	Adj. R^2	Q_{max} [mg g^{-1}]	K [min^{-1}]	Adj. R^2	Q_{max} [mg g^{-1}]	K [mg g^{-1} min^{-1}]	Adj. R^2
AC	7.9	8.3	0.0179	0.999	11.2	0.00139	0.996	8.6	0.0169	0.999	13.3	8.67E-04	0.998
AS	2.7	2.4	0.0247	0.687	2.6	0.01339	0.853	2.1	0.0459	0.892	2.3	0.0294	0.952
MS13X	1.2	1.9	8.78E-04	0.996	3.1	1.75E-04	0.996	1.9	9.12E-04	0.993	3.1	1.79E-04	0.993
A88Y	100.8	138.2	0.00127	0.997	219.0	3.83E-06	0.995	193.2	8.22E-04	0.999	344.8	1.35E-06	0.999
A14Z	14.4	16.2	0.00531	0.999	22.7	1.88E-04	0.998	15.7	5.57E-03	0.999	24.2	1.58E-04	0.999

Table A.19: Kinetic fitting parameters for water adsorption onto industrial porous materials. RH = 10 %, T = 25˚C. Numbers in red represent fits that did not converge.

Sample	$Q_{max, exp}$ [mg g^{-1}]	Uptake range: 0-1 q_{max}						Uptake range: 0-0.85 q_{max}					
		Pseudo first order			Pseudo second order			Pseudo first order			Pseudo second order		
		Q_{max} [mg g^{-1}]	K [min^{-1}]	Adj. R^2	Q_{max} [mg g^{-1}]	K [mg g^{-1} min^{-1}]	Adj. R^2	Q_{max} [mg g^{-1}]	K [min^{-1}]	Adj. R^2	Q_{max} [mg g^{-1}]	K [mg g^{-1} min^{-1}]	Adj. R^2
AC	4.3	4.2	0.117	0.959	4.3	0.0499	0.88	27300	1.06E-05	0.953	988.1	2.98E-07	0.953
AS	40.7	41.5	0.0264	0.986	51.2	5.41E-04	0.961	70.8	0.0117	0.993	126.6	5.22E-05	0.993
MS13X	190.8	269.8	0.00468	0.989	432.1	7.12E-06	0.987	630.8	0.00165	0.999	1193.1	7.34E-07	0.999
A88Y	13.4	14.1	0.0551	0.976	18.6	0.00267	0.957	50.5	0.0106	0.985	99.3	5.43E-05	0.985
A14Z	28.7	29.6	0.0268	0.986	36.3	7.77E-04	0.96	50.9	0.0117	0.992	91.3	7.21E-05	0.992

Table A.20: Kinetic fitting parameters for water adsorption onto industrial porous materials. RH = 30 %, T = 25˚C. Numbers in red represent fits that did not converge.

Sample	$Q_{max, exp}$ [mg g^{-1}]	Uptake range: 0-1 q_{max}						Uptake range: 0-0.85 q_{max}					
		Pseudo first order			Pseudo second order			Pseudo first order			Pseudo second order		
		Q_{max} [mg g^{-1}]	K [min^{-1}]	Adj. R^2	Q_{max} [mg g^{-1}]	K [mg g^{-1} min^{-1}]	Adj. R^2	Q_{max} [mg g^{-1}]	K [min^{-1}]	Adj. R^2	Q_{max} [mg g^{-1}]	K [mg g^{-1} min^{-1}]	Adj. R^2
AC	14.4	14.3	0.0780	0.987	15.8	0.00727	0.941	20.2	0.0446	0.974	35	7.46E-04	0.972
AS	58.0	58.9	0.0546	0.974	67.4	0.00103	0.923	313.2	0.00644	0.982	628.9	5.09E-06	0.982
MS13X	205.3	386.6	0.00848	0.993	675.9	7.26E-06	0.992	1431.2	0.00198	0.996	2832.2	3.53E-07	0.996
A88Y	21.4	21.6	0.0914	0.974	23.7	0.00565	0.911	142.7	0.00854	0.978	290.5	1.44E-05	0.978
A14Z	46.7	47.7	0.0424	0.983	57.4	8.22E-04	0.951	97	0.0151	0.985	179.5	4.54E-05	0.985

Table A.21: Kinetic fitting parameters for water adsorption onto industrial porous materials. RH = 50 %, T = 25˚C. Numbers in red represent fits that did not converge.

Sample	$Q_{max, exp}$ [mg g^{-1}]	Uptake range: 0-1 q_{max}						Uptake range: 0-0.85 q_{max}					
		Pseudo first order			Pseudo second order			Pseudo first order			Pseudo second order		
		Q_{max} [mg g^{-1}]	K [min^{-1}]	Adj. R^2	Q_{max} [mg g^{-1}]	K [mg g^{-1} min^{-1}]	Adj. R^2	Q_{max} [mg g^{-1}]	K [min^{-1}]	Adj. R^2	Q_{max} [mg g^{-1}]	K [mg g^{-1} min^{-1}]	Adj. R^2
AC	93.5	90.6	0.0109	0.979	103	1.45E-04	0.999	79.1	0.0158	0.992	102	1.50E-04	0.999
AS	87.4	87.1	0.0530	0.987	91.7	0.00102	0.928	125.4	0.0299	0.974	217.6	7.99E-05	0.972
MS13X	213.1	214.8	0.0279	0.967	235.6	1.76E-04	0.894	3028.9	0.00114	0.995	6110.2	9.27E-08	0.995
A88Y	30.6	30.6	0.0934	0.982	32.4	0.00493	0.916	62.6	0.0329	0.973	116.8	1.51E-04	0.972
A14Z	65.4	65.3	0.0467	0.988	71.1	1.01E-03	0.935	101.5	0.0234	0.981	178.9	7.46E-05	0.980

Table A.22: Kinetic fitting parameters for water adsorption onto industrial porous materials. RH = 70 %, T = 25˚C. Numbers in red represent fits that did not converge.

Sample	$Q_{max, exp}$ [mg g^{-1}]	Uptake range: 0-1 q_{max}						Uptake range: 0-0.85 q_{max}					
		Pseudo first order			Pseudo second order			Pseudo first order			Pseudo second order		
		Q_{max} [mg g^{-1}]	K [min^{-1}]	Adj. R^2	Q_{max} [mg g^{-1}]	K [mg g^{-1} min^{-1}]	Adj. R^2	Q_{max} [mg g^{-1}]	K [min^{-1}]	Adj. R^2	Q_{max} [mg g^{-1}]	K [mg g^{-1} min^{-1}]	Adj. R^2
AC	232.7	233.7	0.0167	0.998	270.1	7.86E-05	0.971	261.7	0.0135	0.999	411.7	2.19E-05	0.998
AS	159.9	156.5	0.0301	0.977	170.1	2.82E-04	0.994	136.8	0.0441	0.993	179.2	2.27E-04	0.991
MS13X	241.3	241.7	0.0491	0.966	255.6	3.31E-04	0.876	99400	6.82E-05	0.988	32500	6.45E-09	0.988
A88Y	70.6	68.8	0.0336	0.967	74.2	7.45E-04	0.995	59.5	0.0518	0.99	76.3	6.57E-04	0.99
A14Z	98.8	97.9	0.0439	0.992	104.1	7.24E-04	0.963	98.6	0.0449	0.985	147.2	2.19E-04	0.98

Table A.23: Isotherm fitting parameters for water adsorption onto ZIF materials. T = 25ºC. Numbers in red represent fits that did not converge.

Sample	Freundlich			BET			GAB			
	Q_{max} [mg/g]	n [a.u.]	MPSD [%]	Q_{max} [mg/g]	C [a.u.]	MPSD [%]	Q_{max} [mg/g]	C [a.u.]	K [a.u.]	MPSD [%]
ZIF-8	31.0	0.256	101.92	2.33	5.21	48.47	2.06	12.19	1.014	38.56
ZIF-8 (NB-1)	126.3	0.142	117.28	8.27	0.35	77.9	4.23	1.69	1.041	61.07
ZIF-67	63.9	0.175	114.18	3.91	1.42	71.52	2.39	76.53	1.044	13.56
ZIF-67 (NB-1)	179.6	0.126	120.40	12.58	0.21	76.52	4.56	1.77	1.053	53.41
ZIF-67 (ML)	70.4	0.202	111.49	4.38	6.26	52.15	3.20	127.40	1.037	17.36

Table A.24: Isotherm fitting parameters for toluene adsorption onto ZIF materials. T = 25ºC. Numbers in red represent fits that did not converge.

Sample	Langmuir			Freundlich			Sips				Dubinin-Astakhov			
	Q_{max} [mg/g]	K [a.u.]	MPSD [%]	Q_{max} [mg/g]	n [a.u.]	MPSD [%]	Q_{max} [mg/g]	K [a.u.]	N [a.u.]	MPSD [%]	Q_{max} [mg/g]	E [kJ/ mol]	n [a.u.]	MPSD [%]
ZIF-8	325.9	704.5	3.15	376.6	0.068	0.32	796.4	0.287	0.108	0.28	228.0	39.2	0.86	0.28
ZIF-8 (NB-1)	305.4	423.9	6.41	386.9	0.109	1.54	1266.4	0.002	0.137	1.85	210.1	20.8	1.72	0.55
ZIF-67	327.9	739.4	3.23	377.6	0.066	0.23	623.5	19.353	0.127	0.41	241.5	37.3	1.03	0.24
ZIF-67 (NB-1)	334.8	556.9	5.04	404.0	0.086	1.04	932.7	0.095	0.128	1.34	246.0	24.4	1.61	0.36
ZIF-67 (ML)	302.7	844.2	2.00	339.8	0.055	1.16	747.7	0.105	0.088	1.12	120.5	17.8	0.21	0.68

Table A.25: Isotherm fitting parameters for n-hexane adsorption onto ZIF materials. T = 25ºC. Numbers in red represent fits that did not converge.

Sample	Langmuir			Freundlich			Sips				Dubinin-Astakhov			
	Q_{max} [mg/g]	K [a.u.]	MPSD [%]	Q_{max} [mg/g]	n [a.u.]	MPSD [%]	Q_{max} [mg/g]	K [a.u.]	N [a.u.]	MPSD [%]	Q_{max} [mg/g]	E [kJ/ mol]	n [a.u.]	MPSD [%]
ZIF-8	255.7	819.1	2.07	288.6	0.057	0.89	794.9	0.0009	0.082	0.87	149.6	54.9	0.41	0.44
ZIF-8 (NB-1)	242.0	366.2	6.38	313.5	0.120	1.30	1223.8	0.0006	0.145	1.54	152.0	20.3	1.41	0.98
ZIF-67	261.3	739.5	3.23	300.9	0.066	0.23	618.6	0.465	0.107	0.34	192.5	37.3	1.03	0.24
ZIF-67 (NB-1)	252.1	557.0	5.04	304.2	0.086	1.04	835.8	0.007	0.118	1.29	185.3	24.4	1.61	0.36
ZIF-67 (ML)	237.2	739.0	1.57	269	0.061	1.63	592.4	0.121	0.096	1.58	51.2	0.50	0.14	0.68

Table A.26: Isotherm fitting parameters for methanol adsorption onto ZIF materials. T = 25ºC. Numbers in red represent fits that did not converge.

Sample	Langmuir			Freundlich			Sips				Dubinin-Astakhov			
	Q_{max} [mg/g]	K [a.u.]	MPSD [%]	Q_{max} [mg/g]	n [a.u.]	MPSD [%]	Q_{max} [mg/g]	K [a.u.]	N [a.u.]	MPSD [%]	Q_{max} [mg/g]	E [kJ/ mol]	n [a.u.]	MPSD [%]
ZIF-8	913.3	0.241	77.96	15628.2	2.689	49.25	270.5	5.19	13.58	96.05	11.68	11.68	7.41	108.65
ZIF-8 (NB-1)	5058.8	0.093	59.58	5438	2.043	40.29	11.7	11.65	7.02	108.09	5.09	9.24	3.66	30.34
ZIF-67	1064.6	0.247	78.39	12554.7	2.49	46.35	11.4	11.43	6.64	108.38	2.88	9.05	3.87	45.91
ZIF-67 (NB-1)	7813.2	0.119	36.94	1927	1.336	34.07	741.2	3.33	3.17	75.45	10.88	10.88	5.12	52.34
ZIF-67 (ML)	7255.5	0.094	58.38	4302.2	1.77	42.95	10.6	10.56	4.7	112.31	8.98	8.11	2.39	55.24

Table A.27: Kinetic fitting parameters for n-hexane adsorption onto ZIF adsorbents. $P/P_0 = 0.005$, T = 25˚C. Numbers in red represent fits that did not converge.

Material	Q_{exp} [mg/g]	Pseudo first order			Pseudo second order		
		Q_{max} [mg g^{-1}]	K [min^{-1}]	Adj. R^2	Q_{max} [mg g^{-1}]	K [mg g^{-1} min^{-1}]	Adj. R^2
ZIF-8	206.1	209.2	0.0512	0.999	248.6	2.41E-04	0.987
ZIF-8 (NB-1)	166.5	190.3	0.0049	0.998	275.4	1.35E-05	0.994
ZIF-67	212.6	268.0	0.0121	0.994	409.5	2.05E-05	0.991
ZIF-67 (NB-1)	195.5	209.9	0.00572	0.999	292.7	1.59E-05	0.999
ZIF-67 (ML)	190.6	206.3	0.00487	0.991	280.4	1.47E-05	0.980

Table A.28: Kinetic fitting parameters for methanol adsorption onto ZIF adsorbents. $P/P_0 = 0.005$, T = 25˚C. Numbers in red represent fits that did not converge.

Material	Q_{exp} [mg/g]	Pseudo first order			Pseudo second order		
		Q_{max} [mg g^{-1}]	K [min^{-1}]	Adj. R^2	Q_{max} [mg g^{-1}]	K [mg g^{-1} min^{-1}]	Adj. R^2
ZIF-8	3.43	3.24	0.0946	0.851	3.41	4.50E-02	0.941
ZIF-8 (NB-1)	6.14	6.17	0.0214	0.998	6.93	4.34E-03	0.983
ZIF-67	4.50	4.35	0.0672	0.921	4.58	2.62E-02	0.970
ZIF-67 (NB-1)	16.41	15.56	0.0386	0.987	17.53	3.09E-03	0.990
ZIF-67 (ML)	10.79	11.74	0.00604	0.993	16.55	2.93E-04	0.997

Table A.29: Kinetic fitting parameters for toluene adsorption onto ZIF adsorbents. $P/P_0 = 0.005$, T = 25˚C, pre-exposure RH of 0 %. Numbers in red represent fits that did not converge.

Material	Q_{exp} [mg/g]	Pseudo first order			Pseudo second order		
		Q_{max} [mg g^{-1}]	K [min^{-1}]	Adj. R^2	Q_{max} [mg g^{-1}]	K [mg g^{-1} min^{-1}]	Adj. R^2
ZIF-8	261.3	269.9	0.00167	0.999	345.6	4.70E-06	0.995
ZIF-8 (NB-1)	220.1	224.0	0.00158	0.999	290.2	5.15E-06	0.998
ZIF-67	262.8	277.5	0.00145	0.999	370.7	3.46E-06	0.998
ZIF-67 (NB-1)	259.2	265.7	0.00198	0.999	336.6	5.83E-06	0.993
ZIF-67 (ML)	249.8	270.8	0.00129	0.999	371.6	2.90E-06	0.996

Table A.30: Kinetic fitting parameters for toluene adsorption onto ZIF adsorbents. P/P_0 = 0.005, T = 25˚C, pre-exposure RH of 20 %. Numbers in red represent fits that did not converge.

Material	Q_{exp} [mg/g]	Pseudo first order			Pseudo second order		
		Q_{max} [mg g^{-1}]	K [min^{-1}]	Adj. R^2	Q_{max} [mg g^{-1}]	K [mg g^{-1} min^{-1}]	Adj. R^2
ZIF-8	221.1	237.0	6.25E-04	0.998	325.3	1.62E-06	0.999
ZIF-8 (NB-1)	179.8	195.6	5.90E-04	0.999	272.7	1.77E-06	0.999
ZIF-67	230.8	237.6	8.89E-04	0.999	308.5	2.70E-06	0.993
ZIF-67 (NB-1)	217.8	232.8	6.79E-04	0.999	316.1	1.84E-06	0.997
ZIF-67 (ML)	214.9	218.0	8.14E-04	0.997	282.6	2.73E-06	0.999

Table A.31: Kinetic fitting parameters for toluene adsorption onto ZIF adsorbents. P/P_0 = 0.005, T = 25˚C, pre-exposure RH of 40 %. Numbers in red represent fits that did not converge.

Material	Q_{exp} [mg/g]	Pseudo first order			Pseudo second order		
		Q_{max} [mg g^{-1}]	K [min^{-1}]	Adj. R^2	Q_{max} [mg g^{-1}]	K [mg g^{-1} min^{-1}]	Adj. R^2
ZIF-8	217.8	232.8	6.84E-04	0.999	314.4	1.89E-06	0.998
ZIF-8 (NB-1)	182.9	195.1	8.80E-04	0.999	262.2	2.93E-06	0.995
ZIF-67	219.6	236.7	6.76E-04	0.999	325.0	1.74E-06	0.998
ZIF-67 (NB-1)	213.2	224.8	5.91E-04	0.999	303.4	1.69E-06	0.999
ZIF-67 (ML)	208.6	206.6	8.71E-04	0.987	258.1	3.52E-06	0.997

Table A.32: Kinetic fitting parameters for toluene adsorption onto ZIF adsorbents. P/P_0 = 0.005, T = 25˚C, pre-exposure RH of 60 %. Numbers in red represent fits that did not converge.

Material	Q_{exp} [mg/g]	Pseudo first order			Pseudo second order		
		Q_{max} [mg g^{-1}]	K [min^{-1}]	Adj. R^2	Q_{max} [mg g^{-1}]	K [mg g^{-1} min^{-1}]	Adj. R^2
ZIF-8	211.9	214.2	8.75E-04	0.998	268.1	3.36E-06	0.996
ZIF-8 (NB-1)	173.2	179.5	7.14E-04	0.999	235.3	2.79E-06	0.996
ZIF-67	215.3	231.9	6.25E-04	0.998	319.3	1.64E-06	0.999
ZIF-67 (NB-1)	208.7	221.5	5.22E-04	0.999	302.5	1.46E-06	0.999
ZIF-67 (ML)	207.0	213.0	6.36E-04	0.991	290.2	1.91E-06	0.997

Table A.33: Kinetic fitting parameters for toluene adsorption onto ZIF adsorbents. P/P_0 = 0.005, T = 25˚C, pre-exposure RH of 80 %. Numbers in red represent fits that did not converge.

Material	Q_{exp} [mg/g]	Pseudo first order			Pseudo second order		
		Q_{max} [mg g^{-1}]	K [min^{-1}]	Adj. R^2	Q_{max} [mg g^{-1}]	K [mg g^{-1} min^{-1}]	Adj. R^2
ZIF-8	214.7	224.4	7.82E-04	0.998	292.9	2.49E-06	0.996
ZIF-8 (NB-1)	168.9	184.6	5.84E-04	0.999	256.8	1.86E-06	0.998
ZIF-67	210.6	213.0	9.62E-04	0.998	268.7	3.61E-06	0.995
ZIF-67 (NB-1)	198.4	207.2	1.33E-03	0.999	270.5	4.58E-06	0.993
ZIF-67 (ML)	206.3	201.5	7.18E-04	0.975	263.6	2.56E-06	0.989

Table A.34: Kinetic fitting parameters for water adsorption onto ZIF adsorbents. RH = 20 %, T = 25˚C. Numbers in red represent fits that did not converge.

Material	Q_{exp} [mg/g]	Pseudo first order			Pseudo second order		
		Q_{max} [mg g^{-1}]	K [min^{-1}]	Adj. R^2	Q_{max} [mg g^{-1}]	K [mg g^{-1} min^{-1}]	Adj. R^2
ZIF-8	1.14	1.11	0.156	0.983	1.21	1.96E-01	0.965
ZIF-8 (NB-1)	3.63	3.42	0.194	0.878	3.59	8.49E-02	0.921
ZIF-67	2.93	2.89	0.0884	0.939	3.25	3.62E-02	0.879
ZIF-67 (NB-1)	2.95	2.85	0.248	0.935	2.96	1.47E-01	0.926
ZIF-67 (ML)	4.40	4.59	0.00627	0.963	6.31	8.41E-04	0.973

Table A.35: Kinetic fitting parameters for water adsorption onto ZIF adsorbents. RH = 40 %, T = 25˚C. Numbers in red represent fits that did not converge.

Material	Q_{exp} [mg/g]	Pseudo first order			Pseudo second order		
		Q_{max} [mg g^{-1}]	K [min^{-1}]	Adj. R^2	Q_{max} [mg g^{-1}]	K [mg g^{-1} min^{-1}]	Adj. R^2
ZIF-8	2.76	2.67	0.184	0.974	3.02	8.11E-02	0.968
ZIF-8 (NB-1)	4.05	3.79	0.158	0.886	4.00	6.46E-02	0.960
ZIF-67	4.37	3.89	0.0769	0.812	4.27	2.65E-02	0.935
ZIF-67 (NB-1)	3.75	3.66	0.165	0.962	3.94	6.69E-02	0.975
ZIF-67 (ML)	6.22	5.56	0.0965	0.858	6.00	2.40E-02	0.948

Table A.36: Kinetic fitting parameters for water adsorption onto ZIF adsorbents. RH = 60 %, T = 25˚C. Numbers in red represent fits that did not converge.

Material	Q_{exp} [mg/g]	Pseudo first order			Pseudo second order		
		Q_{max} [mg g^{-1}]	K [min^{-1}]	Adj. R^2	Q_{max} [mg g^{-1}]	K [mg g^{-1} min^{-1}]	Adj. R^2
ZIF-8	4.65	4.52	0.194	0.770	4.66	6.39E-02	0.918
ZIF-8 (NB-1)	8.02	7.70	0.0634	0.766	8.02	1.38E-02	0.954
ZIF-67	6.01	5.92	0.0325	0.989	6.30	8.70E-03	0.941
ZIF-67 (NB-1)	9.77	9.07	0.0256	0.680	9.72	4.69E-03	0.881
ZIF-67 (ML)	8.16	7.82	0.105	0.944	8.21	2.26E-02	0.991

Table A.37: Kinetic fitting parameters for water adsorption onto ZIF adsorbents. RH = 80 %, T = 25˚C. Numbers in red represent fits that did not converge.

Material	Q_{exp} [mg/g]	Pseudo first order			Pseudo second order		
		Q_{max} [mg g^{-1}]	K [min^{-1}]	Adj. R^2	Q_{max} [mg g^{-1}]	K [mg g^{-1} min^{-1}]	Adj. R^2
ZIF-8	6.79	6.76	0.218	0.963	6.94	6.15E-02	0.890
ZIF-8 (NB-1)	20.28	19.48	0.109	0.958	20.56	9.22E-03	0.992
ZIF-67	12.28	13.57	0.159	0.990	14.85	1.63E-02	0.978
ZIF-67 (NB-1)	24.76	23.76	0.148	0.960	24.70	1.08E-02	0.961
ZIF-67 (ML)	18.64	18.12	0.147	0.934	18.93	1.38E-02	0.981

Table A.38: Isotherm fitting parameters for water adsorption onto MIL-100 adsorbents. T = 25ºC. Numbers in red represent fits that did not converge.

Sample	Langmuir			BET			GAB			
	Q_{max} [mg/g]	K [a.u.]	MPSD [%]	Q_{max} [mg/g]	C [a.u.]	MPSD [%]	Q_{max} [mg/g]	C [a.u.]	K [a.u.]	MPSD [%]
MIL-100	3.71E+04	0.024	27.07	128.5	21.4	54.34	50200.4	93.7	1.89E-04	65.64
MIL-100/ DPA	1.38E+05	0.0038	42.08	97.5	8.1	55.92	186917.9	27.6	1.02E-04	44.61
MIL-100/ OPA	1.73E+05	0.0033	42.17	100.8	9.1	56.47	250536.4	33.4	6.75E-05	44.71
MIL-100 (NB)	1.19E+03	0.549	18.94	67.6	35.3	59.32	941.6	11.8	5.90E-02	20.21
MIL-100 (NB) DPA	1.22E+04	0.0176	22.45	31.3	14.3	56.3	13197.1	97.8	1.66E-04	23.81
MIL-100 (NB) OPA	2.74E+02	0.5102	8.95	16.9	27.1	47.59	272.3	569.3	9.00E-04	9.49

Table A.39: Isotherm fitting parameters for toluene adsorption onto MIL-100 adsorbents. T = 25ºC. Numbers in red represent fits that did not converge.

Sample	Langmuir			Freundlich			Sips				Dubinin-Astakhov			
	Q_{max} [mg/g]	K [a.u.]	MPSD [%]	Q_{max} [mg/g]	n [a.u.]	MPSD [%]	Q_{max} [mg/g]	K [a.u.]	N [a.u.]	MPSD [%]	Q_{max} [mg/g]	E [kJ/ mol]	n [a.u.]	MPSD [%]
MIL-100	591.7	432.9	2.72	731.5	0.099	2.72	658	595.695	0.506	0.91	617	19.55	2.377	1.05
MIL-100/ DPA	459.2	312	3.87	600.5	0.127	3.43	533.1	296.718	0.5	1.03	486.4	17.692	2.281	0.84
MIL-100/ OPA	446.8	232.2	3.35	621.4	0.159	5.62	488.6	210.682	0.672	2.05	461.2	15.651	2.758	2.11
MIL-100 (NB)	330.9	379.3	2.89	415.9	0.108	3.66	359.8	465.716	0.583	1.62	341	18.19	2.653	1.66
MIL-100 (NB) DPA	224.4	293.9	3.49	294.8	0.131	4.42	248.6	298.066	0.592	1.64	232.9	16.946	2.6	1.5
MIL-100 (NB) OPA	43.5	117	8.68	73.6	0.265	14.75	155.5	0.452	0.338	15.03	390.1	0.461	0.332	19.17

Table A.40: Kinetic fitting parameters for toluene adsorption onto MIL-100 adsorbents. P/P_0 = 0.005, T = 25˚C, pre-exposure RH = 0 %. Numbers in red represent fits that did not converge.

Material	Q_{exp} [mg/g]	Pseudo first order			Pseudo second order		
		Q_{max} [mg g^{-1}]	K [min^{-1}]	Adj. R^2	Q_{max} [mg g^{-1}]	K [mg g^{-1} min^{-1}]	Adj. R^2
MIL-100	412.1	587.8	8.56E-04	0.999	952.7	5.74E-07	0.998
MIL-100/ DPA	293.1	346.9	1.38E-03	0.997	515.4	1.95E-06	0.994
MIL-100/ OPA	248.9	289.7	1.02E-03	0.999	421.5	1.82E-06	0.998
MIL-100 (NB)	225.8	252.7	1.19E-03	0.999	358.7	2.60E-06	0.997
MIL-100 (NB)/ DPA	143.8	145.8	3.65E-03	1	176.6	2.29E-05	0.987
MIL-100 (NB)/ OPA	14.9	14.8	6.00E-03	0.998	16.7	4.88E-04	0.982

Table A.41: Kinetic fitting parameters for toluene adsorption onto MIL-100 adsorbents. P/P_0 = 0.005, T = 25˚C, pre-exposure RH = 20 %. Numbers in red represent fits that did not converge.

Material	Q_{exp} [mg/g]	Pseudo first order			Pseudo second order		
		Q_{max} [mg g^{-1}]	K [min^{-1}]	Adj. R^2	Q_{max} [mg g^{-1}]	K [mg g^{-1} min^{-1}]	Adj. R^2
MIL-100	199.6	224.3	9.84E-04	0.994	317.5	2.44E-06	0.988
MIL-100/ DPA	120.3	127	2.03E-03	0.989	165.4	1.13E-05	0.973
MIL-100/ OPA	170.5	178.1	1.76E-03	0.991	228.9	7.31E-06	0.975
MIL-100 (NB)	130.2	154.1	7.78E-04	0.998	228.1	2.49E-06	0.996
MIL-100 (NB)/ DPA	72.7	74.9	2.22E-03	0.997	95	2.30E-05	0.985

Table A.42: Kinetic fitting parameters for toluene adsorption onto MIL-100 adsorbents. P/P_0 = 0.005, T = 25˚C, pre-exposure RH = 40 %. Numbers in red represent fits that did not converge.

Material	Q_{exp} [mg/g]	Pseudo first order			Pseudo second order		
		Q_{max} [mg g^{-1}]	K [min^{-1}]	Adj. R^2	Q_{max} [mg g^{-1}]	K [mg g^{-1} min^{-1}]	Adj. R^2
MIL-100	63.1	62.2	3.14E-03	0.983	76.4	4.48E-05	0.995
MIL-100/ DPA	40.3	46.1	3.74E-03	0.999	67.2	4.19E-05	0.997
MIL-100/ OPA	40.7	45.9	3.88E-03	0.999	66.3	4.46E-05	0.996
MIL-100 (NB)	50.9	74.5	1.42E-03	0.999	120.4	7.55E-06	0.999
MIL-100 (NB)/ DPA	24.7	27.6	3.50E-03	0.996	38.7	7.28E-05	0.991

Table A.43: Kinetic fitting parameters for water adsorption onto MIL-100 adsorbents. RH = 0.5 %, T = 25˚C. Numbers in red represent fits that did not converge.

Material	Q_{exp} [mg/g]	Pseudo first order			Pseudo second order		
		Q_{max} [mg g^{-1}]	K [min^{-1}]	Adj. R^2	Q_{max} [mg g^{-1}]	K [mg g^{-1} min^{-1}]	Adj. R^2
MIL-100	66.4	66.9	1.90E-02	0.997	79.5	2.77E-04	0.977
MIL-100/ DPA	37.0	37.3	3.35E-02	0.998	45.5	8.02E-04	0.984
MIL-100/ OPA	31.0	28.7	2.04E-02	0.928	32.8	8.37E-04	0.984
MIL-100 (NB)	39.2	39.2	6.69E-03	0.997	50.6	1.27E-04	0.999
MIL-100 (NB)/ DPA	13.3	14.3	9.74E-03	0.999	19.4	4.27E-04	0.994
MIL-100 (NB)/ ODPA	9.8	10.0	5.61E-02	0.998	12.9	4.16E-03	0.994

Table A.44: Kinetic fitting parameters for water adsorption onto MIL-100 adsorbents. RH = 20 %, T = 25˚C. Numbers in red represent fits that did not converge.

Material	Q_{exp} [mg/g]	Pseudo first order			Pseudo second order		
		Q_{max} [mg g^{-1}]	K [min^{-1}]	Adj. R^2	Q_{max} [mg g^{-1}]	K [mg g^{-1} min^{-1}]	Adj. R^2
MIL-100	126	126.6	3.20E-02	0.999	147.2	2.70E-04	0.977
MIL-100/ DPA	73.6	74.1	3.32E-02	0.995	89.3	4.15E-04	0.976
MIL-100/ OPA	74.3	73.3	3.50E-02	0.993	78.0	7.63E-04	0.963
MIL-100 (NB)	93.9	94.2	1.12E-02	0.999	111.9	1.17E-04	0.983
MIL-100 (NB)/ DPA	35.7	35.2	2.31E-02	0.998	40.0	7.72E-04	0.979

Table A.45: Kinetic fitting parameters for water adsorption onto MIL-100 adsorbents. RH = 40 %, T = 25˚C. Numbers in red represent fits that did not converge.

Material	Q_{exp} [mg/g]	Pseudo first order			Pseudo second order		
		Q_{max} [mg g^{-1}]	K [min^{-1}]	Adj. R^2	Q_{max} [mg g^{-1}]	K [mg g^{-1} min^{-1}]	Adj. R^2
MIL-100	379.2	431.6	8.24E-03	0.995	606.5	1.09E-05	0.991
MIL-100/ DPA	320.7	319.9	7.09E-03	0.998	389.5	2.01E-05	0.995
MIL-100/ OPA	315.5	311.1	7.75E-03	0.997	371.5	2.43E-05	0.996
MIL-100 (NB)	257.3	253.1	3.26E-03	0.994	312.3	1.12E-05	0.999
MIL-100 (NB)/ DPA	114.2	108.7	6.96E-03	0.980	128.8	6.51E-05	0.999

Table A.46: Kinetic fitting parameters for water adsorption onto MIL-100 adsorbents. RH = 80 %, T = 25˚C. Numbers in red represent fits that did not converge.

Material	Q_{exp} [mg/g]	Pseudo first order			Pseudo second order		
		Q_{max} [mg g^{-1}]	K [min^{-1}]	Adj. R^2	Q_{max} [mg g^{-1}]	K [mg g^{-1} min^{-1}]	Adj. R^2
MIL-100	657.1	799.9	1.43E-02	0.998	1188.2	8.73E-06	0.997
MIL-100/ DPA	563.1	615.0	1.96E-02	0.994	831.9	2.02E-05	0.985
MIL-100/ OPA	540.5	585.8	1.47E-02	0.996	787.0	1.63E-05	0.988
MIL-100 (NB)	332.3	332.1	3.84E-03	0.990	428.2	8.66E-06	0.997
MIL-100 (NB)/ DPA	159.4	158.9	1.63E-02	0.997	200.5	8.17E-05	0.994

Table A.47: Summary of fitting parameters and adjusted R^2 values for toluene BTCs on industrial adsorbents, at the relative humidity specified in parentheses. Fitting carried out using the Bohart-Adams Logistic model. Gas flowrate = 60 mL/min. C_{in} = 10 ppmv, T = 25˚C.

System	a [a.u.]	b, k_{BA} [mg/mL]	Adj. R^2
GAC (0)	28.28	0.01023	0.998
GAC (40)	16.55	0.01136	0.995
GAC (80)	5.12	0.0126	0.997
A88Y (0)	12.21	0.00703	0.999
A88Y (40)	11.14	0.00792	0.998
A88Y (80)	10.28	0.00748	0.998
MS13X (0)	11.45	0.00555	0.999

Table A.48: Fitting parameters and adjusted R^2 values for toluene BTC of MS13X at 40 % RH. Fitting carried out using the Boltzmann-EMG model. Flowrate = 60 mL/min. C_{in} = 10 ppmv, T = 25˚C.

Material	k	A1	A2	D1	D2	D3	x1	x2	dx	Adj. R^2
MS13X (40)	0.875	0	1.13	0	23.7	24.1	28.6	49.4	0.8	0.994

Table A.49: Comparison of experimental and fitted values for useable capacity, total capacity, and useability of industrial adsorbents and toluene. Fitted values calculated by integrating BTCs generated using the Bohart-Adams Logistic or Boltzmann-EMG model. Gas flowrate = 60 mL/min. C_{in} = 10 ppmv, T = 25˚C.

Material	Experimental			Fitted		
	Useable capacity [mg/g]	Total capacity [mg/g]	Useability	Useable capacity [mg/g]	Total capacity [mg/g]	Useability
GAC (0)	93.8	105.9	0.886	94.6	105.7	0.895
GAC (40)	49.2	57.0	0.863	46.0	56.1	0.819
GAC (80)	7.5	11.2	0.664	6.4	15.4	0.417
A88Y (0)	52.3	66.8	0.783	50.0	66.3	0.755
A88Y (40)	42.5	54.5	0.78	39.4	53.9	0.731
A88Y (80)	40	52.7	0.759	37.0	52.2	0.709
MS13X (0)	59.9	79.5	0.753	58.5	79.2	0.738
MS13X (40) [c]	0.94	0.26 (0.86 [a])	N/A [b]	0.80	0.24 (0.82 [a])	N/A [b]

[a] Quantity of toluene displaced during multicomponent experiment

[b] Could not be determined due to significant rollover in BTC

[c] Fitting carried out using the Boltzmann-EMG model

Table A.50: Summary of fitting parameters and adjusted R^2 values for water BTCs on industrial adsorbents. Fitting carried out using the Bohart-Adams Logistic model. Gas flowrate = 60 mL/min. Humidity specified in parentheses, T = 25˚C.

System	a [a.u.]	b, k_{BA} [mg/mL]	Adj. R^2
GAC (40)	2.24	0.40828	0.966
GAC (80)	0.98	0.12365	0.869
A88Y (40)	13.07	5.38119	0.994
A88Y (80)	4.63	0.97053	0.948
MS13X (40)	17.58	0.73413	0.998

Table A.51: Comparison of experimental and fitted values for useable capacity, total capacity, and useability of industrial adsorbents and water. Fitted values calculated by integrating BTCs generated using the Bohart-Adams Logistic model. Gas flowrate = 60 mL/min. Humidity specified in parentheses, T = 25˚C.

Material	Experimental			Fitted		
	Useable capacity [mg/g]	Total capacity [mg/g]	Useability	Useable capacity [mg/g]	Total capacity [mg/g]	Useability
GAC (40)	11.0	68.5	0.160	0	52.3	0
GAC (80)	40.6	273.5	0.148	0	191.7	0
A88Y (40)	18.2	23.7	0.769	17.1	22.0	0.778
A88Y (80)	59.4	110.8	0.536	30.9	85.3	0.362
MS13X (40)	193.0	224.6	0.860	181.3	218.2	0.831

Table A.52: Summary of fitting parameters and adjusted R^2 values for toluene BTCs on ZIF adsorbents, at the relative humidity specified in parentheses. Fitting carried out using the Bohart-Adams Logistic model. Gas flowrate = 60 mL/min. C_{in} = 10 ppmv, T = 25˚C.

System	a [a.u.]	b, k_{BA} [mg/mL]	Adj. R^2
ZIF-8 (0)	4.92	0.00216	0.987
ZIF-8 (40)	5.02	0.00239	0.995
ZIF-8 (80)	5.02	0.00225	0.997
ZIF-8 (0) n-HEX [a]	12.55	0.00596	0.999 (1)
ZIF-8 (NB-1) (0)	4.99	0.00281	0.989
ZIF-8 (NB-1) (80)	4.32	0.00287	0.993
ZIF-67 (0)	5.44	0.00231	0.993
ZIF-67 (NB-1) (0)	4.95	0.00231	0.985
ZIF-67 (ML) (0)	4.72	0.00214	0.994
ZIF-67 (ML) (80)	4.5	0.0024	0.997

[a] Parameters for n-Hexane breakthrough

Table A.53: Comparison of experimental and fitted values for useable capacity, total capacity, and useability of ZIF adsorbents and toluene. Fitted values calculated by integrating BTCs generated using the Bohart-Adams Logistic model. Gas flowrate = 60 mL/min. C_{in} = 10 ppmv, T = 25˚C.

Material	Experimental			Fitted		
	Useable capacity [mg/g]	Total capacity [mg/g]	Useability	Useable capacity [mg/g]	Total capacity [mg/g]	Useability
ZIF-8 (0)	54.5	90.6	0.601	34.0	86.5	0.393
ZIF-8 (40)	47.1	82.3	0.572	32.8	80.4	0.409
ZIF-8 (80)	37.7	81.3	0.464	34.5	84.8	0.407
ZIF-8 (0) n-HEX [a]	59.4	74.5	0.797	59.3	74.8	0.792
ZIF-8 (NB-1) (0)	42.2	72.5	0.582	27.4	68.6	0.400
ZIF-8 (NB-1) (80)	28.3	60.4	0.468	17.9	57.3	0.313
ZIF-67 (0)	55.5	91.6	0.605	40.2	88.7	0.453
ZIF-67 (NB-1) (0)	50.9	84.8	0.601	32.6	82.1	0.396
ZIF-67 (ML) (0)	45.1	85.9	0.525	31.1	84.6	0.367
ZIF-67 (ML) (80)	33.2	73.0	0.454	24.3	72.0	0.338

[a] Values for n-Hexane breakthrough

Table A.54: Summary of fitting parameters and adjusted R^2 values for toluene BTCs on MIL-100. Fitting carried out using the Bohart-Adams Logistic model. Gas flowrate = 60 mL/min. Humidity specified in parentheses, T = 25˚C.

System	a [a.u.]	b, k_{BA} [mg/mL]	Adj. R^2
MIL-100 (0)	7.79	0.0037	0.996
MIL-100 (20)	7.19	0.00582	0.997

Table A.55: Summary of fitting parameters and adjusted R^2 values for toluene BTCs on MIL-100, at the relative humidity specified in parentheses. Fitting carried out using the Boltzmann-EMG model. Gas flowrate = 60 mL/min. C_{in} = 10 ppmv, T = 25˚C.

Material	k	A1	A2	D1	D2	D3	x1	x2	dx	Adj. R^2
MIL-100 (40)	0.530	0	1.89	0	248.9	381.7	186.7	653.9	26.8	0.986
MIL-100 (80)	0.314	-7.11	0.60	0.81	147.8	82.9	19.9	0	3.4	0.924

Table A.56: Comparison of experimental and fitted values for useable capacity, total capacity, and useability of MIL-100 and toluene. Fitted values calculated by integrating BTCs generated using the Bohart-Adams Logistic or Boltzmann-EMG models. Gas flowrate = 60 mL/min. C_{in} = 10 ppmv, T = 25˚C.

Material	Experimental			Fitted		
	Useable capacity [mg/g]	Total capacity [mg/g]	Useability	Useable capacity [mg/g]	Total capacity [mg/g]	Useability
MIL-100 (0)	59.6	81.6	0.730	53.5	86.1	0.621
MIL-100 (20)	34	47.9	0.709	29.5	50.2	0.588
MIL-100 (40) [c]	6.2	6.3 (14.1[b])	N/A [c]	4.1	6.9 (9.5[b])	N/A [c]
MIL-100 (80) [c]	0.4	0.6 (2.0[b])	N/A [c]	0.3	0.6 (1.6[b])	N/A [c]

[a] Quantity of toluene displaced during multicomponent experiment

[b] Could not be determined due to significant rollover in BTC

[c] Fitting carried out using the Boltzmann-EMG model

Table A.57: Summary of fitting parameters and adjusted R^2 values for water BTCs on MIL-100. Fitting carried out using the Bohart-Adams Logistic model. Gas flowrate = 60 mL/min. Humidity specified in parentheses, T = 25˚C.

System	a [a.u.]	b, k_{BA} [mg/mL]	Adj. R^2
MIL-100 (20)	5.16	0.2109	0.993
MIL-100 (40)	2.72	0.07243	0.946
MIL-100 (80)	2.63	0.07438	0.961

Table A.58: Summary of fitting parameters and adjusted R^2 values for water BTCs on MIL-100, at the relative humidity specified in parentheses. Fitting carried out using the Boltzmann-EMG equation (Equation 8.3). Gas flowrate = 60 mL/min. C_{in} = 10 ppmv, T = 25˚C.

Material	k	A1	A2	D1	D2	D3	x1	x2	dx	Adj. R^2
MIL-100 (40)	0.321	-1.99	0.89	0.72	17.6	-41.0	24.6	43.9	3.6	0.998
MIL-100 (80)	0.043	2.25	18.66	0.30	-8.5	17.0	53.0	5.1	9.8	0.999

Table A.59: Comparison of experimental and fitted values for useable capacity, total capacity, and useability of MIL-100 and water. Fitted values calculated by integrating BTCs generated using the Bohart-Adams Logistic or Boltzmann-EMG models. Gas flowrate = 60 mL/min. C_{in} = 10 ppmv, T = 25˚C.

Material	Experimental			Fitted		
	Useable capacity [mg/g]	Total capacity [mg/g]	Useability	Useable capacity [mg/g]	Total capacity [mg/g]	Useability
MIL-100 (20)	73.0	119.1	0.613	49.4	119.9	0.412
MIL-100 (40)- BAL	186.7	373.6	0.500	0 [a]	376.7	0
MIL-100 (40)- BE [b]	186.7	373.6	0.500	176.2	393.1	0.448
MIL-100 (80)- BAL	209.9	646.9	0.325	0 [a]	652.8	0
MIL-100 (80)- BE [b]	209.9	646.9	0.325	169.3	650.0	0.261

[a] Fitting resulted in initial concentration exceeding C_{out}/ C_{in} = 0.05.

[b] Fitting carried out using the Boltzmann-EMG model.